The Affect of Ash Chemistry and Deposits from Co-Firing Biomass and Coal in Power Plant Systems

By

Victoria Lay

A Doctoral Thesis

Submitted in partial fulfillment of the requirements

for the award of Doctor of Philosophy

of Loughborough University

30th October 2016

© by Victoria Lay 2016

Table of Contents

Table of Contents i

Abstract v

Acknowledgements vii

Table of Figures viii

Table of phases identified in samples presented in this thesis xvii

Thesis structure xix

1. Introduction 1

1.2 Aims and Objectives 2

2 Literature Review 3

2.1 Fuels 6

2.1.1 Fuel Pretreatment 12

2.2 Ash Formation 13

2.3 Deposition Formation Mechanisms 17

2.3.1 The affect of deposits on heat transfer 20

2.4 Deposit Composition 21

2.4.1 Zinc and Lead 22

2.4.2 Slagging 23

2.4.3 Fouling 24

2.5 Corrosion Mechanisms 25

2.5.1 Active Oxidation 25

2.5.2 Sulphidation 27

2.6 Materials 27

2.6.1 Coatings 30

2.7 Ash Utilisation/Disposal 32

2.8 Conclusions 32

3 Materials and Experimental 34

3.1 Data Supplied by E.On 34

3.1.1 As Received Fuel Analysis 34

3.1.2 Ash Analysis 35
3.2 The Combustion Rig 38
3.2.1.1 Corrosion Coupon Probes 40
3.2.1.2 Ash Quenching 43
3.2.1.3 Ceramic Probe Samples 44
3.3 Combustion Conditions 45
3.4 Furnace Procedure for Ashing 45
3.4.2 High Temperature Heat- Treatments of the ash 45
3.5 Materials Characterisation Techniques 46
3.5.1 X-Ray Diffraction (XRD) 46
3.5.1.1 Phase detection limitations 47
3.5.2 Scanning Electron Microscopy (SEM) 49
3.5.3 Energy Dispersive X-ray Spectroscopy (EDS) 49
3.5.4 Micro X-Ray Flourescence (XRF) 49
3.6 Synthesis of Akermanite 51
4 Laboratory Ashing Studies of Selected Biomass Fuels, Hemp, Coal and Eucalyptus and their blends 53
4.1. Hemp 56
4.1.1 Hemp Fuel 56
4.1.2 Hemp Ash 59
4.2 Eucalyptus 82
4.2.1 Eucalyptus Raw Fuel 82
4.2.2 Eucalyptus Ash 83
4.3 Coal 93
4.3.1 Coal Fuel 93
4.3.2 Coal Ash 94
4.4 Hemp and Coal Ash 100
4.5 Eucalyptus and Coal Ash 109
4.6 Conclusions 117

5. Characterisation of the fly ash components of: deposited, quenched, cyclone, and bottom ash samples from the co-firing of biomass and coal in a 1MWth combustion rig 119
5.1 Hemp and coal combustion rig samples 121
5.1.1 Hemp and coal deposit samples 121
5.1.2 Hemp and coal quenched samples 135
5.1.3 Hemp and coal cyclone ash samples 144
5.1.4 Hemp and coal bottom ash 149
5.2 Eucalyptus and Coal Combustion Rig Samples 153
5.2.1 Eucalyptus and Coal Deposit Samples 153
5.2.2 Eucalyptus and coal quenched samples 163
5.2.3 Eucalyptus and coal bottom ash samples 169
5.3 Eucalyptus Ash Combustion Rig Samples 175
5.3.1 Eucalyptus Deposit Samples 175
5.3.2 Eucalyptus Quenched Samples 189
5.3.3 Eucalyptus Cyclone ash sample 199
5.3.4 Eucalyptus Bottom ash samples 205
5.4 Conclusions 210
6. Analysis of deposit build up on boiler probes from a $1MW_{th}$ combustion rig 212
6.1 Introduction 212
6.2 Analysis of the hemp and coal boiler coupon surface deposits 214
6.2.1 Conclusions 230
6.3 Analysis of the eucalyptus and coal boiler coupon surface deposits 231
6.3.1 Conclusions 244
6.4 Analysis of the eucalyptus boiler coupon surface deposits 245
6.4.2 Conclusions 263
7. Discussion and Overview 265
7.1 Hemp and Coal Discussion 265
7.2 Eucalyptus and Coal Discussion 271
7.3 Eucalyptus Discussion 275

7.4 Fuel comparisons and conclusions 278
8. Overall Conclusions and Further Work 281
9. References 284
Appendix 1 – Calculating Patterns for High Temperature In-Situ Data 299
Appendix 1 – Publications 300

Abstract

Hemp, eucalyptus, coal, hemp and coal blended fuel, and eucalyptus and coal blended fuel were ashed and then heat treated for 1 hour at temperatures from 600-1100°C. X-ray diffraction analysis indicated reactions between the phases present after initial ashing of the fuel showed biomass-biomass, biomass-coal and coal-coal interactions. Two phase systems were identified as dominant in the biomass and coal ash blends, these were CaO-MgO-SiO_2 and CaO-Al_2O_3-SiO_2. The phases identified in these systems have also been identified in ceramics produced at high temperatures which have similar compositions to the ash matrix of the laboratory synthesised ash; this indicates that phase diagrams can be powerful tools in phase formation prediction. Structures identified as trichomes (phosphate-silicate structures with melting points above 1100°C) from the hemp fuel which had not decomposed were present in both the hemp ash and the hemp and coal ash. The composition determined by Energy-dispersive X-ray spectroscopy analysis of laboratory synthesised ashes was also in agreement with the phases identified through X-ray diffraction.

Hemp and coal, eucalyptus and coal, and eucalyptus ash samples (deposited, quenched, cyclone, and bottom ash) removed from a full scale $1MW_{th}$ combustion rig were analysed. Phase composition of the fly ash samples are similar to those identified in the analagous samples produced in the laboratory with several of the same phases present; confirming that laboratory testing is useful for the predictions of phases present on the industrial scale combustion rig. Particle morphology is one of the largest differences between the laboratory scale tests and combustion rig samples. The dominant particle shape of fly ash particles removed from the combustion rig is spherical. These particles of characteristic shape are often referred to as plerospheres and cenospheres and were first identified in coal fly ash. The presence of the spheres in the combustion rig when only biomass (eucalyptus) is present indicates the formation mechanism of the particles is similar to that of coal. There are similarities between the chemical composition of the spheres which are solely of biomass origin and co-fired; it is likely that phase composition of the sphere and not the fuel origin contributes to the formation of the spheres. Phases identified in the bottom ash are similar to those identified in the fly ash. High temperature phases such as (e.g. $Ca_9MgK(PO_4)_7$) ocur in the bottom ash suggesting that higher temperatures are reached in the bottom of the rig than in the flue gas.

Analysis of 15Mo3 alloy corrosion coupons with fly ash deposited onto the surface, alongside the interactions between gas phases and coupons, deposits and coupons, and gas phases and deposits, showed that some oxidation/reduction of the metal had occurred. The presence

of metal oxide flakes indicated corrosion. Oxidation of 15Mo3 alloy was observed in hemp and coal, and eucalyptus and coal combustion trials, likely due to the observed deposition of potassium chloride which has caused detachment of several scales. Between the metal-deposit interface, hematite whiskers were observed; magnetite octahedra were also present on the surface of scales. The phases present in the coupon deposit ash differ from those observed in the laboratory and fly ash due to the length of time spent in the high temperature environment. This indicates that some phases will not form until the deposits have built up and are in the furnace for an extended period of time. When the coupon samples were coated, fewer metal scales were observed meaning that the coatings are an affective method of corrosion reduction leading to an increased lifetime of boiler components.

The dominant particle morphology present in the combustion rig is the cenospheres and plerospheres. The phases formed can be broadly catergorised into CaO-MgO-SiO_2, CaO-Al_2O_3-SiO_2, and K_2O-Al_2O_3-SiO_2 phases. Potassium chloride is observed in the laboratory ash and combustion rig ash indicating, alongside the presence of metal oxide scales, that the fuel blends are likely to lead to corrosion during combustion.

Acknowledgements

The process of completing a PhD is not an easy one or everybody would be a doctor. I would like to thank Caroline Kirk for showing enthusiasm in my results, steering me through the minefield of learning that is Rietveld refinement, and for teaching me (moderately successfully) the use of commas. Rebecca Higginson for helping me to find the story in my results, and for helping with my microscopy (they're micrographs, not pictures). Simon Hogg for the feedback on my microscopy, and for helping me improve my metallurgy.

Many thanks to E.On Technology Ltd. (Uniper Technologies Limited) firstly for funding this project, and secondly allowing me to experience the combustion rig co-firing tests; an experience which has been invaluable. I would particularly like to thank Colin Davis for putting up with a large volume of emails asking for information, and his patience in explaining what I did not understand.

Funding from the EPSRC is invaluable to research in this country and I am very grateful to have had my research funded, allowing me to complete this project.

Pauline King, thank you for having immense patience with our lab, being able to make such amazing cakes, being a voice of reason and for being a diffractometer whisperer. The author acknowledges use of the facilities and the assistance of Keith Yendall in the Loughborough Materials Characterisation Centre (LMCC).

Without the happy atmosphere in the small office I would have gone slightly mad, and so thank you to my fellow students in the office for the discussion, cups of tea, lunches and pictures of cats! This sentiment is also extended to the chemistry PhD students who without the cider, the laughter, and the cooking, I would be malnourished. I would like to thank my friends for the adventures that were required, the idea bouncing, and their support through some of my trickier moments. Matt Isaacs, thank you for helping me stay with the process and for your unwavering belief that I could do this. Mum and Dad, thank you for encouraging me to be curious about the world, for supporting me in my decisions, and for always looking out for me.

To the rest of my friends and family, each and every one of you has helped me write this thesis and some of your comments have lead me to "OOH, that's why that works" moments, so thank you.

Table of Figures

Figure 2- 1: Routes of biomass utilisation adapted from[1] 3
Figure2- 2: UK Coal production sites and ports 6
Figure 2-3: Mechanisms involved in ash formation in biomass combustion[244] 13
Figure 2-4: Deposition mechanisms for ash deposits onto a metal surface during combustion[47] 17
Figure 2-5: Deposition mechanisms of (left) Diffusion and Thermophoresis and (right) Inertial Impaction onto a metal surface[46] 18
Figure 2-6: Inertial Impaction Deposition Mechanism.[55] Open particles are sticky, shaded particles are sticky on arrival followed by solidification in the deposit. The two types of cross hatched particles are smooth: fused in the furnace but solid upon arrival or jagged: highly erosive particles which were never fully fused 19
Figure 2-7b: Heat transfer mechanisms through deposits in the furnace region[245] 20
Figure 2-8: Ash Matrix Composition 21
Figure 2- 9: Active oxidation mechanisms under a) oxidising and b) reducing conditions adapted from reference[85] 26
Figure 3-1: A schematic diagram of the 0.8MWth combustion rig[246] a) ash collection hopper b)combustion probe coupons c) ceramic probes d) quenched ash e) the cyclone 38
Figure 3-2: A Schematic Diagram of the boiler and the ports used in the combustion run. .. 39
Figure 3-3: A comparison of XRF spectra a) without a filter and b) with a 250um Al filter to remove Rh 3/interference with Cl 50
Figure 4-1: XRD Pattern for the raw hemp fuel collected on the D2 diffractometer Cu Kα radiation (Qz- quartz, Ca - calcite, ... 57
Figure 4-2: Electronmicrograph of raw hemp fuel showing a clear organic matrix i.e. the fibrous nature, with trichomes, large silicate structures attached 58
Figure 4-3: Au coated EDS spectrum of the trichomes in the raw hemp fuel 58
Figure 4-4: Electronmicrograph of crystals present in the raw hemp fuel with EDS spectrum showing the composition 59
Figure 4-5: Patterns of hemp ash showing phases formed at high temperature, data collected on I-11 (λ 0.82675) beamline PXRD data is truncated to the range 0.2-0.5 1/D for clarity ... 61
Figure 4- 6: Variation in phases in the hemp samples vs weight percent. Laboratory synthesised hemp ash after heat treatment at 600°C-1100°C 64
Figure 4-7: (a) The refinement parameters for rietveld refinements of 600°C heat treated hemp ash. (b) A table presenting the results and errors for the wt% of the phases present in the refinement (c) Experimental (blue), calculated (red) and difference (grey) plots for rietveld refinements of 600°C heat treated hemp ash. 65

Figure 4-8: (a) The refinement parameters for rietveld refinements of 700°C heat treated hemp ash. (b) A table presenting the results and errors for the wt% of the phases present in the refinement (c) Experimental (blue), calculated (red) and difference (grey) plots for rietveld refinements of 700°C heat treated hemp ash. 66
Figure 4-9: (a) The refinement parameters for rietveld refinements of 800°C heat treated hemp ash. (b) A table presenting the results and errors for the wt% of the phases present in the refinement (c) Experimental (blue), calculated (red) and difference (grey) plots for rietveld refinements of 800°C heat treated hemp ash. 67
Figure 4-10: (a) The refinement parameters for rietveld refinements of 900°C heat treated hemp ash. (b) A table presenting the results and errors for the wt% of the phases present in the refinement (c) Experimental (blue), calculated (red) and difference (grey) plots for rietveld refinements of 900°C heat treated hemp ash. 68
Figure 4-11: (a) The refinement parameters for rietveld refinements of 1000°C heat treated hemp ash. (b) A table presenting the results and errors for the wt% of the phases present in the refinement (c) Experimental (blue), calculated (red) and difference (grey) plots for rietveld refinements of 1000°C heat treated hemp ash. 69
Figure 4-12: (a) The refinement parameters for rietveld refinements of 1100°C heat treated hemp ash. (b) A table presenting the results and errors for the wt% of the phases present in the refinement (c) Experimental (blue), calculated (red) and difference (grey) plots for rietveld refinements of 1100°C heat treated hemp ash. 70
Figure 4-13: PXRD patterns of the starting reagents diopside and calcite and the reactions at three temperatures to simulate reaction temperatures in the laboratory ash. Di- diopside ($CaMgSi_2O_6$) Ak - akermanite ($Ca_2MgSi_2O_6$) La- larnite (Ca_2SiO_4) Li - lime (CaO) Qz – quartz (SiO_2)patterns were collected on the D8 Discover using Co $K\alpha_1$ radiation 72
Figure 4-14: Calculated phase diagram of the $CaSiO_3$ - $MgSiO_3$ metasilicates from Jung et al.[164] 73
Figure 4- 15: In-situ HTPXRD patterns of hemp ash showing phase changes undergone in the ash Cu $K\alpha_1$ radiation (Section 2.4.1)..... 76
Figure 4-16: Electronmicrographs of hemp ashed at a) 600°C for 1 hour b) 700°C for 1 hour c) 800°C for 1 hour d) 900°C for 1 hour e)1000°C for 1 hour f) 1100°C for 1 hour..... 77
Figure 4-17: SEM Electronmicrograph of silicate thorn break site at 900°C and EDS analysis of the site 78
Figure 4-18: EDS Maps of hemp ashed for 1 hour at 600°C 79
Figure 4-19: EDS Maps of hemp ashed for 1 hour at 900°C 80
Figure 4-20: EDS Maps of hemp ashed for 1 hour at 1100°C 81
Figure 4-21: XRD Pattern of Eucalyptus Fuel showing large amorphous cellulose peaks collected on the D2 diffractometer with Cu Kα radiation 82

Figure 4-22: Electronmicrograph of Eucalyptus fuel 83
Figure 4-23: P-XRD patterns of laboratory ashed eucalyptus at temperatures 600-1100°C collected on beamline I-11 range (λ 0.826215) presented is 5-29°2θ to present clearer data 86
Figure 4-24: Calculated liquidus surface of the CaO-MgO-SiO2 system at 1 bar pressure. T in °C Crist-Cristobalite Trid, Tridymite, woll, wollastonite,p-woll – pseudo wollastonite, diop-diopside, pig – pigeonite, aker – akermanite, merw- merwinite, mont – monticellite, fors - forsterite 87
Figure 4-25: Electronmicrographs of eucalyptus ashed at a) 600°C for 1 hour b) 700°C for 1 hour c) 800°C for 1 hour d) 900°C for 1 hour e)1000°C for 1 hour f) 1100°C for 1 hour..... 88
Figure 4-26: Ca and O rich crystals present in the eucalyptus fuel from 800°C 90
Figure 4-27: EDS Maps of Eucalyptus ash heat treated at 900C for 1 hour 91
Figure 4-28: EDS maps of eucalyptus ash heat treated at 1000C for 1 hour 92
Figure 4-29: PXRD Pattern for Pulverised Kuzbass Coal Fuel Qz Quartz, Ko kaolinite, Gy gypsum, Ro rozenite, Do dolomite, Il illite collected on the D8 advance diffractometer Cu $K\alpha_1$ radiation 93
Figure 4- 30: Electronmicrograph of pulverised coal showing irregularity of shape 94
Figure 4-31: PXRD patterns of heat treated coal ash showing phase changes with temperature increase, data collected on the I-11 (λ 0.82675) beamline and truncated to 5-30 °2θ for clarity 95
Figure 4-32: EDS map of coal ash at 600°C showing the presence of illite 97
Figure 4-33: EDS Maps of coal ash at 800°C showing clear regions of correlation between Si,O,Al and K as well as Ca, S and O 98
Figure 4-34: EDS analysis of coal ash heat treated at 1000°C for one hour showing CaSO4 and mullite 99
Figure 4-35: PXRD patterns of high temperature heat treated hemp and coal ash showing ash composition and phases present at different temperatures, data 800-1100°C collected on the I-11 beamline (λ 0.82675) 600-700°C collected on the D2 and truncated to 0.1-0.6 1/D. .. 102
Figure 4-36: The $CaO\text{-}SiO_2\text{-}Al_2O_3$ phase diagram 103
Figure 4-37: Electronmicrographs of hemp and coal co-ashing at a)600°C b)700°C c)800°C d)900°C e)1000°C f)1100°C 106
Figure 4-38: EDS Maps of Hemp and Coal at 600°C showing trichome composition and K,Al,Si and O association 107
Figure 4-39: EDS maps of hemp and coal ash after 1000°C high temperature heat treatment for 1 hour 108
Figure 4-40: PXRD patterns of eucalyptus and coal ash from 800-1100°C showing fuel interactions and phases present after high temperature ashes patterns 800-1100C collected

on the I-11 synchrotron beam (λ 0.826215) 1/D for comparison with 600-700 C range, collected on the D2 and truncated to 0.1-0.6. 111
Figure 4-41: Electronmicrographs of the eucalyptus and coal co-ash at a)600°C b)700°C c) 800°C d)900°C e)1000°C and f) 1100°C 112
Figure 4-42: EDS analysis of crystal presented in Figure 4-41f..... 113
Figure 4-43: EDS Maps of crystals present after 800°C heat treatment of eucalyptus and coal ash for 1 hour..... 113
Figure 4-44: EDS Maps of eucalyptus and coal ash heated at 900C for 1 hour..... 115
Figure 4-45: EDS Maps of eucalyptus and coal ash heated at 1100C for 1 hour..... 116
Figure 5-1: Photograph of a hemp deposit onto ceramic probe showing the elliptical shape of the ash. 119
Figure 5-2: Gas conditions at combustion rig exit during the co-combustion of hemp and Kuzbass coal. SO_2, CO and NO should be read from the left concentration (ppm) axis and CO_2 and O_2 from the right concentration (%) axis. Red indicates a deposit, blue indicates a quenched sample. The numbers denote the sample code (Section 3)..... 121
Figure 5-3: PXRD data of deposit samples removed from the combustion rig during co-firing hemp and Kuzbass coal trials. 1/D presented as H7279 D2 data Cu Kα radiation) is presented alongside synchrotron data (λ 0.826215) for H7228, H7274 and H7223..... 124
Figure 5-4: SEM electronmicrographs of hemp and coal deposits a,b) H722-3 c,d) H727-4 e,f) H722-8 g,h) H727-9 showing the different morphologies present in the deposits. 127
Figure 5-5: a) a cenosphere present in H722-8 b) the inside surface of the cenosphere present in H722-8 128
Figure 5-6: A micrograph and EDS maps of H722-3 showing both K_2SO_4 and $CaSO_4$ as well as a trichome present. 129
Figure 5-7: Electron micrograph and EDS Maps of H727-4 showing elemental association indicating the silicate akermanite/diopside and sanidine/microcline also identified in PXRD data..... 130
Figure 5-8: An electronmicrograph and EDS maps of H722-8 showing elemental association similar to the phases identified in the PXRD data..... 131
Figure 5-9: An electronmicrograph and EDS maps of H727-9 illustrating elemental association of Fe and O, indicating hematite/magnetite. 132
Figure 5-10: PXRD patterns collected on the I-11 beamline (λ 0.826215) and analysis of hemp and coal quenched samples 1/D presented to allow easy comparison with the deposit samples..... 137
Figure 5-11: SEM electronmicrographs of the quenched samples in the hemp and coal co-firing a&b) H722-2 c&d) H740-5 e&f) H740-6 g&h) H740-10 illustrating the different morphologies present in the samples. 139

Figure 5-12: an electronmicrograph and EDS Maps of sample H727-2 showing hydroxyapatite and K,Al – silicates present in the quenched sample. 140
Figure 5-13: An electronmicrograph and EDS Maps of sample H740-10 showing a phosphosphere and association between K,Al , Si and O 141
Figure 5-14: PXRD analysis of the hemp and coal cyclone ash collected on the d8 advance diffractometer (Cu Kα1 radiation) *denotes the LaB_6 internal standard 145
Figure 5-15: An electron micrograph of hemp cyclone ash showing a trichome, several spheres, a char particle and a large flake 146
Figure 5-16: Backscattered electronmicrograph of cyclone ash and EDS maps showing the presence of Ca-phosphates, KCl, K,Al-silicates, a trichome and CaSO4 148
Figure 5- 17: A photograph of a large block of bottom ash from the hemp and coal combustion trial 149
Figure 5-18: PXRD diffraction analysis for the hemp and coal bottom ash 150
Figure 5-19: SEM analysis of hemp and coal hopper ash 151
Figure 5-20: An Electronmicrograph and EDS maps of hopper ash encapsulated in resin. Distinct SiO_2 and CaO regions are visible..... 152
Figure 5-21: Gas conditions at combustion rig exit during the co-combustion of eucalyptus and Kuzbass coal. Red indicates a deposit, blue indicates a quenched sample. The numbers denote the sample code (Section 3) 153
Figure 5-22: PXRD eucalyptus and coal deposits synchrotron I-11 beamline data (λ0.826215) is presented, the range is truncated to 0.2-0.5 for clarity..... 156
Figure 5-23: SEM electronmicrographs of eucalyptus and coal ash a) EC727-1 b) EC728-5 c) EC722-6 d) EC 722-8 158
Figure 5-24: EDS maps of EC 727-8 showing areas of sintering in the deposit and their composition..... 159
Figure 5-25: EDS maps of EC 722-6 showing regions of sphere agglomeration and reactions between them 160
Figure 5-26: SEM Electron micrographs of EC740-4 a) large and small spheres present b) a cuboid shaped particle with smaller spherical particles 163
Figure 4-27: PXRD analysis of sample EC740-4 collected on the I-11 beamline (λ 0.826215) 164
Figure 5-28: EDS maps of sample EC740-4 showing distribution of K, Al, Si and O throughout the sample 165
Figure 5-29: EDS maps of sample EC740-4 showing K,Al silicates 166
Figure 5-30: Eucalyptus and coal bottom ash showing a porous texture and regions of slag flow melts as well as the loose bottom ash..... 169

Figure 5-31: PXRD analysis of the glassy blocks and loose bottom ash present in the eucalyptus and coal bottom ash collected on the D2 diffractometer (Cu Kα radiation)..... 170
Figure 5-32a) Ball milled eucalyptus and coal bottom ash electron micrograph showing the glassy texture of the bottom ash b) An electron micrograph of the eucalyptus and coal loose bottom ash. 171
Figure 5-33: EDS analysis and an electromicrograph of eucalyptus and coal blocky bottom ash. Showing areas of leucite and Ca-phosphate. There is also association of Ca,Mg,K,P and O suggesting the presence of the phase identified using PXRD 173
Figure 5-34: EDS maps and an electronmicrograph of the loose bottom ash from eucalyptus and coal combustion trial showing Ca,Mg phosphate. There is also C present in the particles suggesting that they are unburnt char or the carbonates also identified in the sample. 174
Figure 5-35: Gas conditions of eucalyptus combustion test. SO2, CO and NO left axis. CO2, O2 right axis. Purple boxes indicate deposit and quench samples were collected simultaneously 175
Figure 5-36: PXRD data of the eucalyptus deposit samples collected during a combustion trial. Data collected on the I-11 beamline (λ 0.826215) 178
Figure 5-37: Electronmicrographs of the deposit samples from a eucalyptus combustion trial a) E 722-1 b) E 722- 4 c) E 722- 6 d) E 722- 7 e) E 722-9 f) E 722-12 g) E 722-13..... 181
Figure 5-38: SEM Electronmicrograph showing sintering in the deposit E722-12..... 182
Figure 5-39: a) the inside of a deposit from E722-12 b) the inside of a deposit from 722-13 highlighted in Figure 3g..... 182
Figure 5-40: EDS maps of sample E722-6 183
Figure 5-41: EDS maps of sample E722-7 184
Figure 5-42: EDS Maps of sample E722-12 185
Figure 5-43: PXRD data of the eucalyptus quenched samples collected during a combustion trial patterns were collected on the I-11 beamline (λ 0.826215) 191
Figure 5-44: Composite of SEM electronmicrographs from the quenched samples a)E740-2 b)E740-3 c)E740-5 d)E740-8 e)E740-10 f)E740-11 g)E740-14 193
Figure 5-45: EDS maps of a char particle identified in sample E470-5..... 194
Figure 5-46: EDS maps showing association of KAlSiO and SiO_2 cuboids present in sample E740-14 195
Figure 5-47: EDS maps showing a variety of phases and particle morphologies of sample E740-10 196
Figure 5-48: Eucalyptus cyclone ash data collected on the D2 diffractometer Cu Kα radiation 200
Figure 5-49: SEM electronmicrographs of eucalyptus combustion trial cyclone ash showing spherical particles with sintering and char particles..... 201

Figure 5-50: An electronmicrograph and EDS maps of the eucalyptus cyclone ash showing char particles, silicates, KCl and CaSO4 also identified using PXRD analysis 203
Figure 5-51: An electronmicrograph and EDS maps of the eucalyptus cyclone ash showing KCl, carbonates and phosphates. The silicate speeres present in the cracks have not expanded to the same size as those present in the looser ash. 204
Figure 5-52: Eucalyptus combustion trial bottom ash showing large pores, slag flow melt and loose bottom ash 205
Figure 5-53: PXRD analysis of eucalyptus glassy blocks and loose bottom ash pattern collected on the d2 diffractometer (Cu Kα radiation) 206
Figure 5- 54: Electronmicrographs of a) Eucalyptus bottom ash blocks showing a close glassy texture and b) Eucalyptus loose bottom ash showing porous regions and several different particle morphologies 207
Figure 5-55: An electronmicrograph and EDS maps of eucalyptus glassy block bottom ash showing mullite, Fe-Cr spinel and C,aMg Phosphate 208
Figure 6-1: Fe-O phase diagram showing magnetite and hematite as the most common Fe-O phases below 500°C 212
Figure 6-2: Gas conditions sampled every two hours from 15Mo3 probes in the hemp and coal combustion test. a) Hemp A b) Hemp B c) Hemp C d) Hemp D 215
Figure 6-3: Gas conditions sampled every two hours from 15Mo3 probes in the hemp and coal combustion test. a)Hemp E b) Hemp F c) Hemp G d) Hemp H 216
Figure 6-4: Positions of the 15Mo3 hemp and coal combustion probes in the hemp and coal combustion run a) Hemp A b) Hep B c) Hemp C d) Hemp D e) Hemp E f) Hemp F g) Hemp G, h) Hemp H 217
Figure 6-5: PXRD Data analysis of hemp probe deposits, data collected on the D2 diffractometer (Cu Kα radiation) 221
Figure 6-6: SEM electronmicrographs of the 15Mo3 coupon deposits illustrating different morphologies present a) Hemp A b) Hemp B c) Hemp C d) Hemp D e) Hemp E f) Hemp F g) Hemp G h) Hemp H 223
Figure 6-7: An electronmicrograph and EDS maps of a KCl cube present in Hemp B 224
Figure 6-8: An electronmicrograph and EDS maps of showing the needles to be K_2SO4.. 225
Figure 6-9: An electronmicrograph and EDS maps showing K_2SO4 deposition in both needle and droplet morphology 226
Figure 6-10: An electronmicrograph and EDS Maps of K_2SO4 and KCl on a metal oxide flake 227
Figure 6-11: SEM electronmicrograph and EDS maps showing trichomes present in Hemp F 228

Figure 6-12: An electronmicrograph and EDS maps showing pockets of calcium phosphate in a silicate melt. 229
Figure 6-13: Coupon O2 and CO2 gas conditions for the eucalyptus and coal combustion trial a) EUCCO A b) EUCCO B c) EUCCO C d) EUCCO D..... 233
Figure 6-14: Coupon O2 and CO2 gas conditions for the eucalyptus and coal combustion trial a) EUCCO E b) EUCCO F c) EUCCO G d) EUCCO H 234
Figure 6-15: Port positions for probes containing the coupon samples a) EUCCO A b)EUCCO B c)EUCCO C d)EUCCO D e) EUCCO E F) EUCCO F g) EUCCO G h) EUCCO H 235
Figure 6-16: PXRD patterns for EUCCO coupon deposits data collected on the D2 diffractometer (Cu Kα radiation)..... 236
Figure 6-17: SEM micrograph and EDS spectrum of KCl deposition onto the surface of an oxide scale under reducing conditions in sample EUCCO B 238
Figure 6-18:Electronmicrograph and EDS maps of KCl and K_2SO4 deposition onto metal oxide flakes in sample EUCCO G 238
Figure 6-19: SEM electronmicrograph and linescan spectra of K_2SO_4 deposit onto an iron oxide scale 239
Figure 6-20: Magnetite Octahedral Crystals visible under both oxidising and reducing conditions, SEM-EDS analysis of the octahedral regions..... 240
Figure 6-21: Hematite whiskers present under an oxidising atmosphere 240
Figure 6-22: Electronmicrograph of EUCCO E showing a metal oxide with a sintered deposit 241
Figure 6-23: SEM electronmicrograph and EDS maps from sample EUCCO A showing akermanite/gehlenite and leucite deposition alongside unburnt C deposition 242
Figure 6-24: An electronmicrograph and EDS maps of EUCCO D showing silicates present as well as Ni joint grease..... 243
Figure 6-25: Probe positions for the eucalyptus combustion run probes a) EUC A b) EUC B c) EUC C d) EUC D e) EUC E f) EUC F g) EUC G h) EUC H i) EUC I j) EUC J k) EUC K 247
Figure 6-26: Gas conditions sampled every two hours from 15Mo3 probes in the eucalyptus combustion test . a) EUC A b) EUC B c) EUC C d) EUC D..... 248
Figure 6-27: Gas conditions sampled every two hours from 15Mo3 probes in the eucalyptus combustion test . a) EUC E b) EUC F c) EUC G d) EUC H..... 249
Figure 6-28: Gas conditions sampled every two hours from 15Mo3 probes in the eucalyptus combustion test . a) EUC I b) EUC J c) EUC K 250
Figure 6-29: PXRD data for EUC A-E collected on the D2 diffractometer (Cu Kα radiation) 252
Figure 6-30: PXRD data and analysis for EUC F-K collected on the D2 diffractometer (Cu Kα radiation)..... 253

Figure 6-31: SEM electronmicrographs showing different sample morphologies present in the eucalyptus coupon deposits a) EUC A b) EUC B c) EUC C d) EUC D e) EUC E f) EUC F g) EUC G h) EUC H i) EUC I j) EUC J k) EUC K 256
Figure 6-32: Glassy slag flow removed from EUC E 257
Figure 6-33: An electronmicrograph and EDS maps of a porous char particle from EUC J 258
Figure 6-34: SEM electronmicrograph and EDS maps of spheres present in EUC C showing a variety of compositions between spheres and in individual spheres 259
Figure 6-35: SEM Electronmicrograph and EDS maps of a melt incorporating Ca-Phosphate spheres from EUC D 260
Figure 6-36: SEM micrograph and EDS maps showing an Fe scale with deposit build up from sample EUC 261
Figure 6-37: SEM Electronmicrograph and EDS maps of a corrosion scale from EUC H showing regions of Cr enrichment and K_2SO_4 deposition 262
Figure 6-38: An electron micrograph and EDS maps of Fe, Ti and O deposit in sample EUC K 263

Table of phases identified in samples presented in this thesis

Phase	Composition	ICDD CARD
Kaolinite	$Al_2(Si_2O_5)(OH)_4$	14-164
Mullite	$Al_{2.35}Si_{0.64}O_{4.82}$	88-2049
Aluminium Oxide	Al_2O_3	52-803
Corundum	Al_2O_3	10-173
Augite	$Ca(Mg_{0.74}Fe_{0.26})Si_2O_6$	74-201
Portlandite	$Ca(OH)_2$	44-1481
Tremolite	$Ca_2(Mg,Fe)_5Si_8O_{22}(OH)_2$	44-1402
Akermanite-Gehlenite	$Ca(Mg_{0.5}Al_{0.5})(Si_{1.5}Al_{0.5})O_7$	79-2423
Gehlenite	$Ca_2Al_2SiO_7$	35-755
Akermanite	$Ca_2MgSi_2O_7$	35-592
Larnite	Ca_2SiO_4	33-302
Calcium Phosphate	$Ca_3(PO_4)_2$	29-539
Grossular	$Ca_3Al_2(SiO_4)_3$	39-368
Merwinite	$Ca_3Mg(SiO_4)_2$	74-382
Xonotlite	$Ca_6Si_6O_{16}(OH)_2$	23-125
Hydroxyapatite	$Ca_{10}(PO_4)_6(OH)_2$	9-432
Potassium Calcium Magnesium Phosphate	$Ca_9MgK(PO_4)_7$	45-137
Anorthite	$CaAl_2Si_2O_8$	70-287
Calcium Oxalate	CaC_2O_4	20-231
Calcite	$CaCO_3$	5-586
Dolomite	$CaMg(CO_3)_2$	36-426
Diopside	$CaMgSi_2O_6$	78-1390
Lime	CaO	37-1497
Wollastonite	$CaSiO_3$	43-1460
Anhydrite	$CaSO_4$	37-1496
Gypsum	$CaSO_4.2\ H_2O$	21-816

Chromium Oxide	Cr_2O_3	84-314
Hematite	Fe_2O_3	33-664
Iron Silicate	Fe_2SiO_4	52-1141
Magnetite	Fe_3O_4	19-621
Maghemite	$y\text{-}Fe_2O_3$	39-1346
Rozenite	$FeSO_4.4\ H_2O$	19-632
Illite	$KAl_2(Si_3Al)O_{10}(OH)_2$	43-685
Fairchildite	$K_2Ca(CO_3)_2$	21-1287
Arcanite	K_2SO_4	5-613
Leucite	$KAlSi_2O_6$	38-1423
Microcline	$KAlSi_3O_8$	19-926
Orthoclase	$KAlSi_3O_8$	31-966
Sanidine	$KAlSi_3O_8$	70-3751
Kalsilite	$KAlSiO_4$	11-579
Sylvite	KCl	41-1476
Potassium Iron Oxide	$KFe_{11}O_{17}$	87-1546
Magnesium Iron Oxide	$(MgO)_{0.77(}FeO)_{0.23}$	77-2366
Forsterite	Mg_2SiO_4	34-189
Monticellite	$MgCaSiO_4$	35-590
Periclase	MgO	45-946
Albite	$NaAlSi_3O_8$	9-466
Sodium-Melilite	$NaCaAlSiO_7$	71-2066
Natrite	$NaCO_3$	76-628
Nickel Oxide	NiO	44-1159
Quartz	SiO_2	46-1045
Tridymite	SiO_2	71-197
Cristobalite	SiO_2	39-1425

Thesis structure

Outlined are summaries of each chapter in this thesis.

Literature review

An overview of the current status of biomass combustion, and co-firing, will be outlined. Contradictions and conclusions from the literature will be highlighted.

Materials and Experimental

Details of the combustion rig, sample collection, synthesis, and characterisation techniques are presented.

Laboratory Ashing Studies of Selected Biomass Fuels

An overview of hemp, coal, and eucalyptus fuels, alongside hemp and coal, and eucalyptus and coal blends, that have been ashed in the laboratory is presented. Discussion about phases that form under certain conditions, and those that are likely to form, are given in context of previous work as given in the literature with the phases that are formed having the formation pathways highlighted.

Characterisation of deposit, quench, cyclone and bottom ash samples from the co-firing of biomass and coal in a 1MWth combustion rig

Analysis of the deposit and quenched samples collected during large scale combustion trials of the hemp and coal, eucalyptus and coal blends, and eucalyptus fuels is conducted. A comparison to the phases that formed during the laboratory study is given, and any differences between the samples are highlighted. Cyclone ash and bottom ash from the combustion run are analysed and compared to other samples present from the combustion run, to analyse the origin of the phases (e.g. flue gas formation, deposit formation). An analysis of the phases present, how they formed and how they may affect corrosion are given.

Analysis of the deposit build up on boiler probes of the alloy 15Mo3 from a 1MWth combustion rig

Deposits that built up on the surface of corrosion coupons are analysed, corrosion products and their affect on metal scale formation and ash deposition are highlighted. Phases that are

present in deposits, and those also present in the laboratory produced ash are also compared. Any differences between phases are investigated to highlight the differences between combustion regions.

Discussion

In the discussion chapter an analysis of each fuel blend, the phases formed in each sample region of the combustion rig that was analysed and a comparison to the phases identified in laboratory ashing are given, developing a discussion on sample differences.

1. Introduction

The depletion of fossil fuel reserves, coupled with a drive to reduce carbon dioxide emissions, has led to an increased interest in sustainable energy generation.[1] Alongside solar and wind energy, the combustion of biomass is under investigation as a future energy source.[2] The burning of biomass releases CO_2 into the atmosphere. However when the next crop cycle is produced the CO_2 released during combustion is captured creating a carbon neutral cycle.[1] In comparison, the CO_2 released during energy production using fossil fuels cannot be captured in the same way, as it is carbon that has been trapped for millions of years and therefore is being reintroduced into the cycle, giving an increase in free carbon.[1]

The combustion of biomass has been investigated in Denmark and Sweden, particularly using straw husks in power plants that were previously dedicated to coal.[3] These studies encountered problems with corrosion and deposit build up, which led to a reduction in efficiency as well as an increase in plant down time due to component failure. The co-firing of biomass and coal has been shown to decrease some of these issues. Therefore it is important that fuel suitability is investigated prior to use in full scale combustion. Assessment of fuels prior to large scale combustion is presented in Chapter 4.

A reduction in the build up of ash deposits in a combustion environment is a further area of study. The build up of deposits on boiler tubes and superheater regions of power plants leads to a drop in efficiency as heat transfer is retarded. Identification of phases likely to create tenacious deposits which can't be removed, or are so large they will cause damage to components below them in the power station, is an area that needs to be studied. The build up of deposits and analysis of the fly ash removed from a large scale combustion rig are presented in Chapter 5.

Previous investigation of biomass and biomass / coal combustion has identified potassium chloride (KCl) as a phase that increases corrosion. KCl deposits onto cool (in this instance meaning below gas temperature) surfaces in the combustion environment, it then reacts to form metal chlorides which, if left unchecked, can lead to rapid wastage of boiler components. Analysis of scale and deposits onto coupons of the high ferritic steel alloy 15Mo3 (composition in Table 3-4), with and without coatings, are analysed in Chapter 6 to assess the corrosion potential of the fuels investigated in this study.

The aims of this project are to profile ash from the fuels used for the co-firing of hemp and coal, eucalyptus and coal, and eucalyptus. This profiling will be used alongside samples

collected from large scale combustion trials of the fuel blends including deposited fly ash, cyclone ash, corrosion coupon scales and ash deposits, and bottom ash.

The analysis of the fuels and combustion rig samples is a challenge due to the large range of elements present; this in turn leads to a greater variety of phases that can form. The samples all contain multiple phases, many of which have similar compositions, which means that identification of the phases present using PXRD and SEM-EDS will be challenging. This is due to peak overlap and also the penetration depth of the X-rays into the sample during EDS analysis. These techniques only use a small quantity of ash for analysis and therefore, multiple samples have been analysed to try and ensure a more representative analysis of the bulk samples.

Ash samples collected from the combustion rig are from a variety of environments due to fluctuation of gas conditions caused by the fuel combustion and also locally to the samples as phases form and decompose.

1.2 Aims and Objectives

The aims of this project are to profile three fuels: hemp, Kuzbass region coal, and eucalyptus, as well as the blends hemp and coal, and eucalyptus and coal, in a laboratory setting; this will give key information into the phases formed and the interaction of the ashes at high temperature.

These ashes will then be compared with samples collected from a $1MW_{th}$ combustion rig (deposits, quenched ash, cyclone ash, corrosion coupon scale, and bottom ash).

Conclusions about the affect of ash composition and particle morphology, and the affect on corrosion and deposit build up, will be drawn.

2 Literature Review

Biomass - organic matter derived from plants or animals that is available on a renewable basis[4] is considered to be a carbon neutral fuel as CO_2, released on combustion, is then recaptured during the growth of the next crop cycle.[5] One notable exception to this statement are the emissions from the pre-treatment of biomass.[1] Fossil fuels, coal, and gas, have been at the forefront of energy generation for a long time. However, growing concerns about the long term affects of greenhouse gases (CO_2, NO_x, SO_x, CH_4) on the environment have led to increased research into alternative forms of energy generation.

Along with solutions such as wind turbines, solar power, and fuel cells, bioenergy has been proposed as a way of reducing carbon emissions. Bioenergy, the energy derived from biomass either directly or indirectly, is currently considered by the International Energy Agency (IEA) to be the largest renewable energy source today. It is thought bioenergy supplies 10% of the global primary energy supply. This statistic includes the use of wood for both heat and cooking in developing countries; Figure 2- 1 illustrates the routes through which biomass is currently utilised. The reduction of greenhouse gas emissions is of interest worldwide, with the Kyoto

Figure 2- 1: Routes of biomass utilisation adapted from[1]

protocol setting key targets for the reduction of CO_2. The United Kingdom Climate Change Act 2008 set a target of 2050 for the reduction of emissions to a level of at least 80% lower than that of the 1990 baseline.[6] The co-firing of biomass as well as the sole firing of biomass has been highlighted as a method of interest.

Co-firing, the simultaneous combustion of two (or more) different fuels for energy generation, in this instance refers to the burning of biomass and coal simultaneously.[5] Coal has been widely used in energy generation around the world whereas biomass, until recently, has primarily been used for smaller domestic scale energy generation. In the UK co-firing experienced a rapid period of growth from zero in 2002 and then doubling each year until 2005. Since 2005, usage has declined due to a shift in trend towards dedicated biomass, with co-firing being responsible for only 0.5% of the bioenergy generation in 2013.[7] Table 2- 1 illustrates the current status of biomass combustion in the UK. There are multiple powerstations that have been converted from energy generation solely through the use of fossil fuels to biomass/ co-firing powerstations. The IEA Biomass 32 project co-firing database contains 243 co-firing installations, with 183 of them being in Europe ranging from trial to commercial application.

Table 2- 1: UK Biomass and Co-firing Powerstations

Energy Company	Powerstation	Fuel
Drax Power Ltd.	Drax	Coal/biomass
E.On UK	Ironbridge	Biomass
	Steven's Croft	Biomass
EPR Ely Limited	Elean	Straw/gas
EPR Glanford Ltd	Glanford	Meat & bone meal
EPR Scotland Ltd	Westfield	Poultry litter
EPR Thelford Ltd	Thetford	Poultry litter
Unspecified	Ferrybridge C	Coal/biomass
	Fiddler's Ferry	Coal/biomass
	Slough	Coal/biomass / gas/ waste derived fuel
Sembcorp Utilities (UK) Ltd	Wilton 10	Biomass

The fact that existing power stations can be repurposed for co-firing makes co-firing an attractive prospect. Repurposing allows use of existing infrastructure, often utilising a partial substitution of fossil fuels with 5-10% biomass either through existing burners, or through specifically designed ones.[7] Baxter *et al.* also note that co-firing results in a very slight decrease in efficiency compared to coal-firing alone (43-49%)[8] with conversion efficiencies between 30-38%.[9] Conversion has further advantages of fast implementation and low capital cost in comparison to building new installations.[7] The IEA states that the co-combustion of biomass and coal is the most cost-affective use of biomass for power generation.[4] It is also

noted that, prior to full-scale conversion, the low energy density and high moisture content of biomass vs. fossil fuels should be considered.[9]

The coal supply chain is already well established, either through mining or import (Figure2-2).[7] Conversely, the biomass supply chain must take into account competition with foodstocks, alongside sustainability assurance and accreditation.[4] Types of biomass commonly co-fired are forestry products, agricultural products, and waste. Switchgrass, miscanthus and woody crops are seen as potential fuels for combustion due to their relatively short rotations (3-12 years).[4] In England, 0.2% of the 4.6 million hectares of arable land was used for growing miscanthus and short rotation coppice (SRC) in 2012, with 14,000 tonnes of SRC being used for electricity generation.

In order for co-firing and biomass combustion to be a successful long term strategy, energy supply security must be guaranteed. Growth, processing, and storage should all be considered; biomass with a moisture content above 20% has an increased chance of self-ignition and therefore advanced pre-treatment may be required. The importance of adequate storage protocols was highlighted by a fire at Tilbury 'B' powerstation in 2012 where hot dust coming into contact with a hot lamp in the storage facility caused a large fire.[10]

Baxter identified the major technical challenges for co-firing as:[9]

1. Fuel preparation, storage and delivery
2. Ash Deposition
3. Fuel Conversion
4. Pollutant Formation
5. Corrosion
6. Fly Ash Utilisation
7. Impacts on SCR systems
8. Formation of striated flow

This study will focus mainly on ash deposition (2) and corrosion (5) in pulverised fuel fired boilers.

Figure2- 2: UK Coal production sites and ports

2.1 Fuels

Due to the large scale and worldwide nature of coal combustion, there is a lot of published data/knowledge about the elemental composition and phases contained in coal as well as the combustion products.[11] This in turn means affective materials selection[12] and firing conditions can be used. Well-defined classifications of coal already exist and are commonly determined using ASTM D388-12.[13] It is common that power stations are designed for specific types of coal and as such problems may arise when different types of coal are used.[14]

Vassilev *et al.*[15] in their review of the organic and inorganic phase composition of biomass, found that, in comparison to coal, biomass often has larger concentrations of Mn, K, P, Cl, Ca, Mg, O, moisture, and volatile matter. Biomass ash is also commonly depleted in Al, C, Fe, N, S, Si and Ti. These differences from coal and also between the large amount of fuels that the term biomass covers, indicate that both boiler design specifically for biomass/ biomass co-firing, as well as firing in repurposed installations, will create challenges.

Demirbas[16] states that the key differences between coal and biomass are the lower C, Fe, and Al content of biomass and increase in O, Si, and K. Biomass typically has a lower heating value, lower density and higher moisture content.[1] The density of coal can range from 1100kg/m^3 to 2330 kg/m^3 in comparison to biomass which has an average of 100kg/m^3 and 500kg/m^3 for straw and wood respectively.[17] Multiple equations for calculating Higher Heating Value (HHV) have been presented with reviews by Demirbas[18] and Sheng and Azevedo.[19] At present there does not seem to be one equation used by everyone.

The BIOBIB, a fuel database established in 1992, compiles 647 different biofuels falling into the categories:

1. Wood – uncontaminated wood from forests, chipped wood
2. Straw – straw from annual crops
3. Biomass Waste – waste wood, residues from industries, railroad ties
4. Bark – bark from different species
5. Energy Crops – miscanthus, whole crops
6. Husks and Shells – sunflower husks, cocoa hulls, pistachio shells
7. Grass – grass from different species
8. Others – sewage sludge, coconut fibre, cellulose, rapeseed

A further biomass database, Phyllis 2, comprises of almost 3000 records falling into the categories:

1. Untreated Wood
2. Treated Wood
3. Straw
4. Grass/Plant
5. Husk/Shell/Pit
6. Organic residues, manure, sludge
7. Municipal Solid Waste (MSW) and Refuse Derived Fuel (RDF)

Table 2-2 compares the analysis presented in the databases. Both databases acknowledge the limitations imposed by analysis using different methods in different laboratories worldwide, suggesting caution is necessary when comparing with data collected in house.

Table 2-2: A comparison of BIOBIB and Phyllis biomass classification

	Biobib	Phyllis
Ash	Ash Content	% dry, % as received
Ultimate Analysis	C,H,N,S,Cl	as received - C +H+O+N+S+Cl+F+Br+ash+water content = 100 Dry - C +H+O+N+S+Cl+F+Br+ash= 100 Dry, ash free - C +H+O+N+S+Cl+F+Br = 100
Calorific Value	Gross and net	Higher Heating Value Lower Heating Value
Proximate Analysis	Si, Fe, Al, Ca, Mg, Na, K, Ti, CO_2, SO_3, Cl	Ash composition expressed as % oxides (not representitive of form)
Ash – Thermal Behaviour	DIN 51 730 in oxygen atmosphere	
Ash – Heavy Metals	Pb, Cd, Cu, Hg, Mn, Cr	Pb, Cd, Cu, Hg, Mn, Cr mg/kg ash
Water Content		Analysed with caveats that storage and drying can affect content
Biochemical Composition (wt%)		The biochemical composition of materials is expressed in weight% of the dry material (cellulose, hemi-cellulose, lignin, fats, protein, pectin,starch, extractives, C5 and C6 sugars, total non-structural carbohydrates

Further methods of classifying biomass have also previously been explored with one study placing biomass in the following categories according to ash content:[20]

- High silica/ high potassium/ low calcium (agricultural residues)
- Low silica/ low potassium/ high calcium (wood based fuels)
- High calcium/ high phosphorus (manure)

Classification into these categories will only give a limited amount of information on the possible ash/ deposit chemistry expected during biomass combustion.

Coal composition can vary due to pressure, heat, environment (including bacteria present), and the origin of organic matter.[17] Biomass ash composition can vary between region, crop cycle,[21] time of harvest,[22] and genus. Studies into time of harvest have been conducted for

a large variety of fuels. For instance, studies into the affect of harvest time for miscanthus have produced a range of results; from late summer/early autumn[23] through to February.[24] This range of results can be explained by the range of miscanthus genus (22 in total) each of which have an optimum range and set of growth conditions.

The large variety of miscanthus species studied show that a blanket “one size fits all” approach can not be applied to biomass combustion. Similar studies for straw showed that if crops are harvested, but then left in the fields to be washed by rain water ,100mm of rain removes almost all chlorine and 50mm reduces the chlorine content by 50%.[25] It was also found that potassium content is largely reduced; due to the speciation of potassium in the straw (sometimes as complex silicates), the potassium will never be fully leached by rainfall. Xiong *et al.* analysed five types of biomass and concluded that chlorine was the element with most significant correlation with harvest time, culminating in a suggested harvest delay until spring.[22] Further to this, is a comparison of these results with those of European biomass studies as climates in different parts of the world, specifically rainfall, will have a large affect on elemental composition i.e. less rainfall means less chlorine leaching.

Table 2-3 compares 6 fuels used in pilot-scale pulverised fuel investigations. There is significant variation between the ash content of woods and straws and also between straw varieties. Coal has a much larger fixed carbon content than the biomass, which is responsible for the greater higher heating values (HHV) often exhibited by coal. The compositional variations of ash, represented here by their oxides; (often the elements are not present in oxide form e.g. Ca is present as $CaCO_3$) between biomass and coals are illustrated in the ash composition area of Table 2-3. Coal ash is typically comprised of larger amounts of aluminosilicates, reflected in the higher Al_2O_3 proportions in the coal ash.

Further classification of biomass from the six most prevalent ash oxides is proposed by Vassilev et al[26].:

- Wood and woody biomass: $CaO > SiO_2 > K_2O > MgO > Al_2O_3 > P_2O_5$
- Herbaceous and Agricultural Biomass: $SiO_2 > K_2O > CaO > P_2O_5 > MgO > Al_2O_5$
- Herbaceous and Agricultural Straw: $SiO_2 > K_2O > CaO > MgO > P_2O_5 > Al_2O_5$
- Herbaceous and Agricultural Residue: $K_2O > SiO_2 > CaO > P_2O_5 > MgO > Al_2O_5$
- Animal Biomass: $CaO > P_2O_5 > K_2O > SiO_2 > MgO > Al_2O_5$
- Contaminated Biomass: $SiO_2 > CaO > Al_2O_5 > P_2O_5 > MgO > K_2O$

Vassilev *et* al. stated that the large variation in biomass ash is likely due to the variability of inorganic matter in diverse biomass varieties.[27] Ash composition in wood has also been shown to vary between plant tissue with a ranking (from high to low): Shoots/leaves> needles> twigs> bark> wood.[28]

Wood experiences the same seasonal variations seen in other types of biomass and the study also notes that due to the highly inhomogenous nature of the fuel, representative samples are difficult to obtain.

Alongside ash content, moisture content should be given considerable thought prior to biomass co-firing; for instance typically straw is not fired if the moisture content is above 20%.[25] The moisture content of biomass fuel was reported by Sami *et al.*[17] to be a limiting factor in biomass combustion as it lowers flame temperature and stability; if flame temperature drops below 1600K, flame stability is compromised. This can lead to the need for a trade-off between storage, to minimise the moisture content, alongside the identified need for biomass to be washed with rainfall to reduce K^+ and Cl^- content.[29] Much research into the moisture content of wood has been conducted, and is presented in the book "Quality characteristics of biofuel pellets".[30]

Conditions of growth should be carefully monitored, as it has previously been found that a low-chlorine fertiliser can lead to a marked decrease in Cl^- content of biomass.[25,31] Other studies have concluded that high levels of P in fertilisers can lead to hydroxyapatite formation in biomass ash.[32–34] High fertiliser levels can also lead to high N content of the fuels,[31,35] an undesirable quality with respect to NO_x emissions.

Table 2-4 shows a summary of the role of the key inorganic components in biomass. Epstein and Bloom[36] state that elements must satisfy one or both of the following criteria in order to be considered essential elements:

1. The element is part of a molecule that is an intrinsic component of the structure or metabolism of the plant;
2. The plant can be so severely deficient in the element that it exhibits abnormality in growth, development or reproduction i.e: performance in comparison to plants with a milder deficiency.

Further information on the role of these elements in biomass ash deposits will be discussed later.

Table 2-3: Fuel Analysis for 4 types of biomass and 2 types of coal, data is reproduced from reference.[37]

Table 2-4 - the role of key inorganic elements in biomass

Element	Function	Location
Ca	Structural, Osmotic & Signalling Purposes	Vacuoles, cell walls, plasma membrane (oxalates)
Cl	Photosynthesis and osmoregulation	>130 compounds throughout the plant, chloroplats, stomate, vacuole
K	Osmotic and Ionic regulation, carbohydrate and protein metabolism	Cytoplasm and vacuole. High concentration in guard cells
N	Component of organic compounds. E.g. Nucleic Acids	Found throughout the plant
P	Essential for growth, energy transfer and protein metabolism	Cell proteins; taken up as $H_2PO_4^-$, HPO_4^{2-}
Na	Cell Wall structural component	Cell walls and vacuoles
Si	Skeletal structure, protection; no function in some plants	Cell walls, epidermis (phytoliths)

2.1.1 Fuel Pretreatment

In order to combat the low bulk density of biomass, a factor which leads to high-cost handling procedures, pelletisation has been identified as a significant method of reducing this issue. It has been shown that bulk density can be increased from 40-200 kg/m^3 (fuel dependent) to around 700kg/m^3. Shah *et al*.[38] concluded that the role of processing and handling can dramatically alter mineral matter composition, and hence the gaseous release of the minerals. Fuel pretreatment through pelletisation and torrefaction is beyond the scope of this review, a review of pelletisation technology and torrefaction can be found here[39], with further information about exisiting supply chains for both straw and wood pellets in Demark available from[29], and Torrefaction as a method for biomass upgrading here[40].

2.2 Ash Formation

Ash forming elements from biomass most commonly come from two sources, often defined as inherent/included; salts bound in the carbon structure and entrained/excluded; mineral particles introduced during harvest or transport.[1] Vassilev *et al.*[15] suggest that classification of these minerals should be in accordance with coal classification and as such suggested the categories natural and anthropogenic. Natural is further broken down into authigenic, formed in the biomass during growth or after death, and detrital, formed outside biomass but fixed in the structure such as mineral inclusions transported by water suspension and fine grained particles fixed in pores through rainfall or wind. Anthropogenic refers to the constituents formed outside biomass and then collected during harvest, transport and processing. It remains to be seen whether this categorisation will be widely adopted.

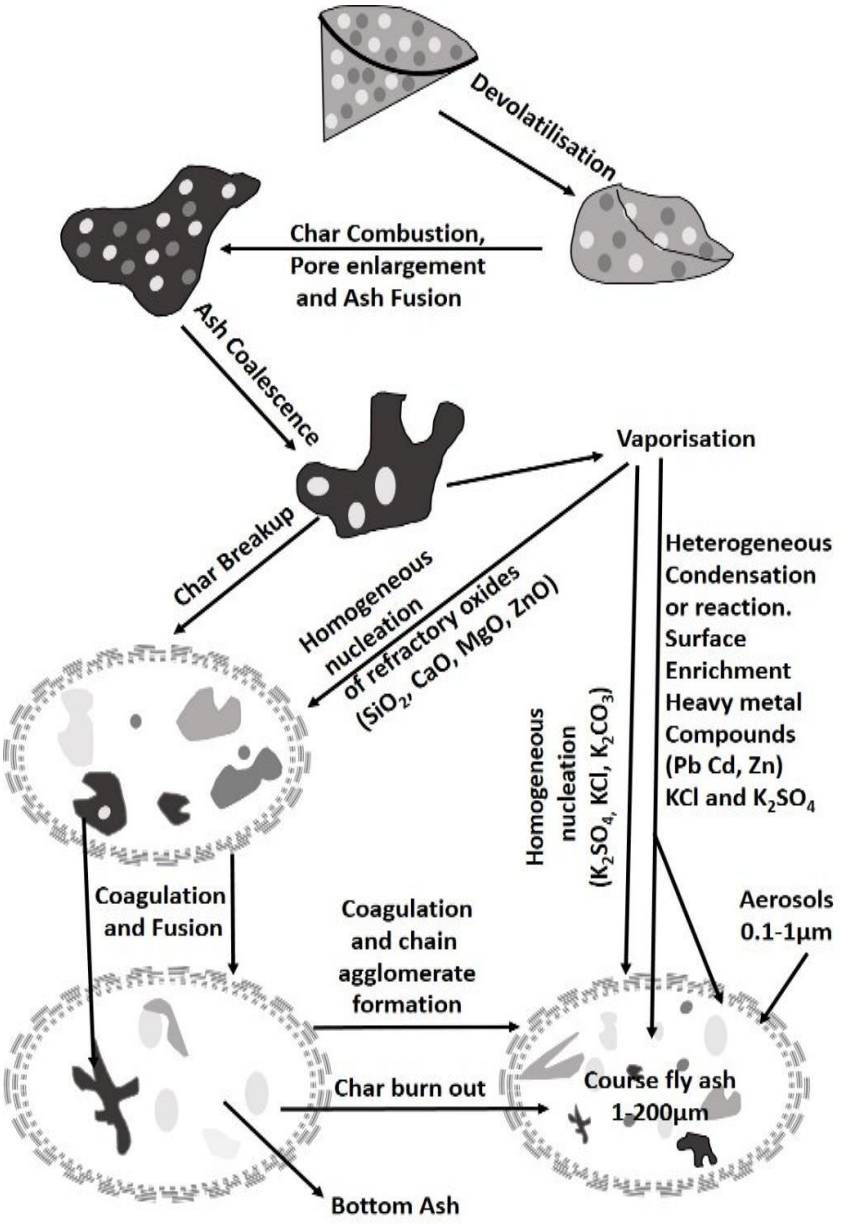

Figure 2-3: Mechanisms involved in ash formation in biomass combustion[244]

When biomass combusts it does so in three stages:[1]

1. Drying – below 100°C moisture evaporates
2. Pyrolysis – Devolatilisation at 200°C, the decomposition of cellulose and hemi-cellulose followed by lignin between 400-500°C. The products are dependent on fuel type, temperature, pressure and atmosphere
   OR
   Gasification – devolatilisation with an externally supplied oxidising agent
3. Combustion – the complete oxidation of the fuel

Ash formation is vastly dependent on the original composition of the biomass, the oxidation/reduction environment, temperature, and residence time in the furnace.[41] Typically the mineral inclusions form a char (200-850°C)[42], volatile elements are then lost and form a fine inorganic aerosol (particle size typically 0.3µm)[43]. Simultaneously with the volatilisation the large char particles fragment (above 500°C)[42], often reacting and agglomerating with other ash particles to form the coarser fraction of the fly ash. This agglomeration takes place in three stages[27]:

- Initial (700-900°C)
- Significant (700-1100°C)
- Extensive (900-1100°C)

Complete fusion of these multicomponent agglomerates takes place at temperatures above 1100°C[42]. The aerosol particles undergo homogenous nucleation, (particularly in the case of KCl, K_2SO_4 and K_2CO_3) or heterogenous nucleation, (particularly with aerosolised heavy metals). In the presence of Zn a slight mechanism variation, where ZnO is acting as a primary nuclei, is observed.[44] The formation of ash is illustrated graphically in Figure 2-3.

The rate of pyrolysis for fuels is dependent on fuel type, with both coal and biomass seeing variation.[17] It has been shown that biomass has a lower activation energy in comparison to coal.[9,17]

Included and excluded mineral matter behave differently during combustion. Minerals characterised as included (Section 2.2) tend to be more volatile, as they heat up and combust faster.[41] These char particles may reach higher temperatures than the gas which then leads to molten particles, which either coalesce or fragment, dependent on a thermal expansion coefficient.[45] Mineral matter characterised as excluded reaches lower temperatures as it is less affected by the locally reducing environment. The particles often remain intact or melt; rarely do they fragment, which is a random process.[41]

Particle shape, size, and density also play a role in the combustion by affecting dynamics, drying, and heating rate, alongside reaction rate between particles. For instance, it has been

shown that spheres devolatilise faster than other particle shapes.[41] Whilst this is ideal for combustion, current methods for the pre-treatment of biomass means it is unlikely that spheres will be the form of biomass during combustion. Large particles have been shown to fragment to a greater degree than small particles due to a temperature gradient that forms across the surface.[41]

Table 2-5 summarises the transformations that the main inorganic compounds present undergo during the combustion process.[27] Biomass ash is said to be comprised of amorphous, semi-crystalline, and crystalline minerals of mostly inorganic origin. Remaining organic matter is present as char and organic minerals, and fluid matter associated with both inorganic and organic matter.[27] A classification of the phases present in ash are primary (those already present in the fuel), secondary (new phases formed during the combustion process), and tertiary (formed during transport and storage) was presented by Vassilev *et al.*[31] This categorisation scheme would allow ease of identification for interactions between coal and biomass when co-fired.

A study by Shah *et al.*[38] correlated the association of elements in the fuel ash and their release during combustion. They concluded that the presence of Si and Al can reduce alkali release where those alkalis are present in highly water soluble forms. It was also found that the higher the total ash and volatiles content the greater the observed elemental release. Ca and Mg were found to have a greater release when not counterbalanced with Si and Al.

Recently, a large scale review of biomass combustion, its mineral phase transformations (inorganic and organic), ash fusion and formation mechanisms, alongside reviews of the classification and application which includes phase-mineral and chemical composition utilisation and challenges was conducted by Vassilev *et al.,*[27,31,42] highlights are discussed throughout this review.

Table 2-5: Inorganic Transformations in Ash taken from reference [27]

2.3 Deposition Formation Mechanisms

Knowledge of the formation mechanism of deposits is necessary if the build up of large deposits is to be minimised. Deposits are formed when the inorganic ash, formed during combustion, is carried in the flue gas through the plant and a portion of it then deposits onto heat transfer surfaces[46]. Laursen *et al.*[47] present the 6 dominant mechanisms of ash deposition (Figure 2-4). Initially deposits form through thermophoresis (small gas-borne ash particles deposit onto cool surfaces due to high temperature gradients), or condensation of small (<4µm) particles of volatilised inorganic compounds (e.g. KCl, K_2SO_4)[1]. An illustration of how the deposit typically looks can be seen in Figure 2-6. Hansen *et al.*[48] analysed deposits from air cooled probes that were inserted into the top of the furnace and convective pass (1-8h collection), alongside mature deposits removed from the boiler after approximately 1 year. It was found that a thin layer of iron oxide mixed with KCl formed on the probe at the top of the furnace. In the convective pass, the structure of the deposit was similar to that of the inner layers of the mature deposits, supporting the initial deposition mechanism proposed by Laursen *et al*[47]*.*

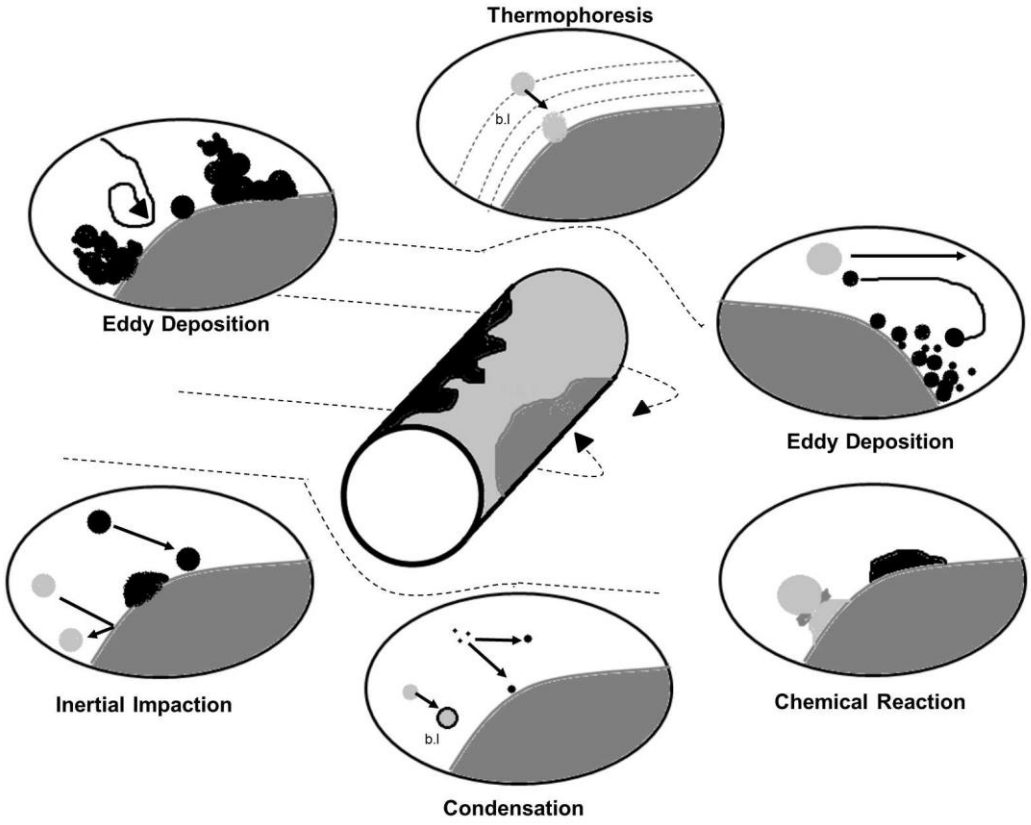

Figure 2-4: Deposition mechanisms for ash deposits onto a metal surface during combustion[47]

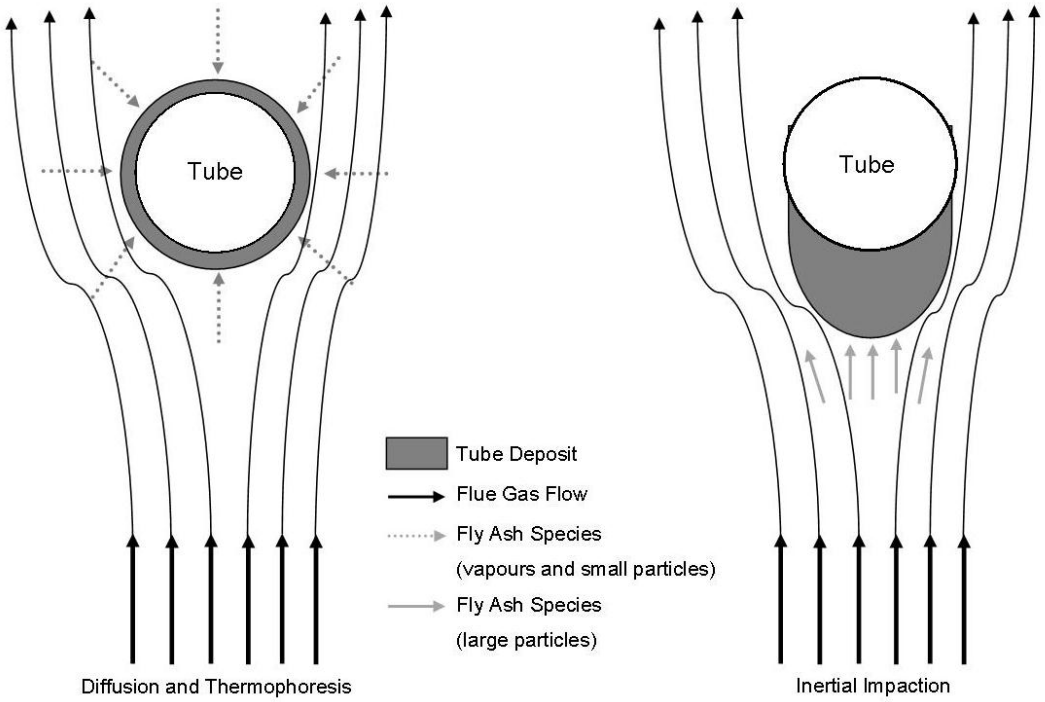

Figure 2-5: Deposition mechanisms of (left) Diffusion and Thermophoresis and (right) Inertial Impaction onto a metal surface[46]

Eddy diffusion occurs in the turbulent area around the boundary layer surrounding the tube; heterogenous condensation on heat transfer surfaces, deposits or in existing pores leads to a thickening of the deposit.[46] This was observed by Jensen *et al.;* [49] As a layer of KCl described as "gluing" several deposit layers together. Eddy diffusion also occurs on the non-flue gas side of the tube. It is thought that these particles "bounce off" rather than undergo inertial impaction and therefore get caught in an eddy, which is followed by deposition onto the tube, affecting particles with sizes in the region of 4-10µm.[46] Koer *et al.*[50] noted that eddy impaction caused by surface related turbulent flow should not be confused with vortex shedding, where two opposing gas flows (one from above and one below the tube) remove particles which are then redeposited.[51]

The mechanism of deposition for species which are not stable at the gas temperature is by chemical reaction. Baxter[52] states that this is the most common method of deposition for alkali sulphates, heterogenous reaction between the gas phase species and the lower temperature deposit surface being the mechanism of deposition. The most important chemical reactions are listed as sulphation, alkali absorption, and oxidation.[1,52]

After the initial deposition phase, larger particles (>10µm) start to deposit through the inertial impaction mechanism.[1] Inertial impaction occurs when the large particles have too much mass and inertia to deviate from the gas flow, and so hit the surface of the tube/deposit.[46] These deposits often form a characteristic elliptical deposit (Figure 2-5). Hansen *et al*.[48] note that

particles are often molten during impaction, this is evidenced by deformation of particles imaged in the deposits. Factors influencing inertial impaction are: particle size distribution, particle density (if not sufficiently high the particle can deviate with the gas flow), angle of impaction, and gas flow.[46] Cieplik *et al.*[41] found that gas density, related to CO_2/O_2 or N_2/O_2, may have an affect on deposition rate through inertial impaction, as oxyfuel conditions had slightly higher deposition rates; it was also noted that this may be due to longer residence times in the flame.

Frandsen *et al.*[53] reported both thickness and compositional variation of deposits in relation to gas flow direction. Baxter[52] reports other key factors for deposition to be surface composition, morphology, and viscosity. Coleman *et al*.[54] note that deposition is often enhanced when deposit surfaces are sticky at lower temperatures. Figure 2-6 illustrates the mechanisms of deposit growth; it is stated that a clean tube only collects sticky particles, which then solidify if a deposit is thin.[55] The deposit surface temperature increases, and so particles may remain sticky, leading to an increase in collection efficiency.[46] Inertial impaction is often seen as the dominant mechanism for deposit growth; however, it should be noted that for fuels with lower ash content, eddy impaction, condensation and thermophoresis may be equally important[56]. Deposits may be removed by erosion of the solid surface by large solid particles impacting, by melting, or by thermal shock.[46]

Ash and deposit build up comes with associated issues. During pulverised fuel combustion ash deposition on burner surfaces and quarls can lead to large ‘eyebrow shaped’ deposits,[57]

Figure 2-6: Inertial Impaction Deposition Mechanism.[55] Open particles are sticky, shaded particles are sticky on arrival followed by solidification in the deposit. The two types of cross hatched particles are smooth: fused in the furnace but solid upon arrival or jagged: highly erosive particles which were never fully fused

which are not cleared during soot blowing. This has lead to burner light-up and operation failures.[1] In addition large slag bridges and regions of partially fused deposits can lead to blockages which result in unexpected shut-downs.[58] The build up of large deposits on heat transfer surfaces is discussed below. Soot-blowing is an affective mechanism of deposit removal, although large deposit removal can result in mechanical damage to components lower down in the boiler.[1]

2.3.1 The affect of deposits on heat transfer

Large ash deposits often build up in co-fired installations (Figure 2-7). These large deposits can affect heat transfer which in turn leads to a decrease in thermal efficiency.[59] Without the presence of a deposit, heat should transfer from the flue gas to the steam via the tube. In the presence of a deposit, the heat must first be transferred by radiation and convection before being conducted through to the steam[60] (Figure 2-7). Heat is also lost through reflection and emission, which are related to surface emissivity and density.[60]

Alongside reflection, absorbance into the deposit at depths up to 1mm should be considered. Wall *et al*.[61] noted that the factors affecting heat transfer in large deposits are thermal conductivity, absorbance, and emittance; when deposits are not significant, the gas and steam temperatures are roughly equivalent therefore thermal conductivity is not affected. Radiative properties are affected by surface conditions whereas conductive properties are affected by the physical structure inside the deposit (particle size, porosity and sintering).[60] Baxter et al.[62] identified the degree of particle connectivity as one of the key factors in affective heat transfer. Emissivity is affected by the chemical composition (which can affect colour), particle size on the surface (discussed later in deposition mechanisms), and the state of the surface (e.g. solid,

Figure 2-7a: Deposit formation in the superheater region of the Amager power station co-firing straw and coal[60]

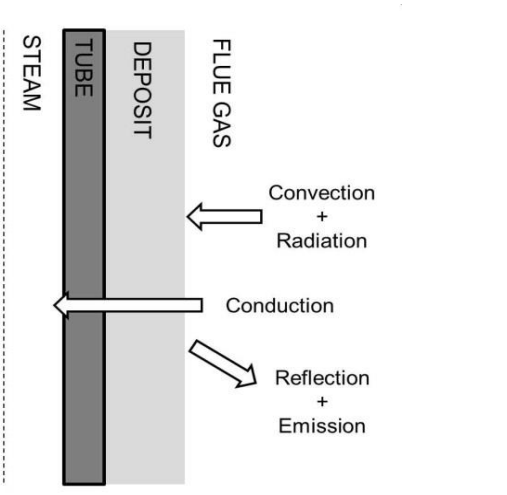

Figure 2-7b: Heat transfer mechanisms through deposits in the furnace region[245]

molten, slag).[61] The deposition onto heat transfer surfaces can also give an increase in the flue gas temperature, which can in turn lead to deposition in areas further along the convective sections of the boilers.[1]

2.4 Deposit Composition

As would be expected, ash composition in deposits can vary wildly from the bulk ash composition of the fuel.[63] Frandsen[44] notes that whilst coal ash largely comprises of aluminosilicates, biomass ash has a much wider variety of salts, illustrated in Figure 2-8. During co-firing, a large portion of potassium is thought to be 'captured' by silicates from the coal[64]. As well as in-deposit reactions between alkali cations/metals and silicon, reactions can also occur between gas phase and condensed phases.[37] Incorporation of alkali metals into silica can create issues with slagging and fouling, as the melting point is lowered from 1700°C to 750°C.[65] Frandsen found that ash from pulverised fuel boilers was rich in aluminosilicates.[44] Dayton *et al*. also noted that when co-firing Pittsburgh #8 coal variety and various biomass fuels, increasing the content of aluminium and silicates gave rise to an increase in alkali retention in the condensed phase.[66]

Metal			Counter Ion
K^+			SO_4^{2-}
Na^+		x	CO_3^{2-}
Mg^{2+}			Cl^-
Ca^{2+}			PO_4^{3-}
Zn^{2+}			

Figure 2-8: Ash Matrix Composition

Robinson *et al.*[37] divided the elements in deposit chemistry into non-volatile (Si, Al, Fe, Ca), semi-volatile (Na, K) and volatile (Cl, S). Co-firing biomass (wood and straw) with coal showed an enhancement of Ca in the coal-wood deposits; the coal-straw deposits showed a K enrichment alongside a sevenfold enrichment of S in the deposits and a Cl reduction.

Deposits have been shown to contain distinct layers.[48,53] Miles *et al.*[67] describe three layers formed on a probe during the co-firing of wheat straw

1. A fine white deposit shown to be KCl
2. A porous intermediate network
3. Sintered ash particles

It was also reported that in respect to the fuel, Si was enriched in the outer layers, K was enriched close to the probe-deposit interface, and P is enriched in the outer layers. In contrast Hansen *et al*.[68] found there to be six layers in straw co-fired deposits.

1. A thin layer of Fe/Cr-oxide
2. A dense layer of K_2SO_4 containing threads of Fe_xO_y
3. Porous KCl
4. Dense KCl
5. KCl including ash particles
6. Porous sintered fly ash particles

Heinzel *et al*.[69] investigated multiple types of biomass in a pulverised fuel 0.5MW_{th} combustion chamber. It was found that with biomass: coal (25:75%), only light easily removable deposits were formed. A comparison between pure straw and 50:50 straw:coal highlighted that the Al content in the slags close to the burner was high in comparison to the fuel in both the pure and blended straw fires. The silicon content in slag deposits was also higher in respect to the fuel. The S content was significantly higher in the co-fired blend, due to fuel differences and was found to have condensed on cooler parts of the probes.

Khodier *et al*.[70] characterised deposits from co-firing miscanthus and Daw Mill coal (0:100, 20:80, 40:60, 60:40, 80:20, 100:0) in a 100kWth PF combustion rig. It was found that for probes at 500°C the deposits formed on the gas side of the probe were larger for those with higher levels of coal in the co-fire; in comparison, deposits on the down-stream surface increased with a higher biomass share. Gas side deposits were found to decrease in Al, Si, and Fe as the coal composition was decreased but an increase in K, S, and P were seen. These results are due to the increased mobility of these elements in the biomass, theorised from chemical fractionation results.[70] KCl was only detected on the probes of 500 and 600°C, suggesting thermophoresis and diffusion as the mechanisms of deposition.

2.4.1 Zinc and Lead

The roles of Zn and Pb in deposits and ash are of interest in relation to deposit build up and corrosion. It is thought that Zn and Pb have largely similar vaporisation mechanisms to alkali metals[1]. Zn and Pb are typically found in higher content in waste wood,[71] however external factors mean that they can be found in high concentrations in tree bark,[72] and also when there are longer rotation times for woody biomass growth.[1]

Heavy metals generally become trapped in ash[73] rather than being released in flue gases, Pb and Zn are typically found in fly ash compared to bottom ash due to their volatile nature.[1] Despite their often low concentrations in the fuel matrix, ash enrichment in the fly ash can cause significant problems with respect to corrosion. Backman *et al*. extensively studied the

affect of the Cl/S ratio on volatilisation of Pb and Zn. It was found that the concentration of chlorine directly affects the amount of Zn retained in the bed bottom ash as ZnO or $ZnSO_4$.[74]

Zn typically volatilises as $Zn^{2+}(g)$ which then forms ZnO,[31,74] and often goes on to form $ZnCl_2$, whereas Pb typically volatilises and reacts to form silicates in the gas phase.[75] If Zn and Pb are deposited they can cause significant corrosion problems.[76] As is the case with alkali salts, Zn and Pb salts also form lower melting point eutectics. It has previously been found that the formation of alkali salt eutectics lowers the melting point of metal oxides and chlorides that may already have formed.[77] The presence of Zn and Pb salts further lower these melt temperatures (Table 2-6), which can lead to an increase in corrosion.[78]

Table 2-6:Melt temperatures for pure compounds and eutectics of common salts[78]

Melting Temperatures			
Pure Compounds		**Eutectics**	
$PbSO_4$	1170°C	$PbSO_4.K_2SO_4$	814°C
K_2SO_4	1069°C	$PbSO_4.Na_2SO_4$	719°C
Na_2SO_4	884°C	$ZnSO_4.K_2SO_4$	566°C
NaCl	801°C	$ZnSO_4.Na_2SO_4$	674°C
KCl	771°C	$PbCl_2$.NaCl	485°C
$ZnSO_4$	730°C	$PbCl_2$.KCl	435°C
$PbCl_2$	501°C	$ZnCl_2$.NaCl	294°C
$ZnCl_2$	318°C	$ZnCl_2$.KCl	288°C
		$PbCl_2.ZnCl_2$	243°C

2.4.2 Slagging

Slagging is defined as “the formation of fused or sintered deposits on heat-transfer surfaces and refractory in the furnace cavity subjected to radiant heat surfaces”.[20] Factors affecting slagging are similar to those affecting deposition; in general, slagging typically occurs at temperatures above 1000°C.[1] The formation of slag is very much dependent on the combustor and furnace design used in co-firing[1,65]. Nussbaumer[79] compiled a report on factors and design to minimise slag formation during biomass combustion. Van Loo *et al*. state that the boiler design should have intelligent furnace design to prevent high gas temperatures adjacent to a furnace wall, which would allow slag to form.[1]

The key deposition mechanism for slagging is inertial impaction,[69] although it was noted by Van Loo *et al.*[1] that during the initial stages of slag build up, other mechanisms are likely to take place. Particle adhesion is dependent on both the particle, and the surface. A sticky

molten surface is the norm with particles being either molten or partially molten. As the outer surface temperature increases, the slag becomes denser and more bulk ash is collected. When the outer temperature of the ash deposit reaches the melting point of the deposit, slag flow often initiates.[80] After slag flow formation, the deposition rate remains at a steady state as particle deposition is balanced by the flow rate of molten slag.[80] Henizel *et al.*[69] noted that the main elements present in slags are aluminium and silicon, suggesting that if these elements are present in high quantities, slags are increasingly likely to form. Nutapatali *et al*. calculated that the presence of silicon in ash deposits increased the sequestration of potassium, however the higher the portion in these deposits the greater the chance of the deposits forming a slag melt.[81]

2.4.3 Fouling

Fouling in comparison is a lower temperature process (300-900°C), which relies upon a volatilising and condensing mechanism in order to deposit.[1] The rate of condensation has been shown to impact on deposit morphology and mechanical properties.[65] Fouling deposits are often loose and lightly sintered with volatile species; the alkali chlorides often serve as a bond between non-volatile ash components which then stick to the deposit surface.[82] At these temperatures, sulphation of the alkali metal compounds commonly occurs due to reaction with SO_2(g) in the flue gas.[1] The tenacity of deposits formed through the fouling mechanism are temperature dependent. Deposits formed at temperatures below 600°C are commonly unfused, in comparison to those formed in the higher temperatures of the convective passes. These higher temperatures result in partially fused, highly tenacious, deposits.[1]

Khodier *et al*.[70] reported that an increase in deposit size on the downstream side of probes for co-firing ratios higher in biomass indicated a higher risk of fouling.

2.5 Corrosion Mechanisms

Through the study of the combustion of coal, then the study of co-firing, the main factors influencing corrosion have been determined as:[1]

1. Tube Material
2. Flue gas temperature, metal temperature, flux temperature
3. Chemical deposit composition
4. Chemical composition of the flue gas
5. Plant operating regime

For biomass, co-firing temperatures are often limited to 400-450°C as higher temperatures can often lead to harsher conditions related to the nature of the fuels. Before investigating corrosion mechanisms, the reaction of oxygen with a metallic surface should first be explored.

Oxidation is initiated by adsorption of oxygen at the metal surface, this is followed by the growth of a bidimensional layer (oxide materials consisting of one atomic layer).[83] The bidimensional layer then grows to form a tridimensional oxide growth, across which both metal and gas species diffuse. Following this, cracks in the metal and the oxide can form which may lead to cracks in the protective surface scale, in turn leading to spallation and an increase in corrosion.[84]

The formation of a protective oxide layer is a key consideration during the selection of alloys for use in co-firing as power plant components, as it can increase the protection of the alloy from other forms of corrosion. The use of thermal cycling (heat up and cool down of power stations) can lead to spalling of the oxides, therefore reducing the lifetime of the components.

2.5.1 Active Oxidation

A Cl^- containing atmosphere, formed either through the presence of deposited KCl or gaseous HCl, can lead to active oxidation; a schematic illustration can be seen in Figure 2- 9. Under reducing conditions, a defective oxide barrier (which is far less protective than an oxide layer) forms as little O_2 is present to react and form a protective layer.[85] The presence of CO at concentrations higher than 2% has previously been shown to increase the corrosive rate of HCl by 2.5 times.[86] A high $\%O_2$ indicates oxidising conditions, under which protective oxide scales are more likely to form.[85] Under a high $p(O_2)$, metal chlorides diffuse to the scale surface

and upon encountering a higher p(O_2) gradient, solid metal oxides are formed in a loosely adherent non-protective, porous layer.[86]

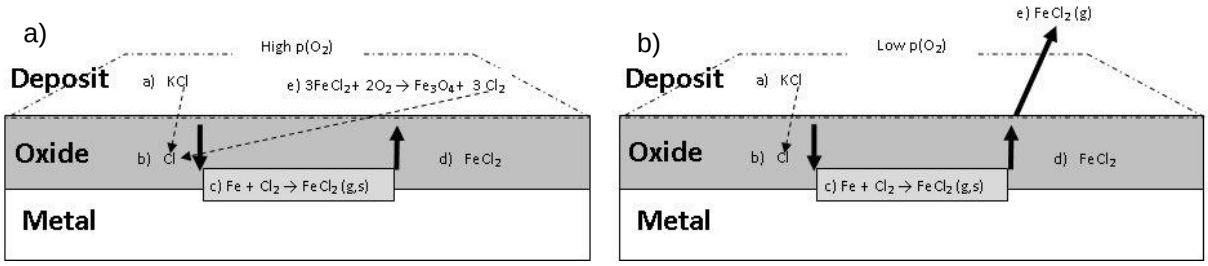

Figure 2- 9: Active oxidation mechanisms under a) oxidising and b) reducing conditions adapted from reference[85]

Zahs *et al*.[87] show the reaction for the equilibrium of HCl in oxidising conditions as:

$$4HCl(g) + O_2(g) = 2Cl_2(g) + 2H_2O(g)$$

Equation 2-1

Cl_2 is the main aggressor for short metal exposure times, however it was also shown that metal oxides catalyse this reaction.[87] This in turn led to the assumption of Equation 2-1 reaching equilibrium in the oxide layer.

Cha and Spiegel stated possible reactions between KCl and Fe (Equation 2-2), and Cr (Equation 2-3). Investigation into the affect of 0.05 vol.% HCl addition[88] showed an increase in the partial pressure of Cl^- led to more $FeCl_3$ forming, which promoted the formation of the low melting point KCl-$FeCl_3$ eutectic. A chlorine rich layer formed on the surface of the Fe substrates which led to the increased adhesion of salt particles, and therefore an increase in deposit build up. At temperatures above 600°C, it was shown that Cl^- diffuses through the oxide layer of a Cr/Cl interface, and increases corrosion through active oxidation.[88]

$$2\,KCl + Fe_2O_3 + 0.5O_2 \rightarrow K_2Fe_2O_5 + Cl_2$$

Equation 2-2

$$2KCl + Cr_2O_3 + 2.5O_2 \rightarrow 2K_2CrO_4 + Cl_2$$

Equation 2-3

2.5.2 Sulphidation

The corrosion of metals under sulphidation conditions (gas containing, H_2S, COS and SO_x) is reported to be much more severe than corrosion observed in purely oxidation enviroments.[89] It has been found that in the presence of oxidation-sulfidation atmospheres, sulphide corrosion occurs as S molecules diffuse through the oxide layer to reach the oxide-metal interface. Once this penetration has occurred, a sulphide layer rapidly grows on the surface of the alloy.[90] This sulphidation is described as internal and can then cause retardation of protective oxide layer formation, leading to a rapid increase in oxidation. This in turn can increase the corrosion rate which is referred to as sulphidation/oxidation.[91]

Sulphidation of Cl^- containing phases, present in surface deposits and the oxide layer, can also lead to corrosion, as the replacement of Cl^- with SO_2 releases the Cl^- to undergo active oxidation once again.[1] However, Petterson *et al.*[92] present research indicating that the growth of a K_2SO_4 scale over the top of an oxide scale can also form a protective barrier.

2.6 Materials

In relation to materials selection for use in power plants, mechanical, physical, and chemical properties must be considered[84]. The mechanical and physical properties of metals can be viewed as constants, the chemical properties are dependent on the conditions the materials are subjected to,[84] therefore testing of alloys under conditions used in co-firing is necessary to give information into whether they are suitable for use in large scale applications. The theory behind corrosion protection is the minimisation and disruption of the electrochemical processes.[93]

One method of materials selection presented by Antunes and Oliviera[94] is the Ashby approach, which follows the steps:

1. All available materials
2. Defining the functions, constraints, objectives and variables of the material required (translation)
3. Materials which don't meet the constraints are removed (screening)
4. Materials that passed the screening test are classified according the objectives in step 2 (ranking)
5. Documentation of the top-ranked candidates are sought and materials are selected. (Seek documentation)

Shriers corrosion states that the goal of alloy selection is to maximise oxidation lifetime by accounting for thermodynamic, kinetic, mechanical, physical and metallurgical factors.[84]

Materials being used in supercritical steam conditions must be resistant to creep, corrosion, and thermal fatigue, whereas materials at lower temperatures must be resistant to acid corrosion exhibited in flue gases.[29] A material that was suitable for coal-fired conditions may be highly susceptible to corrosion from the type of biomass to be co-fired. For example it has been found that high-Cr steels are far more susceptible to attack when straw is being co-fired.[95]

Birks *et al.*[96] produced a table showing the hierarchy of common engineering alloys with respect to temperature (Table 2-7).

Table 2-7: Alloys and their applications[96]

Alloy	Protective Product	Temperature Limit (°C)
Low Alloy Steels	M_3O_4 (M= Fe, Cr)	500
Titanium – Base	TiO_2	600
Ferritic Stainless Steel	Cr_2O_3	650 (Creep Dependent)
Austenitic Fe-Ni-Cr	Cr_2O_3	850
Austenitic Ni-Cr	Cr_2O_3	950
Austenitic Ni-Cr-Al Plus Coating	MCrAlY (M= Ni,Co or Fe)	1100
Ceramics or Coatings		Above 1100

Investigation of the reaction of KCl with Fe, Cr, and Ni by Cha and Spiegel[88] showed active oxidation had a severe affect on Fe at 300°C, Cr at 500-600°C, corrosion was not enhanced in Ni. This led to the conclusion that Ni based superalloys and steels were best suited for biomass combustion plant superheater regions.

Studies conducted by ELSAM showed that the combustion method had a significant affect on corrosion.[97] It was shown that a 10 wt% addition of straw in a pulverised fuel boiler showed no, or only a minor increase (1.5 times), in corrosion in comparison to when coal is fired alone. In comparison, firing biomass on a (circulating fluidised bed) CFB or grate firing led to corrosion rates of 2-25 times higher when straw was co-fired.[97] The difference in corrosion rates was explained as differences in the Cl speciation. In the CFB boilers, KCl was formed and condensed onto the superheater tubes whereas in the PF boilers there is a higher heating rate and so the Cl is present as HCl which leaves the boiler alongside the flue gases.

Research at the Jordbro 70MW hot water boiler, firing pulverised wood as the fuel, indicated the alloys X20 and TP321 had the highest corrosion rates at 600°C. A chromium oxide was formed close to the metal interface with depletion seen below, on top of this chromium oxide was iron oxide. Creep strength of the materials at 600°C steam were also tested; X20, TP 321, 825, and 800 H were shown not to be suitable, however E 1250, HR3C, and AC 66 were

suitable for metal temperatures up to 650°C.[98] HR3C was shown to have the best creep strength, however cold working caused low ductility and therefore cracking. It was also noted that there was no clear correlation between the composition of materials and the corrosion rate observed during the tests.

Research on HR3C exposed to 600 & 650°C removed from a pulverised fuel boiler firing 100% wood showed three general regions of a corrosion reaction.[99] The gas phase/deposit interface, the initial iron oxides (scale), and the iron-depleted alloy (internal corrosion zone). It was concluded that the position of the probe relative to the gas flow would give differing corrosion results, with the deposit/gas interface playing a large part. Where inertial impaction was the dominant mechanism, there was a lower partial pressure of O and Cl. In the presence of KCl deposition by thermophoresis, or where no deposit was present, the corrosion was higher due to the increased partial pressure of O and Cl.[99]

Liu *et al.*[99] investigated the corrosion of TP347H FG probes exposed in a wood-firing PF boiler for 3770h at 600 and 650°C. Three distinct layers are found under deposits. Firstly an internal corrosion layer as a result of inter granular corrosion; secondly an intermediate scale layer, comprising general corrosion products, and sometimes unreacted alloy; and finally an outermost scale, which is parallel to the metal surface and may contain sintered deposits.[99] It was also shown that intergranular corrosion is often unrelated to the outermost scale. Cr enrichment was reported at the inner scale and is thought to enhance corrosion protection[99].

Hussain *et al.*[100] studied the affects of temperature (600, 650 and 700°C), air (1300 vppm SO_2, 400 vppm HCl)/oxy-fuel (6260 vppm SO_2, 1700 vppm HCl) conditions and the deposit Na_2SO_4:K_2SO_4:Fe_2O_3 in the ratio 1.5:1.5:1 on the alloys T92, HR3C, 347HFG and Alloy 625. Gas simulations were based on experimental data obtained from pilot plants for combined cereal product: Daw mill coal (20:80). The deposit is considered to be aggressive and likely to form alkali-iron-trisulphates. Data showed that, due to the nature of the deposit accelerated corrosion, the alloys were damaged in the order T92> 347HFG > HR3C. The authors stated the Cr content of the alloys was the reason for this ranking.[100] It was also stated that peak corrosion damage was experienced at 650°C in air-firing conditions, and that the Cr content did not seem to affect protective scale formation under these conditions.

Dudziak *et al*.[101] used the deposit recoat method whilst investigating the affect of oxy-fired conditions on fireside corrosion of 15Mo3, T22, T21, and T91 at 600°C. Sample corrosion was studied for 1000h (5 recoats after each 200h) under gas simulation conditions from Daw Mill. The study concluded that the deposit containing Na_2SO_4:K_2SO_4:Fe_2O_3 will lead to the formation of alkali trisulphates, and therefore increase the corrosion rate. 15Mo3, the alloy

containing no Cr, showed good corrosion resistance when no deposit was present up to 800h of testing, after which spalling was observed. The alloy containing the highest Cr content, T91, exhibited similar corrosion resistance properties to T22, T23, and 15Mo3 under most conditions.

Skrifvar *et al*.[102] simulated deposit corrosion on alloys in a furnace for 1 week. It was found that in the presence of synthetic salt deposits, containing Na, K, S, Cl, and O in varying concentrations and compositions, on 10CrMo9-10 showed extensive corrosion at high temperatures, particularly when chlorine was present. Alloy 625, containing a high nickel content, showed very few signs of corrosion with only thin oxide layers forming in the high chloride salts. It has previously been noted that the Ni based alloy 625 has some resistance to chloride attack.[103] Eriksson concluded from a variety of materials sampled both in lab and in plant, that an optimum Cr and Ni content seems to be of greater importance than additional elements.[103] Hussain *et al*.[100] reported results agreeing with this assessment; under oxy-fuel conditions with the simulated deposit (Na_2SO_4:K_2SO_4:Fe_2O_3 =1.5:1.5:1) at 750°C, alloy 625 experienced more corrosion than HR3C, this was attributed to the differences in Cr content (HR3C more Cr by 2-5%).

Petterson et al. studied the affect of KCl induced high temperature corrosion on Sanicro 28 and 304L. It was found that in the presence of KCl, Cr depletion occurs for both alloys in the form of K_2CrO_4.[104] This leads to Cr loss from the scale and therefore Fe rich scales are exposed. 304L also experienced corrosion far away from the grain boundaries due to the formation of chromium oxyhydride, followed by its evaporation.[104] It is noted that after the formation of K_2CrO_4, corrosion rates are rapidly decreased as a protective layer is formed. A further study showed K_2CrO_4, formed as a spinel on 304L at 600°C.[92] Large amounts of research into Sanicro 28 and 304L, and their corrosion at 600°C have been undertaken, and are mostly in good agreement in both simulated deposits, and also for the co-combustion of wood.[105] Addition of sulphate to the fuel showed a reduction in chromate formation and therefore retarded corrosion.[106]

2.6.1 Coatings

Alloy design is often combined with the use of coatings in order to use materials for an increase in operation time under the service conditions whilst co-firing biomass and coal.[84] A coating is a barrier layer between the material and the corrosive environment which is optimised to be as inert and impermeable to corrosion as possible.[93] The coatings are used to protect against oxygen, nitrogen, SO_2/SO_3, Cl, and liquid deposits.[107] It is noted that these factors must be in low concentrations as otherwise coatings will rapidly fail.[107] The composition of the coatings

are often similar to those of high Ni based alloys. Coatings are employed as these alloys are often ten times the price of conventional ferritic steels.[108]

The principle behind coatings is the presence of a reservoir phase (commonly Al_2O_3), which allows for the formation of a protective and slow growing oxide scale.[107] Once this reservoir is depleted, corrosion occurs.[84] Schutze *et al*. present a list of criteria for the development of coatings.[107]

- A thermodynamically stable protective phase should form on the surface of the coating, this is commonly Al_2O_3, Cr_2O_3, and SiO_2, combined with spinels
- These coatings should be slow growing, meaning the reservoir depletion is not as rapid.
- Interdiffusion between the coating and the substrate alloy must be minimal, meaning the diffusion will occur at a slow rate.
- Thermal expansion co-efficients of the coatings, substrate, and oxide scales should be as close as possible to minimize stress and strain when caused during thermal cycling.

Further expansion behind these principles are presented in Shriers Corrosion.[84] One of the limitations of coatings is that defects form during the coating process which will allow the corrosive atmosphere to reach the bulk material.[93]

Most coating methods use thermal spraying, where small molten/ softened particles are deposited on to the alloy surface. These particles then flatten onto the surface and adhere to one another.[109] The other two methods of deposition are Chemical Vapour Deposition (CVD) and Physical Vapour Deposition (PVD); these are not widely used, as thermal spraying is viewed as more versatile and can be used for new installations or to spray old components.[110] It should also be noted that the adherence of coatings is greatly increased when the surface to be coated has been correctly prepared[93].

The most common method of thermal spray coating is High-Velocity Oxy-Fuel (HVOF). A fuel is mixed with oxygen in chamber, propelling the powder coating (1000-2000m/s, 5500K). The advantages of the process are cited as high bond strength, low residual stress, and low porosity.[111] A review of the advantages and disadvantages of the HVOF system is presented by Sidhu *et al*.[111]

2.7 Ash Utilisation/Disposal

Biedermann and Obernberger[59] identified chemical composition as a key factor in ash utilisation and disposal. The elements Cl, S, Na, K, As, Cd, Hg, Pb, and Zn have been identified as those creating the greatest concern.[32,59,64] Jenkins *et al.*[112] identify a need for further characterisation of biomass fuel ash to include heavy metals, rather than the 15 elements often present; it is thought that this would help in classification for disposal of the ash. Vamvuka *et al*.[113] however, reported the observed environmental impact of disposal of ash containing these elements to be negligible. As such it can be concluded that further work is needed prior to the production of comprehensive strategy of biomass ash disposal.

The utilisation of biomass ash is viewed as important for the ongoing cost-affectiveness of firing or co-firing biomass.[114] Use of ash as a soil enhancer, due to the high K content, has been reported several times.[42,115,116] A review by Vassilev *et al*.[42] indicated that water solubility of phases in biomass ash should be considered prior to ash being used as a soil enhancer, as they could lead to water contamination and eventually enter the food chain. The presence of harmful phases can be controlled to some extent by the combustion temperature.[42]

Teixera *et al*.,[117] in a comparison of concretes using biomass and coal fly ash as cement filler, concluded that the use of biomass ash was possible. They concluded that the use of biomass ash would improve the sustainability of concrete and the biomass combustion process. However it was also noted that further study of biomass ash incorporation should be conducted prior to large scale utilisation.

Whilst progress has been made towards the disposal of biomass and co-fired ashes, adequate disposal and utilisation methods are still under investigation.

2.8 Conclusions

The combustion of biomass, both alone and co-fired with coal, provides many complex challenges as a sustainable energy source. Initially, selection of a suitable biomass as a fuel source is followed by the creation of a sustainable infrastructure to ensure that future energy demands are met. A choice on whether to convert existing infrastructure e.g. coal power stations or to build new ones must be made. Each of these options will present complex challenges related to materials selection, areas of deposition, ash forms, and waste disposal. This selection process will also yield different rates of efficiency, with higher efficiencies being desirable.

To ensure the best possible outcomes for these decisions, there are multiple steps that should be followed, from small scale fuel tests (e.g. in a laboratory, in a furnace, or chemical fractionation) to large scale tests in a combustion setting (e.g. at Elsam). There are multiple technologies currently being used for the co-firing of biomass including pulverised fuel, bubbling fluidised bed, and circulating fluidised bed. Each of these methods has been shown to produce different results and also different phases in the ash post-combustion.

Ash deposition during co-firing is one of the key issues faced when converting a power station from dedicated coal firing to co-firing. The build up of ash in places different to those observed during coal firing have been observed during large scale fuel tests. This is due to the differing composition of the ash when biomass is fired. One of the key concerns during biomass combustion is the formation, and deposition, of the phase KCl. This has previously been shown to deposit onto the cooler surfaces in the combustion environment (e.g. boiler pipes and superheaters). This in turn leads to the active oxidation corrosion mechanism outlined in Section 1.5.1. This is undesirable as it can then lead to component failure, which then leads to plant downtime, and increased operations costs.

The deposition of ash during firing can also lead to a drop in efficiency of the power plant as the build up of ash onto a heat transfer surface will mean more energy is required to heat the water. A large build up may halt this transfer altogether. The deposit composition will vary greatly between biomass fuel type with some types exhibiting a wider range of slagging and fouling, creating tenacious and harder to remove deposits.

The disposal of the fly ash, post combustion, is an area of research with great interest in the industry as it is desirable for the process to be as environmentally friendly as possible, coupled with further use of the ash being a possible economic incentive. The disposal of the fly ash is being investigated, with two of the main methods of disposal being used as a fertilizer and use as a filler material in cement/concrete. In order for deposit build up, possible corrosion mechanisms, and disposal of the fly ash to be comprehensively understood, profiling of the ash formed during biomass and coal co-firing must be conducted.

3 Materials and Experimental

3.1 Data Supplied by E.On

The following data were supplied by E.On to supplement the rig data collected during the combustion trials. Results were produced in house in a lab conforming to reccomendations presented in BS 17025:2005.[118] Sampling of the bulk fuel was undertaken as outlined in BS 14778[119] and prepared according to BS 14780.[120]

3.1.1 As Received Fuel Analysis

Analysis for moisture,[121] volatile matter,[122] fixed carbon,[123] calorific value,[124] sulphur, chlorine,[125] and hydrogen[126] were also provided for each fuel and the data are presented in Table 3-1. Things to note in particular are the large differences between moisture content of the fuels, and the high ash content of the hemp fuel in comparison to the other fuels. As is typical between biomass and coal, the coal has a much higher calorific value and fixed carbon than the biomass. These data represent partial analysis of the composition and therefore will not reach 100%.

Table 3-1: As received analysis for the fuels used in the combustion trials

	% As received		
	Kuzbass Coal	Hemp Fuel	Eucalyptus
Moisture	7.3	14.5	8.2
Volatile Matter	35.8	56.3	76.8
Fixed Carbon	48.2	13.00	14.40
Ash	8.7	16.2	0.6
Calorific Value (CV)	27440 (kJ/kg)	14050 (kJ/kg)	18570 (kJ/kg)
Sulphur	0.34	0.09	0.01
Chlorine	0.01	0.21	0.03
Hydrogen	4.48	4.43	5.63

3.1.2 Ash Analysis

The analysis presented in Table 3-2 shows the compositional data, presented as oxides, for each fuel matrix calculated according to EN ISO 16967[127] for Al, Ca, Fe, Mg, P, K, Si, Na and Ti and BS EN 15297[128] for Mn. Detection was carried out using Inductively Coupled Plasma – Optical Emission Spectroscopy (ICP-OES).[129] The elements analysed do not give the total composition (they do not add up to 100%). This indicates the presence of other elements or oxides (e.g. Cl), it is also likely as a result of high carbonate content.[130] The elements analysed are those considered of most interest in the co-firing trials. The calculation of the elemental composition is presented below:

$$w_i = \frac{(c_i - c_{i,0}) \times V}{m} x \frac{100}{(100 - M_{ad})}$$

Equation 3-1 : Calculation of % of element present

W_i = concentration of the element in the sample on a dry masis (mg/kg)

C_i = concentration of the element in the diluted sample digest (mg/l)

$C_{i,0}$= concentration of the element in the blank experiment (mg/l)

V = volume of diluted sample digest solution (ml)

m = mass of test portion (g)

M_{ad} = moisture content in the test sample (% m/m)

Table 3-2: Matrix Analysis of Fuel ash used in the combustion trials

	Result (wt%)		
Analyte	**Pulverised Kuzbass Coal**	**Hemp Fuel**	**Eucalyptus Fuel**
Al_2O_3	6.21	1.68	7.60
BaO	0.49	0.02	0.22
CaO	23.1	17.7	21.8
Fe_2O_3	4.50	0.84	5.13
K_2O	3.57	11.8	10.25
MgO	2.55	3.89	5.88
Mn_3O_4	0.57	0.17	2.03
Na_2O	1.52	0.32	2.52
P_2O_5	1.13	6.52	2.88
SiO_2	44.8	44.0	26.5
SO_3	3.53	1.44	2.53
TiO_2	4.07	0.11	0.33
Total	**96.04**	**88.49**	**87.67**

Conversion factors for the elements to their oxides are as follows, Al 1.89, Ca 1.40, Fe 1.43, Mg 1.66, Mn 1.29, P 2.29, K 1.20, S 2.50, Si 2.14, Na 1.35, Ti 1.67. These results are used as an integrity check in accordance with BS EN ISO 16993.[130]

Reproducibility and repeatability standard deviation was calculated and used in conjunction with data presented in Annex B in BS 16967.127 Repeatability (r) is calculated according to equations Equation 3-2 andEquation 3-3130

$$r = 2\sqrt{2} \times s_r = 2.8 \times s_r$$

Equation 3-2 absolute comparison of two measurements at repeatibility conditions

$$r = 2\sqrt{2} \times CV_r = 2.8 \times CV_r$$

Equation 3-3 Relatively comparison of two measurements at repeatability conditions

r = repeatability limit

s_r = repeatability standard deviation

CV_r = coefficient of the variation of repeatability

Reproducibility (R) is calculated according to equations Equation 3-4 and Equation 3-5[130]

$$R = 2\sqrt{2} \times s_R = 2.8 \times s_R$$

Equation 3-4 absolute comparison of two measurements at reproducibility conditions

$$R = 2\sqrt{2} \times CV_R = 2.8 \times CV_R$$

Equation 3-5 Relatively comparison of two measurements at reproducibility conditions

R = reproducibility limit

s_R = reproducibility standard deviation

CV_R = coefficient of the variation of reproducibility

These data are then used in comparison with round robin data, like that presented in Annex B of BS 16967127 and data within the repeatability and reproducibility parameters is accepted.

Table 3-3 shows the calculated compositional data, presented as oxides, for each co-fired blend presented in this study.

$$wt\% = \frac{(fuel\ 1\ \times \%mass\ of\ fuel1)}{100} + \frac{(fuel\ 2\ \times \%mass\ of\ fuel2)}{100}$$

Equation 3-6 calculation of co-fired blends ash composition

SiO_2 is higher in the Kuzbass coal and hemp fuel in comparison to the eucalyptus. The eucalyptus fuel has similar amounts of Al and Fe to the Kuzbass coal.

Table 3-3: Ash Matrix Analysis of the co-fired blends fuels used in the combustion trials

Analyte	Result (wt%)	
	Kuzbass coal (23% by mass) and hemp	**Kuzbass coal (12% by mass) and eucalyptus**
Al_2O_3	2.72	7.28
BaO	0.13	0.28
CaO	18.94	22.10
Fe_2O_3	1.68	4.99
K_2O	9.91	8.71
MgO	3.58	5.11
Mn_3O_4	0.26	1.69
Na_2O	0.60	2.29
P_2O_5	5.28	2.48
SiO_2	44.18	30.71
SO_3	1.92	2.76
TiO_2	1.02	1.19
Total	**90.22**	**89.59**

3.2 The Combustion Rig

Hemp, eucalyptus, wood, and coal samples were fired in a 0.8MW_{th} combustion test rig (Figure 3-1). Ash samples were taken from the ash hopper (a), the end of probes (b), the ceramic probes (c), and superheater region quenched (d), as well as the cyclone (e).

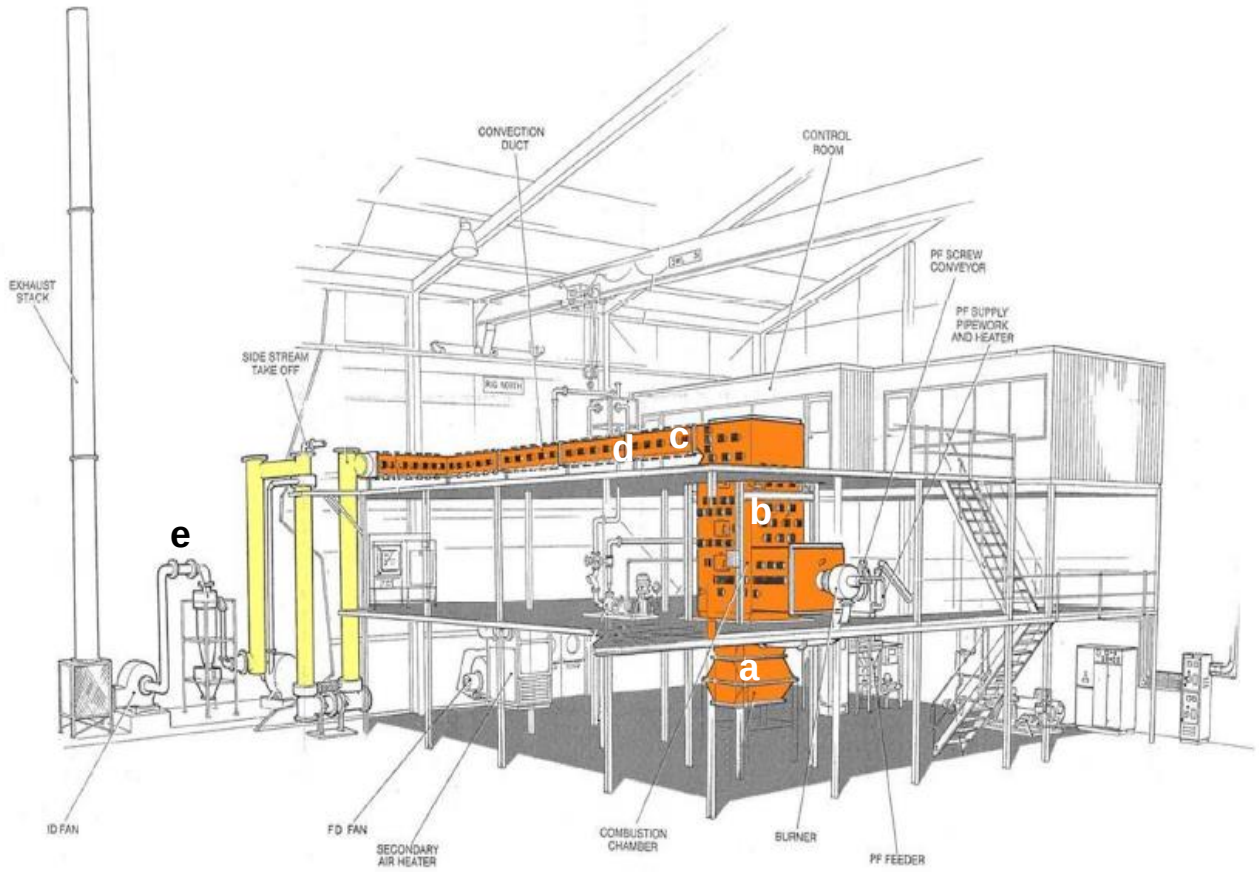

Figure 3-1: A schematic diagram of the 0.8MWth combustion rig[246] a) ash collection hopper b)combustion probe coupons c) ceramic probes d) quenched ash e) the cyclone

Figure 3-1a: Ash Collection Hopper

Figure 3-1 b: Corrosion coupon probes

Figure 3-1c: Ceramic probe inserted into the combustion rig to collect deposits

Figure 3-1d: Apparatus used to collect samples quenched in water

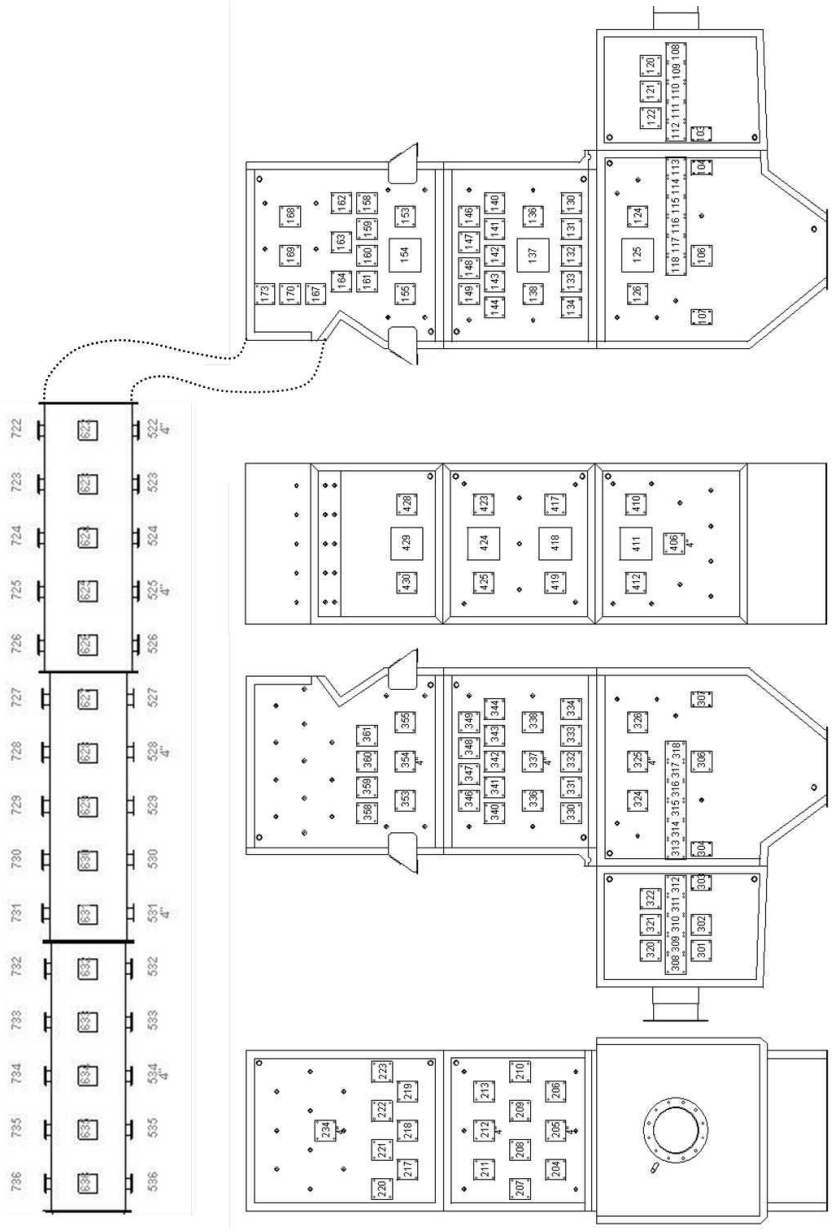

Figure 3-2: A Schematic Diagram of the boiler and the ports used in the combustion run.

Figure 3-2 is a schematic diagram of the combustion rig showing the ports used for sample collection. Ports 522-740 correspond with the superheater regions of the combustion rig, ports 101-440 correspond with the boiler region of the combustion rig.

3.2.1.1 Corrosion Coupon Probes

Corrosion coupons were used to assess the amount of corrosion that alloys used in the test runs undergo. Corrosion coupons of 15Mo3 (measured composition in Table 3-4) were analysed, sometimes coated, and bare metal surface ground to a 0.4RA surface finish. These coupons were inserted into the boiler ports (Figure 3-2,) flush with the lining of the boiler so as to experience the same gas and temperature conditions that would be experienced in a full scale operation; these conditions were also used to minimise deviation of gas flow. The mechanisms securing the coupons in the probe were lubricated using Belzona 8211 (H.P. Anti-Seize) mineral based nickel grease. A Eurotherm temperature controller with a continuously variable output was used to drive a proportional air throttle valve, enabling the flow of cooling air to the probe to be regulated.

Table 3-4: Measured composition of the 15Mo3 alloy used for the corrosion test probes

	Wt %					
Alloy	**Cr**	**Mn**	**Fe**	**Ni**	**Mo**	**Cu**
15Mo3	0.22	0.48	98.59	0.24	0.29	0.18

Table 3-5: Corrosion Probe Test Matrix for Hemp and Coal Combustion Test

Probe	Port Number	Material	Target Temperature(°C)
HEMP A	325	15Mo3	475
HEMP B	331	15Mo3	450
HEMP C	419	15Mo3	425
HEMP D	409	15Mo3	475
HEMP E	410	15Mo3	475
HEMP F	417	15Mo3	475
HEMP G	117	15Mo3	450
HEMP H	116	15Mo3	425

Table 3-6: Corrosion Probe Test Matrix for Eucalyptus and Coal Combustion Test

Probe	Port Number	Material	Target Temperature (°C)
EUCCO A	318	15Mo3	475
EUCCO B	333	15Mo3	450
EUCCO C	419	15Mo3	425
EUCCO D	409	15Mo3	475
EUCCO E	408	15Mo3	475
EUCCO F	410	15Mo3	475
EUCCO G	117	15Mo3	450
EUCCO H	116	15Mo3	425

Table 3-7: Composition of the coatings applied to EUC A-N

						%					
Coatings	**Al**	**Si**	**Cr**	**Mn**	**Fe**	**Ni**	**Nb**	**Mo**	**W**	**Y**	**O**
FeCrAl	8	0.4	23		65.1						3.4
IN625		0.4	19.2		3.5	58.7	3.4	9.4			4.4
NiCrAlY	9	0.4	21.9		3.6	62.8				1	1.3
50Cr50Ni	0.2	2.3	42.1		5.7	44.6					3
Claddings	**Al**	**Si**	**Cr**	**Mn**	**Fe**	**Ni**	**Nb**	**Mo**	**W**	**Y**	**O**
FeCrAl	4.6	0.9	17.9	0.8	75.9						
IN625		0.7	21.3	0.5	3.4	60.6	4	9.9			
50Cr50Ni		2.6	44.7		4.6	48.2					
C276		0.6	14.1	1.2	8.6	53.2		16.9	4.7		

Table 3-8: Corrosion Probe Test Matrix for Eucalyptus Combustion Test Red denotes coating application using HVOF method Blue denotes coatings applied using the laser cladding method Table 3-7 gives the coating compositions

Probe	Port Number	Material	Mean surface Temperature (°C)
EUC A	317	15Mo3 (FeCrAl + IN625)	400
EUC B	318	15Mo3 (NiCrAlY + 50Cr50Ni)	400
EUC C	324	15Mo3 (FeCrAl + IN625)	425
EUC D	325	15Mo3 (NiCrAlY + 50Cr50Ni)	440
EUC E	326	15Mo3 (FeCrAl + IN625)	440
EUC F	333	15Mo3 (NiCrAlY + 50Cr50Ni)	450
EUC G	334	15Mo3 (FeCrAl + IN625)	485
EUC H	419	15Mo3 (NiCrAlY + 50Cr50Ni)	475
EUC I	412	15Mo3 (FeCrAl + IN625)	425
EUC J	409	15Mo3 (50Cr50Ni + C276)	425
EUC K	411	15Mo3 (FeCrAl + IN625)	500
EUC L	406	15Mo3 (50Cr50Ni + C276)	435
EUC M	408	15Mo3 (FeCrAl + IN625)	500
EUC N	410	15Mo3 (NiCrAlY + 50Cr50Ni)	450

3.2.1.2 Ash Quenching

A probe was inserted into rig port 722 or 740 (Figure 3-2), water was pumped through the probe and ash extracted through the probe, then quenched into a conical flask, this ash was then separated by filtration. Samples and collection time are listed in Table 3-9 to 3-11.

Table 3-9: Hemp and Kuzbass Coal Ash Quenching

Sample	Duration
H722-2	71 minutes
H740-6	30 minutes
H722-7	118 minutes
H740-10	86 minutes

Table 3-10: Eucalyptus and Kuzbass Coal Ash Quenching

Sample	Duration
EC740-4	105 minutes

Table 3-11: Eucalyptus Ash Quenching

Sample	Duration
E740-2	120 minutes
E740-3	120 minutes
E740-5	120 minutes
E740-8	120 minutes
E740-10	120 minutes
E740-11	120 minutes
E722-13	120 minutes

3.2.1.3 Ceramic Probe Samples

Ceramic probes were inserted into the rig at ports 722, 727, or 728 (Figure 3-2). Samples are listed in Table 3-12-14. Samples were removed and air cooled before being stored. Differing sampling times for the first two combustion tests are due to combustion trials being used for multiple purposes; proper protocols were established in later trials.

Table 3-12: Hemp and Kuzbass Coal Ceramic Probe Deposit Samples

Sample	Duration	Temperature (°C)
H722-3	38 minutes	971
H727-4	57 minutes	Not Available
H722-8	66 minutes	1013
H727-9	58 minutes	980

Table 3-13: Eucalyptus and Coal Ceramic Probe Deposit Samples

Sample	Duration	Temperature (°C)
EC722-1	163 minutes	978
EC728-5	202 minutes	914
EC722-6	184 minutes	1012
EC729-8	117 minutes	932

Table 3-14: Eucalyptus Ceramic Probe Deposit Samples

Sample	Duration	Temperature (°C)
E722-1	120 minutes	962
E722-4	120 minutes	968
E722-6	120 minutes	1015
E722-7	120 minutes	Not Available
E722-9	120 minutes	1045
E722-12	120 minutes	1040
E722-14	120 minutes	1045 (30 mins after sampling)

3.3 Combustion Conditions

Knowledge of the combustion conditions allows greater context to be given to the results. Table 3-15 gives information about the air composition, fuel blends, and feed calculations given for the fuel trials

Table 3-15: Combustion conditions for the corrosion test runs

	Hemp and Coal	**Eucalyptus and Coal**	**Eucalyptus**
Burner	Low NO_x coal	Low NO_x coal	Low NO_x coal
Overfire Air	15-22%	9-21%	13-16%
O_2	1.5-2.5%	1.4-2%	0.9-3.5%
Fuel	40:57% coal + 59:43% hemp	12% coal + 88% eucalyptus	100% eucalyptus
Feed	41.8 kg/h Kuzbass coal + 140.10 kg/h hemp	18.89 kg/h Kuzbass coal + 138.5 kg/h eucalyptus	168 kg/h eucalyptus

3.4 Furnace Procedure for Ashing

Into an oven dried (105°C) porcelain crucible, biomass (approx. 1g) was added. The crucibles were heated in a furnace to 150°C for one hour, 250°C for two hours, 450°C for 90 minutes, 575°C for 3 hours and then cooled to 105°C. The samples were cooled in a dessicator, then weighed and returned to the oven at 575°C for 1 hour until a constant weight (±3mg) was obtained. Coal was also ashed using this method.

3.4.2 High Temperature Heat- Treatments of the ash

After initial ashing (Section 3.5.1) the biomass, coal, and blends were further heated. The samples were heated in a Pt crucible from 600-1100°C at 100°C increments for one hour, a small portion of the sample was removed and the crucible was returned to the furnace.

3.5 Materials Characterisation Techniques

3.5.1 X-Ray Diffraction (XRD)

Powder-XRD has been selected to identify the phases present in each sample. PXRD is a powerful technique to carry out this, due to the large and extensive database of powder diffraction patterns housed in the International Centre for Diffraction Data (ICDD) Powder Diffraction File (PDF).

Samples were prepared by grinding to a powder in a mortar and pestle and mounted either in a silicon miniwell or made as a smear between 2 layers of Scotch Tape™. Where there was too little sample to analyse using the above preparative methods, a suspension of sample in acetone was placed on silicon wafers. LaB_6 (ICDD card: 34-427) was occasionally used as an internal standard due to sample mounting difficulties. PXRD data were collected using 3 different powder X-ray diffractometers: either a Bruker D8 Advance in reflection geometry using Cu $K\alpha_1$ radiation and a LYNXEYE ™ 1D detector, a Bruker D2 Phaser in reflection geometry using Cu Kα radiation and a LYNXEYE ™ 1D detector, or a Bruker D8 Discover in transmission geometry using Co $K\alpha_1$ radiation and a Braun Position Sensitive detector. Data was collected on the D8 Advance over the 2θ range 5-60˚ with a step size of 0.013˚ 2θ and a count time of 0.55s per step, and on the D2 over the 2θ range 7-60˚ with a step size of 0.012˚ 2θ and a count time of 0.122s per step. Phases in the samples were identified using the STOE WinXPOW software suite and the ICDD 2011 database.

The high temperature XRD data were collected using a Nonius PDS 120 diffraction system consisting of an Inel-curved, position-sensitive detector within a static beam-sample-detector reflection geometry[131]. This system allowed for the simultaneous measurement of diffracted X-ray intensities at all angles of 2θ across 120°. A 100-μm-diameter beam was selected from a 300-μm-diameter primary beam by a pinhole at the end of a collimator evacuated tube to reduce air scattering. High brightness Cu Kα radiation was generated by a GeniX system with a Xenocs FOX2D CU 10_30P mirror operating at 50 kVand 1 mA. Silicon and silver behenate were used as external standards. The sample was loaded onto an Anton Paar HTK10 high temperature attachment. Calibration and data collection were performed using Diffgrab™. Data were collected every 100ºC on heating, with an average data collection time of 180 min. The instrumentation description was taken from.[132]

Samples collected on the I-11 beamline at the Diamond Light Source are also presented. Data collection method is noted at the bottom of each XRD pattern presented. The use of the I-11

beamline allows resolution of the complex phases identified in the samples due to the variety of the sample matrix. Samples were ground in a pestle and mortar, the resulting powder was packed into 0.3mm capillaries and mounted onto brass sample holders using wax and superglue.

Samples were then placed on the auto-carousel which mounted the samples onto a spinner on the θ circle. The data were then collected on both the MAC detectors mounted on the 2θ circle, and the PSD mounted on the δ circle. Wavelengths used for collection were PSD 0.826215 and MAC 0.82675.

3.5.1.1 Phase detection limitations

The limit of detection for XRD diffraction is commonly defined as the equivalent of two standard deviations of the observed background level[133]. It is commonly cited to be anywhere between 1-5%[133]. Synchrotron radiation due to a higher signal to noise ratio and intensity can have a limit of detection as low as 0.2%[134]. Where possible synchrotron data has been used for analysis. Collection method is noted in figure captions.

3.5.1.2 Topas Procedure

A diffraction pattern was collected for the Si standard using the PSD detectors on the Diamond I-11 beamline. The pattern was then used for a Pawley fit using the parameters from ICDD card 27-1402. The fitted pattern gave peakshape information:

TCHZ_Peak_Type
pku,-0.00022
pkv, -0.00042
pkw, -0.00051
pkz, 0.00058
pky, 0.01171
pkx, 0.00254`
Simple_Axial_Model axial, 2.30888

This information was used as a peakshape model in the initial refinement of the data.

The ICDD cards for the phases that were identified in the qualitative analysis of the data were used as starting input for the Pawley fit. The number of background parameters was varied until a good fit was achieved (i.e. no deviation from the pattern). Each phase was entered

individually with fixed peakshape parameters. These peakshapes were then refined one by one (axial peakshape was not refined as it remains constant) and finally all together. Lattice parameters were checked against the ICDD cards to check that there were no significant changes. The calcite was refined using the hexagonal setting of the rhombahedral space group. Once the parameters had converged and no significant changes in r_wp (the weighted profile factor) and closeness to the r_exp (expected R factor, the best case-scenario) occurred the peakshapes were fixed and the Rietveld refinement was started. The goodness of fit (gof) is calculated using the Equation 3-7. The closer the gof gets to 1, the closer the refinement. Pawley fit data is presented in Table 3-16

$$X^2 = (R_{wp}/R_{exp})^2$$

Equation 3-7 calculation of the goodness of fit

Table 3-16: Pawley fit parameters for the refinement of the high temperature heat treatment of the hemp ash

Lab ash at Temperature (°C)	r_wp	r_exp	gof
600	3.89	1.53	2.54
700	4.58	1.61	2.84
800	4.26	1.58	2.71
900	4.49	1.34	1.49
1000	2.09	1.4	1.49
1100	1.92	1.27	1.51

.cif files were obtained from the American Mineralogist Crystal Structural Database[135]**.**
The lattice parameters and peakshapes that were refined in the Pawley fit were used in conjunction with the atom position information from the cif files. The refinement was run for each phase with the atom positions, lattice parameters, and peakshape all fixed. The peakshape for each phase was then refined. Atom positions were then refined according to the Wyckoff positions. Thermal parameters were fixed at 1.

Table 3-17: Rietveld fit parameters for the refinement of the high temperature heat treatment of the hemp ash

Lab ash at Temperature (°C)	r_wp	r_exp	gof
600	6.30	1.75	3.61
700	6.52	1.84	3.54
800	5.62	1.58	3.05
900	6.35	1.76	3.59
1000	3.42	2.02	1.69
1100	3.2	2.02	1.59

3.5.2 Scanning Electron Microscopy (SEM)

SEM was used to determine the morphology and size of the particles in the samples, information on morphology can give insights into how particles may travel through a system. SEM can also be used to show how samples change in the different environments of the combustion rig through monitoring the shape and degree of agglomeration.
Samples were prepared by mounting pre-ground samples on carbon pads attached to aluminium stubs, followed by gold coating for 30s using a gold sputter coater. Leo-Zeiss 1530 VP Field emission gun SEM was used for analysis at 5kV, aperture size 30µm using an SE2 detector.

3.5.3 Energy Dispersive X-ray Spectroscopy (EDS)

SEM-EDS was used to show regions of closely occurring elements and map elemental variation across samples, this was used alongside PXRD to allow swift phase identification. Leo-Zeiss 1530 VP Field emission gun SEM was used for analysis at 20kV, 60µm aperture size, working distance 8.5mm using an SE2/ backscatter detector. Energy dispersive X-ray spectroscopy (EDS) using Oxford Instruments X-Max 80mm^2 Detector. Aztec software was used for analysis. Both mapping and whole sample spectral analysis were used.

This technique has several limitations, there is a limit of detection of 1000-3000 ppm and only elements heavier than Be can be analysed. The spatial resolution of elements is atomic number dependent with higher atomic number having a resolution of 0.2-1 µm^3 and lower having a resolution of 1-5 µm^3. The accuracy of the EDS analysis is ±5% for the ash samples analysed due to the rough surface of the particulate. A high accelerating volume was used and as such spatial resolution was decreased as the X-rays were generated from deeper in the samples.

3.5.4 Micro X-Ray Flourescence (XRF)

To complement the analysis performed by E.ON for the ash composition analysis, samples were prepared by grinding to a powder in a pestle and mortar. SPEX™ SamplePrep Prep-Aid™ Grinding Aid was added in a 10-20% ratio to allow pelletisation. Pelletisation was performed in a Specac 15T manual hydraulic press using a 10mm pellet die. Pellets were pressed for 3 minutes at 10T.

Data was collected using an EDAX Orbis Micro XRF analyser in vacuum mode whilst applying Rh-tube radiation (40kV and 300µA). The x-ray primary beam was focused to a spot of 2mm

diameter. Analysis of two sites per sample disc was used, data is presented as an average with e.s.d of both sites. No beam filter was used except for the quantification of Cl where a 250µm Al filter was used to eliminate Rh interference (peak overlaps ClK 2.622, RhL 2.697, illustrated in Figure 3-3). Results were recorded using the Orbis Vision Software.

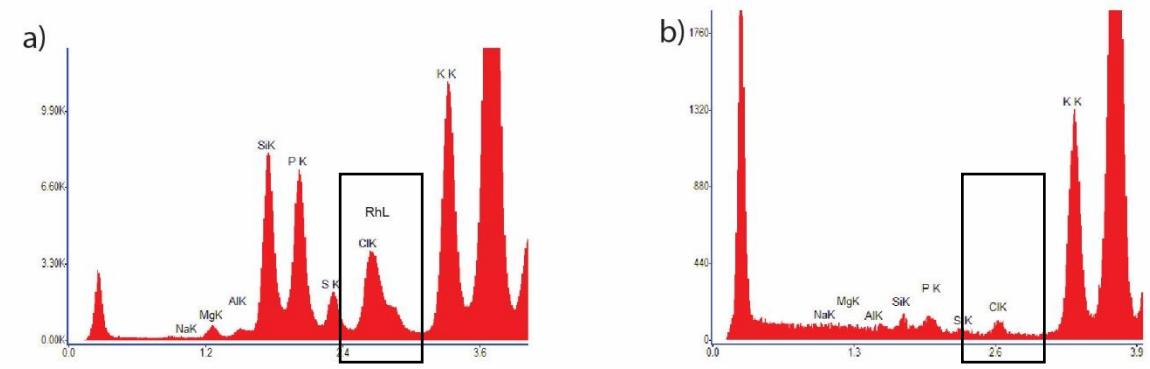

Figure 3-3: A comparison of XRF spectra a) without a filter and b) with a 250um Al filter to remove Rh 3/interference with Cl

Results of the ash analysis are presented in Table 3-18. There is variation between the composition presented here and those presented in Table 3-2 and 3-3. The most significant variation is between the Si contents of the hemp ash and the hemp and coal ash which are much lower than those determined by ICP. The Ca also shows variation in comparison to the ICP results.

One study which accounts for discrepancy between the ICP-OES results from E.On and the XRF results can be attributed to the conclusion drawn by Xing *et al.*[136] who state that biomass ash prepared at 550°C can give inaccurate results from XRF analysis owing to significant unburnt carbon retained in the ash. This means that the results should be used in conjunction when looking at the lower temperature ashes i.e. up to 800°C. The temperature 800°C is used here as they also state that use of an ashing temperature above 800°C is more suitable for XRF testing. Therefore the XRF results for the laboratory high temperature ash (Chapter 4) and the deposits, quench and cyclone ashes (Chapter 5) can be used as stand alone as they are comparable to those produced using wet digestion[136].

Variations between the provided data and the collected data can be accounted for through the ashing procedure. In house ashing was undertaken using a different method than BS 18122[137]. The key differences between the two methods which accounts for the variation in Ca and Si present are the absence of a lid in the ashing procedure of the provided results, which may have resulted in the volatilisation of Ca in the samples giving a lower composition than observed in the collected data. A further difference is the loading of the ashing container in

the in house collected data exceeded 0.1g/cm^3 of the bottom area, increasing the chance of incomplete incineration of the lower layer of biomass and increasing the CO_2 absorption onto the top ash layer which increases the likelihood of $CaCO_3$ formation in calcium rich samples.[137] This in turn could change the amount of Ca present in the samples for the analysis and as such accounts for the data variation between provided and collected data.

These variations should be anticipated as BS 16967 states that unless the ashing procedure is performed exactly as in BS18122[137] methodical deviations will influence the results.[127] As such general comparisons, e.g. trends between the data sets can be drawn however direct comparison, e.g. Ca content should be used with caution. Comparison with combustion rig data can be drawn from both data sets as the ash formation mechanism in the combustion rig is vastly different to either the provided data or the collected data.

There are also significant differences between the calculated results for the biomass and coal blends (Table 3-5) and those determined using XRF. This is due to one set being calculated and one set being measured. The calculation does not account for ash matrix reactions.

Calibration of the results was performed using the 'no standards fundamental parameters(FP)' approach, incorporated into the software. Fundamental parameters (FP) were first proposed in 1955[138] and are based on the characteristic spectral line radiation emitted by an analyte and the concentration[139]. The FP algorithm solves non linear equations which describe the intensity variation via concentration and layer thickness for each element[140]. It is cited as accurate for both layered and bulk samples[140]. A stored reference for each pure element is stored after measurement by the instrument manufacturer, this is then used by the algorithm to create a reference intensity ratio[139]. The EDAX algorithm is patented[141] and has a non disclosed method for the quantitative method of FP using a standardless method. Further information on the instrument and software can be found in the 'X-Ray Flourescence Metrology Tools' guide provided by EDAX[142].

Results of the ash analysis are presented in Table 3-18.

3.6 Synthesis of Akermanite

Diopside ($CaMgSi_2O_6$, 0.5580g) and calcite ($CaCO_3$, 0.2807g) were ground together in a pestle and mortar. The mixture was placed in a Pt crucible and heated to 900°C for 1 hour. The sample was then heated to 1000°C for 1 hour, followed by a final heating to 1100°C for 1 hour. The samples were then analysed using PXRD and diopside, akermanite, larnite, and lime were identified.

Table 3-18: Elemental composition of the ash of biomass fuels presented in this thesis as determined by XRF

Analyte	Kusbass Coal	Hemp	Eucalyptus	Hemp and Coal	Eucalyptus and Coal
Al	15.24 ±0.21	0.95 ±0.03	4.86 ±0.11	4.01 ±0.16	10.54 ±0.08
Ca	8.52 ±0.37	39.95 ±0.47	36.70 ±0.64	31.91 ±0.01	17.75 ±0.13
Cl	0.13 ±0.02	1.32 ±0.11	0.11 ±0.00	0.94 ±0.04	1.02 ±1.17
Fe	11.13 ±0.62	1.41 ±0.04	9.61 ±0.33	3.13 ±0.02	11.93 ±0.49
K	3.53 ±0.08	14.62 ±0.86	11.24 ±0.18	13.91 ±0.13	7.81 ±0.01
Mg	2.38 ±0.31	6.81 ±0.46	6.03 ±0.33	5.27 ±0.19	2.81 ±0.05
Mn	0.12 ±0.00	0.38 ±0.01	4.02 ±0.14	0.34 ±0.00	1.28 ±0.01
Na	1.11 ±0.37	0.88 ±0.16	0.70 ±0.98	0.78 ±0.25	1.23 ±0.10
Ni	0.03 ±0.01	0.07 ±0.00	0.09 ±0.01	0.02 ±0.00	0.04 ±0.01
P	1.59 ±0.12	13.56 ±0.23	4.25 ±0.13	11.94 ±0.05	2.48 ±0.02
S	11.16 ±0.13	2.22 ±0.16	2.55 ±0.05	4.55 ±0.21	9.16 ±0.08
Si	43.17 ±0.49	13.41 ±0.23	16.92 ±0.21	23.41 ±0.49	31.25 ±0.35
Sr	0.49 ±0.04	0.11 ±0.00	0.39 ±0.00	0.18 ±0.01	0.39 ±0.03
Ti	1.41 ±0.03	0.47 ±0.37	0.92 ±0.03	0.42 ±0.06	1.35 ±0.01
Zn	0.08 ±0.01	0.16 ±0.01	0.28 ±0.01	0.10 ±0.01	0.14 ±0.00
Zr	0.08 ±0.00	0.05 ±0.00	0.02 ±0.01	0.07 ±0.04	0.05 ±0.01
Total	**100.14**	**96.33**	**98.66**	**100.94**	**99.20**

4 Laboratory Ashing Studies of Selected Biomass Fuels, Hemp, Coal and Eucalyptus and their blends

Fuel characteristics such as calorific value, elemental composition, and the presence of heavy metals (e.g. Cd, Pb, and Zn) can give important information into the feasibility for large scale combustion. Ash behaviour, including the formation of corrosive phases and the melting temperature (high or low) of silicates will give insight into the potential deposition areas, and therefore likely areas of corrosion in a full scale power plant. It is advisable that fuel should be investigated prior to full application, with the IEA Bioenergy Taskforce 32 publishing a report into advanced characterisation of solid biomass fuels.[143]

Vassilev *et al*.,[15,27,31,42,144] published multiple reviews of the current state of biomass ash research, giving indications of phases present and formation temperatures. The information gathered about phase transformations in the ash can also be used to identify phases that may cause issues during combustion, e.g. K-Silicates with low melting temperatures which can increase the likelihood of slagging and fouling. Information on phases formed at high-temperature can also compliment research into the use of biomass ash disposal or utilisation.

Vassilev *et al*.[144] noted that as woody biomass typically has a lower ash content than conventional fossil fuels, they will be of benefit in energy production as less fouling, deposition, and agglomeration will be observed. They also noted however, that the highly variable composition of biomass ash between different sources of biomass can lead to problems when predicting where slagging and fouling are likely to occur.

A further study by Vassilev *et al*.[15] indicates that the higher Ca, K, Mg, Mn, Na, P, carbonates, chlorides, and phosphates values, and lower Al, Fe, N, S, Si, Ti, oxyhydroxides, and silicates compared to coal are responsible for the lower ash fusion temperature of biomass. This lower ash fusion temperature can in turn lead to the formation of low temperature melts. One of the most cited methods of predicting whether a fuel will foul or slag is the alkali index Equation 4-8, where m = weight % in the ash).[145]

$$\frac{mFe_2O_3 + mCaO + mMgO + mK_2O + mNa_2O}{mSiO_2 + mTiO_2 + mAl_2O_3}$$

Equation 4-8

The alkali index, typically expressed by alkali metal oxide mass per unit fuel energy produced thermally (GJ) is often used in conjunction with modelling to predict boiler furnace slagging.[146–

[148] Fuels with alkali index below 0.17kg/GJ are of low fouling and slagging index whereas those with an index above 0.34 kg/GJ are likely to foul severely.[147]

Fuels can also be ashed under laboratory conditions to determine the fate of elements considered important due to their potential to foul boilers and propagate corrosion; high interest elements such as K,Cl, and S are often monitored. Niu *et al*.[149] investigated capsicum stalks, cotton stalks, and wheat stalks over the temperature range 1000-1400°C to observe the speciation of these elements at high temperature. Suarez-Garcia *et al*.[150] characterised ash formed from vegetable biomass feedstocks using PXRD and Fourier transform infrared spectroscopy (FTIR); at low temperatures (373 – 427K) quartz, carbonates, halites and phosphates were found to dominate, whereas at higher temperatures (823K) other transformations were observed.

XRF data for each of the fuels was collected and is presented in Table 4-1. The difference between the data provided by E.On (Table 3-2) and the data collected using XRF can be attributed to both the presence of unburnt carbon in the ash matrix produced at 575°C and the difference in the ashing methods (previously discussed in section 3.5.3). This carbon may also be present as carbonates, which are identified in X-ray diffraction data. It has previously been shown that XRF analysis of biomass ash heated below 800°C can be inaccurate due to retained unburnt carbon[136]. When comparing the results of ash formed at 575°C and 900°C XRF data is used as comparison is for the general trends.

Table 4-1: XRF data for the composition of the fuel ashes

Analyte	Kusbass Coal		Hemp		Eucalyptus		Hemp and Coal		Eucalyptus and Coal	
Al	15.24	±0.21	0.95	±0.03	4.86	±0.11	4.01	±0.16	10.54	±0.08
Ca	8.52	±0.37	39.95	±0.47	36.70	±0.64	31.91	±0.01	17.75	±0.13
Cl	0.13	±0.02	1.32	±0.11	0.11	±0.00	0.94	±0.04	1.02	±1.17
Fe	11.13	±0.62	1.41	±0.04	9.61	±0.33	3.13	±0.02	11.93	±0.49
K	3.53	±0.08	14.62	±0.86	11.24	±0.18	13.91	±0.13	7.81	±0.01
Mg	2.38	±0.31	6.81	±0.46	6.03	±0.33	5.27	±0.19	2.81	±0.05
Mn	0.12	±0.00	0.38	±0.01	4.02	±0.14	0.34	±0.00	1.28	±0.01
Na	1.11	±0.37	0.88	±0.16	0.70	±0.98	0.78	±0.25	1.23	±0.10
Ni	0.03	±0.01	0.07	±0.00	0.09	±0.01	0.02	±0.00	0.04	±0.01
P	1.59	±0.12	13.56	±0.23	4.25	±0.13	11.94	±0.05	2.48	±0.02
S	11.16	±0.13	2.22	±0.16	2.55	±0.05	4.55	±0.21	9.16	±0.08
Si	43.17	±0.49	13.41	±0.23	16.92	±0.21	23.41	±0.49	31.25	±0.35
Sr	0.49	±0.04	0.11	±0.00	0.39	±0.00	0.18	±0.01	0.39	±0.03
Ti	1.41	±0.03	0.47	±0.37	0.92	±0.03	0.42	±0.06	1.35	±0.01
Zn	0.08	±0.01	0.16	±0.01	0.28	±0.01	0.10	±0.01	0.14	±0.00
Zr	0.08	±0.00	0.05	±0.00	0.02	±0.01	0.07	±0.04	0.05	±0.01
Total	**100.14**		**96.33**		**98.66**		**100.94**		**99.20**	

4.1. Hemp

Competition for land use between food, animal feed, and energy production is high. This means crops with the best energy yield per hectare are selected for growth for use as biomass.[151] Annual biomass, biomass in which the whole plant can be used for energy production, and crop rotation (alongside food and feed) have been identified as critical.[151] Hemp (*Cannabis Sativa L.)* previously cultivated for fibre production, fits the above criteria as a biomass suitable for energy production. The hemp fibre cultivation process does not require excessive pesticide use, as it is a natural weed suppressant.[151,152] Its natural resilience means it is also suitable for growth in multiple climates around the world.[153] Hemp has been reported to grow 50cm/month with the leaf shedding increasing the organic matter in the surrounding soil and improving its quality.[154]

Hemp cultivation has been widespread for the past 5000 years.[154] EU legislation prevented the growth of hemp for around 40 years due to the presence of d-9-tetrahydrocannibinol (THC).[154] Much investigation into breeding hemp cultivars with low THC content has occurred since a legislation change in 2001.[153] This legislation states that crops with a THC content below 0.2% may be grown; in the UK this is subject to license.[155]

4.1.1 Hemp Fuel

PXRD data (Figure 4-1) collected on the unburnt pulverised hemp fuel has two broad peaks in the 15-25° 2θ region, which can be identified as the poorly crystalline cellulose, hemi-cellulose, and lignin.[156] Crystalline phases are also present in the fuel and have been identified as SiO_2 (quartz), $CaCO_3$ (calcite), CaC_2O_4 (calcium oxalate), and $KAlSi_3O_8$ (microcline), which is thought to be extraneous in origin (from the soil/ collected during the harvesting process). The speciation of silica in plants is complex and yet to be fully understood. It is widely accepted that Si is usually taken up as orthosilicic acid ($Si(OH)_4$). The pathways it takes before final deposition in the cells are still under investigation.[157]

SEM imaging (Figure 4-2) of the hemp fuel shows a distinct fibrous nature to the un-ashed fuel, also present on the surface of the fuel are large thorn- like structures, thought to be trichomes (small epidermal protrusions).[158] EDS analysis of these structures (Figure 4-3) shows them to be largely comprised of Si, O, Mg, and Ca with P, S, Cl, and K present in smaller quantities. Carbon is also present in the spectra. However as the fuel is stuck on a C sticky pad it is not possible to distinguish from the background.

SEM-EDS (Figure 4-4) analysis of the raw fuel also shows the presence of crystals with the main composition of Ca, C, and O. This could indicate the presence of CaC_2O_4 (calcium oxalate) or $CaCO_3$ (calcium carbonate); both are present in the XRD data. The presence of CaC_2O_4 in hemp has been well established[159] with K content affecting the size and shape of the oxalate crystals.

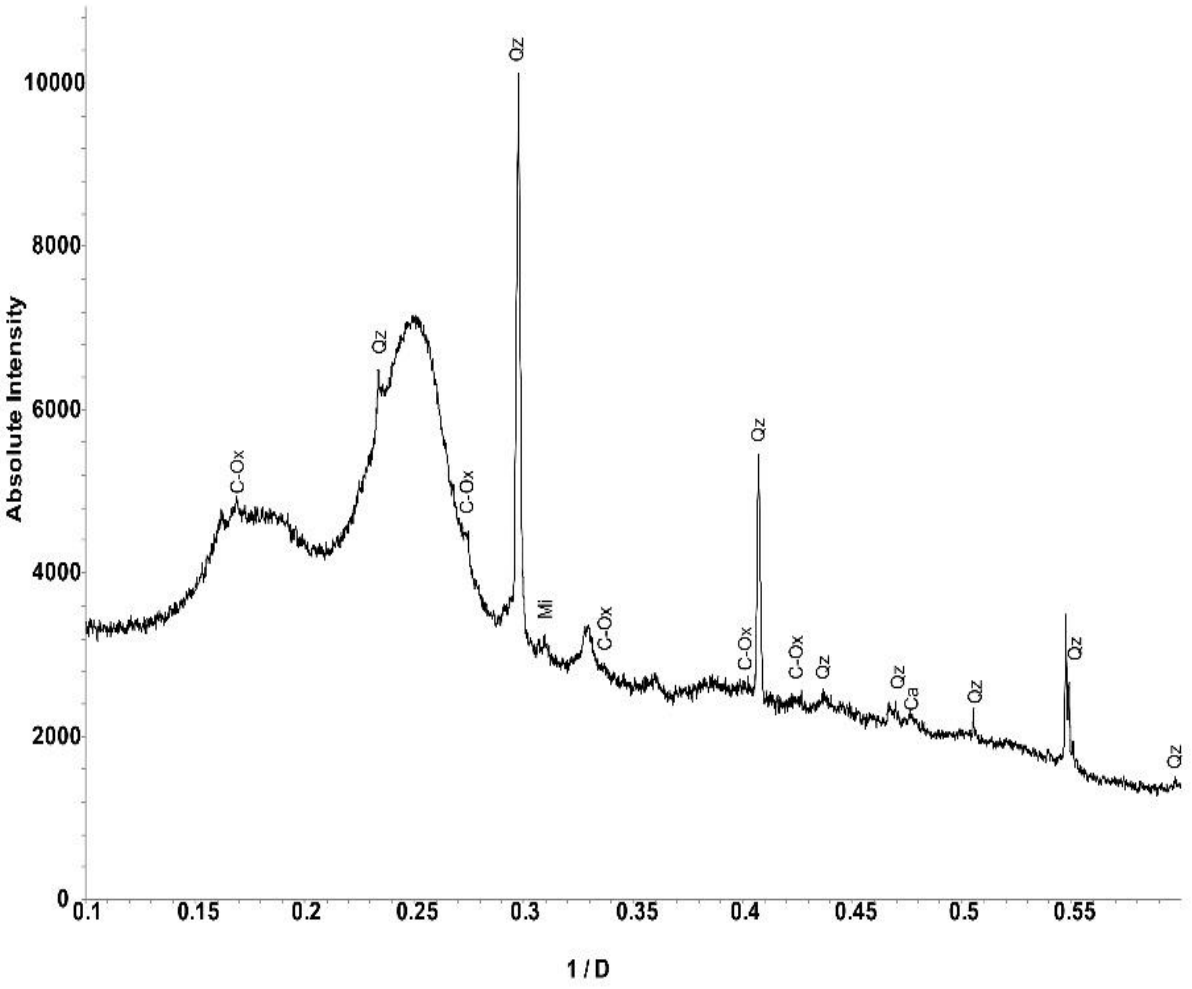

Figure 4-1: XRD Pattern for the raw hemp fuel collected on the D2 diffractometer Cu Kα radiation (Qz- quartz, Ca - calcite, C-Ox- calcium oxalate Mi - microcline)

Figure 4-2: Electronmicrograph of raw hemp fuel showing a clear organic matrix i.e. the fibrous nature, with trichomes, large silicate structures attached

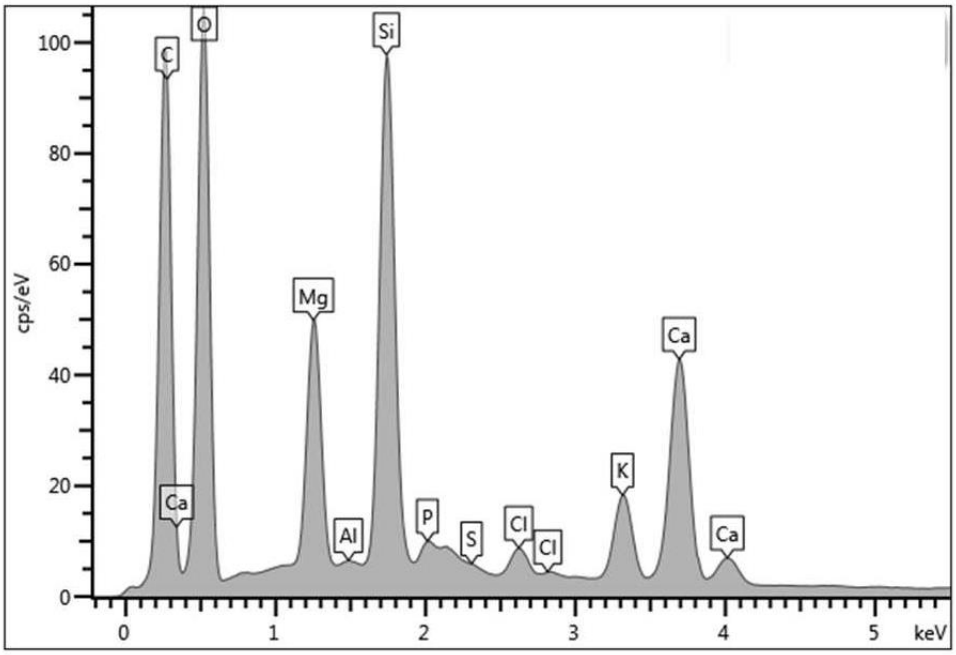

Figure 4-3: Au coated EDS spectrum of the trichomes in the raw hemp fuel

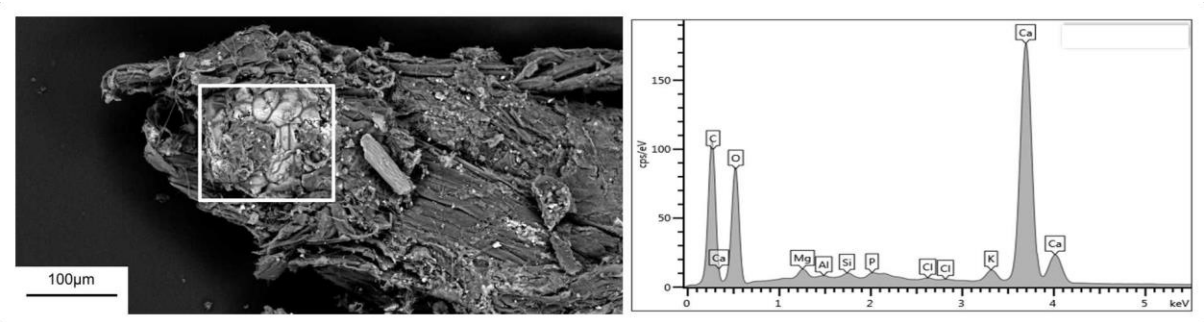

Figure 4-4: Electronmicrograph of crystals present in the raw hemp fuel with EDS spectrum showing the composition

4.1.2 Hemp Ash

Hemp was ashed according to the procedure outlined in Section 3.5.1. After ashing, the organic components (cellulose, hemi-cellulose, and lignin) were removed with the inorganic ash components remaining. Analysis of the PXRD data (Figure 4-5) shows the collected patterns for the hemp ash after heat treatment at 600-1100°C with Table 4-2 showing the phases present at each temperature.

PXRD analysis of the ash showed the presence of SiO_2 (quartz), in agreement with the Si identified in the fuel ash (Table 3-18, Table 3-2). $CaCO_3$ was present after ashing and could be present in the fuel itself or through decomposition of CaC_2O_4 (Equation 4-2, Equation 4-10)

$$CaC_2O_4 \xrightarrow{500°C} CaCO_3 + CO$$

Equation 4-9

$$2CaC_2O_4 + O_2 \xrightarrow{420°C} 2CaCO_3 + 2CO_2$$

Equation 4-10

The presence of $K_2Ca(CO_3)_3$ (fairchildite), $Ca_{10}(PO_4)_6(OH)_2$ (hydroxylapatite (HA)), and KCl (sylvite) agree with previous research by Vassilev *et al*.,[15] who stated that the formation of secondary carbonates, phosphates and chlorides will occur below 500°C. Work by Vassilev *et al*.[27] has shown multiple occurrences of both apatites and hydroxyaptites which are thought to have been derived from organic matter. Vamvuka *et al.*[33] suggest that the HA formation may also be due to fertiliser used during the growth of the biomass. MgO is present, and multiple theories have been proposed for its formation[27] including the thermal decomposition of chlorophyll ($C_{55}H_{72}O_5N_4Mg$).

Table 4-2: Phases present at each temperature in the furnace ashing of hemp

			Temperature (°C)					
Phase	**Key**	**Composition**	**600**	**700**	**800**	**900**	**1000**	**1100**
Quartz	Qz	SiO_2	•	•	•	•	•	•
Calcite	Ca	$CaCO_3$	•	•	•			
Sylvite	Sy	KCl	•	•	•	•		
Fairchildite	Fa	$K_2Ca(CO_3)_2$	•	•	•			
Hydroxyapatite	Ha	$Ca_{10}(PO_4)_6(OH)_2$	•	•	•	•	•	•
Microcline	Mi	$KAlSi_3O_8$	•	•	•	•	•	•
Periclase	P	MgO	•	•	•	•	•	•
Dolomite	Do	$CaMg(CO_3)_2$	•	•	•			
Wollastonite	Wo	$CaSiO_3$				•	•	•
Diopside	Di	$CaMgSi_2O_6$			•	•	•	•
Akermanite	Ak	$Ca_2MgSi_2O_7$					•	•
Larnite	La	Ca_2SiO_4					•	•
Kalsilite	Ka	$KAlSiO_4$					•	•

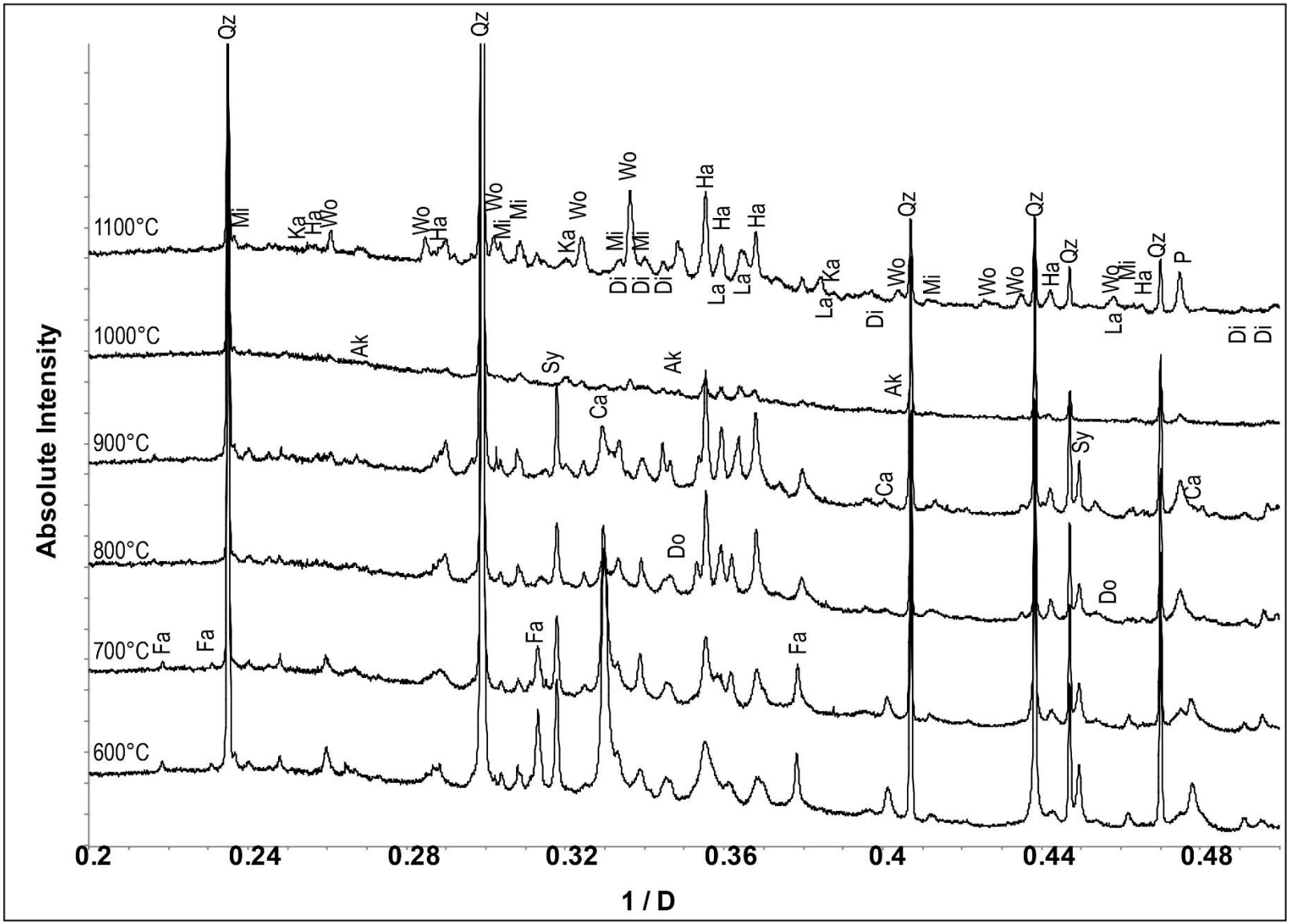

Figure 4-5: Patterns of hemp ash showing phases formed at high temperature, data collected on I-11 (λ 0.82675) beamline PXRD data is truncated to the range 0.2-0.5 1/D for clarity

At lower temperatures, carbonates ($CaCO_3$, $CaMg(CO_3)_2$, and $K_2Ca(CO_3)_2$) are present as is found in the original raw fuel ash. On heating, the carbonates begin to decompose and new phases form through reaction.

$CaCO_3$ decomposes to form CaO according to the reaction outlined in Equation 4-11.[160] There are many temperatures presented for this decomposition:[31]

$$CaCO_3 \rightarrow CaO + CO_2$$

Equation 4-11

The presence of CaO, formed through the decomposition of $CaCO_3$, is not observed in the PXRD patterns presented here, suggesting that upon formation it may react with another phase in the samples. Research by Vassilev *et al.,*[15] estimates the formation of lime (CaO) occurs between 500-700°C. The composition of the ash, and the atmosphere the ashing is carried out at, will have an affect on the decomposition temperature. Research by Cultrone *et al*.[161] into ceramic carbonate silicate, phases formed during ceramic firing, suggests reactions at the carbonate/ silicate interface through mass diffusion and viscous flow. This would eliminate the detectable decomposition to CaO.

The diffraction peak of MgO at 22.6°2θ (Figure 4-5) sharpens with increasing temperature, suggesting the MgO present becomes more crystalline at higher temperatures. This could also be due to an increase in MgO due to the decomposition of dolomite

$CaMg(CO_3)_2$ decomposes according to the reaction:[162]

$$CaMg(CO_3)_2 \rightarrow CaCO_3 + MgO + CO_2 \qquad 500 - 900℃$$

Equation 4-12

At temperatures above 800°C, the silicate phases $CaSiO_3$ (wollastonite), $CaMgSi_2O_6$ (diopside), $Ca_2MgSi_2O_7$ (akermanite), Ca_2SiO_4 (larnite), and $KAlSiO_4$ (kalsilite) begin to form. Formation of these phases is proposed through the reaction of $CaO/MgO/SiO_2$ at the elevated temperatures during heat treatment. This fits with previous work undertaken on ceramic and clay systems with similar compositions (Table 4-3) to those in the hemp ash where it was shown that MCO_3 (M = Mg, Ca) reacts with SiO_2 during decomposition to form alkali silicates:[162]

$$CaCO_3 + SiO_2 \rightarrow CaSiO_3 + CO_2$$

Equation 4- 13

$$CaMg(CO_3)_2 + SiO_2 \rightarrow CaMgSi_2O_6 + 2CO_2$$

Equation 4-14

Table 4-3: Composition of clays with high dolomite and calcite composition[162]

Element (wt %)	Calcite Rich Clay	Dolomite Rich Clay
SiO_2	25.7	23.8
Al_2O_3	9.39	9.33
TiO_2	0.49	0.38
Fe_2O_3 (total)	5.41	3.97
MgO	1.81	11.9
MnO	0.05	0.11
CaO	27.6	17.7
Na_2O	0.06	0.23
K_2O	2.11	3.93
P_2O_5	0.11	0.11
Loss on ignition	26.1	27.8

Topas Academic (version 6) was used for the Rietveld refinement of high resolution powder X ray diffraction data collected on the beamline I11 (Diamond Light Source) of the hemp laboratory synthesised ash samples (600-1100°). Initially, a Pawley fit of the data was carried out to obtain starting unit cell and peak shape parameters. The phases were modelled according to information on the ICDD 2004 database cards. Calcite was modelled using the hexagonal setting of the rhombahedral space group.

This was followed by Rietveld refinement using atom position information from CIF files. Lattice parameters, atom positions, peakshape, and thermal parameters were modelled for each phase with the thermal parameters of the Ca-silicate phase(s) being constrained to 1 to give the most consistent results.The pathways of formation for the Ca-silicates which have previously been identified are corroborated by the by the quantitative analysis. A general trend was observed (Figure 4- 6) in that the amount of quartz decreases as a function of temperature due to reaction of this phase with Ca^{2+} (present from the decomposition of carbonate phases) to form complex calcium silicate phases (i.e: diopside, wollastonite, larnite, and akermanite). At 1000°C, the background increased (Figure 4-11) in comparison to the other patterns

collected; whilst some Ca-silicates were observed at this temperature, it is likely that they were present as glassy amorphous phases which then crystallised out at 1100°C.

The proportions of the phases refined doesn't take into account the presence of any amorphous phases, so it can artificially enhance the proportions of some crystalline phases (making the peak appear higher than it is). Hydroxyapatite, the Ca-P phase present in each of the samples exhibits peak sharpening at 800°C (Figure 4-8) which suggests that it undergoes recrystallization or annealing. At lower temperatures the, Ca^{2+} source for the formation of diopside is the calcite ($CaCO_3$) which shows a dramatically reduced quantity at 800°C. At higher temperatures, the hydroxyapatite is thought to contribute some of the Ca for the phases to form.

The reaction of diopside with $CaCO_3$ was conducted, results are presented in Section 4.1, where larnite and akermanite were identified alongside residual diopside. The quantity of diopside decreased as the temperature the samples were held at increased. This suggests that as diopside forms it may be further converted into other Ca-silicates, either through a phase transformation or through reaction with quartz or CaO/MgO to form akermanite.

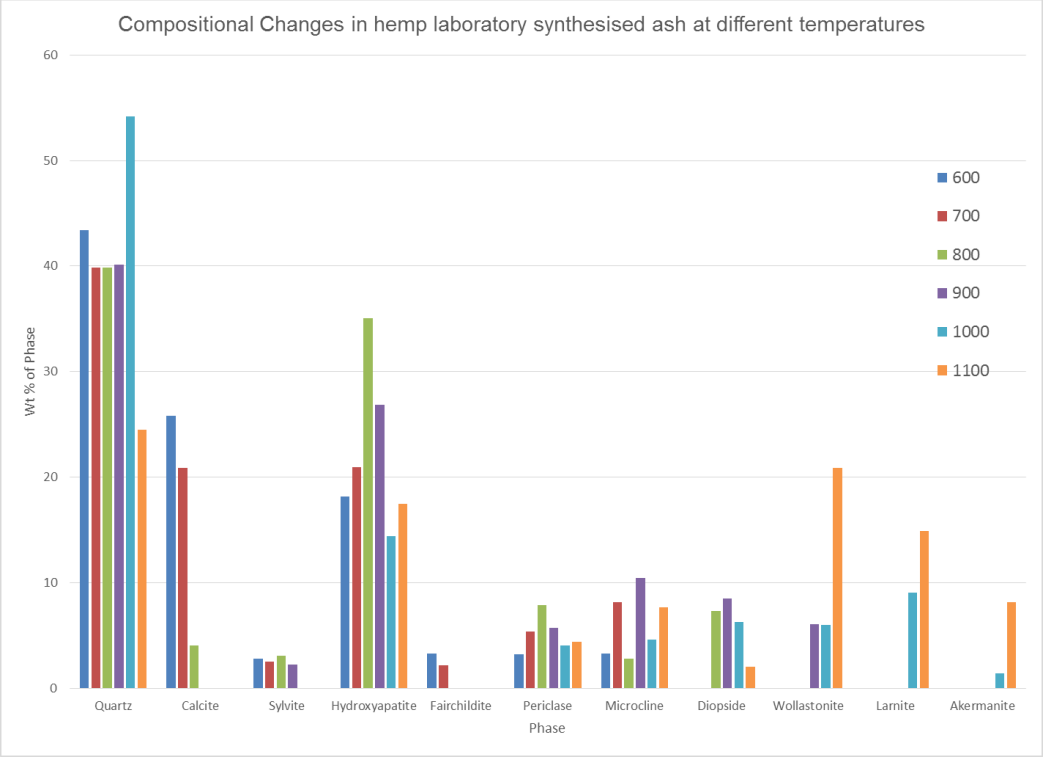

Figure 4- 6: Variation in phases in the hemp samples vs weight percent. Laboratory synthesised hemp ash after heat treatment at 600°C-1100°C

a)

R_wp	6.20
R_exp	1.89
gof	3.41

b)

Phases	Wt %	Error
Quartz	43.12	0.14
Calcite	25.83	0.13
Hydroxyapatite	18.37	0.17
Microcline	3.46	0.14
Fairchildite	3.32	0.05
Periclase	3.1	0.09
Sylvite	2.81	0.04

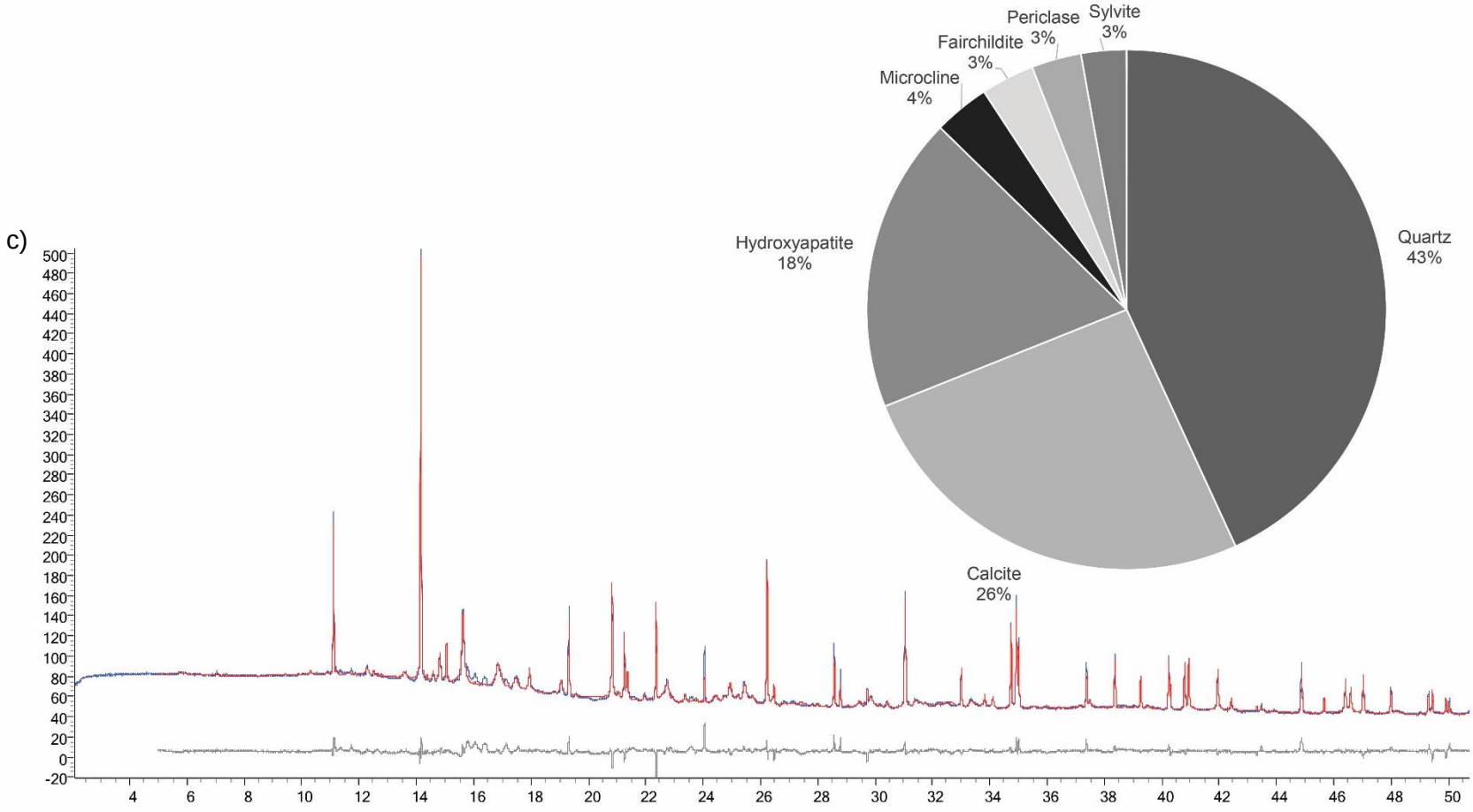

Figure 4-7: (a) The refinement parameters for rietveld refinements of 600°C heat treated hemp ash. (b) A table presenting the results and errors for the wt% of the phases present in the refinement (c) Experimental (blue), calculated (red) and difference (grey) plots for rietveld refinements of 600°C heat treated hemp ash.

a)

R_wp	6.39
R_exp	1.92
gof	3.33

b)

Phases	Wt %	Error
Quartz	39.90	0.14
Calcite	20.95	0.14
Hydroxyapatite	20.87	0.17
Microcline	8.13	0.15
Periclase	5.45	0.13
Sylvite	2.51	0.04
Fairchildite	2.19	0.04

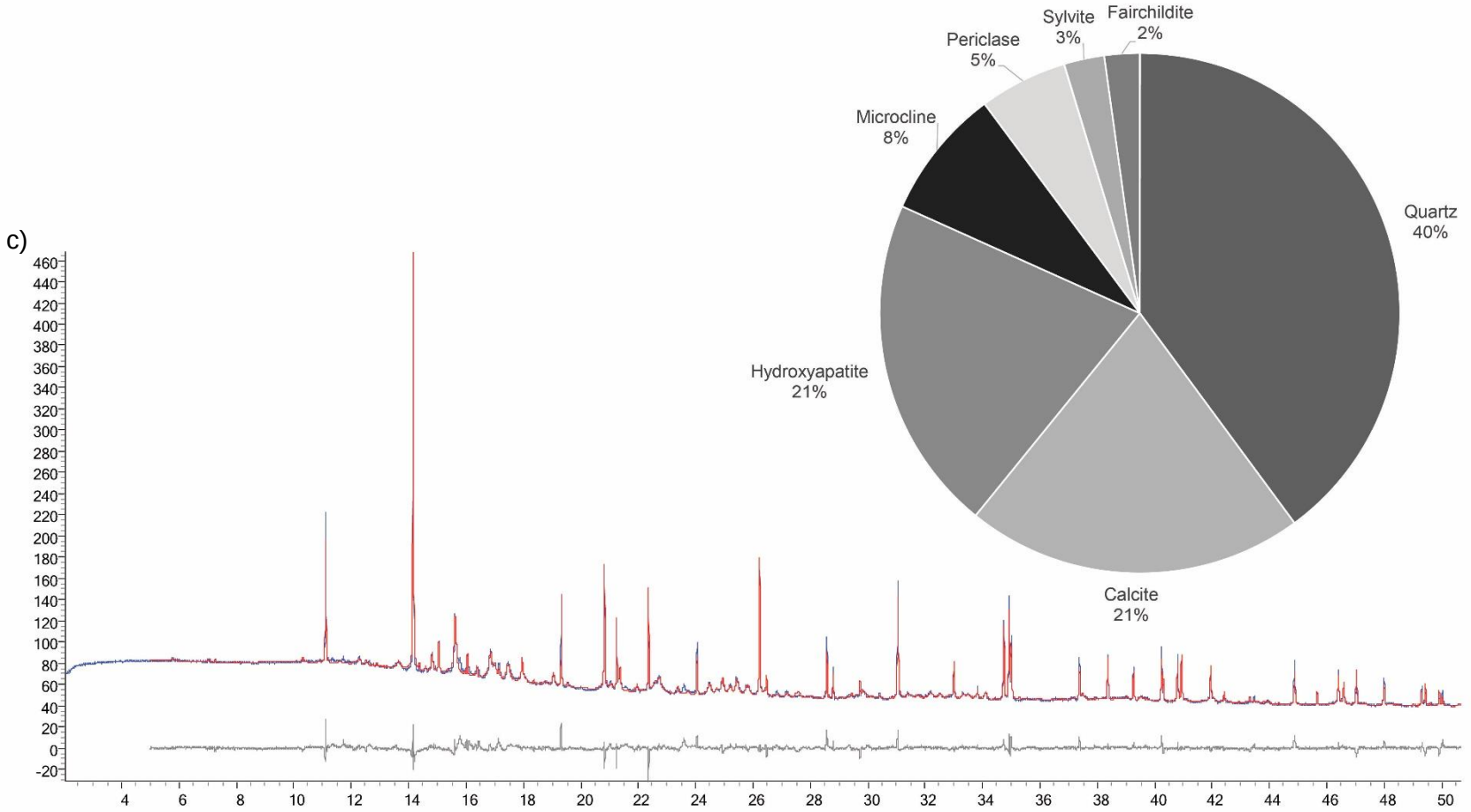

c)

Figure 4-8: (a) The refinement parameters for rietveld refinements of 700°C heat treated hemp ash. (b) A table presenting the results and errors for the wt% of the phases present in the refinement (c) Experimental (blue), calculated (red) and difference (grey) plots for rietveld refinements of 700°C heat treated hemp ash.

a)

R_wp	5.52
R_exp	1.92
gof	2.87

b)

Phases	Wt %	Error
Quartz	37.94	0.16
Hydroxyapatite	30.95	0.18
Diopside	11.33	0.20
Periclase	7.21	0.10
Microcline	6.39	0.18
Calcite	4.02	0.10
Sylvite	2.18	0.04

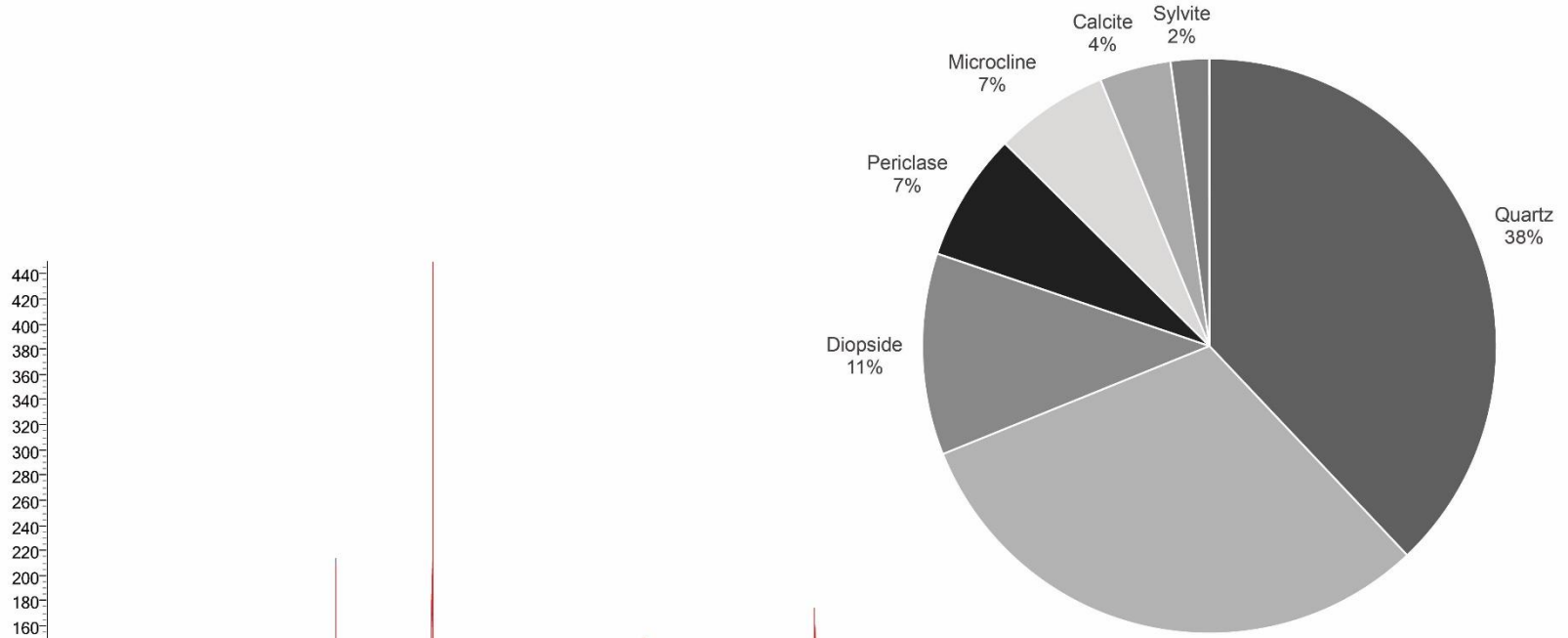

c)

Figure 4-9: (a) The refinement parameters for rietveld refinements of 800°C heat treated hemp ash. (b) A table presenting the results and errors for the wt% of the phases present in the refinement (c) Experimental (blue), calculated (red) and difference (grey) plots for rietveld refinements of 800°C heat treated hemp ash.

a)

R_wp	6.23
R_exp	1.84
gof	3.38

b)

Phases	Wt %	Error
Quartz	40.09	0.16
Hydroxyapatite	26.83	0.18
Microcline	10.47	0.15
Diopside	8.42	0.17
Wollastonite	6.19	0.19
Periclase	5.73	0.10
Sylvite	2.28	0.04

c)

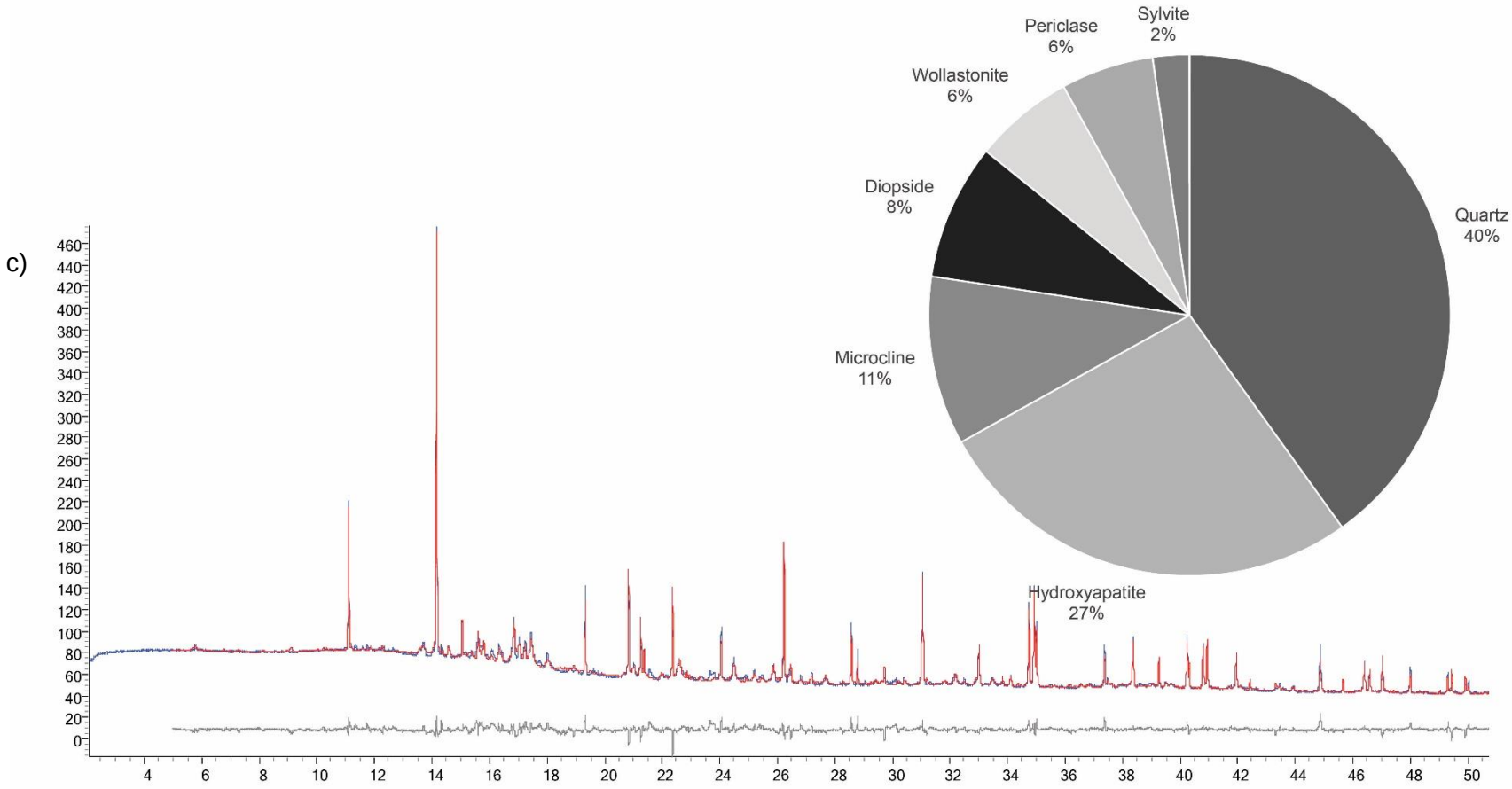

Figure 4-10: (a) The refinement parameters for rietveld refinements of 900°C heat treated hemp ash. (b) A table presenting the results and errors for the wt% of the phases present in the refinement (c) Experimental (blue), calculated (red) and difference (grey) plots for rietveld refinements of 900°C heat treated hemp ash.

a)

R_wp	3.31
R_exp	2.21
gof	1.57

b)

Phases	Wt %	Error
Quartz	55.72	0.37
Hydroxyapatite	14.22	0.27
Larnite	8.36	0.23
Diopside	5.64	0.24
Wollastonite	5.54	0.26
Microcline	4.89	0.32
Periclase	4.35	0.12
Akermanite	1.27	0.14

c)

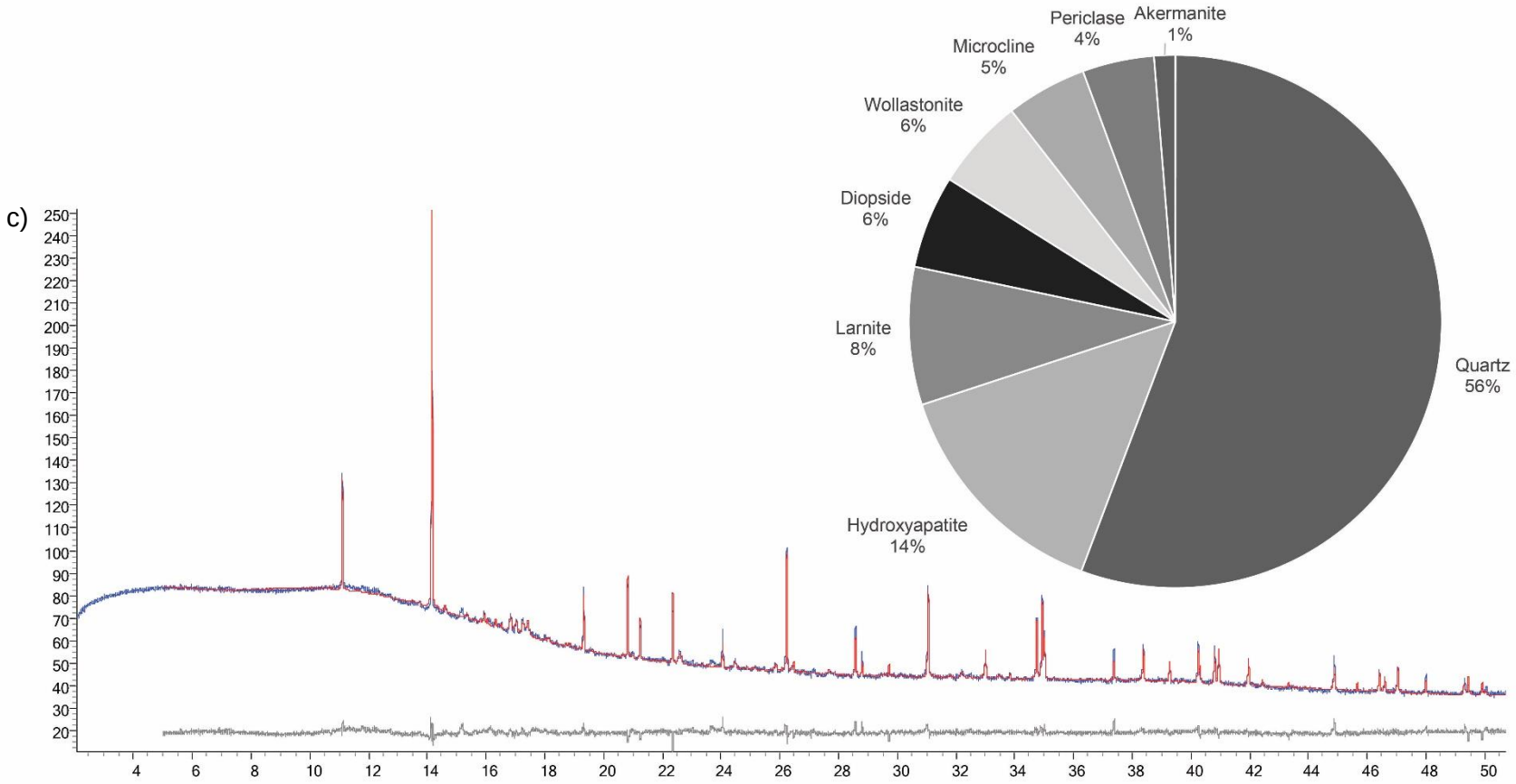

Figure 4-11: (a) The refinement parameters for rietveld refinements of 1000°C heat treated hemp ash. (b) A table presenting the results and errors for the wt% of the phases present in the refinement (c) Experimental (blue), calculated (red) and difference (grey) plots for rietveld refinements of 1000°C heat treated hemp ash.

a)

R_wp	3.89
R_exp	1.92
gof	2.02

b)

Phases	Wt %	Error
Quartz	24.16	0.13
Wollastonite	21.27	0.19
Hydroxyapatite	18.00	0.14
Larnite	12.17	0.15
Akermanite	10.07	0.16
Microcline	6.76	0.31
Periclase	4.58	0.06
Diopside	2.99	0.18

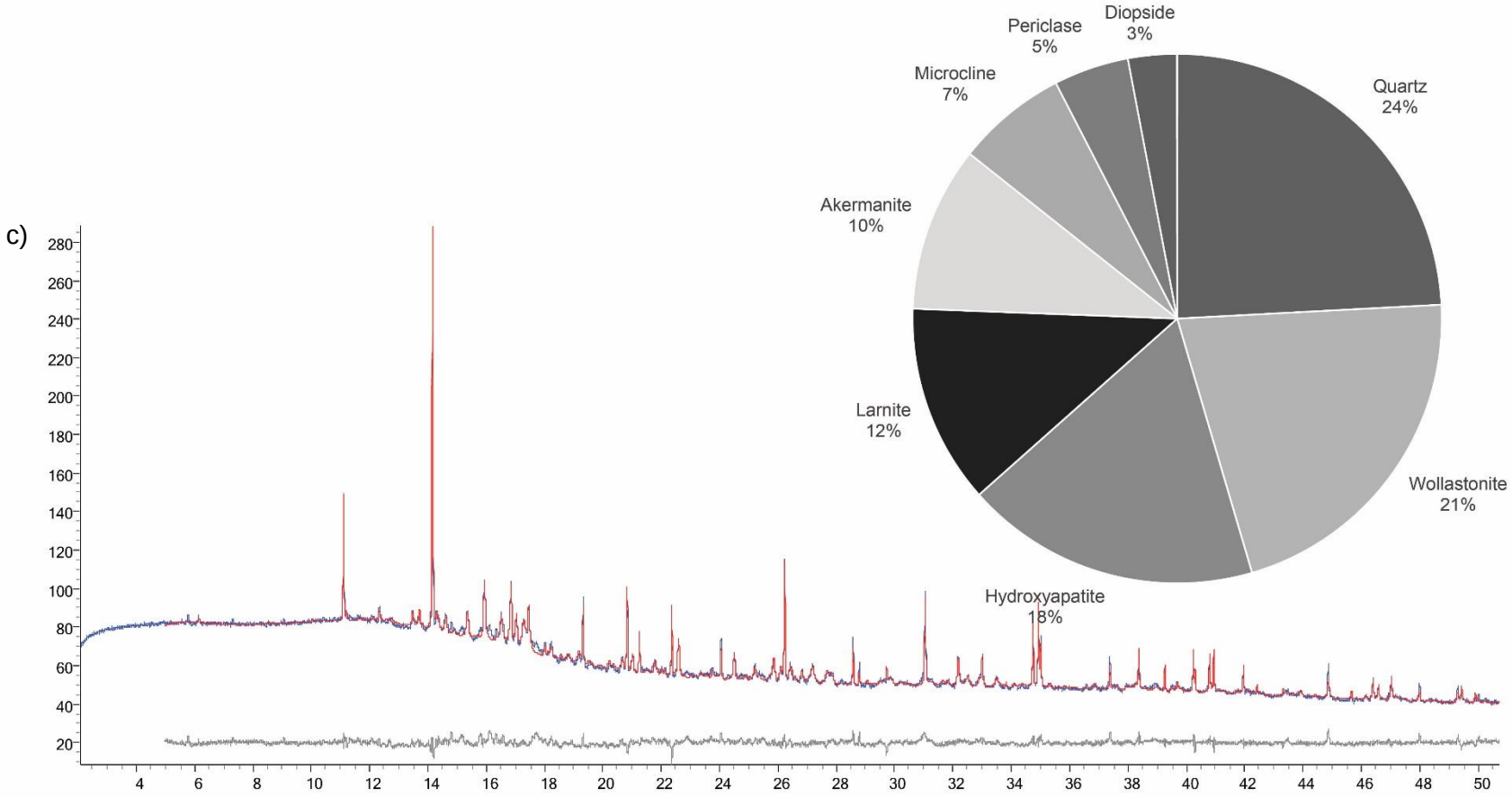

Figure 4-12: (a) The refinement parameters for rietveld refinements of 1100°C heat treated hemp ash. (b) A table presenting the results and errors for the wt% of the phases present in the refinement (c) Experimental (blue), calculated (red) and difference (grey) plots for rietveld refinements of 1100°C heat treated hemp ash.

Table 4-4: XRF data for hemp ash and high temperature hemp ash treated at 900°C

	Wt%			
	Hemp Ash		Hemp 900°C	
Al	0.95	±0.03	1.14	±0.06
Ca	39.95	±0.47	32.93	±0.12
Cl	1.32	±0.11	0.71	±0.08
Fe	1.41	±0.04	1.30	±0.03
K	14.62	±0.86	14.78	±0.57
Mg	6.81	±0.46	5.64	±0.26
Mn	0.38	±0.01	0.31	±0.01
Na	0.88	±0.16	0.62	±0.03
Ni	0.07	±0.00	0.10	±0.00
P	13.56	±0.23	13.11	±0.29
S	2.22	±0.16	2.55	±0.11
Si	13.41	±0.23	24.05	±0.35
Sr	0.11	±0.00	0.11	±0.00
Ti	0.47	±0.37	0.19	±0.04
Zn	0.16	±0.01	0.14	±0.00
Zr	0.05	±0.00	0.03	±0.00
	96.33		**97.67**	

XRF data comparing the 900°C ash composition to the hemp ash is presented in Table 4-4. Reduction in the Ca content (39.95 to 32.93 wt%) is observed, this indicates that some of the Ca may have volatilised when the carbonate (calcite, fairchildite and dolomite) decomposed. The loss of the Ca explains the increase in Si content (13.41 to 24.05 wt%) which also corresponds with the formation of the wollastonite ($CaSiO_3$) and diopside ($CaMgSi_2O_6$). The decrease in Ca content indicates a change in the form of the Ca (e.g. from $CaCO_3$ to CaO) which would have then reacted more readily with the SiO_2 to form the complex silicates. The P content of the ash does not change significantly (13.56 and 13.11 wt%). This agrees with the XRD data, which indicates that there is no change in the phase hydroxyapatite ($Ca_{10}(PO_4)_6(OH)_2$) which contains the majority of the P.

A decrease in the Cl content (1.31 to 0.71 wt%) is also seen, this suggests sylvite (KCl) is released at various intervals throughout the high temperature treatment. This decrease is not as visible through the rietveld analysis of the XRD data with a decrease in KCl from 2.81 wt% to 2.28 wt%. It is worth noting that as other phases in the ash decompose or transform the need for the quantitative analysis to add up to 100% accounts for this discrepancy.

The Mn is not observed in any of the phases identified in the XRD data suggesting that it is present as amorphous manganese oxide. Some manganese may be incorporated into the silicates formed at high temperatures e.g. wollastonite ($CaSiO_3$).[163]

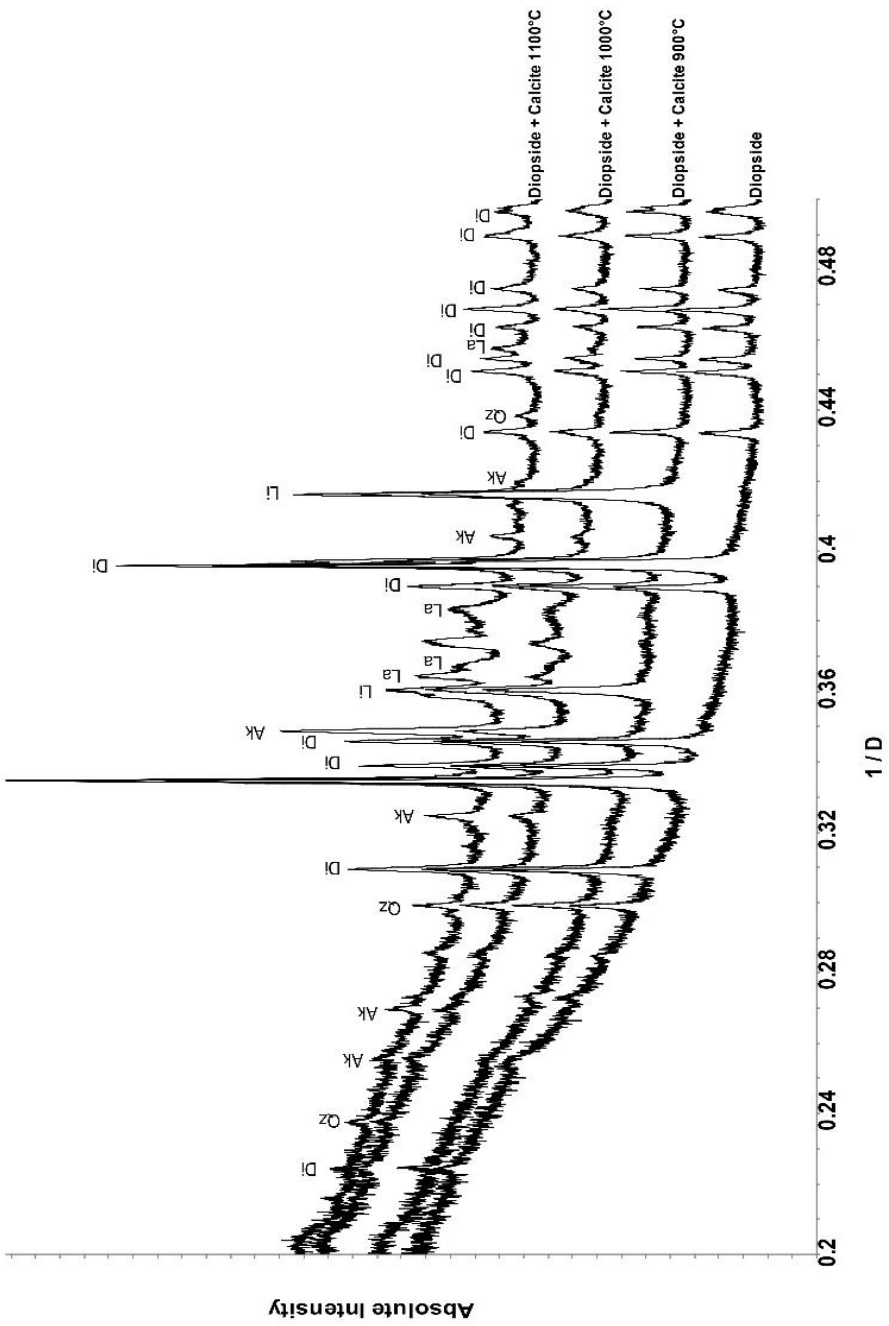

Figure 4-13: PXRD patterns of the starting reagents diopside and calcite and the reactions at three temperatures to simulate reaction temperatures in the laboratory ash. Di- diopside ($CaMgSi_2O_6$) Ak - akermanite ($Ca_2MgSi_2O_6$) La- larnite (Ca_2SiO_4) Li - lime (CaO) Qz – quartz (SiO_2)patterns were collected on the D8 Discover using Co Kα$_1$ radiation

The synthesis of akermanite ($Ca_2MgSi_2O_6$) from diopside ($CaMgSi_2O_6$) was carried out to determine whether the excess Ca^{2+} present in the biomass ash would drive the formation of akermanite. XRD data collected on a synthetic sample of akermanite, produced through the high temperature reaction of diopside and calcite, is presented in Figure 4-13. The synthesis was carried out under the same conditions (temperatures and atmosphere) as the high temperature heat treatment of the biomass ashes. This suggests that Ca^{2+} rich phases and diopside are likely to react to synthesise akermanite. Larnite (Ca_2SiO_4) was identified as an

impurity phase. This suggests an excess of available Ca^{2+} in the ash will react with SiO_2 to form larnite.

Figure 4-14 shows the $CaSiO_3$-$MgSiO_3$ phase diagram by Jung et al.,[164] highlighting the phases formed over the temperature range 800-1800°C. The presence of both wollastonite and diopside in the hemp ash samples are supported by the phase diagram from this study.[164] Diopside ($CaMgSi_2O_6$) is present from 800°C, akermanite (Ca_2MgSiO_7) is present only above 1000°C). The results presented in Figure 4-13 indicate that Ca_2MgSiO_7 only forms once an excess of reactive Ca is present and may require a higher temperature to be synthesised.

Further high temperature experiments were carried out using a high temperature stage coupled to an X-ray diffractometer (details given in section 3.5.1, data presented in Figure 4-15). This was to monitor in-situ phase transformations and potential solid-solid interactions. Analysis of the data showed the phases identified were similar to those identified in the ex-situ high temperature treated ash. In the in-situ data, the thermal decomposition of calcite to lime was observed between 500-600°C, much lower than the decomposition observed in the ex-situ data. This suggests that when the sample was removed from the furnace, the CaO reacted with CO_2 in the air to form $CaCO_3$, rather than reacting further to form silicates.

In-situ HT-PXRD also showed the presence of Ca-silicates at lower temperatures than those observed in the ex-situ data collected at ambient temperature. Calculation of peak positions of wollastonite, larnite, and akermanite at different temperatures could not be performed due to insufficient thermal expansion data. The sets of peak positions for these silicates fit with the phases identified in data collected at room temperature and shift accordingly with further

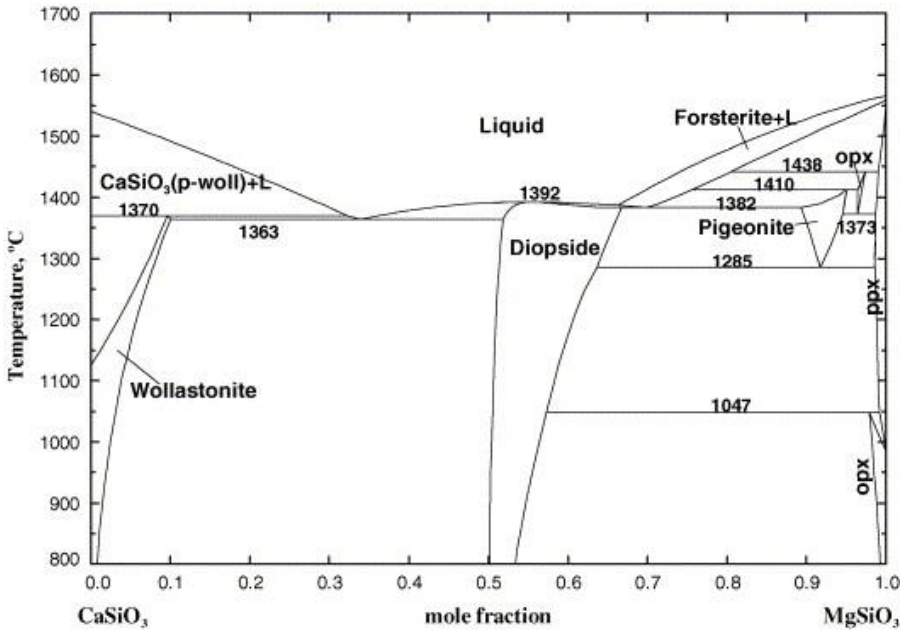

Figure 4-14: Calculated phase diagram of the $CaSiO_3$ - $MgSiO_3$ metasilicates from Jung et al.[164]

heating. Akermanite is present whilst diopside is not, suggesting that as it forms a full conversion from diopside to akermanite is undergone. Trindade *et al*.[153] report that CaO is consumed more rapidly than MgO during formation of phases in the CaO-MgO-SiO_2 system and therefore under the conditions studied, where Ca is much more abundant akermanite may be more likely to form.

Hydroxyapatite is present in the in-situ data (Table 4-5), thermal expansion data was used to calculate powder diffraction patterns at non-ambient temperatures[165] using a theoretical diffraction pattern calculation program. It is shown that hydroxyapatite is present up to 1000°C, and this is confirmed through the matching of patterns to calculated patterns (Appendix 1).

Table 4-5: Phases present in in-situ HT-PXRD

			Temperature (°C)					
Phase	Key	Composition	500	600	700	800	900	1000
Quartz	Qz	SiO_2	•	•	•	•	•	•
Sylvite	Sy	KCl	•	•				
Calcite	Ca	$CaCO_3$	•	•	•	•		
Lime	Li	CaO			•	•	•	
Larnite		Ca_2SiO_4				•	•	
Wollastonite	Wo	$CaSiO_3$		•	•	•	•	•
Hydroxyapatite	Ha	$Ca_{10}(PO_4)_6(OH)_2$	•	•	•	•	•	•
Microcline	Mi	$KAlSi_3O_8$	•	•				
Akermanite	Ak	$Ca_2MgSi_2O_6$					•	•

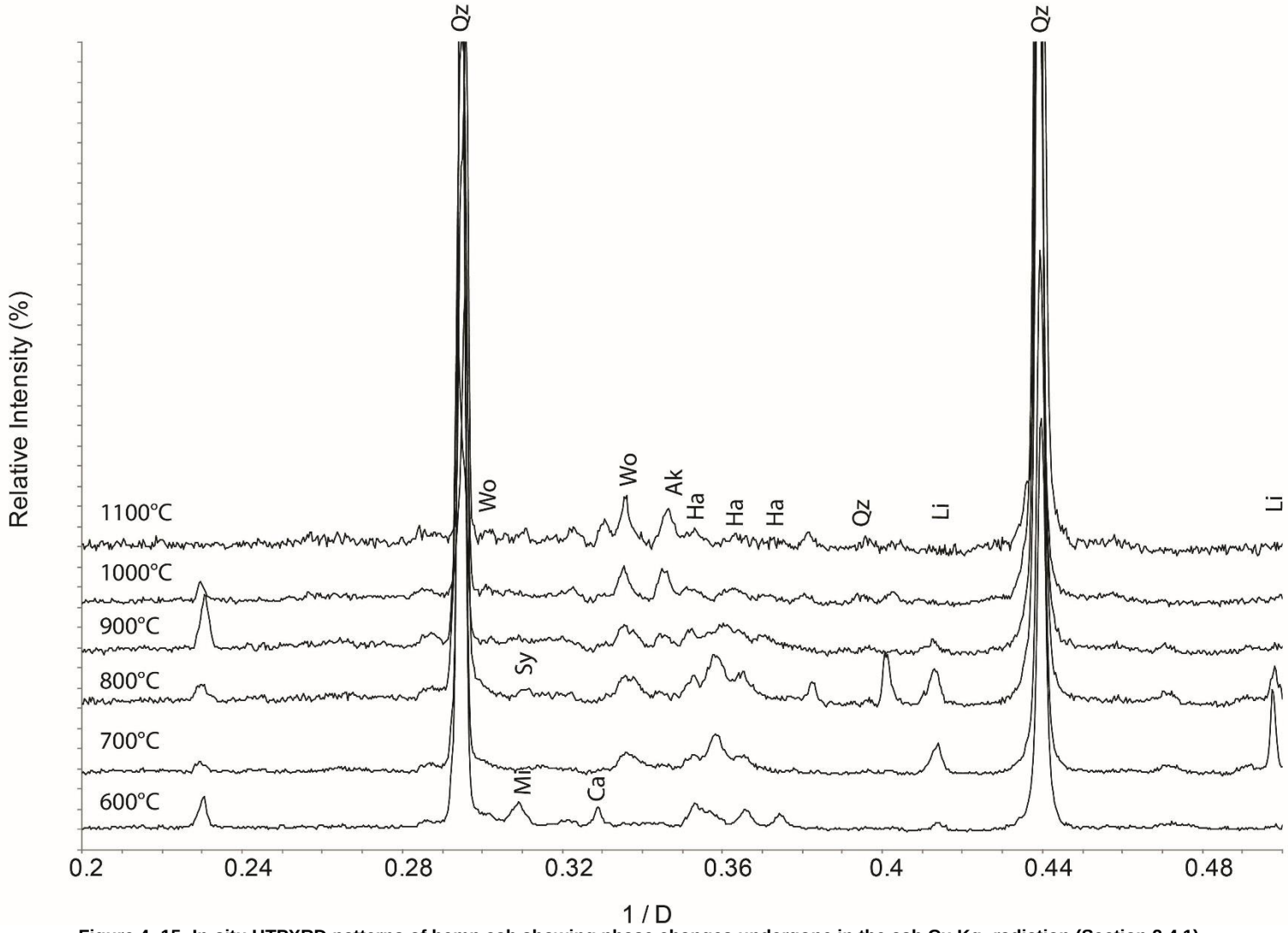

Figure 4- 15: In-situ HTPXRD patterns of hemp ash showing phase changes undergone in the ash Cu $K\alpha_1$ radiation (Section 2.4.1)

SEM imaging of the samples heated at temperatures between 600-1100°C (Figure 4-16) shows a decomposition of the organic matter from the raw hemp fuel (Figure 4-2) to ash at 600°C i.e: the large organic structures can no longer be observed. The trichomes present in the raw fuel (Figure 4-2) are still clearly visible at the higher temperatures and have not decomposed or melted suggesting they are highly thermally stable. The point where the thorns connected to the organic structure prior to ashing can also be observed (circled in Figure 4-16c and d), EDS analysis of these sites (Figure 4-17) shows that they have an incredibly similar composition to that of the trichomes themselves (Figure 4-3). With increasing

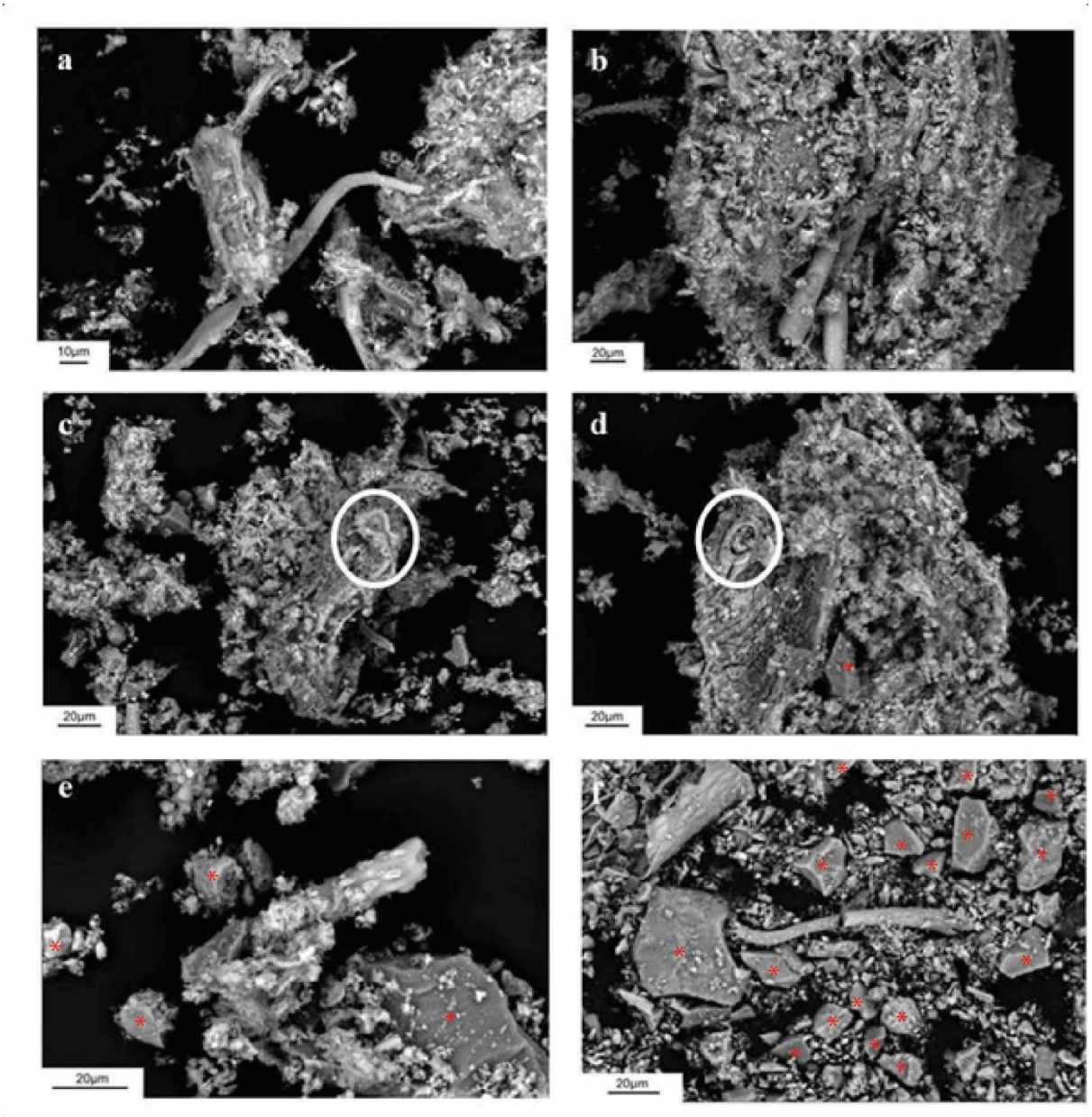

Figure 4-16: Electronmicrographs of hemp ashed at a) 600°C for 1 hour b) 700°C for 1 hour c) 800°C for 1 hour d) 900°C for 1 hour e)1000°C for 1 hour f) 1100°C for 1 hour

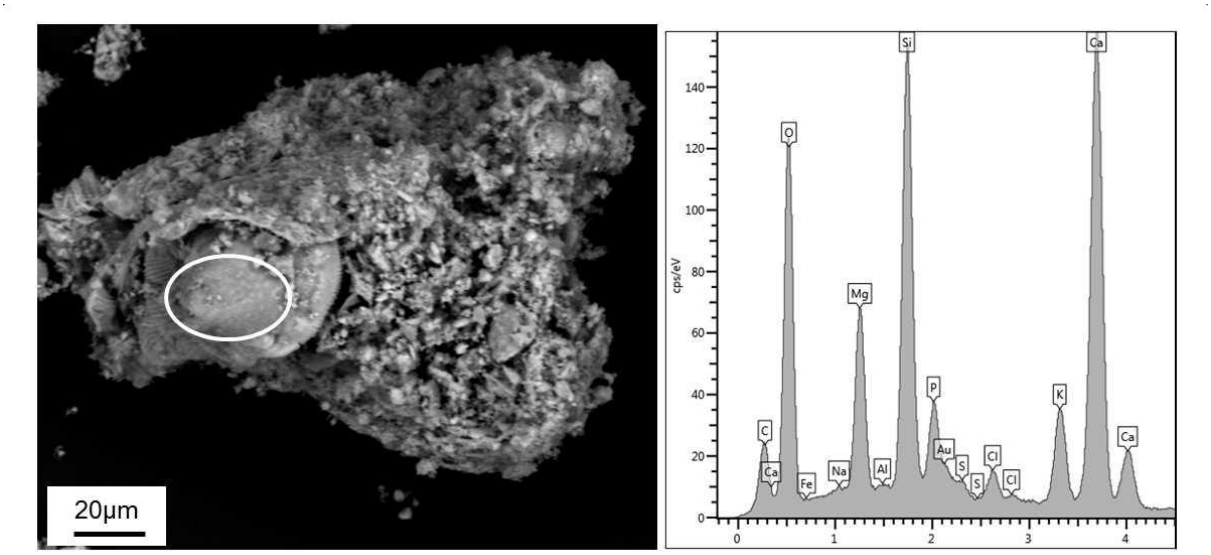

Figure 4-17: SEM Electronmicrograph of silicate thorn break site at 900°C and EDS analysis of the site

temperature, a higher number of large glass-like particles are present (*). This suggests melting, reaction and agglomeration of particles in the fuel.

Figure 4-18, shows EDS maps of the hemp ash at 600°C giving clear association between K^+ and Cl^- confirming the presence of KCl. Regions of close association of Si with other elements are not clearly observed at the low temperature, this is in agreement with the PXRD data which shows that the Ca-Mg-silicates do not form until 800°C.

EDS maps of the hemp ash at 900°C (Figure 4-19) where a distinct region of association between Si and O is visible, this is likely to be quartz. Ca, Si, Mg, and O show clear associations confirming the presence of diopside. The association of Ca, P, and O also contain Mg, suggesting the incorporation of Mg into the hydroxyapatite lattice; evidence of this incorporation was not observed during analysis of the PXRD data.[166] This potential incorporation is also observed in the 1100°C ash sample (Figure 4-20). Figure 4-20 shows EDS maps of the hemp ash at 1100°C illustrating clear correlation between K,Al,Si and O which is likely to be present as microcline. The Ca, Mg, Si, and O are also still associated therefore confirming the presence of diopside ($CaMgSi_2O_6$) and akermanite ($Ca_2MgSi_2O_7$).

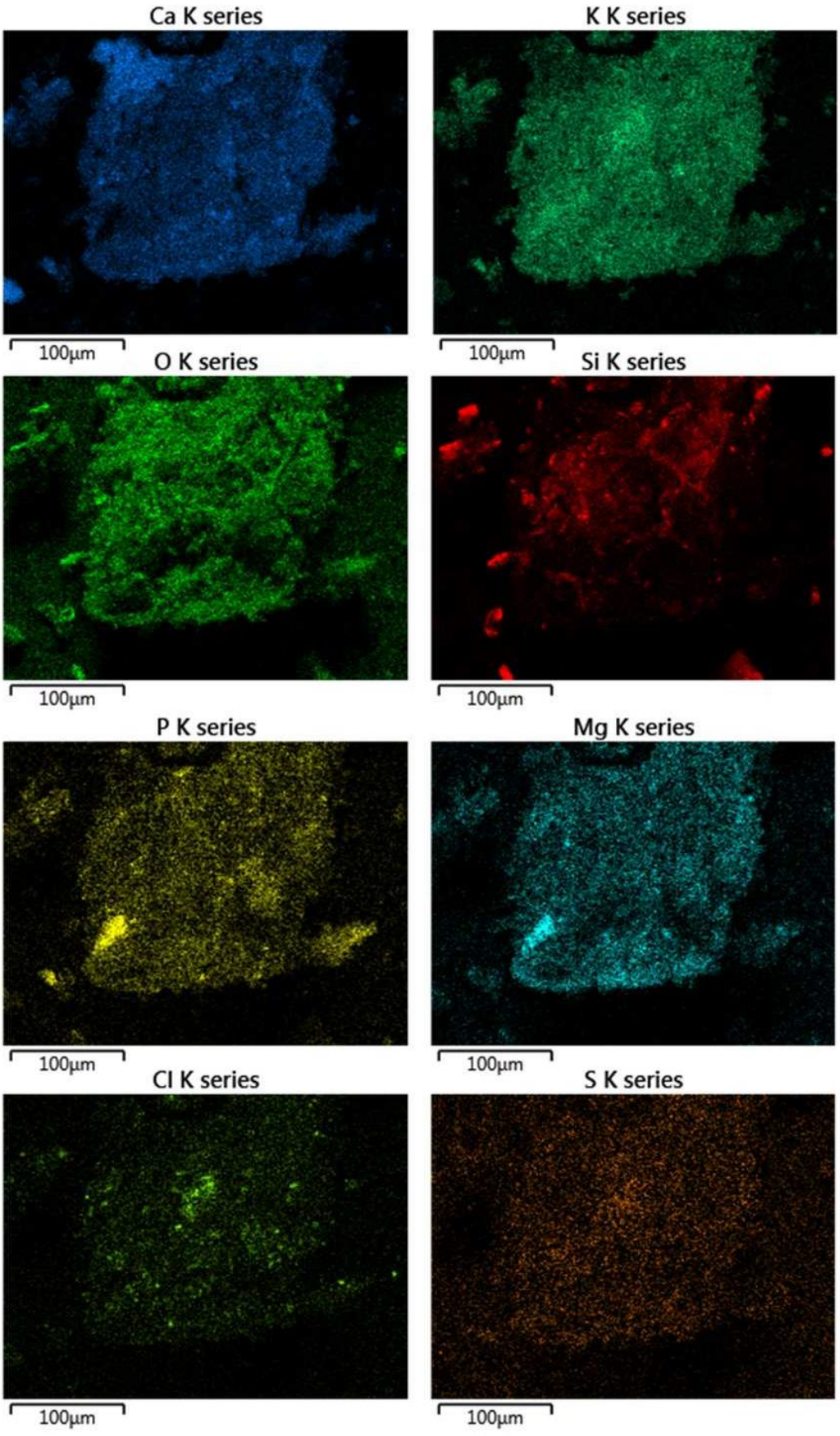

Figure 4-18: EDS Maps of hemp ashed for 1 hour at 600°C

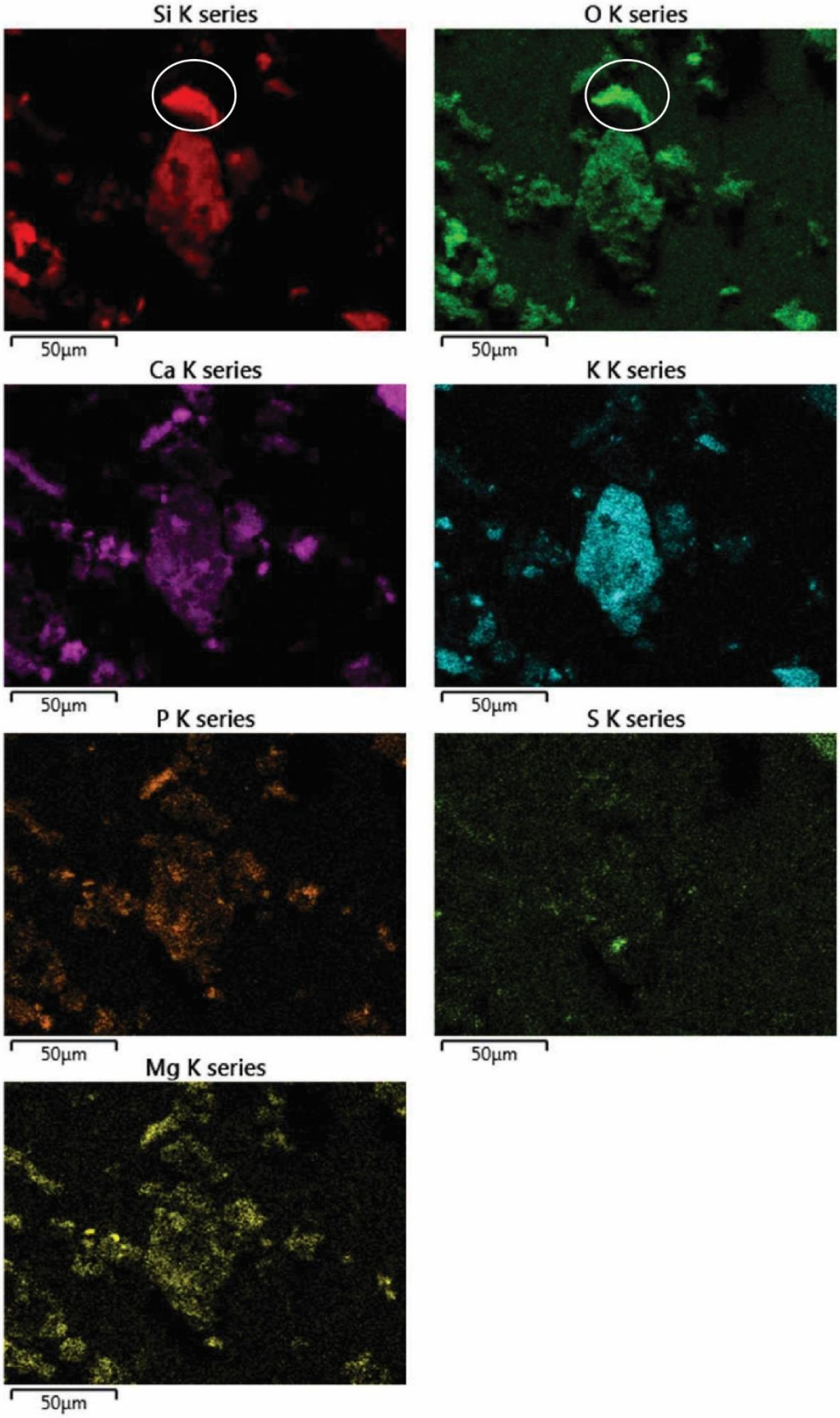

Figure 4-19: EDS Maps of hemp ashed for 1 hour at 900°C

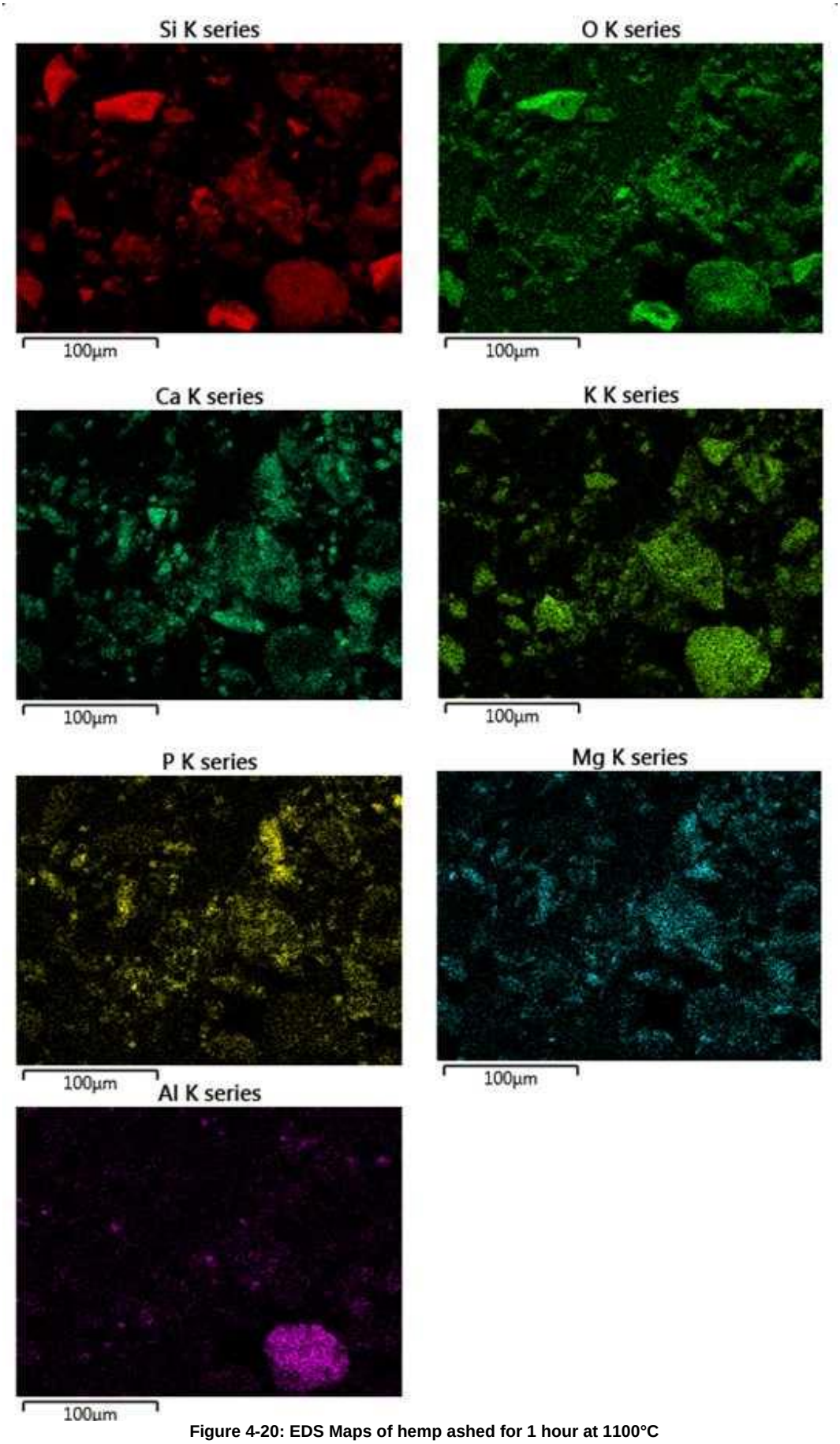

Figure 4-20: EDS Maps of hemp ashed for 1 hour at 1100°C

4.2 Eucalyptus

Eucalyptus is classified as a fast growing woody biomass[167] and has been shown to have a high calorific value.[168] When used as an energy crop it is grown in a coppice system over periods of 3-6 years or 6-12 years.[4] Eucalyptus is often widely used in the paper and pulp industry therefore study of the stumps that remain in the ground after harvesting has also been undertaken.[169] In comparison to slower growing woody biomass, it has been found that eucalyptus may contain 0.04-0.43 wt% of K, Cl, and S.[170] This information is important when considering coals to co-fire with a potential biomass.

As well as stumps, analysis of eucalyptus bark, leaves and the whole biomass has been undertaken.[171] Between the BIOBIB and Phyllis databases there are 27 entries concerning eucalyptus showing that it is being considered as a fuel for energy production.[172,173] Neilan *et al.*[168] reviewed the growth of eucalyptus in Ireland, and concluded that there is potential for several species to be used for energy production.

4.2.1 Eucalyptus Raw Fuel

PXRD of the raw eucalyptus fuel (Figure 4-21**)** shows broad peaks for the organic phases of cellulose, hemi-cellulose and lignin. The sharp peaks, indicative of crystalline phases in the hemp fuel are not present in the eucalyptus fuel. The ash content of the eucalyptus fuel is

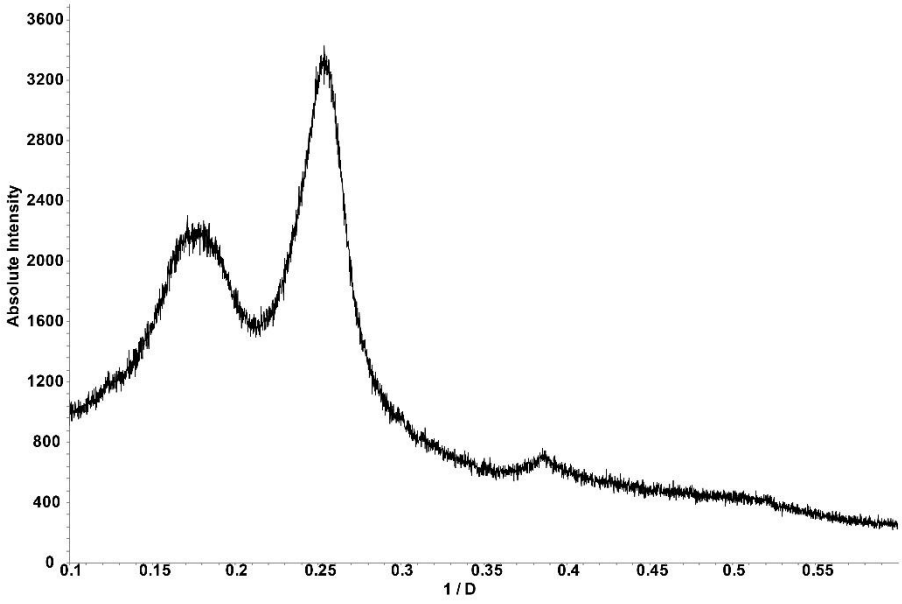

Figure 4-21: XRD Pattern of Eucalyptus Fuel showing large amorphous cellulose peaks collected on the D2 diffractometer with Cu Kα radiation

much lower than that of the hemp (0.7% in comparison to 16.9%), this suggests that the crystallinity of the raw fuel is directly related to components later observed in the ash i.e. if crystalline inorganics/organics phases present in raw fuel and organics are observed then the elemental make-up of the fuel is more complex, potentially leading to more complex reactions in the ash.

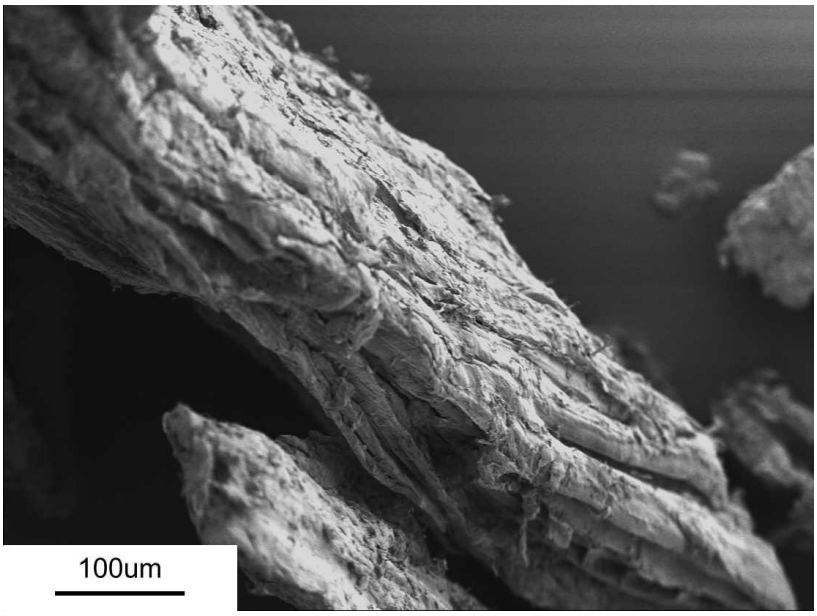

Figure 4-22: Electronmicrograph of Eucalyptus fuel

Figure 4-22, an electronmicrograph of the eucalyptus fuel shows a wood-like structure with some hemicellulose deposits on the surface, previously identified by Lima *et al*..[174] Analysis of the fuel shows a structure characteristic of whole eucalyptus, with both morphology of eucalyptus bark and cellulose fibres present.[169,174]

4.2.2 Eucalyptus Ash

The eucalyptus was ashed according to the procedures outlined in Section 3.5. Analysis of the PXRD data of the ashes after high temperature heat treatment (Figure 4-23, Table 4-6) showed the phases present at each temperature. At 600°C the hemicellulose, cellulose, and lignin that were identified as present from the PXRD of the raw fuel have decomposed. The carbonates calcite, fairchildite and dolomite are formed during the thermal treatment of the raw fuel; formation of these phases has previously been explained by Vassilev *et al.*.[15] Sylvite (KCl) and arcanite (K_2SO_4) were both present. In the analysis of the fuel ash, the chlorine and sulfur content of the fuels were shown to be (0.011% and 0.033%). The KCl is often reported as forming first, K_2SO_4 is then formed. After the decomposition of arcanite (between 800-900°C), anhydrite ($CaSO_4$) is formed, secondary sulphates (Table 2-5) have been seen to form at these temperatures.[15]

Table 4-6: Phases present from 600-1100°C in the high temperature heat treatment of eucalyptus ash

			Temperature (°C)					
Phase	Key	Composition	600	700	800	900	1000	1100
Quartz	Qz	SiO_2	•	•	•	•	•	•
Calcite	Ca	$CaCO_3$	•	•				
Fairchildite	Fa	$K_2Ca(CO_3)_2$	•	•	•			
Microcline	Mi	$KAlSi_3O_8$	•	•	•	•		
Sylvite	Sy	KCl	•					
Periclase	P	MgO		•	•	•	•	•
Hematite	He	Fe_2O_3	•	•	•	•	•	•
Arcanite	Ac	K_2SO_4	•	•	•	•		
Kalsilite	Ka	$KAlSiO_4$		•	•	•	•	•
Lime	Li	CaO	•	•				
Monticellite	Mo	$MgCaSiO_4$			•	•	•	
Portlandite	Po	Ca(OH)2			•	•	•	
Dolomite	Do	$CaMg(CO_3)_2$		•				
Anhydrite	An	$CaSO_4$				•	•	•
Grossular		$Ca_3Al_2(SiO_4)_3$						•
Magnetite	Mag	Fe_3O_4		•	•			
Forsterite	Fo	Mg_2SiO_4			•	•		
Akermanite	Ak	$Ca_2MgSi_2O_6$				•	•	•
Wollastonite	Ao	$CaSiO_3$				•	•	•
Tridymite	Tri	SiO_2				•	•	•
Gehlenite	Ge	$Ca_2Al_2SiO_7$					•	•
Merwinite	Mw	$Ca_3Mg(SiO_4)_2$					•	•
Potassium Iron Oxide	Not Shown	$KFe_{11}O_{17}$					•	•

The origin of the feldspar microcline is likely authigenic, present due to the harvesting methods of the biomass, as it is present at 600°C. The Fe containing phases hematite (Fe_2O_3) and magnetite (Fe_3O_4) are present due to the high Fe content of the eucalyptus ash (9.61% (XRF), 5.13% (ICP-OES)) and not external in origin.

As the heating temperature increases above 900°C, silicates begin to form. The Ca,(Mg)-silicates that are present in high temperature heat treatment of hemp ash are also present in the high temperatures heat treated ash of the eucalyptus. In contrast to the hemp samples, diopside ($CaMgSiO_6$) is not present whereas akermanite (Ca_2MgSiO_6) is present over the temperature range 900-1100°C. Previous work by Courtial *et al*.[175] has shown that diopside may experience early melting affects up to hundreds of degrees lower than the congruent melting point, and as such may react with excess Ca present in the samples to form akermanite, this is thought to be due to matrix impurities.

Figure 4-24, illustrates the similarites between diopside ($CaMgSi_2O_6$), wollastonite ($CaSiO_4$) and akermanite ($Ca_2MgSi_2O_7$). Diopside is favoured under conditions with increased SiO_2 and MgO content whereas akermanite is favoured with a higher CaO content.[164]

The presence of monticellite ($MgCaSiO_4$) and merwinite ($Ca_2Mg(SiO_4)_2$) can also be related to the phase diagram (Figure 4-24), as a lower Si content will also lead to the formation of these phases. Trindade *et al.*[162] show a reaction between dolomite and quartz at 800°C is responsible for the formation of monticellite.

$$SiO_2 + CaMg(CO_3)_2 \rightarrow CaMgSiO_4 + CO_2$$

Equation 4-15

The transformation of monticellite to merwinite may be facilitated by the decomposition of portlandite to lime, increasing the amount of available Ca to react with the monticellite to form merwinite. Vassilev *et al*.[27] in their compilation of biomass phase transformations report the formation of monticellite at temperatures between 575-1300°C; solid state reactions are also reported in this temperature range supporting the formation of merwinite.

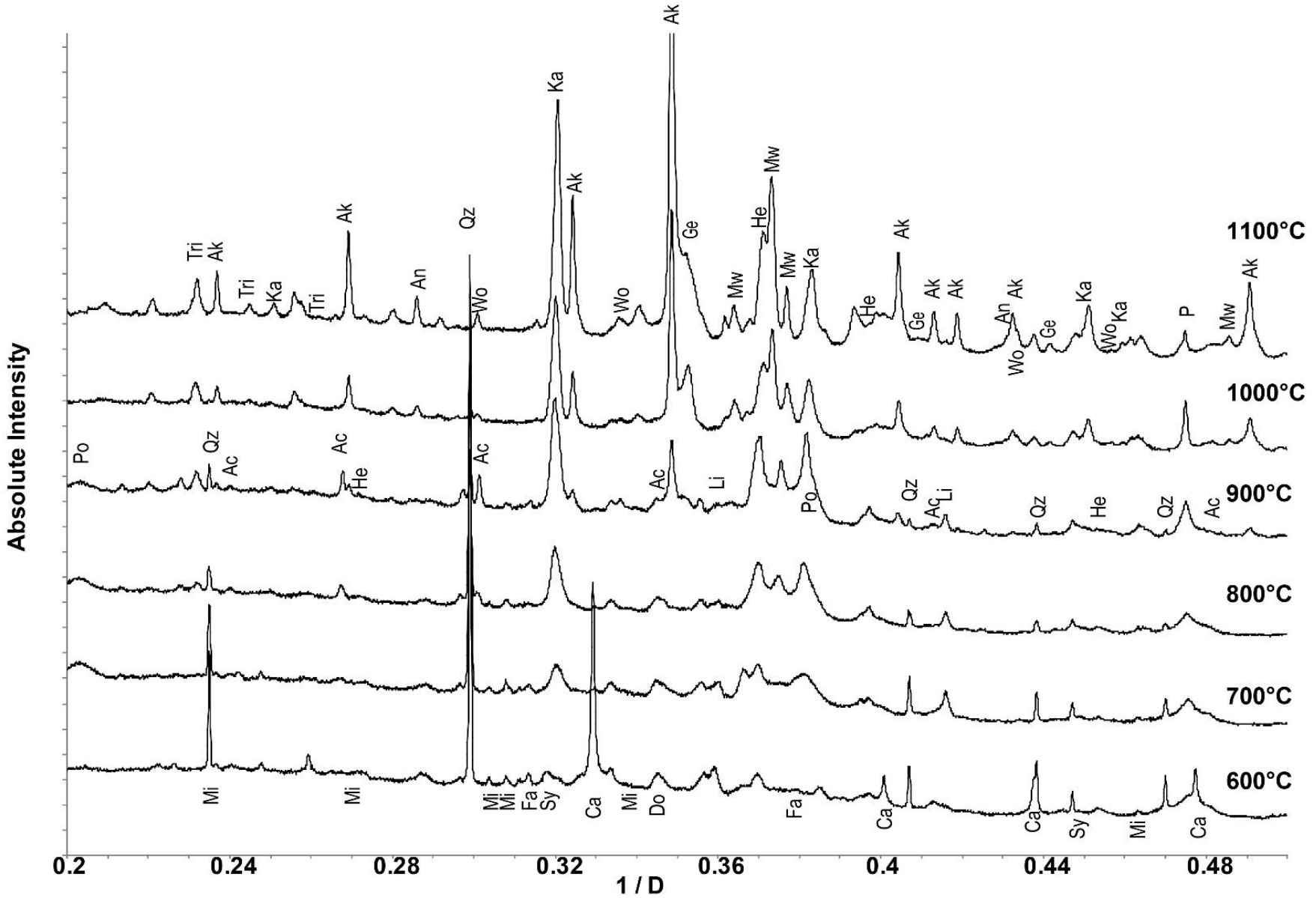

Figure 4-23: P-XRD patterns of laboratory ashed eucalyptus at temperatures 600-1100°C collected on beamline I-11 range (λ 0.826215) presented is 5-29°2θ to present clearer data

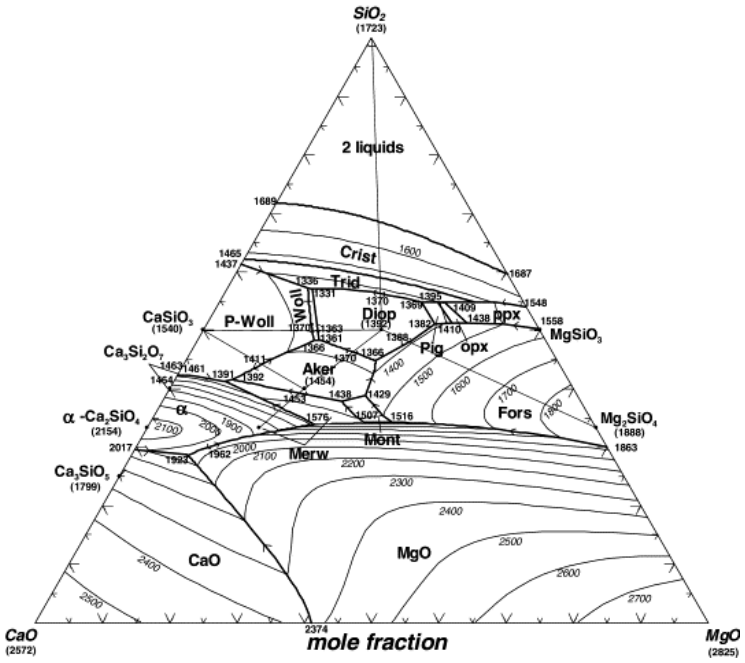

Figure 4-24: Calculated liquidus surface of the CaO-MgO-SiO2 system at 1 bar pressure. T in °C Crist-Cristobalite Trid, Tridymite, woll, wollastonite,p-woll – pseudo wollastonite, diop- diopside, pig – pigeonite, aker – akermanite, merw- merwinite, mont – monticellite, fors - forsterite

Trindade *et al.*[162] also indicate the reaction of periclase (MgO) with diopside may lead to the formation of forsterite, which is also present in the high temperature heat treated ash.

$$CaMgSi_2O_6 + 3MgO \rightarrow 2Mg_2SiO_4 + CaO$$

Equation 4-16

Trindade et al.[162] further state that Ca is consumed prior to Mg, with Ca-Mg silicates expected to form prior to Mg-silicates which will then form due to an excess of MgO. The early formation of these compounds may be due to the inhomogenous nature of the fuels, and as such if MgO is situated close to SiO_2 in the sample, forsterite will form prior to diopside.

The Ca,Al-silicate phase gehlenite ($Ca_2(Al(Al\ Si)O_7$) was shown in research by Cultrone *et al*.[161] to form in high temperature systems alongside wollastonite. Gehlenite is formed in the heat treated ash between 900-1000°C. The presence of gehlenite alongside akermanite as a solid solution with the composition ($2CaO.(1-x)MgO.xAl_2O_3.(2-x)SiO_2$ is suggested by Ventura *et al.*.[176] in their study of akermanite based glass ceramics. These studies show similar pathways of reaction to those in the biomass ash.

At 1100°C the quartz is no longer detected and has transformed to the polymorph cristobalite (main peak at 11.7, Figure 4-5), as well as reaction with CaO and MgO to form the aforementioned Ca-Mg silicate phases. The reaction of all the SiO_2 to silicates and other polymorphs is likely due to the lower SiO_2 content of the fuel in comparison to hemp (26.5% compared to 44%), therefore if conditions favour the formation of other phases full conversion could take place.

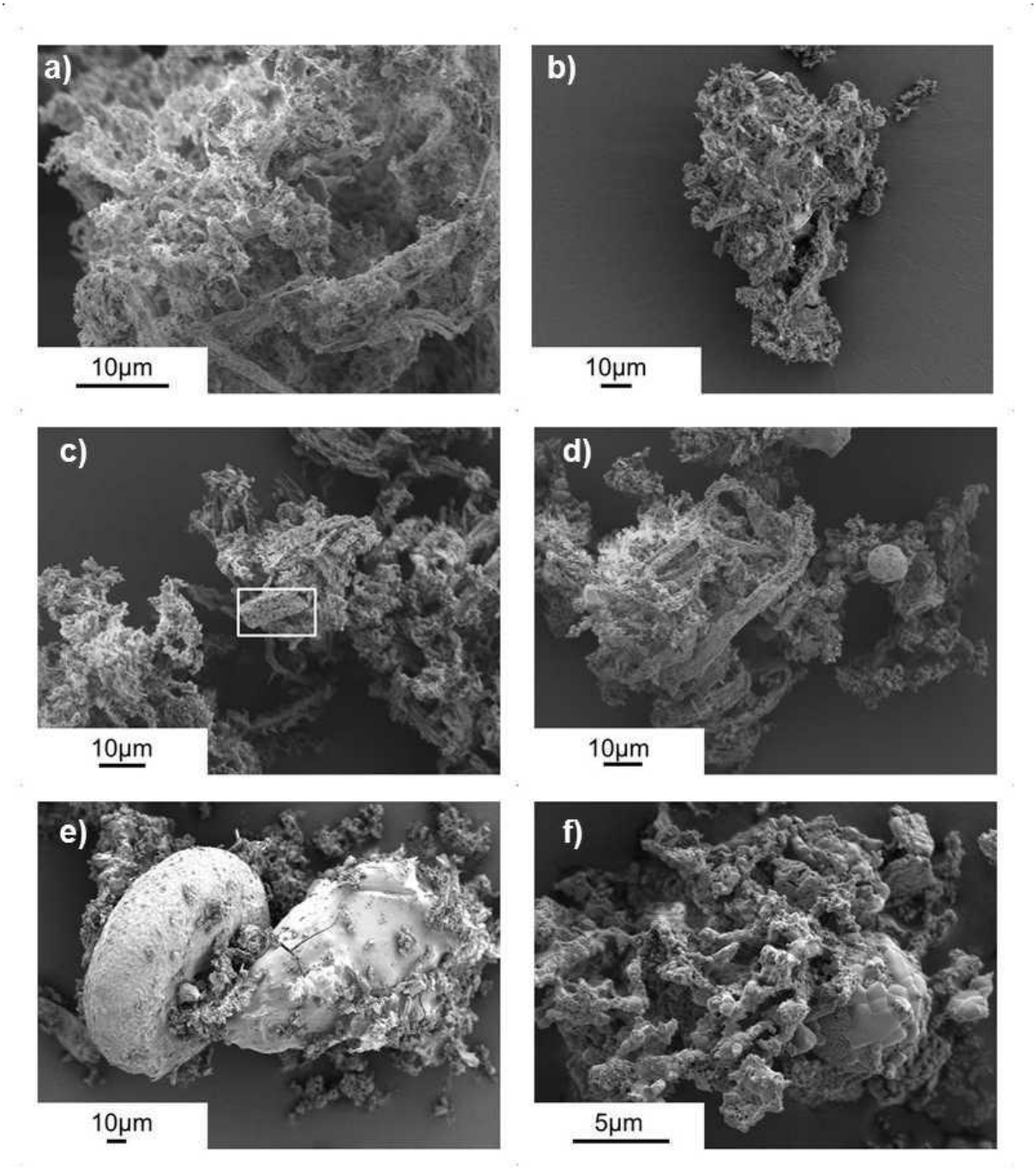

Figure 4-25: Electronmicrographs of eucalyptus ashed at a) 600°C for 1 hour b) 700°C for 1 hour c) 800°C for 1 hour d) 900°C for 1 hour e)1000°C for 1 hour f) 1100°C for 1 hour

Table 4-7: XRF analysis of the eucalyptus ash and high temperature eucalyptus ash treated at 900°C

	Wt%			
	Eucalyptus		Eucalyptus 900°C	
Al	4.86	±0.11	5.68	±0.04
Ca	36.70	±0.64	35.36	±0.39
Cl	0.11	±0.00	0.12	±0.04
Fe	9.61	±0.33	8.58	±0.16
K	11.24	±0.18	9.58	±0.17
Mg	6.03	±0.33	7.91	±0.48
Mn	4.02	±0.14	3.65	±0.09
Na	0.70	±0.98	0.47	±0.66
Ni	0.09	±0.01	0.04	±0.00
P	4.25	±0.13	4.84	±0.04
S	2.55	±0.05	3.03	±0.05
Si	16.92	±0.21	18.28	±0.16
Sr	0.39	±0.00	0.39	±0.04
Ti	0.92	±0.03	0.69	±0.04
Zn	0.28	±0.01	0.26	±0.01
Zr	0.02	±0.01	0.03	±0.00
	98.66		**98.87**	

The changes in elemental composition between the eucalyptus ash and the heat treated eucalyptus as are presented in Table 4-7. There are no large changes in the composition (above 3 wt%). There are minor increases in both Al (4.85 to 5.68 wt%) and Si (16.92 to 18.28 wt%). This is likely to be due to the formation of the phase kalsilite ($KAlSiO_4$). The decrease in the K content of the ash (11.24 to 9.58 wt%) may correspond with the loss of the phase KCl.

There is an increase in the Mg content of the ash (6.03 to 7.91 wt%); this corresponds with the decomposition of dolomite to form periclase (MgO). This is also visible in the XRD patterns where a visible sharpening of the MgO peak is also observed.

The Mn is not observed in any of the phases identified in the XRD data suggesting that it is present as amorphous manganese oxide. Some manganese may be incorporated into the silicates formed at high temperatures e.g. wollastonite ($CaSiO_3$).[163]

SEM electronmicrographs of the high temperature heat treated eucalyptus show that significant agglomeration and melting take place in the fuel as the temperature increases. At 600°C the carbon matrix of cellulose, hemicellulose, and lignin has degraded; whilst the inorganic components still seem to have held some of this structure (Figure 4-25a). As the

temperature increases the structure degrades further and distinct shapes are observed e.g. the spheres present in Figure 4-25d and f, and the donut shaped particle in Figure 4-25f.

The glass like particle melt present in Figure 4-25e illustrates a possible area of high-temperature reaction to form the K-silicates/ Ca,Mg- silicates. The agglomeration of several smaller particles together (Figure 4-25f) alongside melting on the surface of a sphere also highlights areas where the phase interactions may be taking place in the local environment.

Above 800°C, clear cuboid shaped crystals (Figure 4-25c, Figure 4-26) with the composition of Ca and O are present. The phase identified through PXRD with these elements is portlandite ($Ca(OH)_2$) which crystallises with trigonal geometry. The shape and composition of these Ca rich crystals indicate they are portlandite.

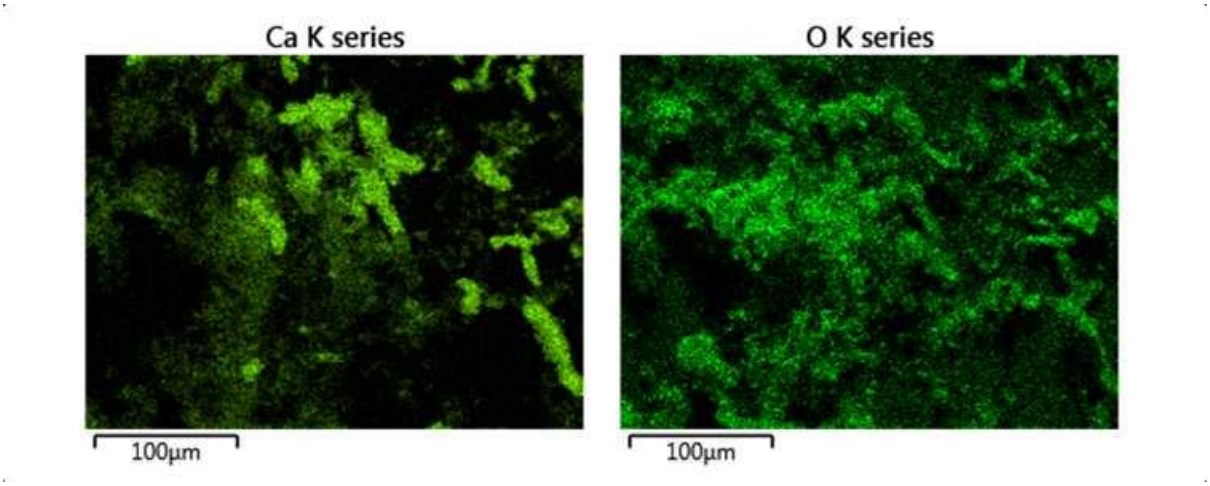

Figure 4-26: Ca and O rich crystals present in the eucalyptus fuel from 800°C

EDS maps of the eucalyptus which were heat treated for 1 hour at 900°C (Figure 4-27), show a region of clear association between Mg and O, which is likely to be periclase (MgO). The association of K, Al, Si, and O confirms the XRD result, which shows that $KAlSiO_4$ is present. There are also regions of distribution of Ca, however these do not seem to correspond with minerals found in PXRD data and these are likely to be regions where phases will form at higher temperatures.

Figure 4-28, EDS maps of eucalyptus heat treated at 1000°C for 1 hour. Close association of Ca, K, Al, Si, Mg, and O indicate that the reactions forming the silicates identified by PXRD may rely on elements required for formation to be in close proximity e.g. phases that are next to each other will react with one another.

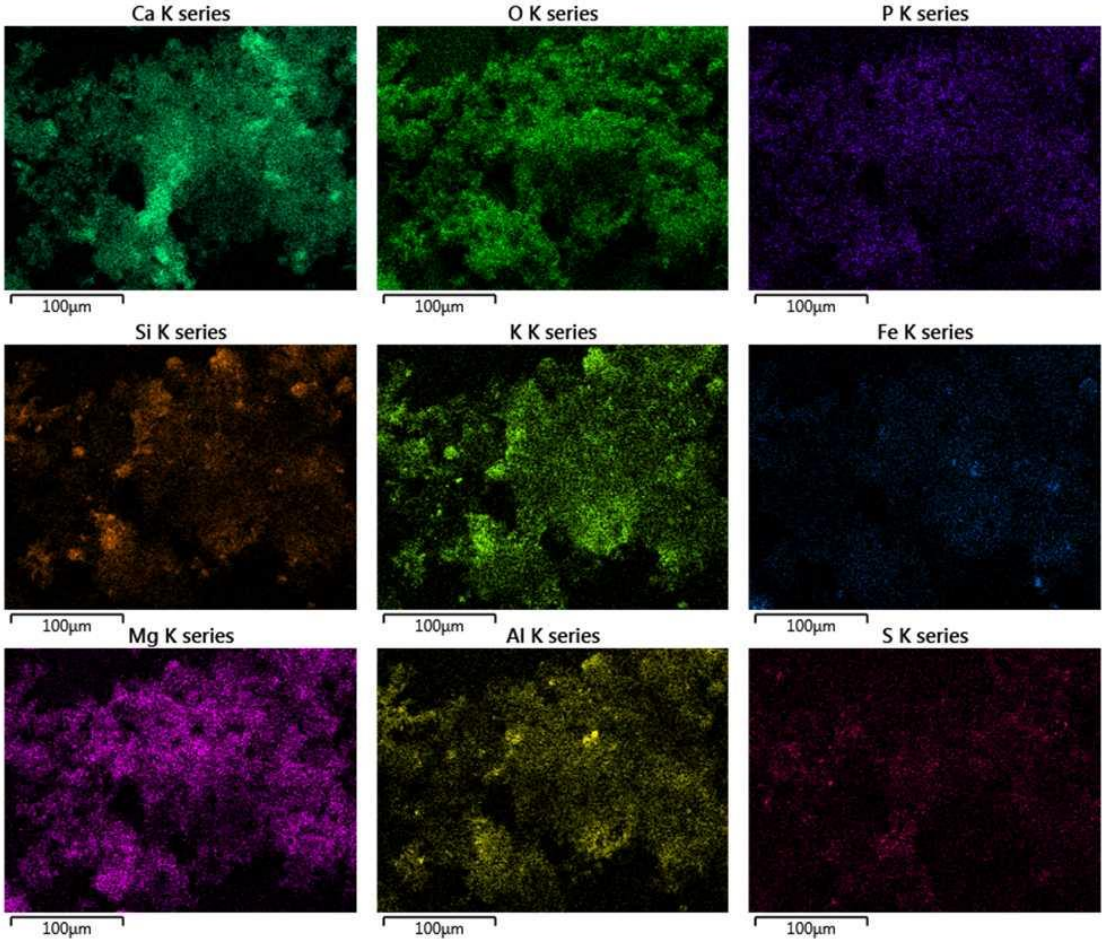

Figure 4-27: EDS Maps of Eucalyptus ash heat treated at 900C for 1 hour

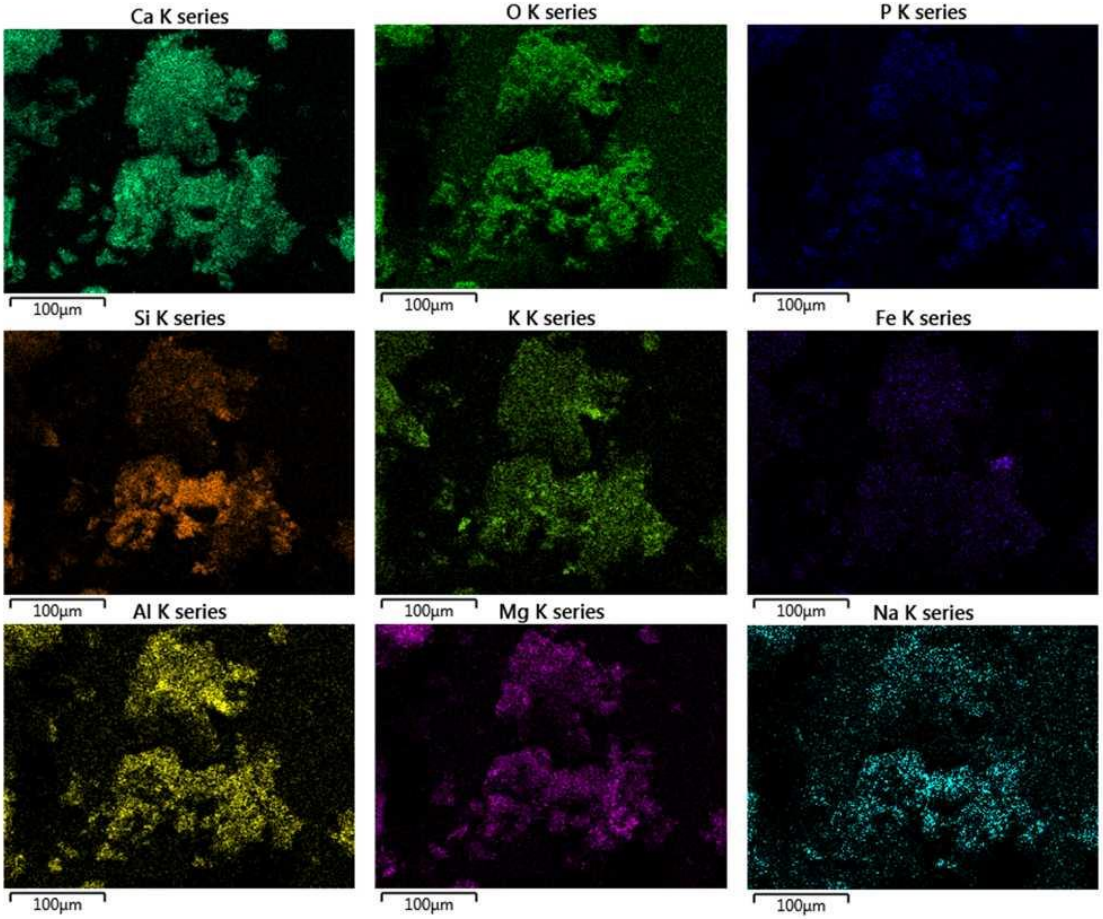

Figure 4-28: EDS maps of eucalyptus ash heat treated at 1000C for 1 hour

4.3 Coal

As coal has been used as a fuel since the early 1800s,[177] there have been many investigations into the phases formed in ash from coal combustion.[11,61,178,179] Fly ash is often used as a filler material in concrete, tarmac, and other building materials.

4.3.1 Coal Fuel

PXRD analysis of the pulverised coal fuel (Figure 4-29) shows a large amorphous bump at 0-30° 2θ, indicating the complex carbon organic matrix. Crystalline inorganic phases are also present in the fuel with quartz, illite ($KAl_2(Si_3Al)O_{10}(OH)_2$), kaolinite ($Al_2(Si_2O_5)(OH)_4$), dolomite($CaMg(CO_3)_2$), rozenite ($FeSO_4.4H_2O$), and gypsum ($CaSO_4.2H_2O$) comprising the main phases identified. The S containing minerals (rozenite and gypsum) are likely to account for the 0.34%(as received, Table 3-1) S value of the fuel.

The morphology of the coal fuel (Figure 4- 30) is largely small particles of irregular shape, it differs to the structure of the biomass in that there are no clear organic structures left.

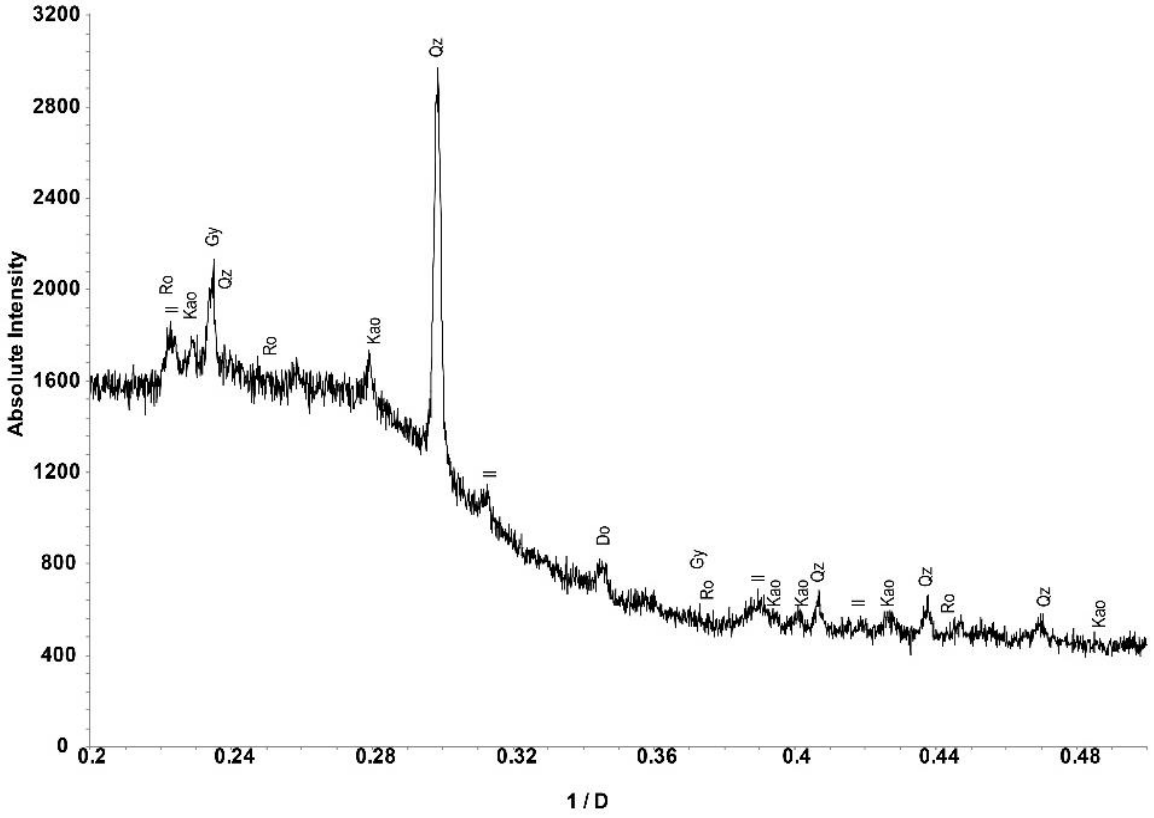

Figure 4-29: PXRD Pattern for Pulverised Kuzbass Coal Fuel Qz Quartz, Ko kaolinite, Gy gypsum, Ro rozenite, Do dolomite, Il illite collected on the D8 advance diffractometer Cu $K\alpha_1$ radiation

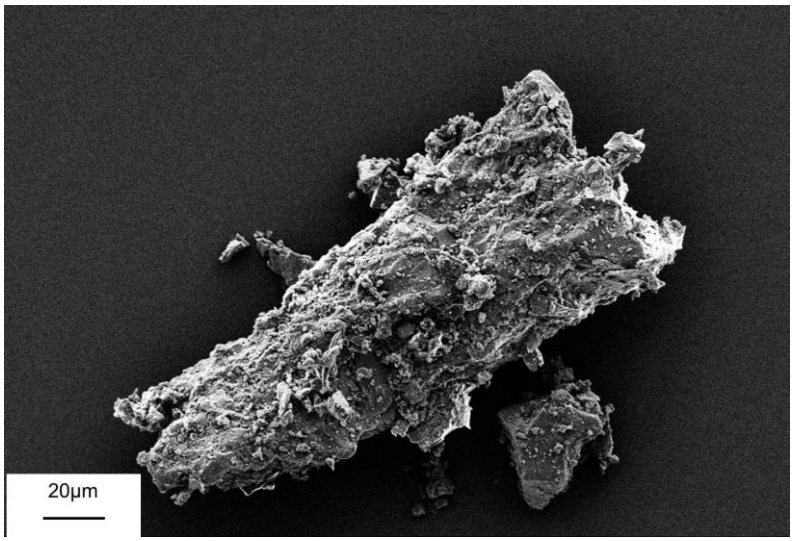

Figure 4- 30: Electronmicrograph of pulverised coal showing irregularity of shape

4.3.2 Coal Ash

After the initial ashing process, the organic amorphous phases are removed from the coal as shown by the lack of large amorphous bumps in the PXRD pattern background. Table 3-18 which shows the elemental composition, indicates a large portion of the ash is SiO_2, likely to be quartz and or Illite, both of which have been identified in the PXRD data (Table 4-8, Figure 4-31). Gypsum ($CaSO_4.2H_2O$), which has been identified in the coal fuel is no longer present after heating to 800°C, has most likely been dehydrated to form anhydrite ($CaSO_4$). Dolomite and calcite decompose above 600°C and 700°C respectively in the samples presented here. It is proposed the decomposition products undergo further reaction with SiO_2 to form phases such as Augite, a Ca,Mg,Fe-silicate with a similar structure to diopside. The illite $KAl_2(Si_3Al)O_{10}(OH)_2$, present in the fuel itself is also present in the heat-treated ash up to 900°C, after which thermal decomposition occurs.

Table 4-8: PXRD composition of high temperature heat treated ashes of coal

			Temperature (°C)					
Phase	Key	Composition	600	700	800	900	1000	1100
Quartz	Qz	SiO_2	•	•	•	•	•	•
Calcite	Ca	$CaCO_3$	•	•				
Dolomite	Do	$CaMg(CO_3)_2$	•					
Illite	Il	$KAl_2(Si_3Al)O_{10}(OH)_2$	•	•	•	•		
Anhydrite	An	$CaSO_4$	•	•	•	•	•	•
Hematite	He	Fe_2O_3	•	•	•	•	•	•
Albite	Ab	$NaAlSi_3O_8$	•	•	•	•	•	•
Mullite	Mu	$Al_{2.35}Si_{0.64}O_{4.82}$					•	•
Periclase	P	MgO			•	•	•	•
Cristobalite	Cr	SiO_2					•	•
Augite	Au	$Ca(Mg_{0.74}Fe_{0.26})Si_2O_6$					•	•

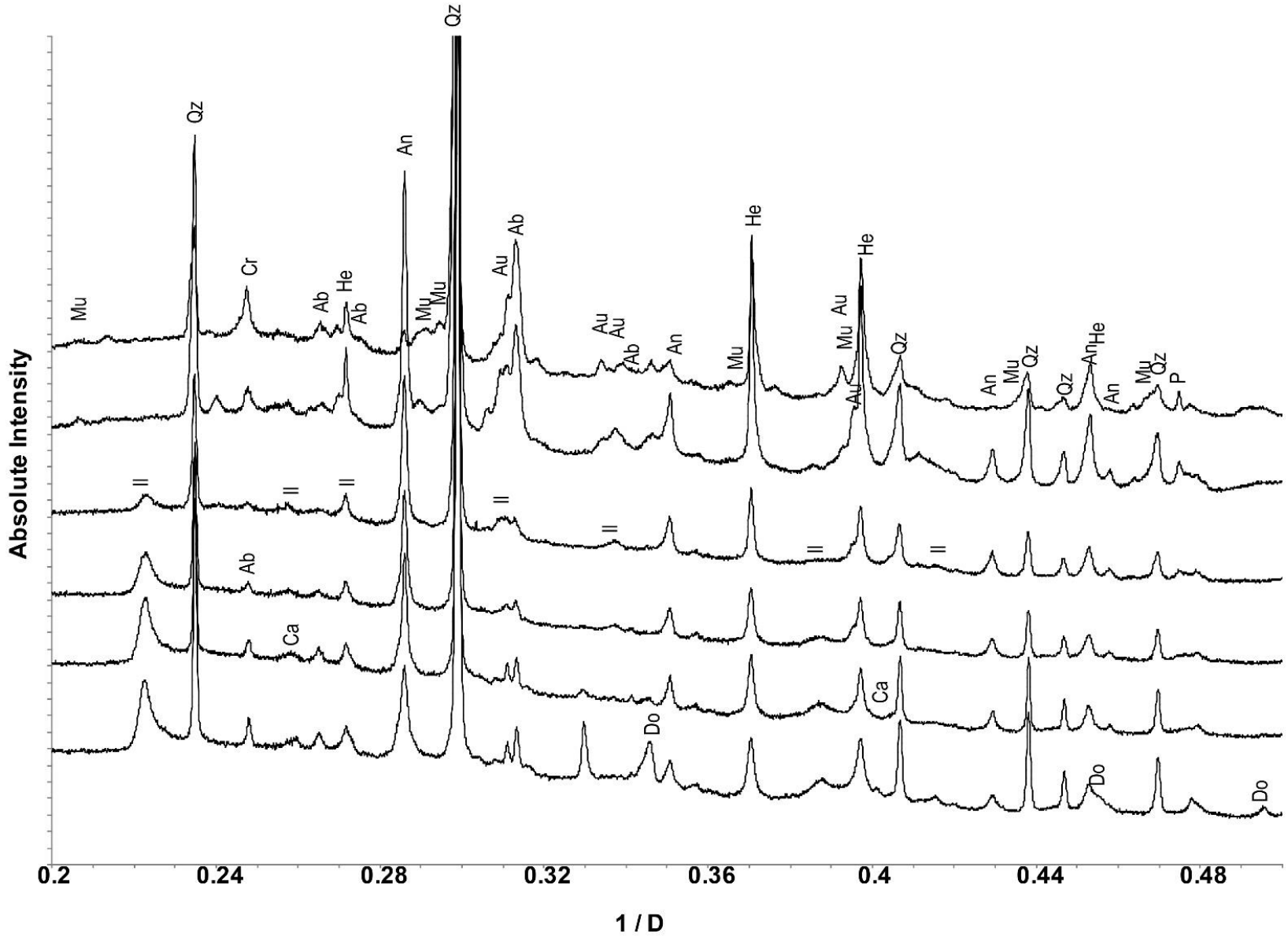

Figure 4-31: PXRD patterns of heat treated coal ash showing phase changes with temperature increase, data collected on the I-11 (λ 0.82675) beamline and truncated to 5-30 °2θ for clarity

Table 4-9: XRF elemental analysis for coal ash and high temperature coal ash treated at 900°C

	Wt%			
	Coal		Coal 900°C	
Al	15.24	±0.21	16.10	±0.05
Ca	8.52	±0.37	8.55	±0.04
Cl	0.13	±0.02	0.00	±0.58
Fe	11.13	±0.62	10.68	±0.16
K	3.53	±0.08	3.90	±0.09
Mg	2.38	±0.31	2.66	±0.01
Mn	0.12	±0.00	0.12	±0.29
Na	1.11	±0.37	1.26	±0.01
Ni	0.03	±0.01	0.03	±0.01
P	1.59	±0.12	1.77	±0.18
S	11.16	±0.13	7.78	±0.56
Si	43.17	±0.49	45.17	±0.03
Sr	0.49	±0.04	0.44	±0.00
Ti	1.41	±0.03	1.45	±0.01
Zn	0.08	±0.01	0.07	±0.00
Zr	0.08	±0.00	0.07	±0.05
	100.14		**100.00**	

A comparison of the ash composition at 900°C with the untreated fuel ash is presented in Table 4-9. There are few significant changes between the two indicating that the ash composition is largely unchanged. This is supported by the similar phases present at 600°C and 900°C in the PXRD data.

EDS maps of the coal ash shows the association of K, Al, Si, and O indicating the presence of illite at 600°C (Figure 4-32). This is in agreement of with the PXRD data at the same temperature.

Figure 4-33 shows EDS maps of the coal ash at 800°C; there is clear correlation between Ca, S, and O but also Fe, Mg, S, and O, suggesting that the rozenite which was shown to be present in the coal fuel has decomposed into $Fe_2(SO_4)_3$.[160]

EDS maps of the coal ash at 1000°C (Figure 4-34) show correlation between Ca, S, and O indicating the presence of anhydrite ($CaSO_4$), confirmed by analysis of the P-XRD data. Al, Si and O are also in close association, this suggests the presence of mullite also present in the PXRD pattern at 1000°C. Na is also in close association with Al, Si, and O likely to be the phase albite. K is present in this region too, however no K,Al-silicates were shown to be present through analysis of the PXRD data, suggesting it is present in minor quantities (less than 3wt% or amorphous) which are undetectable by PXRD.

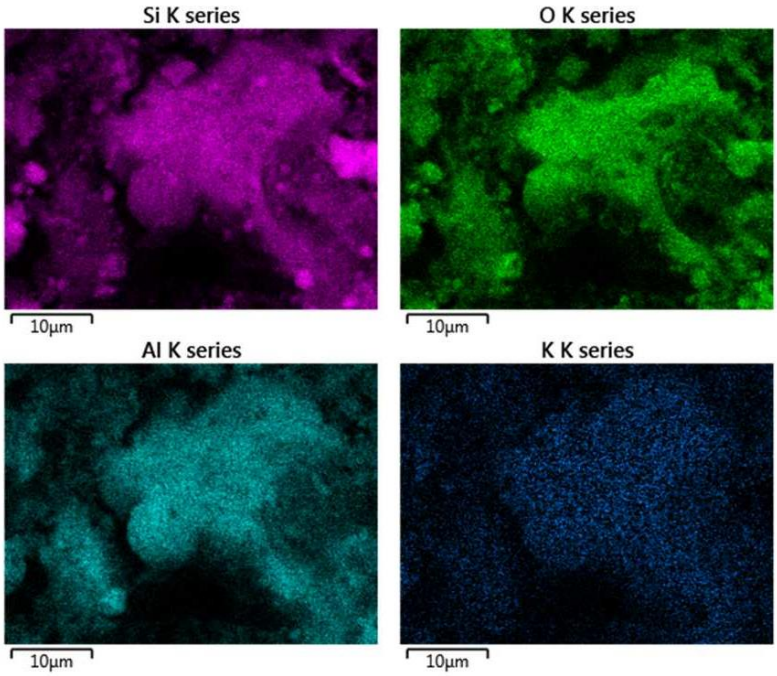

Figure 4-32: EDS map of coal ash at 600°C showing the presence of illite

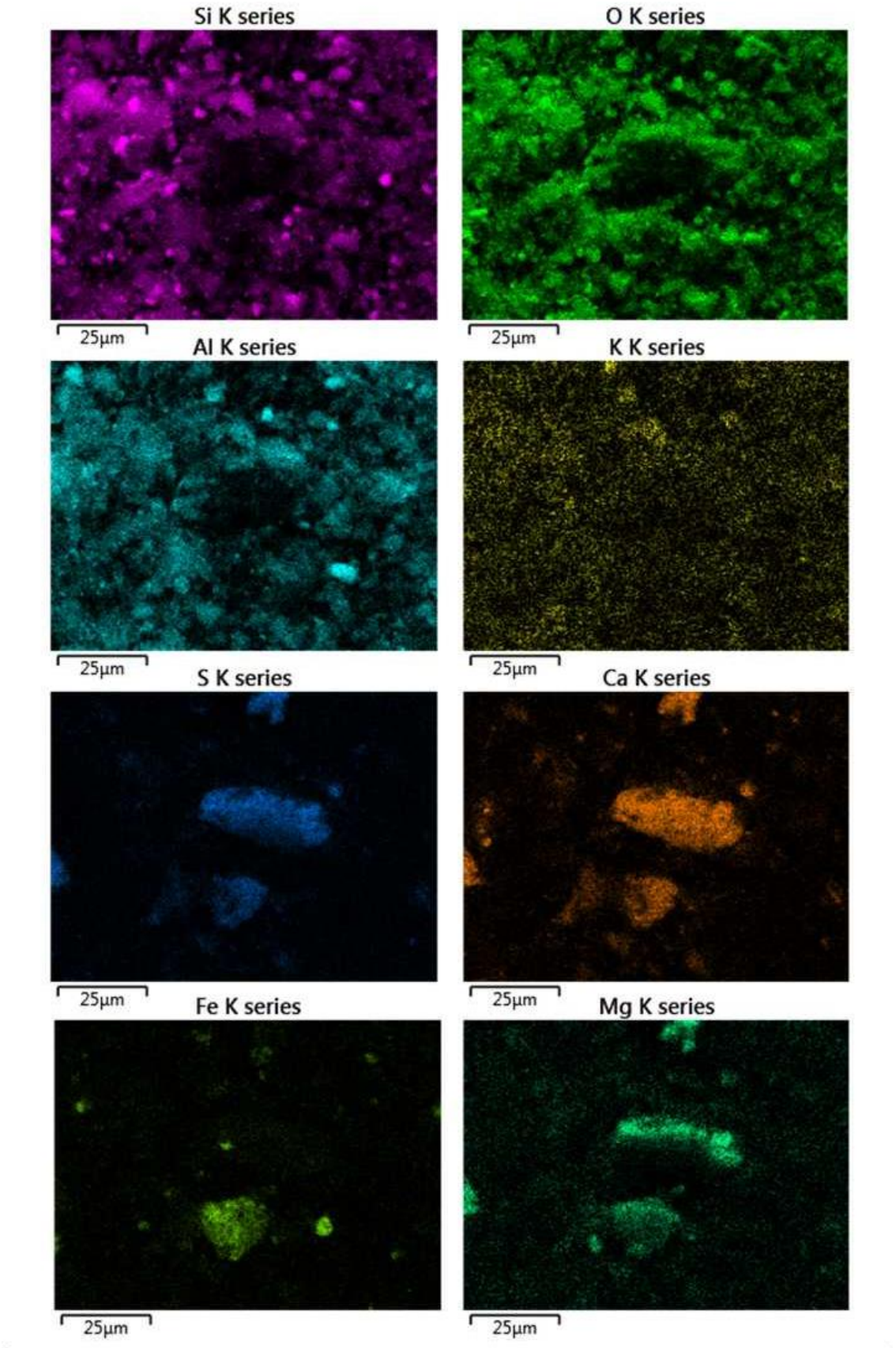

Figure 4-33: EDS Maps of coal ash at 800°C showing clear regions of correlation between Si,O,Al and K as well as Ca, S and O

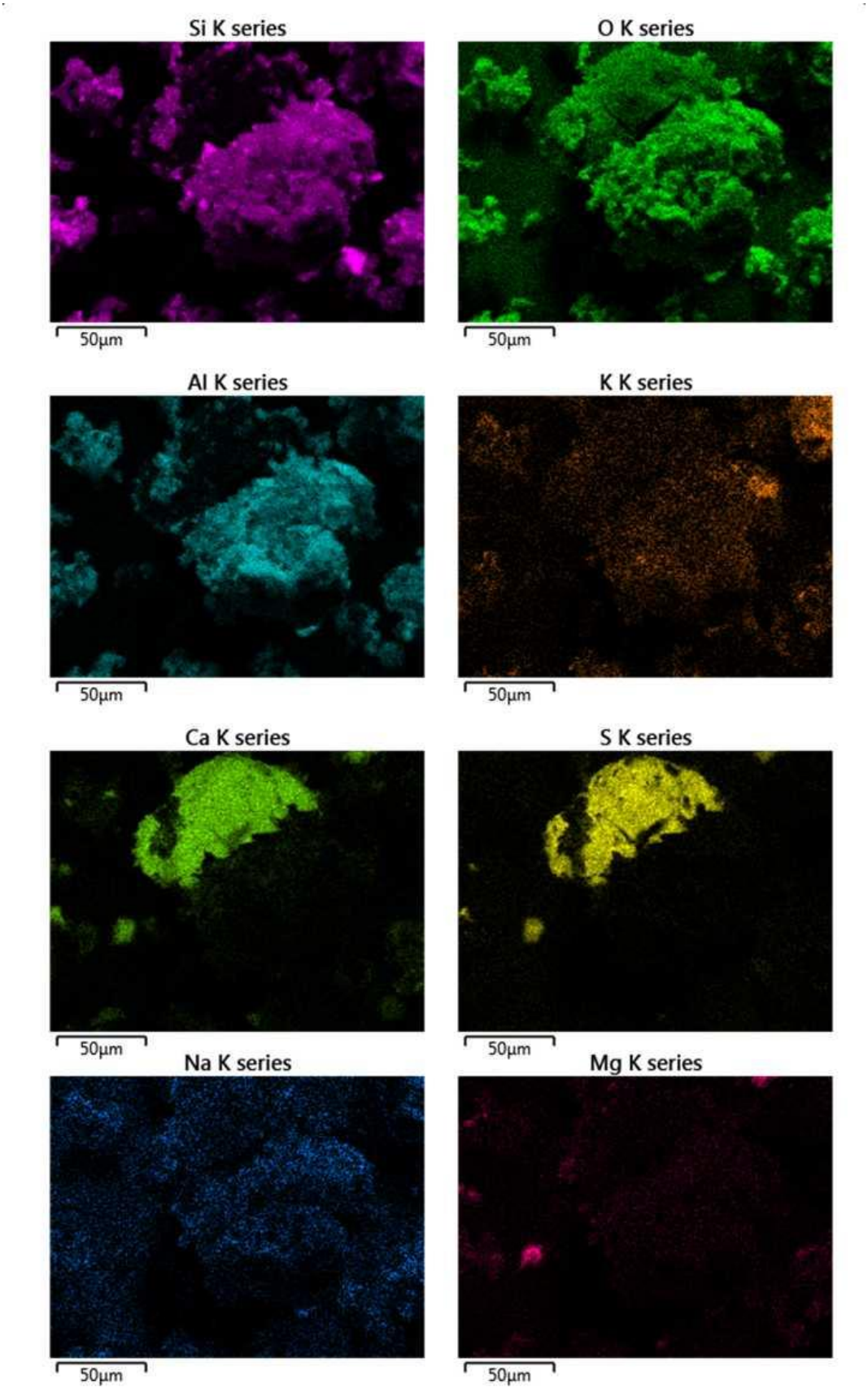

Figure 4-34: EDS analysis of coal ash heat treated at 1000°C for one hour showing CaSO4 and mullite

4.4 Hemp and Coal Ash

Hemp and coal (77:12 % by mass) were co-ashed according to the procedure outlined in Section 3.5.1. A large amount of the phases present in the separate fuel components are also in the blended ash after heat treatment (Table 4-10, Figure 4-35). The hydroxyapatite present in the hemp fuel is also present in the hemp and coal co-ash, and does not seem to react with other phases from either hemp or coal. Periclase is present in the heat treated ash, presumably through the decomposition of the dolomite ($CaMg(CO_3)_2$) present in both fuels (Equation 4-12).

Arcanite (K_2SO_4) is present in the heat treated ash, this forms through a reaction of KCl present in the hemp and the SO_2 liberated during the ashing of the coal (Equation 4-17). SO_2 is likely to form through decomposition of rozenite ($FeSO_4.4H_2O$). Due to the low S content of the hemp fuel (Table 3-1), K_2SO_4 is unlikely to form in the hemp ash. The reaction of KCl and SO_2, to form K_2SO_4, is of much interest in biomass firing and co-firing. KCl has frequently been cited as one of the most harmful components formed during the combustion of biomass as it condenses on surfaces which are cold in comparison to the gas. The KCl then reacts with the metal surface which often undergoes active oxidation (section 2.5.1).[48] Promotion of the formation of K_2SO_4, due to high S content in co-fired fuels, is one possible way of mitigating aggressive KCl corrosion[1].

$$2KCl + SO_2 + H_2O + \frac{1}{2}O_2 \rightarrow K_2SO_4$$

Equation 4-17

Microcline is present in both the hemp ash and the heat treated co-ashes; orthoclase ($KAlSi_3O_8$) another K-feldspar, is also present in the data. Microcline often forms through the slow cooling of orthoclase,[180] so the rapid cooling after removal from the furnace accounts for the formation of the orthoclase as the thermodynamic product microcline does not have time to form exclusively.

Table 4-10: Phases identified in high temperature ashed hemp and coal blend

			Temperature (°C)					
Phase	**Key**	**Composition**	**600**	**700**	**800**	**900**	**1000**	**1100**
Quartz	Qz	SiO_2	•	•	•	•	•	•
Calcite	Ca	$CaCO_3$	•	•	•	•		
Hydroxyapatite	Ha	$Ca_{10}(PO_4)_6(OH)_2$	•	•	•	•	•	•
Sylvite	Sy	KCl	•	•	•			
Microcline	Mi	$KAlSi_3O_8$	•	•	•	•	•	•
Periclase	P	MgO	•	•	•	•	•	•
Hematite	He	Fe_2O_3	•	•	•	•	•	•
Albite	Ab	$NaAlSi_3O_8$			•			•
Illite	Il	$KAl_2(Si_3Al)O_{10}(OH)_2$	•	•	•	•		
Arcanite	Arc	K_2SO_4			•	•		
Wollastonite	Wo	$CaSiO_3$				•	•	•
Diopside	Di	$CaMgSi_2O_6$				•	•	•
Akermanite	Ak	$Ca_2MgSi_2O_7$			•	•	•	•
Kalsilite	Ka	$KAlSiO_4$			•	•	•	•
Orthoclase	Or	$KAlSi_3O_8$					•	•
Larnite	La	Ca_2SiO_4			•	•	•	•
Mullite	Mu	$Al_{2.35}Si_{0.64}O_{4.82}$					•	•
Anhydrite	An	$CaSO_4$					•	•
Cristobalite	Cr	SiO_2						

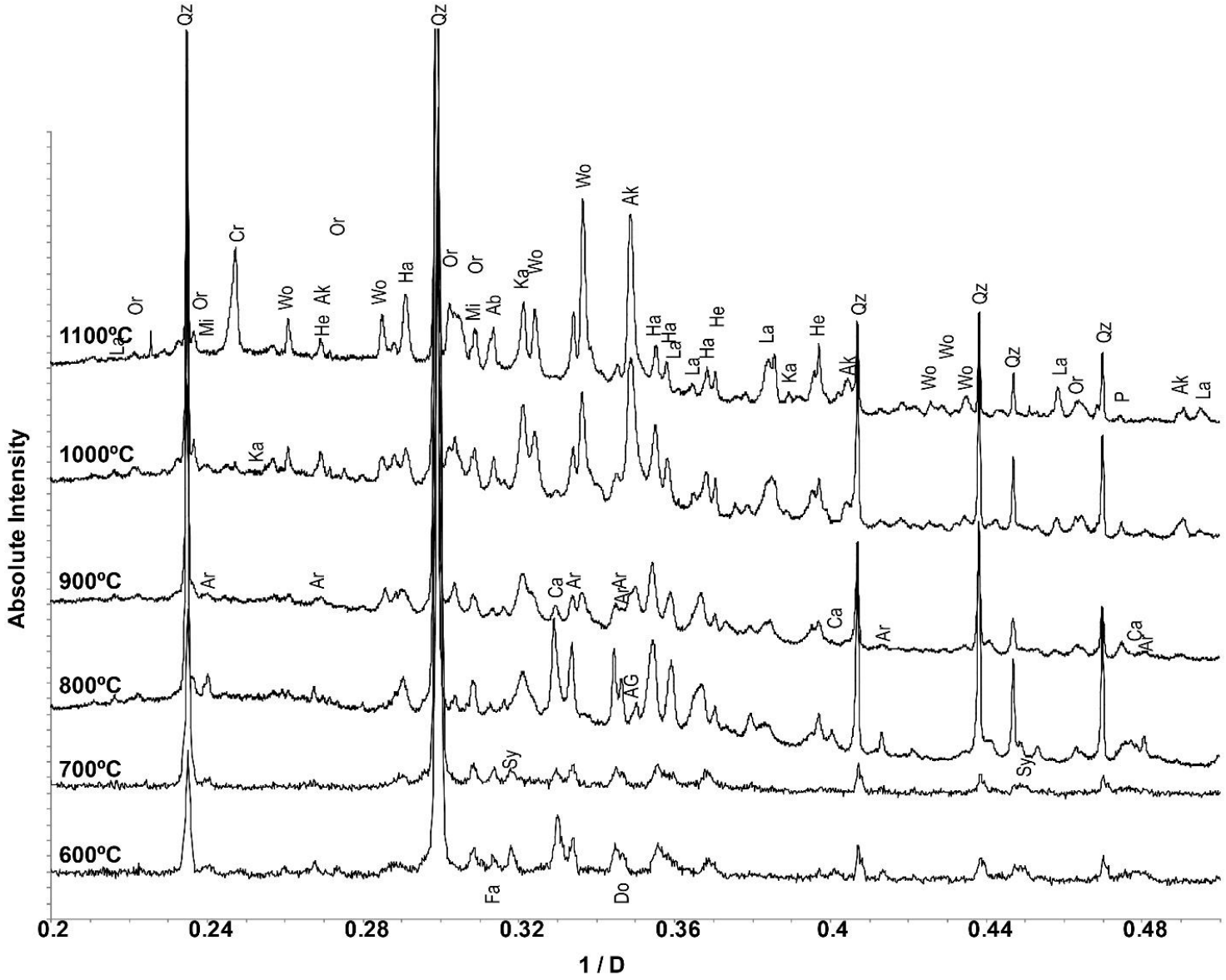

Figure 4-35: PXRD patterns of high temperature heat treated hemp and coal ash showing ash composition and phases present at different temperatures, data 800-1100°C collected on the I-11 beamline (λ 0.82675) 600-700°C collected on the D2 and truncated to 0.1-0.6 1/D.

Cultrone *et al*.[161] show K-feldspars (such as microcline and orthoclase) forming through the reaction of illite and calcite.

$$KAl_2(Si_3Al)O_{10}(OH)_2 + 2CaCO_3 + 4SiO_2 \rightarrow 2KAlSi_3O_8 + 2Ca_2Al_2SiO_8 + 2CO_2 + H_2O$$

Equation 4-18

Previous investigation of high temperature heat treatment of the hemp and coal blend showed the presence of anorthite[181] ($Ca_2Al_2SiO_8$), the presence of this phase was not observed in the ashes studied here suggesting the local environment of the phases is of great importance for formation i.e: phases that are in direct contact. Mao *et al*.[182] present a calculated phase diagram (Figure 4-36) for the system CaO-SiO_2-Al_2O_3 which suggests that $CaSiO_4$ or pseudo-wollastonite may form instead.

Albite is present at 800°C and 1100°C. Its absence at 900 and 1000°C is likely due to the inhomogeneous nature of the samples. Albite is present from the coal fuel and therefore, due to the ratios of the fuel, less will be present in the sample. The anhydrite ($CaSO_4$) may have formed during heat treatment of the ashes, potentially as a component of the coal ash. $CaSO_4$ is present above 1000°C; Vassilev *et al*. note the crystallisation of secondary sulphates above 900°C.[27] Also present from the coal fuel is mullite ($Al_{2.35}Si_{0.64}O_{4.82}$) suggesting formation without interaction with the hemp ash.

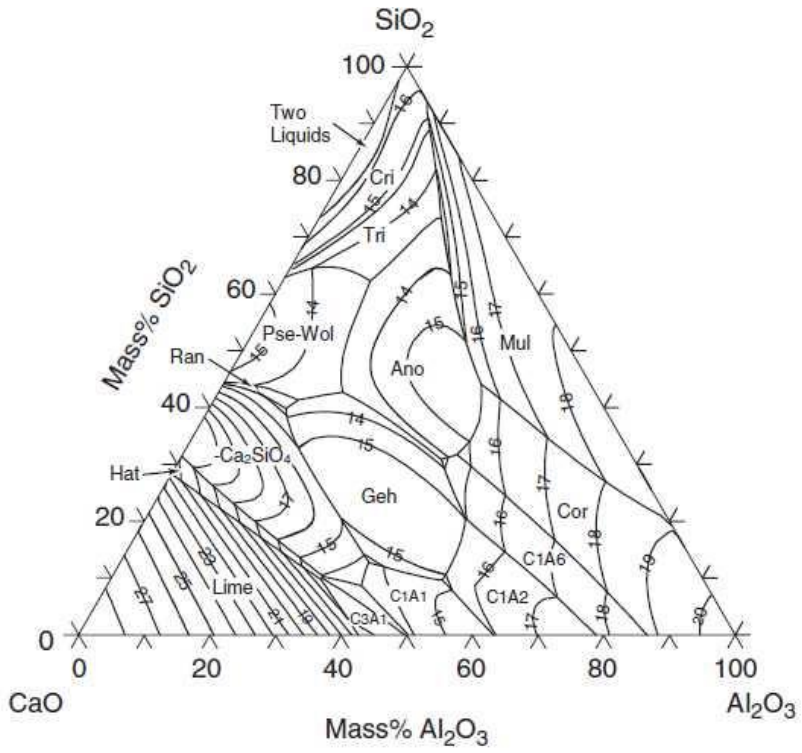

Figure 4-36: The CaO-SiO_2-Al_2O_3 phase diagram

The Ca-silicates and Ca,Mg-silicates formed in the high temperature heat treatment of the hemp ash are also present in the co-ash. Akermanite ($Ca_2MgSi_2O_6$) is present prior to diopside. This is in agreement with the CaO-SiO_2-MgO phase diagram (Figure 4-24),[164] which indicates that a low MgO content will influence the formation of these phases; in this case the Mg content of the hemp and coal ash is 5.27%.The larnite (Ca_2SiO_4) is present in the co-ash at high temperature, as well as the hemp ash. This is likely to be a by product of the reactions to form akermanite and diopside.

Table 4-11: XRF data for hemp and coal ash and high temperature hemp and coal ash blend treated at 900°C

	Wt%			
	Hemp and Coal		Hemp and Coal 900°C	
Al	4.01	±0.16	3.37	±0.04
Ca	31.91	±0.01	31.66	±0.63
Cl	0.94	±0.04	0.42	±0.03
Fe	3.13	±0.02	3.03	±0.32
K	13.91	±0.13	11.51	±0.27
Mg	5.27	±0.19	5.09	±0.17
Mn	0.34	±0.00	0.32	±0.01
Na	0.78	±0.25	1.24	±0.30
Ni	0.02	±0.00	0.02	±0.01
P	11.94	±0.05	11.85	±0.07
S	4.55	±0.21	4.42	±0.06
Si	23.41	±0.49	24.57	±0.76
Sr	0.18	±0.01	0.18	±0.01
Ti	0.42	±0.06	0.32	±0.00
Zn	0.10	±0.01	0.10	±0.00
Zr	0.07	±0.04	0.05	±0.01
	100.92		**98.13**	

Comparison of the elemental composition of the ash at 900°C and the fuel blend ash (Table 4-11) indicates little change. There is a decrease in Cl content (0.94 to 0.42 wt%). This also corresponds with a loss of K (13.91 to 11.51 wt%), potentially indicating the loss of KCl as a gas. There is an increase in Na (0.78 to 1.24 wt%) which suggests that there may be a greater percentage of albite in the sample prepared for analysis of the 900°C ash.

Electronmicrographs of the hemp and coal co-ash (Figure 4-37) at 600 and 700°C show trichomes in the ash from the high temperature heat treatment of hemp are also present in the hemp and coal high temperature ash. At lower temperatures there seems to be separation between the two types of ash, however at higher temperatures the ash appears to have formed agglomerates. In comparison to high temperature hemp ash there are less large glassy

particles. The agglomeration of the particles suggests that the fuel blend may be disposed towards slagging and fouling.

EDS maps of hemp and coal co-ash after heat treatment at 600°C (Figure 4-38), clearly show the presence of the trichomes present from the hemp. Also closely associated are K, Al, Si, and O suggesting that this may be illite present from the coal ash. On the surface of the K, Al, Si, O region is a Na, Al, Si, O region; this is likely to be the phase albite, also present from the coal. Ca, S, and O are also clearly associated suggesting the presence of anhydrite, also from the coal. The separation of the phases present from the coal ash and hemp ash at this temperature suggests interaction begins at higher temperatures and this is supported by the PXRD data.

At higher temperatures (Figure 4-39), there is less evidence of separation between the phases from hemp and coal ash individually. There is association between Ca, P, and O indicating the presence of the hydroxyapatite identified through PXRD analysis. Ca, S, and O are once again present in close association indicating the presence of anhydrite.

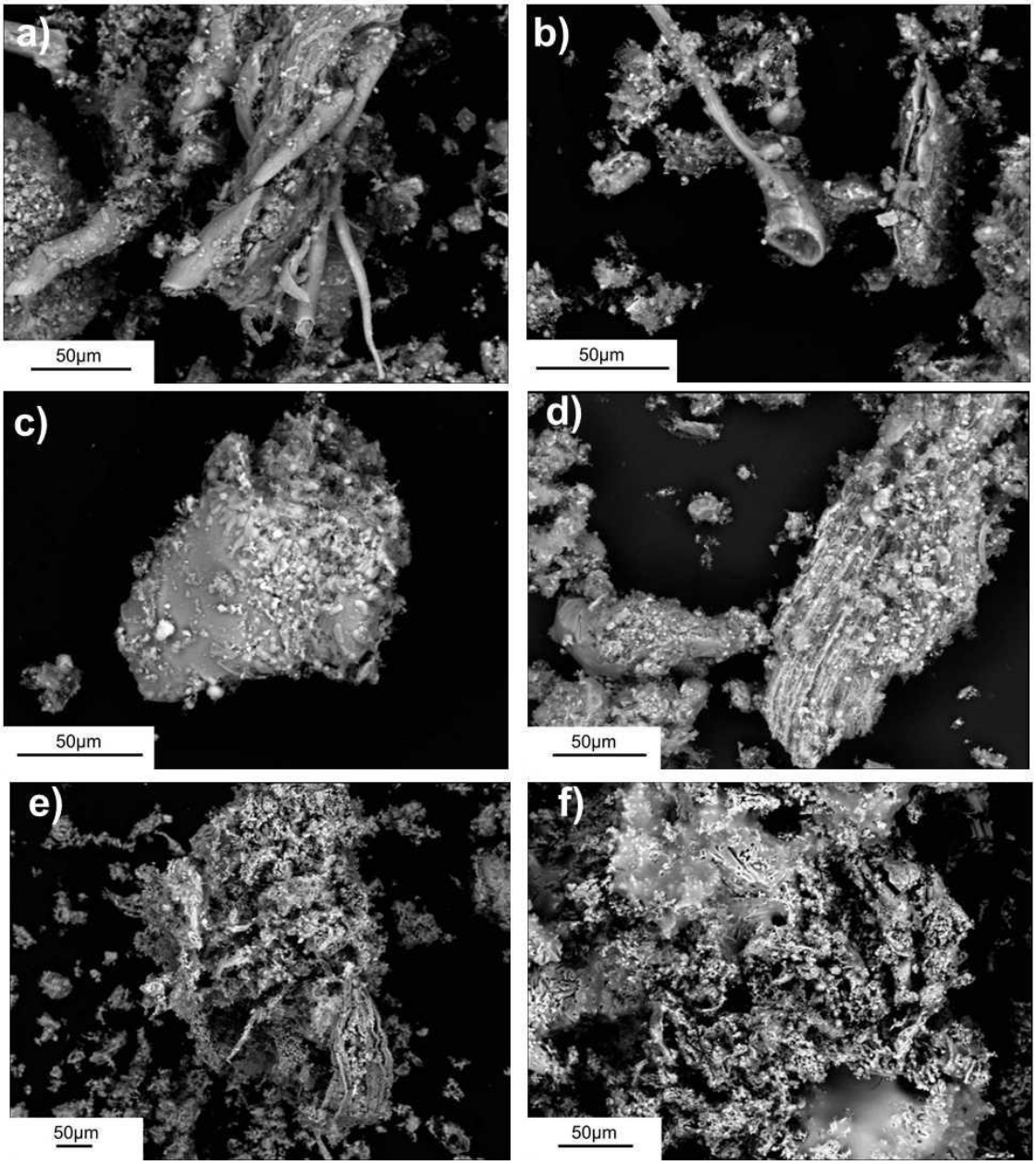

Figure 4-37: Electronmicrographs of hemp and coal co-ashing at a)600°C b)700°C c)800°C d)900°C e)1000°C f)1100°C

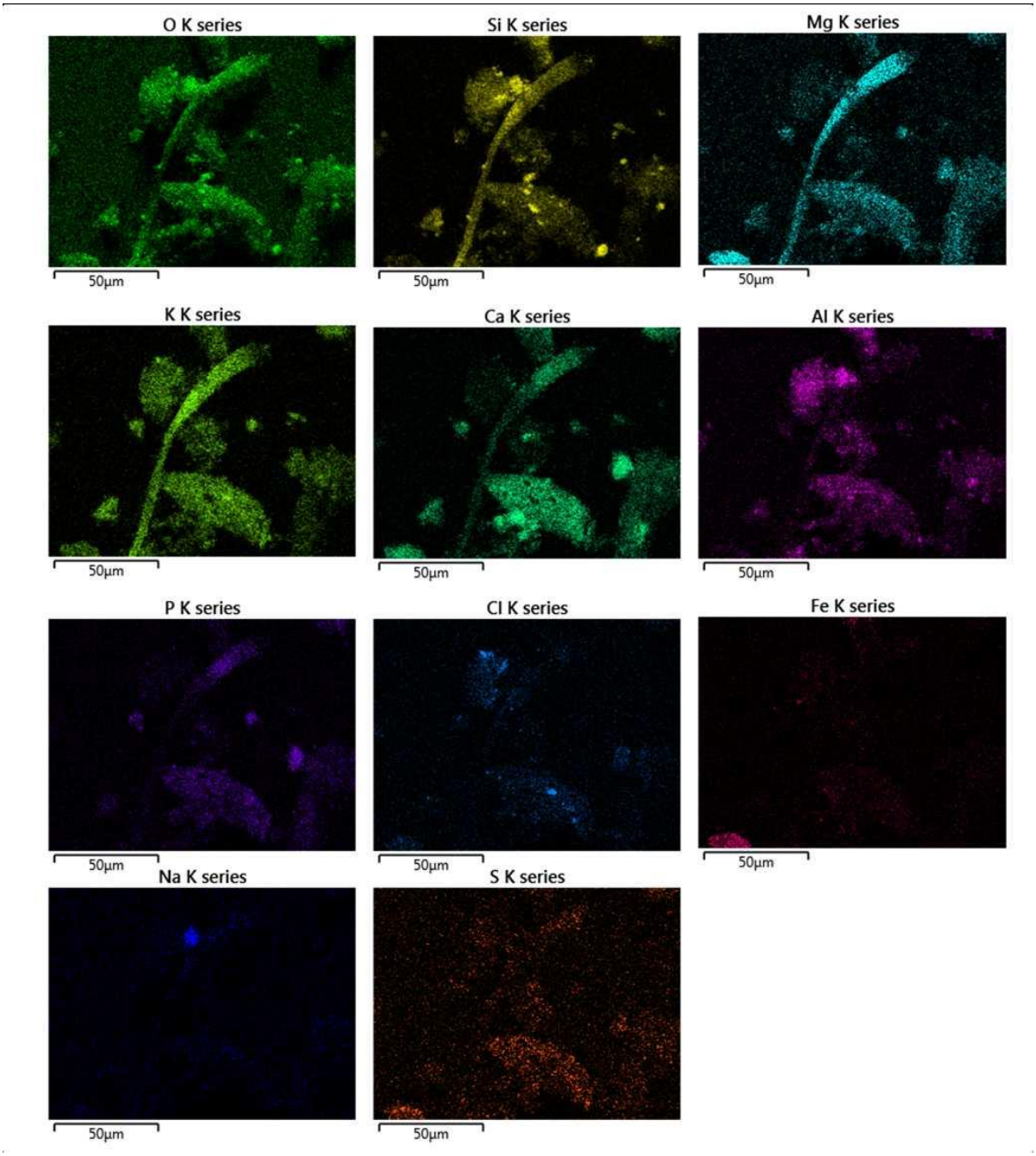

Figure 4-38: EDS Maps of Hemp and Coal at 600°C showing trichome composition and K,Al,Si and O association

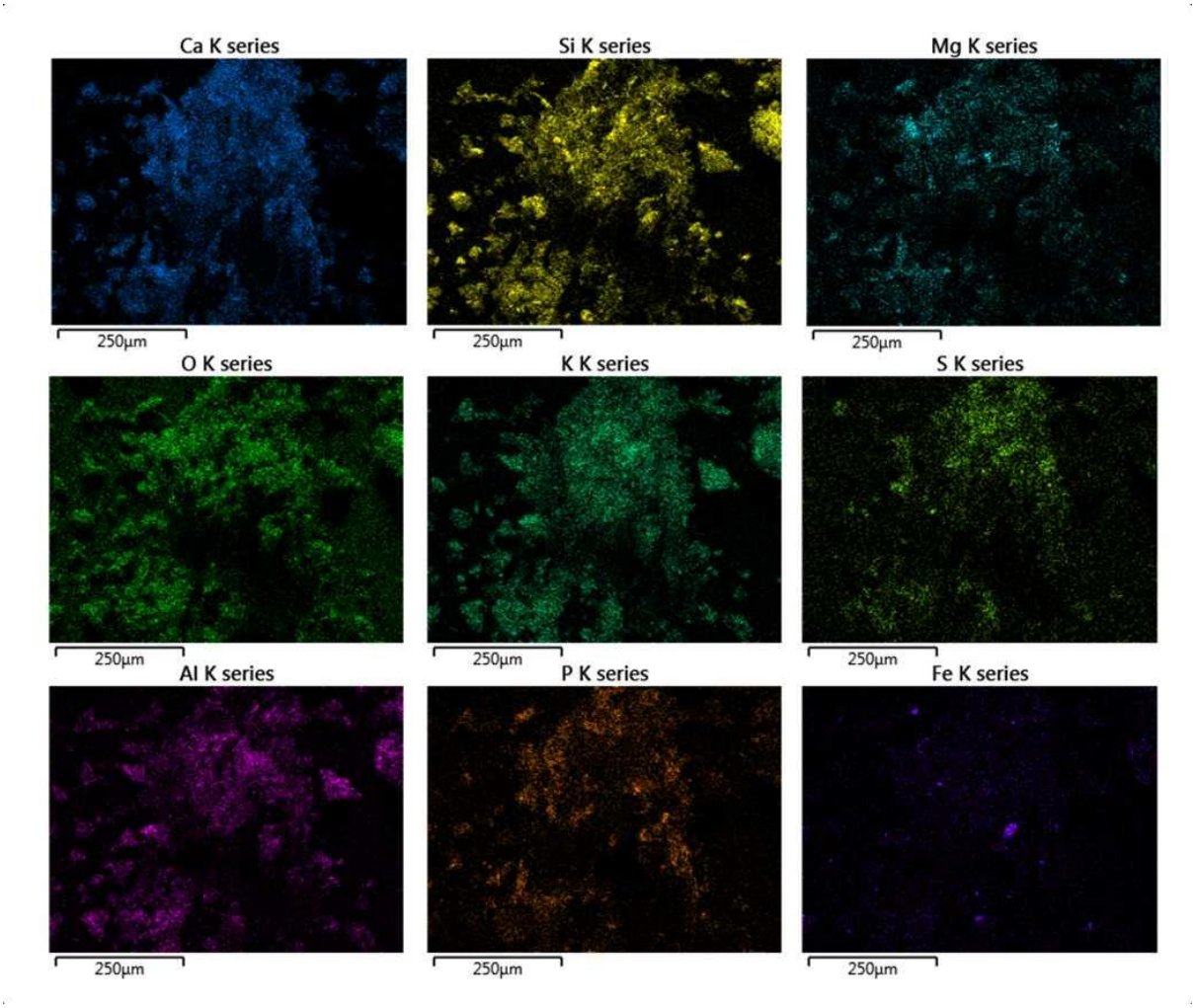

Figure 4-39: EDS maps of hemp and coal ash after 1000°C high temperature heat treatment for 1 hour

4.5 Eucalyptus and Coal Ash

Eucalyptus and coal (12:88% by mass) were co-ashed according to the procedure outlined in section 3.5.1**.** Similar to results seen in the heat treatment of the hemp ashes, phases present in both the eucalyptus and coal ashing were identified (Figure 4-40,Table 4-12).

The K,Al-silicate leucite ($KAlSi_2O_6$) is thought to have formed through the reaction of kalsilite $KAlSiO_4$ with quartz, as was shown synthetically by Zhang *et al*.[183] where $KAlSiO_4$ was synthesised followed by heat treatment at 750-900°C in 50°C increments to yield $KAlSi_2O_6$.

Periclase is likely to have formed through the decomposition of dolomite (Equation 4-10), which was shown to be present at lower temperatures in the coal and eucalyptus ash. In comparison to the heat treated eucalyptus ash, where the Ca,Mg-silicate formed is akermanite, the dominant Ca-Mg silicate is diopside. This can be explained by the SiO_2 content in the samples, in the co-ash blend there is 31.28% SiO_2 in comparison to 16.92% in the eucalyptus ash. Figure 4-24, the CaO-MgO-SiO_2 phase diagram shows that a lower SiO_2 content will lead to the preferential formation of diopside. The change in SiO_2 composition of the ash also accounts for the disappearance of the Ca,Mg-silicate phases monticellite and merwinite that were seen in the eucalyptus heat treatment.

Mao *et al*.[182] studied the CaO-$Al_2O_3SiO_2$ system (Figure 4-36), this shows that gehlenite ($Ca_2Al_2SiO_7$) will form under the conditions present in the eucalyptus ash systems. Cultrone *et al*.[161] presented the reaction of illite and calcite, both of which are present in the ash, to form gehlenite:

$$KAl_2(Si_3Al)O_{10}(OH)_2 + 6CaCO_3 \rightarrow 3Ca_2Al_2SiO_7 + 6CO_2 + 2H_2O + K_2O + 3SiO_2$$

Equation 4-19

Cultrone *et al.* also note that the formation of gehlenite is likely due to ease of crystallisation, where under laboratory conditions it is easier for Al to form in 4-co-ordinate compounds.[161] Trindade *et al*.[162] note that gehlenite and wollastonite are often precursors to anorthite, however at the temperatures reached in this heat treatment (up to 1100°C) they are stable.

Table 4-12: Phases present in the high temperature heat treatment of eucalyptus and coal ash

			Temperature (°C)					
Phase	**Key**	**Composition**	**600**	**700**	**800**	**900**	**1000**	**1100**
Quartz	Qz	SiO_2	•	•	•	•	•	•
Hematite	He	Fe_2O_3	•	•	•	•	•	•
Calcite	Ca	$CaCO_3$	•	•				
Fairchildite	Fa	$K_2Ca(CO_3)_2$	•	•	•			
Albite	Ab	$NaAlSi_3O_8$	•	•	•	•	•	•
Anhydrite	An	$CaSO_4$	•	•	•	•	•	•
Illite	Il	$KAl_2(Si_3Al)O_{10}(OH)_2$	•	•	•	•		
Periclase	P	MgO	•	•	•	•	•	•
Microcline	Mi	$KAlSi_3O_8$			•	•	•	•
Kalsilite	Ka	$KAlSiO_4$				•	•	
Wollastonite	Wo	$CaSiO_4$					•	•
Diopside	Di	$CaMgSi_2O_6$					•	•
Akermanite	Ak	$Ca_2MgSi_2O_6$					•	
Leucite	Le	$KAlSi_2O_6$					•	•
Cristobalite	Cr	SiO_2					•	•
Mullite	Mu	$Al_{2.35}Si_{0.64}O_{4.82}$					•	•
Grossular	Gr	$Ca_3Al_2(SiO_4)_3$						•
Magnetite	Mag	Fe_3O_4						•
Gehlenite	Ge	$Ca_2Al_2SiO_7$					•	•

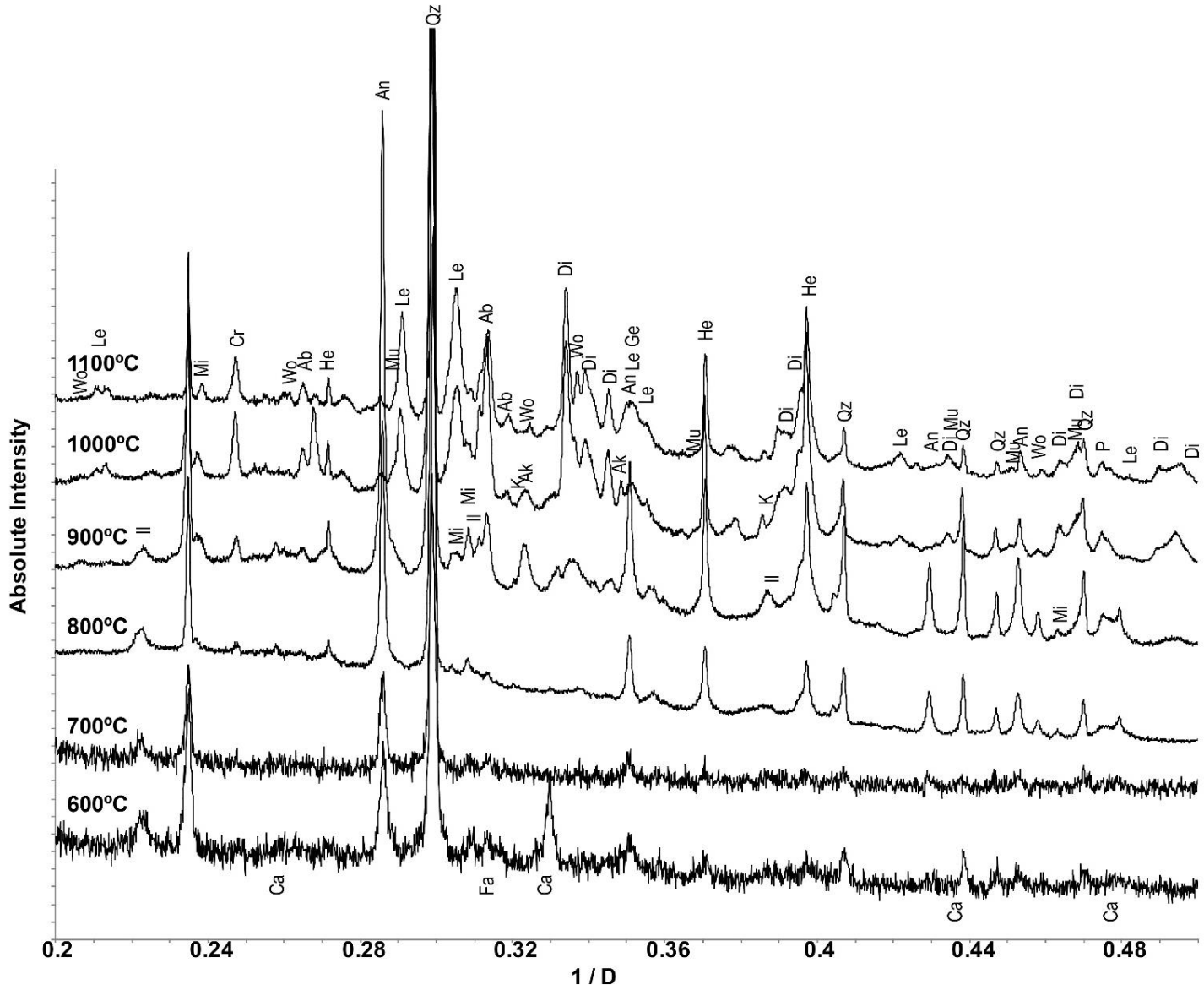

Figure 4-40: PXRD patterns of eucalyptus and coal ash from 800-1100°C showing fuel interactions and phases present after high temperature ashes patterns 800-1100C collected on the I-11 synchrotron beam (λ 0.826215) 1/D for comparison with 600-700 C range, collected on the D2 and truncated to 0.1-0.6.

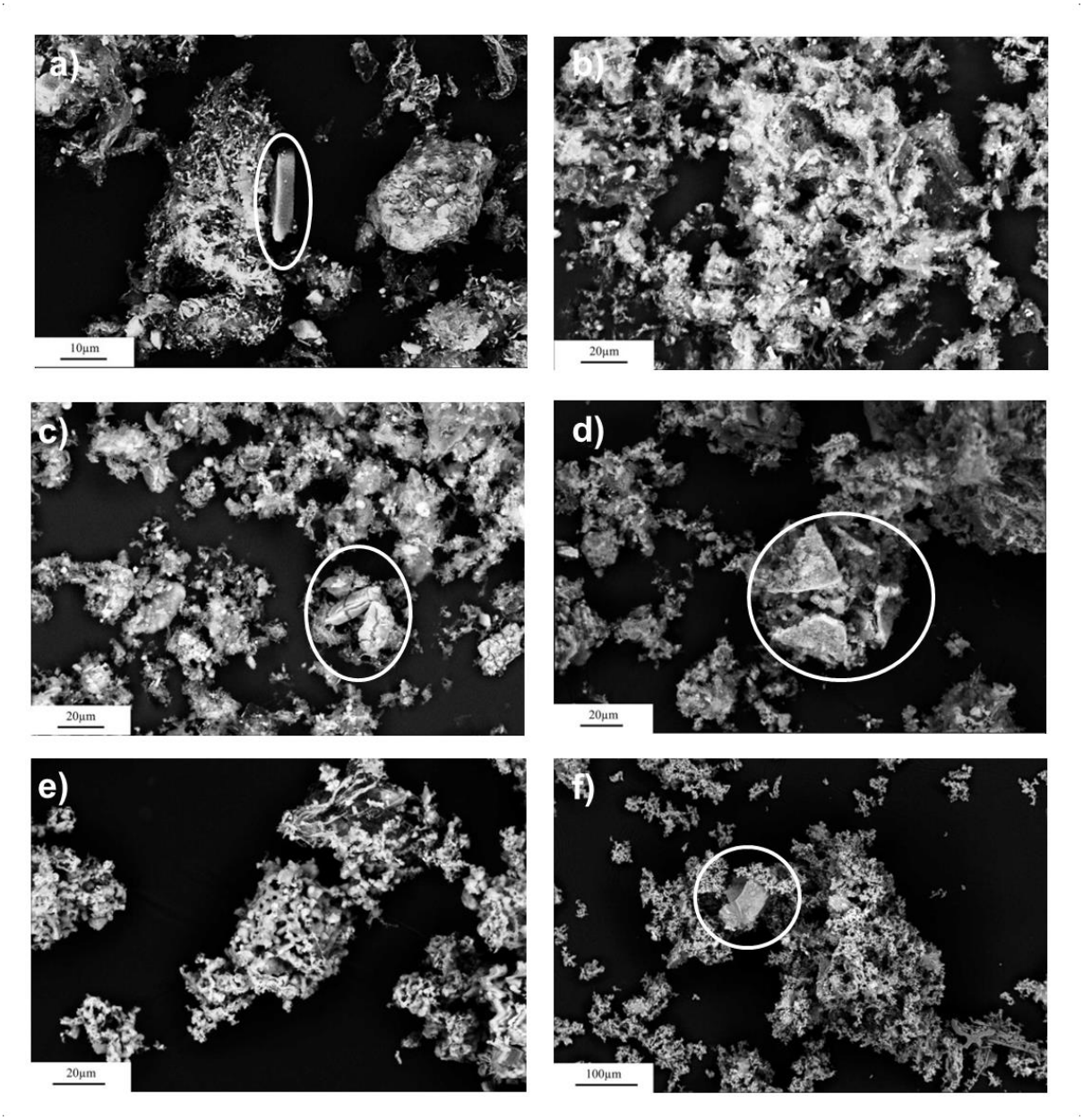

Figure 4-41: Electronmicrographs of the eucalyptus and coal co-ash at a)600°C b)700°C c) 800°C d)900°C e)1000°C and f) 1100°C

Electronmicrographs of the eucalyptus and coal ash (Figure 4-41) show that once the organic matrix has been lost, some distinct crystals are observed (circled). The general morphology of the ash does not appear to change dramatically throughout the high-temperature treatment. This could be related to the low ash content of the eucalyptus, which has a greater content in the fuel blend. This also indicates that the fuel blend is likely to have a low slagging potential when used in larger scale combustion.

The parallelepiped crystal circled in Figure 4-41a has the composition of K, Al, Si, and O. This suggests it may be microcline present from harvesting in the soil, or illite which will not have

decomposed at 600°C but may have been exposed during the loss of organic matter. The crystal morphology is closer to that typically presented as monoclinic, and is therefore likely to be Illite which is in the monoclinic crystal system. The limitations of EDS analysis mean the H will be unable to be detected.

The parallelepiped crystals present in Figure 4-41c have the composition Ca, S, and O (Figure 4-43). This is anhydrite ($CaSO_4$), also seen in the PXRD data at 800°C, which is present from the dehydration of gypsum ($CaSO_4.2H_2O$) in the initial ashing of the fuel. These crystals have the characteristic orthorhombic dipyramidal shape, further confirming the presence of anhydrite.

The crystal circled in Figure 4-41f has a composition of O, Si, Al, Ca, K, Mg, Fe, and Mn (Figure 4-42) suggesting a complex system. The crystal may contain several minerals and therefore identification of each is not possible.

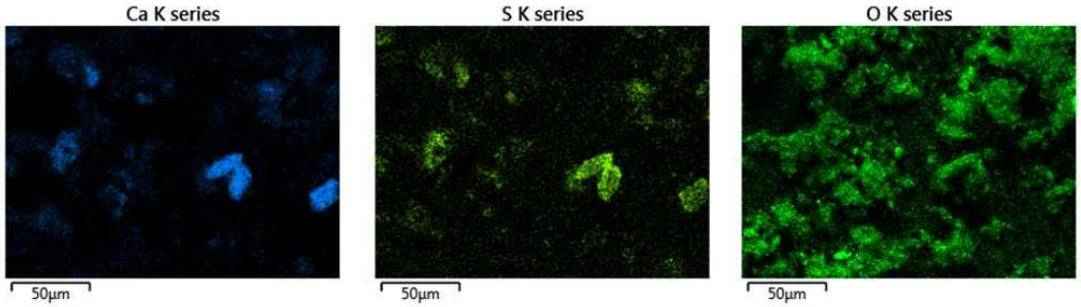

Figure 4-43: EDS Maps of crystals present after 800°C heat treatment of eucalyptus and coal ash for 1 hour

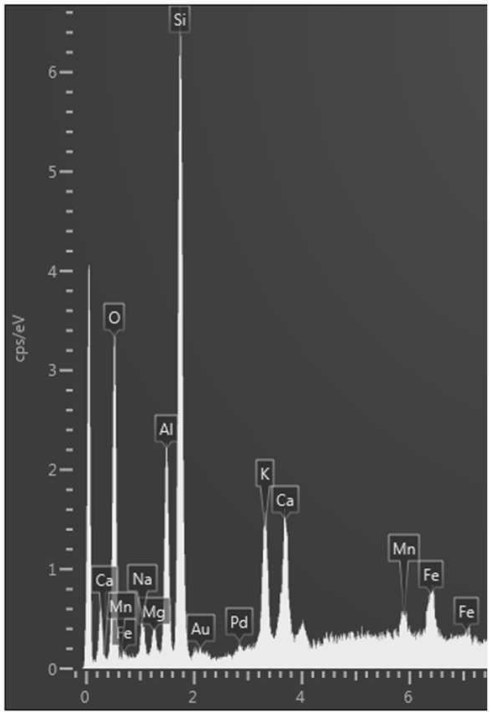

Figure 4-42: EDS analysis of crystal presented in Figure 4-41f

Analysis of the EDS maps of the co-ash heated at 900°C for 1 hour (Figure 4-44) shows there is distinct association between Ca, S, and O, indicative of anhydrite. Present is a region of K, Mg, Ca, Al, Si, and O interaction, this suggests the region my contain Illite or $KAlSiO_4$ alongside forming akermanite and gehlenite. In this block there is also a region rich in Si and O, suggestive of unreacted quartz.

EDS Maps of eucalyptus and coal ash heat treated at 1100°C for 1 hour (Figure 4-45), shows regions of association between Si, O, K, Al, Ca, and Mg. This region is likely to contain akermanite, gehlenite, leucite, and quartz. In the bottom right hand corner of the image is association between Al, Si, and O, the needle shape of these crystals is indicative of mullite, formed from the coal ash, also shown to be present at this temperature in PXRD data analysis.

Table 4-13: XRF data for eucalyptus and coal ash and high temperature eucalyptus and coal ash treated at 900°C

	Wt%			
	Eucalyptus and Coal		**Eucalyptus and Coal 900°C**	
Al	10.54	±0.08	12.16	±0.11
Ca	17.75	±0.13	16.20	±0.09
Cl	1.02	±1.17	0.14	±0.01
Fe	11.93	±0.49	9.04	±0.28
K	7.81	±0.01	7.32	±0.05
Mg	2.81	±0.05	3.95	±0.06
Mn	1.28	±0.01	1.07	±0.01
Na	1.23	±0.10	1.71	±0.30
Ni	0.04	±0.01	0.02	±0.00
P	2.48	±0.02	2.44	±0.04
S	9.16	±0.08	10.39	±0.04
Si	31.25	±0.35	32.87	±0.08
Sr	0.39	±0.03	0.40	±0.01
Ti	1.35	±0.01	1.06	±0.03
Zn	0.14	±0.00	0.11	±0.01
Zr	0.05	±0.01	0.05	±0.00
	99.20		**98.90**	

A comparison of the elemental composition of the fuel blend ash and the high temperature treatment of the ash at 900°C shows few changes (Table 4-13). This corresponds with changes to the phase composition of the ash which has changed relatively little with only a decomposition of the carbonates identified in the XRD data. The S present in the ash can be attributed to the presence of the phase anhydrite ($CaSO_4$).

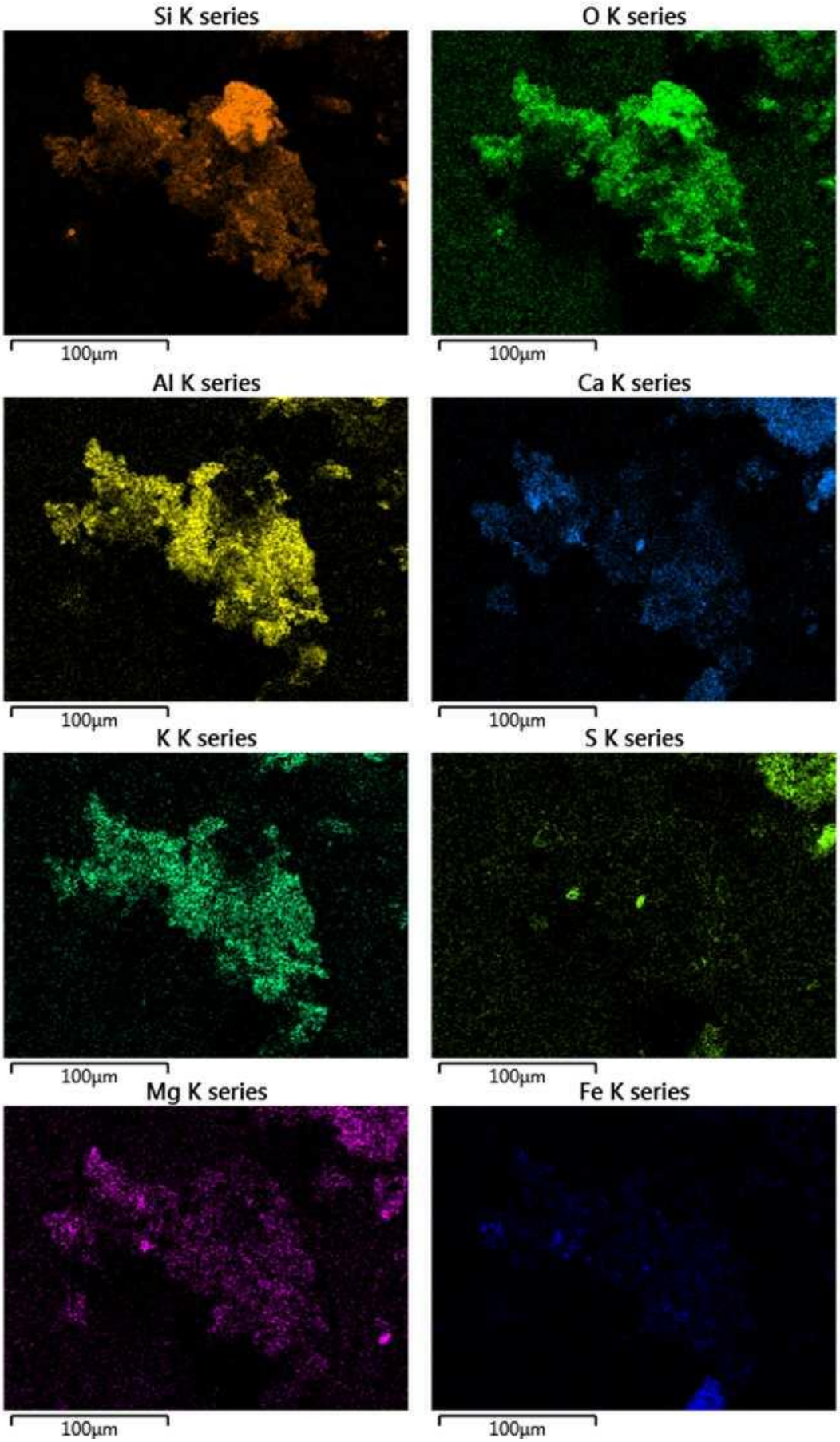

Figure 4-44: EDS Maps of eucalyptus and coal ash heated at 900C for 1 hour

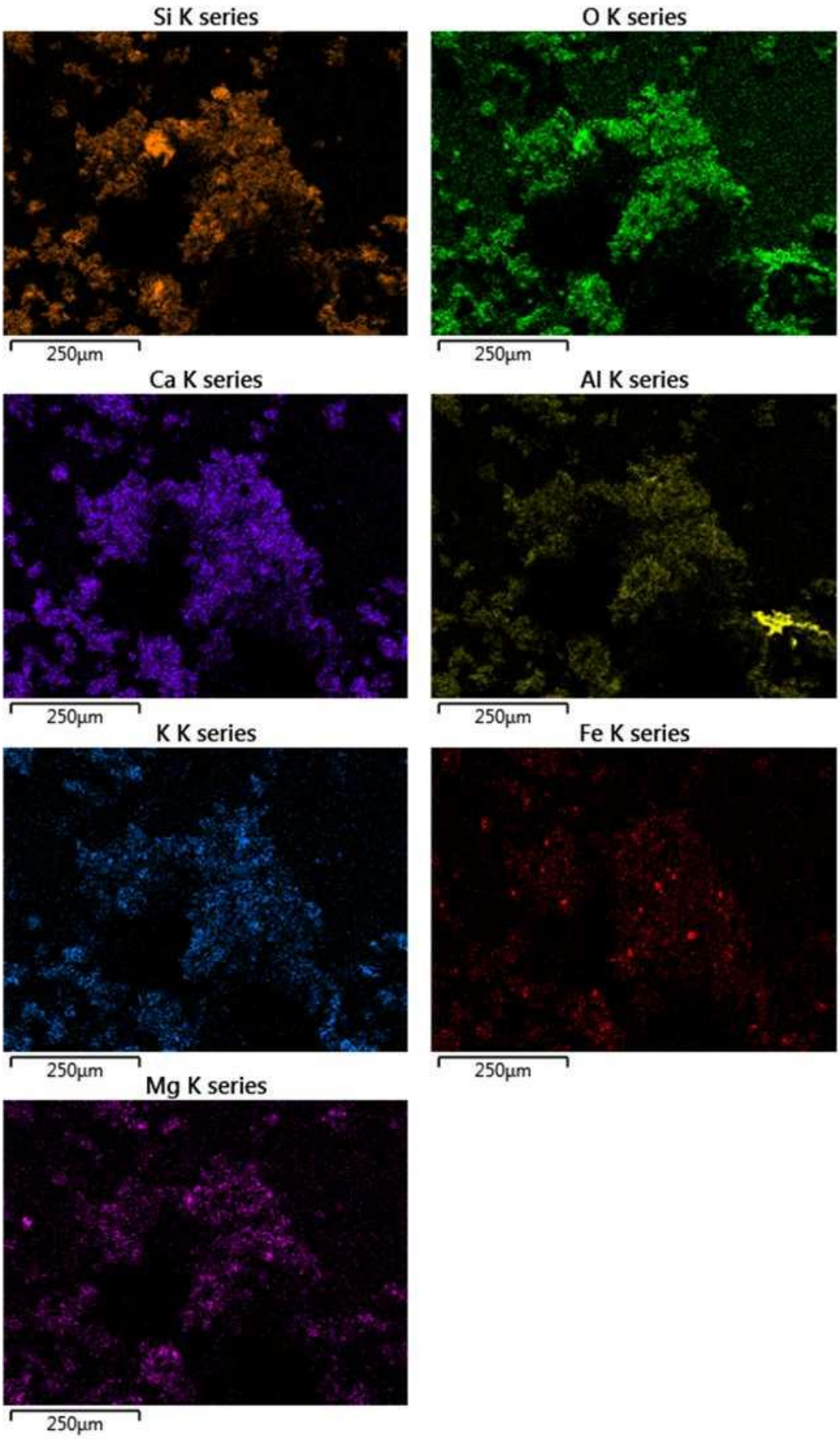

Figure 4-45: EDS Maps of eucalyptus and coal ash heated at 1100C for 1 hour

4.6 Conclusions

Evaluation of the biomass, coal, and the blends used in the co-firing trials has given information about the fuels that can be used when analysing the impact of using the blends and biomass in large scale combustion tests. As the temperature that the ash is treated at increases, reactions often happen in the ash; this can be biomass-biomass, coal-coal, or biomass-coal. The different proportions of the elements in the fuel can result in the formation of proportionally different phases containing the same elements as illustrated by the CaO-MgO-SiO_2 and CaO-Al_2O_3-SiO_2 phase diagrams presented above.

Ceramic systems with similar compositions to the biomass ashes, like those presented by Trindade *et al.*[162] and Cultrone *et al*.[161] can also be used alongside phase diagrams to predict which phases will be present in different conditions. This would be of particular use when investigating ashes where the additives lime and kaolin are used[184,185] in an attempt to limit corrosion.

The decomposition temperature of calcite ($CaCO_3$) varies between the fuels (last detection varies from 700-900°C). This suggests that fuel content also has an affect on the decomposition and/or reaction of the calcite. For hemp, the last identification of $CaCO_3$ is 800°C. When the fuel is blended with coal, the last identification is 900°C. For eucalyptus the last detection is at 700°C, and when mixed with coal it remains at 700°C. The presence of Ca in the trichome structures in the hemp fuel could explain the later decomposition of the $CaCO_3$ as it is incorporated into the complex structure, and is therefore less accessible for decomposition.

The formation of K-silicates should be noted as the incorporation of alkali metals into Si-containing materials has been shown to reduce the melting points of slag deposits to below 750°C[65]. This can lead to issues with rapid deposit build up, and highly tenacious deposits due to the glassy sintered nature. It is also often stated that alkali metal capture in silicate form is preferable to the volatilisation of KCl.

The Si component of the ash appears to be an important parameter when determining the phases that are likely to form in the high temperature heat treated ash. In the ashes with the higher SiO_2-CaO/MgO/K_2O, quartz was still present at the higher temperatures. In comparison when the ratio was lower (e.g. eucalyptus) a greater variety of silicates were present suggesting different reactions between the CaO and SiO_2 present in the ashes. When the coal and eucalyptus were ashed simultaneously, quartz was still observed suggesting that an excess of SiO_2 was present compared to that of the eucalyptus alone.

No Mn containing phases were identified in the samples despite each fuel containing Mn, this suggests that the Mn either incorporates into other phases or is present as an amorphous oxide.

The chemical composition of biomass ash has been identified as a parameter which will affect its disposal/ utilisation[59]. Liodakis *et al*.[116] report that high alkali wood ash has been used as a soil amendment due to the high K content of the ash. Disposal of fly ash should be given special consideration as water solubility of the elements present in the ash has been reported to be as high as 61% in strongly alkali ash;[32] without careful monitoring, ground water contamination could be a serious concern. Vassilev *et al*.[32] highlighted the presence of Ca containing phases (e.g. portlandite, calcite and ettringite) may bind hazardous elements such as Hg, Pb and Zn and reduce the risk of groundwater mobility. No heavy metal containing compounds have been identified during high-temperature heat treatment of the ashes, this coupled with the high Ca content of the fuel, suggests several disposal routes for the ash are possible.

Analysis and phase quantification on the full selection of fuels is a future aim, phase quantification on the hemp and coal sample set has been presented. This identifies a general trend of a decrease of quartz present in the ash alongside an increase of Ca-Mg silicates indicating the reaction pathways identified above are correct. Hydroxyapatite showed peak sharpening above 800°C indicating it may anneal at high temperatures.

Small scale investigation of fuels, such as the one presented in this chapter are essential to gain information into ash behaviour before larger scale application. Knowledge of phases likely to form, including those responsible for corrosion (e.g KCl) or slagging and fouling (K-Al silicates) can be useful as oxidation/ reduction conditions in large scale tests may be altered to avoid some of the worst implications. Environmentally, the categorisation of ash is important as it disposal methods should be analysed to ensure no danger is posed.

5. Characterisation of the fly ash components of: deposited, quenched, cyclone, and bottom ash samples from the co-firing of biomass and coal in a 1MWth combustion rig

Each of the samples is comprised of fly ash; the fine ash particles which are driven from the boiler in the flue gas. Quenched, cyclone and bottom ash samples and deposits formed on boiler components for the hemp and coal and eucalyptus and coal fuel blends as well as the pure eucalyptus fuel, were collected during a 50h combustion and corrosion test. These samples were characterised using PXRD, SEM and EDS and the results are presented here. Comparisons between these results and the findings from Chapter 4 will be made.

Combustion conditions and sample collection parameters are presented in Chapter 3. The sample identification code is presented as H (refers to the fuel) 722 (refers to the collection port) 3 (refers to the number of the collection in the sample set). Samples were collected in the superheater region of the combustion rig (Figure 3-1, Figure 3-2). Temperatures in the superheater region often fluctuate; the higher a port number the cooler the sample temperature will be i.e: 722 is at a higher temperature than 740.

Cyclone ash is the ash removed through cyclone filtration of the flue gas prior to the exit from the combustion rig (Figure 3-1d). The cyclone ash is fly ash which did not deposit onto any of the boiler surfaces during the combustion trials, and therefore will give information to compare and contrast with the deposits. A comparison of the cyclone ash and the deposited ash gives insight into which of the phases formed in the flue gas, and which phases formed in the deposits.

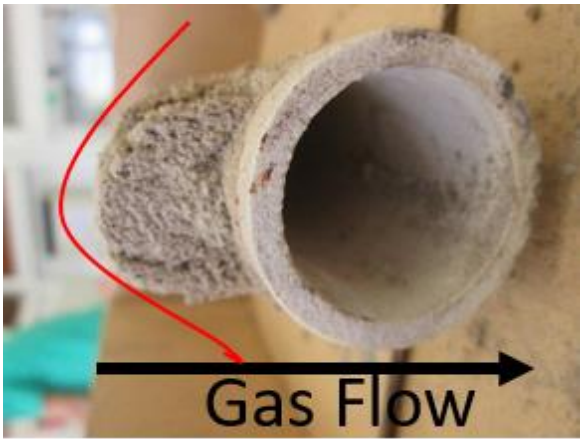

Figure 5-1: Photograph of a hemp deposit onto ceramic probe showing the elliptical shape of the ash.

The bottom ash is formed via the fusion of fly ash and raw fuel particles that fall to the bottom of the furnace hopper (Figure 3-1a) and are not carried in the flue gas. Bottom ash typically contains varying forms of low melting point silica, these are often highly crystalline. Upon cooling these melts form glassy porous structures. Analysis of the bottom ash formed during the combustion trial can be used to suggest phases that may form in the deposits which could lead to an increase in slagging and fouling.

The shape of the deposit samples is elliptical (Figure 5-1), with little or no deposit build up on the side facing away from the gas flow, indicating that the main deposition method onto the ceramic pipes (Figure 3-1c) is inertial impaction (section 2.3). The surface temperature of the ceramic that the deposits impact onto is not air cooled, and therefore will be at or around the gas temperature (during sample collection it was observed as glowing orange/red). These high temperatures indicate that little thermophoresis and diffusion will take place, as these mechanisms require a cold surface to initiate on to.

There are several limitations related to the information gathered from the quenched ash samples. After removal of any solid via filtration, analysis of the quench water using inductively coupled plasma-mass spectroscopy (ICP-MS) would have been desirable. This would have allowed information on phases that dissolved in the water to be gathered. This was outside the scope of the investigation as the quench water used was tap water and so had unknown concentrations of Ca^{2+} and Mg^{2+}. These analyses could not be carried out by the author (due to sample collection not being performed by the author) and sample collection of this nature was outside the scope of the larger study. As such, accurate concentrations of elements/phases dissolved in the water are not obtainable.

5.1 Hemp and coal combustion rig samples

Gas composition collected at the exit of the combustion rig at the time of sampling are presented in Figure 5-2. Clear fluctuations in conditions are visible, with the largest monitored components of the gas being CO and CO_2. Data was collected by E.On during the co-firing trial. Cyclone ash and bottom ash are not indicated in this figure as they were collected at the end of the combustion trials.

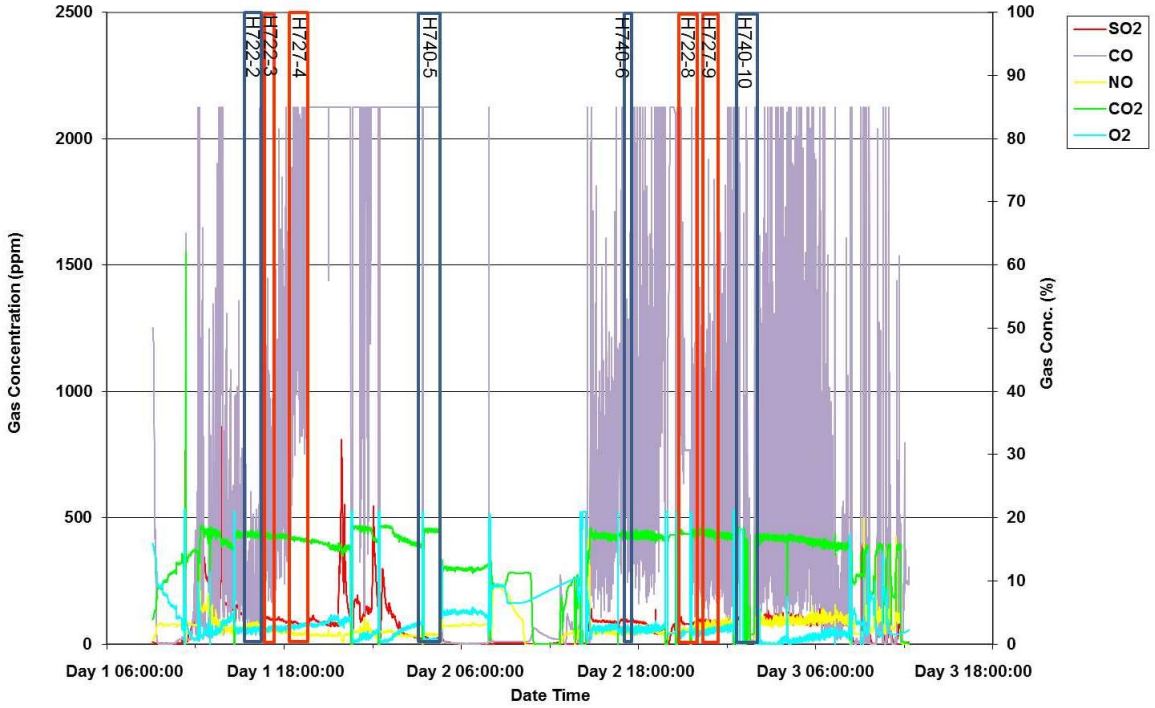

Figure 5-2: Gas conditions at combustion rig exit during the co-combustion of hemp and Kuzbass coal. SO_2, CO and NO should be read from the left concentration (ppm) axis and CO_2 and O_2 from the right concentration (%) axis. Red indicates a deposit, blue indicates a quenched sample. The numbers denote the sample code (Section 3)

5.1.1 Hemp and coal deposit samples

As was observed in the ashing of the raw fuels (Chapter 3), the organic matrix of the fuels was removed during combustion. The release of this carbon is confirmed by the CO and CO_2 observed in the flue gas Figure 5-2. The hemp and coal have ash contents of 16.2% and 8.7% respectively, both of which are considered high, combining them in the ratio 77:23 giving a calculated ash content for the co-fired fuels of 14.5%. Collection times and sample temperatures for the deposit samples are presented in Table 5-1.

Table 5-1: Collection time and sample temperatures of hemp and coal deposit samples

Sample	Duration	Temperature (°C)
H722-3	38 minutes	971
H727-4	57 minutes	Not Recorded
H722-8	66 minutes	1013
H727-9	58 minutes	980

The phases present, as determined by analysis of PXRD data in each of the samples, are presented in Table 5-2 and Figure 5-3. Clear differences between each deposit are visible. The variation in probe temperatures (971-1013°C) and gas atmosphere accounts for some of these differences. Whilst in the combustion rig the deposit will be growing as more particles impact onto the surface. This means that not only will the composition of individual samples be changing, but also that each deposit may have a different composition due to the heterogeneous nature of the fuel. Additionally, the sample will only be deposited from a small portion of the flue gas and fly ash that is passing the ceramic deposition probe.

The presence of carbonates ($CaCO_3$, $CaMg(CO_3)_2$) despite the high temperatures in the combustion rig is thought to be through the reaction of CaO, which forms through the initial decomposition of $CaCO_3$, with CO_2(g) in the air during the cooling of the probe and deposit. The deposit is constantly changing and phases undergo internal reaction in the deposit, indicated by the formation of Ca-Mg silicates. There are two pathways of reaction for the deposited CaO. Either it may react further, whilst at high temperature, with other phases present in the ash sample e.g. SiO_2/MgO to form complex silicate phases or it may react with CO_2 in the air on cooling.

Anhydrite ($CaSO_4$) is shown to be present in each deposit sample. In Chapter 3 anhydrite was identified as being present through the dehydration of gypsum ($CaSO_4.2H_2O$). In the combustion rig anhydrite may also form through the sulphation of CaO in the deposit through reaction of the SO_2 in the flue gas (Equation 5-17)[27]. The decomposition of anhydrite into lime and SO_3 may occur, as previous research has shown it to decompose between 900-1300°C. However, it is also stated that this decomposition often occurs at 1050-1200°C,[27] temperatures which are not reached in the flue gas.

$$CaO + SO_2 + O_2 \rightarrow CaSO_4$$

Equation 5-20

Table 5-2: Phases present in deposit samples from hemp and coal co-firing, identified through analysis of PXRD data

Phase	Key	Composition	H722-3	H727-4	H722-8	H727-9
Quartz	Qz	SiO_2	•	•	•	•
Calcite	Ca	$CaCO_3$	•	•	•	
Kalsilite	Ka	$KAlSiO_4$	•	•	•	•
Anhydrite	An	$CaSO_4$	•	•	•	•
Arcanite	Not shown	K_2SO_4	•	•	•	•
Hydroxyapatite	Ha	$Ca_{10}(PO_4)_6(OH)_2$	•	•	•	•
Hematite	He	Fe_2O_3	•	•	•	•
Microcline	Mi	$KAlSi_3O_8$	•			•
Albite	Ab	$NaAlSi_3O_8$	•	•	•	
Gehlenite	Ge	$Ca_2Al_2SiO_7$	•	•	•	
Wollastonite	Wo	$CaSiO_3$	•			•
Forsterite	Fo	Mg_2SiO_4	•		•	
Magnetite	Mag	Fe_3O_4	•		•	
Augite	Au	$Ca(Mg_{0.74}Fe_{0.26})Si_2O_6$	•			
Monticellite	Mo	$MgCaSiO_4$	•	•		•
Andalusite	Not Shown	Al_2SiO_5	•	•	•	•
Periclase	P	MgO	•	•	•	•
Diopside	Di	$CaMgSi_2O_6$		•		•
Dolomite	Do	$CaMg(CO_3)_2$		•		
Sylvite	Sy	KCl		•		
Sanidine	Sa	$KAlSi_3O_8$			•	•
Mullite	Mu	$Al_{2.35}Si_{0.64}O_{4.82}$			•	•
Merwinite	Mw	$Ca_2Mg(SiO_4)_2$			•	
Akermanite	Ak	$Ca_2MgSi_2O_6$			•	•

Hematite (Fe_2O_3) is thought to be present from the coal, which has a 11.13 wt% Fe_2O_3 content in comparison to the 1.41% in the hemp. The combined fuels contain 3.13 wt% Fe_2O_3 (Table 3-18). Hematite may have formed through decomposition of rozenite ($FeSO_4.H_2O$) observed in the coal fuel (Figure 4-29). In samples H722-3 and H722-8, magnetite (Fe_3O_4) is present, this forms through the reduction of hematite (Equation 5-21).[186]

$$3Fe_2O_3 + CO \rightarrow 2Fe_3O_4 + CO_2$$

Equation 5-21

The cause of this reduction is due to the gas conditions at the time of sampling (Figure 5-2). For samples H722-3 and H722-8, the gas CO content was fluctuating and was lower than in H727-4 and H727-9; this could indicate incomplete combustion of the organic matter, causing some C to build up in the deposit. Monsen[187] investigated the affect of CO on the reduction of hematite, and concluded that for controlled reduction of hematite to magnetite carbon deposition should be avoided. Therefore a greater C content in the deposit could lead to reduction to magnetite.

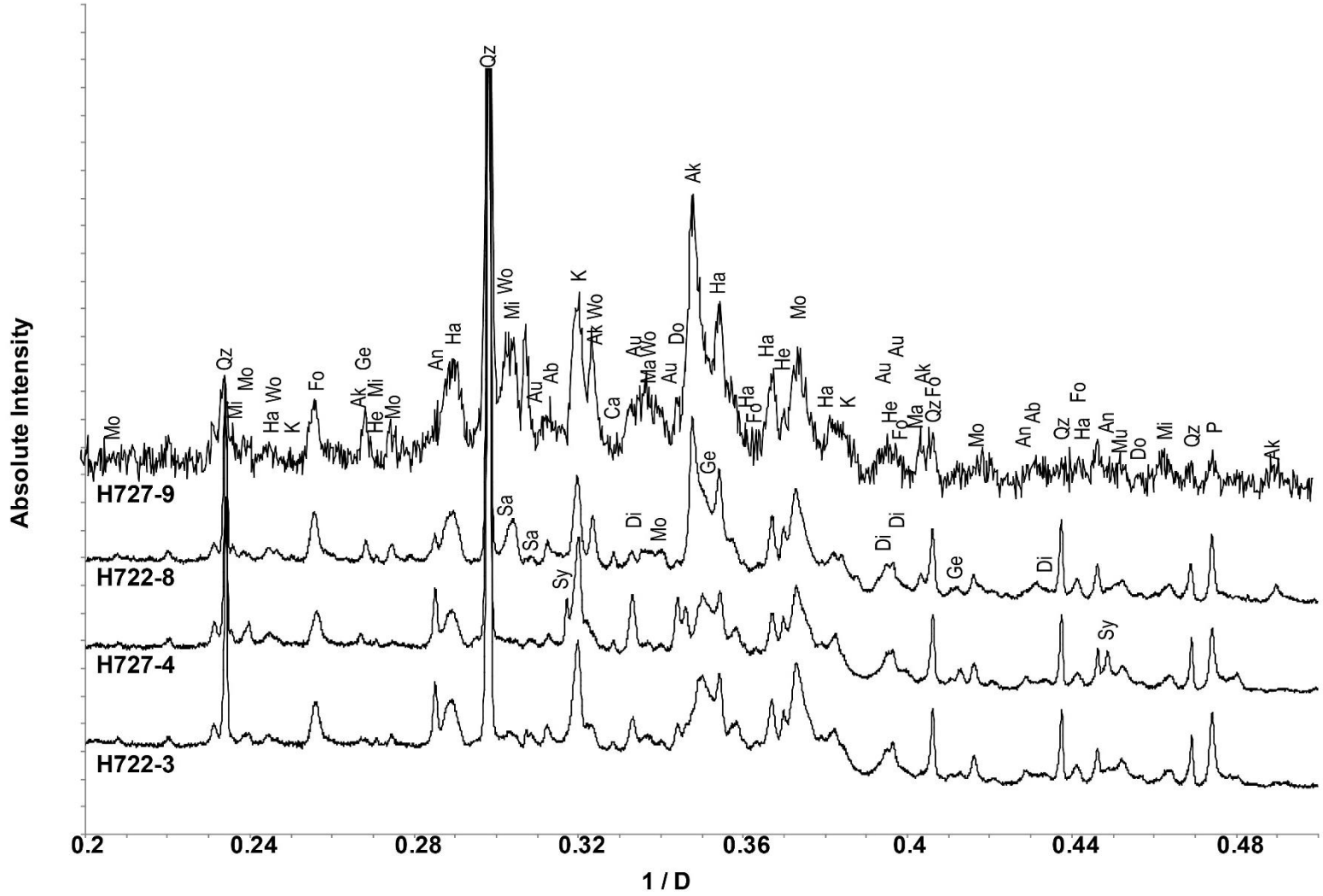

Figure 5-3: PXRD data of deposit samples removed from the combustion rig during co-firing hemp and Kuzbass coal trials. 1/D presented as H7279 D2 data Cu Kα radiation) is presented alongside synchrotron data (λ 0.826215) for H7228, H7274 and H7223.

Also observed in deposit H722-3 is augite ($Ca(Mg_{0.74}Fe_{0.26})Si_2O_6$), an iron substituted analogue of diopside ($CaMgSi_2O_6$). This phase was observed in the high temperature coal ash in section 3.1.3.2. It may also be due to the oxidation state of the Fe; Sørensen *et al*.[188] observed that Fe^{2+} was more mobile and likely to substitute into the diopside structure than Fe^{3+}. As hematite (which contains Fe^{3+}) has been reduced to magnetite (which contains some Fe^{2+}) in the deposit, substitution of Fe^{2+} into the diopside structure is possible. Diopside is present in samples H727-4 and H727-9, supporting the proposed substitution mechanism as no magnetite was observed in these samples. Akermanite ($Ca_2MgSi_2O_6$) is observed in H722-8 and H727-9, and may have formed through reaction of diopside with CaO present in the deposit (chapter 3).

Arcanite (K_2SO_4) is present in all of the samples. This phase has previously been observed to have formed in the deposit through sulphation of K_2O released from the organic components of the fuel[31]. Vassilev *et al*.[31] state that arcanite is likely to crystallise at temperatures between 500-1100°C, the collection temperatures are inside this temperature bracket. The formation of K_2SO_4, through the sulphation of KCl, is also possible in the deposits.

The feldspar microcline ($KAlSi_3O_8$), which probably originates from soil contamination through the harvesting process of the biomass, is present in H722-3 and H727-9. Sanidine ($KAlSi_3O_8$), the high temperature form of microcline, is also present in several deposits (Table 5-2). Cultrone *et al*.[161] investigated the formation of sanidine in ceramic firing (as presented in Section 4.1.2) and found that microcline often transforms to sanidine at high temperature. Deposit exposure time may also play a role in the conversion of microcline to sanidine as in samples with an exposure time of above 58 minutes it was observed as present. In sample H722-3 however, with a shorter exposure time of 37 minutes, microcline was observed as present. H727-4 has a similar exposure time to that of H722-8, 57 and 58 minutes respectively, no specific temperature data is available but it will be in the temperature range 971-1013°C.

As well as the high temperature transformation of microcline to sanidine, formation of the high-temperature feldspar could also be attributed to the reaction of illite, present in the coal fuel (Table 4-8), with SiO_2 (Equation 5-22).[161]

$$\underset{\text{illite}}{3KAl_2(Si_3Al)O_{10}(OH)_2} + 2SiO_2 \rightarrow \underset{\text{sanidine}}{3KAlSi_3O_8} + \underset{\text{mullite}}{Al_6Si_{12}O_{13}} + H_2O + melt$$

Equation 5-22

Monticellite ($MgCaSiO_4$) was observed in samples H722-3, H727-4, and H727-9, whereas merwinite ($Ca_2Mg(SiO_4)_2$) was identified in H722-8. The temperature of H722-8 is higher than

the other samples, suggesting this may contribute towards merwinite formation. It should also be noted that the deposit containing merwinite may be more Ca rich as it also contains akermanite. This also suggests that a significant factor in the formation of certain phases is down to what phases impact next to one another in the deposit.

Andalusite (Al_2SiO_5), is a phase that is present in the deposits which was not observed in the high temperature heat-treated ashes (Section 3.1). Andalusite often co-occurs with mullite ($Al_{2.35}Si_{0.64}O_{4.82}$), also identified in the ashes, through the decomposition of kaolinite.[189] Kaolinite is present in the coal fuel itself but was not identified after ashing to 575°C suggesting it had already volatilised. Mullite may also be present due to the decomposition of illite.

KCl is present in deposit H727-4. It was thought unlikely that KCl would form in any of the deposits, as the main deposition mechanism it undergoes is diffusion (deposition onto a cool surface) and the deposit probe is at gas temperature. The gas conditions at the time of deposition were high in CO, suggesting a strong reducing atmosphere (As shown in Figure 5-2). Previous work has shown KCl deposition increases under a reducing atmosphere.[190]

Analysis of the SEM data (Figure 5-4) shows variation between the morphologies of the particles. The spherical particles present in Figure 5-4a-e are either cenospheres (a microsphere of aluminosilicate glass encapsulating gas)[191] or a plerosphere (a sphere encapsulating smaller pre-existing particles)[191]. A sphere is present in sample H722-8 Figure 5-5a), the interior of the sphere is hollow (inside the hole is imaged in Figure 5-5b) and so it can be identified as a cenosphere. Cenospheres are formed through the expansion of a silicate droplet; the droplet must contain a small amount of carbon which in turn forms a gas causing the droplet to expand. Often a small amount of iron is present in the sphere which catalyses the sphere expansion.[191] Plerospheres form with the same mechanism however they also encapsulate smaller droplets from the flue gas.

Distinct agglomeration of the particles is observed in the samples, the clearest example of these are presented in H727-4 (Figure 5-4c). The growth of deposits this way also confirms the deposition mechanism as inertial impaction, as the size of the deposit grows rapidly when the deposit surface becomes sticky. The particle indicated by the red box in sample H722-3 (Figure 5-4a, indicated in the red box) may be one of the trichomes previously identified in the hemp fuel.

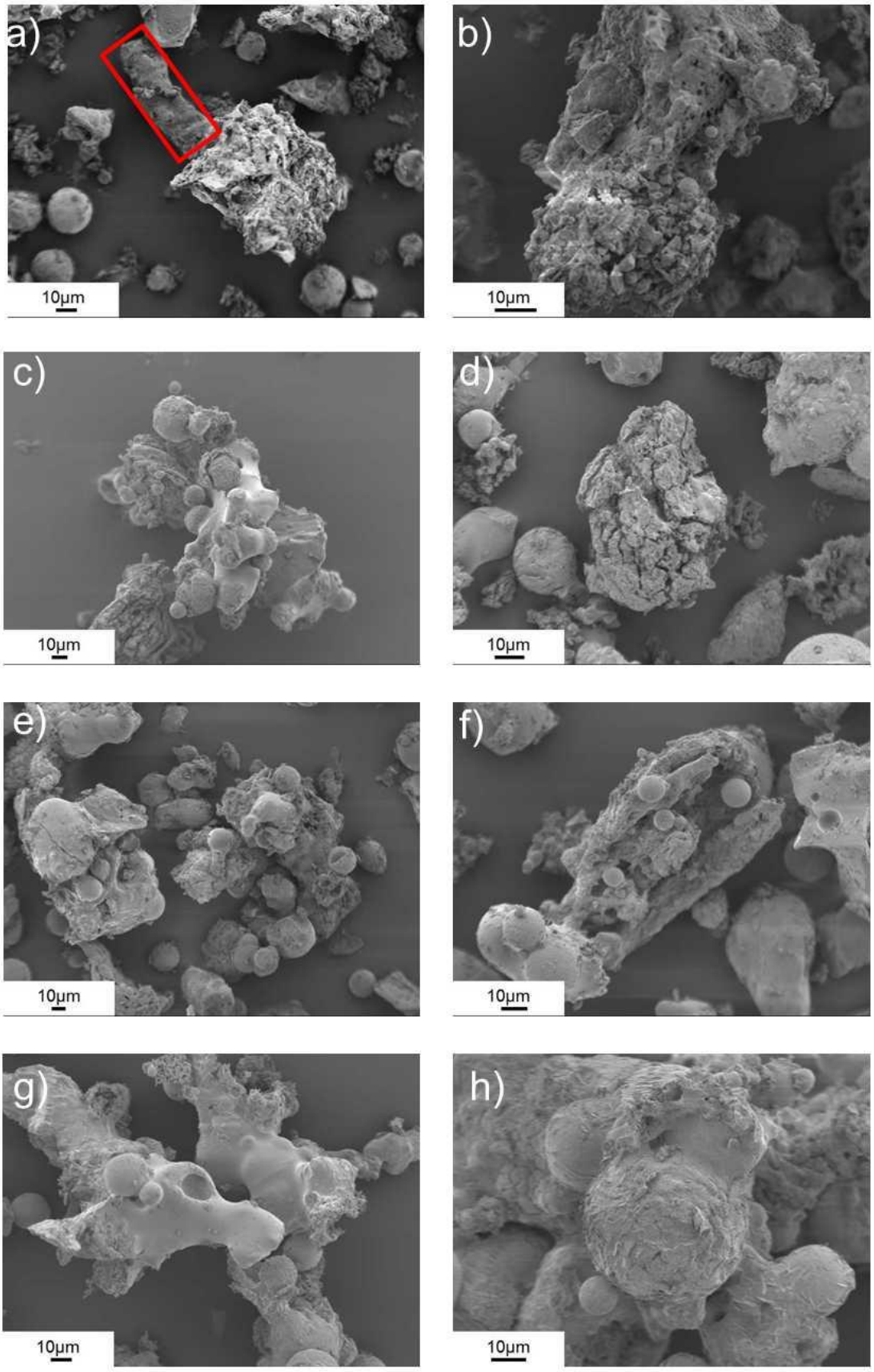

Figure 5-4: SEM electronmicrographs of hemp and coal deposits a,b) H722-3 c,d) H727-4 e,f) H722-8 g,h) H727-9 showing the different morphologies present in the deposits.

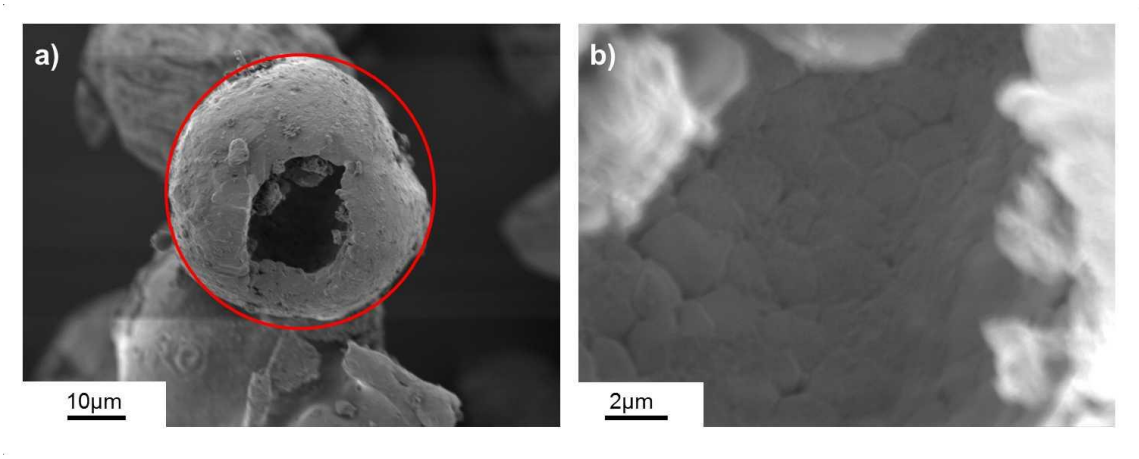

Figure 5-5: a) a cenosphere present in H722-8 b) the inside surface of the cenosphere present in H722-8

Analysis of the deposits using SEM-EDS mapping (Figure 5-6) confirms the phases identified through analysis of the PXRD data. K, S, and O are associated, this is in agreement with the phase arcanite. K, Al, Si, and O are associated (not presented here), this indicates the presence of microcline and kalsilite. In the top right third a trichome, highlighted in the red box, is intact; this has the composition of S, Na, Ca, P, Mg, Si, and O, similar to the analysis of the trichomes presented in Figure 4-3. This suggests that the trichome is multiphase. Albite ($NaAlSi_3O_8$) can be identified through the association of Na, Al, Si, and O (data not presented here).

The EDS maps (Figure 5-7) and PXRD data of sample H727-4 complement each other. The KCl identified in the PXRD data is also observed in the EDS maps, KCl was present in multiple analysed areas. The mechanism of deposition is still unclear, it may also have formed in situ in the deposit. There are areas of association between K, S, and O confirming the presence of K_2SO_4, also identified in the PXRD data. There are regions of association between Ca, P, Mg and O, this suggests some substitution into hydroxyapatite by Mg, this was also suggested in Chapter 3.

Analysis of the EDS maps for sample H7228 (Figure 5-8) indicate the presence of K_2SO_4, identified as present through PXRD analysis. S is also associated with Ca, confirming the presence of anhydrite ($CaSO_4$) thought to originate from the coal. There is also association of Ca and O, this is likely to be the $CaCO_3$ identified using PXRD, the C map is not presented here as the analysis matrix is a C tab which causes inaccuracy in the C map. KCl is observed in the bottom right hand corner of the map, this was not identified through PXRD suggesting that it is a minor contributor in this deposit.

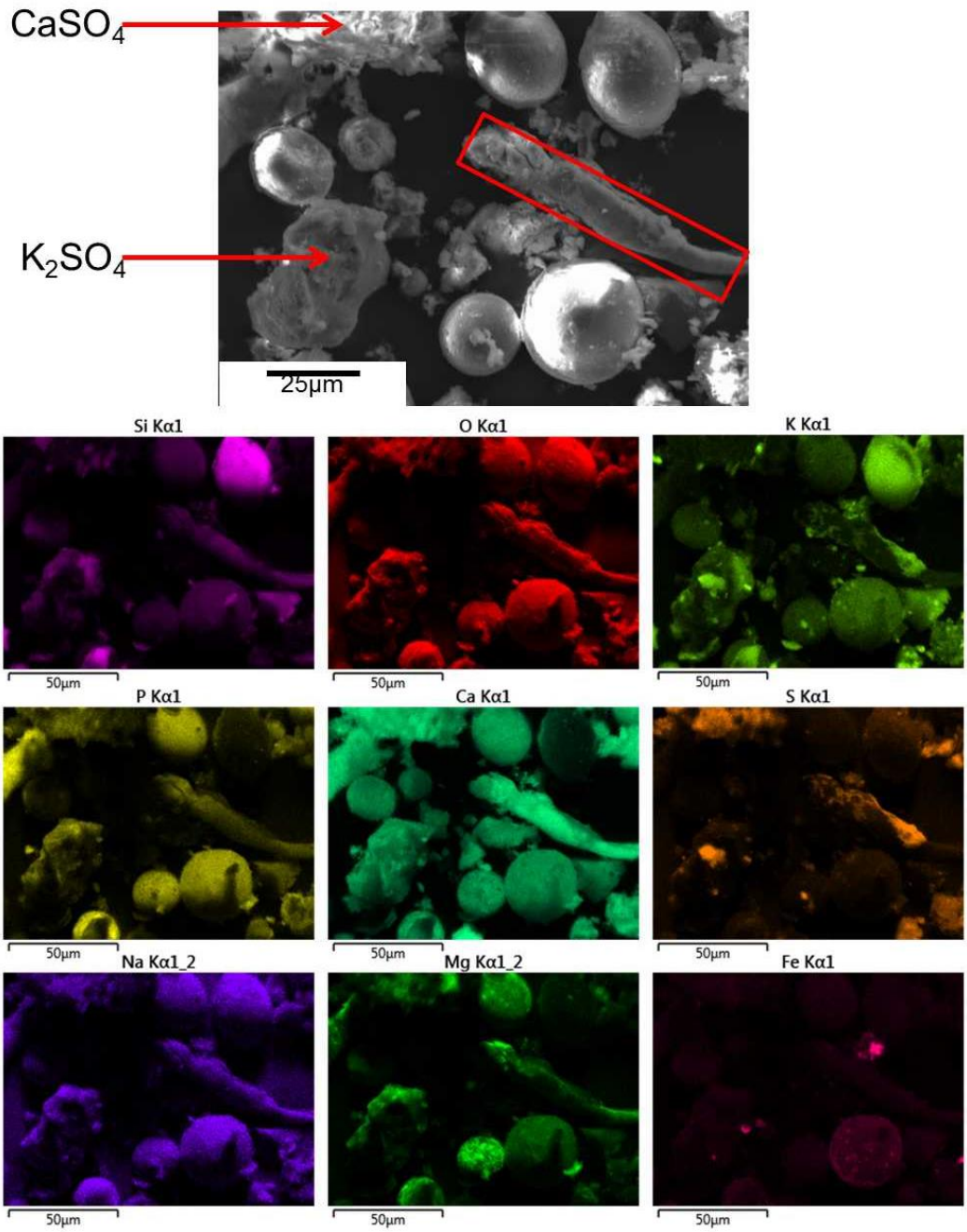

Figure 5-6: A micrograph and EDS maps of H722-3 showing both K_2SO_4 and $CaSO_4$ as well as a trichome present.

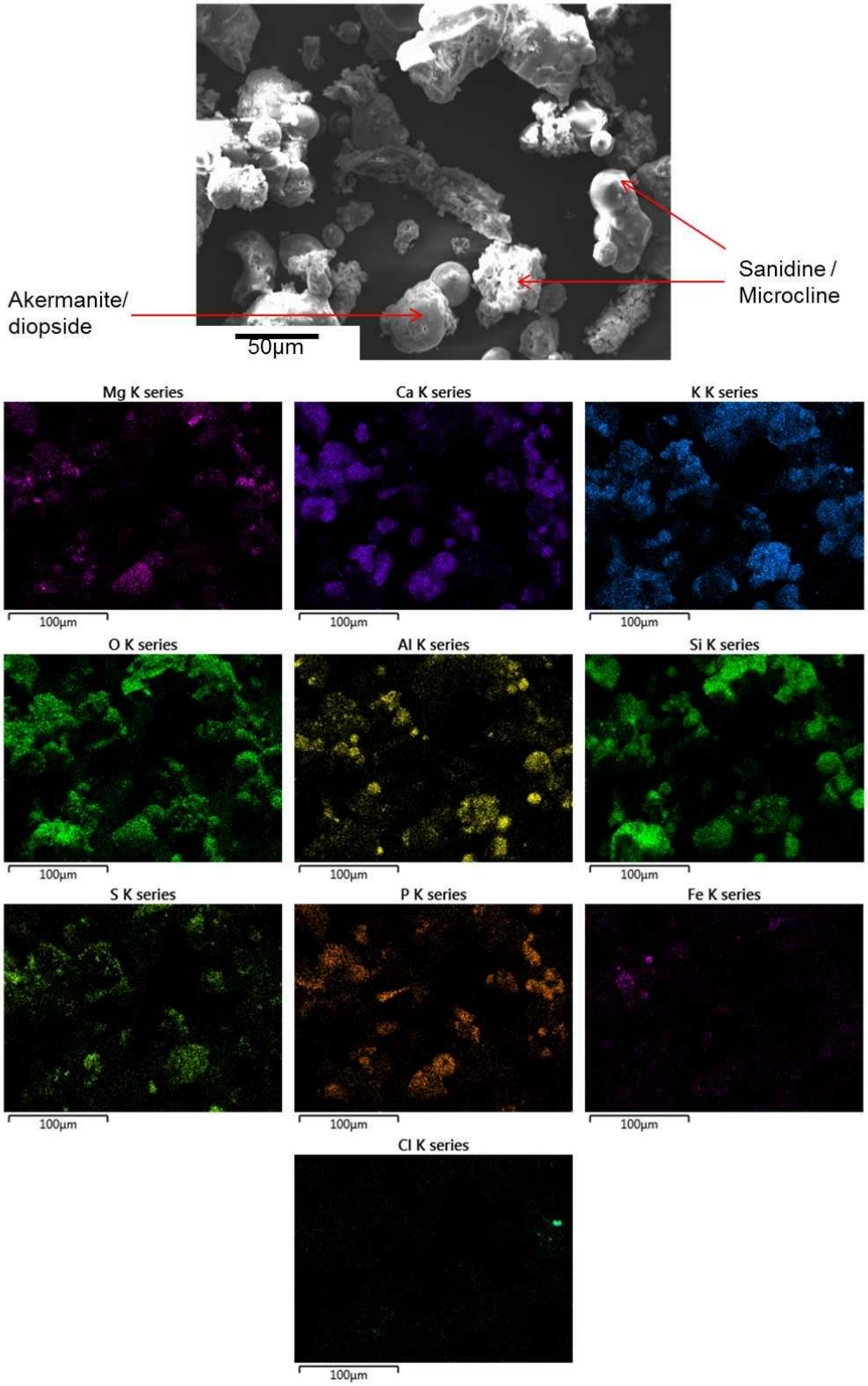

Figure 5-7: Electron micrograph and EDS Maps of H727-4 showing elemental association indicating the silicate akermanite/diopside and sanidine/microcline also identified in PXRD data

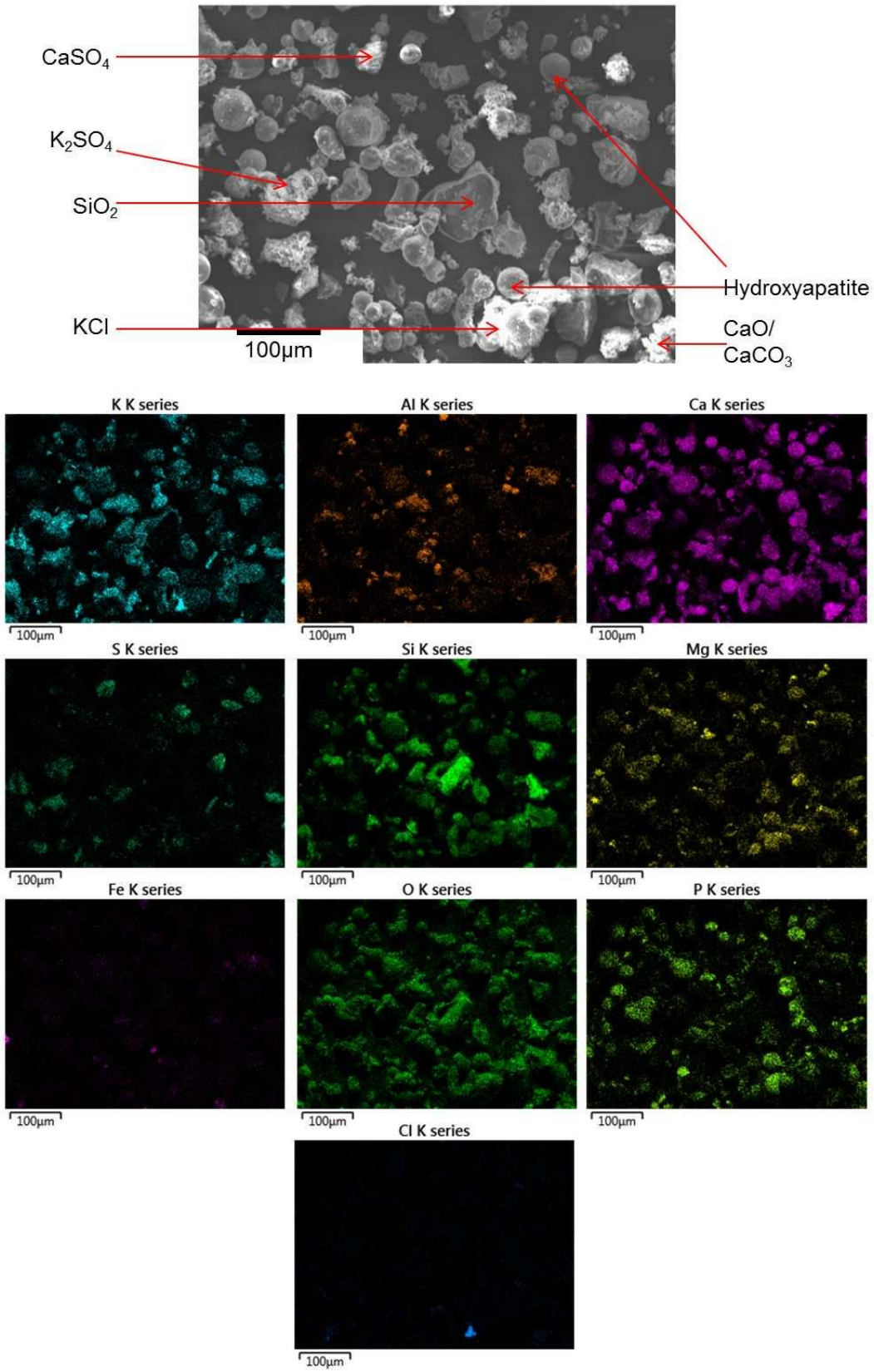

Figure 5-8: An electronmicrograph and EDS maps of H722-8 showing elemental association similar to the phases identified in the PXRD data.

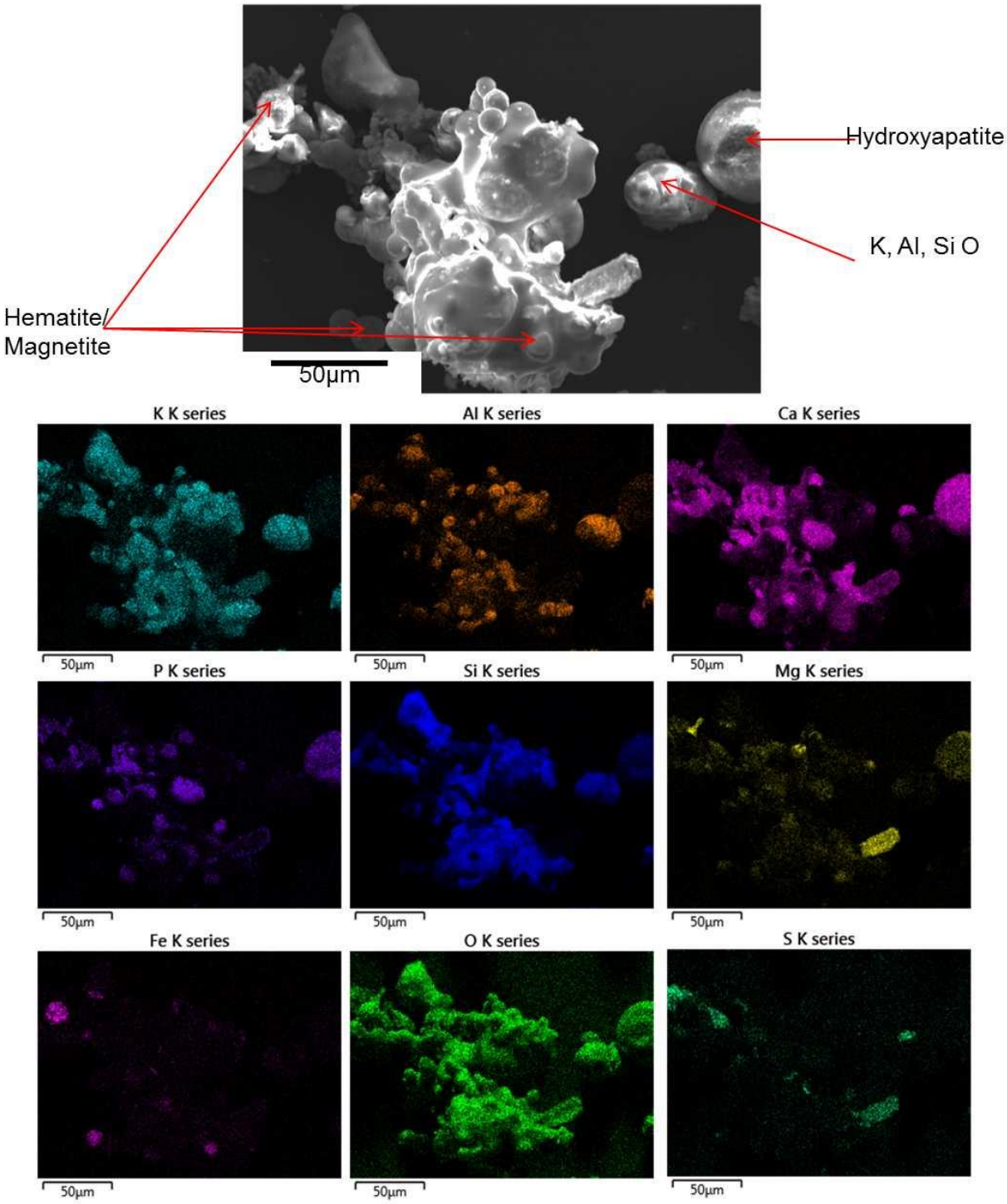

Figure 5-9: An electronmicrograph and EDS maps of H727-9 illustrating elemental association of Fe and O, indicating hematite/magnetite.

Analysis of the H727-9 EDS maps is presented in Figure 5-9. In each sample there is Fe distributed about, this largely corresponds with presence of spheres. The formation of cenospheres and plerospheres by Raask,[191] stated the need for a catalytic amount of Fe to be present in order for the spheres to swell. The presence of Fe in some of the spheres is in agreement with this statement. Not all of the spheres contain aluminosilicates, with some containing Ca, Mg, P, and O and no Al suggesting that more than just the aluminosilicates shown by Raask can form ceno/plerospheres.

Valentim *et al*.[192] have identified these spheres as phosphospheres, no mechanism has been put forward as a reason for the spheres in comparison to the cenosphere formation mechanism presented by Raask.[191] Phosphospheres have been identified in both biomass and coal, the internal structure has been compared to that of a pomegranate.

The presence of K_2SO_4 and KCl in the deposits onto the probes was unexpected, as the main mechanism of deposition being thermophoresis/diffusion, which relies on a cold surface for the phases to nucleate. However during ash formation stages, surface enrichment of K_2SO_4 and KCl have been reported on the surface of coarse fly ash particles (1-200μm). The presence of these phases on the surface could be a further mechanism for presence in this deposit.

Table 5-3: XRF data comparison for hemp and coal ash, heat treated hemp and coal ash and samples H722-3 and H727-9

	Wt%			
	Hemp and Coal	**Hemp and Coal 900°C**	**H722-3**	**H727-9**
Al	4.01 ±0.16	3.37 ±0.04	3.39 ±0.24	4.18 ±0.18
Ca	31.91 ±0.01	31.66 ±0.63	36.03 ±1.37	32.62 ±1.63
Cl	0.94 ±0.04	0.42 ±0.03	0.19 ±0.01	0.16 ±0.06
Fe	3.13 ±0.02	3.03 ±0.32	4.07 ±0.05	3.89 ±0.35
K	13.91 ±0.13	11.51 ±0.27	13.35 ±0.33	15.70 ±0.25
Mg	5.27 ±0.19	5.09 ±0.17	4.42 ±0.21	4.17 ±0.25
Mn	0.34 ±0.00	0.32 ±0.01	0.36 ±0.01	0.33 ±0.03
Na	0.78 ±0.25	1.24 ±0.30	0.66 ±0.93	0.87 ±0.27
Ni	0.02 ±0.00	0.02 ±0.01	0.02 ±0.01	0.01 ±0.00
P	11.94 ±0.05	11.85 ±0.07	9.59 ±0.11	8.77 ±0.44
S	4.55 ±0.21	4.42 ±0.06	6.47 ±0.71	6.68 ±0.63
Si	23.41 ±0.49	24.57 ±0.76	19.67 ±2.12	20.85 ±2.47
Sr	0.18 ±0.01	0.18 ±0.01	0.23 ±0.01	0.24 ±0.02
Ti	0.42 ±0.06	0.32 ±0.00	0.47 ±0.06	0.55 ±0.04
Zn	0.10 ±0.01	0.10 ±0.00	0.07 ±0.00	0.09 ±0.01
Zr	0.07 ±0.04	0.05 ±0.01	0.06 ±0.01	0.05 ±0.01
	100.92	**98.13**	**99.01**	**99.12**

The elemental composition of H722-3 and H727-9 are presented in Table 5-3. The elemental compositions of the samples are similar indicating that gas conditions, temperature, and what the elemental composition of the ash that impacts in proximity to reactive phases are important factors to consider. Zbogar *et al*.[46] report that ash depositied in the superheater region, where the samples were collected, and the fly ash will be very similar. General composition of the fly ash can be considered to be similar to the laboratory synthesised sample at 900°C. An enrichment of the alkali metals in deposits has previously been reported by Baxter *et al.,*[65] it was also reported that in areas of high mass transfer (i.e. the front of probes) the deposits are enriched in alkali and sulphate content. This enrichment is visible in the deposit analysis

Averaged data from the whole area analysis of the deposit regions is presented in Table 5-4. The data is largely similar to that presented in Table 5-3. The exceptions are the P content which is almost double in the XRF collected data. The region of analysis for the XRF data is a greater size and therefore will give greater information on the bulk data.

Table 5-4: Averaged data for whole area analysis data collected during SEM-EDS analysis of multiple sample regions of the hemp and coal deposits. C and O removed due to interference from the samples mounting process

	H722-3		H727-4		H722-8		H722-9		Average	
Al	4.73	±1.66	4.26	±1.48	4.53	±1.23	5.39	±4.19	4.73	±0.48
Ca	36.83	±5.86	36.04	±7.95	32.78	±3.90	42.97	±17.07	37.15	±4.25
Cl	0.31		0.59	±0.45	0.42	±0.20	0.39	±0.15	0.43	±0.12
Cr	0.59				0.11			±0.21	0.35	
Cu			0.45	±0.08	0.39	±0.07	0.82	±4.19	0.55	
Fe	3.95	±0.81	2.51	±0.31	3.75	±3.30	4.07	±5.01	3.57	±4.58
K	14.15	±4.62	16.54	±7.39	17.84	±3.27	12.47	±1.17	15.25	±5.48
Mg	4.46	±1.23	7.35	±5.44	5.14	±0.41	5.65		5.65	±1.51
Mn			0.22		0.29	±0.02		±0.68	0.25	
Na	1.36	±0.31	0.97	±0.27	1.23	±0.25	1.80	±2.22	1.34	±1.64
P	5.48	±1.57	4.55	±1.62	5.93	±1.28	4.46	±5.85	5.10	±1.41
S	6.05	±0.71	7.40	±3.13	6.56	±1.42	7.90	±10.88	6.98	±3.44
Si	19.70	±4.01	18.51	±6.80	21.11	±1.91	13.46	±0.06	18.19	±9.70
Ti	0.38	±0.08	1.48	±2.41	0.28	±0.06	0.48		0.66	±0.67

5.1.2 Hemp and coal quenched samples

Quenched samples are portions of the ash removed from the combustion rig through a suction probe followed by rapid quenching in water. Composition of the quenched fly ash gives information of composition of bulk fly ash. This is in comparison to the deposit samples, which will give information about how phases will react in fly ash when in close proximity post deposition. Sample collection times for the quenched samples are presented in Table 5-5.

Table 5-5: Sample collection times for the hemp and coal quenched samples

Sample	Duration
H722-2	71 minutes
H740-6	30 minutes
H722-7	118 minutes
H740-10	86 minutes

Analysis of the PXRD data is presented in Table 5-6 and Figure 5-10. Similar to the deposited samples, there are variations between the samples. The heterogeneous nature of the fuel explains some of these differences. Gas temperatures at the time of sampling were unavailable and so comparison based on temperature could not be made. Whilst information (e.g. phases present, particle morphology) about the bulk fly ash can be gathered, it is also important to note that the samples may react with the water that they are quenched in.

Calcite ($CaCO_3$) is present in the quenched samples as well as the deposit samples. The formation of the calcite in the quenched samples is thought to happen in two stages (Equation 5-23&5). The CO_2(g) is assumed to be dissolved in the water.

$$CaO(s) + H_2O(l) \rightarrow Ca(OH)_2(s)$$

Equation 5-23

$$Ca(OH)_2(s) + CO_2(g) \rightarrow CaCO_3(s) + H_2O(l)$$

Equation 5-24

Both larnite (Ca_2SiO_4) and wollastonite ($CaSiO_3$) are present in the quenched samples. However in the deposit samples there is wollastonite but no larnite present. Mazzucato *et al*.[193] reported that wollastonite forms through a two-step reaction; firstly larnite forms, then reacts with excess SiO_2 to form wollastonite. This suggests that in the deposits the excess SiO_2 present will drive the reaction towards wollastonite

Table 5-6: Phases present in quenched samples from hemp and coal co-firing as identifed through analysis of the PXRD data

Phase	Key	Composition	H727-2	H740-5	H740-6	H740-10
Quartz	Qz	SiO_2	•	•	•	•
Calcite	Ca	$CaCO_3$	•	•	•	•
Kalsilite	Ka	$KAlSiO_4$	•	•	•	•
Hydroxyapatite	Ha	$Ca_{10}(PO_4)_6(OH)_2$	•	•	•	•
Hematite	He	Fe_2O_3	•	•	•	
Gehlenite	Ge	$Ca_2Al_2SiO_7$	•	•	•	•
Wollastonite	Wo	$CaSiO_3$		•		•
Forsterite	Fo	Mg_2SiO_4	•		•	•
Magnetite	Ma	Fe_3O_4	•		•	•
Monticellite	Mo	$MgCaSiO_4$	•	•	•	
Larnite	La	Ca_2SiO_4	•	•	•	•
Andalusite	Not Shown	Al_2SiO_5	•	•	•	•
Periclase	P	MgO	•	•	•	•
Sanidine	Sa	$KAlSi_3O_8$	•	•	•	•
Mullite	Mu	$Al_{2.35}Si_{0.64}O_{4.82}$			•	
Merwinite	Mw	$Ca_2Mg(SiO_4)_2$				•
Akermanite	Ak	$Ca_2MgSi_2O_6$	•	•	•	•

In a study of glass-ceramic formation in fly ash, Vu et al.[194] found larnite formed through a reaction of CaO with amorphous SiO_2 (Equation 5-25). The background features of the PXRD patterns of these quenched samples (Figure 5-10) indicate that there may be amorphous SiO_2 present in the quenched samples. However it does not correspond with the expected 1/D of 0.496.

$$2CaO + amorphous\ SiO_2 \rightarrow Ca_2SiO_4$$

Equation 5-25

Sanidine ($KAlSi_3O_8$) is present in all of the quenched samples, suggesting that the speed of the cooling of the sample did not allow microcline, the low temperature structure, to crystallise. Cultrone *et al*.[161] reported that with rapid cooling, amorphous sanidine may be present, therefore some contribution by sanidine to the amorphous region of the PXRD pattern is expected.

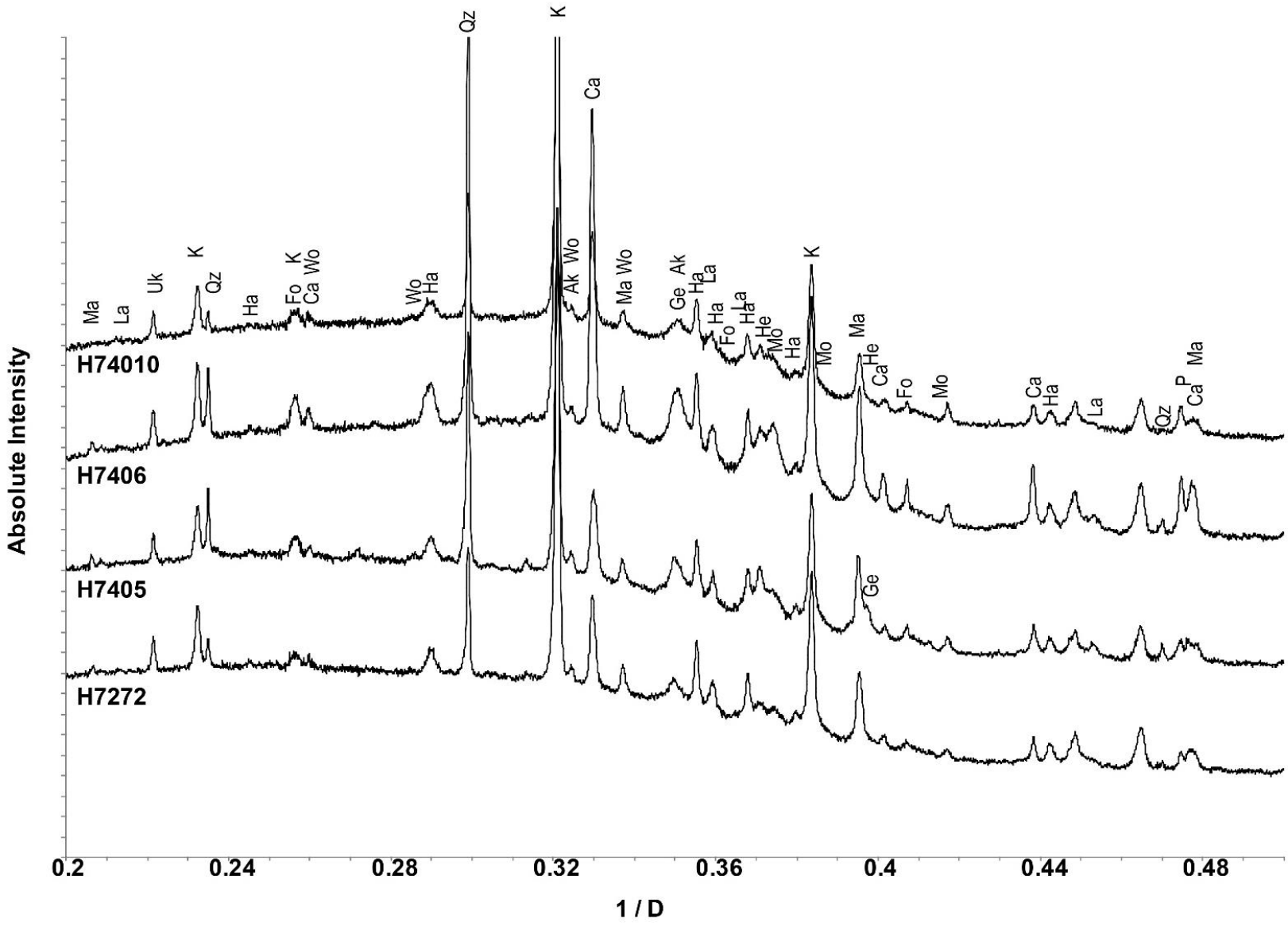

Figure 5-10: PXRD patterns collected on the I-11 beamline (λ 0.826215) and analysis of hemp and coal quenched samples 1/D presented to allow easy comparison with the deposit samples.

Akermanite ($Ca_2MgSi_2O_6$) and gehlenite ($Ca_2Al_2SiO_7$) are both present in all of the quenched samples. The peaks associated with akermanite and gehlenite are broad, and merge into one another, suggesting that they may be forming a solid solution.[195]

Hematite and magnetite are both present in H727-2 and H740-6; in comparison only hematite is present in H740-5 and magnetite in H740-10. It is unclear what has caused this variation in the samples.

KCl, which was detected in H727-4, the deposit sample, was not detected in any of the quench samples. 360g/Kg of KCl is soluble in water at 25°C,[196] so as the samples are quenched in water it would have to be present in extremely high quantities to precipitate out in detectable amounts. Arcanite (K_2SO_4) is also soluble in water[27] and so will be absent from the quenched samples. The anhydrite ($CaSO_4$) present in the deposit sample is likely to rehydrate to gypsum ($CaSO_4.2H_2O$) which is then moderately soluble in water,[27] the full transformations are explained in “the crystal forms of calcium sulphate”.[197]

Analysis of the SEM data collected from the quenched samples (Figure 5-11) shows similarities with the deposit samples as there are the ceno- or plerospheres present. The spheres present in the quenched samples are much less agglomerated than in the deposit samples, i.e. the spheres present in the quenched samples show much less melting between one another (Figure 5-11c and Figure 5-11g). The surface of the spheres can vary widely (Figure 5-11f and g) which may be due to compositional variations of the sample, or the heating rate across the particle.

Observed in the sample are distinct porous regions (Figure 5-11c), thought to contribute to the amorphous region observed in the PXRD data (Figure 5-11). The plate shaped crystal present in Figure 5-11b may be portlandite ($Ca(OH)_2$) which has been previously identified as a precursor to calcite. During the precipitation of calcite from the quenched samples, the $Ca(OH)_2$ may be present but in quantities undetectable in PXRD.

The surfaces of some of the spheres are not smooth (Figure 5-11h). Research into spheres present in ash by Valentim *et al*.[192] states that the texture is likely due to immiscible phases being included in the droplet. This results in a punctuated appearance in SEM images. It should also be noted that the surface texture cannot be relied on to identify spheres as either largely P bearing or Si bearing as both sphere types can exhibit this texture.[190]

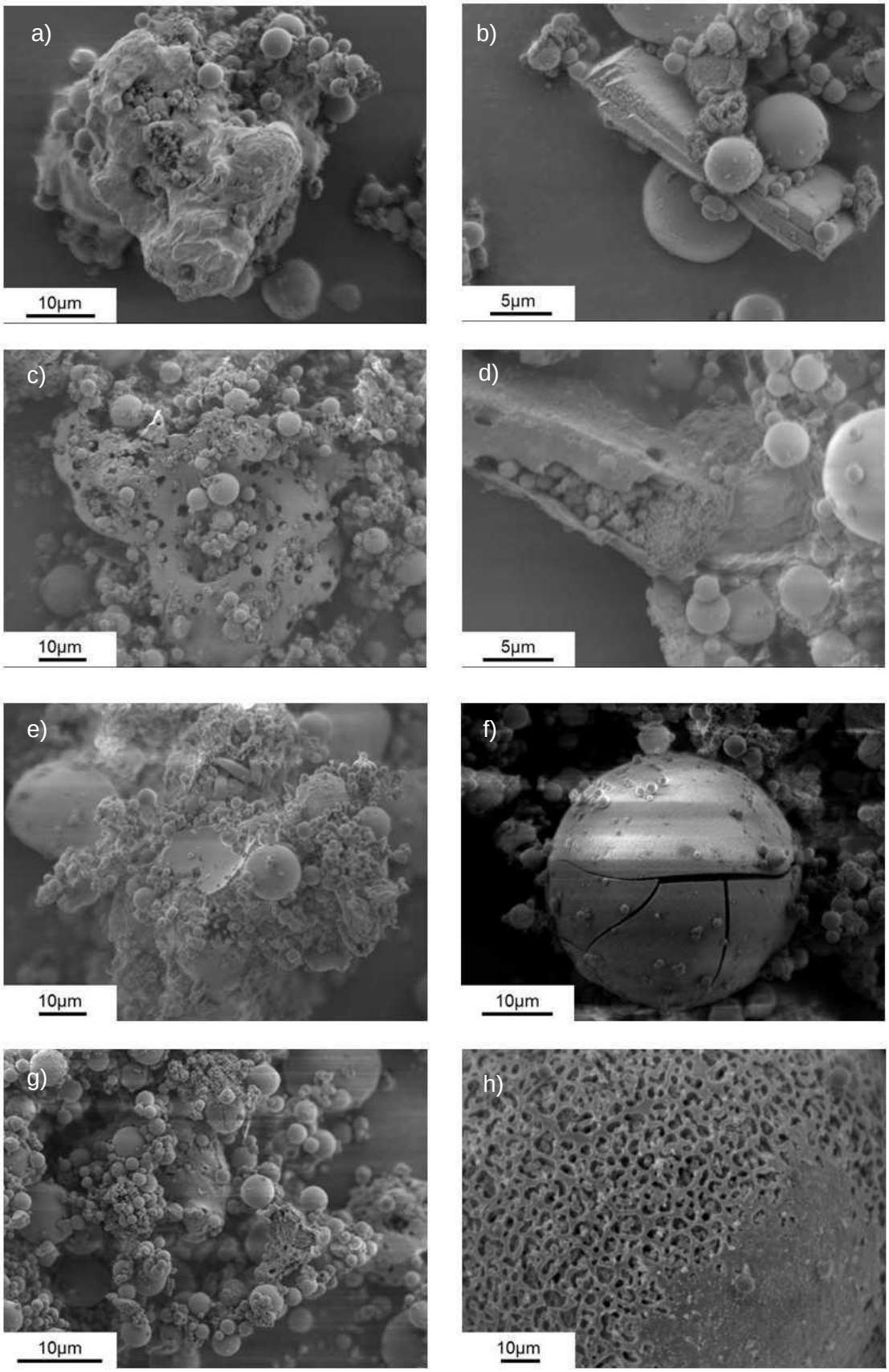

Figure 5-11: SEM electronmicrographs of the quenched samples in the hemp and coal co-firing a&b) H722-2 c&d) H740-5 e&f) H740-6 g&h) H740-10 illustrating the different morphologies present in the samples.

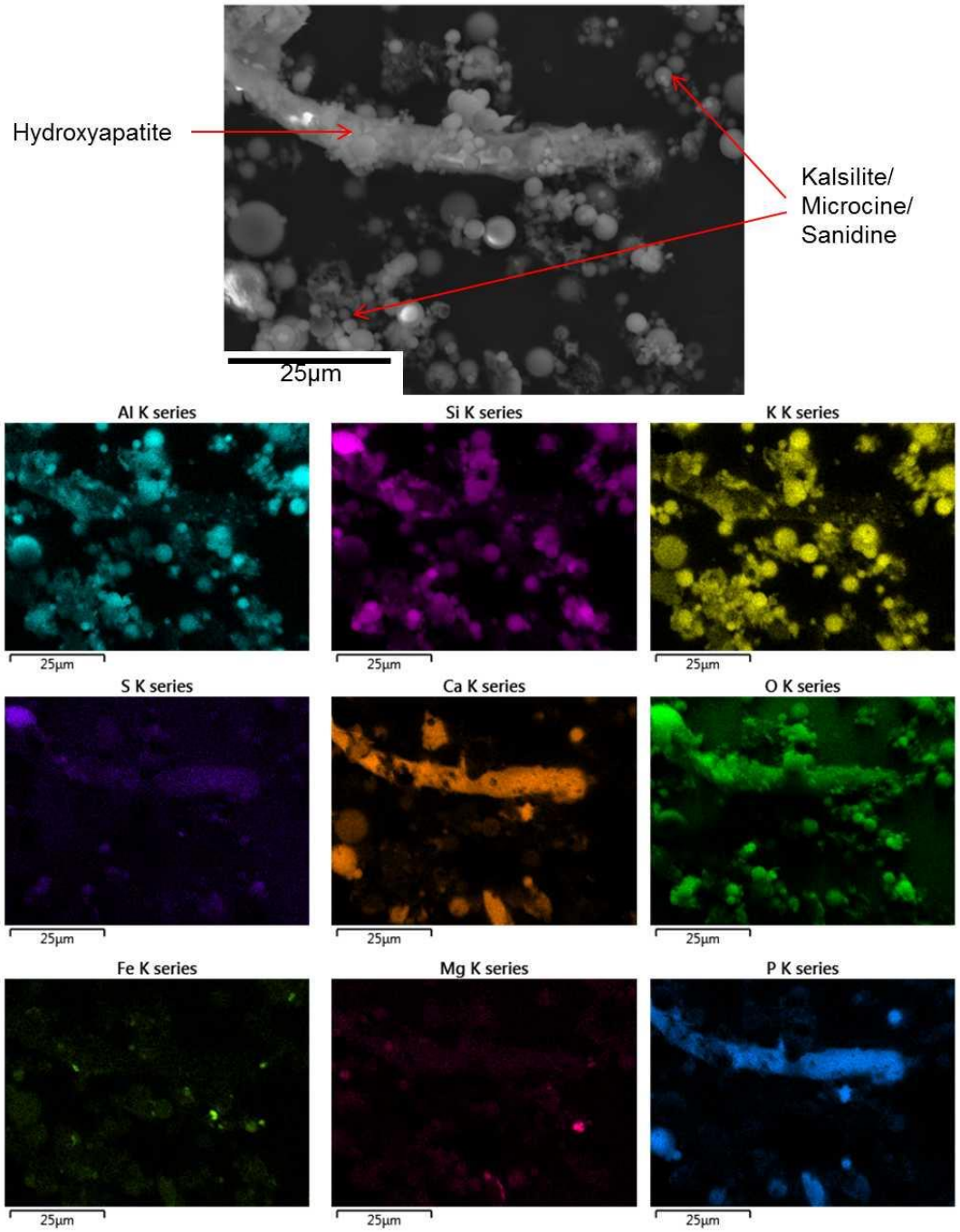

Figure 5-12: an electronmicrograph and EDS Maps of sample H727-2 showing hydroxyapatite and K,Al – silicates present in the quenched sample.

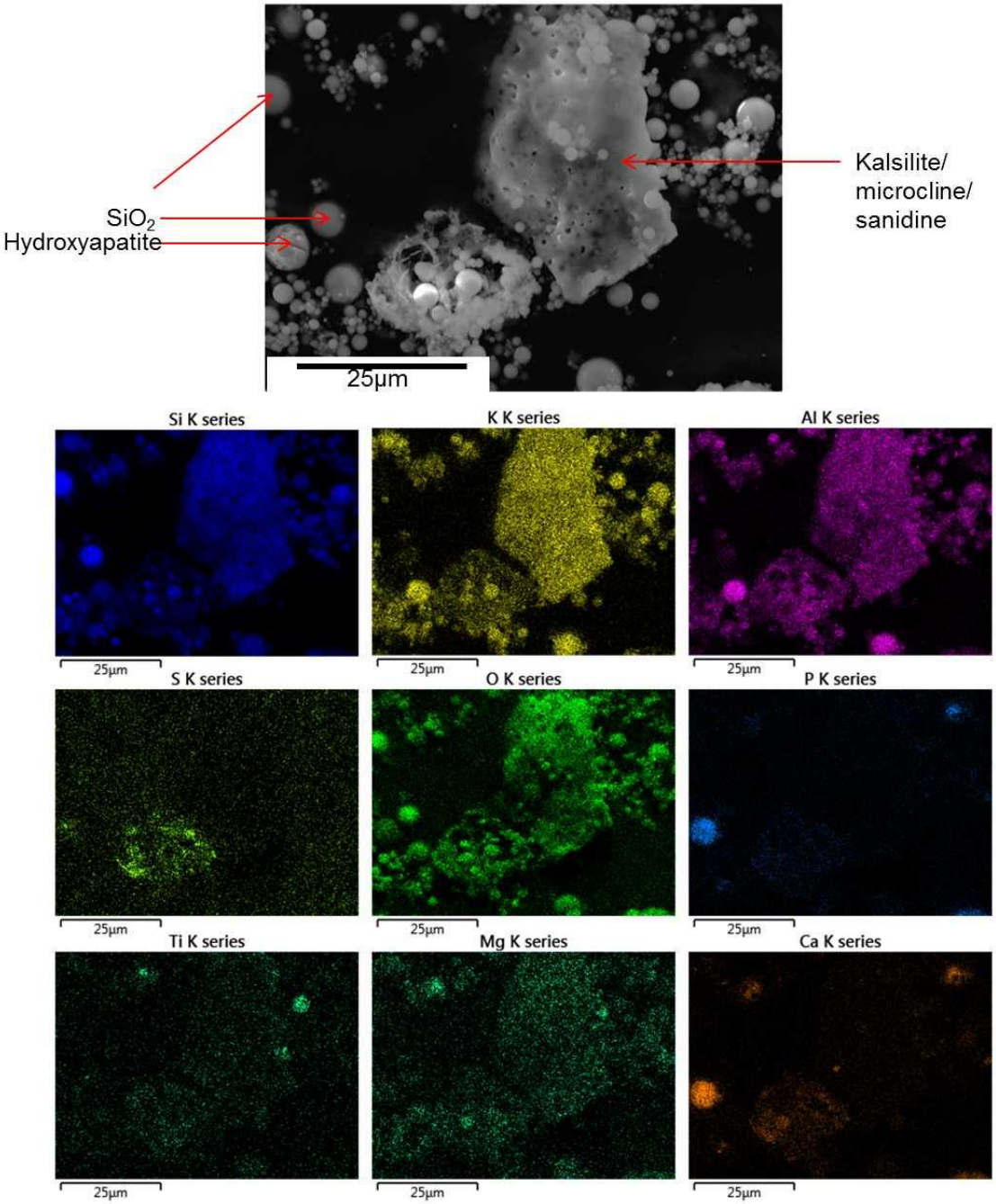

Figure 5-13: An electronmicrograph and EDS Maps of sample H740-10 showing a phosphosphere and association between K,Al , Si and O

EDS maps of the quenched sample H727-2 (Figure 5-12) show clear agreement with the PXRD analysis, as multiple associations which can be linked to the phases identified using PXRD are shown. K, Al, Si, and O make up a large portion of the sample. These indicate the presence of kalsilite, microcline, and sanidine. Peaks for kalsilite have greater intensity in the quenched samples in comparison to the deposits, indicating the samples contain larger amounts of K in comparison to the deposits. Ca, P, Mg, and O are associated, once again indicating the presence of hydroxyapatite. The trichome structure present in the raw fuel, laboratory ashed samples, and the deposits is also present in the quenched samples.

EDS map analysis of samples H740-5 and H740-6 identified similar trends with K, Al, Si, and O largely being the composition of the spheres and trichome structures largely containing Ca, P, and O.

In sample H740-10 (Figure 5-13) a large plate of K, Al, Si, and O is visible, this could be sanidine or kalsilite identified through PXRD analysis. As well as the large plate there are also spheres containing K, Al, Si, and O presumably formed through the expansion mechanism outlined by Raask.[191] Several of the phosphospheres presented by Valentim *et al*.[192] can also be observed.

Averaged data from the whole area analysis of the quenched samples is presented in Table 5-7, XRF analysis of H722-2 is presented in Table 5-8. Elemental analysis is in close agreement between the two techniques. In comparison to the high temperature ash at 900°C the quenched samples contain much less S, this indicates that the species are either largely soluble (K2SO4 identified in the deposits is soluble in water) or were in phases too small to be removed from the gas flow by the equipment (K2SO4 is often present in aerosol size).

In comparison to the deposits and the lab synthesised ash there is a decrease in Ca. This suggests that the Ca is present in the gas flow in a form that is soluble in water. It is also indicative that the Ca phase responsible for the formation of the complex silicates in the deposits may be water soluble.

The decrease in the Ca wt% of the sample goes hand in hand with an increase in the K, Al and Si wt%. The PXRD data shows strong peaks for the phase kalsilite ($KAlSiO_4$) and as such this increase confirms the presence of kalsilite in large quantities (alongside sanidine, $KAlSi_3O_8$).

Table 5-7: Averaged data for whole area analysis data collected during SEM-EDS of multiple sample regions of the hemp and coal quenched samples. C and O removed due to interference from the sample mounting process

	Element	H722-2	H740-5	H740-6	H740-10	Average
	Al	13.89	12.70	10.69	11.18	12.12
	Ca	14.78	21.83	19.24	20.51	19.09
	Cl	0.14	0.28	0.35	0.27	0.26
	Cu		0.48	0.72	0.64	0.61
	Fe	5.09	5.19	8.08	3.99	5.59
	K	21.41	19.04	15.25	18.75	18.61
Wt%	Mg	1.86	2.03	5.25	2.91	3.01
	Mn		0.45	0.47	0.45	0.45
	Na	2.66	1.38	2.17	1.70	1.98
	P	5.62	7.17	6.61	7.32	6.68
	S	3.02	1.57	2.52	2.06	2.29
	Si	30.22	27.52	28.19	29.72	28.91
	Ti	0.74	0.71	0.64	0.70	0.70
	Zn		0.26	0.52	0.47	0.42

Table 5-8: XRF data for the comparison of lab collected ash and sample H722-2

	Wt%					
	Hemp and Coal Ash		Hemp and Coal Ash at 900°C		H722-2	
AlK	4.01	±0.16	3.37	±0.04	10.17	±0.05
CaK	31.91	±0.01	31.66	±0.63	19.10	±0.03
ClK	0.94	±0.04	0.42	±0.03	0.19	±0.01
FeK	3.13	±0.02	3.03	±0.32	6.42	±0.13
K K	13.91	±0.13	11.51	±0.27	18.84	±0.46
MgK	5.27	±0.19	5.09	±0.17	2.27	±0.02
MnK	0.34	±0.00	0.32	±0.01	0.32	±0.01
NaK	0.78	±0.25	1.24	±0.30	0.84	±0.12
NiK	0.02	±0.00	0.02	±0.01	0.03	±0.01
P K	11.94	±0.05	11.85	±0.07	7.95	±0.16
S K	4.55	±0.21	4.42	±0.06	0.96	±0.11
SiK	23.41	±0.49	24.57	±0.76	30.18	±0.01
SrK	0.18	±0.01	0.18	±0.01	0.28	±0.00
TiK	0.42	±0.06	0.32	±0.00	0.92	±0.04
ZnK	0.10	±0.01	0.10	±0.00	0.51	±0.09
ZrK	0.07	±0.04	0.05	±0.01	0.06	±0.00
	100.92		**98.13**		**98.99**	

5.1.3 Hemp and coal cyclone ash samples

Analysis of the hemp and coal cyclone ash is presented in Table 5-9 and Figure 5-14 . Quartz is present in the fly ash, but no cristobalite (SiO_2) is present suggesting that formation conditions are favourable in the deposited ash but not the quenched ash. Also present in the fly ash is KCl, indicating that the surfaces present in the combustion rig were not suitable for condensation of KCl. This is likely due to the absence of lots of cool surfaces, in larger scale power plants more cool surfaces (defined here as below gas temperature (approx. 1100°C), in the form of heat transfer and superheater pipes, will be present. This may lead to an increase in deposition of KCl onto areas susceptible to corrosion, in comparison to the surfaces present in the combustion rig, as they will provide much cooler surfaces. This in turn often leads to corrosion of the boiler components.

Table 5-9: Phases present in hemp and coal cyclone ash

Phase	Key	Composition
Quartz	Qz	SiO_2
Sylvite	Sy	KCl
Periclase	P	MgO
Calcite	Ca	$CaCO_3$
Hematite	He	Fe_2O_3
Gehlenite	Ge	$Ca_2Al_2SiO_7$
Merwinite	Mw	$Ca_3Mg(SiO_4)_2$
Kalsilite	Ka	$KAlSiO_4$
Hydroxyapatite	Ha	$Ca_{10}(PO_4)_6(OH)_2$

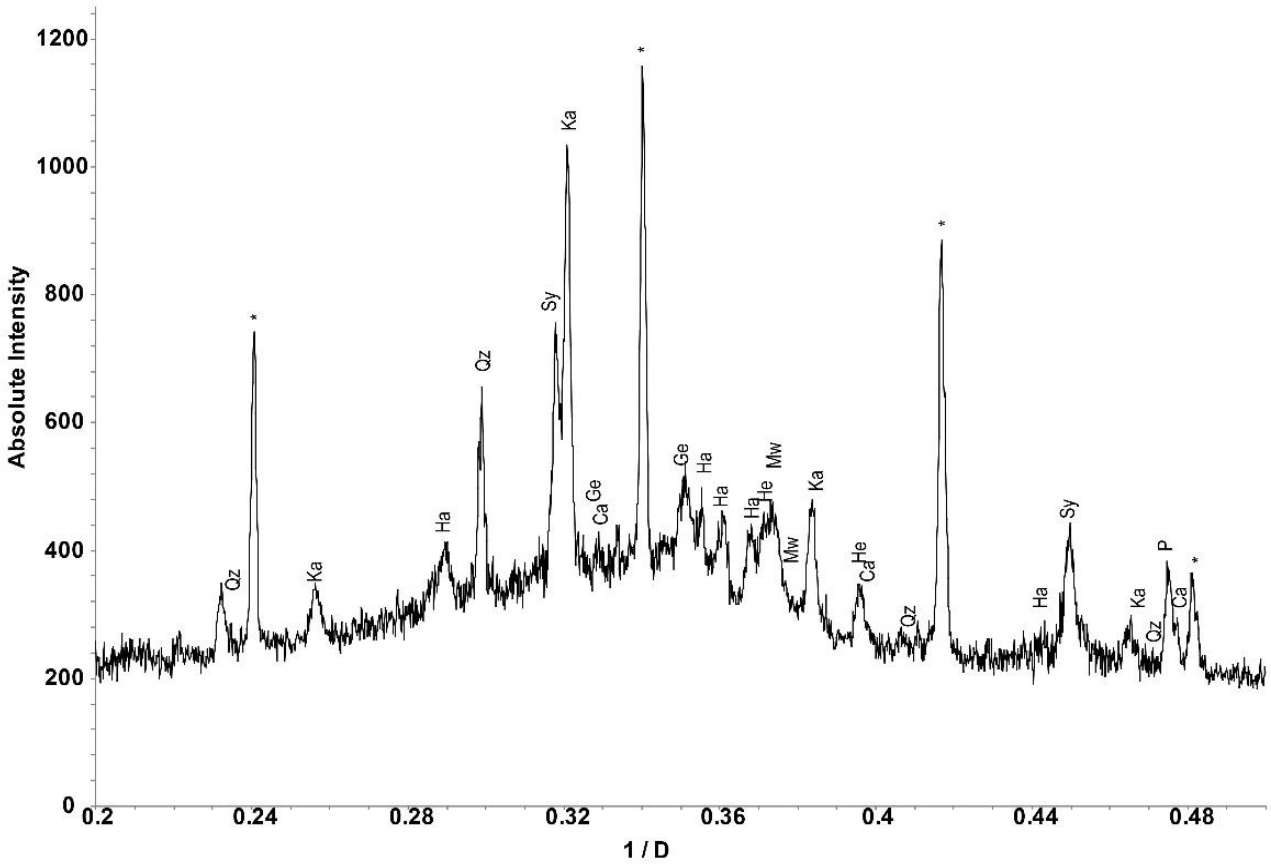

Figure 5-14: PXRD analysis of the hemp and coal cyclone ash collected on the d8 advance diffractometer (Cu Kα1 radiation) *denotes the LaB_6 internal standard

Hydroxyapatite is present in the cyclone ash, which is also present in the laboratory heat treated samples, deposits, quenched, and coupon probe samples. This suggests that the hydroxyapatite is either present in the biomass itself, or formed in the flue gas, rather than post-deposition. Gehlenite ($Ca_2Al_2SiO_7$) is present in the cyclone ash, this suggests that it formed in the flue gas through agglomeration of the parent oxides (Figure 2-3).

Periclase (MgO), calcite ($CaCO_3$), which decomposes to form CaO, and SiO_2 are present in the cyclone ash; these are the endmembers of the CaO-MgO-SiO_2 phase system identified as one of the dominant systems of phases present in the ash. This accounts for the formation of Merwinite ($Ca_3Mg(SiO_4)_2$) in the ash, and suggests that the cyclone ash is rich in CaO (from the phase diagram presented in Figure 4-24).

Kalsilite is also identified in the ash but, in comparison to the laboratory and deposit samples, there are no other K,Al-silicates e.g. leucite, microcline, sanidine, and orthoclase identified as present. This suggests that the feldspars (microcline, sanidine, and orthoclase) or illite did not reach the cyclone ash as they had impacted and deposited, fallen into the bottom ash or they

formed kalsilite in the flue gas. The absence of leucite suggests that it is also a phase that forms in the deposit.

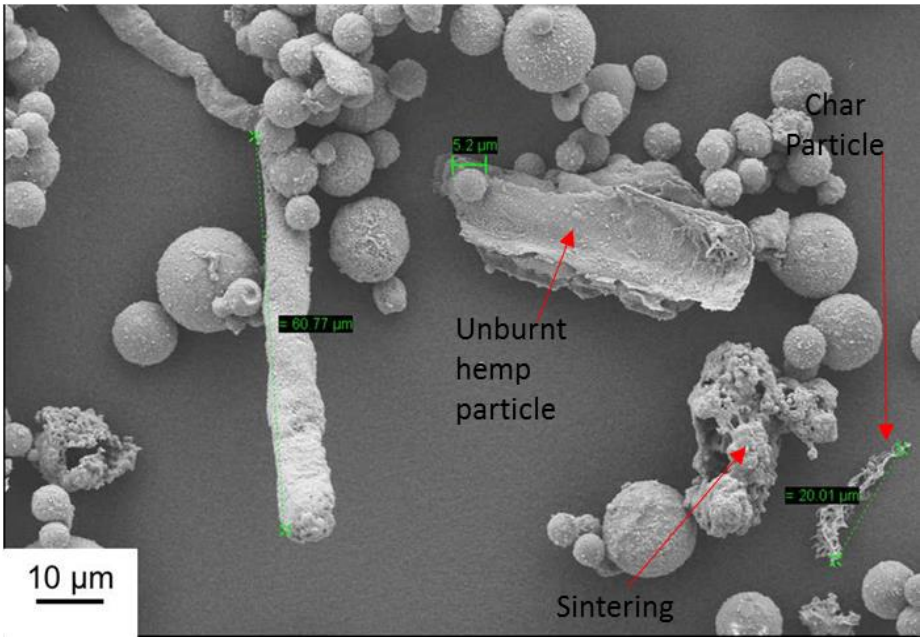

Figure 5-15: An electron micrograph of hemp cyclone ash showing a trichome, several spheres, a char particle and a large flake

An electron micrograph of the wide variety of morphologies present in the hemp and coal cyclone ash is presented in Figure 5-15. The majority of the fly ash comprises of the plerospheres and cenospheres, which are also present in the deposit ash as well as the quenched portion of the fly ash. The surface texture of the spheres shows multiple variations suggesting there may be phase composition differences between the spheres. The particles deposited onto the surface of the spheres are either surface enrichment of KCl (Figure 2-3), or gold particles from the coating used.

A large particle with stick-like morphology is present alongside the spheres. This is likely to be one of the trichomes present in the hemp raw fuel. These structures are also present in the laboratory ash, deposits, and quench. Char particles, those particles still containing some C, are present in the deposits and quenched ash, which suggests incomplete combustion of the fuel. The 20µm particle in the bottom right hand corner is similar in morphology to char particles present in other samples.

The large flake like particle present in the sample is thought to be unburnt hemp due to the morphological similarities shared with the raw fuel. There is also evidence of particle sintering in the sample suggesting that the high temperatures of the flue gas can cause sintering prior to deposition of the fly ash. The sintering may also have been removed from deposits through

erosion by other particles in the flue gas, explaining the presence of sintered particles in the cyclone ash.

SEM-EDS analysis of the samples confirms that the stick-like particles are the trichomes, as identified in the raw fuel. The particles are comprised of the same elements, and are the same shape as the trichomes identified in the high-temperature lab ash samples, (Figure 4-2) the deposit (Figure 5-4), and quenched (Figure 5-11) samples.

The KCl identified through analysis of the PXRD data is also shown to be present through analysis of the EDS maps. The KCl is distributed throughout the sample which suggests that it is enriched on the surface of the other particles. This is in agreement with research by Backman *et al*.[198] who state that KCl often forms as an aerosol. Figure 2-3 indicates that KCl often nucleates on the surface of larger particles.

The composition of the spheres is largely K, Al, Si, and O which suggests that the composition of the hemp and coal quench samples is largely similar to the cyclone ash and therefore bulk composition of the fly ash.

Table 5-10: XRF data comparing laboratory synthesised ash with the hemp and coal cyclone ash

	Wt%		
	Hemp and Coal Ash	**Hemp and Coal Ash 900°C**	**Cyclone Ash**
Al	4.01 ±0.16	3.37 ±0.04	8.04 ±0.25
Ca	31.91 ±0.01	31.66 ±0.63	21.71 ±0.71
Cl	0.94 ±0.04	0.42 ±0.03	1.23 ±0.00
Fe	3.13 ±0.02	3.03 ±0.32	5.315 ±0.06
K	13.91 ±0.13	11.51 ±0.27	23.02 ±0.52
Mg	5.27 ±0.19	5.09 ±0.17	2.985 ±0.02
Mn	0.34 ±0.00	0.32 ±0.01	0.215 ±0.01
Na	0.78 ±0.25	1.24 ±0.30	0.93 ±0.11
Ni	0.02 ±0.00	0.02 ±0.01	0.02 ±0.00
P	11.94 ±0.05	11.85 ±0.07	6.38 ±0.23
S	4.55 ±0.21	4.42 ±0.06	1.805 ±0.21
Si	23.41 ±0.49	24.57 ±0.76	24.295 ±0.57
Sr	0.18 ±0.01	0.18 ±0.01	0.315 ±0.01
Ti	0.42 ±0.06	0.32 ±0.00	0.8 ±0.06
Zn	0.10 ±0.01	0.10 ±0.00	0.16 ±0.00
Zr	0.07 ±0.04	0.05 ±0.01	0.05 ±0.00
	100.92	**98.13**	**97.27**

The elemental composition of the hemp and coal combustion trial cyclone ash is presented in Table 5-10. The composition of the ash is similar to the quenched ash (Table 5-8). The

presence of kalsilite in both these samples and the increase in K and Al suggests that kalsilite is formed in the gas stream. There is an enrichement of Cl in the cyclone ash. This is likely to be as sylvite which also presents strong diffraction peaks in the XRD data (Figure 5-14).

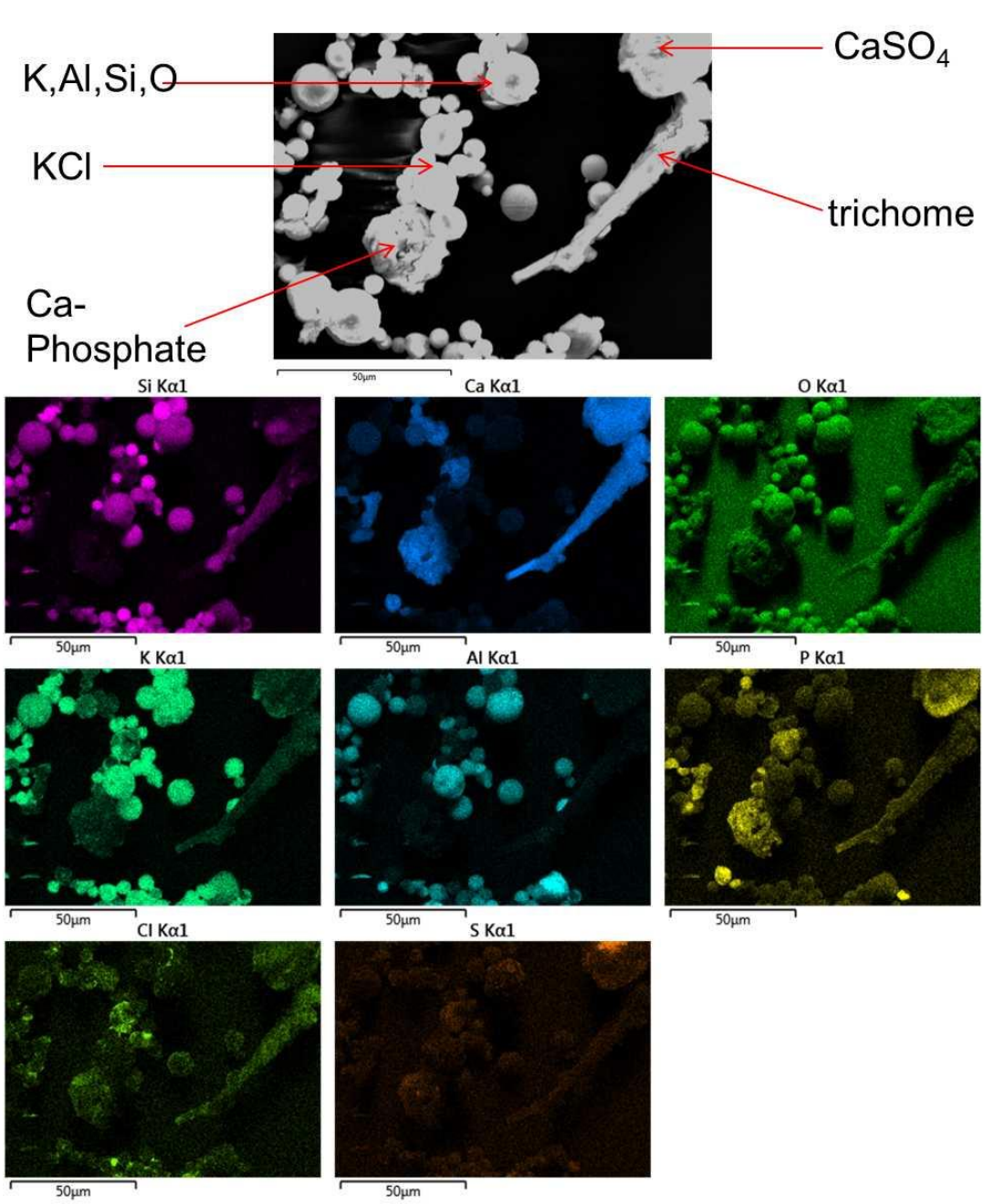

Figure 5-16: Backscattered electronmicrograph of cyclone ash and EDS maps showing the presence of Ca-phosphates, KCl, K,Al-silicates, a trichome and CaSO4

5.1.4 Hemp and coal bottom ash

Whilst the cyclone ash was largely comprised of fine particles, the hopper bottom ash consists of large agglomerated blocks (Figure 5- 17). These blocks are not uniform in appearance, both large pores and sintering are present, these are also visible as several different coloured layers. These layers also show a variety of textures. The top sintered layer is pale green, the middle pale turquoise layer is more closely packed and the bottom grey layer is much more porous.

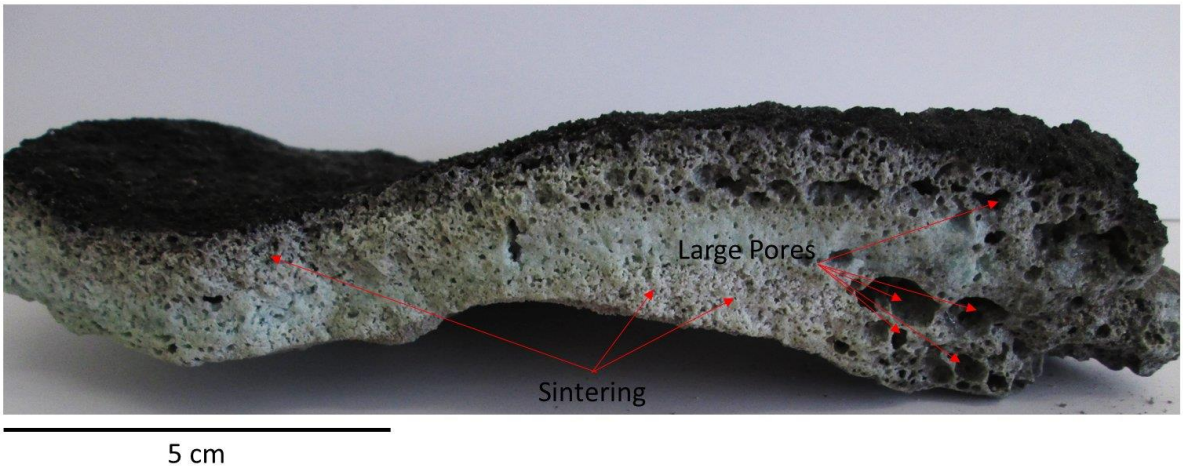

Figure 5- 17: A photograph of a large block of bottom ash from the hemp and coal combustion trial

PXRD analysis of the bottom ash (Table 5-11, Figure 5-18) indicates that three quartz polymorphs are present. At the conditions in the combustion rig quartz, cristobalite and tridymite are the polymorphs expected to form. The formation of cristobalite suggests that the temperature of the ash in the hopper must have reached temperatures close to 1400°C. The hopper ash is mostly comprised of the large particles that did not follow the path of flue gas through the combustion rig, and as such fell into the bottom ash hopper.

The feldspar albite ($NaAlSi_3O_8$) is also present in the bottom ash; it may have formed in the high-temperature melt, or it could be present from the coal ash, as it is identified in the high temperature laboratory produced ash as well as the hemp and coal ash. The phase KCl is also present in the bottom ash; due to the high temperature in the ash hopper, it is unlikely that it has condensed onto the surface of the melt. Instead it is likely that partially combusted, or uncombusted, fuel fell into the hopper and decomposed leaving behind KCl. Uncombusted biomass in the high temperature melt may also be responsible for the large pores visible in the ash blocks. The decomposition of the fuel to yield gas (likely CO_2) may have caused the large bubbles visible in the sample.

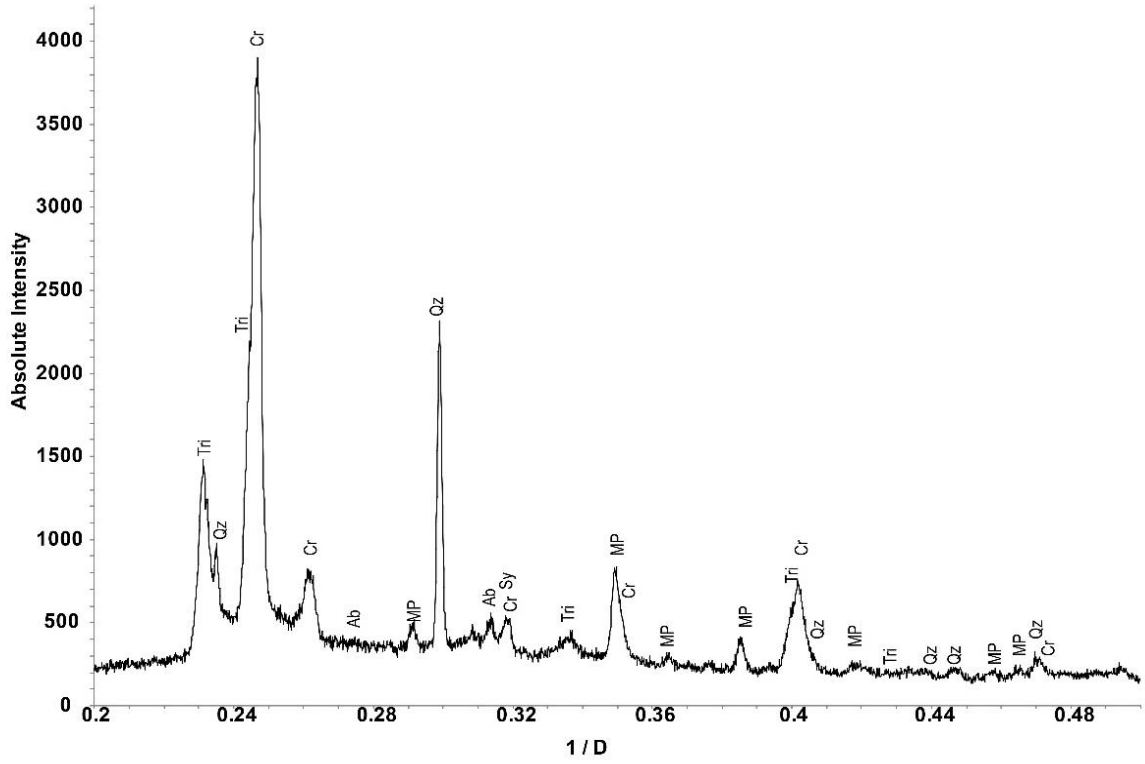

Figure 5-18: PXRD diffraction analysis for the hemp and coal bottom ash

Table 5-11: Phases identified through PXRD analysis in the hemp and coal hopper ash collected during a combustion trial.

Phase	Key	Composition
Quartz	Qz	SiO_2
Cristobalite	Cr	SiO_2
Tridymite	Tr	SiO_2
Sylvite	Sy	KCl
Albite	Ab	$NaAlSi_3O_8$
Potassium Calcium Magnesium Phosphate	MP	$Ca_9MgK(PO_4)_7$

The phosphate $Ca_9MgK(PO_4)_7$ is present in the bottom ash. Hydroxyapatite ($Ca_{10}(PO_4)_6(OH)_2$) has previously been identified in the high temperature lab ash, the deposits, quenched samples, and in coupon deposits. Queiroz *et al*.[199,200] have previously synthesised $Ca_9MgK(PO_4)_7$ after melting glass of the composition 0·45 SiO_2–0·405 MgO–0·045 K_2O–0·1($3CaO.P_2O_5$) at 1500°C for 1 hour. The temperature of the hopper ash is known to be above 1500°C (due to the formation of cristobalite). Further investigation of the formation of $Ca_9MgK(PO_4)_7$[199] showed crystallisation from the above glass composition occurred via

oxyapatite (or hydroxyapatite) at temperatures above 850°C. This suggests that the formation of this phase occurred via the hydroxyapatite previously identified in the ash blend.

The structure of the bottom ash is presented in Figure 5-19. The glass like structure of the bottom ash blocks is also visible in these images. Figure 5-19a shows a particle of compact ash with other smaller particles on the surface. There is little variation in the particle morphology, which also suggests that the melt is fairly uniform. Figure 5-19b shows several particles being absorbed into the surface of a glassy melt. As these particles are still visible, it suggests that they comprise of high melting point compounds.

EDS analysis of the hopper ash after encapsulation in resin (Figure 5-20) shows that there are distinct regions in the melt that do not have clearly visible morphological differences. EDS analysis shows that there are distinct SiO_2 regions, which are the quartz, cristobalite, or tridymite, identified through analysis of the PXRD data. There also appears to be lime (CaO) which has not reacted with SiO_2 as there are distinct regions. K, Si, and O are present in the

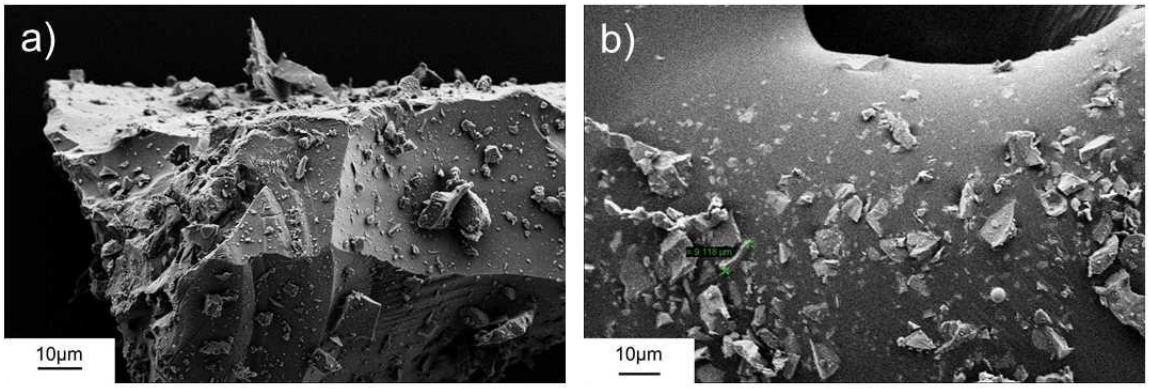

Figure 5-19: SEM analysis of hemp and coal hopper ash

melt too, this was not identified in the PXRD analysis, however it may be present in small quantities or as a glassy amorphous phase.

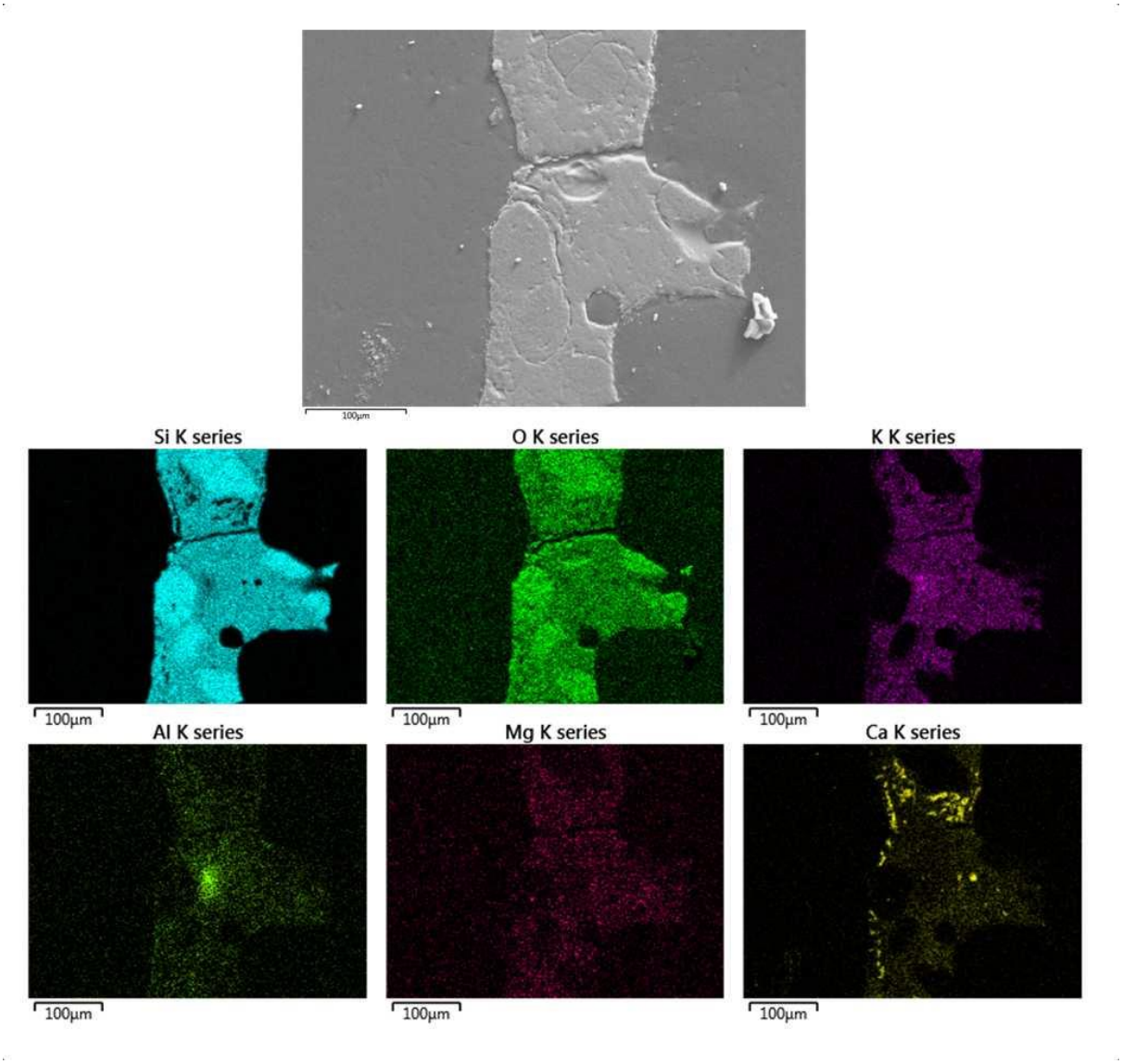

Figure 5-20: An Electronmicrograph and EDS maps of hopper ash encapsulated in resin. Distinct SiO_2 and CaO regions are visible

5.2 Eucalyptus and Coal Combustion Rig Samples

Gas conditions collected at the exit of the combustion rig are presented in Figure 5-21, samples coloured red are deposit samples, samples coloured blue are quenched samples. SO_2, CO and NO should be read from the left concentration (ppm) axis, and CO_2 and O_2 from the right concentration (%) axis. Similarly to the conditions in the hemp combustion run, there is significant fluctuation in the CO concentration during the fuel trial. In contrast, the CO_2 concentration remains fairly constant.

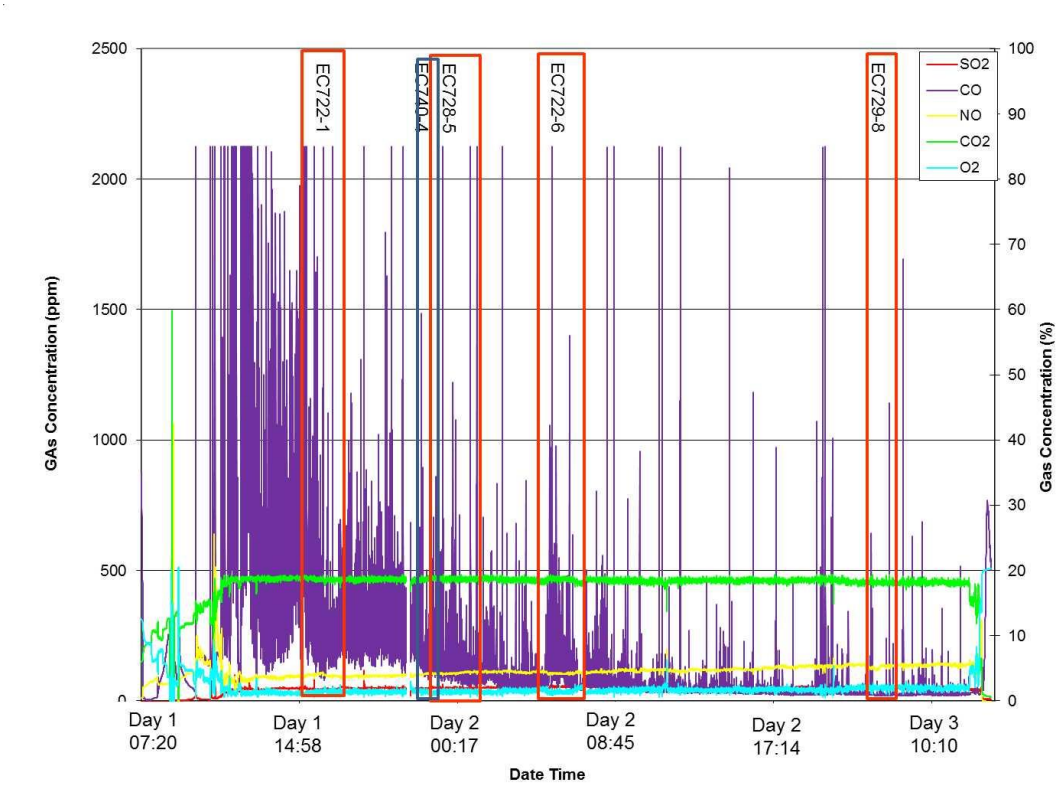

Figure 5-21: Gas conditions at combustion rig exit during the co-combustion of eucalyptus and Kuzbass coal. Red indicates a deposit, blue indicates a quenched sample. The numbers denote the sample code (Section 3)

5.2.1 Eucalyptus and Coal Deposit Samples

The organic matrix observed in the raw fuels (Figure 4-22) decomposed during combustion, leaving the inorganic ash components behind. The release of the C is observed as CO/CO_2 in the flue gas (Figure 5-21). The ash contents of the fuel are 0.6% for eucalyptus, and 8.7% for coal; the fuels were fired in the ratio 88:12 eucalyptus:coal which gives a combined ash content of 1.57%. This is much lower than the ash content of the hemp and coal fuel blend.

Table 5-12: Sample collection times and temperature for eucalyptus and coal deposit samples

Sample	Duration	Temperature (°C)
EC 722-1	163 minutes	978
EC 728-5	202 minutes	914
EC 722-6	184 minutes	1012
EC729-8	117 minutes	932

The temperature range of the eucalyptus and coal samples was between 914-1012°C (Table 5-12). Analysis of the PXRD data is presented in Table 5-13 and Figure 5-22. Whilst there is a significant variation in temperatures between the samples, this does not appear to have had a large affect on the phases present i.e. a large portion of the same phases are present in each sample. This can be observed as the XRD patterns are similar yet not identical. The SO_2, CO_2, O_2 and NO content of the gas fluctuated very little through the duration of the combustion run.

In contrast to the hemp and coal deposits, there are no carbonates e.g. $CaCO_3$ or $CaMg(CO_3)_2$ observed. This could be due to the length of time that the sample was collected for e.g. 117 minutes – 202 minutes for eucalyptus and coal, in comparison to 37-58 minutes for hemp and coal. The longer the sample is in the combustion environment the more stable the deposit may become, i.e. the most stable phases are likely to form and not react further. Lime (CaO) is present in the sample. Previously it was thought that the CaO (s) may react with CO_2(g) during cooling to form the $CaCO_3$ a phase observed in the hemp and coal sample (Section 4.1.1). It may be that some $CaCO_3$ is present in the deposit but in undetectable quantities. The CaO may also have been too deep in the deposit to react with CO_2 from the air, as the outside of the deposit would cool and solidify first and almost "seal" the outside.

Both the eucalyptus and coal have a high Fe content (Table 3-18), which is reflected through the presence of hematite (Fe_2O_3) and maghemite (y-Fe_2O_3). Maghemite forms from the incomplete oxidation of Fe_3O_4. Incomplete combustion of the fuel can lead to an increase of C in the deposits, and this can in turn affect the reduction/oxidation conditions in the deposit.

Table 5-13: Phases present in deposit samples from eucalyptus and coal co-firing as identified through PXRD analsysis

Phase	Key	Composition	EC727-1	EC728-5	EC722-6	EC729-8
Quartz	Qz	SiO_2	•	•	•	•
Diopside	Di	$CaMgSi_2O_6$	•	•	•	•
Hematite	He	Fe_2O_3	•	•	•	•
Kalsilite	Ka	$KAlSiO_4$	•	•	•	•
Periclase	P	MgO	•	•	•	•
Anhydrite	An	$CaSO_4$	•	•	•	•
Cristobalite	Cr	SiO_2	•	•	•	•
Microcline	Mi	$KAlSi_3O_8$	•	•	•	•
Sanidine	Sa	$KAlSi_3O_8$	•			
Forsterite	Fo	Mg_2SiO_4	•	•	•	•
Mullite	Mu	$Al_{2.35}Si_{0.64}O_{4.82}$	•	•	•	•
Aluminium Oxide	Al_2	Al_2O_3	•	•	•	•
Akermanite-Gehlenite	Ak-Geh	$Ca_2(Mg_{0.5}Al_{0.5})(Si_{1.5}Al_{0.5})O_7$	•	•	•	•
Leucite	Le	$KAlSi_2O_6$	•			
Arcanite	Ac	K_2SO_4	•	•	•	•
Albite	Ab	$NaAlSi_3O_8$	•	•	•	•
Merwinite	Me	$Ca_3Mg(SiO_4)_2$	•	•	•	•
Lime	Le	CaO	•	•	•	•
Grossular	Gr	$Ca_3Al_2(SiO_4)_3$		•	•	•
Maghemite	Magh	y-Fe_2O_3	•	•	•	•

Cristobalite, a high temperature SiO_2 polymorph, is present in the samples (Table 5-13). The presence of cristobalite highlights that there is either an excess of SiO_2 in the fuel, or that the conditions have not reached stability.[201] Under stable conditions all SiO_2 would react to form Ca/Mg/K silicates or form slags; if cristobalite is present it is an indicator that this stability hasn't been reached.[202] Cristobalite has been reported to have a high affinity to alkali metals at high temperature.[202] Farny *et al.*[203] state that this is due to the low density, porous nature of the structure which leads to a large surface area more susceptible to reaction. This suggests that reactions to form the silicates observed could proceed with cristobalite as the SiO_2 source, which further explains the formation of these phases at lower temperatures than predicted.

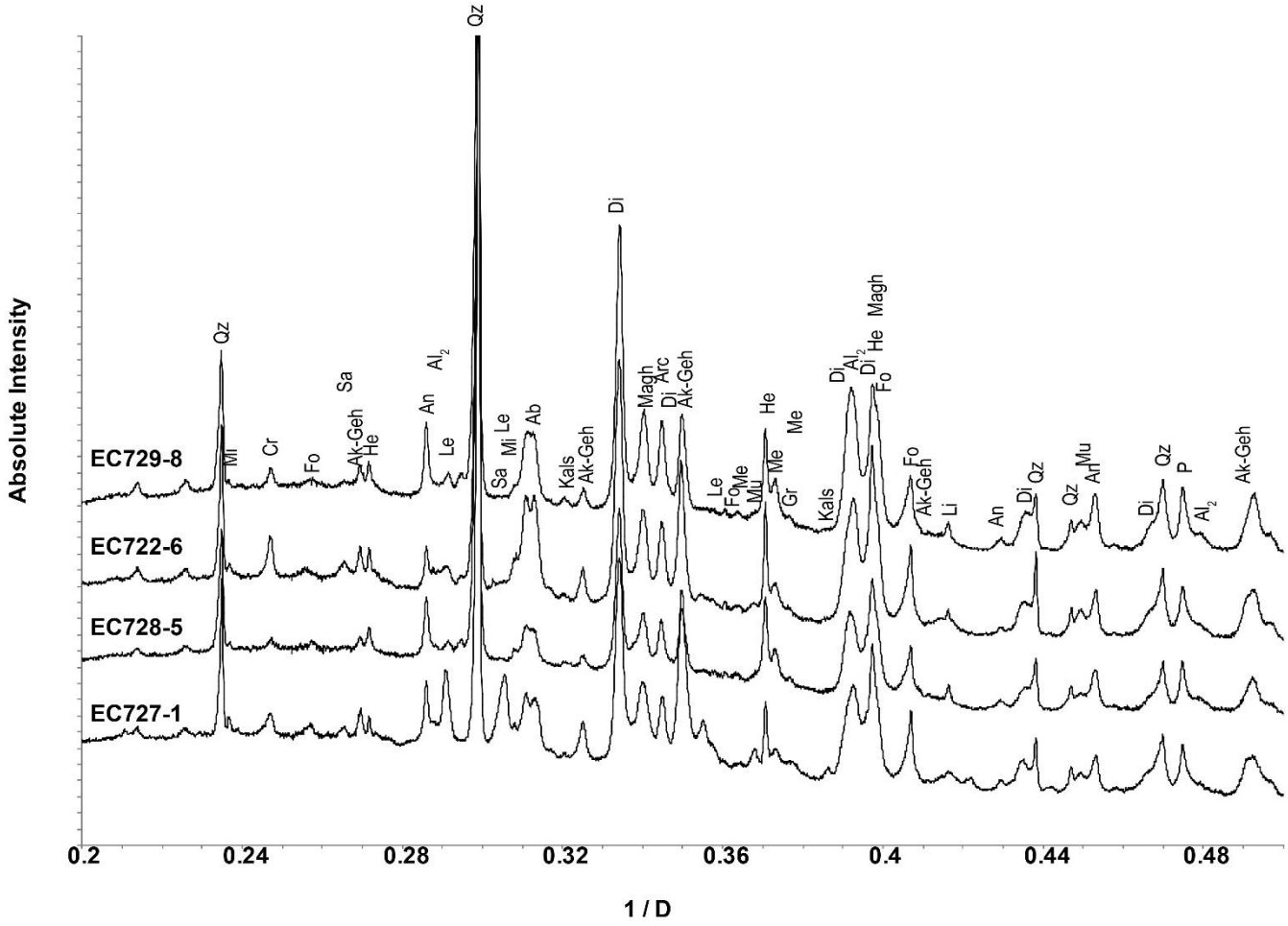

Figure 5-22: PXRD eucalyptus and coal deposits synchrotron I-11 beamline data (λ0.826215) is presented, the range is truncated to 0.2-0.5 for clarity

The presence of cristobalite has both disposal and environmental implications. Cristobalite can lead to the lung condition silicosis[204] and therefore the presence of crystalline cristobalite in particulate emissions is subject to monitoring.[205] This monitoring has also been extended to further use of the ash eg: fly ash in the concrete industry, where monitoring of respirable quartz and cristobalite is already used[206] suggesting that as long as the presence of cristobalite is monitored, health hazards can be limited.

As shown in Table 5-13 the phases present in the different samples are similar. However in EC722-1 leucite and sanidine are also present. The gas temperature of EC722-1 is 978°C, a temperature in the middle of the recorded range. The gas conditions were not vastly different to those recorded during for the other samples (Figure 5-21). Therefore it is not immediately obvious why these two K,Al-silicates have formed. The inhomogeneity of the samples i.e: the difference of what deposits next to one another is likely to contribute.

Al is present in the ash matrix at 10.54 wt%, Al_2O_3 is confirmed by PXRD to be present in the ash. The increased content of Al in the fuel will have led to the formation of the akermanite-gehlenite solid solution identified to be present by analysis of the PXRD data. Increased Al_2O_3 in the ash is desirable as it increases the ash fusion temperature,[207] this in turn means that a deposit is less likely to sinter.[56] The presence of Al_2O_3 in quantities lower than 8.6 wt% has previously been shown to favour the formation of diopside over anorthite in ceramic systems.[176,208] Kurama *et al*.[209] reported that gehlenite forms at lower temperatures than anorthite, and therefore an increase in temperature of the deposit, or presence for a greater amount of time (e.g. formation on boiler/superheater tubes during power plant service) could potentially lead to further reaction of gehlenite to form anorthite.

Analysis of the SEM electron micrographs of the samples show that, similarly to the deposits in the hemp and coal combustion run, there is agglomeration of the spherical particles (Figure 5-23). As well as the spherical particles there are clear sintered and porous regions of the deposit (Figure 5-23) which appear to join larger spheres together. Sintering of deposits can lead to melting and flow and, this can create very tenacious deposits that are not able to be removed with soot blowing.[65] This sintering commonly accompanies fuels high in alkali and silicate content;[65] the blend of coal with the eucalyptus decreases the K_2O content from 10.25% in eucalyptus to 8.71% in the co-fire blend, which may reduce the likelihood of sintering.

Figure 5-24 shows areas of sintering in deposit sample EC 727-8. The area of sintering is largely comprised of K, Al-silicate confirming that alkali silicates give an increased chance of sintering in ash deposits. Also present in this region of the deposit are Ca, Mg, Al, and Si

suggesting these could be particles of the akermanite-gehlenite solid solution identified as present through analysis of the PXRD data. In the EDS maps, an area of Ca,Mg phosphate is also identified. This was not observed in analysis of the PXRD data suggesting it is either present in minor quantities that cannot be detected, or due to the number of different crystalline phases present, there is a large degree of peak overlap.

EDS maps of melted agglomerated spheres from a deposit in sample EC 722-6 are presented in Figure 5-25. Distinct regions of overlap between Ca, Mg, Al, Si, and O can be observed which suggests that these melt regions may be the origin of formation of the akermanite-gehlenite solid solution.

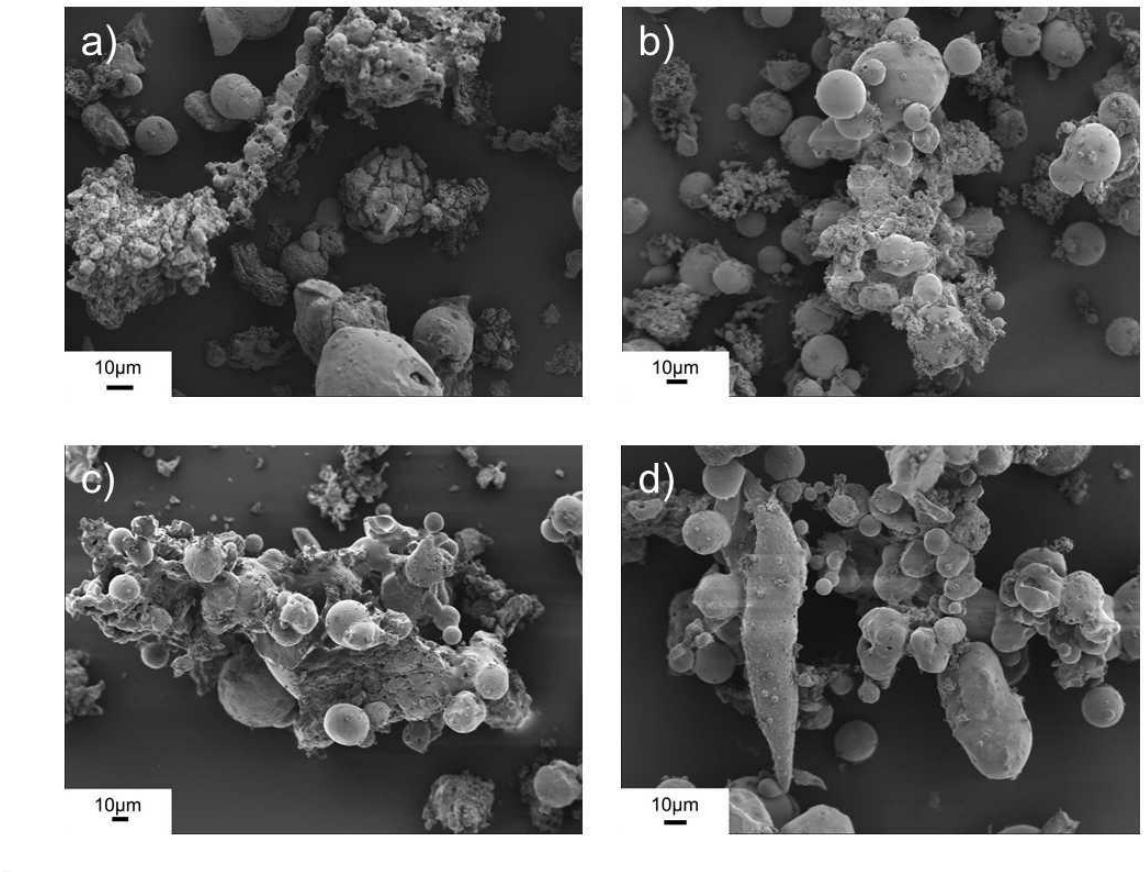

Figure 5-23: SEM electronmicrographs of eucalyptus and coal ash a) EC727-1 b) EC728-5 c) EC722-6 d) EC 722-8

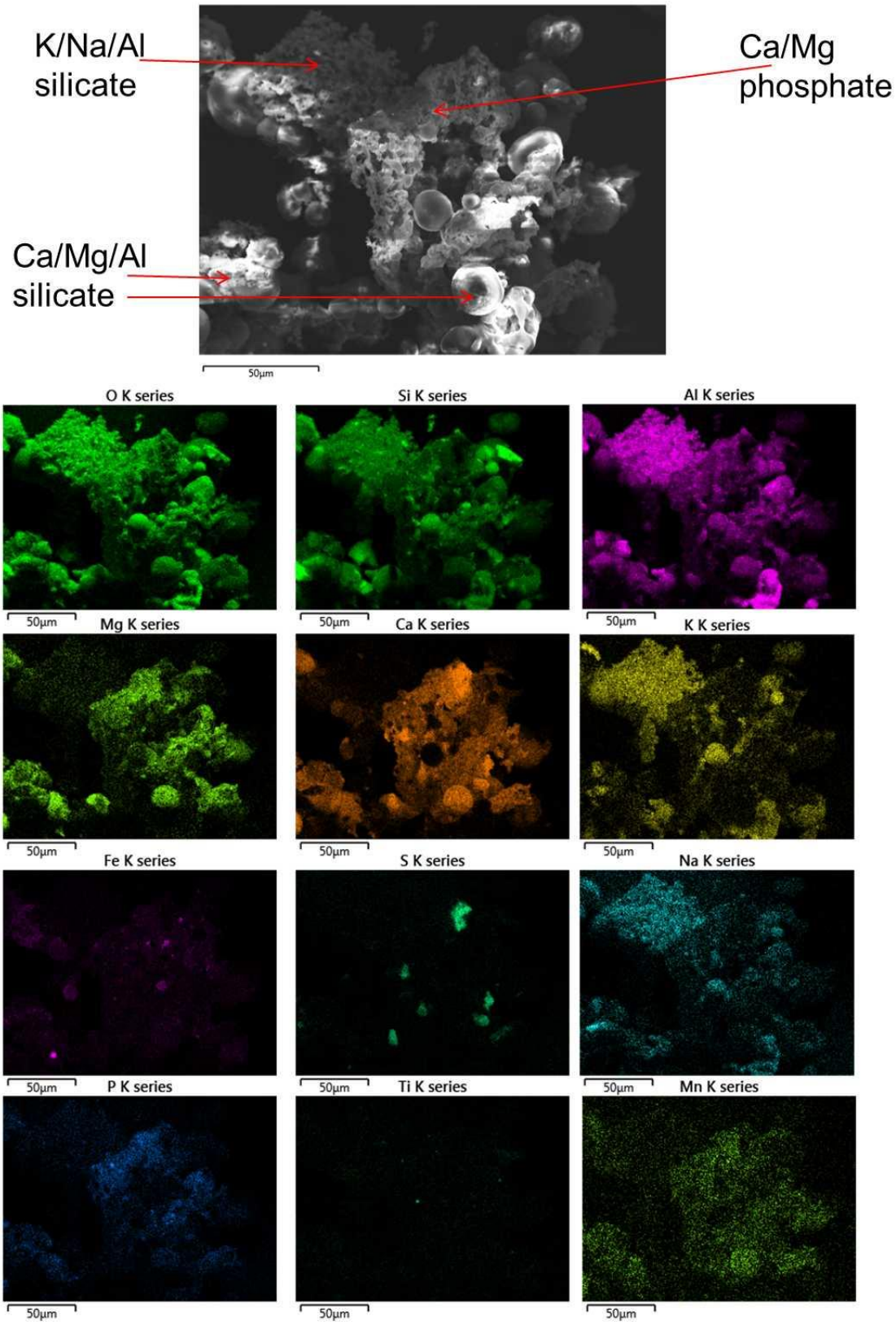

Figure 5-24: EDS maps of EC 727-8 showing areas of sintering in the deposit and their composition

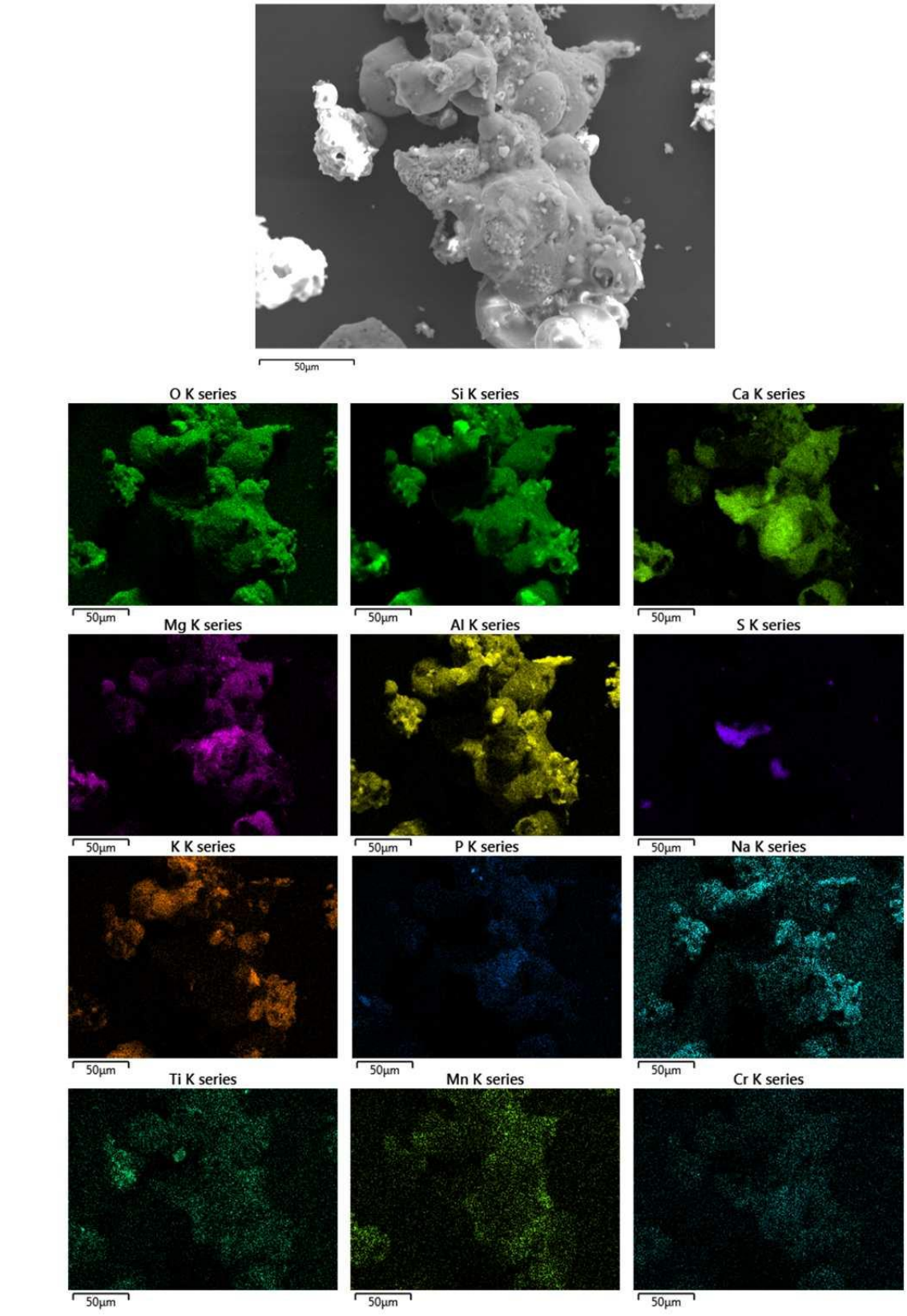

Figure 5-25: EDS maps of EC 722-6 showing regions of sphere agglomeration and reactions between them

Table 5-14: Averaged data for whole area analysis data collected during SEM-EDS of multiple sample regions of the eucalyptus and coal deposits. C and O removed due to interference from the sample mounting process

	Wt %									
	722-1		728-5		722-6		729-8		Average	
Al	10.83	±1.31	16.25	±1.41	15.43	±1.22	17.00	±1.84	14.88	±2.77
Ca	28.99	±4.23	14.21	±2.53	19.89	±5.77	16.75	±2.72	19.96	±6.45
Cu	0.55	±0.12	0.60	±0.08	0.64	±0.25	0.59	±0.23	0.59	±0.04
Fe	7.98	±0.79	8.80	±0.77	10.19	±4.34	9.37	±3.17	9.08	±0.93
K	5.25	±0.44	7.39	±0.86	5.27	±0.91	5.52	±0.55	5.86	±1.03
Mg	4.68	±0.58	3.45	±0.46	4.08	±0.67	3.95	±0.63	4.04	±0.51
Mn	1.09	±0.27	1.05	±0.12	1.34	±0.40	1.32	±0.44	1.20	±0.15
Na	1.96	±0.19	3.02	±0.90	2.90	±0.76	2.96	±0.44	2.71	±0.50
P	2.60	±0.30	1.48	±0.70	1.46	±0.59	1.84	±0.73	1.84	±0.53
S	5.88	±2.31	3.14	±0.64	3.68	±1.31	3.25	±1.42	3.99	±1.28
Si	28.46	±3.72	39.33	±1.60	34.39	±5.23	36.46	±1.53	34.66	±4.60
Ti	0.76	±0.11	1.07	±0.25	0.90	±0.08	0.94	±0.19	0.92	±0.13

Table 5-15: XRF data comparing deposit samples EC722-6, EC729-8, eucalyptus and coal ash and eucalyptus and coal ash heat treated to 900°C

	Wt%							
	EC722-6		EC729-8		Eucalyptus and Coal		Eucalyptus and Coal 900°C	
Al	11.09	±0.18	11.50	±0.09	10.54	±0.08	12.16	±0.04
Ca	22.15	±0.28	21.73	±0.59	17.75	±0.13	16.20	±0.39
Cl	0.15	±0.04	0.23	±0.02	1.02	±1.17	0.14	±0.04
Fe	10.68	±0.31	10.38	±0.32	11.93	±0.49	9.04	±0.16
K	4.96	±0.01	4.77	±0.06	7.81	±0.01	7.32	±0.17
Mg	4.17	±0.01	3.69	±0.06	2.81	±0.05	3.95	±0.48
Mn	1.80	±0.01	1.77	±0.06	1.28	±0.01	1.07	±0.09
Na	1.60	±0.37	1.26	±0.43	1.23	±0.10	1.71	±0.66
Ni	0.03	±0.01	0.02	±0.00	0.04	±0.01	0.02	±0.00
P	2.75	±0.09	2.57	±0.09	2.48	±0.02	2.44	±0.04
S	1.70	±0.12	3.31	±0.03	9.16	±0.08	10.39	±0.05
Si	35.60	±0.80	35.64	±0.62	31.25	±0.35	32.87	±0.16
Sr	0.64	±0.02	0.63	±0.02	0.39	±0.03	0.40	±0.04
Ti	1.11	±0.01	1.12	±0.03	1.35	±0.01	1.06	±0.04
Zn	0.05	±0.00	0.05	±0.01	0.14	±0.00	0.11	±0.01
Zr	0.09	±0.01	0.09	±0.01	0.05	±0.01	0.05	±0.00
	98.52		**98.71**		**99.20**		**98.90**	

TablesTable 5-14 and Table 5-15 show analysis of the elemental composition of the deposit samples using SEM-EDS and XRF data. Overall the analysis between both methods are in agreement. In comparison to the samples produced in the laboratory there is a decrease in the K content (7.32 wt% to 4.96 and 4.77wt%, from XRF data) of the deposits. This

corresponds with the SEM-EDS data which also shows a decrease across the majority of the samples with EC 728-5 being the exception. Comparison with the XRD data shows several K containing silicates are identified in the samples but the peaks associated with them are not dominant. However, without phase quant on the samples no conclusion of K content from XRD can be drawn.

There is slight increase in the Si content (35.6 wt% for the deposits from 32.87 wt% in the laboratory ash at 900°C) and a minor decrease in the Al content of the ash (11.09 wt% and 11.50 wt% from 12.16 wt% in the laboratory ash at 900°C). This suggests that the dominant method of deposition is inertial impaction as these are larger particles which will not deviate around the probe with gas flow and so will impact causing the build up of sticky deposits. It is suggested that a large amount of the Al and Si will come from the coal fuel with phases such as mullite being present in the deposits (Table 5-13) and as the coal fuel contains more Si than the eucalyptus fuel (43.17 wt% to 16.92 wt%).

The deposits are enriched in Ca in comparison to the high temperature laboratory ashed samples (22.15 and 21.73 wt% to 16.20 wt% Ca). In contrast to the hemp and coal deposit samples there are fewer Ca,Mg silicates (e.g. diopside and merwinite) and more Ca as non-silicate phases (e.g. anhydrite and lime). Suggesting that the Ca deposited in forms available for reaction rather than as silicates, Figure 5-24 andFigure 5-25 show clear association between Ca and S indicating these are regions where $CaSO_4$ deposited.

Mn and Ti are identified in both the XRF and SEM-EDS averaged results. No phases containing them are in the XRD analysis. In Figures Table 5-14 andTable 5-15 there are clear regions of Mn and Ti. This suggests that the phases are either amorphous or present in amounts undetectable by XRD. This observation is also true for the P identified as Ca/Mg phosphate in Figure 5-24.

5.2.2 Eucalyptus and coal quenched samples

Sample EC740-4 was collected according to the method described in Section 2.2.1.2. The sample collection time was 105 minutes and no temperature was recorded; from previous combustion runs the temperature is estimated to be around 700-800°C.

Table 5-16: Phases present in sample EC740-4

Phase	Key	Composition
Quartz	Qz	SiO_2
Hematite	He	Fe_2O_3
Magnetite	Ma	Fe_3O_4
Corundum		Al_2O_3
Microcline	Mi	$KAlSi_3O_8$
Mullite	Mu	$Al_6Si_2O_{13}$

PXRD analysis of EC740-4 is presented in Table 5-16 and Figure 4-27. The phases present in EC740-4 identified through analysis of the PXRD data are mainly insoluble oxides. These have formed through decomposition of the fuels during combustion. In comparison to the quenched samples from the hemp and coal (5.1.2), and eucalyptus (5.3.2), there are comparatively fewer silicates identified in the PXRD data. There is however a high background in the sample suggesting the presence of amorphous phases; these may be silicate compounds that did not crystallise during the water quenching process as the amorphous compounds do not show distinct patterns.

Analysis of the SEM data (Figure 5-26) shows that particles of several different morphologies are present. The majority of the ash is comprised of the smaller spheres often found in the quenched samples. There are also cuboid structures similar to those of microcline observed in previous samples.

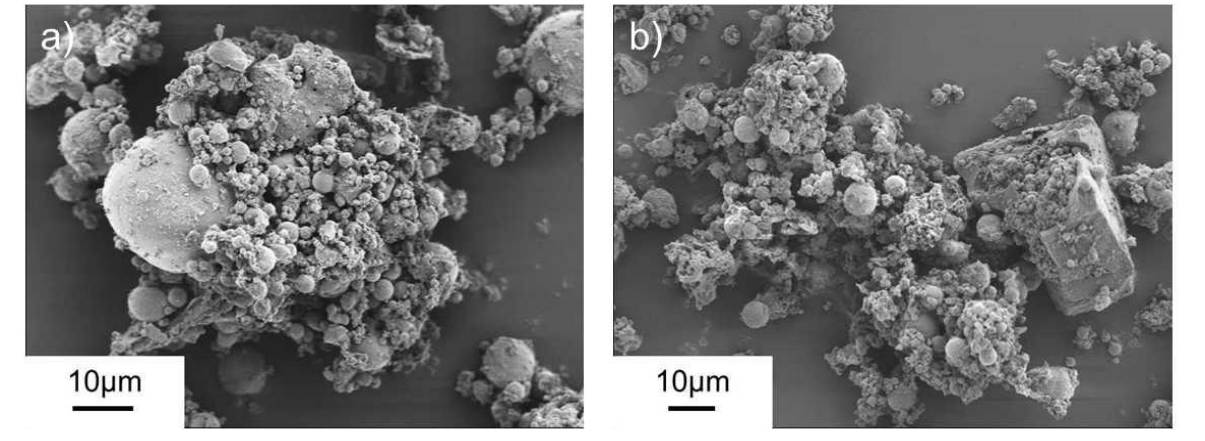

Figure 5-26: SEM Electron micrographs of EC740-4 a) large and small spheres present b) a cuboid shaped particle with smaller spherical particles

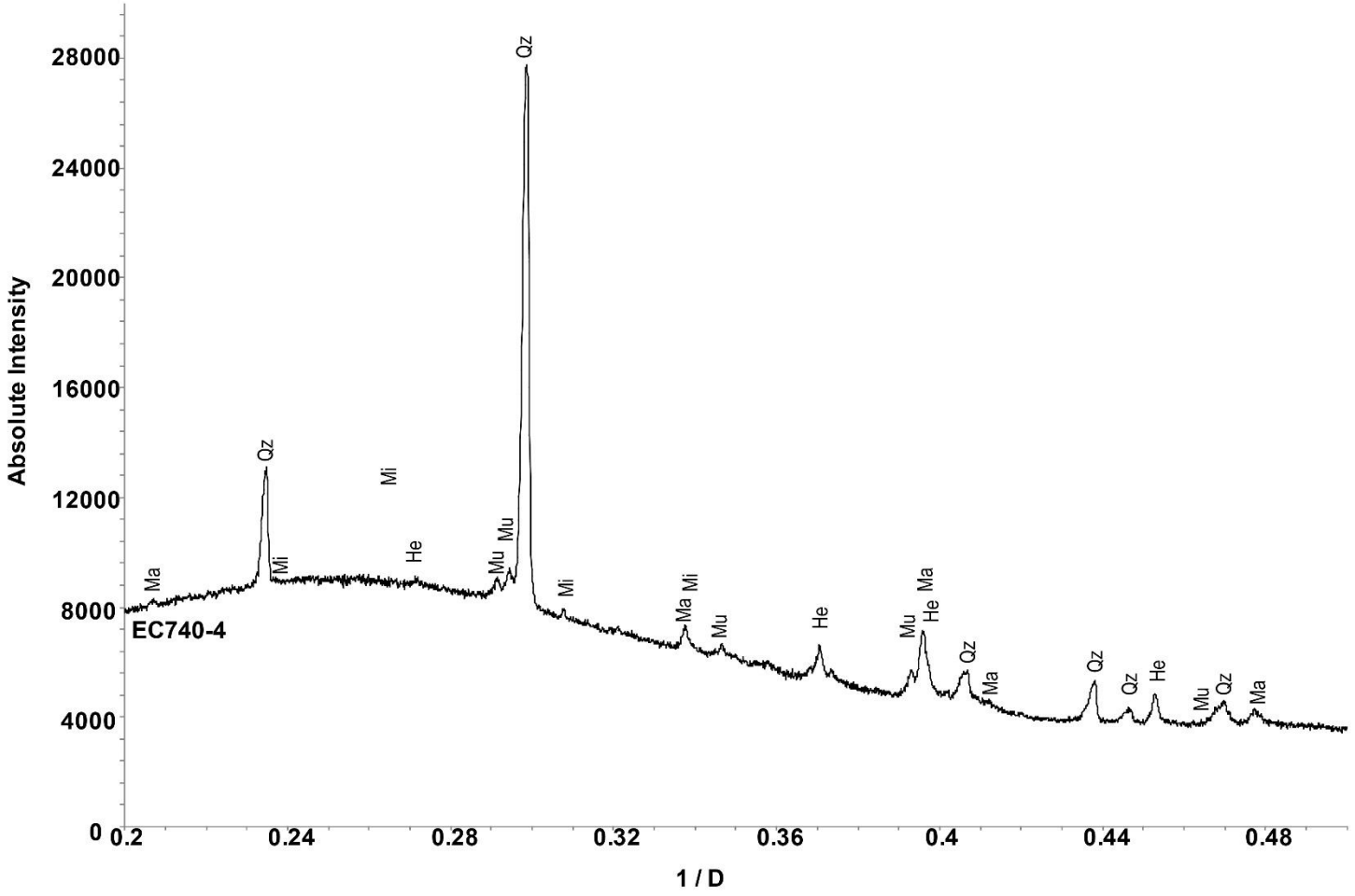

Figure 4-27: PXRD analysis of sample EC740-4 collected on the I-11 beamline (λ 0.826215)

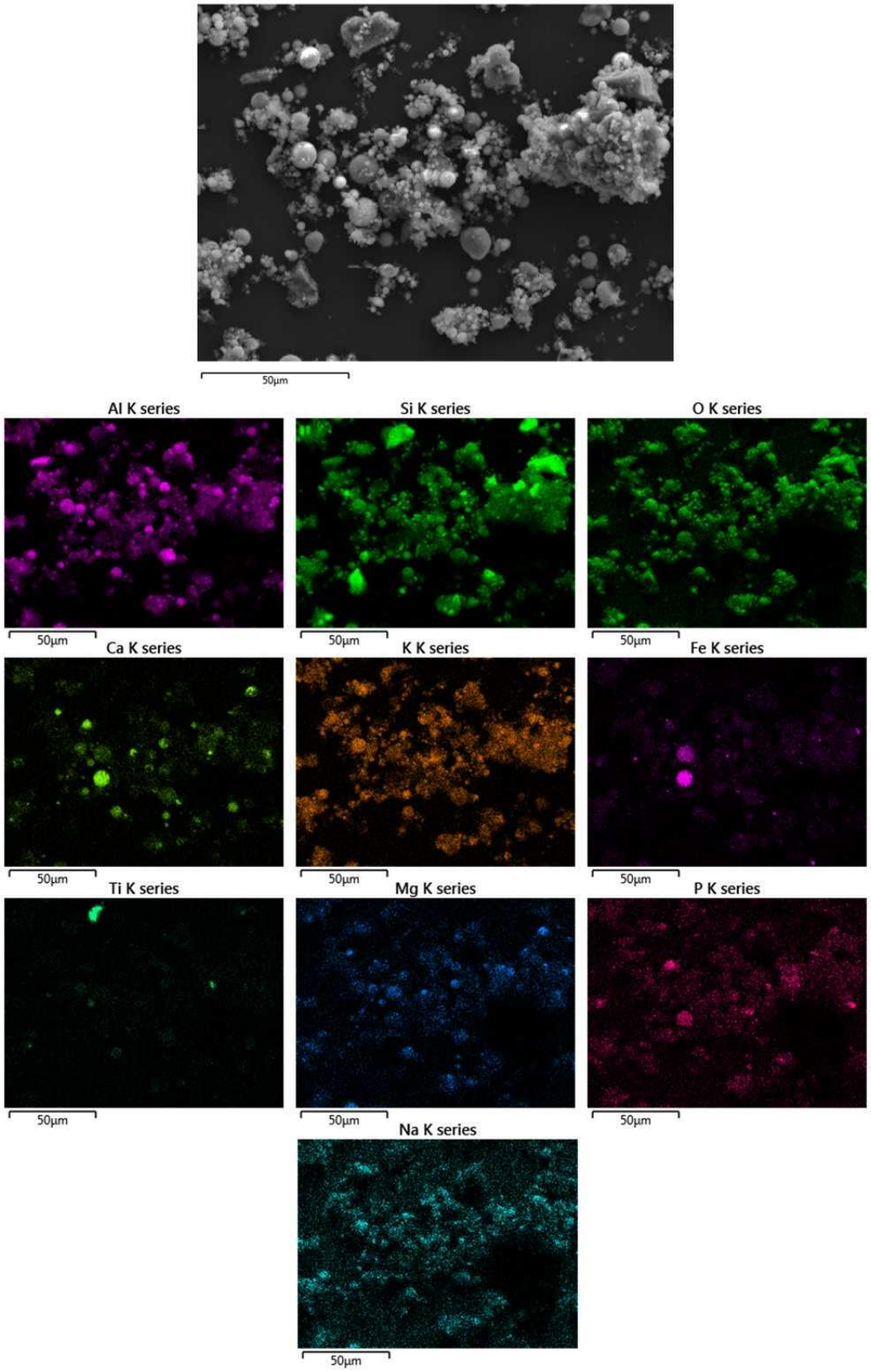

Figure 5-28: EDS maps of sample EC740-4 showing distribution of K, Al, Si and O throughout the sample

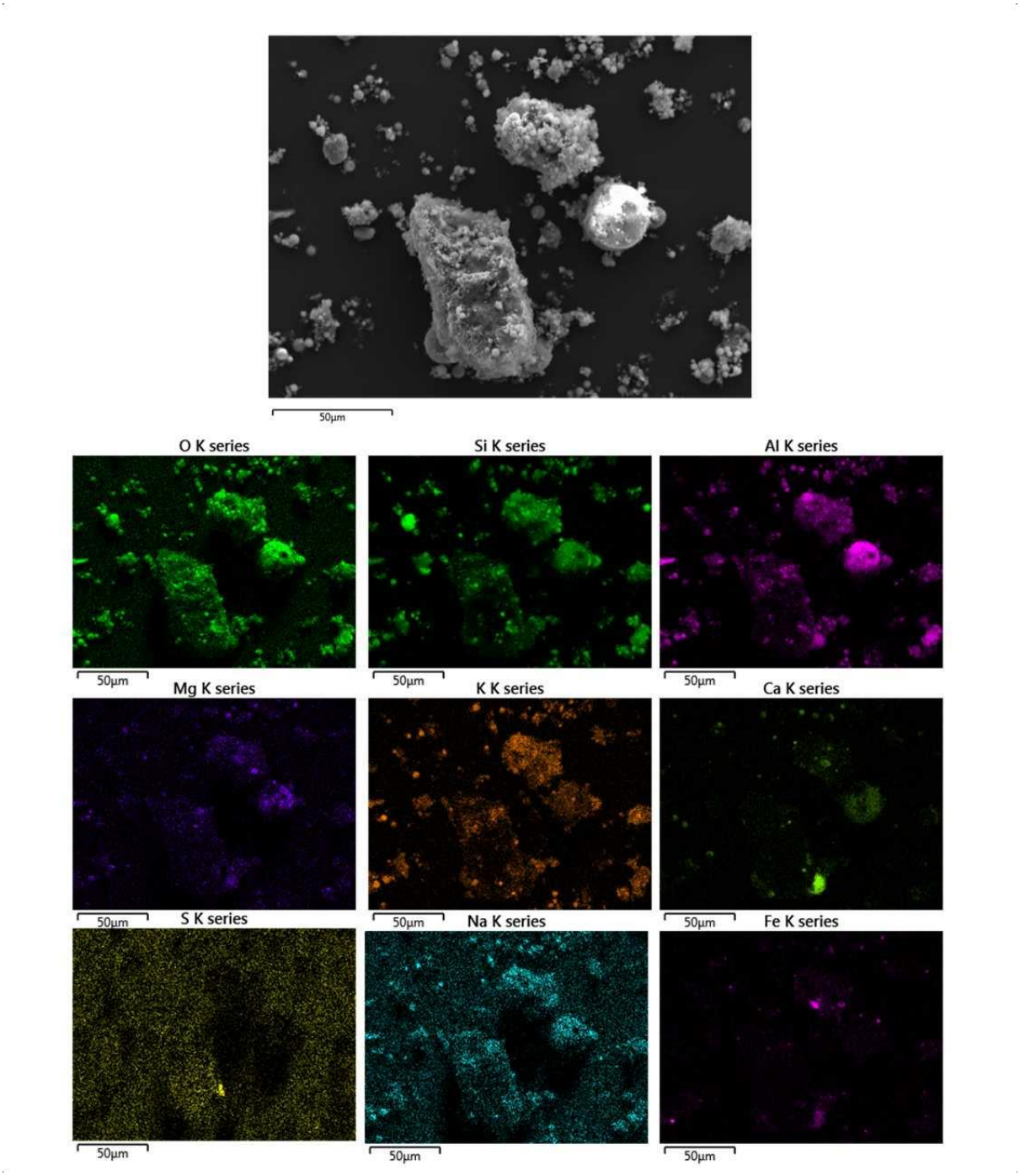

Figure 5-29: EDS maps of sample EC740-4 showing K,Al silicates

Analysis of the EDS maps presented in Figure 5-28 indicates a large portion of the ash in the samples is comprised of K, Al, Si, and O. The glassy phase which has a similar composition to sanidine ($KAlSi_3O_8$) is likely to be responsible for the amorphous region in the background of the PXRD data samples. There is association between Ca, P, and O (Figure 5-28), suggesting the presence of calcium phosphate, but this was not observed in the PXRD analysis. The cuboid structured crystals observed in the SEM data (Figure 5-26) and Figure

5-29 are largely comprised of K,Al Si and O suggesting that they are the microcline identified through PXRD data analysis.

Table 5-17: Averaged data for whole area analysis data collected during SEM-EDS of multiple sample regions of the eucalyptus and coal quenched sample EC740-4. C and O removed due to interference from the sample mounting process

	Element	EC 740-4	
Wt%	Al	18.30	±0.47
	Ca	4.53	±1.83
	Cu	0.97	±0.33
	Fe	6.10	±1.17
	K	11.27	±1.72
	Mg	1.63	±0.12
	Mn	0.37	
	Na	4.52	±0.52
	P	1.88	±0.33
	S	5.03	±2.33
	Si	44.84	±4.95
	Ti	1.09	±0.20

Table 5-18: XRF analysis of EC 740-4 compared with Eucalyptus and Coal and Eucalyptus and coal at 900°C

	Element	EC 740-4		Eucalyptus and Coal		Eucalyptus and Coal 900°C	
Wt%	Al	13.68	±0.62	10.54	±0.08	10.54	±0.08
	Ca	10.59	±2.84	17.75	±0.13	17.75	±0.13
	Cl	0.12	±0.00	1.02	±1.17	1.02	±1.17
	Fe	11.91	±0.62	11.93	±0.49	11.93	±0.49
	K	10.98	±0.39	7.81	±0.01	7.81	±0.01
	Mg	2.10	±0.42	2.81	±0.05	2.81	±0.05
	Mn	0.58	±0.04	1.28	±0.01	1.28	±0.01
	Na	2.14	±0.40	1.23	±0.10	1.23	±0.10
	Ni	0.03	±0.01	0.04	±0.01	0.04	±0.01
	P	3.13	±0.04	2.48	±0.02	2.48	±0.02
	S	0.37	±0.02	9.16	±0.08	9.16	±0.08
	Si	39.74	±2.21	31.25	±0.35	31.25	±0.35
	Sr	0.57	±0.04	0.39	±0.03	0.39	±0.03
	Ti	1.49	±0.08	1.35	±0.01	1.35	±0.01
	Zn	0.33	±0.04	0.14	±0.00	0.14	±0.00
	Zr	0.11	±0.01	0.05	±0.01	0.05	±0.01
		97.84		**99.20**		**99.20**	

Table 5-17 andTable 5-18 show elemental analysis of the sample EC 740-4 through EDS analysis and XRF. Overall the results agree fairly well with the EDS analysis indicating higher levels of Al and Si compared to the XRF results (Al,18.3 wt% to 13.68 wt% and Si, 44.84 wt% to 39.74 wt%). These variations are likely due to the sample area variations as the XRF samples a much larger volume and therefore will give more bulk information.

An increase in Si in the quenched ash is likely as a result of the loss of soluble species into the quench water. The species where Si is present (i.e. quartz, microcline and mullite) are insoluble and are also present in the ash which has not been heat treated (**Table 4-12**) and as such are unlikely to have form in the flue gas. The large background present in the PXRD pattern for EC 740-4 is likely to have large contribution of amorphous silicates e.g. Sanidine, which was unable to crystallise during the rapid cooling in the quench water[161]. It is likely that the P identified in the analysis is also present as an amorphous part of the matrix.

The sample is reported to contain between 6.10 wt% Fe (EDS) and 11.91 wt% Fe (XRF) which is present as the oxides hematite and magnetite (Table 5-16). This suggests that these phases do not react in the flue gas.

5.2.3 Eucalyptus and coal bottom ash samples

No cyclone ash was collected from the eucalyptus and coal co-fire. There were two types of hopper ash collected; the glassy blocks similar to those observed in the hemp and coal combustion trial and loose bottom ash (Figure 5-30). There were clear phase compositional differences between the two. The loose ash contained more carbonates than the glassy blocks as well as MgO. The presence of SiO_2, $CaCO_3$, and MgO in the loose ash and the presence of diopside in the glassy block suggests that these oxides and carbonates react together to form the diopside. This may occur in several reaction steps as was outlined previously (4.1.2.1).

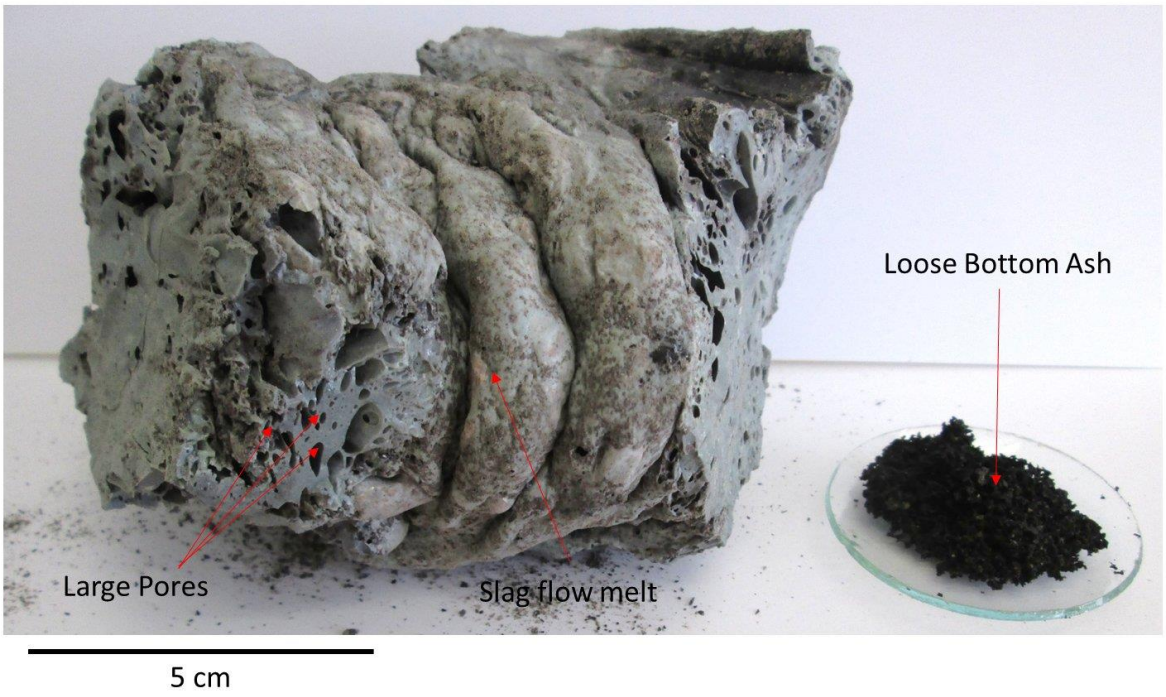

Figure 5-30: Eucalyptus and coal bottom ash showing a porous texture and regions of slag flow melts as well as the loose bottom ash

The glassy blocks have a much closer texture in comparison to the loose ash which is much more porous. The samples were ground, prior to analysis, in order for PXRD to be carried out on the samples. The loose ash was able to be ground by hand, but the large glassy blocks required ball milling.

PXRD data are presented in Figure 5-31 and Table 5-19. The presence of KCa(CO3)2 and MgO in the loose ash, alongside hydroxyapatite is likely to lead to the formation of the phase Ca9MgK(PO4)7 which is seen in the glassy blocks and was also identified in the hemp and coal bottom ash. This is in agreement with the work by Queiroz et al.[200] who showed that the Ca,Mg,K phosphate can form via hydroxyapatite.

Table 5-19: Phases identified in the eucalyptus and coal co-fired bottom ash through analysis of PXRD

Phase	Key	Composition	Glassy Blocks	Loose
Quartz	Qz	SiO_2	•	•
Hematite	He	Fe_2O_3	•	
Anorthite	An	$CaAl_2Si_2O_8$	•	
Cristobalite	Cr	SiO_2	•	•
Leucite	Le	$KAlSi_2O_6$	•	
Akermanite-Gehlenite	Ak-Geh	$Ca_2(Mg_{0.5}Al_{0.5})(Si_{1.5}Al_{0.5}O_7)$		•
Diopside	Di	$CaMgSi_2O_6$	•	
	MP	$Ca_9MgK(PO_4)_7$	•	
Calcite	Ca	$CaCO_3$		•
Fairchildite	Fa	$KCa(CO_3)_2$		•
Periclase	P	MgO		•
Hydroxyapatite	Ha	$Ca_{10}(PO_4)_6(OH)_2$		•

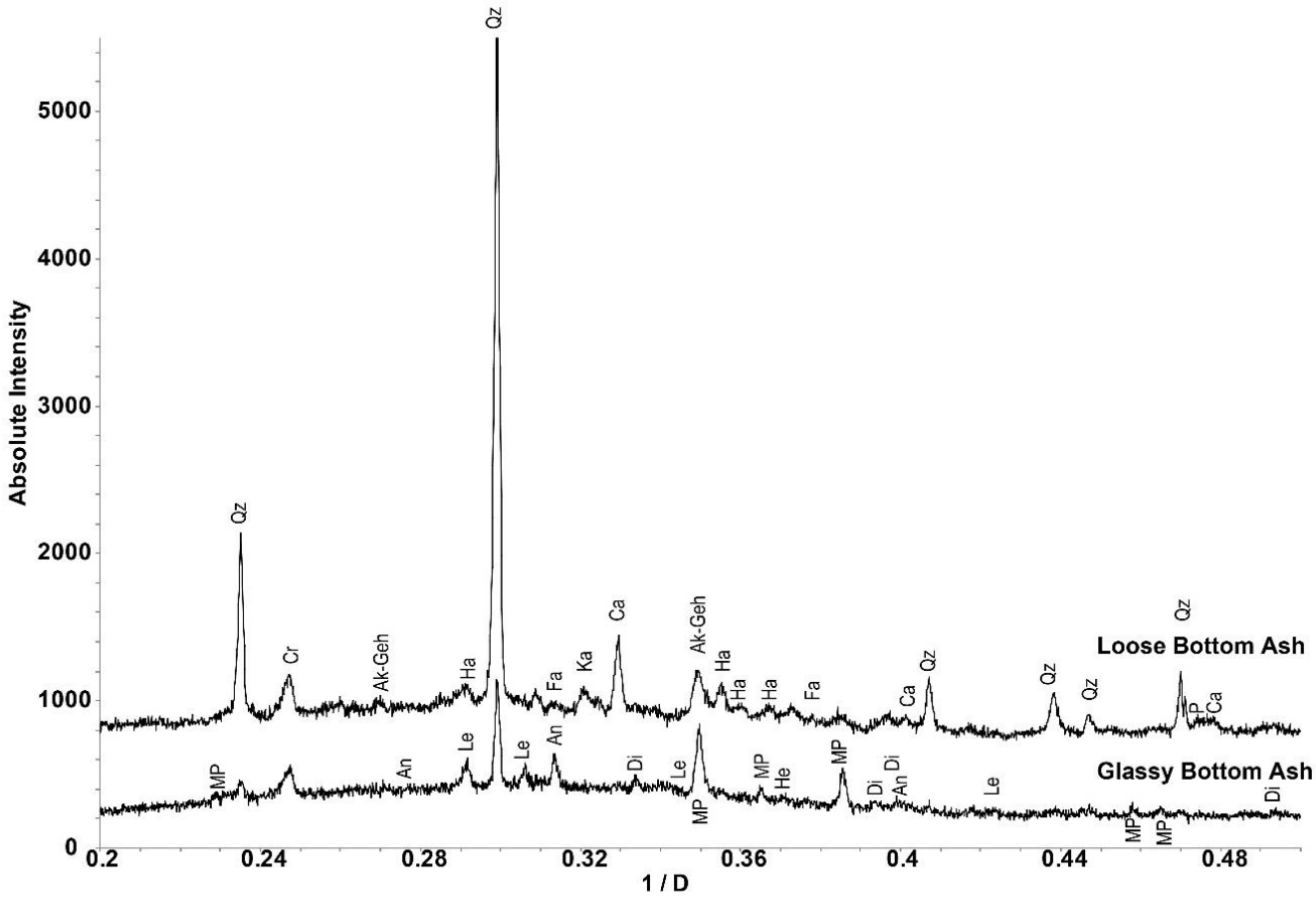

Figure 5-31: PXRD analysis of the glassy blocks and loose bottom ash present in the eucalyptus and coal bottom ash collected on the D2 diffractometer (Cu Kα radiation)

The akermanite-gehlenite solid solution is present in both the glassy blocks and the looser ash; it is also present in the deposit samples (Table 5-13). This suggests that formation occurs post deposition at the higher temperatures often present in the deposits. The presence of this phase in three sample sets suggests this solid solution is the most favourable and stable composition of the phases in relation to the basic composition of the ash.

The glassy nature of the solid blocky bottom ash is visible when imaged using SEM (Figure 5-32a). Figure 5-32b presents the loose bottom ash electron micrograph. The structure is more porous than the bottom ash glassy blocks, suggesting that it did not reach the high temperatures that are typical of the centre of the bottom ash slag. The colour of the loose particles is black (Figure 5-30) suggesting that they contain a large amount of unburnt carbon. This may also be responsible for the large pores observed in the loose bottom ash melts. There are also small particles observed in the loose bottom ash; these are likely to contain the carbonates identified using PXRD.

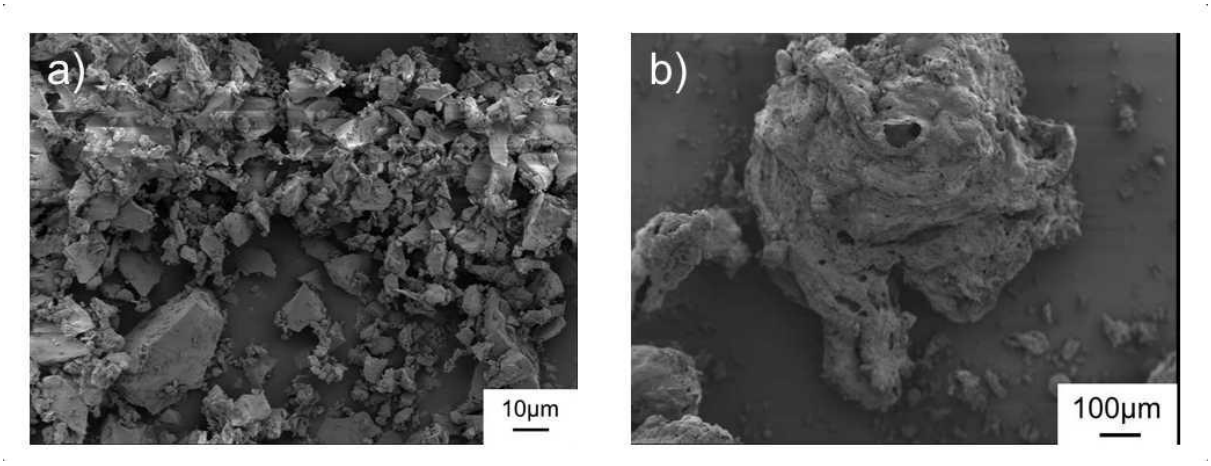

Figure 5-32a) Ball milled eucalyptus and coal bottom ash electron micrograph showing the glassy texture of the bottom ash b) An electron micrograph of the eucalyptus and coal loose bottom ash.

Analysis of the blocky bottom ash using EDS (Figure 5-33) shows the areas of Ca phosphate, which indicate hydroxyapatite, which is also in agreement with the PXRD analysis. Also identified in association are Ca ,K, Mg, P, and O which is in agreement with the PXRD data analysis indicating the phase $Ca_9MgK(PO_4)_7$. The presence of hydroxyapatite in the loose ash and the $Ca_9MgK(PO_4)_7$ in the blocky bottom ash is in agreement with the proposed formation mechanism. The association of Ca, Mg/Al, Si, and O together also indicates the akermanite-gehlenite solid solution identified in the PXRD analysis. The association of these elements also suggests the presence of diopside. The patches of association of K, Al, Si, and O are likely to be the leucite previously identified.

EDS analysis of the loose bottom ash (Figure 5-34) shows areas of Ca, Mg phosphate. Only hydroxyapatite was identified using PXRD. However it is likely that there was some substitution of Mg into the structure as has been discussed in 4.1.1.1. In several of the particles analysed indicate that C is present. This suggests that these are unburnt char particles that did not follow the flue gas through the boiler; these are also likely to be responsible for the porous structure present in the solid bottom ash blocks. K and Ca are also present in these particles, suggesting the presence of fairchildite and calcite identified through PXRD analysis. There is also Cl present in the loose deposits, which may be present as small quantities of KCl. This was also observed in the hemp and coal bottom ash, suggesting it may be present in the bottom ash of other fuel combinations.

The data for the averaged composition of the bottom ash samples from the eucalyptus and coal co-firing test is presented in Table 5-20. In the loose bottom ash the composition of the ash is largely similar to that of the fuel blend ash suggesting that relatively little change occurred in the ash. This is also supported by the presence of un-combusted fuel in the sample (Figure 5-30). The increase in the presence of K and Na compared to the deposit ash and fuel blend ash is probably due a small percentage of the feldspars microcline and albite, which although they are not identified in the PXRD analysis are likely to be present as soil impurities.

In contrast the glassy bottom ash shows a significant increase in Si from 21.72 wt% to 46.05 wt%. This is present as both quartz and cristobalite. Amorphous SiO_2 may also be present, indicated by the bump in the baseline of the PXRD pattern (Figure 5-31).

Table 5-20: Averaged data for whole area analysis data collected during SEM-EDS of multiple sample regions of the eucalyptus and coal bottom ash samples. C and O removed due to interference from the sample mounting process

	Element	Glassy Blocks		Loose Ash	
Wt %	**Al**	3.51	±0.19	11.86	±5.62
	Ca	21.66	±6.63	24.98	±7.81
	Cr	0.33	±0.01	0.92	±0.19
	Fe	3.14	±0.24	6.53	±4.29
	K	9.18	±5.62	14.05	±1.15
	Mg	3.84	±0.04	5.12	±2.04
	Mn	0.31	±0.02	2.25	±1.54
	Na	0.79	±0.07	4.72	±2.31
	P	5.17	±0.40	3.01	±1.21
	S	0.61		4.60	±2.25
	Si	46.05	±0.72	21.72	±2.98
	Ti	12.32	±17.02	0.66	±0.03

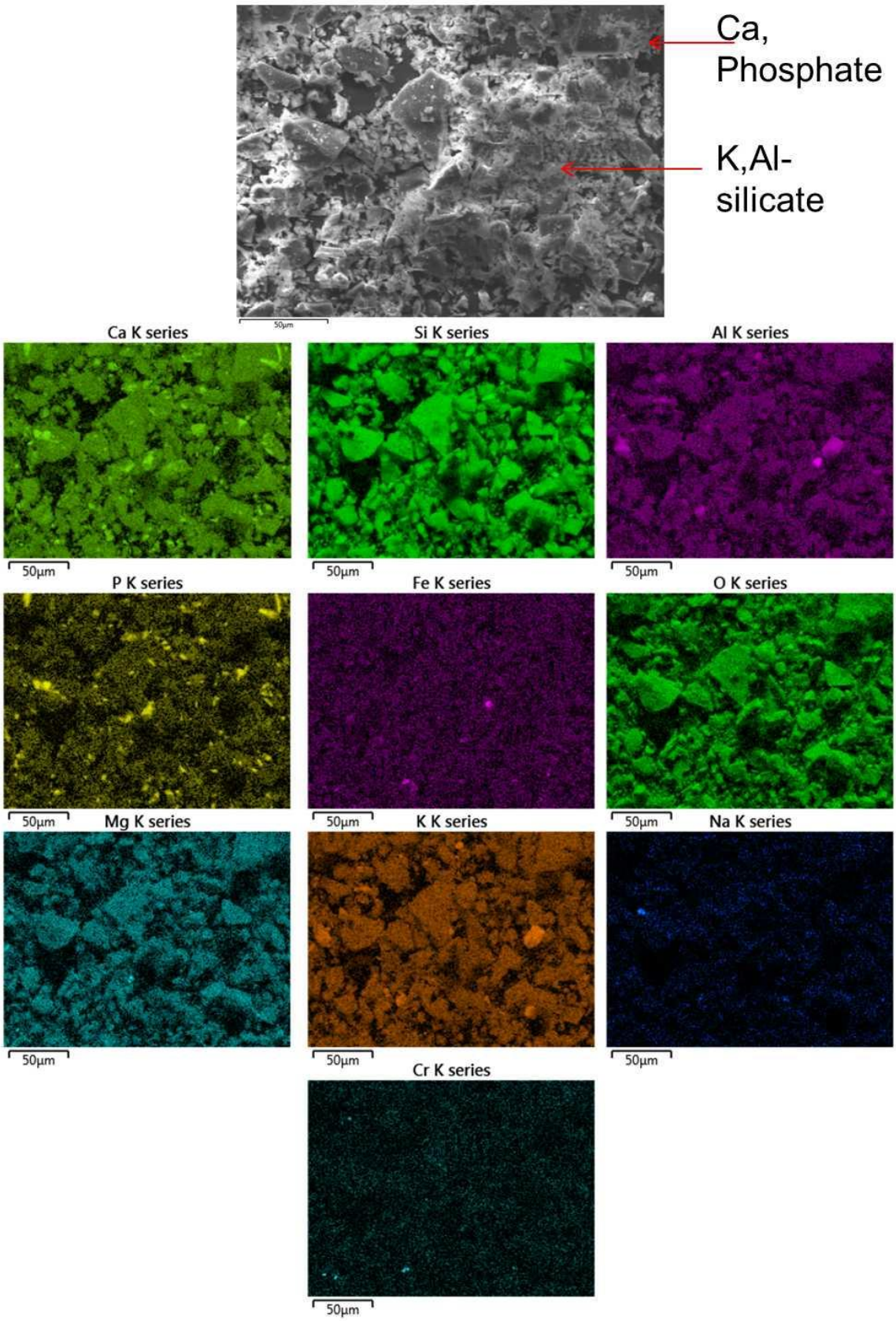

Figure 5-33: EDS analysis and an electromicrograph of eucalyptus and coal blocky bottom ash. Showing areas of leucite and Ca-phosphate. There is also association of Ca,Mg,K,P and O suggesting the presence of the phase identified using PXRD

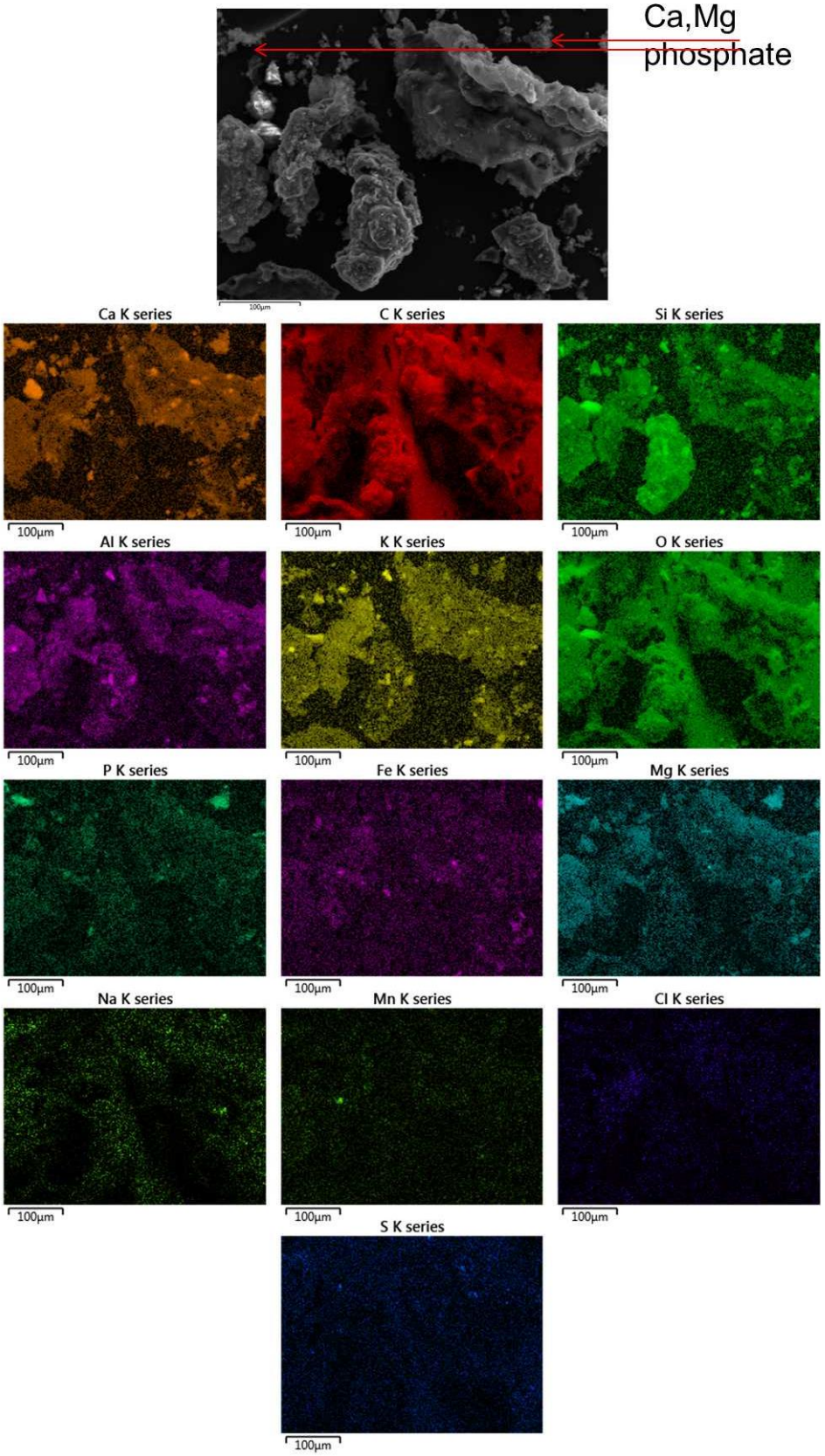

Figure 5-34: EDS maps and an electronmicrograph of the loose bottom ash from eucalyptus and coal combustion trial showing Ca,Mg phosphate. There is also C present in the particles suggesting that they are unburnt char or the carbonates also identified in the sample.

5.3 Eucalyptus Ash Combustion Rig Samples

The gas conditions at the time of sampling for the deposit and quenched samples are presented in Figure 5-35. Each sample was collected for 120 minutes, and the deposit and quench samples were collected at the same time. Combustion gas conditions remained fairly stable throughout the test, with little fluctuation in CO_2 and O_2. In comparison there is greater fluctuation in the CO concentration.

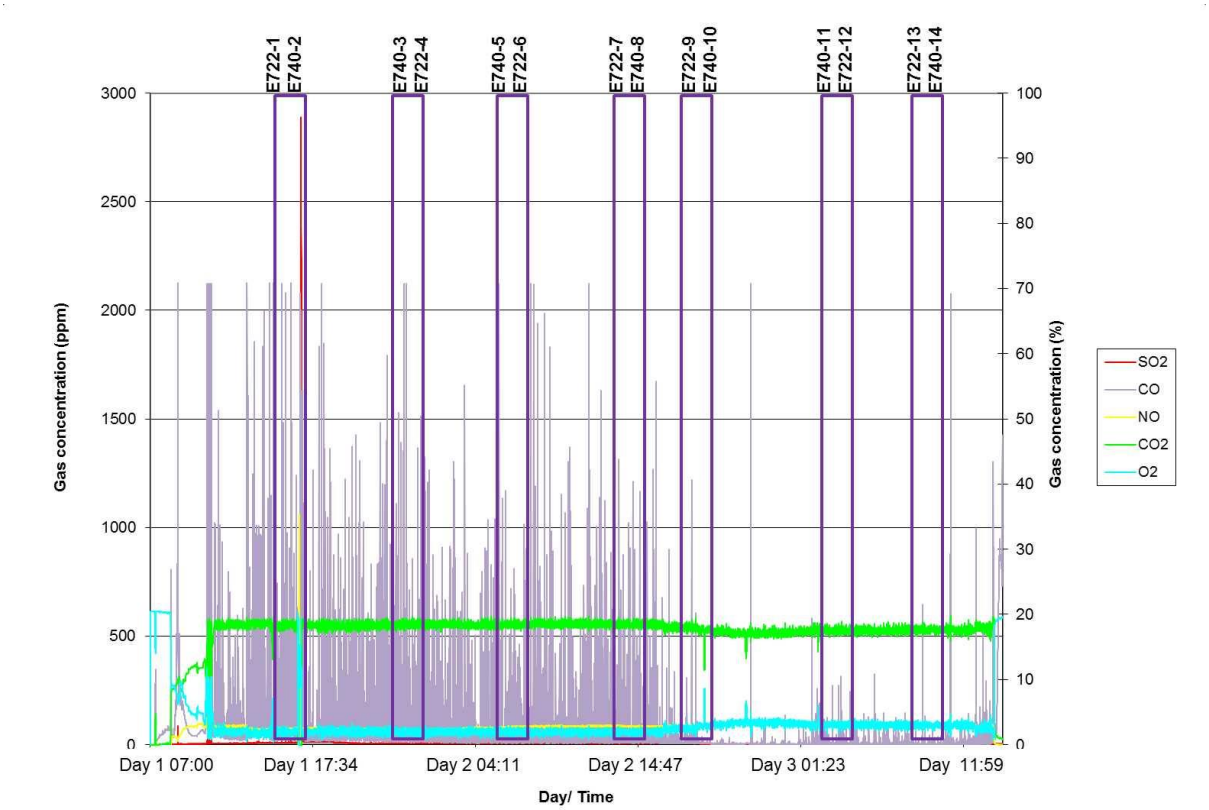

Figure 5-35: Gas conditions of eucalyptus combustion test. SO2, CO and NO left axis. CO2, O2 right axis. Purple boxes indicate deposit and quench samples were collected simultaneously

5.3.1 Eucalyptus Deposit Samples

Similar to the hemp and coal, and eucalyptus and coal combustion tests, the fuel has lost the majority of the organic matrix. The presence of CO and CO_2 in the flue gas confirms the loss through combustion (Figure 5-35). The eucalyptus fuel has an ash content of 0.7% which is considered low, and therefore deposits are likely to be smaller.

Collection times and temperatures of the deposits are presented in Table 5-21. Collection time remained constant through the trial. (Sample port 722 can be identified using Figure 3-2). The temperatures increased during the trial by around 80°C which can have some bearing on deposit composition.

Table 5-21: Deposit sampling conditions in the eucalyptus combustion trial

Sample	Duration	Temperature (°C)
E722-1	120 minutes	962
E722-4	120 minutes	968
E722-6	120 minutes	1015
E722-7	120 minutes	Not given
E722-9	120 minutes	1045
E722-12	120 minutes	1040
E722-13	120 minutes	1045 (30 mins after sampling)

Analysis of the phases present in deposits, identified through PXRD analysis, are presented in Table 5-22 and Figure 5-36. 13 core phases were identified in the deposit samples. These were mainly the Ca-silicates, Mg-silicates, Ca, Mg, silicates and Ca and Mg oxides. Fewer Al and K phases were identified. A more detailed discussion about the phases present in this sample set will now be presented.

The phase anhydrite ($CaSO_4$) is present in the samples. In the co-fired blends it was previously thought this was formed through the dehydration of gypsum ($CaSO_4.2H_2O$) in the coal fuel. However as there is no coal present in this combustion test, this suggests a reaction of CaO, present in the deposit with SO_2(g).

The eucalyptus ash has a high Fe content at 9.16 wt%. Boström *et al.*[210] noted that when considering Fe during biomass combustion, it often exists just as the oxides e.g. hematite and magnetite. The iron oxide hematite (Fe_2O_3) is present in the ash. However, they also noted that reactions of Fe with solid and liquid solutions may take place e.g. diopside is also present in the ash, this phase can incorporate Fe into it to form the phase augite.

The eucalyptus fuel contains 4.25 wt% P, present as $Ca_3(PO_4)_2$ which has previously been identified in biomass combustion ashes[31,210]. This phase is formed through the reaction of lime and P_2O_5 (Equation 5-26)[27].

$$3CaO + P_2O_5 \rightarrow Ca_3P_2O_8$$

Equation 5-26

Table 5-22: Phases identifed in deposits from the eucalyptus combustion trial analysed using PXRD

Phase	Key	Composition	E722-1	E722-4	E722-6	E722-7	E722-9	E722-12	E722-13
Quartz	Qz	SiO_2	•	•	•	•	•	•	•
Akermanite	Ak	$Ca_2Mg(Si_2O_7)$	•	•	•	•	•	•	•
Merwinite	Me	$Ca_3Mg(SiO_4)_2$	•	•	•	•	•	•	•
Periclase	P	MgO	•	•	•	•	•	•	•
Wollastonite	Wo	$CaSiO_3$	•	•	•	•	•	•	•
Forsterite	Fo	Mg_2SiO_4	•	•	•	•	•	•	•
Hematite	He	Fe_2O_3	•	•	•	•	•	•	•
Lime	Li	CaO	•	•	•	•	•	•	•
Diopside	Di	$CaMgSi_2O_6$	•	•		•	•	•	•
Anhydrite	An	$CaSO_4$	•	•	•	•	•	•	•
Mullite	Mu	$Al_6Si_2O_{13}$	•				•		
Cordierite	Not shown	$Mg_2Al_4Si_5O_8$	•	•	•	•	•	•	•
Kalsilite	Ka	$KAlSiO_4$	•	•					
Microcline	Mi	$KAlSi_3O_8$	•	•	•	•	•	•	•
Calcium Phosphate	Not labelled	$Ca_3(PO_4)_2$	•	•	•	•	•	•	•
Sodium-Melilite	N-Me	$NaCaAlSiO_7$	•	•					
Grossular	Not Labelled	$Ca_3Al_2(SiO_4)_3$	•	•	•	•	•	•	•
Cristobalite	Cr	SiO_2			•	•		•	•
Leucite	Le	$KAlSi_2O_6$				•		•	•
Corundum	Co	Al_2O_3					•	•	•

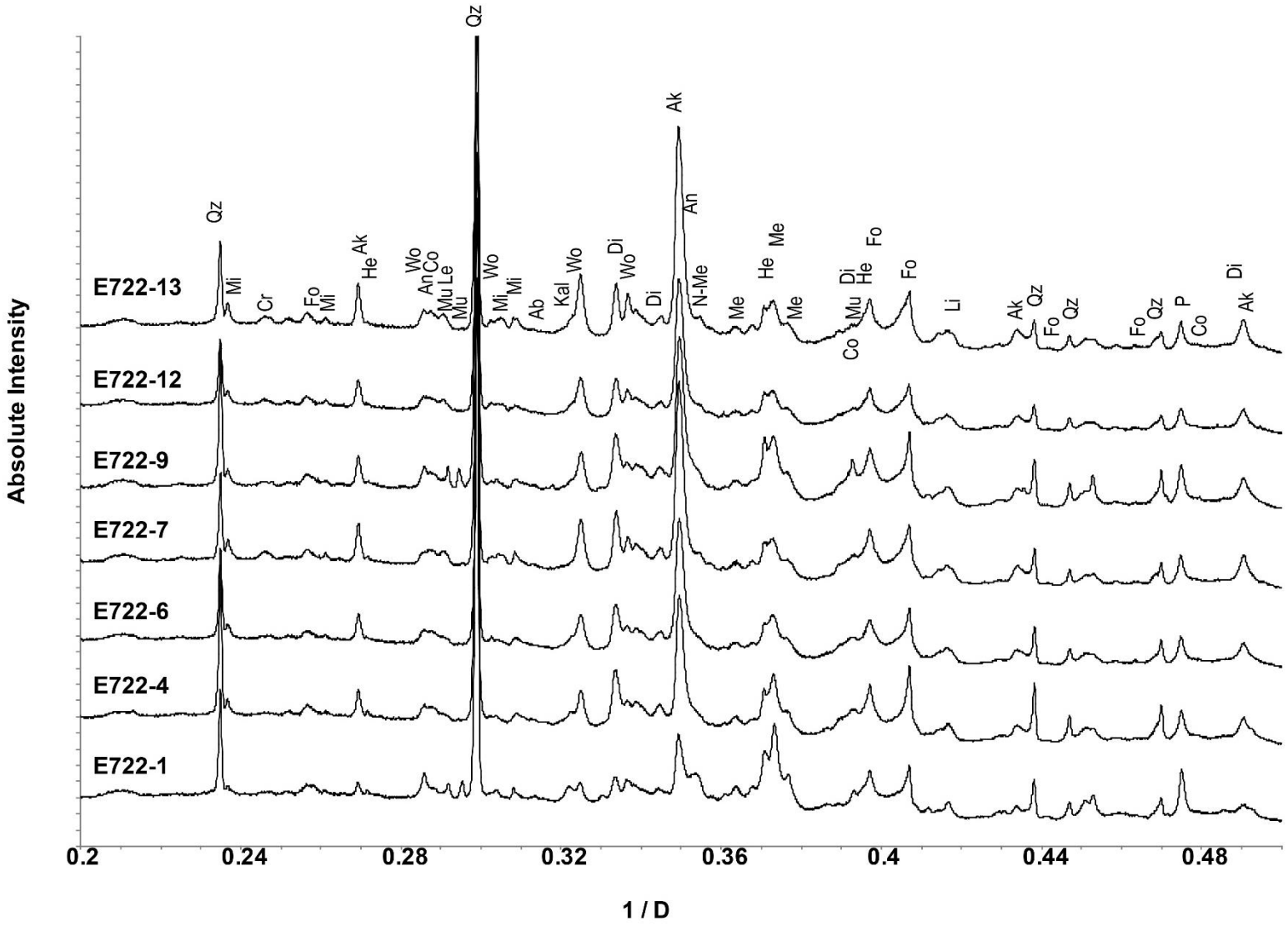

Figure 5-36: PXRD data of the eucalyptus deposit samples collected during a combustion trial. Data collected on the I-11 beamline (λ 0.826215)

Quartz (SiO_2) and cristobalite are present in most of the samples. The SiO_2 content was determined as 16.92 wt% and these phases have been previously discussed in section 5.2

Microcline ($KAlSi_3O_8$), is present in the samples and is thought to originate from the harvesting and processing of the raw eucalyptus fuel. Two other K, Al-silicates are present, leucite ($KAlSi_2O_6$) and kalsilite ($KAlSiO_4$) and they are thought to have formed in the combustion rig either in the flue gas or the deposit. Vassilev *et al*.[31] report multiple methods of kalsilite formation; those involving kaolinite are discounted as it is not present in the eucalyptus fuel. Reaction of $Al_2O_3.2SiO_2$ with either KCl or KOH (in the flue gas) is the proposed mechanism of formation. Leucite, when present, probably forms through the reaction of $KAlSiO_4$ with SiO_2 as proposed by Zhang *et al.*.[211]

The fuel ash contains 36.70 wt% CaO, 6.03 wt% MgO, and 16.92 wt% SiO_2 (Table 3-18) meaning that 60% of the ash composition falls into the CaO-MgO-SiO_2 system. Multiple silicates in this system are present i.e. wollastonite, forsterite, akermanite, diopside and merwinite. As over half of the ash comprises of the individual components of the CaO-MgO-SiO_2 system a wide variety of Ca, Mg-silicates can be expected. If the samples were homogenous, akermanite would be the dominant Ca, Mg-silicate due to the ratio of the CaO, MgO and SiO_2. However, as deposit samples are not homogenous and are dependent on what particle deposits next to another, so the local ratios could favour the formation of other Ca, Mg silicates. The formation of forsterite (Mg_2SiO_4) in the deposits would seem unlikely, as MgO would have to be in relative excess compared to CaO as the ratio in the fuel is 1 MgO: 4 CaO. However if MgO and SiO_2 are in close proximity and correct proportions, they are likely to react to form forsterite.

Al_2O_3 is present in the ash at 4.86 wt%. In a homogenously distributed deposit gehlenite would be the dominant Ca,Al silicate. Gehlenite forms solid solutions with akermanite as they are both end members of the melilite system. A further member of the melilite family, soda-mellilite, has also been identified using PXRD in the deposit samples which suggests that these phases are relatively stable in the deposit. Mullite and corundum are also present in the deposits from the CaO-Al_2O_3-SiO_2 system. These two phases are Al rich, and may form in the deposit in areas depleted of CaO. SiO_2 reacting with the refractory oxide lining of the combustion rig that has been dislodged during the combustion trial may also have formed mullite.

Analysis of SEM micrographs (Figure 5-37) shows a large amount of spheres present in the deposits. These are formed due to the high rate of heating present in the combustion rig. Clear agglomeration of the spheres is visible; Figure 5-37f illustrates two of the spheres joining

together, potentially forming the start of a melt. This is visible on a larger scale in Figure 5-37e and g, where a large number of spheres have joined together. The joining of these spherical particles is also indicative of the inertial impaction mechanism (Figure 2-5) as the spheres may impact into regions that are already partially or fully melted.

Also present in the samples are more porous regions; these often surround and link some of the spheres together (Figure 5-38). This porosity is likely due to sintering of smaller particles. Sintering is commonly identified as a problem when firing biomass, due to the high K-silicate composition. Steenari *et al*.[212] reported that the presence of potassium silicates, in combination with high ratio Ca/K phosphates, are associated with low melting point and low sintering point ashes. In the eucalyptus ash, several potassium silicates (kalsilite and leucite) alongside calcium phosphate have been identified through PXRD explaining the presence of sintering.

Also visible in the deposits are large holes. Figure 5-39 shows the inside of two of the large holes. Figure 5-39a shows a plate like structure inside the deposit suggesting the condensation or formation of one phase. In contrast Figure 5-39b has much less structured texture suggesting it may be multiphase melt, and made of phases with lower melting points than those in Figure 5-39a.

Analysis of the EDS maps of the deposits is in good agreement with the PXRD data. There are clear regions of association between Ca, Mg, Si, and O (Figure 5-40) indicative of the phases previously identified as belonging to the $CaO\text{-}MgO\text{-}SiO_2$ system. In some regions of the deposits Al is also present (Figure 5-40) suggesting the presence of the mellilite system containing akermanite and gehlenite. Na is also present in some of these regions, suggesting the presence of soda-melilite, identified in several of the samples through PXRD.

The $CaSO_4$ identified through PXRD is also shown to be present through analysis of the EDS data (Figure 5-40). The S present in the deposits is mostly associated with Ca, with small amounts being associated with K, suggesting K_2SO_4. This may be present in small quantities undetectable using PXRD. The Ca-phosphate identified as present in the PXRD data is also identified in the EDS analysis. Clear association between K, Al, Si, and O can be seen (Figure 5-40). These areas are likely to be kalsilite ($KAlSiO_4$), microcline ($KAlSi_3O_8$), or leucite ($KAlSi_2O_7$), as identified through PXRD analysis.

Present in several regions of the deposits is Cr (Figure 5-41, Figure 5-40). Cr is present in the fuel as 1.77mg/kg dry fuel, determined using ICP-OES (data provided by E.On). Previous investigation of Cr speciation during the combustion of bituminous and sub-bituminous coal has shown that Cr often associates with anhydrite[213]. This study did not find that to be the

case, instead the Cr was associated with Ca, Mg, Si, Fe, Al and O suggesting incorporation into silicate structures Figure 5-42). In small quantities this incorporation would not be detected using PXRD.

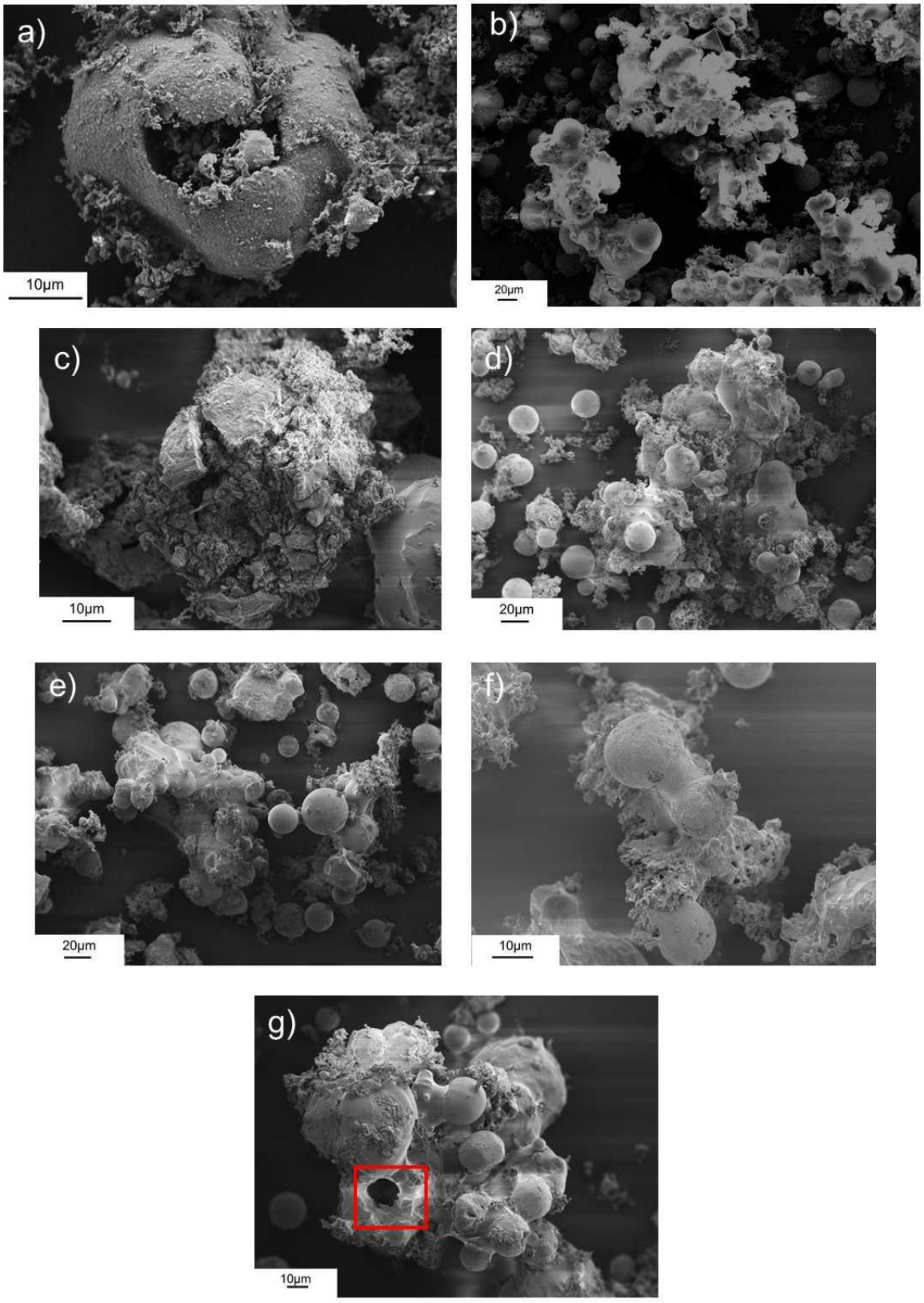

Figure 5-37: Electronmicrographs of the deposit samples from a eucalyptus combustion trial a) E 722-1 b) E 722- 4 c) E 722- 6 d) E 722- 7 e) E 722-9 f) E 722-12 g) E 722-13

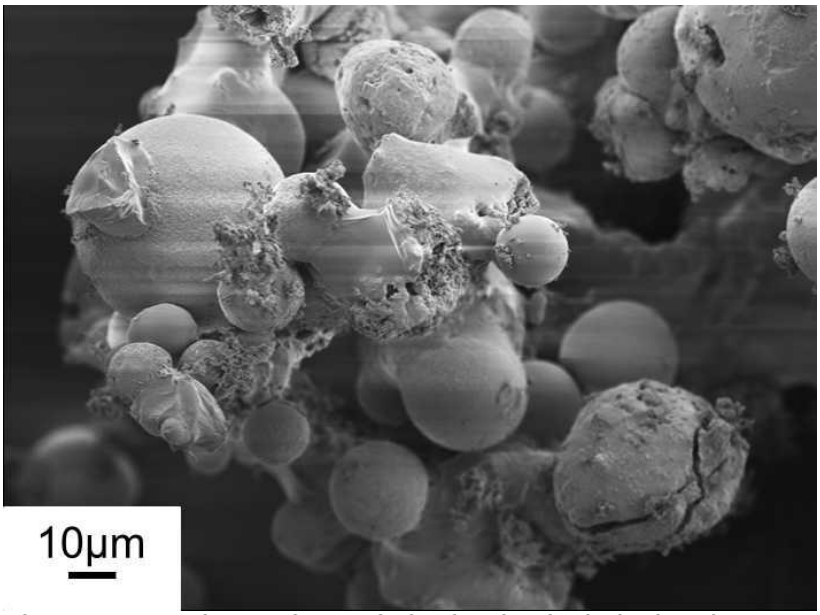

Figure 5-38: SEM Electronmicrograph showing sintering in the deposit E722-12

.

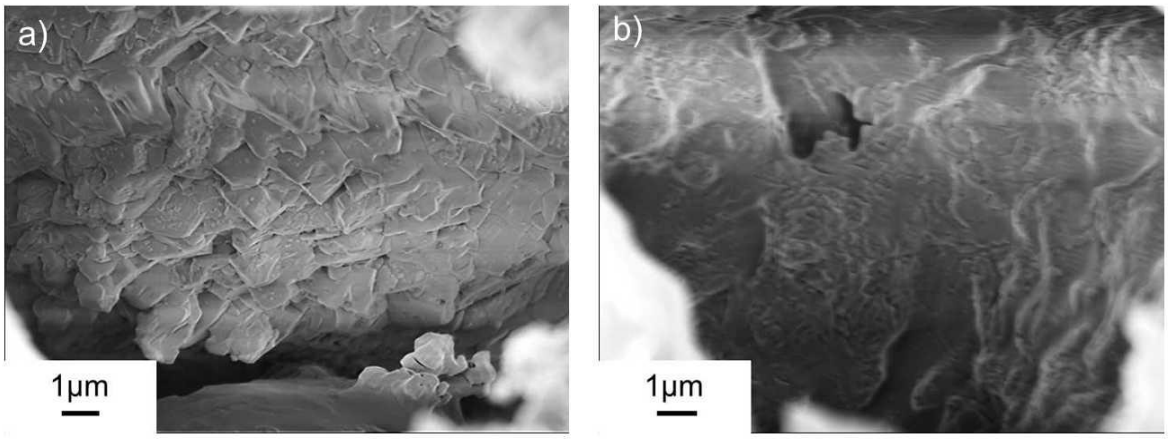

Figure 5-39: a) the inside of a deposit from E722-12 b) the inside of a deposit from 722-13 highlighted in Figure 3g

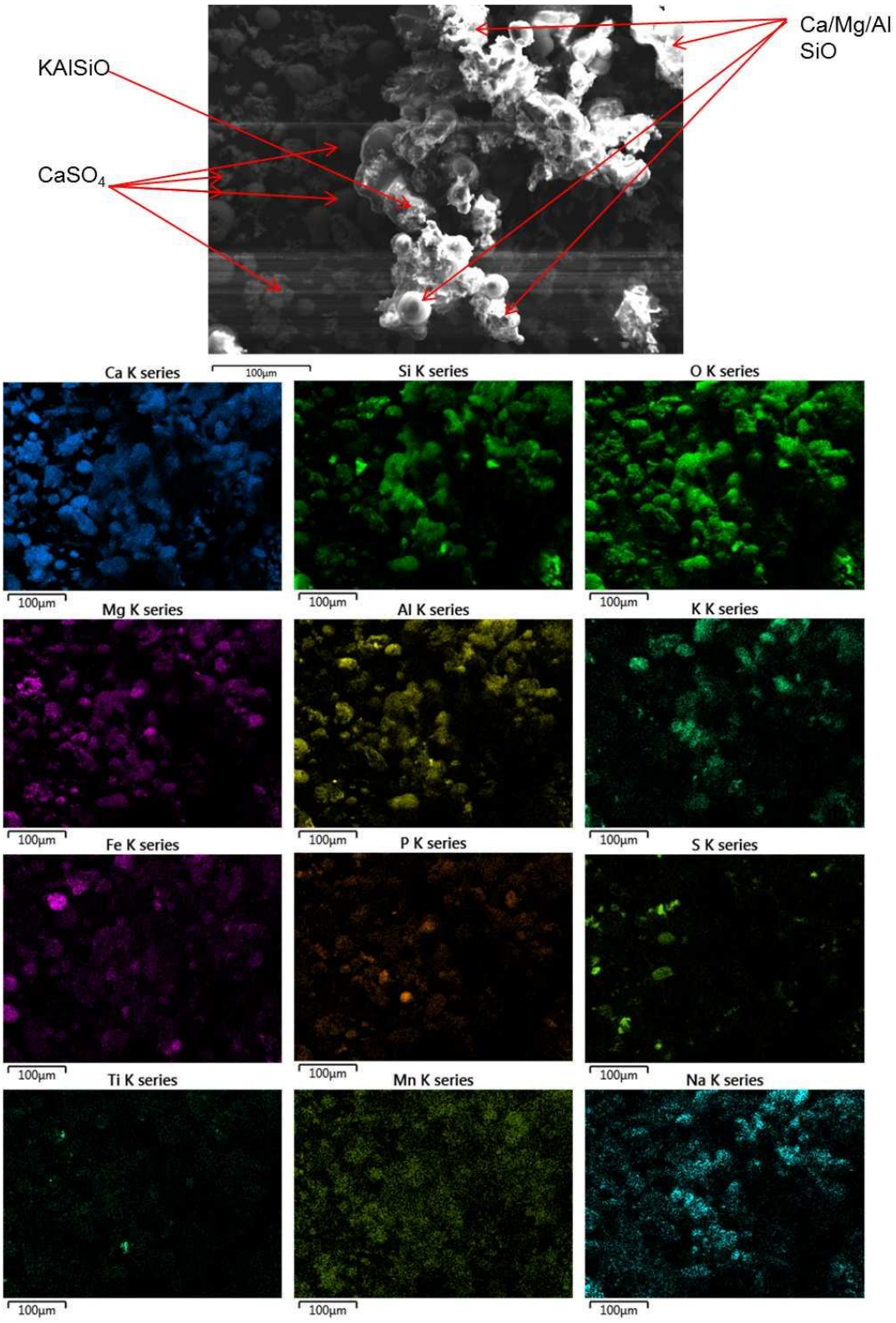

Figure 5-40: EDS maps of sample E722-6

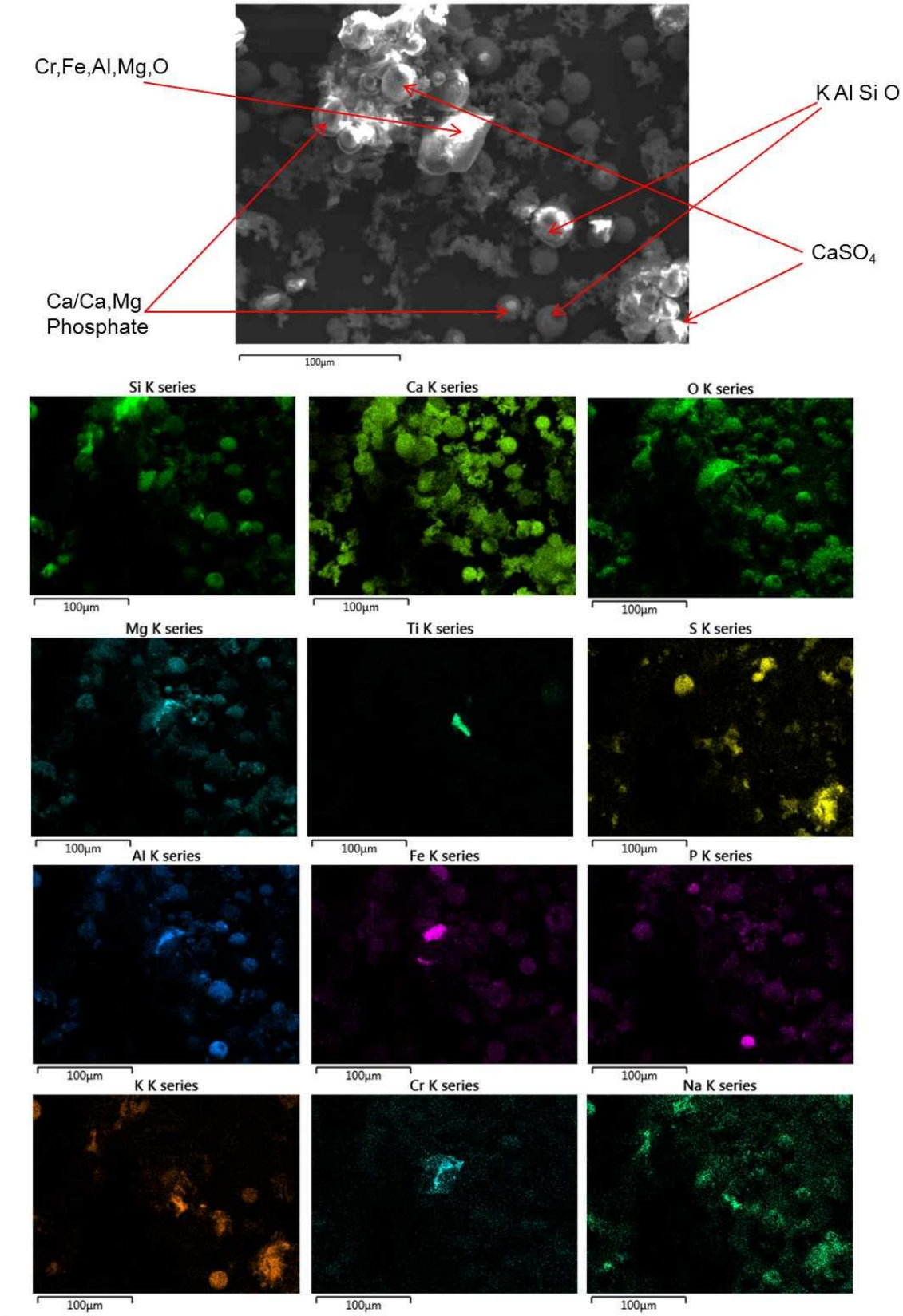

Figure 5-41: EDS maps of sample E722-7

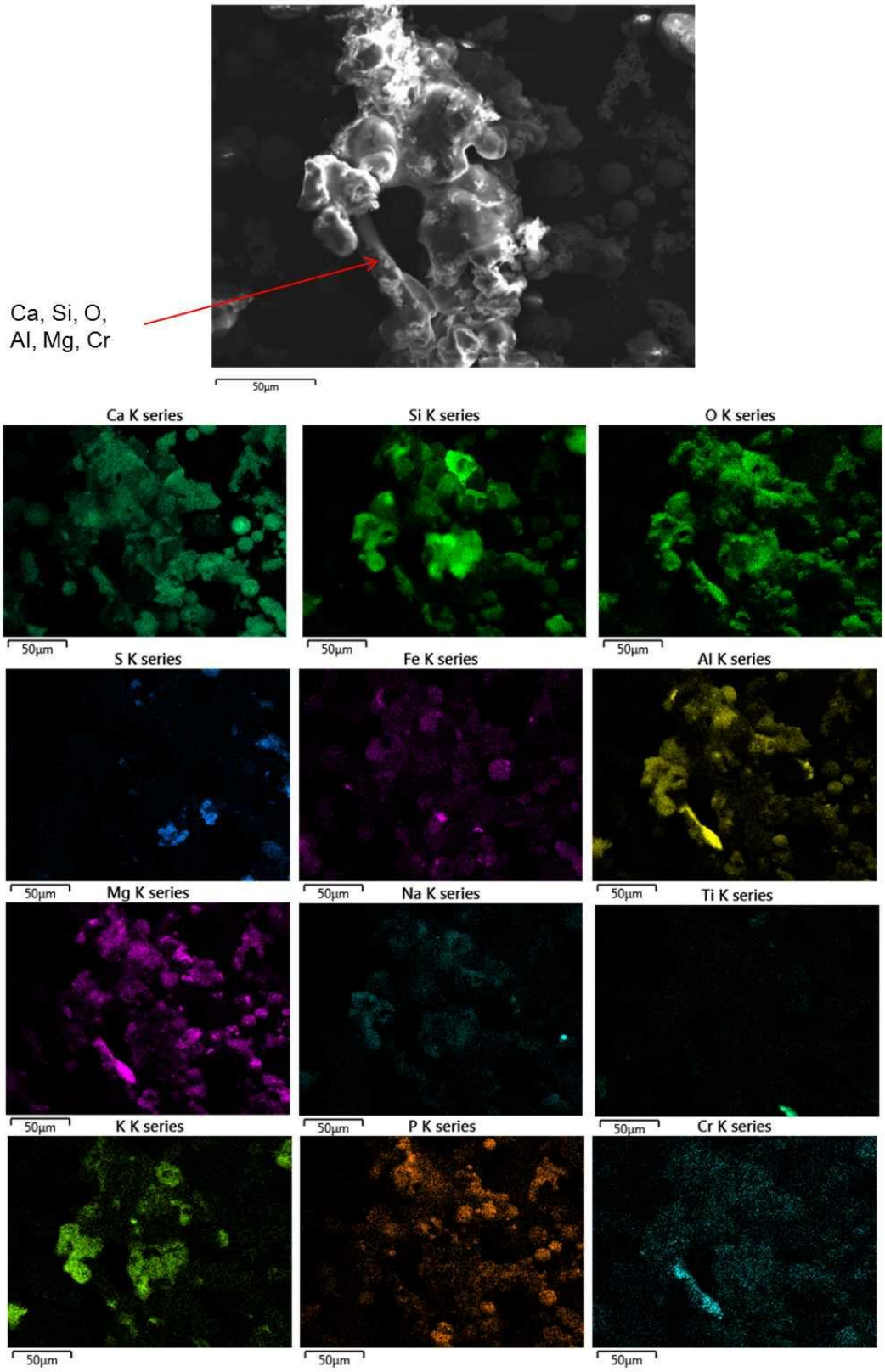

Figure 5-42: EDS Maps of sample E722-12

Table 5-23: Averaged data for whole area analysis data collected during SEM-EDS of multiple sample regions of the eucalyptus deposit samples. C and O removed due to interference from the sample mounting process

	Wt%											
Element	**E722-6**		**E722-7**		**E722-9**		**E722-12**		**E722-13**		**Average**	
Al	7.09	±2.18	8.44	±0.45	8.58	±0.84	7.61	±0.79	7.77	±0.84	7.90	±0.61
Ca	39.06	±11.22	34.22	±1.69	35.24	±3.21	38.96	±6.05	33.84	±3.63	36.26	±2.56
Cl	0.08	±0.08			0.03	±0.03					0.06	±0.06
Cr									0.59	±0.54	0.59	±0.59
Cu	0.45	±0.45	0.64	±0.04	0.77	±0.24	0.99	±0.99	0.51	±0.51	0.67	±0.22
Fe	8.38	±1.92	10.92	±1.31	8.43	±0.29	7.12	±1.91	12.98	±8.18	9.57	±2.35
K	2.45	±0.60	3.02	±0.31	2.57	±0.82	3.03	±1.97	4.24	±0.62	3.06	±0.71
Mg	8.58	±1.06	8.65	±1.21	8.34	±0.63	8.37	±2.29	7.78	±0.56	8.35	±0.34
Mn	3.35	±0.88	3.71	±0.13	3.44	±0.36	3.34	±0.95	3.08	±0.22	3.38	±0.23
Na	1.98	±0.66	2.12	±0.28	3.23	±1.19	3.30	±1.26	2.45	±0.18	2.62	±0.62
P	3.04	±0.30	2.97	±0.54	2.92	±0.29	3.06	±1.38	2.98	±0.44	2.99	±0.06
S	3.92	±0.80	5.15	±2.03	5.25	±1.67	3.08	±2.04	4.18	±1.46	4.32	±0.91
Si	21.37	±6.12	19.25	±4.18	20.61	±3.38	21.41	±12.46	19.60	±5.64	20.44	±0.99
Ti	0.59	±0.22	0.93	±0.52	0.54	±0.14	0.48	±0.05	0.76	±0.31	0.66	±0.18
Zn	0.39	±0.11	0.56	±0.00	0.41	±0.41					0.45	±0.09

Table 5-24: XRF data for the samples E722-4 and E722-6 alongside a comparison of eucalyptus ash and high temperature eucalyptus ash at 900°C

	Wt%			
	E722-4	**E722-6**	**Eucalytpus Ash**	**Eucalyptus Ash at 900°C**
Al	7.13 ±0.21	6.02 ±1.42	4.86 ±0.11	5.68 ±0.04
Ca	28.28 ±0.20	31.17 ±3.63	36.70 ±0.64	35.36 ±0.39
Cl	0.17 ±0.09	0.18 ±0.03	0.11 ±0.00	0.12 ±0.04
Fe	12.24 ±0.39	9.33 ±3.97	9.61 ±0.33	8.58 ±0.16
K	4.35 ±0.07	5.23 ±0.28	11.24 ±0.18	9.58 ±0.17
Mg	5.56 ±0.04	6.12 ±0.54	6.03 ±0.33	7.91 ±0.48
Mn	3.62 ±0.02	3.03 ±0.81	4.02 ±0.14	3.65 ±0.09
Na	1.33 ±0.15	1.59 ±0.11	0.70 ±0.98	0.47 ±0.66
Ni	0.03 ±0.92	0.02 ±0.00	0.09 ±0.01	0.04 ±0.00
P	5.26 ±0.07	4.45 ±1.05	4.25 ±0.13	4.84 ±0.04
S	2.08 ±0.06	1.74 ±0.46	2.55 ±0.05	3.03 ±0.05
Si	26.35 ±0.33	28.05 ±3.45	16.92 ±0.21	18.28 ±0.16
Sr	0.47 ±0.00	0.5 ±0.01	0.39 ±0.00	0.39 ±0.04
Ti	0.85 ±0.01	0.75 ±0.16	0.92 ±0.03	0.69 ±0.04
Zn	0.56 ±0.01	0.13 ±0.49	0.28 ±0.01	0.26 ±0.01
Zr	0.06 ±0.01	0.06 ±0.01	0.02 ±0.01	0.03 ±0.00
	98.3	**98.37**	**98.66**	**98.87**

Elemental composition analysis of the deposit samples from EDS (Table 5-23) and XRF (Table 5-24) show differences between technique. This is likely to be a result of the XRF sampling more of a bulk sample compared to the small area sampled in EDS. The deposits are enriched in Al and Si in comparison to the fuel ash. This change in composition is due to the deposition method of inertial impaction meaning that the heavier particles will impact onto the surface of obstacles in the path of the gas flow. Thirteen of the twenty phases identified in the XRD pattern (Table 5-21, Figure 5-36) contain Si indicating the deposition mechanism is highly likely.

A large amount of the phases identified in PXRD contain Ca with the akermanite, diopside and wollastonite all exhibiting strong and sharp peaks confirming that the EDS and XRF data and PXRD analysis are in good agreement. The decrease in the amount of K present in the deposit samples could be due to the volatitility of the K-bearing phases in the eucalyptus fuel differing from those of the phases present in the fuel blends. i.e. the K is released and forms other phases which deposit elsewhere in the powerplant. A portion of this may be the phase KCl which would not deposit on the ceramic probes as a cooler surface is required for the dominant deposition mechanism.

EDS maps and whole sample analysis identify Cr as present in the samples. Eucalyptus is a fast growing plant species[79] and has been used as a phytoremediant species[214] (a species which will accumulate certain metals quickly from contaminated soils) suggesting that the Cr is present from the fuel itself. Figure 5-42 shows the Cr is present alongside Ca, Si, O, Al and Mg indicating it is likely to be present in an oxide cluster or substituted into a silicate.

5.3.2 Eucalyptus Quenched Samples

The quenched samples were removed from the combustion rig in accordance with the method described in Chapter 3. The sample duration and temperatures are presented in Table 5-25. During this combustion trial deposit and quenched samples were taken simultaneously allowing a comparison between the two. PXRD analysis of the samples is presented in Table 5-26 and Figure 5-43.

Table 5-25: Duration and temperatures of eucalyptus quenched ash samples

Sample	Duration	Temperature (°C)
E740-2	120 minutes	752
E740-5	120 minutes	766
E740-8	120 minutes	785
E740-10	120 minutes	Not stated
E740-11	120 minutes	815
E740-14	120 minutes	823 (30 min after sample)

The carbonates calcite, dolomite, and fairchildite that have previously been observed in quench ash are present in these samples. A mechanism for the formation of calcite is presented in Section 4.1.2. Similarly to the hemp and coal quenched samples, there is larnite present in the quenched ash but not the deposit ash. Wollastonite forms in the deposit after the deposition or formation of larnite, which is the first product in a two step reaction resulting in wollastonite.[193] The larnite may form in the flue gas through reaction of CaO and SiO_2 followed by further reaction with SiO_2, to wollastonite in the deposit. Research by Jung *et al*.[164] shows that larnite can react with forsterite to form the Ca,Mg silicate phases of merwinite and monticellite and these phases are present in the quenched ash.

In comparison to the hemp and coal quenched samples, where a significant portion of the ash is comprised of K,Al-silicates, the eucalyptus ash does not contain kalsilite in such great quantities. There is 36.70 wt% Ca in the fuel in comparison to 1.24% K, meaning that more Ca is available for reaction. The SiO_2 content of the eucalyptus fuel is lower than the hemp and coal and eucalyptus and coal (16.92, 23.41 and 31.25 wt% respectively), and so the formation of the Ca containing silicates could be preferential

Table 5-26: Phases identified through PXRD analysis of quenched samples in a eucalyptus combustion trial

Phase	Key	Composition	E740-2	E740-3	E740-5	E740-8	E740-10	E740-11	E740-14
Quartz	Qz	SiO_2	•	•	•	•	•	•	•
Calcite	Ca	$CaCO_3$	•	•	•	•	•	•	•
Hematite	He	Fe_2O_3	•	•	•	•	•	•	•
Magnetite	Ma	Fe_3O_4	•	•	•	•	•	•	•
Akermanite	Ak	$Ca_2Mg(Si_2O_7)$	•	•	•	•	•	•	•
Merwinite	Me	$Ca_3Mg(SiO_4)_2$	•	•	•	•	•	•	•
Grossular	Gr	$Ca_3Al_2(SiO_4)_3$	•	•	•	•	•	•	•
Forsterite	Fo	Mg_2SiO_4	•	•	•	•	•	•	•
Dolomite	Do	$CaMg(CO_3)_2$	•	•	•	•	•	•	•
Wollastonite	Wo	$CaSiO_4$	•	•	•	•	•	•	•
Larnite	La	Ca_2SiO_4	•	•	•	•	•	•	•
Microcline	Mi	$KAlSi_3O_8$	•	•	•	•	•	•	•
Albite	Ab	$NaAlSi_3O_8$	•	•					
Fairchildite	Fa	$K_2Ca(CO_3)_2$	•		•	•	•	•	•
Xonotlite	Not shown	$Ca_6Si_6O_{16}(OH)_2$		•	•	•	•	•	•
Kalsilite	Ka	$KAlSiO_4$		•	•			•	•
Iron Silicate	Not Shown	Fe_2SiO_4	•	•	•	•	•	•	•

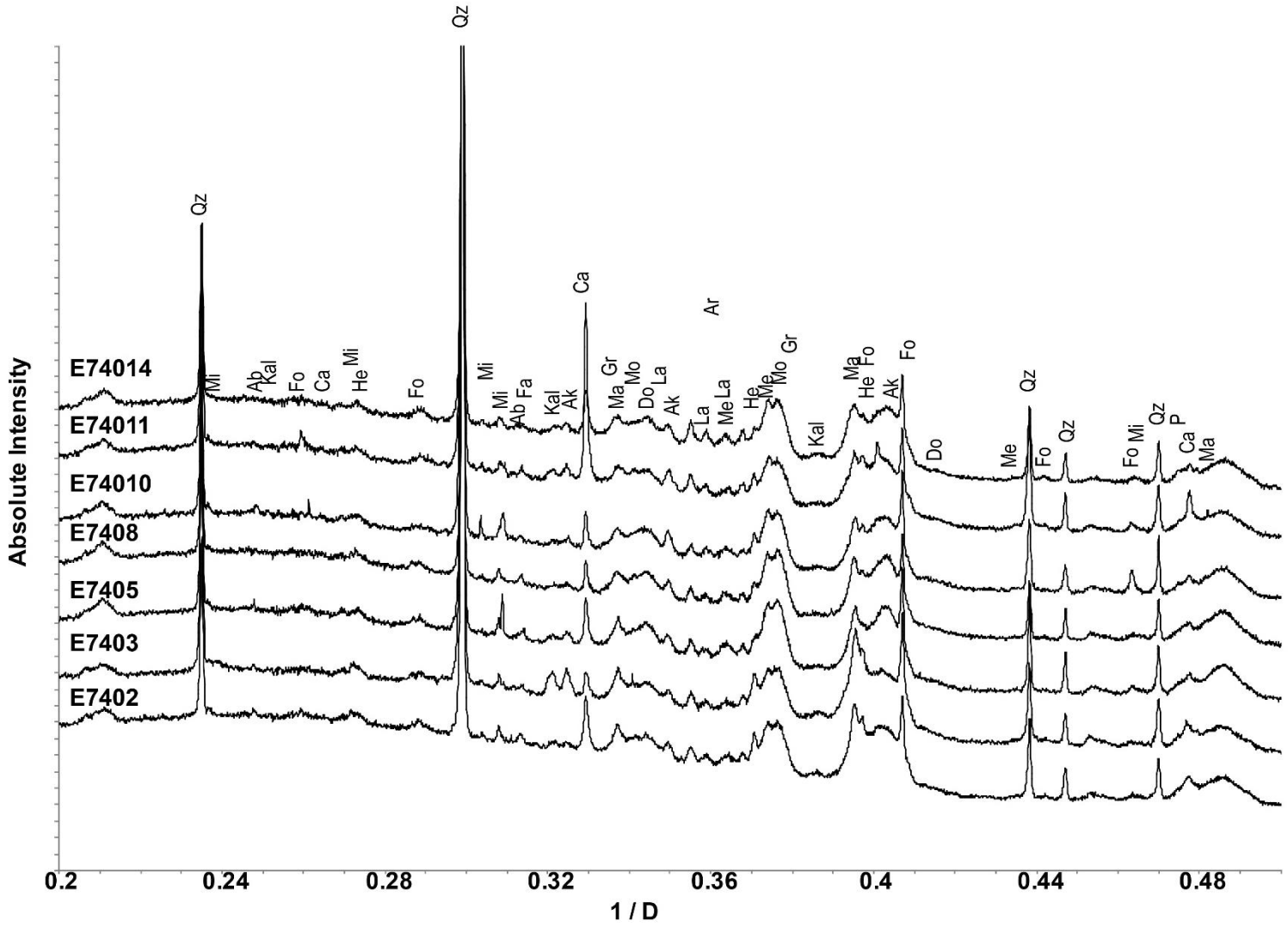

Figure 5-43: PXRD data of the eucalyptus quenched samples collected during a combustion trial patterns were collected on the I-11 beamline (λ 0.826215)

Analysis of the SEM electronmicrographs (Figure 5-44) shows different morphologies in the quenched samples compared to the deposit samples. This appears not to be the case in the quenched samples, where the surfaces of the large areas are much less smooth, and contain more well defined individual particles. This also indicates that a large amount of the melting occurs in the deposits.

The porous structures visible in Figure 5-44b&c are thought to be char particles, carbon rich areas of the ash that have not undergone full combustion during the trial. Analysis of the EDS data shows that these particles are large C structures (Figure 5-45). Any particles of char that were present in the deposit are likely to have decomposed, due to the 120 minute time period that they were exposed to the high temperature (962-1045°C) of the flue gas.

The spheres that are present in the deposit samples of both the hemp and coal, and eucalyptus and coal samples, are also present in the quenched samples. This indicates that they are formed in the flue gas due to the high rate of heating in the combustion rig, following the formation mechanism of plenospheres/cenospheres. Alongside the spheres there are several other distinct particle morphologies present. Figure 5-44 d, f and g show orthoganal particles present in the samples; analysis of the EDS maps (Figure 5-46) shows that they are largely comprised of K, Al, Si, and O or just Si and O indicating that they may be the feldspar microcline, present from harvesting of the biomass. Particles containing K,Al,Si and O are also present in the spherical morphology suggesting that they are leucite/kalsilite phases that have formed in the combustion rig.

The Ca silicates, Ca,Mg silicates and Ca, Al silicate phases presented in the PXRD can also be identified by analysing the EDS maps. The phases can't be distinguished from one another and multiple phases may be present in each area as reaction may have been taking place in this region.

Through the samples there is also an even distribution of Mn and Fe. No Mn phases were identified from the PXRD, however previous research by Wu *et al.*[215] and Lumpkin *et al.*[216] has indicated that MnO and CaO/MgO can have some substitution of Mn into the silicates.

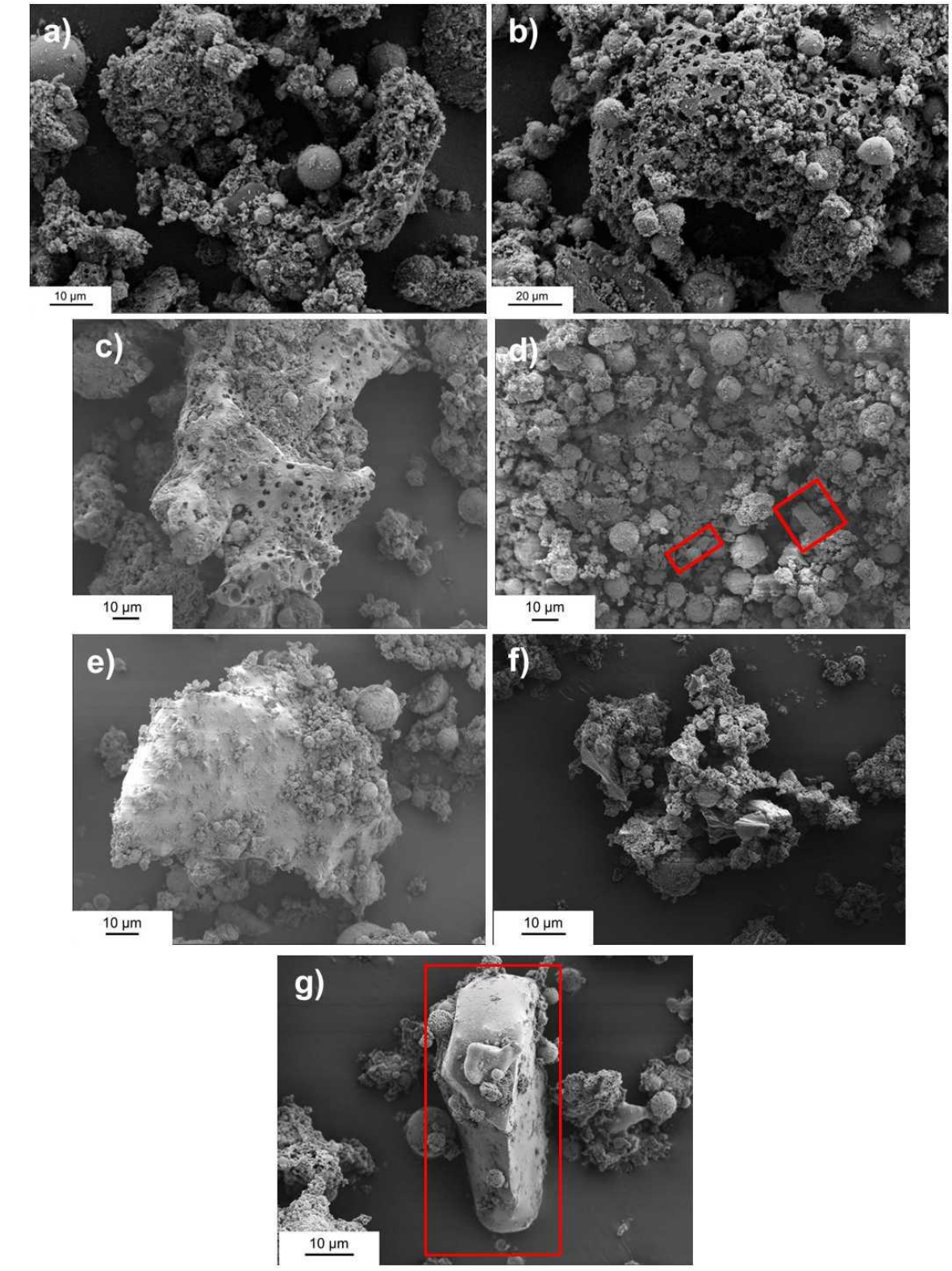

Figure 5-44: Composite of SEM electronmicrographs from the quenched samples a)E740-2 b)E740-3 c)E740-5 d)E740-8 e)E740-10 f)E740-11 g)E740-14

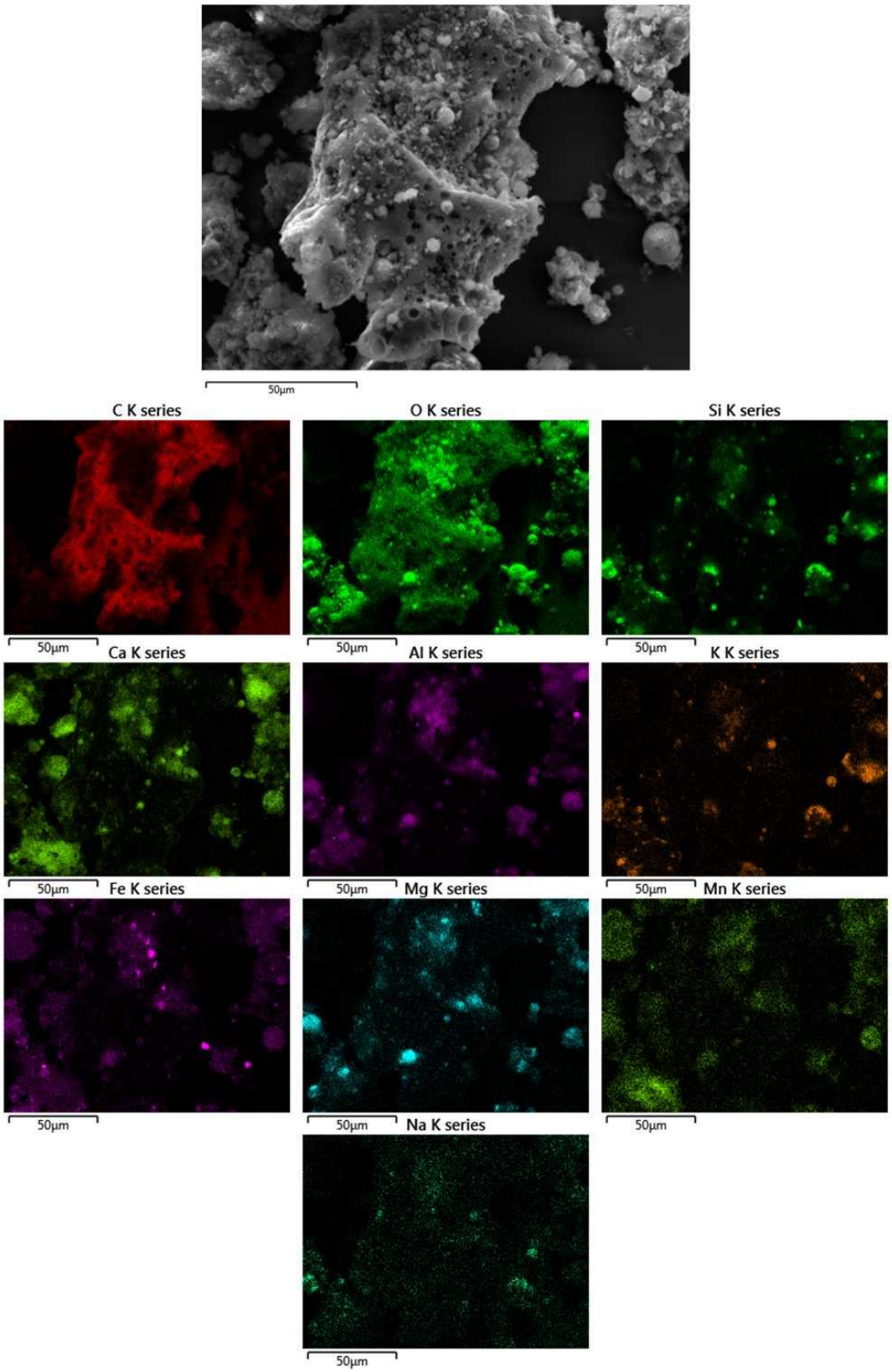

Figure 5-45: EDS maps of a char particle identified in sample E470-5

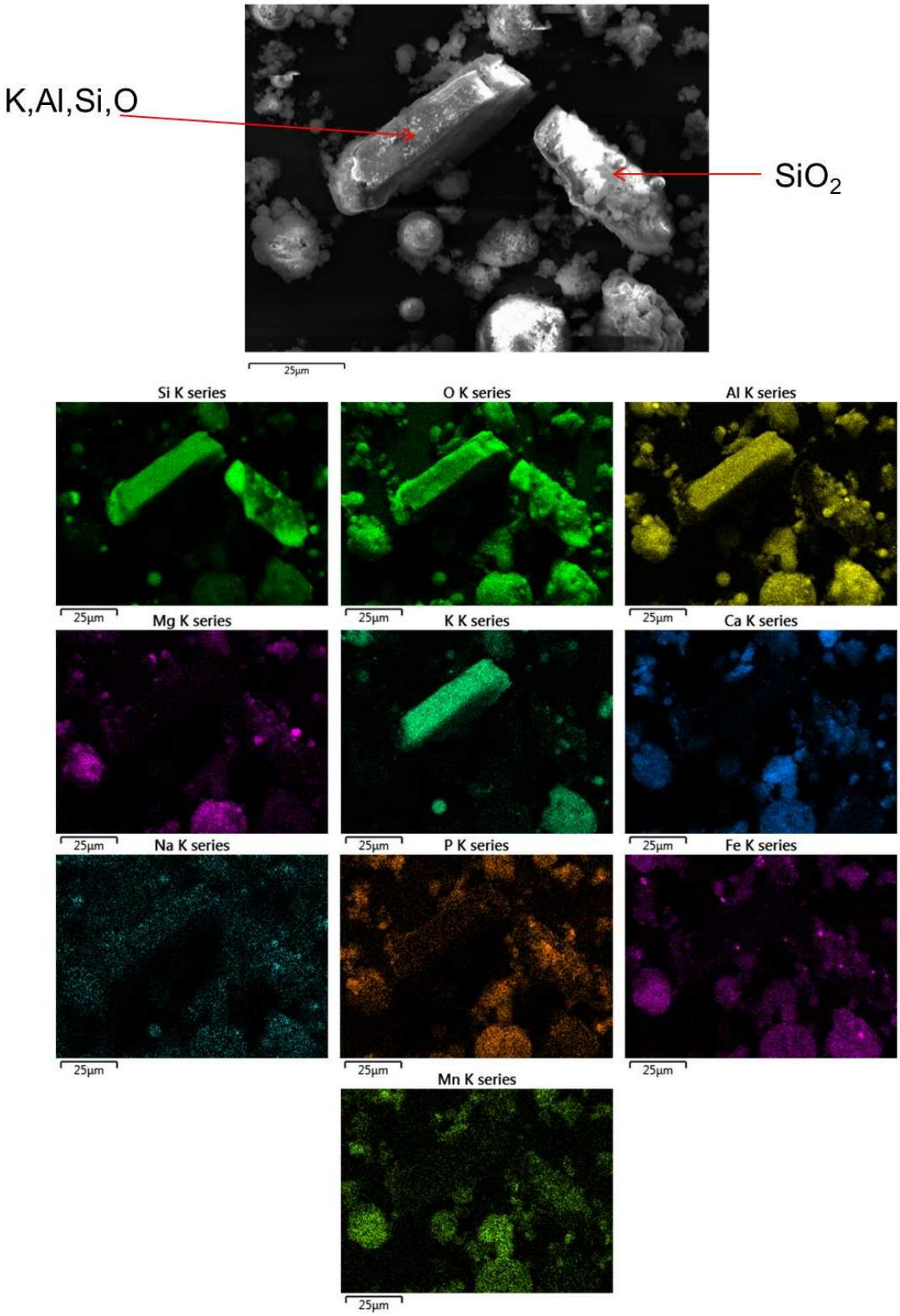

Figure 5-46: EDS maps showing association of KAlSiO and SiO_2 cuboids present in sample E740-14

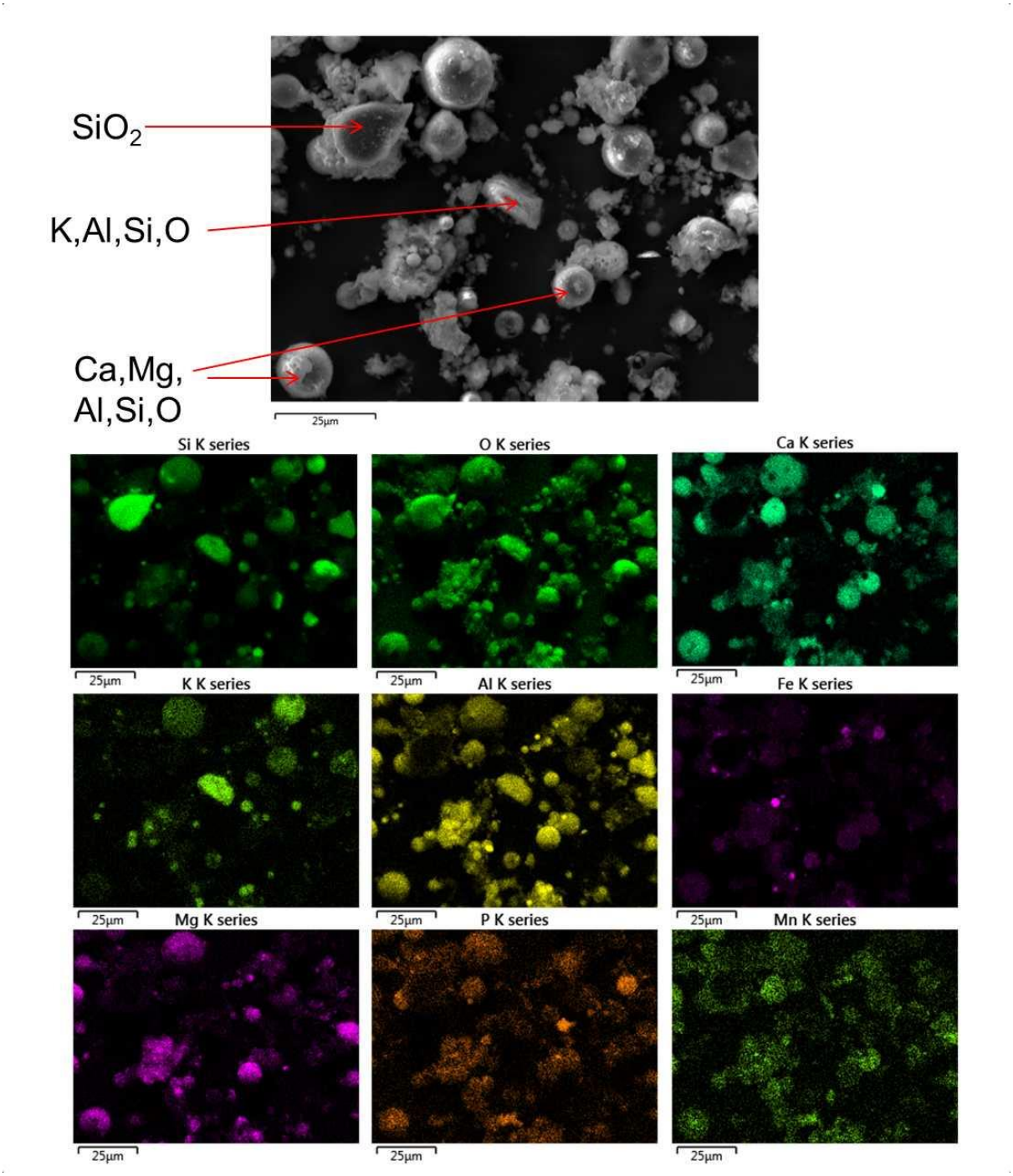

Figure 5-47: EDS maps showing a variety of phases and particle morphologies of sample E740-10

Ash composition data collected by EDS and XRF is presented in Table 5-28 and Table 5-27. The quenched ash for eucalyptus is similar to that of the co-fired blends in showing an increase in Al (from 5.68 wt% to 10.58 wt%). The phases containing Al are largely feldspar or silicate in origin. The feldspars are usually crystalline when present in the fly ash and are in the ash via the harvesting process.As a large portion of the phases identified in the XRD patterms do not contain Al it is likely that they are present as amorphous Al, silicates.

In both collected compositional datasets there is an increase in the Fe content of the ashes. This is likely enriched due to the insolubility of the Fe containing magnetite, hematite and Fe_2SiO_4. The increase in the Na content (from 8.58 wt% to 19.55 wt%) can also be explained by the insolubility of albite.

As was observed in the eucalyptus and coal quenched samples there are no P containing species identified in the XRD data Table 5-28. There are however P containing species in the EDS maps (Figure 5-41 and Figure 5-42) and XRF analysis, which indicates that these phases are either amorphous or in undetectable quantities.

Table 5-27: XRF analysis for the sample E 740-2 and Eucalyptus ash and high temperature 900°C Eucalyptus ash

	Wt%		
	E740-2	**Eucalyptus Ash**	**Eucalyptus 900°C**
Al	10.58 ±0.03	4.86 ±0.11	5.68 ±0.04
Ca	20.65 ±0.28	36.70 ±0.64	35.36 ±0.39
Cl	0.26 ±0.06	0.11 ±0.00	0.12 ±0.04
Fe	19.55 ±0.02	9.61 ±0.33	8.58 ±0.16
K	3.79 ±0.06	11.24 ±0.18	9.58 ±0.17
Mg	4.62 ±0.17	6.03 ±0.33	7.91 ±0.48
Mn	5.13 ±0.09	4.02 ±0.14	3.65 ±0.09
Na	1.82 ±0.07	0.70 ±0.98	0.47 ±0.66
Ni	0.05 ±0.01	0.09 ±0.01	0.04 ±0.00
P	7.50 ±0.10	4.25 ±0.13	4.84 ±0.04
S	0.60 ±0.01	2.55 ±0.05	3.03 ±0.05
Si	20.11 ±0.13	16.92 ±0.21	18.28 ±0.16
Sr	0.43 ±0.01	0.39 ±0.00	0.39 ±0.04
Ti	1.07 ±0.01	0.92 ±0.03	0.69 ±0.04
Zn	1.64 ±0.03	0.28 ±0.01	0.26 ±0.01
Zr	0.05 ±0.00	0.02 ±0.01	0.03 ±0.00
	97.81	**98.66**	**98.87**

Table 5-28: Averaged data for whole area analysis of multiple sample regions of the eucalyptus quenched samples

	Element	E740-5	E740-8	E740-10	E740-11	E740-14	Average
Wt%	Al	17.90 ±0.50	16.56 ±2.01	16.06 ±1.49	14.99 ±0.92	14.83 ±2.03	16.07 ±1.25
	Ca	17.47 ±2.91	17.31 ±2.98	17.28 ±2.50	15.90 ±2.03	19.67 ±8.89	17.53 ±1.36
	Cl	0.51 ±0.05	0.53 ±0.53		1.04 ±1.39		0.69 ±0.30
	Cr				0.68 ±0.09		0.68 ±0.09
	Cu	0.95 ±0.44	1.23 ±0.12	0.90 ±0.05	1.12 ±0.16	1.03 ±0.17	1.04 ±0.13
	Fe	14.23 ±1.43	15.45 ±1.76	13.91 ±2.30	17.82 ±1.66	14.96 ±3.42	15.27 ±1.54
	K	4.31 ±1.95	3.37 ±0.32	3.52 ±0.54	3.07 ±0.50	4.42 ±1.99	3.74 ±0.60
	Mg	6.64 ±0.74	5.69 ±1.16	5.65 ±0.63	4.77 ±0.79	4.45 ±0.66	5.44 ±0.86
	Mn	5.44 ±0.69	5.23 ±0.86	5.08 ±1.01	4.34 ±0.39	5.77 ±1.50	5.17 ±0.53
	Na	2.61 ±0.20	3.36 ±0.64	2.89 ±0.32	3.82 ±0.86	4.29 ±3.17	3.39 ±0.68
	P	5.16 ±0.74	4.74 ±0.56	4.09 ±0.56	5.59 ±0.64	4.93 ±0.93	4.90 ±0.55
	S	2.43 ±1.05	2.84 ±1.23	1.94 ±0.63	3.87 ±0.82	2.18 ±0.73	2.65 ±0.76
	Si	21.47 ±4.42	22.01 ±7.43	26.97 ±7.75	21.87 ±4.87	24.12 ±9.58	23.29 ±2.30
	Ti	0.72 ±0.05	0.83 ±0.12	0.79 ±0.24	0.65 ±0.09	0.72 ±0.18	0.74 ±0.07
	Zn	1.23 ±0.19	1.28 ±0.31	0.94 ±0.10	1.42 ±0.11	1.35 ±0.42	1.24 ±0.19

5.3.3 Eucalyptus Cyclone ash sample

The phases present in the eucalyptus cyclone ash that were identified are presented in Figure 5-48 and Table 5-29. The oxides and carbonates identified in the co-ash blends are also present in the eucalyptus cyclone ash. SiO_2 is present as quartz, not the polymorph cristobalite; this indicates that the gas temperature during combustion was not high enough to form cristobalite. Similarly to the hemp and coal sample, there is also sylvite (KCl) present in the ash. KCl was present in the boiler coupon flake samples, meaning that if a surface is cool enough to condense onto during the combustion trial, KCl will deposit there; this can have severe implications in regard to corrosion.[53]

Table 5-29: Phases identified in PXRD analysis of the Eucalyptus combustion trial cyclone ash

Phase	Key	Composition
Quartz	Qz	SiO_2
Sylvite	Sy	KCl
Periclase	P	MgO
Calcite	Ca	$CaCO_3$
Hematite	He	Fe_2O_3
Gehlenite Magnesian	Ge-Mg	$Ca_2(Mg_{0.25}Al_{0.75})(Si_{1.25}Al_{0.75}O_7)$
Merwinite	Mw	$Ca_3Mg(SiO_4)_2$
Anhydrite	An	$CaSO_4$
Soda Melilite	N-Me	$CaNaAlSi_2O_7$

Also present in the samples are $CaCO_3$ and MgO and the presence of these two phases is in agreement with the presence of gehlenite-magnesian and merwinite previously identified in the PXRD analysis. The formation of these phases has been discussed previously (Section 4.1); at present it is unclear if these phases formed in the flue gas or form in a deposit and are then removed by the flue gas through erosion. There is no Na carbonate/oxide identified in the cyclone ash. However, as it is present in the fuel ash as 0.70 wt% the formation and incorporation into the melilite system, which gehlenite is a member of, is plausible. The hematite (Fe_2O_3) is present in the cyclone ash, the high Fe content of the fuel is the origin of this oxide. It has not been reduced to magnetite (Fe_3O_4), indicating that conditions in the flue gas are not sufficient for reduction. This is in contrast to the quenched samples, which suggests water may play a role in the reduction.

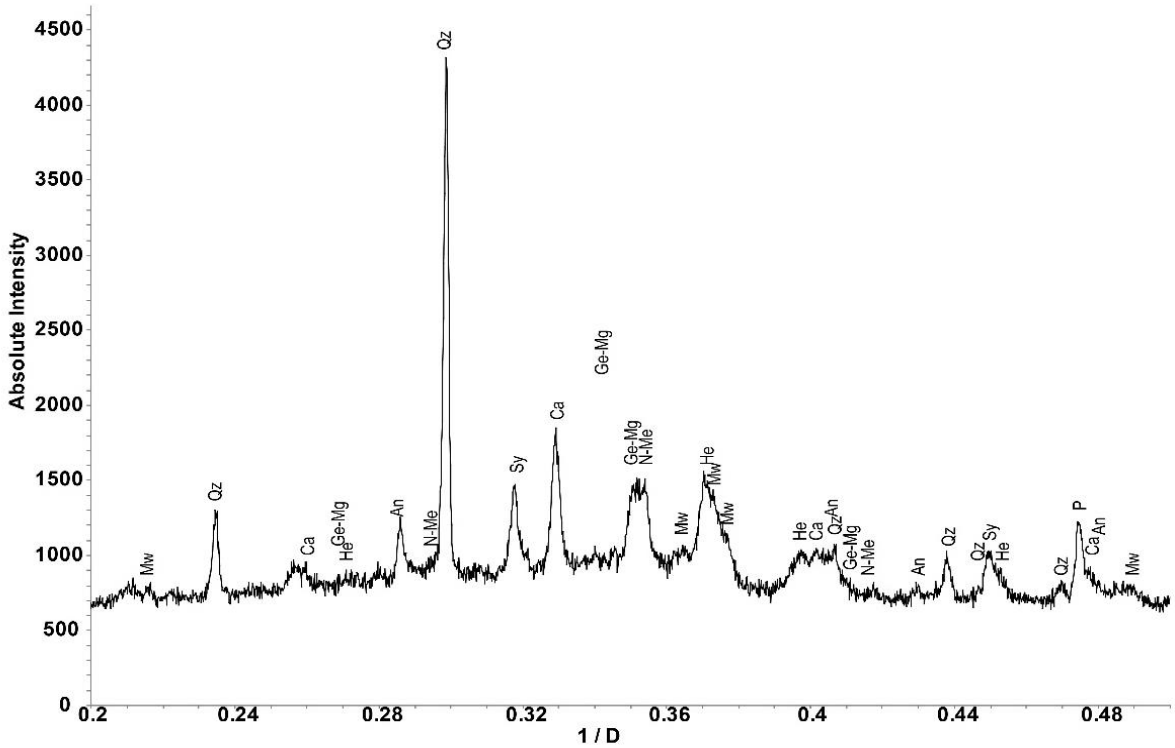

Figure 5-48: Eucalyptus cyclone ash data collected on the D2 diffractometer Cu Kα radiation

SEM analysis of the cyclone ash (Figure 5-49) shows the different morphologies present in the cyclone ash. Similar to the deposit and quench samples, the dominating morphology that is observed in are the spherical particles. These spheres form due to the heating rate in the combustion rig and so far fewer are present in the high temperature laboratory samples.

Also visible in the samples is some evidence of sintering; this may be a region of deposit that has been removed through erosion of deposits with flue gas particulate, as similar sintering has been observed the deposit samples (Figure 5-44 c, f). Alternatively these large particles could also have formed in the flue gas and agglomerated as they impacted together due to the high temperature of the flue gas. Also present in the cyclone ash are particles with similar morphology to char; this suggests that combustion of the fuel is incomplete. The presence of $CaCO_3$ in the ash, as previously, also suggests incomplete combustion.

EDS mapping of the sample (Figure 5-50, Figure 5-51) indicates that there are still char particles present in the cyclone ash and this suggests incomplete combustion of the eucalyptus. The spherical particles show varying composition, similar to the compositions previously observed in deposit (Figure 5-40) and quenched (Figure 5-47) samples. Several of the spheres are embedded in a crack of a large particle. These spheres are smaller than the

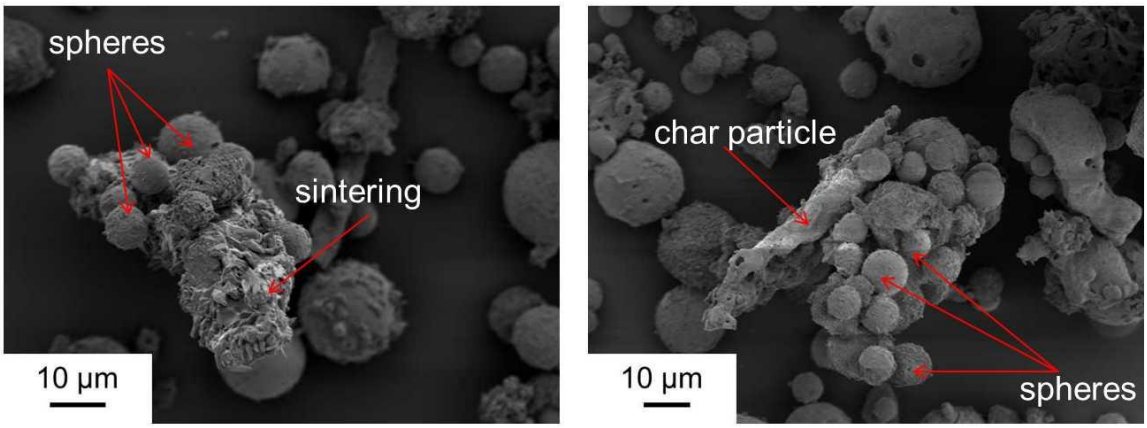

Figure 5-49: SEM electronmicrographs of eucalyptus combustion trial cyclone ash showing spherical particles with sintering and char particles

spheres present in other portions of the ash, suggesting that they could not expand as much as other spheres due to being compressed.

Also present in the samples is the phase $CaSO_4$ which was also identified through PXRD analysis, this is likely a reaction of CaO with SO_2 present in the flue gas (Figure 5-35). There were also regions where carbonates could be identified (Figure 5-51). At higher temperatures they will decompose to oxides and are likely to then form the complex silicates identified in the deposits and quenched samples, through the formation mechanisms previously presented. The phosphates present were not identified in the PXRD data analysis; these phosphates may be amorphous, rather than crystalline, explaining their absence from the PXRD pattern analysis.

KCl is identified in both EDS maps and PXRD data. As has been outlined previously, large amounts of Cl in the fuel can be concerning as it can lead to aggressive corrosion in the boiler environment. KCl was not present in the deposit or quenched ash due to the lack of cool surfaces to condense onto for the deposits, and the solubility of KCl in water.

Elemental composition analysis data is presented in Table 5-30 and Table 5-31. The most noticeable change is the increase in Cl content (0.12 wt% to 2.00 wt%, from XRF data). This corresponds with the presence of KCl identified in the XRD pattern (Figure 5-48). The presence of KCl in the cyclone ash indicates few cool surfaces for the phase to condense on during the combustion test.

$CaCO_3$ was identified in the ash alongside fewer Ca silicates suggesting the formation of the silicates in deposit as opposed to during flight in the flue gas. The suggested mechanism for formation is the deposition of the $CaCO_3$ (or CaO) followed by reaction with the viscous high silicate melt.

There is a decrease in the amount of K present in the cyclone ash compared to the high temperature ash (6.86 wt% to 9.58 wt%). This decrease can be attributed to the increased likelihood of free alkali metal condensation on boiler surfaces.[54]

Table 5-30: Averaged data of several EDS spectra of the cyclone ash samples from the eucalyptus co-firing test.

	Element	Average	
Wt %	Al	8.21	±2.74
	Ca	29.49	±3.75
	Cl	6.70	±4.07
	Fe	9.50	±2.46
	K	5.26	±0.91
	Mg	4.08	±0.81
	Mn	2.16	±0.19
	Na	5.83	±2.18
	P	19.84	±9.33
	S	1.25	±1.25
	Si	8.21	±2.74
	Ti	29.49	±3.75

Table 5-31: XRF data analysis of the cyclone ash compared with the eucalyptus ash and the high temperature eucalyptus ash at 900°C

	Wt%					
	Cyclone Ash		Eucalyptus Ash		Eucalyptus Ash 900°C	
Al	6.53	±0.11	4.86	±0.11	5.68	±0.04
Ca	31.62	±0.38	36.70	±0.64	35.36	±0.39
Cl	2.00	±0.13	0.11	±0.00	0.12	±0.04
Fe	9.59	±0.02	9.61	±0.33	8.58	±0.16
K	6.86	±0.07	11.24	±0.18	9.58	±0.17
Mg	4.63	±0.18	6.03	±0.33	7.91	±0.48
Mn	2.40	±0.01	4.02	±0.14	3.65	±0.09
Na	1.75	±0.23	0.70	±0.98	0.47	±0.66
Ni	0.06	±0.00	0.09	±0.01	0.04	±0.00
P	3.95	±0.02	4.25	±0.13	4.84	±0.04
S	4.72	±0.02	2.55	±0.05	3.03	±0.05
Si	20.81	±0.09	16.92	±0.21	18.28	±0.16
Sr	0.52	±0.01	0.39	±0.00	0.39	±0.04
Ti	0.75	±0.04	0.92	±0.03	0.69	±0.04
Zn	0.13	±0.00	0.28	±0.01	0.26	±0.01
Zr	0.04	±0.00	0.02	±0.01	0.03	±0.00
	96.32		**98.66**		**98.87**	

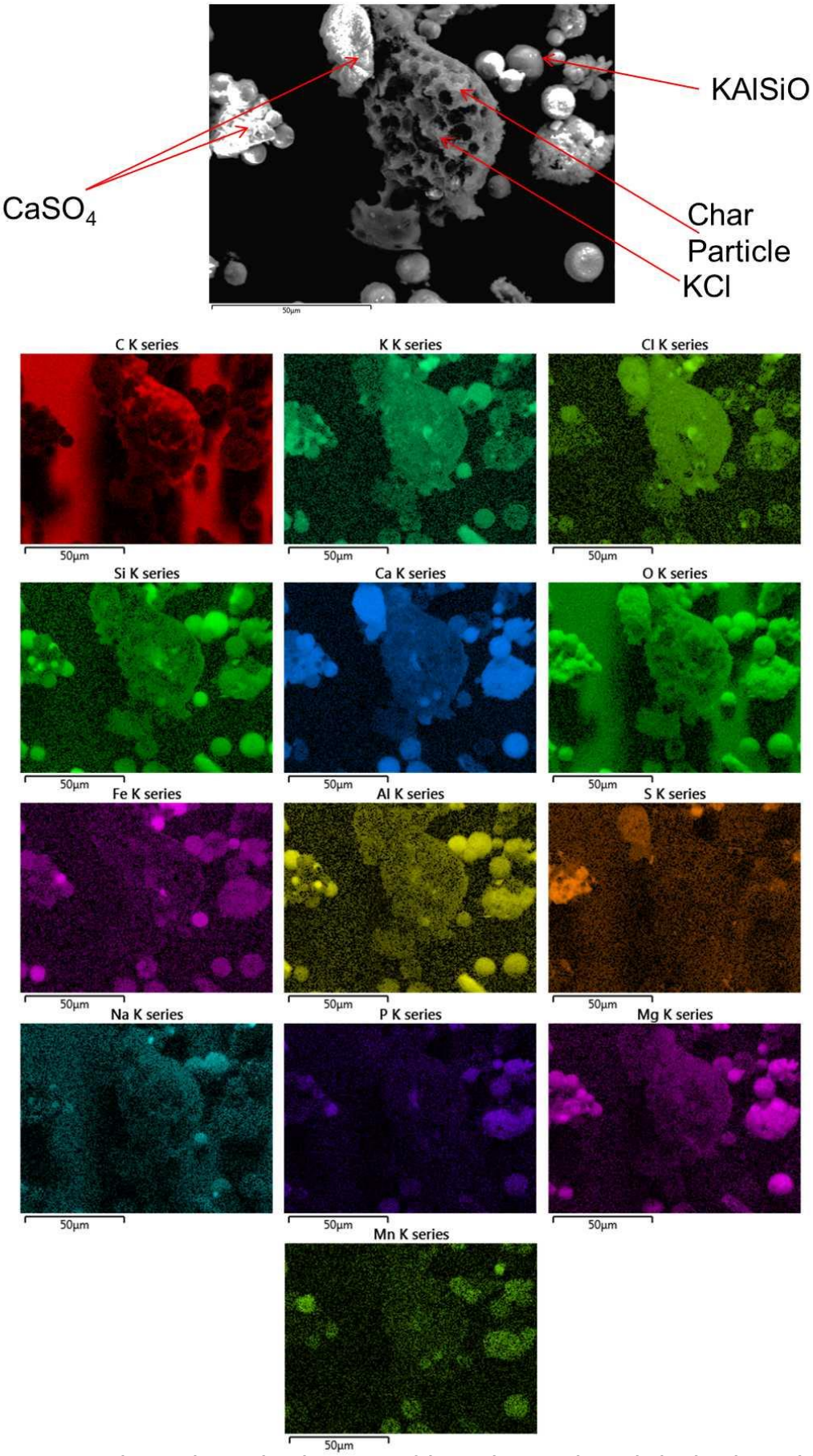

Figure 5-50: An electronmicrograph and EDS maps of the eucalyptus cyclone ash showing char particles, silicates, KCl and CaSO4 also identified using PXRD analysis

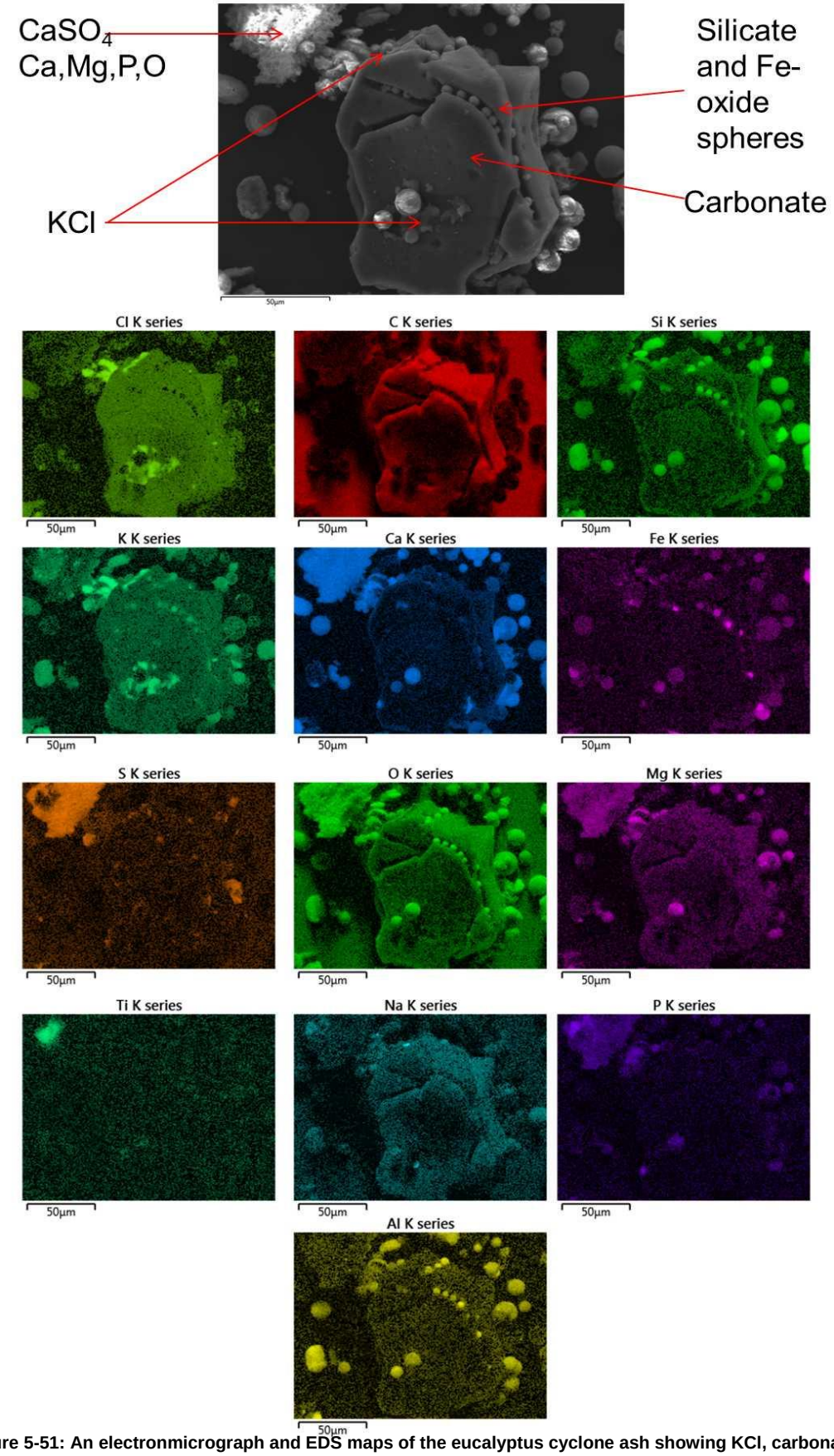

Figure 5-51: An electronmicrograph and EDS maps of the eucalyptus cyclone ash showing KCl, carbonates and phosphates. The silicate speeres present in the cracks have not expanded to the same size as those present in the looser ash.

5.3.4 Eucalyptus Bottom ash samples

Similar to the eucalyptus and coal bottom ash, there are both glassy blocks and loose ash. (Figure 5-52). The phases present in the loose ash (Figure 5-53, Table 5-32) allow insight into the phases that are likely to form in the glassy blocks. As has been previously mentioned, kalsilite can be a precursor to leucite (Section 3.1.5).The calcite likely loses CO_2 to form lime (CaO) which then reacts with SiO_2 to form wollastonite; further reaction with MgO (not identified) to form the diopside was identified in the glassy blocks. The akermanite identified in the loose bottom ash may have reacted with MgO to form the diopside. The $Ca_9MgK(PO_4)_7$ present in the co-fired bottom ash is present in the eucalyptus ash. Hydroxyapatite was previously identified as the precursor to this phase, but it has not been identified in the eucalyptus ash. However, the phase $Ca_3(PO_4)_2$ has been identified in the eucalyptus deposits suggesting that this may also be a precursor to the formation of $Ca_9MgK(PO_4)_7$.

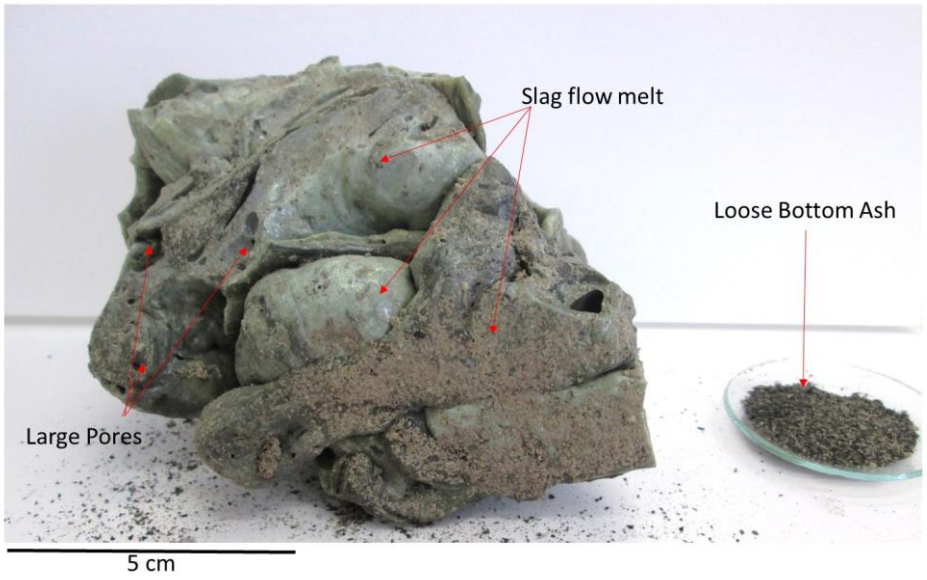

Figure 5-52: Eucalyptus combustion trial bottom ash showing large pores, slag flow melt and loose bottom ash

Table 5-32: Phases identified through PXRD data analysis of loose and glassy bottom ash

Phase	Key	Composition	Glassy Blocks	Loose
Quartz	Qz	SiO_2	•	•
Hematite	He	Fe_2O_3	•	
Albite	Ab	$NaAlSi_3O_8$	•	
Cristobalite	Cr	SiO_2	•	•
Leucite	Le	$KAlSi_2O_6$	•	
	MP	$Ca_9MgK(PO_4)_7$	•	
Diopside	Di	$CaMgSi_2O_6$	•	
Wollastonite	Wo	$CaSiO_3$	•	
Mullite	Mu	$Al_{4.56}Si_{1.44}O_{9.72}$	•	
Grossite	Gr	$CaAl_4O_7$	•	
Calcite	Ca	$CaCO_3$		•
Kalsilite	Ka	$KAlSiO_4$		•
Microcline	Mi	$KAlSi_3O_8$		•
Akermanite	Ak	$Ca_2MgSi_2O_7$		•

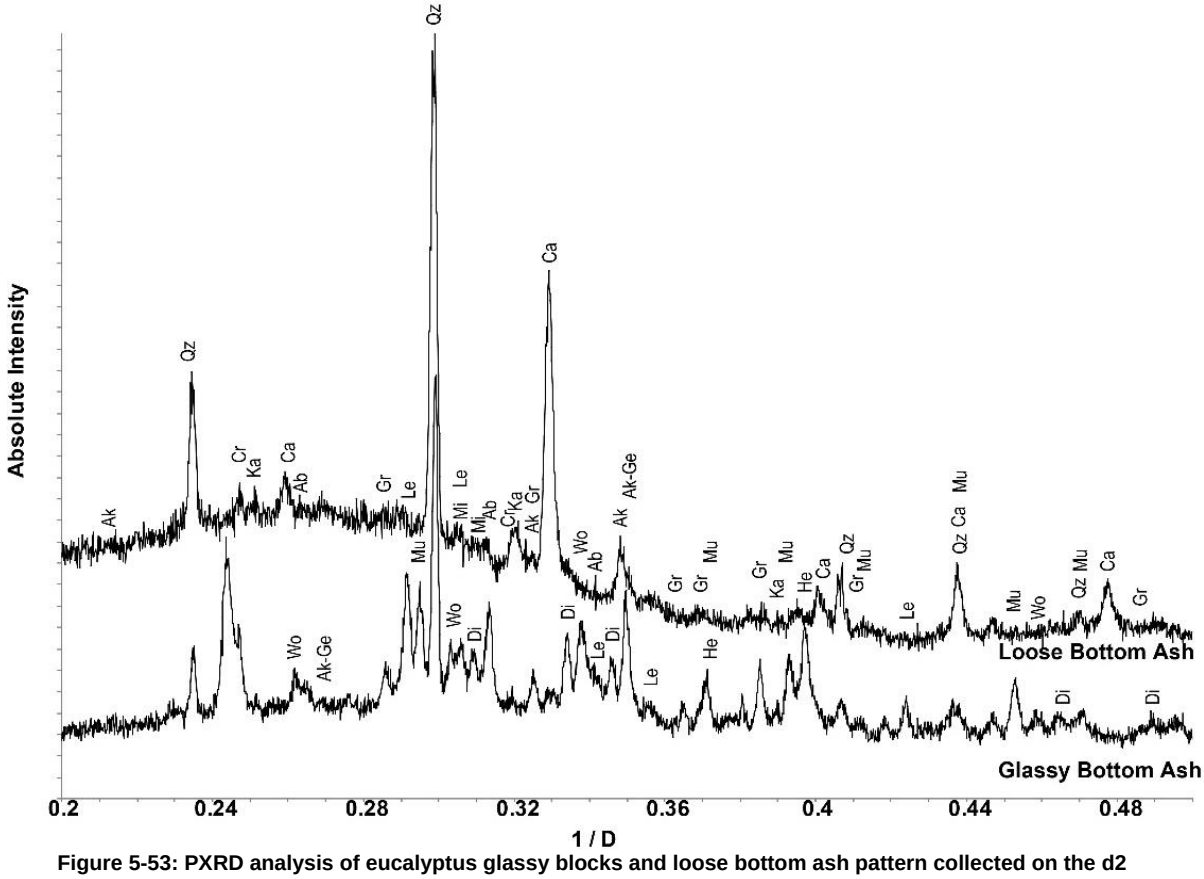

Figure 5-53: PXRD analysis of eucalyptus glassy blocks and loose bottom ash pattern collected on the d2 diffractometer (Cu Kα radiation)

SEM analysis of the samples (Figure 5- 54) shows morphology differences between the loose ash and the glassy blocks. The glassy blocks have a much closer texture in comparison to the loose ash which is much more porous. The samples were ground, prior to analysis in order for PXRD to be carried out on the samples. The loose ash was able to be ground by hand however the large glassy blocks required ball milling.

Analysis of the EDS maps of the glassy block bottom ash shows (Figure 5-55) distinct association between Al, Si, and O confirming the presence of the mullite which was also identified through analysis of the PXRD data (Table 5-32). Mullite present in the combustion rig samples has previously been attributed to the decomposition of kaolinite. As there is no kaolinite present from the coal in these samples, because only eucalyptus is fired it is possible that SiO_2 reacted with the refractory lining of the boiler. Also clearly visible are regions of Ca,Mg silicate which are likely to be the diopside or akermanite which were also identified from the PXRD data.

Fe,Cr-O is also associated in the glassy block and this is likely to be in the spinel type phase. Magnetite has been identified in several other forms of the fuel ash. This suggests that the spinel may have formed via Cr substitution into the magnetite. Also present in the EDS analysis is Ca,Mg phosphate which is also associated with K; this was also identified through PXRD as $Ca_9MgK(PO_4)_7$.

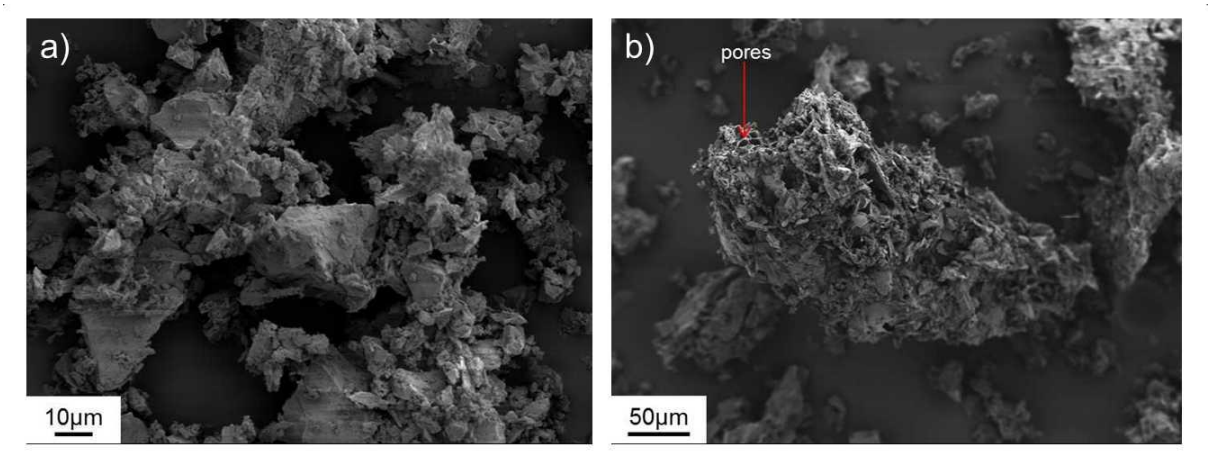

Figure 5- 54: Electronmicrographs of a) Eucalyptus bottom ash blocks showing a close glassy texture and b) Eucalyptus loose bottom ash showing porous regions and several different particle morphologies

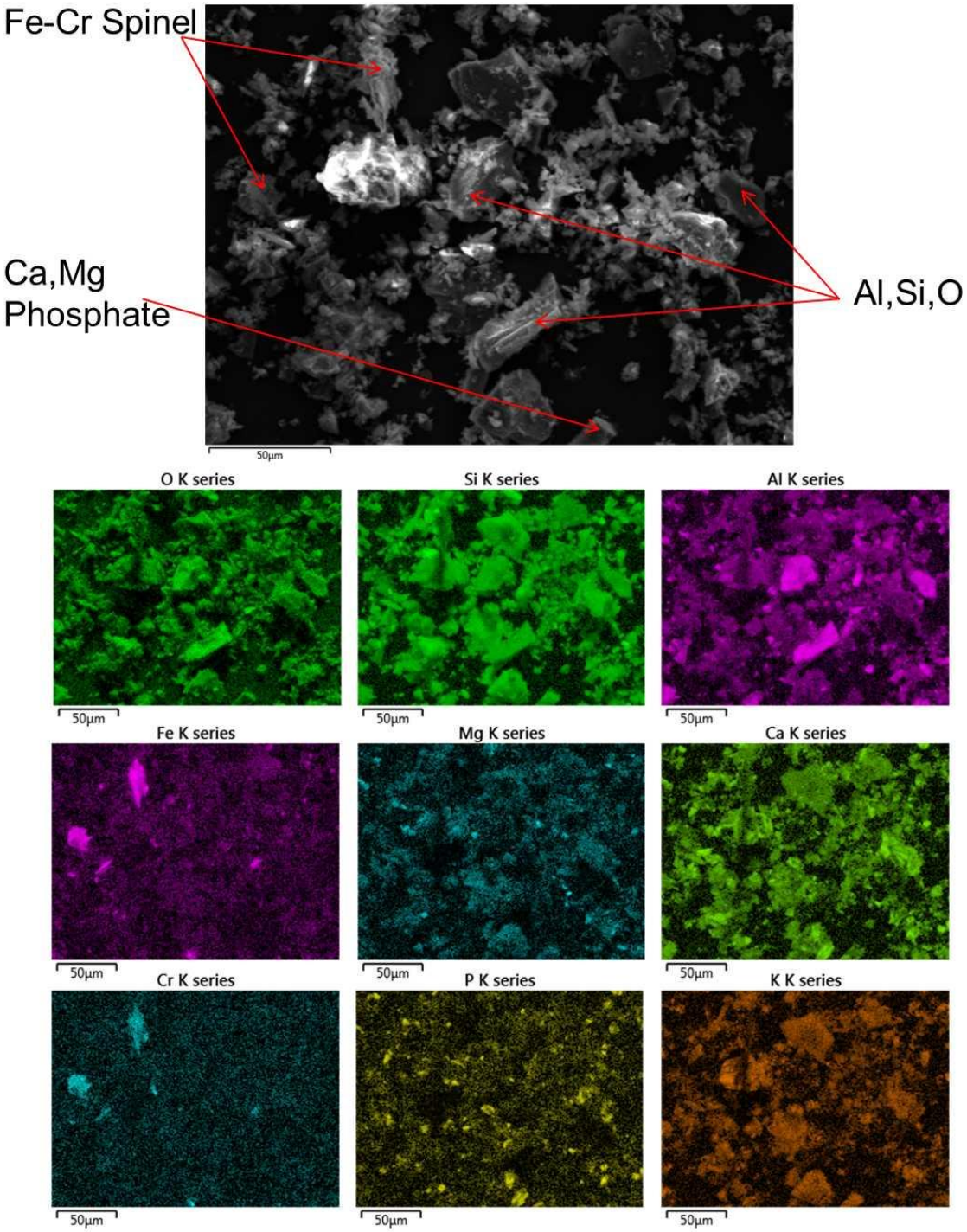

Figure 5-55: An electronmicrograph and EDS maps of eucalyptus glassy block bottom ash showing mullite, Fe-Cr spinel and C,aMg Phosphate

Data collected from analysis of the glassy blocks and loose bottom ash through SEM-EDS is presented in Table 5-33. The loose bottom ash shows a similar composition to the eucalyptus fuel ash A minor increase in the Ca and K content of the loose bottom ash can be attributed to the presence of the phase fairchildite ($KCa(CO_3)_2$), which was also identified in the PXRD data.

In contrast to the loose bottom ash the glassy blocks show a very different composition to the eucalyptus fuel. There is a large increase in the Si content (from 16.92 wt % to 45.52 wt %) suggesting the more volatile elements are lost through the gas stream before the heavier silicates fall to the bottom ash hopper. The increase in Al and K corresponds with the presence of leucite ($KAlSi_2O_6$) in the PXRD data.

Table 5-33: Averaged analysis of the EDS data for the glassy blocks and loose bottom ash of the eucalyptus combustion run

	Element	Glassy Blocks		Loose	
Wt %	**Al**	14.26	±2.51	6.85	±1.04
	Ca	17.50	±3.00	25.49	±2.41
	Cl			1.17	±0.24
	Cr	0.69	±0.35		
	Fe	5.02	±1.93	5.34	±0.60
	K	7.91	±0.60	18.91	±2.05
	Mg	2.37	±0.30	5.92	±0.74
	Mn			2.71	±0.42
	Na	1.20	±0.11	7.32	±1.34
	P	3.81	±0.12	2.70	±0.36
	S	1.39	±0.41	6.38	±2.35
	Si	45.52	±1.57	17.53	±2.71
	Ti	0.69	±0.15		

.

5.4 Conclusions

There are several phases identified in the combustion rig deposits that were not identified in the laboratory ashed samples. Mullite, one of the decomposition products of illite, is present, suggesting decomposition of illite in the flame. Mullite, alongside andalusite, is also a decomposition product of kaolinite. Kaolinite was present in the raw coal fuel but had decomposed in the initial ashing process up to 575°C; this explains the absence of andalusite in the HT heat treated ash, as the product it forms from is not present at the high temperatures in the furnace.

The silicates that are present in the HT lab ash, but not the deposit e.g. wollastonite (eucalyptus and coal), can be considered precursors to other silicates present e.g. diopside and akermanite which may have formed in the deposit via wollastonite. The akermanite and gehlenite present in some deposit samples have formed a solid solution in comparison to the laboratory HT ash samples, where they are present as individual phases. This can be attributed to two affects. Firstly the deposit is present in the combustion rig for 2-3 times longer than the 60 minutes the samples are in the furnace for. This means that reactions between phases that require longer to form can occur. Secondly, the deposit is continuously having ash impacted onto it, meaning that the composition is constantly changing; consequently more Mg/Al may become available to alter the composition of the solid solution.

The hemp and coal cyclone ash has a composition similar to that of the quenched samples. The main difference between these samples is the absence of water soluble phases in the quenched samples i.e: KCl. The samples are morphologically similar, containing spheres which comprise of silicates and phosphates alongside the rod-like particles which are the remainder of the trichomes present on the raw fuel.

There are significant morphology differences between the HT lab ash and deposit, quenched, and cyclone ash samples. The spheres that are present in the hemp and coal, and eucalyptus and coal combustion trials are also present in the eucalyptus combustion trials; this suggests that the plero and cenospheres originally identified by Raask[191] as forming through coal will form from ash of the same composition from biomass. In the deposit samples there are multiple examples of sintering between the large spheres, and significant melt in the deposits seems to have occurred. The deposits are not so tenacious however that they are unable be removed from the probes. The deposit and quenched samples also have a greater number of large spheres present in the ash. The formation of the spheres is thought to be influenced by the heating rate of the ash and so is challenging to reproduce in a lab environment. The

spheres are not the only morphology present in the cyclone ash, some of the particles show evidence of sintering. This indicates that particle collision in the flue gas stream may have occurred to form these particles, or that some of the deposits were removed through an erosion mechanism.

The microcline that was present in the HT ash is present in several of the rig samples, however sanidine is also present suggesting temperature and gas conditions in the combustion rig are favourable for formation of sanidine. This may be due to the heating rate and temperatures experienced in the combustion rig. Kalsilite ($KAlSiO_4$) is present in the deposit, quenched, and HT ash. The greater peak intensities of kalsilite in the quenched samples suggest rapid quenching of the sample may lead to formation, indicating it could be a kinetic product i.e. the product that forms first and due to rapid cooling is unable to convert into a more stable thermodynamic product.

KCl is identified in both the loose bottom ash and the cyclone ash for the eucalyptus fuel suggesting that not all KCl formed in the combustion process will deposit.

There are several polymorphs of SiO_2 present in the glassy blocks. This means that the temperatures in the ash hopper were similar during both co-firing combustion trials. Also present in the glassy blocks is the phase $Ca_9MgK(PO_4)_7$, which has formed via hydroxyapatite present in the loose ash (eucalyptus and coal). Several silicate phases are present in the glassy block ash; in comparison the loose ash contains more carbonates, these in turn are thought to degrade into oxides (e.g. CaO which are identified in some of the deposit ash samples and MgO). These oxides will then react with SiO_2 to form the silicates. The phases present in the loose ash have feasible pathways to form the phases present in the glassy blocks.

A comparison of the HT ash, deposits, and quench samples shows that the vast majority of the phases present in the combustion rig samples can be predicted if a fuel is ashed prior to large scale combustion. The sintering in the deposits is of some concern, however, deposit sintering and increased molten flow can be directly related to the presence of potassium silicates and KCl, which are not present in large quantities. Zbogar *et al*.[46] note that a high content of SiO_2 and Ca also contribute to the formation of porous deposits and therefore these deposits are weaker and easier to remove.

6. Analysis of deposit build up on boiler probes from a 1MW$_{th}$ combustion rig

6.1 Introduction

Low alloy steels, such as 15Mo3 are often used as structural materials in power plants due to their lower cost in comparison to other ferritic and heat-resistant steels. 15Mo3 is typically used at temperatures up to 475°C. However, oxidation can lead to serious problems including pipe failure and wall thinning at high temperatures. Chang and Wei[217] have previously reviewed high temperature oxidation of low alloy steels, and found that hematite and magnetite are the most commonly formed oxides. Higginson *et al*.[218] characterised the oxides formed on low alloy steels and concluded that hematite, magnetite, and wustite are most commonly

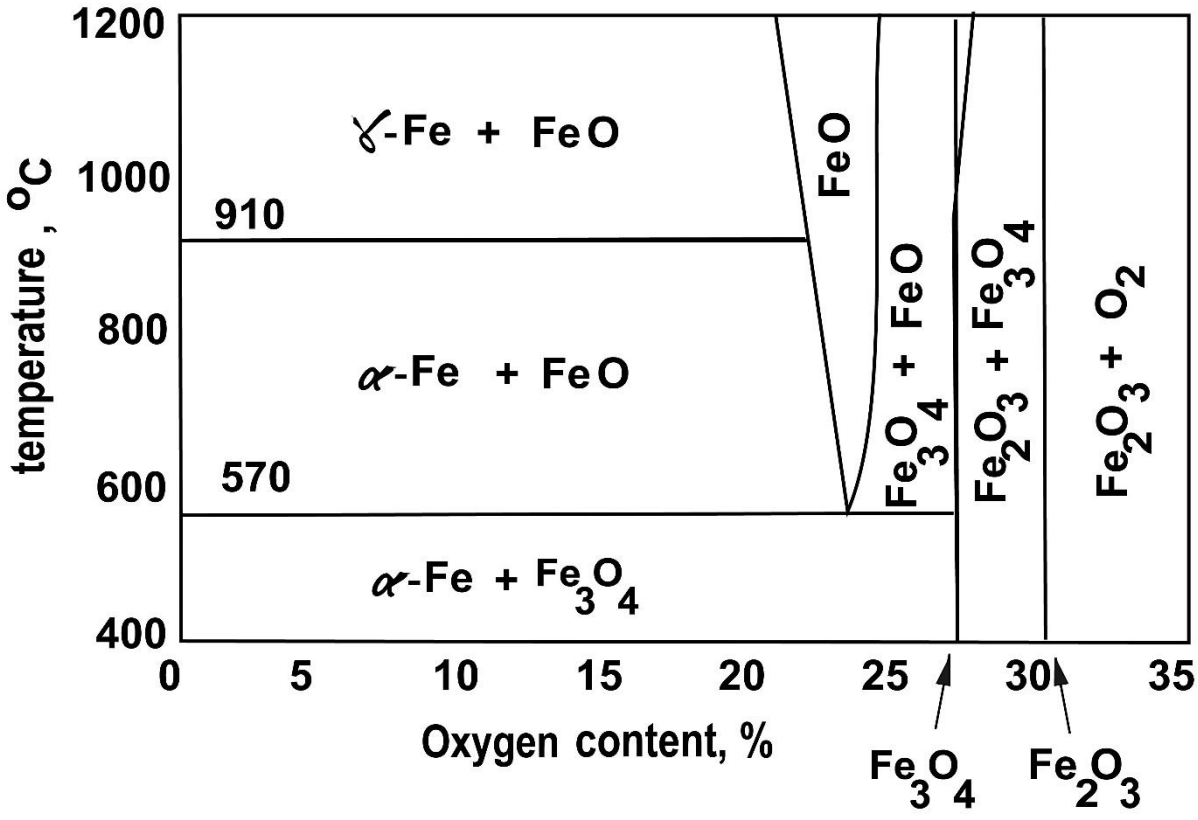

Figure 6-1: Fe-O phase diagram showing magnetite and hematite as the most common Fe-O phases below 500°C

formed. The phase diagram of Fe-O is presented in Figure 6-1, showing that hematite and magnetite are the phases predicted at the temperatures in relation to the O content (below 500°C) in the combustion trial. Later work by Chang[219] showed that long term oxidation of metals could not accurately be predicted, as different alloys possess widely different spalling characteristics. It is therefore important to investigate different alloys and their compatabilities with different fuels. The as-measured composition of the alloy 15Mo3 used in this study is presented in Table 6-1.

Table 6-1: Measured composition of the 15Mo3 coupons used in the combustion trials

Alloy	Cr	Mn	Fe	Ni	Mo	Cu
15Mo3	0.22	0.48	98.59	0.24	0.29	0.18

Heat transfer to the boiler tubes is often affected by deposit build up, and depending on composition, these deposits can also contribute to premature boiler failure. Information on oxidation products and deposit interaction on 15Mo3 during the combustion of biomass is essential to minimise plant downtime. In this chapter, analysis of the deposits onto the surface of the 15Mo3 coupons during hemp and coal, eucalyptus and coal, and eucalyptus combustion trials will be presented.

6.2 Analysis of the hemp and coal boiler coupon surface deposits

Eight samples (Hemp A-H) were analysed; each sample was in a different port of the combustion rig (Figure 6-4). Gas profiles of CO and O_2 (sampled locally to the probe every two hours through the combustion run) for the probes are presented in Figure 6-2 and Figure 6-3, and clear differences in the gas composition surrounding the samples were visible. A higher %CO suggests the sample conditions are reducing, a high $\%O_2$ indicates oxidising conditions. Under oxidising conditions, a protective oxide scale is more likely to form. The target temperatures of the samples are presented in Table 6-2; whilst the temperatures of the samples are duplicated, the atmospheres surrounding the samples are different (the position of the samples in the boiler are presented in Figure 6-4) and so some variation between oxidation and deposit composition is expected.

Table 6-2: Target temperatures of the 15Mo3 probes in the hemp and coal combustion test

Sample	Target Temperature (°C)	Atmosphere
Hemp A	475	Reducing
Hemp B	450	Oxidising
Hemp C	425	Oxidising
Hemp D	475	Oxidising
Hemp E	475	Oxidising
Hemp F	475	Oxidising
Hemp G	450	Oxidising
Hemp H	425	Oxidising

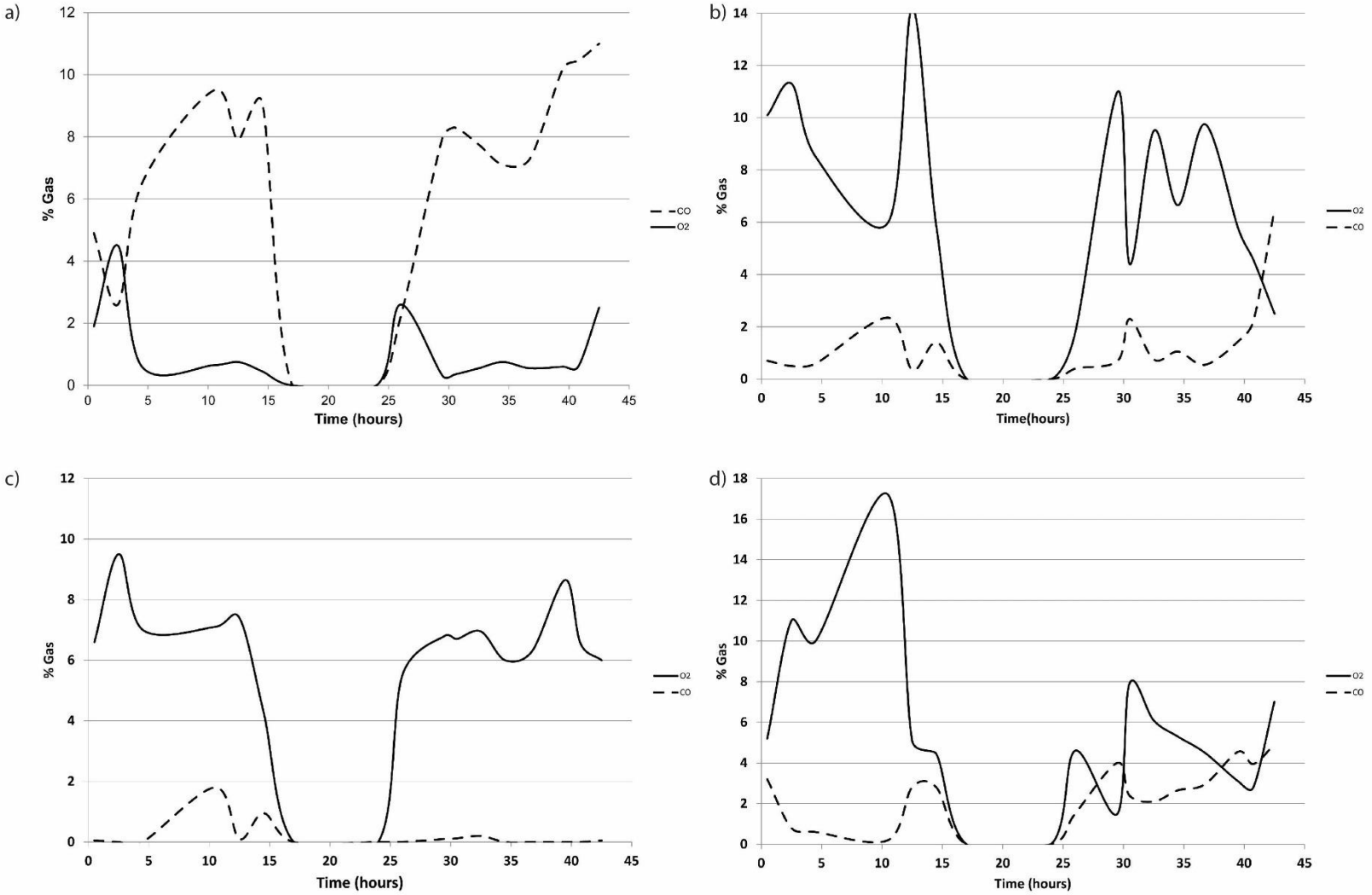

Figure 6-2: Gas conditions sampled every two hours from 15Mo3 probes in the hemp and coal combustion test. a) Hemp A b) Hemp B c) Hemp C d) Hemp D

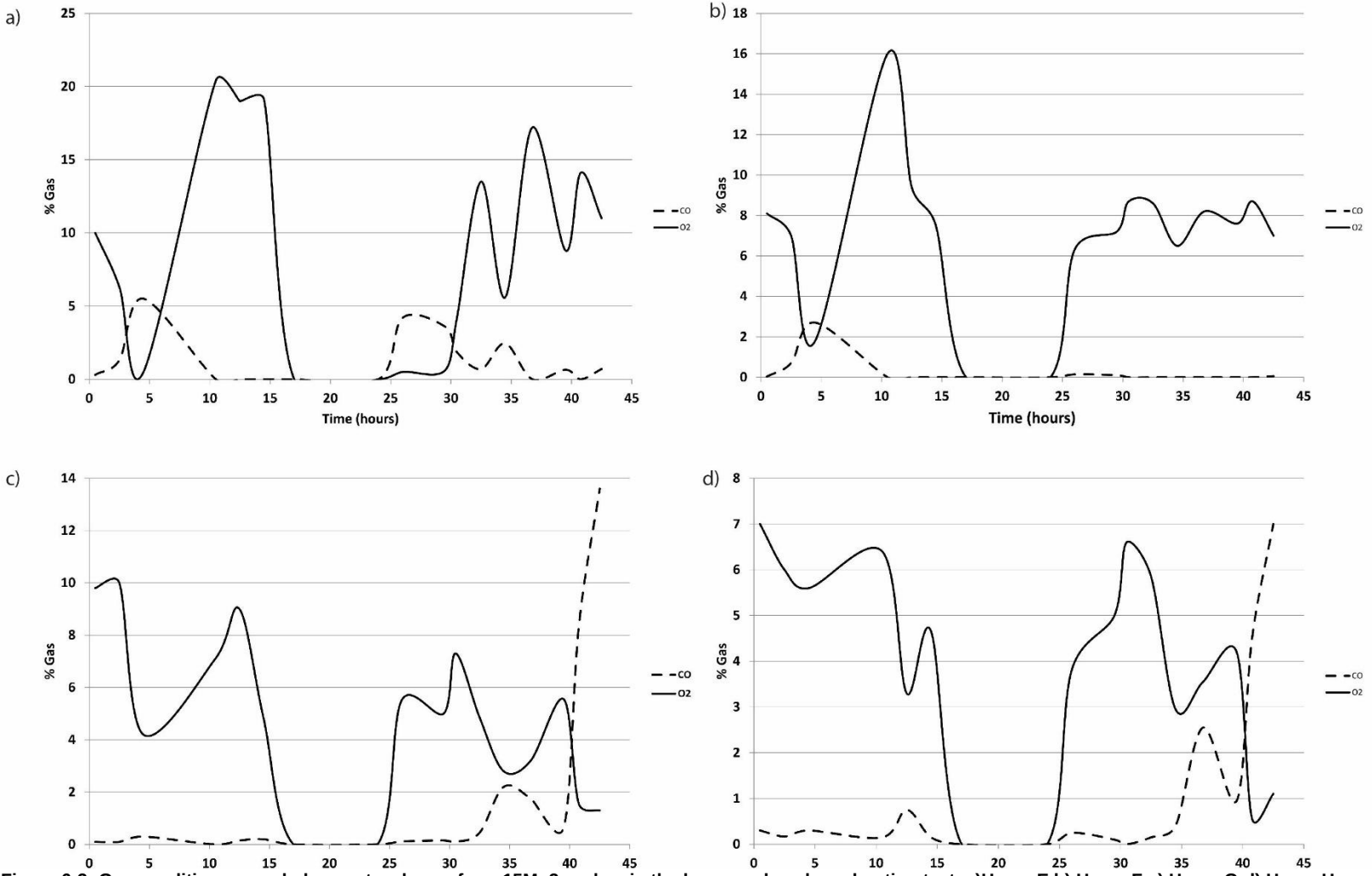

Figure 6-3: Gas conditions sampled every two hours from 15Mo3 probes in the hemp and coal combustion test. a)Hemp E b) Hemp F c) Hemp G d) Hemp H

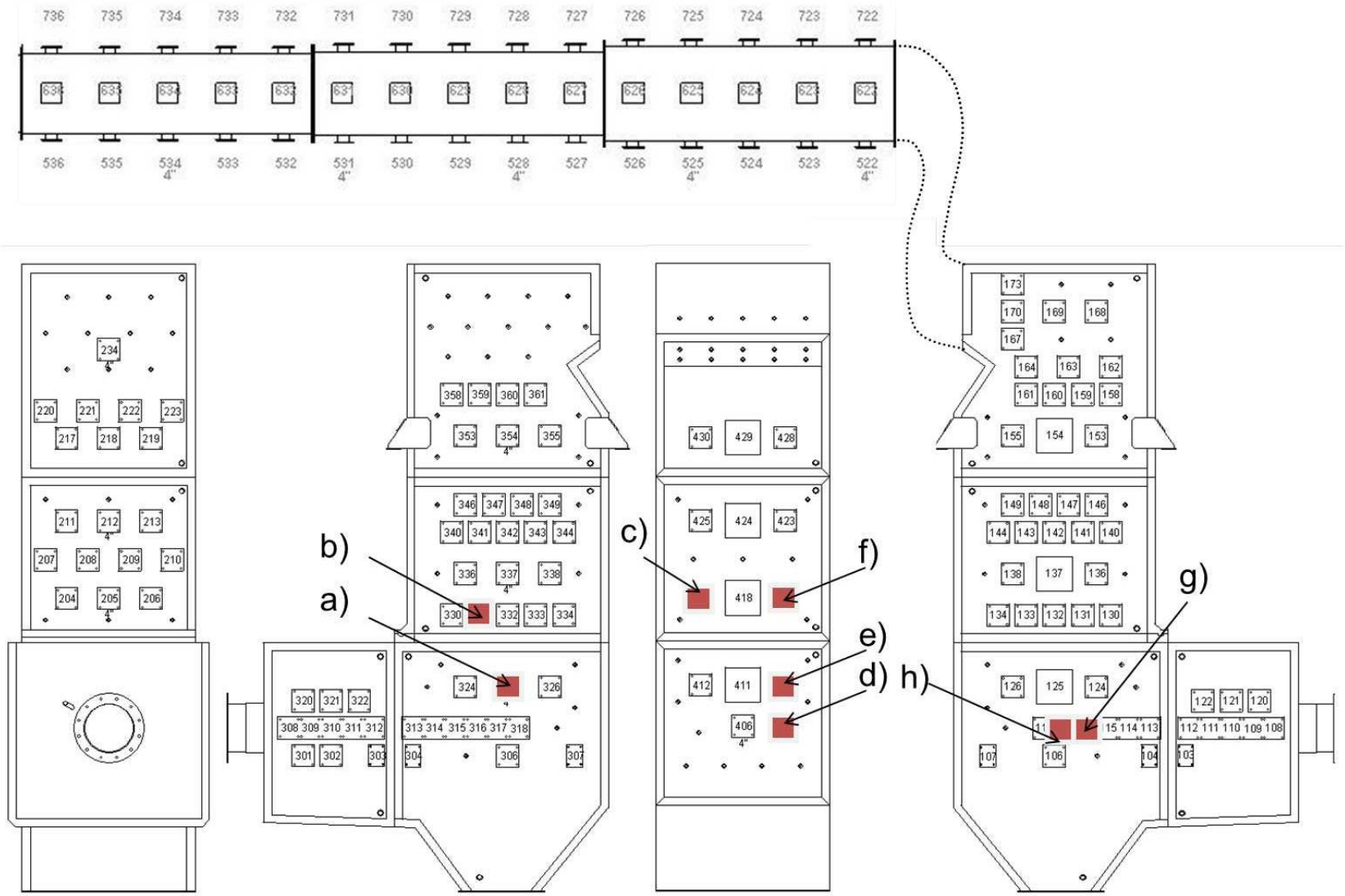

Figure 6-4: Positions of the 15Mo3 hemp and coal combustion probes in the hemp and coal combustion run a) Hemp A b) Hep B c) Hemp C d) Hemp D e) Hemp E f) Hemp F g) Hemp G, h) Hemp H

Table 6-3: Phases present in the probe scales from the hemp and coal combustion run (* indicates solid solution between two phases)

Phase	Key	Composition	Hemp A	Hemp B	Hemp C	Hemp D	Hemp E	Hemp F	Hemp G	Hemp H
Quartz	Qz	SiO_2	•	•	•	•	•	•	•	•
Hematite	He	Fe_2O_3	•	•	•		•	•		
Sylvite	Sy	KCl	•	•	•	•	•		•	
Calcite	Ca	$CaCO_3$	•	•						
Cristobalite	Cr	SiO_2	•	•	•			•	•	•
Diopside	Di	$CaMgSi_2O_6$	•						•	•
Arcanite	Ac	K_2SO_4	•	•		•	•			
Akermanite	Ak	$Ca_2MgSi_2O_7$	•		•			•	•	*
Anhydrite	An	$CaSO_4$	•	•						
Kalsilite	Ka	$KAlSiO_4$	•		•			•	•	
Leucite	Le	$KAlSi_2O_6$	•		•			•	•	•
Microcline	Mi	$KAlSi_3O_8$		•	•	•		•		
Hydroxyapatite	Ha	$Ca_{10}(PO_4)_6(OH)_2$		•	•			•	•	•
Gehlenite	Ge	$Ca_2Al(AlSiO_7)$		•						*
Fairchildite	Fa	$KCa(CO_3)_2$			•			•	•	
Periclase	P	MgO			•					
Orthoclase	Or	$KAlSi_3O_8$							•	
Albite	Ab	$NaAlSi_3O_8$								•

Analysis of the PXRD data and phases present in the hemp probe deposits are presented in Table 6-3 and Figure 6-5. KCl has been identified in the hemp probe samples; as has been mentioned previously, KCl is often highlighted as a phase of concern when co-firing biomass. Figure 2- 9 shows the widely accepted mechanism for active oxidation. KCl is often one of first phases to deposit during biomass combustion.[47,220] The main deposition mechanisms of KCl are diffusion and thermophoresis (Section 2.3). The probe temperatures are 425-475°C and therefore the KCl will deposit on to the probes as they are significantly cooler than the flame / combustion air, which can be in excess of 1000°C.

Arcanite (K_2SO_4) is also shown to be present through analysis of the PXRD data. K_2SO_4 could have deposited through the diffusion and thermophoresis mechanisms similarly to KCl.[1] Kassman *et al*.[221] give an equation (Equation 6-27) for the sulphation of KCl in the deposit. Figure 5-2 shows the gas composition leaving the rig, therefore the reaction is likely to happen. This SO_2 could be present due to the decomposition of the rozenite identified in the PXRD of the coal fuel. Baxter *et al*.[205] list sulphation, alkali absorption, and oxidation as the three most important reactions in the chemical reaction category of the deposition mechanisms.

$$2KCl + SO_2 + H_2O + {}^{1}/_{2}\,O_2 \rightarrow K_2SO_4 + 2HCl$$

Equation 6-27

Also identified in the samples is cristobalite (SiO_2). Cristobalite is a high temperature polymorph of SiO_2 which, due to a highly porous structure, is more reactive than quartz as an SiO_2 source.[222] This suggests the cristobalite is the SiO_2 source for the formation of the complex silicates identified e.g. akermanite and diopside. The larger particles which deposit on to the probe samples are too large to follow the gas flow through the convective pass. Therefore, they either impact into the boiler walls and stick to the probes, or fall into the bottom ash collector.

Ca,Mg,Al silicates have been identified through PXRD data analysis and are present in both the high temperature lab ash and the deposit samples, once again indicating that formation ocurrs after deposition. Tite and Maniatis report that the melting point of Ca compounds is decreased by aprroximately 50°C in reducing atmospheres,[223] which explains the presence of both diopside and akermanite in hemp A. However, both Ca-Mg silicates are also present in samples G and H, which are in a largely oxidising atmosphere, suggesting that the atmosphere does not have a large affect on which of these silicate phases form. The gas conditions also seem to have little affect on the formation of K,Al silicates with kalsilite, with leucite being present under both reducing and oxidising conditions. Rathossi and Pontikes[224] report that for

clays with compositions of SiO_2 (42.03-51.17wt%), Al_2O_3 (10.48-12.8wt%), and CaO (9.48-13.97wt%), between 850-950°C no significant mineral or structural differences between oxidising and reducing atmospheres were seen. At temperatures above 1050°C, the atmosphere was shown to be more important, with an increase in vitreous and viscous glassy phases.[224] The formation of glassy phases is undesirable in a combustion environment as it can lead to tenacious deposits which will decrease heat transfer and therefore efficiency.

SEM electronmicrographs are presented in Figure 6-6**Error! Reference source not found.**. Several clear morphologies are visible in the deposits. Distinct cubes are of KCl are present in hemp B (Figure 6-6b, Figure 6-7), which are also identified as present by analysis of the PXRD data (Table 6-3). These cubes of KCl formed through heterogeneous condensation onto the comparatively cooler surface of the probe coupons. Surrounding the cubic KCl in Figure 6-7 was a region high in Al,Si and O. The close proximity of these two phases suggests that if left at high temperature in the boiler for long periods of time, they may react to form one of the K,Al-silicates identified through PXRD analysis.

Needle shaped crystals are present in several of the probe deposit samples (Figure 6-6a,b,d and e); these are likely to have formed after deposition. Zbogar[46] lists chemical reaction as a method of deposit formation; the formation of these needle crystals may be due to the reaction of phases present in the deposit with CO, CO_2, SO_2, or O_2 from the flue gas. EDS analysis of these needles is presented in Figure 6-8, and close association between K, S, and O suggests that they are the phase K_2SO_4 also identified in the PXRD data. The close proximity of these needles to a large region of KCl suggests that SO_2 in the flue gas reacts with the deposited KCl to form the K_2SO_4. This is in agreement with the formation mechanism presented Equation 6-27.

A different morphology of K_2SO_4 is observed in sample Hemp C (Figure 6-9), where deposition onto a large particle of FeS is observed. This could be from the decomposition of rozenite ($FeSO_4.4H_2O$) to form FeS, the S present may then react with KCl that deposited onto the surface of the particle.

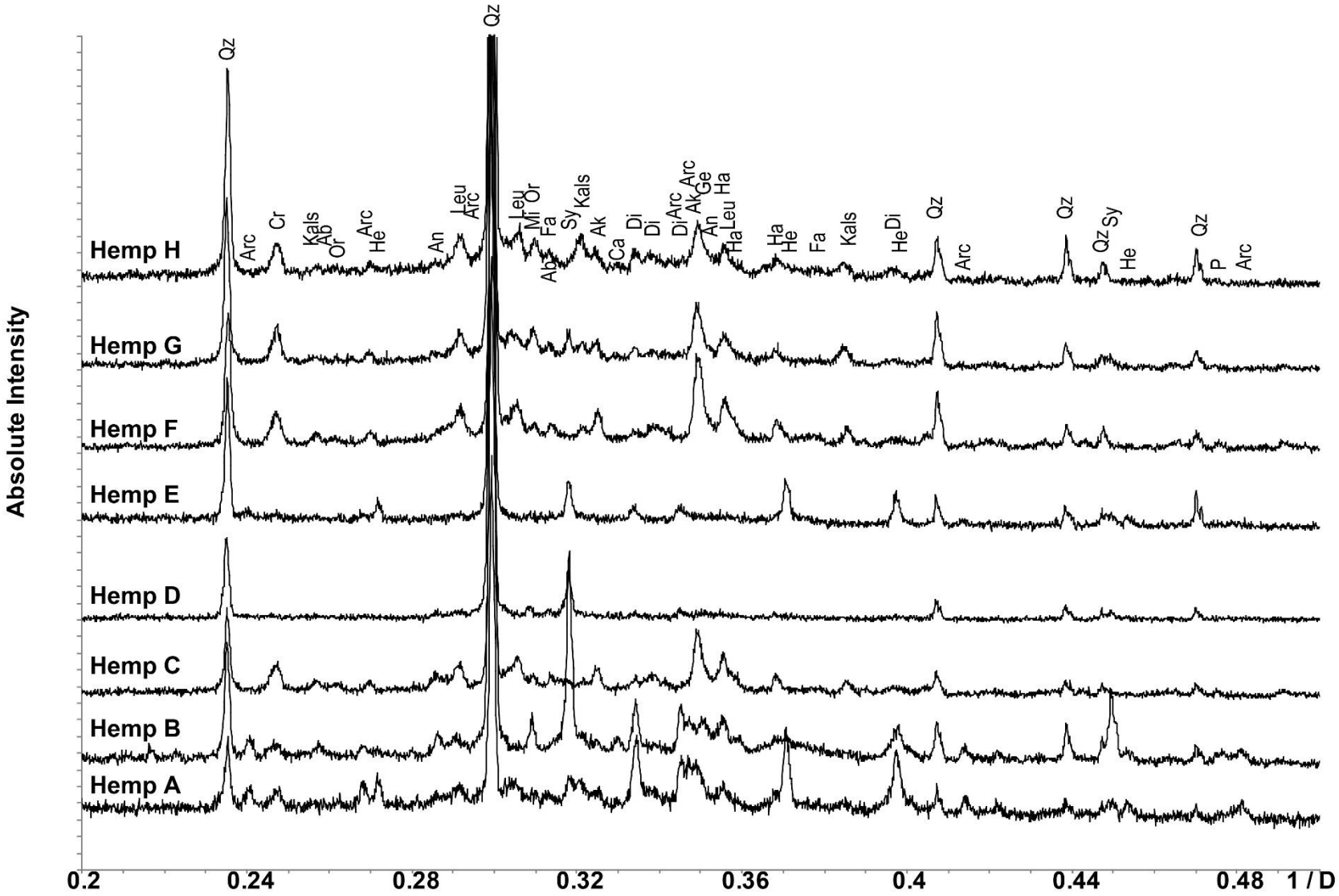

Figure 6-5: PXRD Data analysis of hemp probe deposits, data collected on the D2 diffractometer (Cu Kα radiation)

In several samples, metal oxide flakes are present (Figure 6-6e); these are thought to form through breakaway oxidation, followed by the loss of scales on cooling.[225] The needles observed in several other samples are also present at the oxide-deposit surface, further suggesting in deposit growth.

Also visible on the deposit surface were spheres which may have formed in the flue gas and deposited through inertial impaction. At the deposit-interface, there was also some evidence of sintering (particle-particle attachment during heating). Sintering can increase the tenacity of a deposit, therefore making it harder to remove.[46] Figure 6-10 presents an electronmicrograph and EDS maps of a metal oxide flake; clear KCl cubes can be seen on the surface of the flake as well as in the large deposit region. K_2SO_4 was also present in this deposit suggesting the sulfation of KCl at the metal oxide interface. In close association in the deposit is Ca,P and O confirming the presence of the hydroxyapatite identified in the samples through PXRD analysis. Figure 6-10 further confirms the presence of the hydroxyapatite as there is a distinct visible region in the sample. There is also evidence of the formation of K, Al silicates as there are several distinct regions present in the deposit.

The trichomes that were present in the raw hemp fuel were also present in some of the probe deposits, Figure 6-6f shows trichomes present in Hemp F. The shape is similar to those seen in the raw fuel, and also the trichomes that did not degrade in the high temperatures of the deposits or the HT laboratory ashed samples. EDS maps (Figure 6-11) confirm that these are the trichome like structures, as they have the same composition that was observed from the raw fuel (Section 4.1.1) suggesting that decomposition of these structures requires harsher conditions than those present in most regions of the combustion rig.

Presented in the electronmicrograph and EDS maps of Figure 6-12 is a deposit which has melted and incorporates several spheres. The spheres that have not melted are phosphospheres;[192] melting points of phosphates are typically higher than melting points of silicates. The phosphates could have formed in the deposit, firstly through the formation of KPO_3 in the gas phase, followed by deposition and reaction with CaO in the deposit.[210] The presence of the phosphospheres suggests that the spheres formed in the flame, and therefore deposited onto the probe surface. The presence of lower melting point silicates surrounding the Ca-phosphate pockets also supports the deposition mechanism of formation.

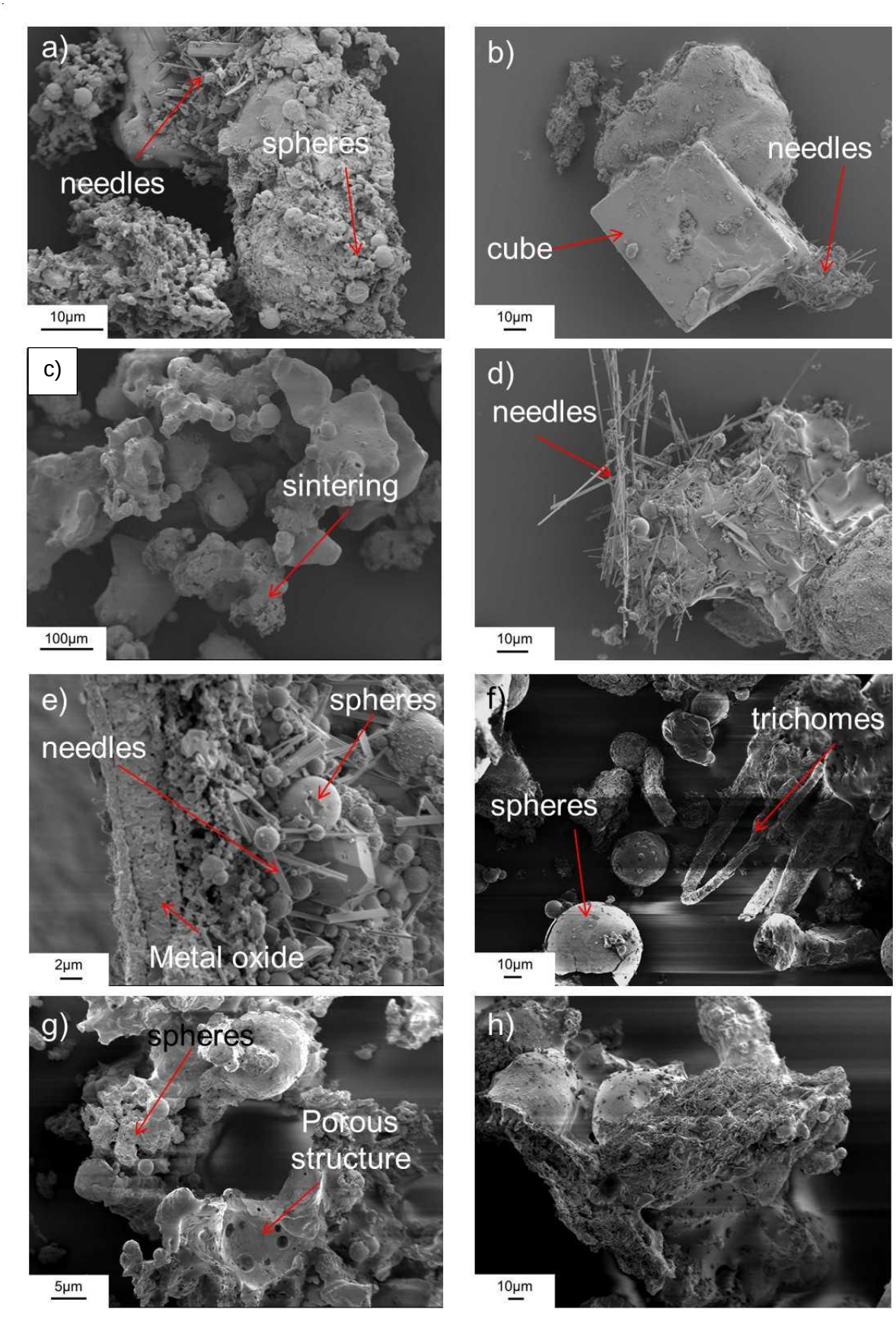

Figure 6-6: SEM electronmicrographs of the 15Mo3 coupon deposits illustrating different morphologies present a) Hemp A b) Hemp B c) Hemp C d) Hemp D e) Hemp E f) Hemp F g) Hemp G h) Hemp H

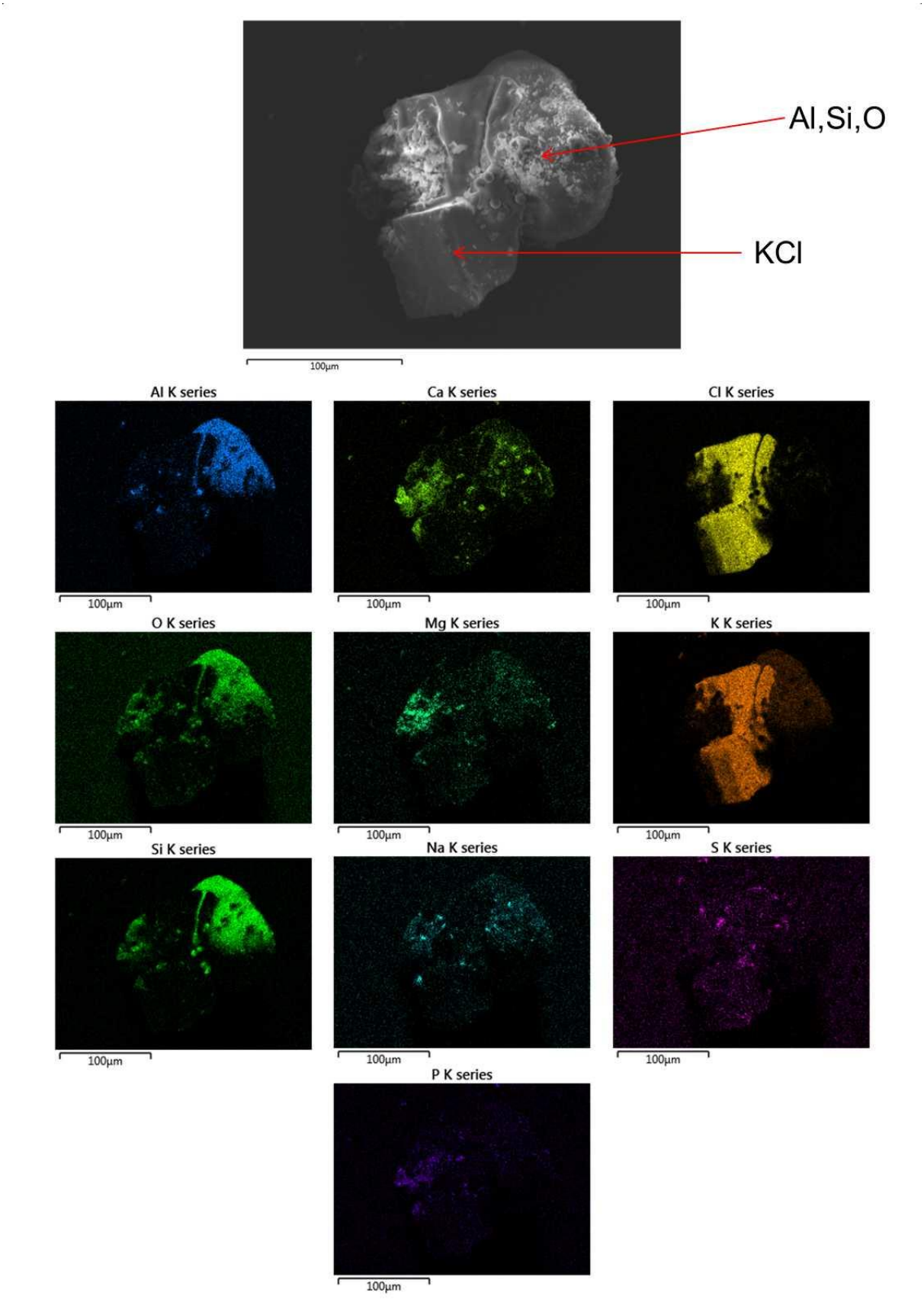

Figure 6-7: An electronmicrograph and EDS maps of a KCl cube present in Hemp B

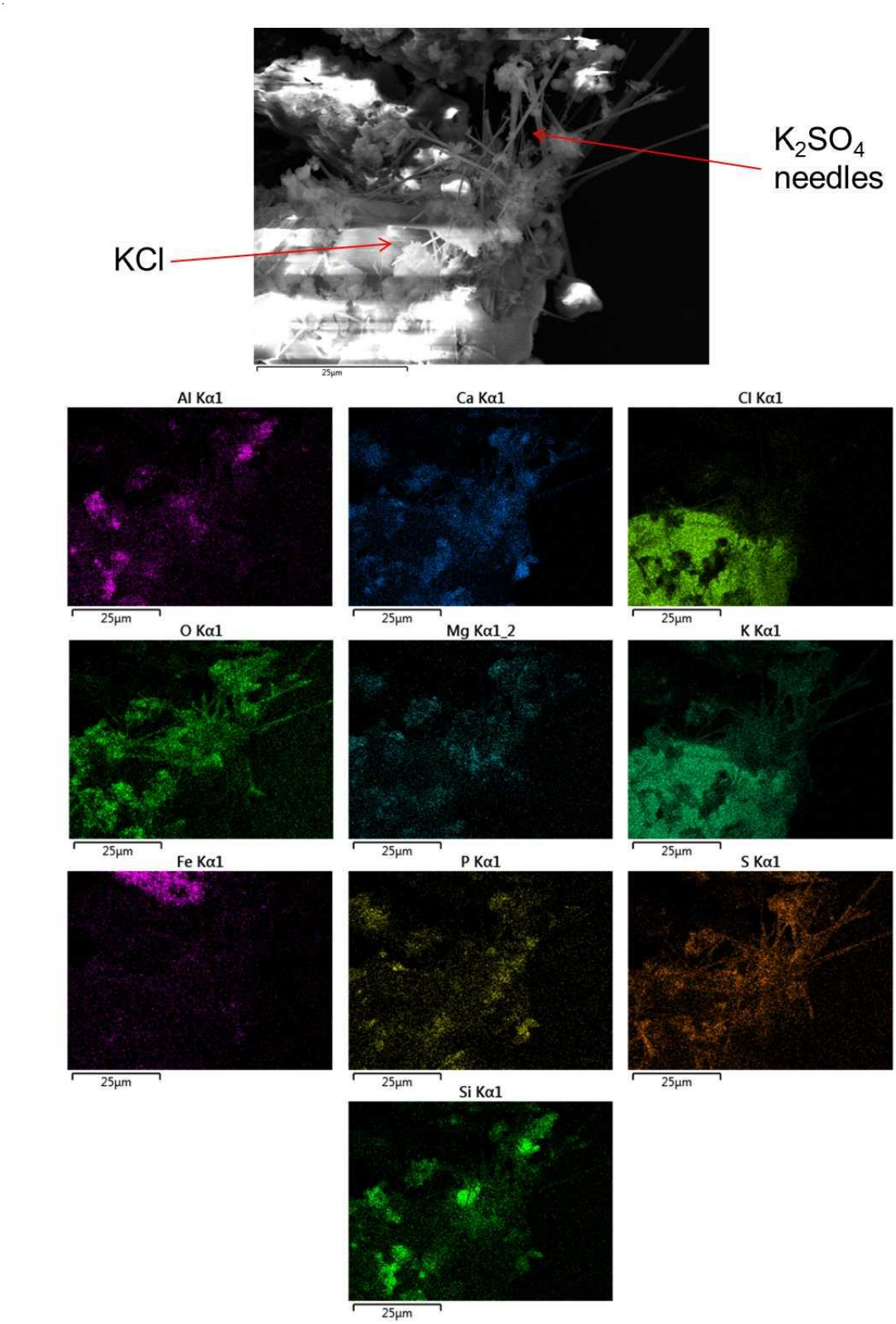

Figure 6-8: An electronmicrograph and EDS maps of showing the needles to be K_2SO4

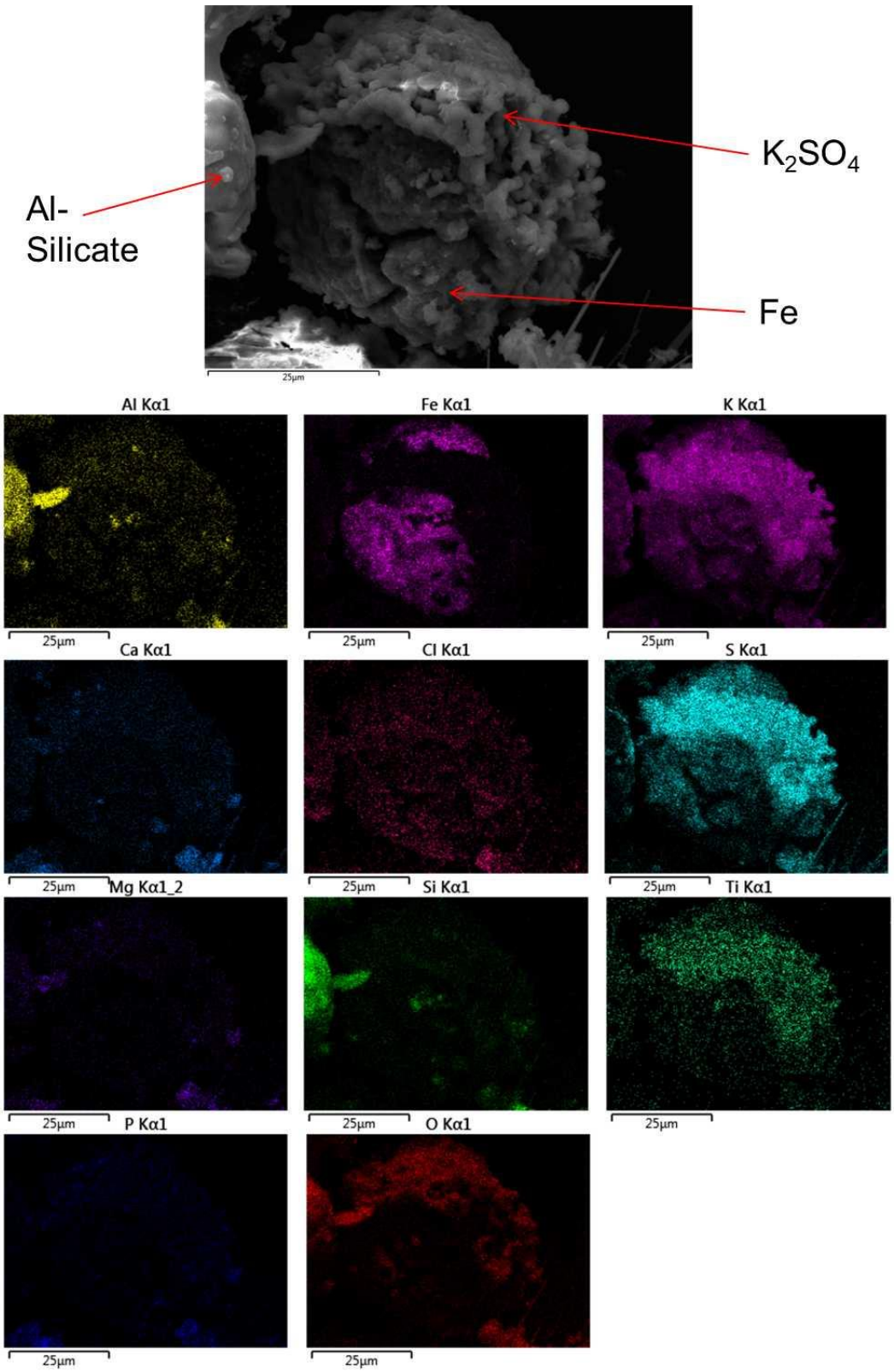

Figure 6-9: An electronmicrograph and EDS maps showing K_2SO4 deposition in both needle and droplet morphology

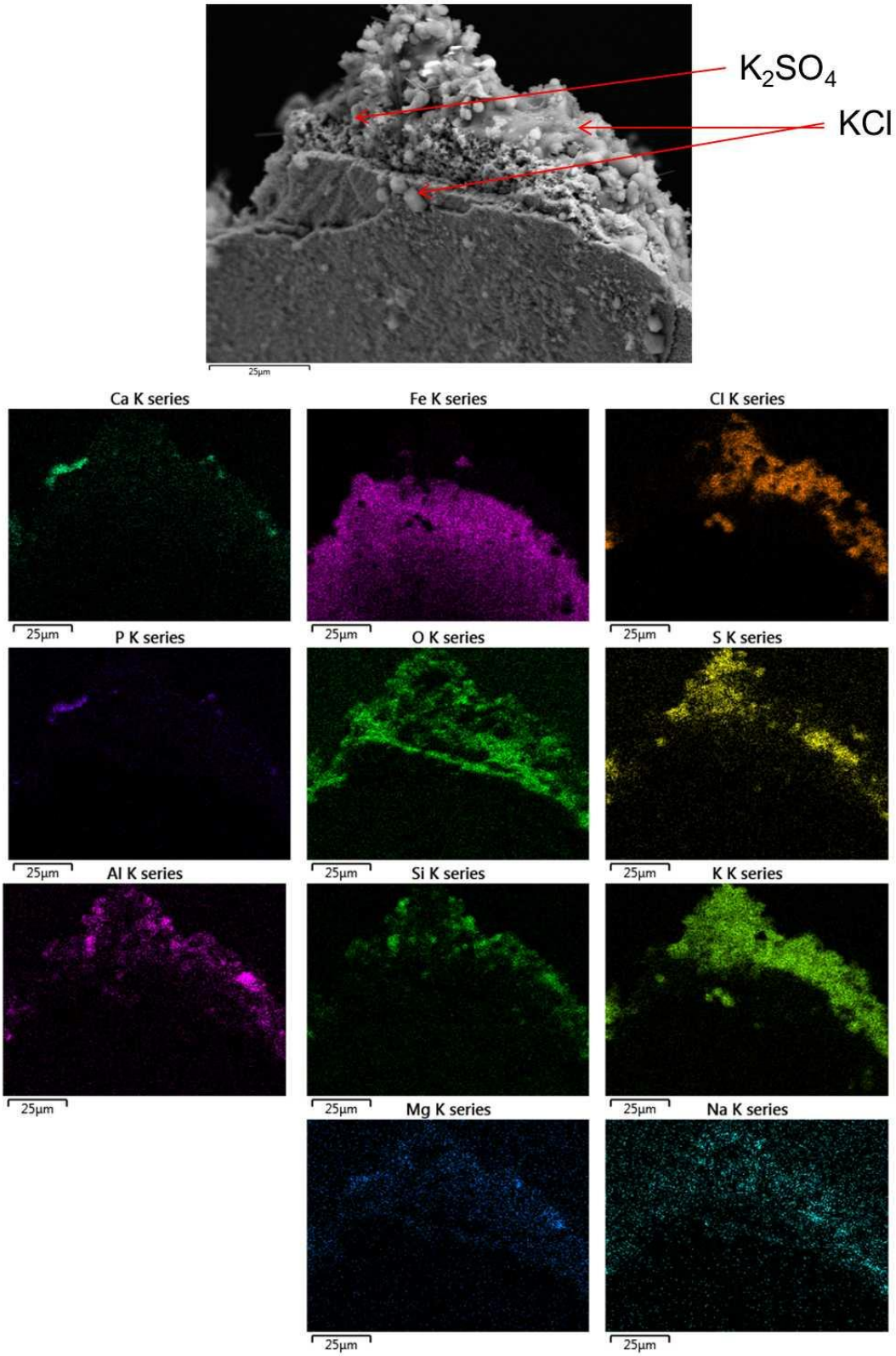

Figure 6-10: An electronmicrograph and EDS Maps of K_2SO4 and KCl on a metal oxide flake

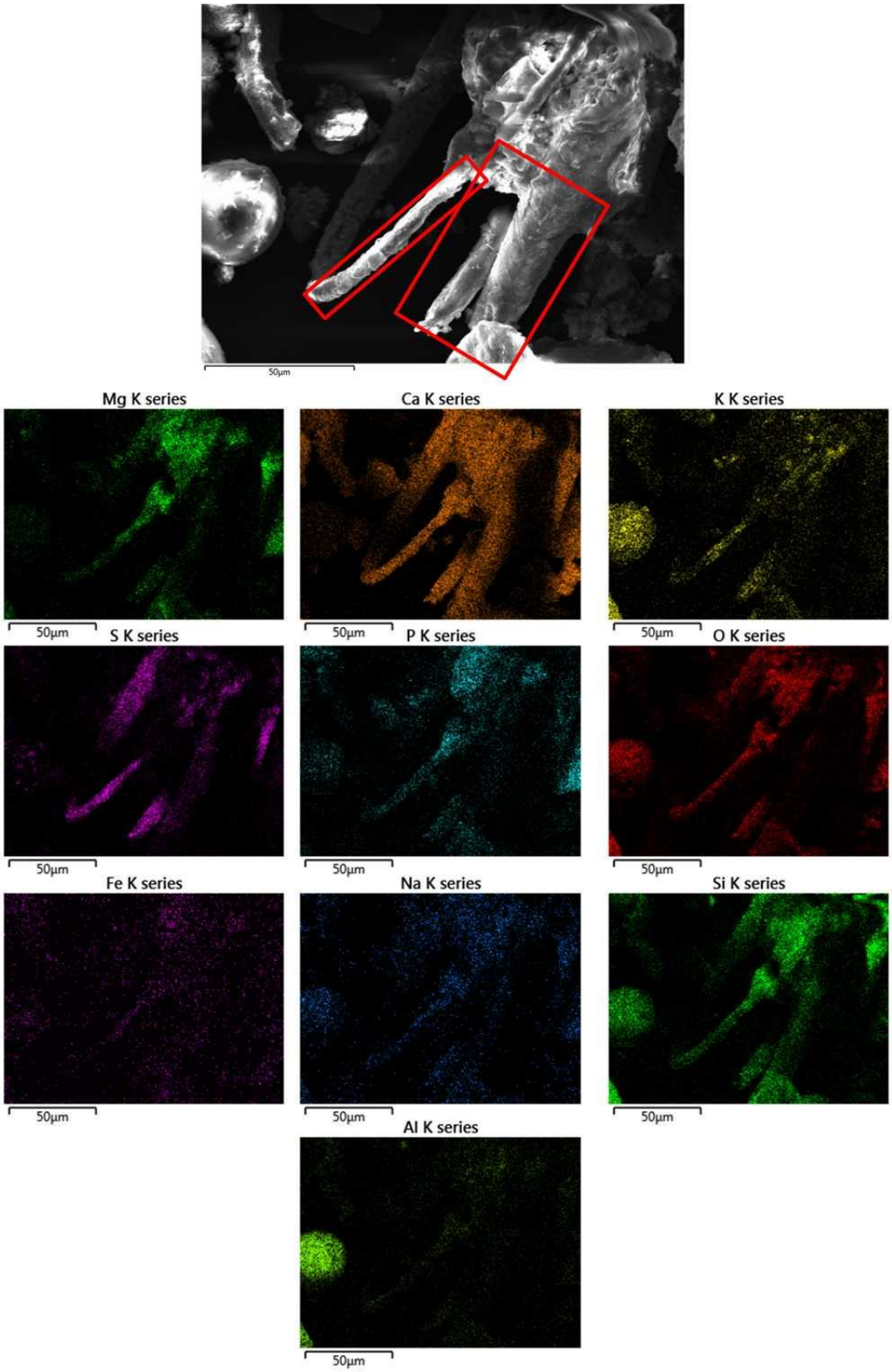

Figure 6-11: SEM electronmicrograph and EDS maps showing trichomes present in Hemp F

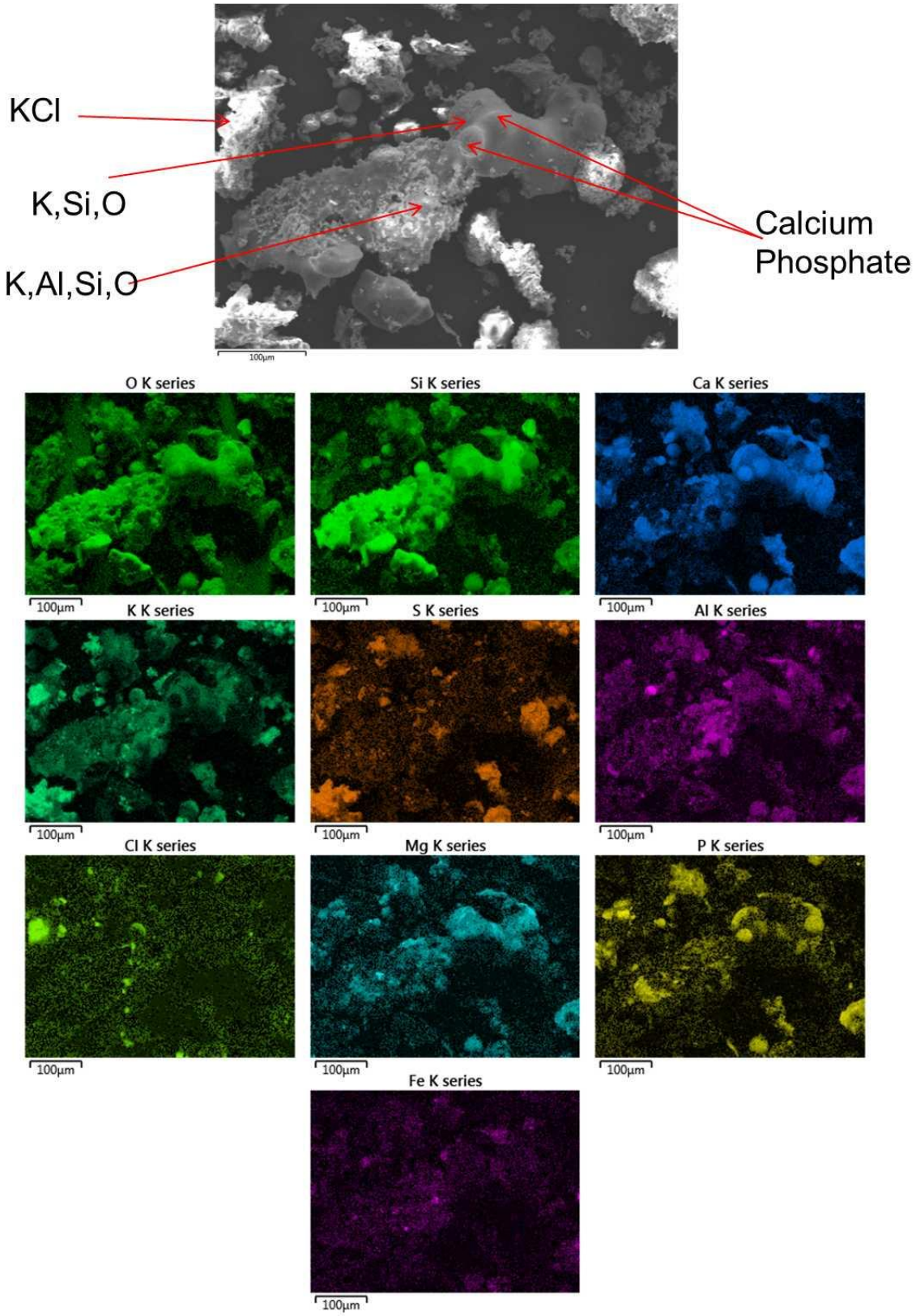

Figure 6-12: An electronmicrograph and EDS maps showing pockets of calcium phosphate in a silicate melt.

6.2.1 Conclusions

The deposits that have attached to the 15Mo3 probe coupons have a largely similar composition to the deposits formed on the ceramic probes in the superheater region of the combustion rig. This is also similar to the high temperature heat treated samples from the laboratory. The trichomes identified in the previous deposits are also present in these samples.

Large cubic KCl particles are visible under reducing atmospheres; these are thought to have deposited through a diffusion mechanism as the surface of the coupons are cooler than the gas temperature. The deposition of KCl can lead to active oxidation of the coupon surface, which can in turn lead to oxide spalling upon cooling, and therefore an increase in corrosion. Evidence of metal oxide flakes with KCl deposition is presented in Figure 6-10. The KCl on this sample is also associated with K_2SO_4, and therefore the reaction according to, Equation 6-27, can be assumed. The presence of K_2SO_4 needles in several of the samples also confirms this mechanism of formation as reaction of KCl in the deposit with SO_2, released during the combustion of the fuel, to allow the formation of needle crystals.

There is evidence of sintering in the deposits which can then lead to slagging and flow. This is undesirable as it can retard heat transfer. The presence of higher melting point silicates, e.g. akermanite and diopside, indicates less slagging may occur.

6.3 Analysis of the eucalyptus and coal boiler coupon surface deposits

Gas profiles of CO and O_2 for the probes are presented in Figure 6-13 and Figure 6-14. Clear differences in the gas conditions local to each probe coupon are visible. Under oxidising conditions (those with high% O_2), oxide scales are more likely to form. Target temperatures and whether the sample was exposed to a largely oxidising or reducing atmosphere are presented in Table 6-4. Sample collection points in the boiler are presented in Figure 6-15; variation between samples, due to boiler position, is expected.

Table 6-4: Temperature and gas conditions of Eucalyptus Co-fire boiler probe deposit samples

Sample	Temperature (°C)	Atmosphere
EUCCO A	475	Reducing
EUCCO B	450	Reducing
EUCCO C	425	Oxidising
EUCCO D	475	Reducing
EUCCO E	475	Oxidising
EUCCO F	475	Oxidising
EUCCO G	450	Oxidising
EUCCO H	425	Oxidising

Table 6-5: Phases present in eucalyptus and coal probe deposit samples. There was an insufficient amount of EUCCO D and E to analyse with PXRD.

Phase	Key	Composition	EUCCO A	EUCCO B	EUCCO C	EUCCO F	EUCCO G	EUCCO H
Quartz	Qz	SiO_2	•	•	•	•	•	•
Leucite	Le	$KAlSi_2O_6$	•					
Diopside	Di	$CaMgSi_2O_6$	•					
Albite	Ab	$NaAlSi_3O_8$	•					
Akermanite	Ak	$Ca_2MgSi_2O_7$	•					
Gehlenite	Ge	$Ca_2Al_2SiO_7$	•					
Periclase	P	MgO	•					•
Arcanite	Ac	K_2SO_4	•	•				
Magnetite	Ma	Fe_3O_4	•	•	•	•	•	•
Cristobalite	Cr	SiO_2	•					
Calcium Chromium Oxide	Not shown		•					
Fairchildite	Fa	$K_2Ca(CO_3)_2$			•			
Microcline	Mi	$KAlSi_3O_8$				•		
Sylvite	Sy	KCl		•				
Hematite	He	Fe_2O_3		•	•		•	•
Grossular	Gr	$Ca_3Al_2(SiO_4)_3$		•				•
Anhydrite	An	$CaSO_4$			•	•	•	•
Anorthite	Ao	$CaAl_2Si_2O_8$				•		
Nickel Oxide	Ni	NiO					•	•
Tremolite	Not shown	$Ca_2(Mg,Fe)_5Si_8O_{22}(OH)_2$					•	
Chomium Oxide	CrO	Cr_2O_3						•
Natrite	Na	$NaCO_3$						•

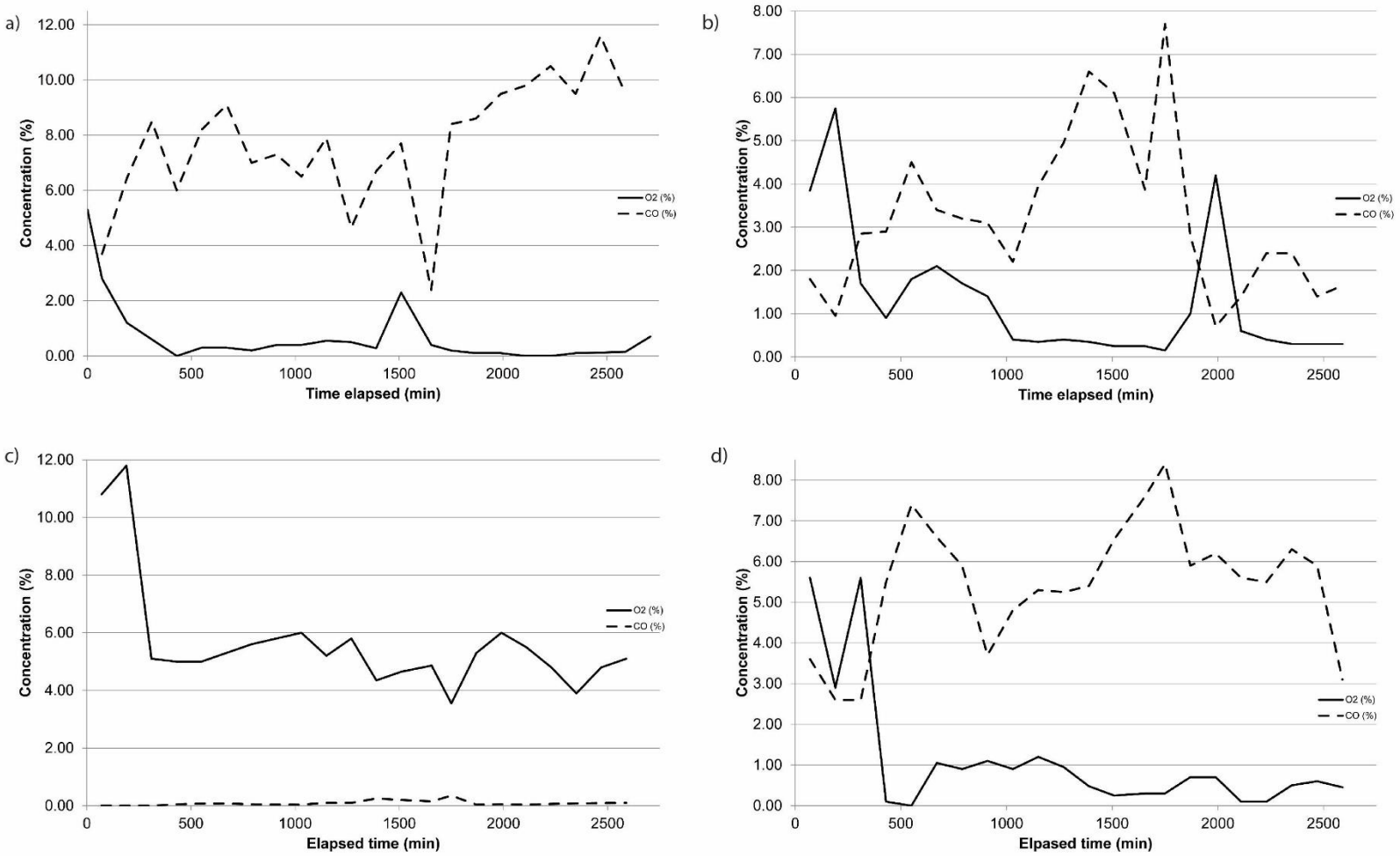

Figure 6-13: Coupon O2 and CO2 gas conditions for the eucalyptus and coal combustion trial a) EUCCO A b) EUCCO B c) EUCCO C d) EUCCO D

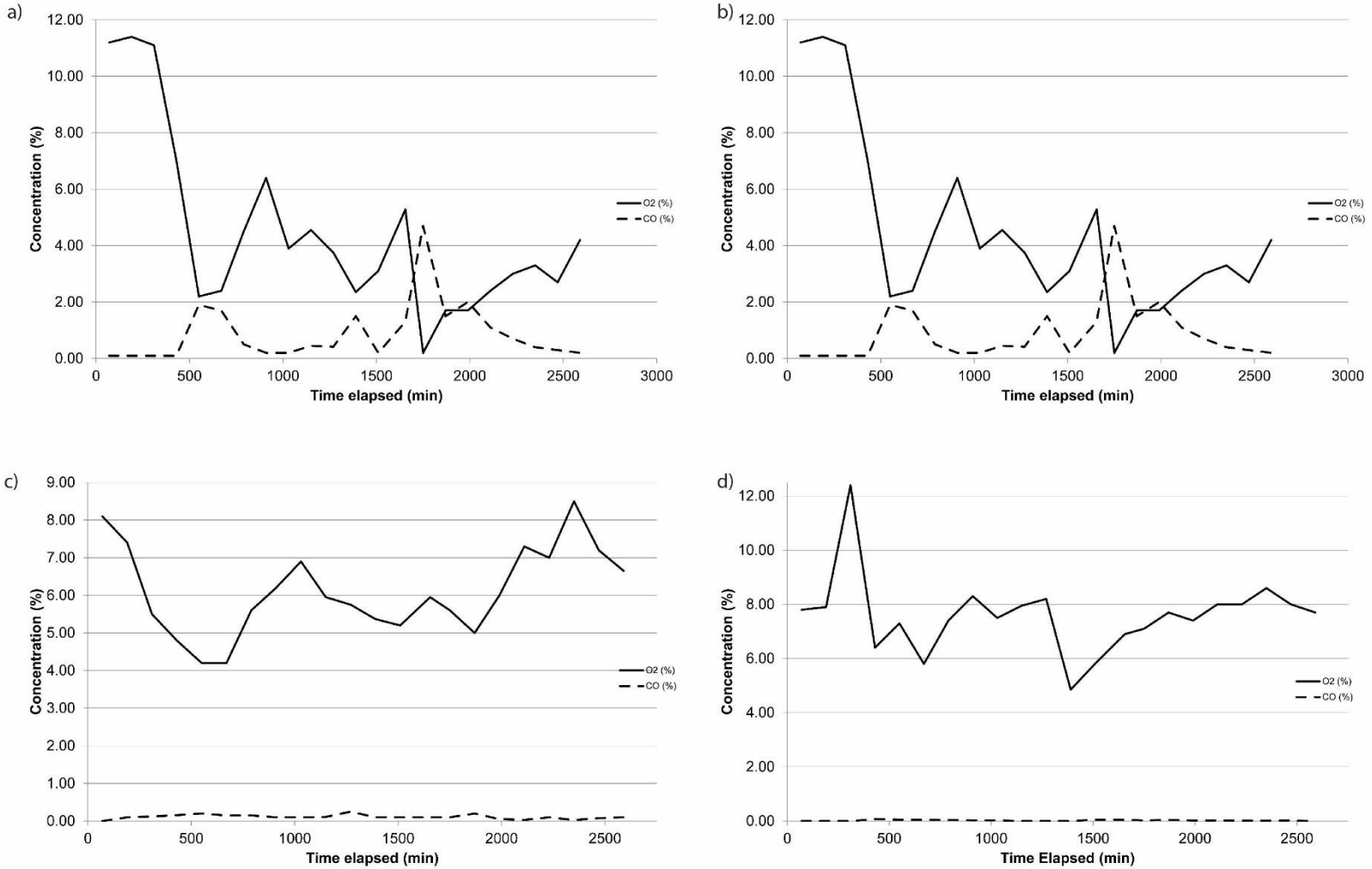

Figure 6-14: Coupon O2 and CO2 gas conditions for the eucalyptus and coal combustion trial a) EUCCO E b) EUCCO F c) EUCCO G d) EUCCO H

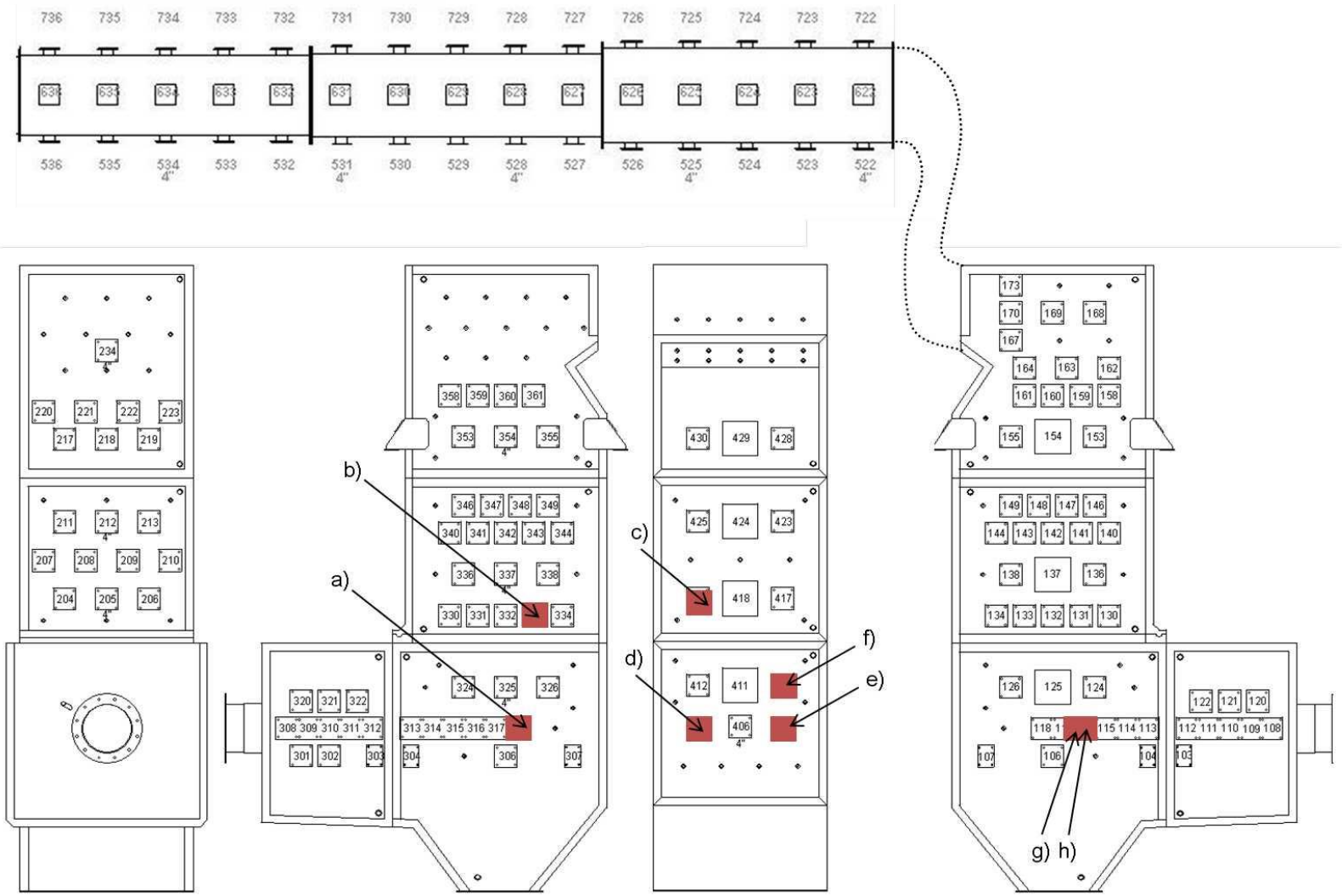

Figure 6-15: Port positions for probes containing the coupon samples a) EUCCO A b)EUCCO B c)EUCCO C d)EUCCO D e) EUCCO E F) EUCCO F g) EUCCO G h) EUCCO H

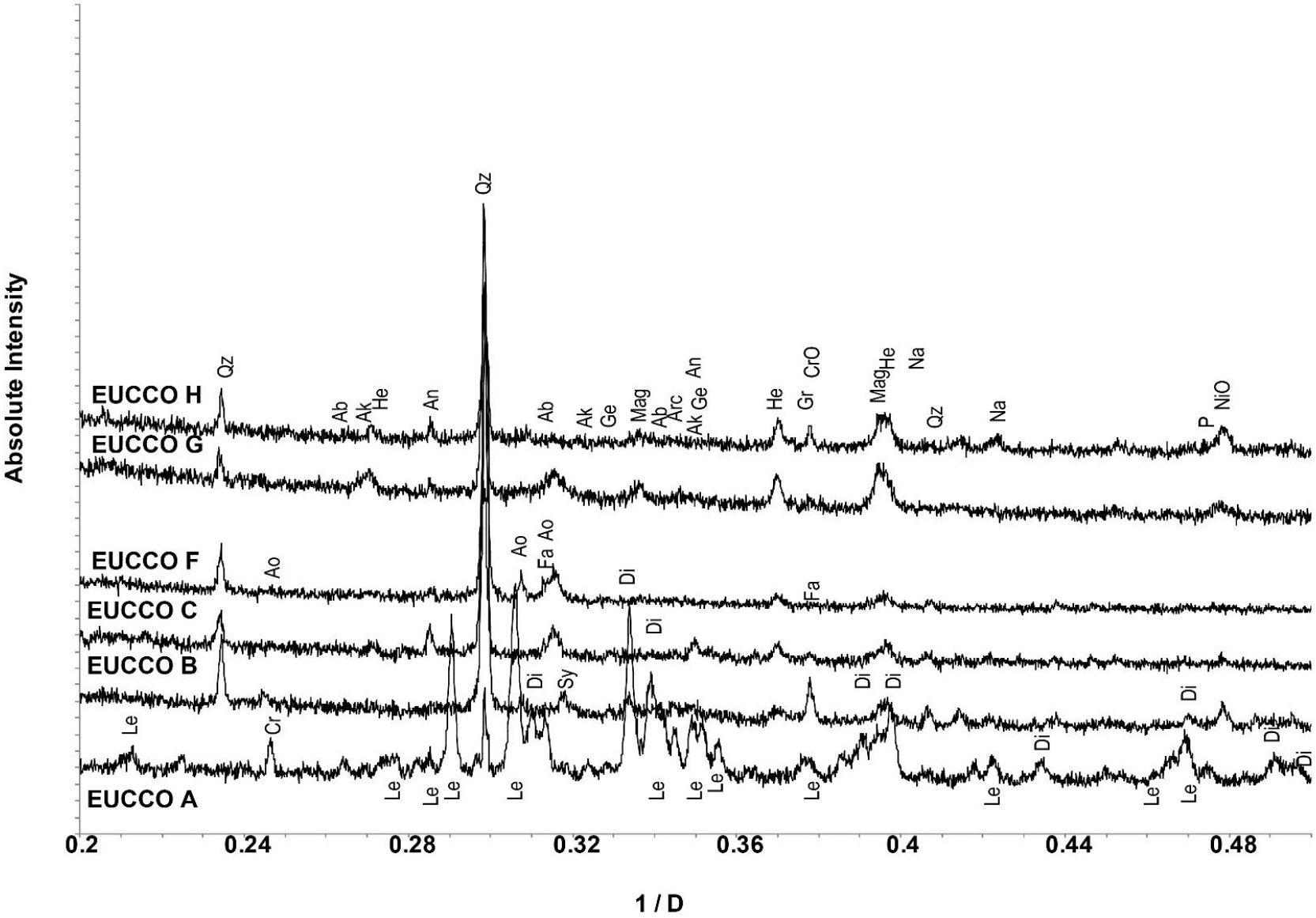

Figure 6-16: PXRD patterns for EUCCO coupon deposits data collected on the D2 diffractometer (Cu Kα radiation)

The metal oxides hematite, magnetite and Cr_2O_3 are present (Figure 6-16, Table 6-5), this suggests oxidation of the 15Mo3 coupons. These metal oxides were present under both oxidising and reducing conditions, suggesting that some breakaway oxidation (significant changes in oxidation rate which creates oxide cracks resulting in a loss of oxide scales upon cooling) has occurred. Chang *et al*.[219] state that at temperatures below 570°C the Fe-oxides magnetite and hematite will be present. As the temperature increases the phase wüstite (FeO) will also form. Characterisation of low alloy steels at high temperatures by Higginson *et al*.[218] agreed with these conclusions. The NiO present in the samples is from the anti-seize grease, used to allow coupon removal from the probe, and is unlikely to be an oxidation product from the minimal amount of Ni present in the alloy.

Anhydrite ($CaSO_4$) was present in the samples that experienced oxidising atmospheres, suggesting preferential formation under these conditions irrespective of temperature. The carbonates natrite ($NaCO_3$) and fairchildite ($K_2Ca(CO_3)_2$) were also only present under oxidising conditions, suggesting they formed through oxidation and reaction in the deposit between char particles and oxides present in the fuels.

The feldspars albite, microcline, and anorthite were present in reducing and oxidising conditions. This suggests that, either formation is unaffected by redox conditions, or that they are already present as large debris present from harvesting, in the biomass ash which do not deviate with the gas flow and therefore impact into the probes and deposit. Under reducing conditions, cristobalite (SiO_2) had formed; in Section 4.2.1 the reactivity of polymorphs of SiO_2 is discussed. Cristobalite is only identified in EUCCO A; this sample also has the greatest variation in silicates present, further indicating it is the more reactive SiO_2 polymorph. Research by Ringdalen[222] suggests that cristobalite is not as readily formed under reducing conditions in comparison to inert conditions, however cristobalite formation was also dependent on the SiO_2 source meaning that many factors (e.g. particle size and Si speciation in the biomass) may affect the formation.

Also identified in samples under reducing conditions are KCl and K_2SO_4. Petterson *et al*.[92] showed that KCl deposits onto 304-type austenitic alloys leading to an increase in breakaway oxidation, in particular around grain boundaries. As the KCl is present under reducing conditions, it may be that more breakaway oxidation has occurred in the samples formed under a reducing atmosphere. K_2SO_4 is most commonly formed through the sulphation of KCl.

Figure 6-17 presents an electronmicrograph of an oxide scale with a large amount of KCl deposited onto the surface, the deposition mechanism of KCl onto the surface of the probe is diffusion (Section 2.3). The particles are fairly large in size which suggests that some may have formed through homogenous nucleation in the flue gas. These large deposits were only imaged on flakes found under reducing conditions, although EDS mapping of other samples indicate that regions of KCl are present under oxidising conditions (Figure 6-18).

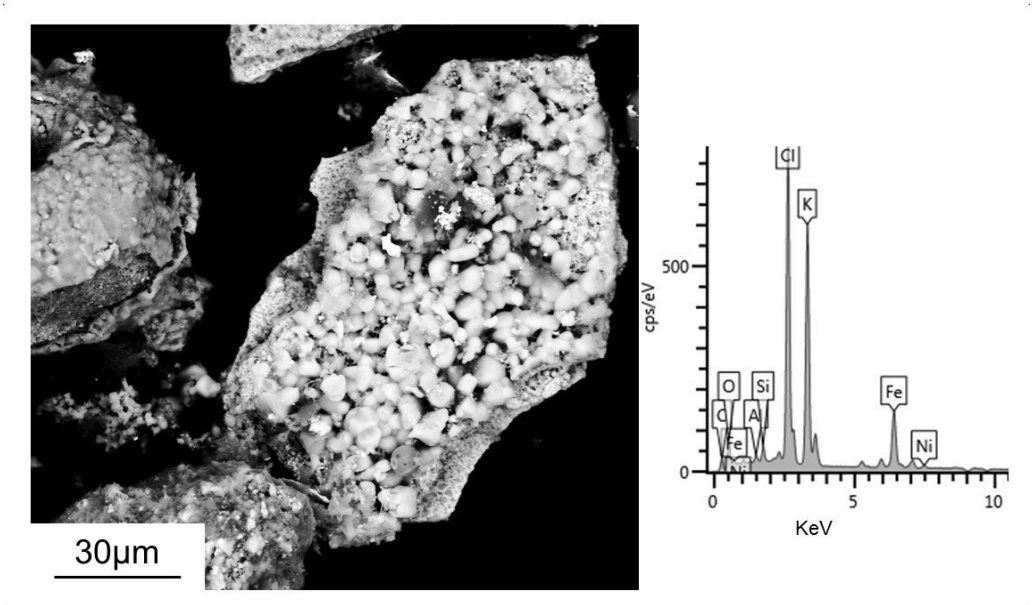

Figure 6-17: SEM micrograph and EDS spectrum of KCl deposition onto the surface of an oxide scale under reducing conditions in sample EUCCO B

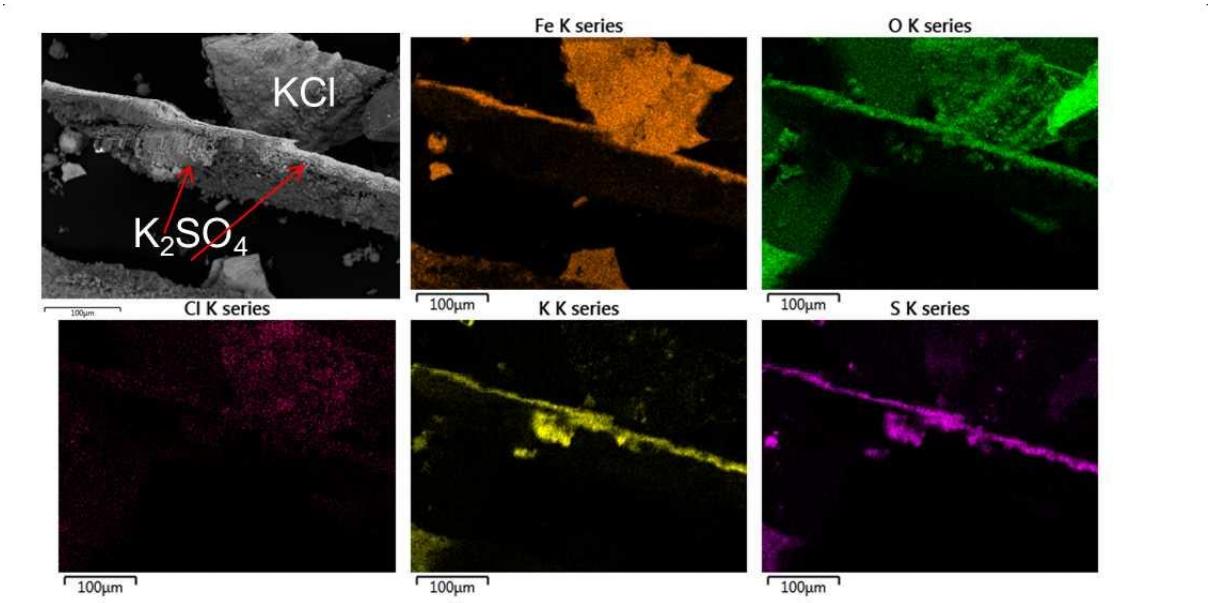

Figure 6-18:Electronmicrograph and EDS maps of KCl and K_2SO4 deposition onto metal oxide flakes in sample EUCCO G

A linescan of an oxide scale in sample EUCCO G (Figure 6-19) shows clear separation between oxide and deposit regions. There is also clear association of K and S. This is similar to the oxide scale observed in Figure 6-18. The K_2SO_4 present is likely to have deposited through the diffusion mechanism proposed by Zbogar *et al.*,[60] or through the reaction of SO_2 with KCl that had previously deposited onto the scale, causing an increase in the active oxidation cycle. The silicate spheres present in the deposit region of the scale deposit through the inertial impaction mechanism, and may undergo reaction post deposition.

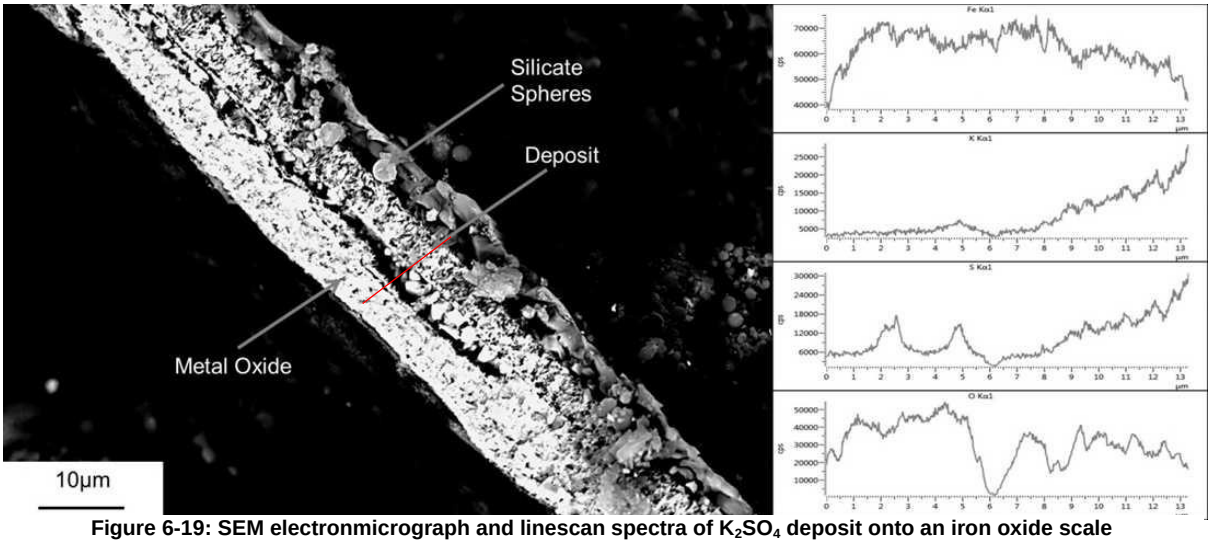

Figure 6-19: SEM electronmicrograph and linescan spectra of K_2SO_4 deposit onto an iron oxide scale

EDS analysis of the oxide scale formed under a reducing atmosphere in EUCCO B shows the presence of Cr oxide and Mn oxide, alongside Fe oxide. Considering the Cr content of 15Mo3 is 0.22% (Table 3-4) the Cr enrichment in the scale appears high. The enrichment of Cr in scales formed on low-alloy steels under reducing conditions, was also found in research by Uusitalo *et al*..[109] Wood[225] stated that the initial oxidation of Cr (when the alloy contains less that 0.2%) is more rapid in comparison to the oxidation of Fe; this in turn can lead to a Cr maximum at the inner/outer scale interface. Oxidation rates are likely to be faster under reducing conditions than oxidising conditions.[225] The increase in Cr content of the scale can be explained by this preferential oxidation. Fe and Cr are present in close association with one another which suggests the presence and formation of Fe,Cr spinel. Also associated in the EDS maps are K_2SO_4 present on metal oxide scales. The presence of the Ni is likely to be due to the grease used in the lubrication of the probe.

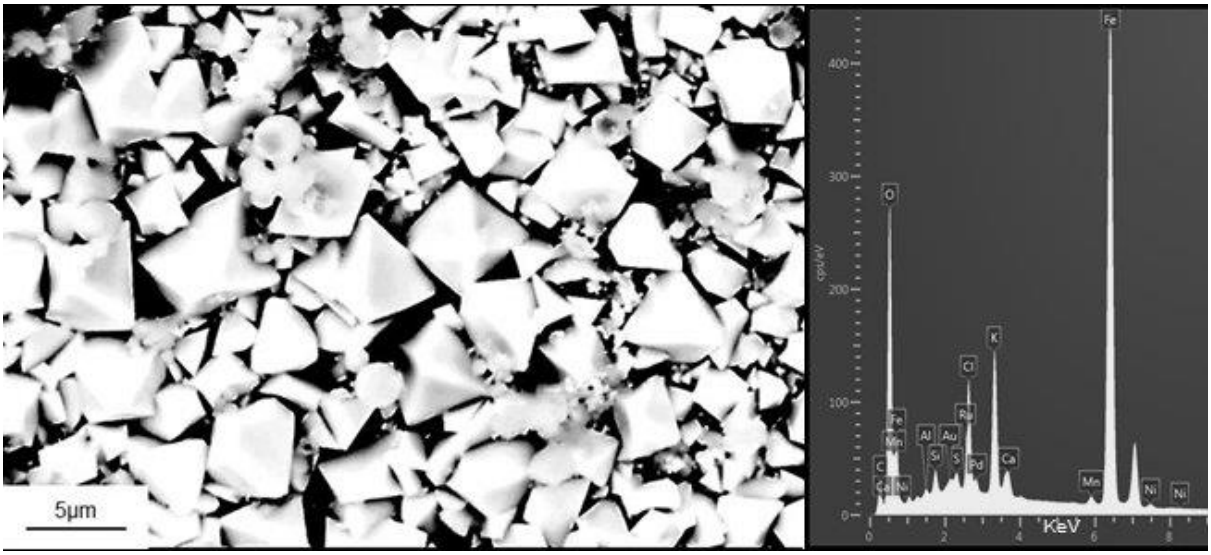

Figure 6-20: Magnetite Octahedral Crystals visible under both oxidising and reducing conditions, SEM-EDS analysis of the octahedral regions

The iron oxide magnetite (Fe_3O_4) that was shown as present through PXRD analysis (Figure 6-16). On several oxide scales in EUCCO B octahedral crystals characteristic of magnetite are visible (Figure 6-20). EDS analysis of these octahedral crystal shows that they are largely comprised of Fe and O which, coupled with their morphology, confirms that they are Fe_3O_4. Small amounts of Mn and Ni are also present in the scale suggesting that this oxide flake was removed from the 15Mo3 alloy coupon. The Ca, Al, Si and O present in the spectrum are from the spheres present on the magnetite deposit surfaces. The K and Cl, which is likely to be present as KCl, is thought to have induced $FeCl_2$ transport to the surface of the deposit. After encountering O_2 at the deposit surface octahedral crystals will form through the active oxidation mechanism.[85]

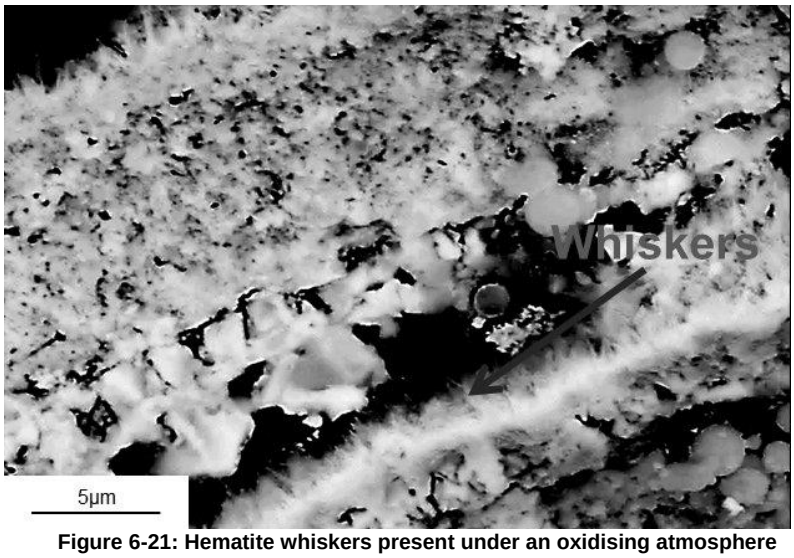

Figure 6-21: Hematite whiskers present under an oxidising atmosphere

Cracks in the oxide scales, either at the deposit oxide interface or between an oxide-oxide interface, were observed. Whiskers were observed in these cracks in the scales formed under oxidising conditions only (Figure 6-21). Higginson *et al.*[226] in their study on whisker growth morphology of high temperature oxides showed that these whiskers are highly likely to be hematite. There is a difference in opinion to how these whiskers form. Yuan *et al*.[227] state that whisker growth occurs at the hematite/magnetite boundary. In comparison Higginson *et al*.[226] and Pettersson *et al*.[104] found that the whiskers were most likely to form in areas where breakaway oxidation has occurred.

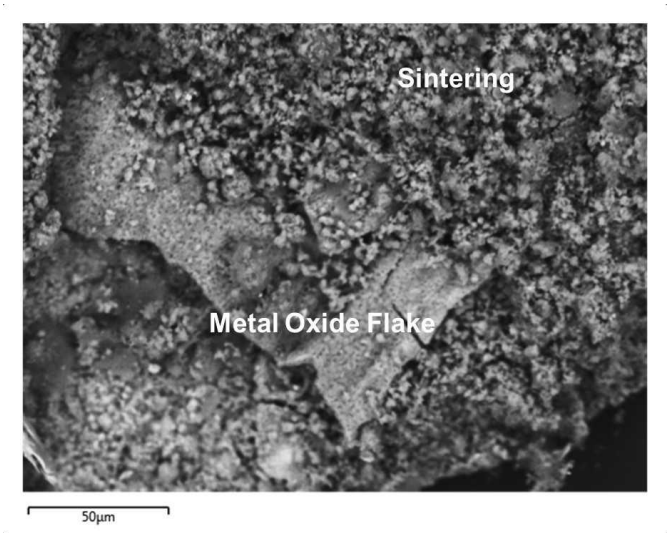

Figure 6-22: Electronmicrograph of EUCCO E showing a metal oxide with a sintered deposit

Alongside the alloy oxidation products there was also evidence of sintering in the deposit. An electronmicrograph of EUCCO E (Figure 6-22) shows sintering in a deposit onto a metal oxide surface. Sintering is often caused by low melting point silicates, which can then cause an in-deposit heat flux, and create a corrosive environment. This potentially explains the presence of the metal oxide flake in the deposit.

Sintering was also observed in EUCCO A deposits (Figure 6-23) . Strong association between Ca, Al/Mg Silcates, corresponds to the gehlenite and akermanite identified in PXRD analysis of the sample. There is also close association between K, Al, Si, and O which is likely to be leucite identified in PXRD. Present in this deposit is also a close association of K,Ca, C and O which is suggestive of the carbonate fairchildite, this has not been identified using PXRD however it could be present in minor quantities undetectable using PXRD. The C through the deposit is likely to be from unburnt char particles which did not undergo complete combustion.

Loose silicates, unattached from oxide flakes were also observed, Figure 6-24 illustrates several spheres often observed during biomass and coal combustion. Ca, Al silicates and K,Al-silicates were observed. There were some areas of association between K, Al silicates and K_2SO_4, suggesting an in deposit reaction forming the silicates through a reaction of K_2SO_4 and SiO_2. Also visible in this area were the Ni flakes probably from the joint grease which allows removal of the probe coupon after the combustion trial.

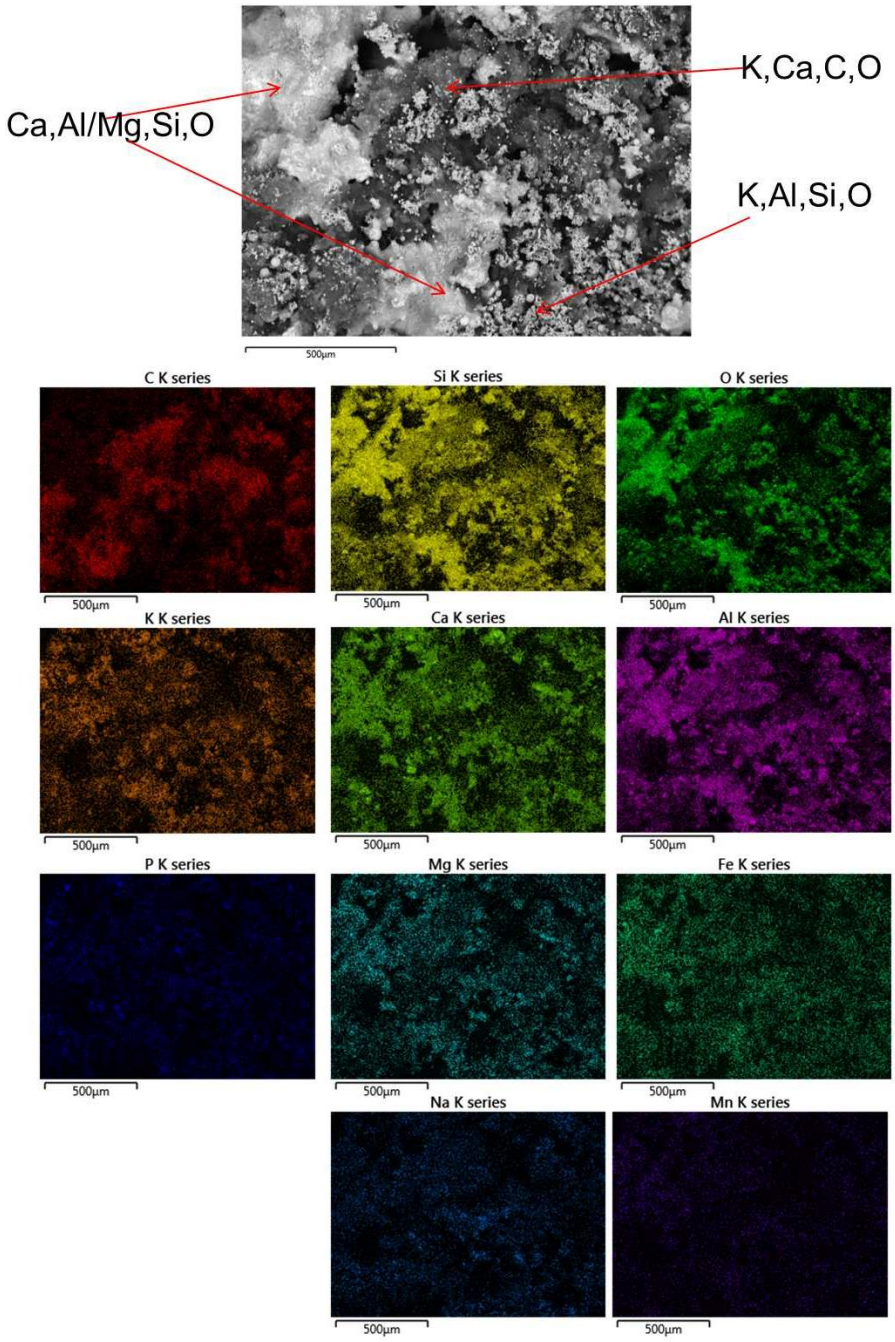

Figure 6-23: SEM electronmicrograph and EDS maps from sample EUCCO A showing akermanite/gehlenite and leucite deposition alongside unburnt C deposition

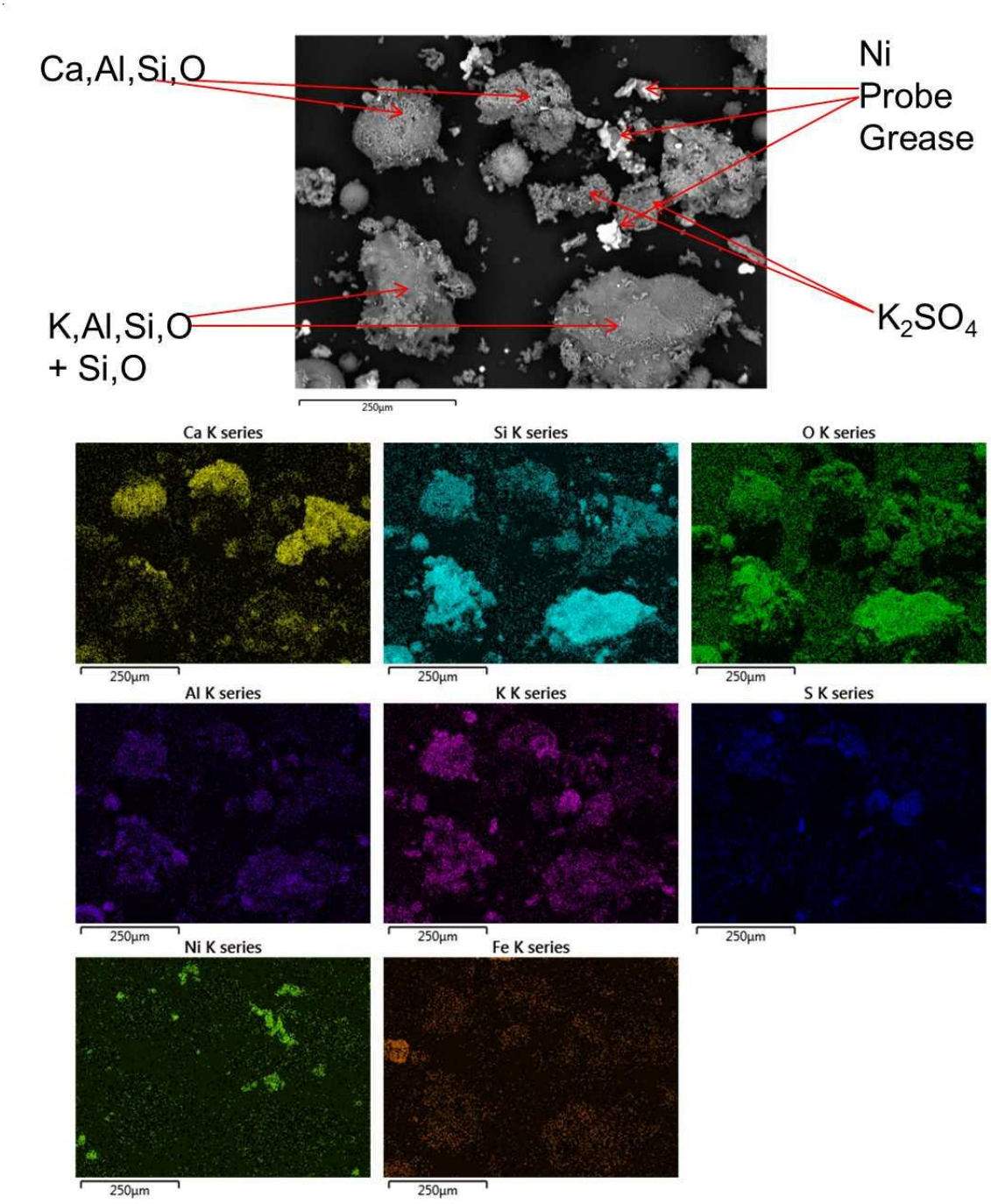

Figure 6-24: An electronmicrograph and EDS maps of EUCCO D showing silicates present as well as Ni joint grease

6.3.1 Conclusions

There is clear evidence of oxidation of the 15Mo3 coupons during the eucalyptus and coal combustion trials. The samples under a reducing atmosphere showed large KCl deposits onto the coupons, which can lead to an increased rate of breakaway oxidation.

Magnetite octahedra have been observed under both reducing and oxidising conditions, KCl was also visible around these octahedra suggesting their formation occurs during active oxidation. Hematite whiskers, which are present under oxidising conditions are observed, although reasons for their formation are still unclear.

There are multiple silicates present in the deposits; the akermanite and gehlenite, which were observed in the laboratory high temperature heat-treated eucalyptus and coal ash, are also identified in these samples, confirmed through PXRD and EDS analysis. Leucite, a K-Al silicate, is present in the scale deposits; this phase was also observed in the HT eucalyptus and coal ash analysed during the in house experiments.

6.4 Analysis of the eucalyptus boiler coupon surface deposits

Eleven samples (EUC A-K) were analysed, each sample was in a different port of the combustion rig (Figure 6-25). The gas profiles of CO and O_2 for the probes are presented in Figure 6-26, Figure 6-27 and Figure 6-28. Clear differences in the gas composition surrounding the samples are visible. The mean temperatures of the samples are presented in Table 6-6, alongside the sample atmosphere (oxidising or reducing). The base alloy of the samples is 15Mo3 however the samples are also coated or clad with other materials (Table 6-6). The composition of these coatings is presented in Table 3-7. These coatings aim to present an economic way of increasing lifetime of boiler components.

Table 6-6: Corrosion Probe Mean surface temperature and atmosphere Red denotes coating application using HVOF method Blue denotes coatings applied using the laser cladding method

Probe	Material	Mean surface Temperature (°C)	Atmosphere
EUC A	15Mo3 (NiCrAlY + 50Cr50Ni)	400	Reducing
EUC B	15Mo3 (NiCrAlY + 50Cr50Ni)	440	Reducing
EUC C	15Mo3 (NiCrAlY + 50Cr50Ni)	450	Reducing
EUC D	15Mo3 (FeCrAl + IN625)	485	Reducing
EUC E	15Mo3 (NiCrAlY + 50Cr50Ni)	475	Reducing
EUC F	15Mo3 (FeCrAl + IN625)	425	Reducing
EUC G	15Mo3 (50Cr50Ni + C276)	425	Reducing
EUC H	15Mo3 (FeCrAl + IN625)	500	Reducing
EUC I	15Mo3 (50Cr50Ni + C276)	435	Reducing
EUC J	15Mo3 (FeCrAl + IN625)	500	Oxidising
EUC K	15Mo3 (NiCrAlY + 50Cr50Ni)	450	Oxidising

PXRD analysis of the samples is presented in Figure 6-29, Figure 6-30, and Table 6-7. The Fe oxides hematite, magnetite, and wüstite were present in the samples, suggesting oxidation of the 15Mo3 samples. Wüstite (FeO) is only present under reducing conditions (EUC C,D and E). The Fe-O phase diagram indicates that under reducing conditions (low wt% O_2) wüstite will form alongside α-Fe and magnetite at temperatures above 570°C. Magnetite is present in samples EUC C, D and E suggesting reduction of magnetite to wustite during the combustion test. Samples EUC C, D and E are in similar positions in the boiler (Figure 6-25), and they may have been in the flame, and therefore reached higher temperatures than the other samples. Other metal oxides (e.g. Cr_2O_3) are not present in the XRD analysis of the samples, which suggests some of the metal oxide scales may have come from the rings used to secure the coupons to the probes.

Figure 6-25: Probe positions for the eucalyptus combustion run probes a) EUC A b) EUC B c) EUC C d) EUC D e) EUC E f) EUC F g) EUC G h) EUC H i) EUC I j) EUC J k) EUC K

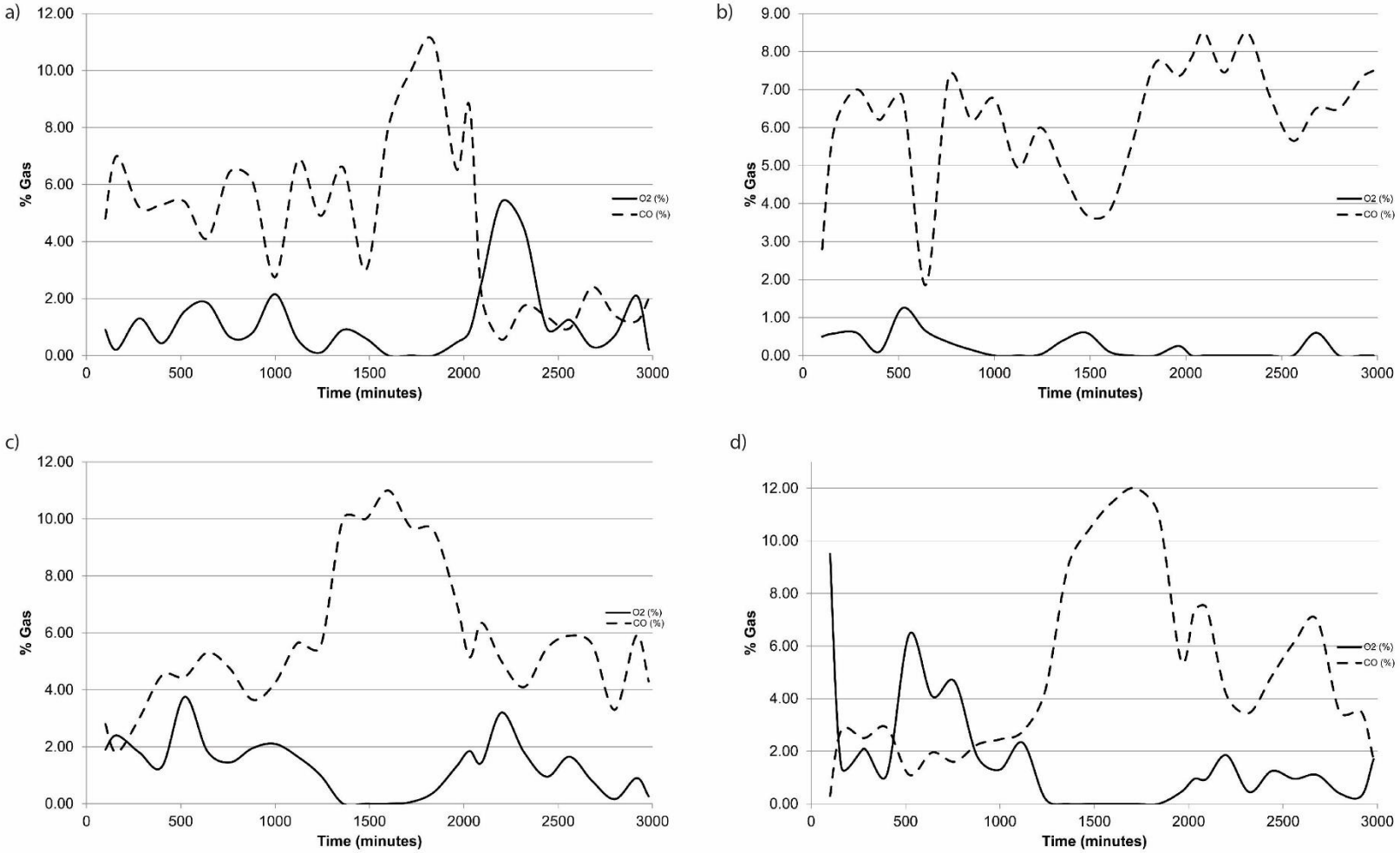

Figure 6-26: Gas conditions sampled every two hours from 15Mo3 probes in the eucalyptus combustion test . a) EUC A b) EUC B c) EUC C d) EUC D

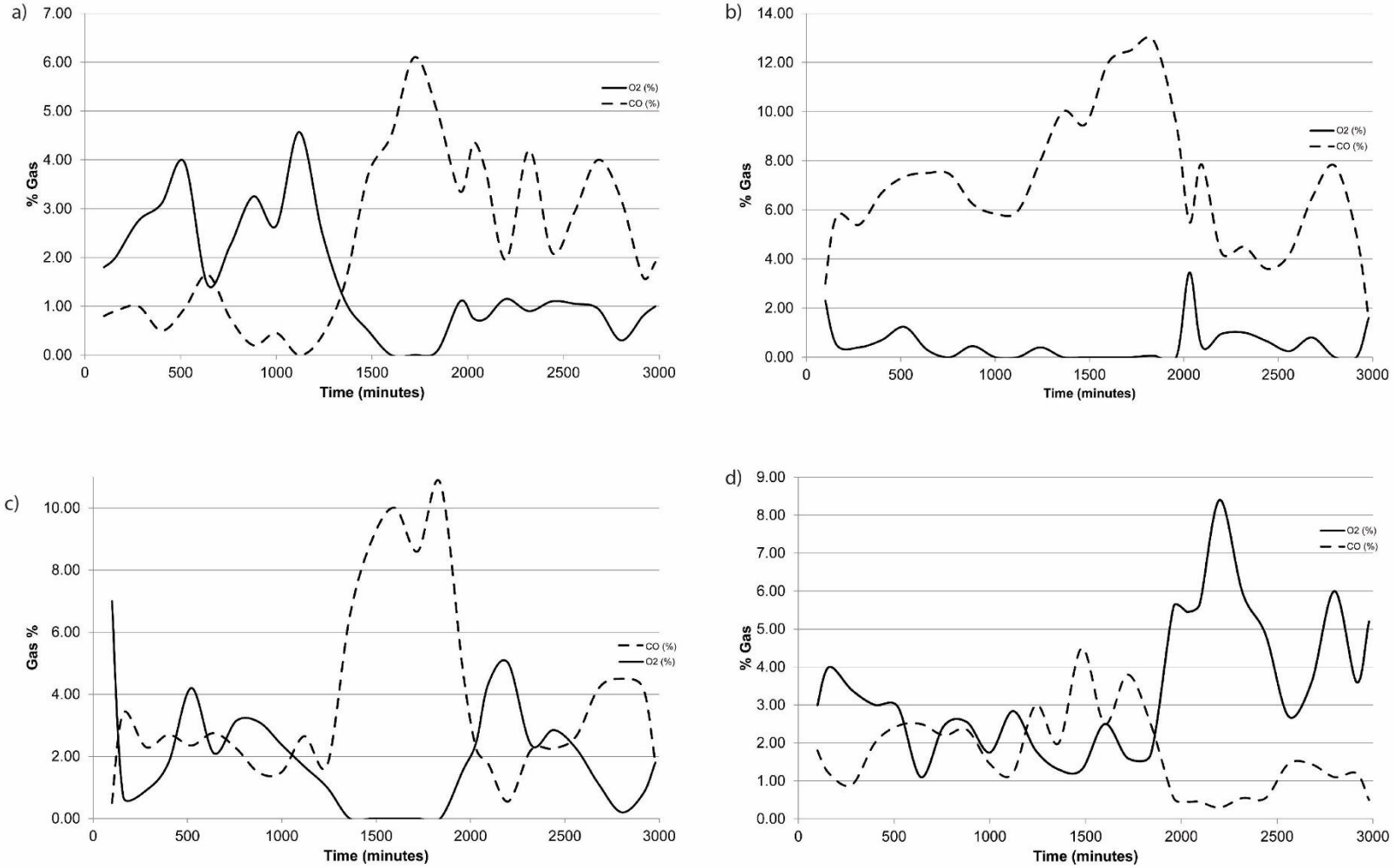

Figure 6-27: Gas conditions sampled every two hours from 15Mo3 probes in the eucalyptus combustion test . a) EUC E b) EUC F c) EUC G d) EUC H

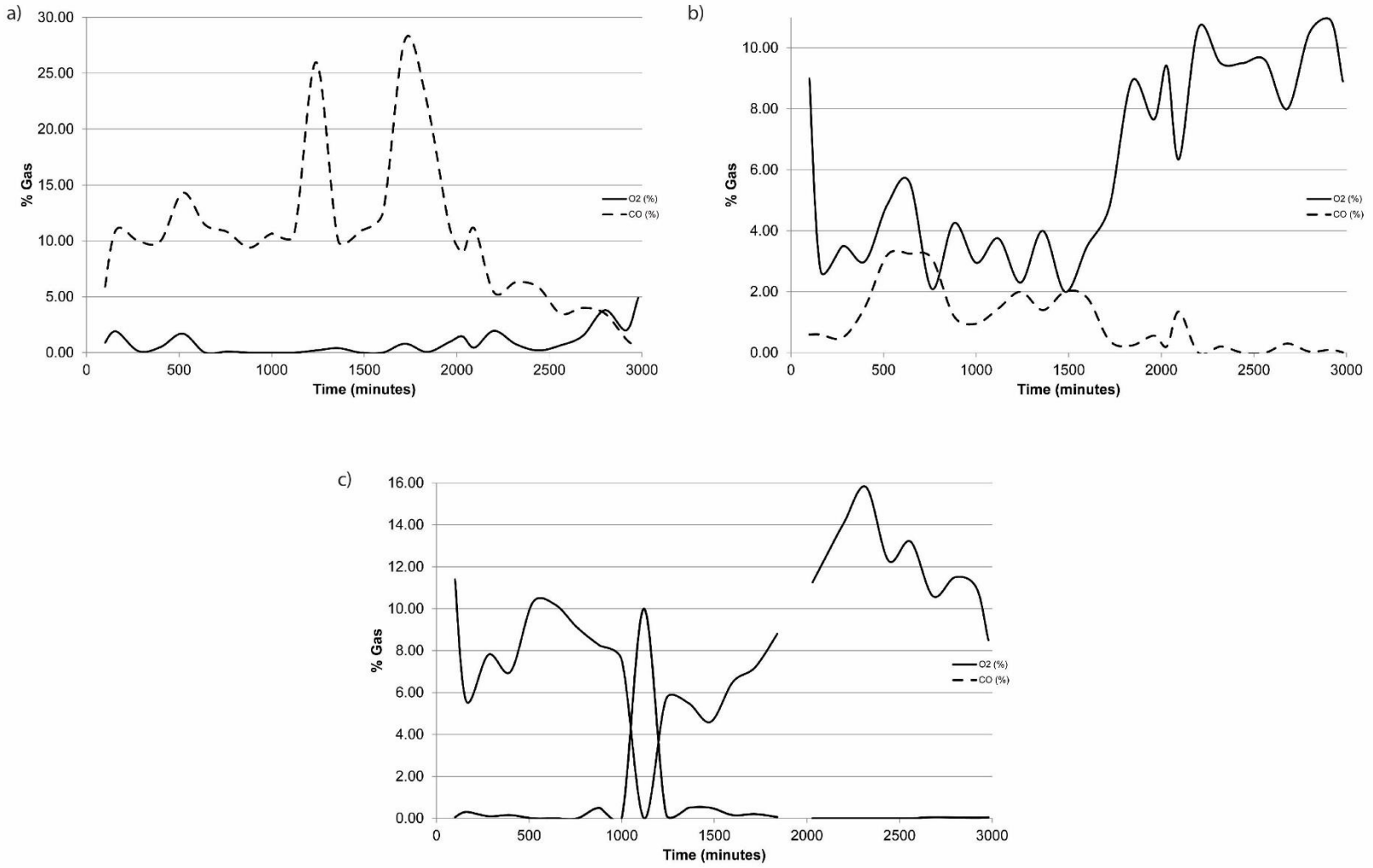

Figure 6-28: Gas conditions sampled every two hours from 15Mo3 probes in the eucalyptus combustion test . a) EUC I b) EUC J c) EUC K

Table 6-7: Phases present in the probe scales from the eucalyptus combustion run

Phase	Key	Composition	EUC A	EUC B	EUC C	EUC D	EUC E	EUC F	EUC G	EUC H	EUC I	EUC J	EUC K
Magnetite	Mag	Fe_3O_4	•	•	•	•	•	•	•	•	•		•
Akermanite	Ak	$Ca_2Mg(Si_2O_7)$	•	•	•	•		•	•	•	•	•	•
Quartz	Qz	SiO_2	•		•	•		•	•	•	•	•	•
Hematite	He	Fe_2O_3	•		•		•		•	•	•	•	•
Fairchildite	Fa	$K_2Ca(CO_3)_2$	•										•
Anhydrite	An	$CaSO_4$	•					•	•	•	•	•	•
Diopside	Di	$CaMgSi_2O_6$	•	•	•	•		•	•	•	•	•	•
Leucite	Le	$KAlSi_2O_6$	•	•	•	•		•	•	•	•	•	•
Magnesio-Wustite	Mg-Fe	$(MgO)_{0.77}(FeO)_{0.23}$		•									
Sylvite	Syl	KCl			•							•	
Wustite	Wu	FeO			•	•	•						
Calcium Phosphate	Ca-P	$Ca_{3(}PO_4)_2$				•		•				•	
Orthoclase	Or	$KAlSi_3O_8$						•		•			•
Cristobalite	Cr	SiO_2									•	•	•
Microcline	Mi	$KAlSi_3O_8$											•

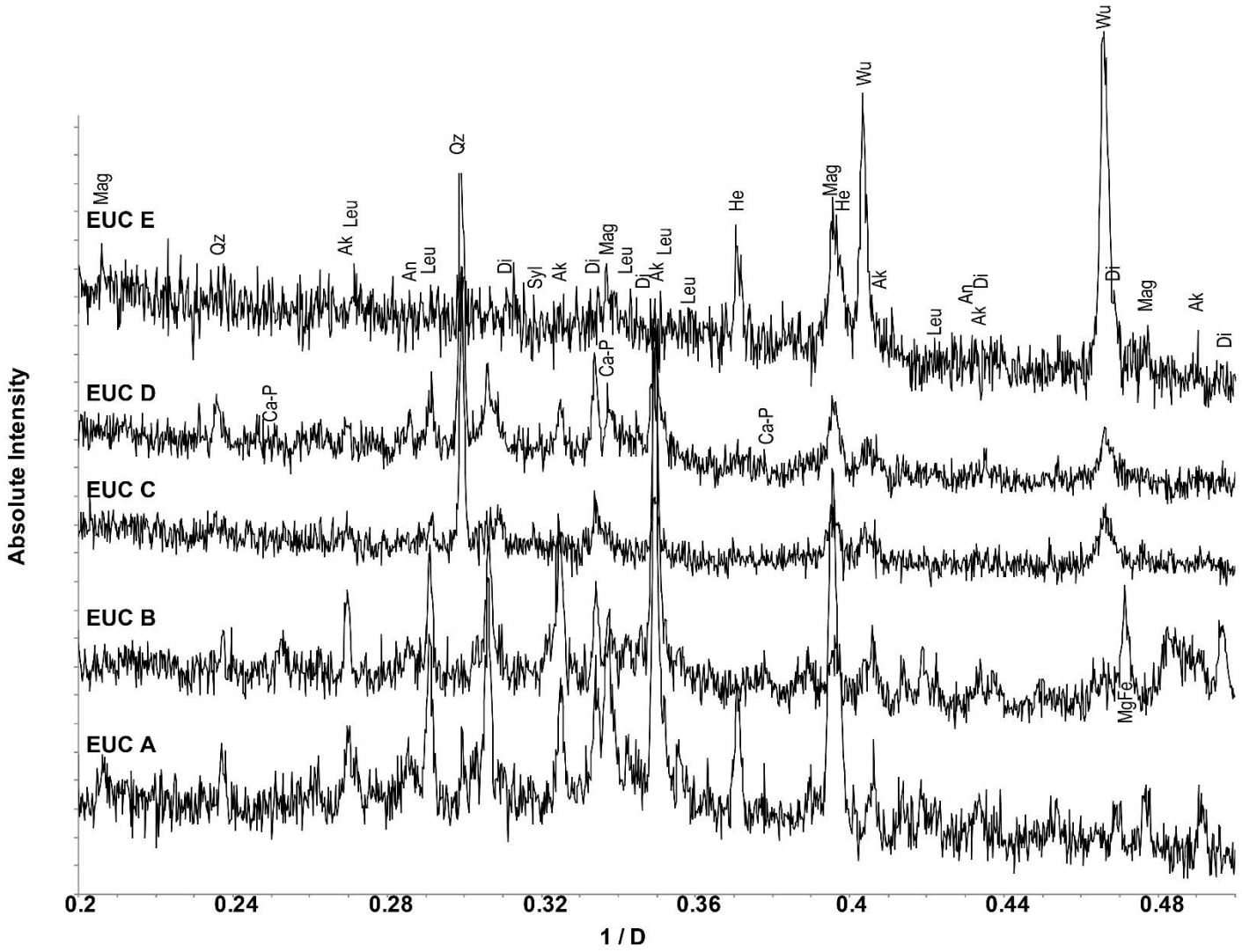

Figure 6-29: PXRD data for EUC A-E collected on the D2 diffractometer (Cu Kα radiation)

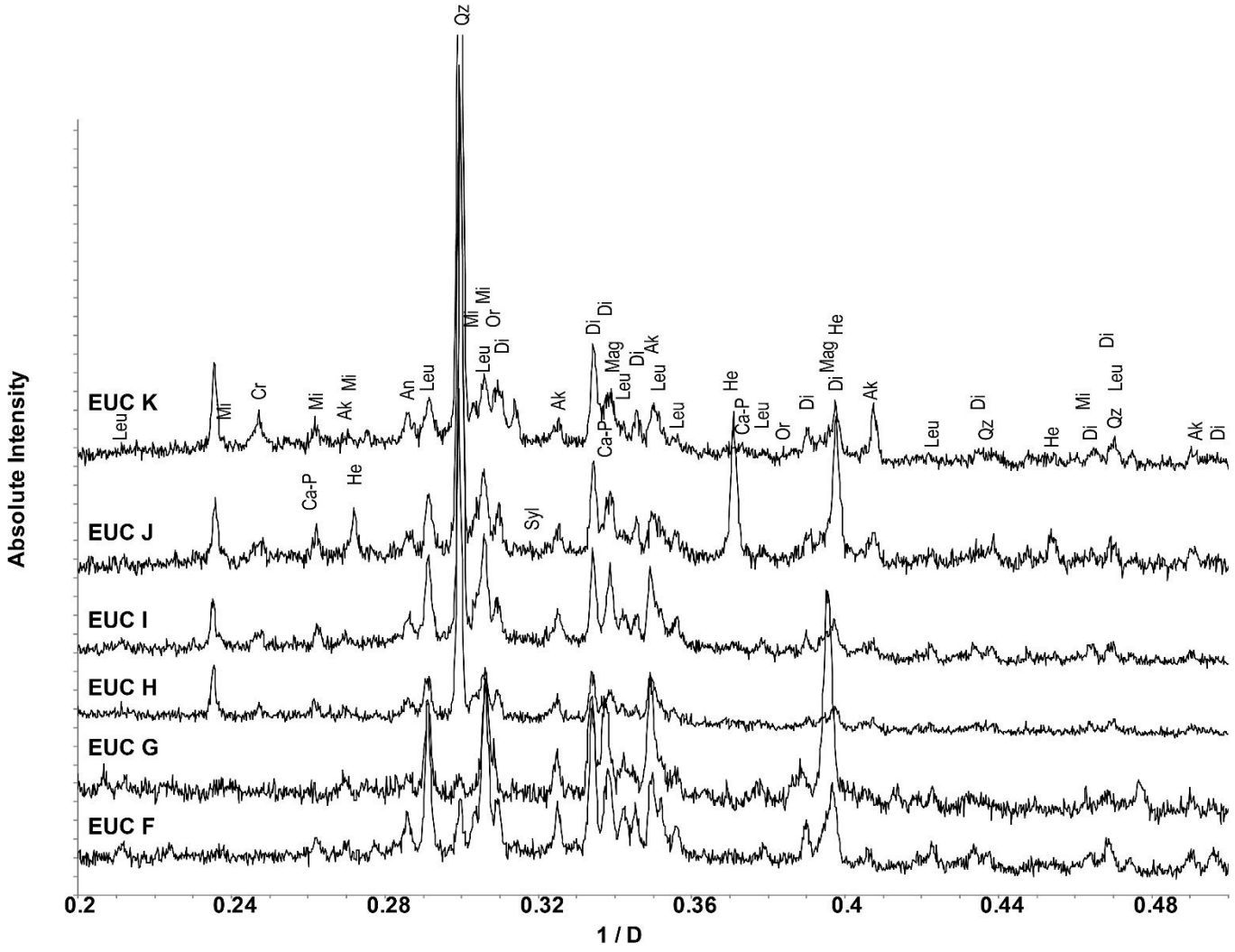

Figure 6-30: PXRD data and analysis for EUC F-K collected on the D2 diffractometer (Cu Kα radiation)

KCl was identified in samples EUC C and J. There is little correlation between the samples with regards to temperature, atmosphere, and position. The average surface temperature of EUC C and EUC J differ by 50°C; however with the flame temperature being higher than 500°C, sample surfaces will still be the coolest surface for KCl to condense on to. The K_2SO_4 that often co-occurs with KCl is not identified in these samples, suggesting that SO_2 from the coal is often responsible for the sulphation of KCl during the combustion.

$CaSO_4$ is present in multiple samples, suggesting combustion conditions are favourable for its formation through sulphation of CaO. Ca-phosphate is present in samples EUC C, D and J; these samples are in the temperature range of 475-500°C, indicating that higher temperatures are favoured during the formation of this phase. Ca-phosphate is present under both reducing and oxidising conditions, indicating that the formation is unaffected by atmosphere.

Quartz was present in several of the combustion probe samples. The Ca,Mg silicates akermanite and diopside that were present in the HT lab ash, deposits, and quenched samples are also present in the deposits analysed from the probe coupons (Table 6-7, Figure 6-29, Figure 6-30). Formation of these phases is covered in previous chapters.

Figure 6-31 presents electronmicrographs of the samples EUC A-K. The samples show several common characteristics with a large degree of sintering in the deposits being observed. There were also several regions where melting has occurred indicating that use of fuel may lead to slagging or fouling if used in larger scale combustion rigs. A large deposit had built up on EUC E (Figure 6-32), the colouring and shape of it suggests a melt region that has flowed and formed a droplet, which may be undesirable. The site of attachment to the boiler is also porous and exhibits sintering, this suggests that the conditions surrounding EUC G are undesirable during large scale combustion.

EUC E (Figure 6-31e) had a metal oxide scale present in the coupon scale deposit. This oxide scale corresponds with the PXRD data obtained from the sample where hematite, magnetite, and wustite are present. The scale probably detached from the coupon during the cooling of the probe after the test. Cracking on the surface of the scale is clearly visible, which can indicate breakaway oxidation (previously discussed in Section 2.5.1). There are also spherical particles present on the surface, likely to be silicates that are present in several other samples.

The spherical particles were present in multiple samples (Figure 6-31 A, D, G, H, I, and J). In several samples these spheres are being incorporated into the sample melt. This incorporation is particularly visible in EUC A and D, where a large region of melt and agglomeration surrounds the sphere.

Regions of the deposit also show a high degree of porosity (Figure 6-31f and j). These porous regions may indicate a degree of C-rich char particles that impacted onto the deposit, which then released CO_2 and formed the large visible pores. EDS analysis of one of these porous char particles is presented in Figure 6-33. The porous region largely consists of C and O, it is likely to be unburnt C from the eucalyptus fuel. Regions of Ca,Mg, Si and O are visible, suggesting the presence of the akermanite and diopside also identified through PXRD. There is also close association of KCl in the maps presented. The presence of KCl in the char particle suggests it may not have been released during combustion, it could also have condensed on the surface of the particle leading to enrichment.

An electron micrograph and EDS maps of spheres present in EUC C are presented in Figure 6-34. Whilst the morphology of the spheres is similar, in that they are all spheres, there is variation between the surfaces of the spheres and also elemental composition. The differences in the surfaces are illustrated in the spheres present in the micrograph of Figure 6-34. Spheres one and two show a smoother surface in comparison to spheres three and four. Various different sphere surfaces can also be observed in Figure 6-31.

The surface variation in sphere three is also visible in the EDS maps. On the surface of the sphere to the right hand side there are clear regions of Ca, Mg silicate interspersed with regions of K,Al,Si and O. This indicates that there is little reaction between the two phases. Fe is associated with O in the sphere; previous research by Raask[191] has shown a catalytic amount of Fe is often required to form the spheres from aluminosilicate droplets in the gas stream. Sphere one, in comparison, has a much more uniform composition comprising largely of Ca, Mg, Si, O, P, and Fe. The variations between the spheres suggests that heating rate has a far greater affect on the formation compared to the elemental composition of the spheres.

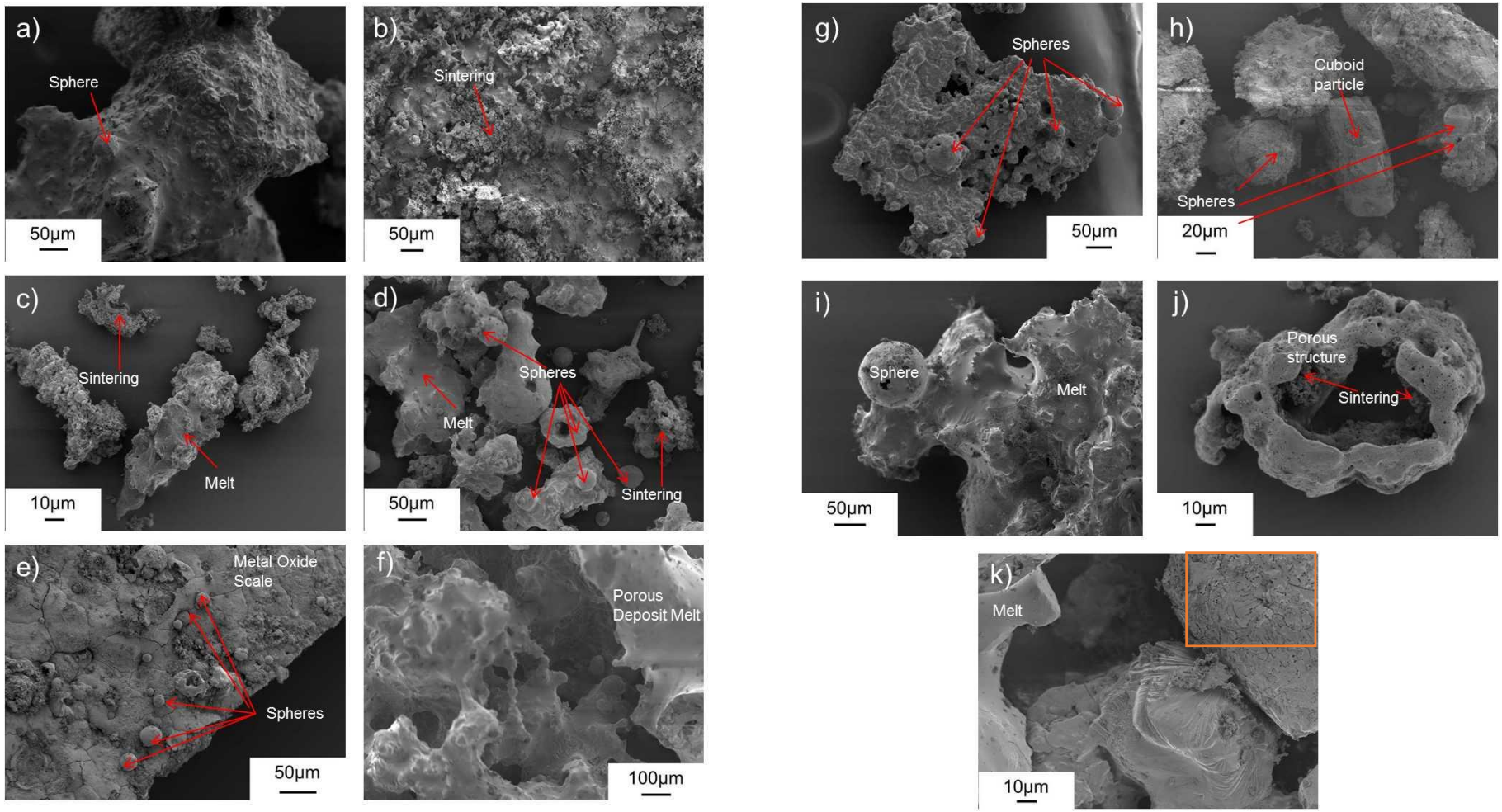

Figure 6-31: SEM electronmicrographs showing different sample morphologies present in the eucalyptus coupon deposits a) EUC A b) EUC B c) EUC C d) EUC D e) EUC E f) EUC F g) EUC G h) EUC H i) EUC I j) EUC J k) EUC K

Figure 6-32: Glassy slag flow removed from EUC E

Due to the variable composition of the spheres the melting points of the spheres will differ. This is illustrated in Figure 6-35, an electron micrograph and EDS maps of a melt region containing both Ca, Mg, phosphate spheres, and K, Al silicate spheres. The composition of the melt surrounding these spheres is largely uniform, exhibiting little variation between region, suggesting that the most thermodynamically stable phase under the combustion conditions has formed. The incorporation of the spheres into this melt indicates that the melt may have formed around the spheres, as the spheres present comprise of two distinct phases as opposed to the less uniform composition visible in Figure 6-34. If the spheres had impacted after the formation of the melt it is likely they would consist of multiple phases.

There are several metal oxide flakes present in the samples, Figure 6-31e shows one of the most distinct scales. A metal oxide flake is presented in Figure 6-36, one end of the flake is Fe- oxide rich and also incorporates K, this indicates that it is likely to be a corrosion scale that has detached from the coating of 15Mo3 alloy. The Si build up on the other side of the flake indicated deposition onto the metal surface.

A further metal oxide is presented in Figure 6-37, throughout the flake there is both Fe and Cr distribution suggesting formation of a Cr,Fe oxide spinel. Mechanisms of Cr enrichment in high Fe alloys has been discussed in Section 5.2. The scale could also originate from either of the claddings on the sample (FeCrAl or IN 625). The presence of both K_2SO_4, potentially formed through reaction with KCl, and Cr-oxide suggests that this is corrosion scale formed during the combustion trial which has then been removed from the main oxide layer.

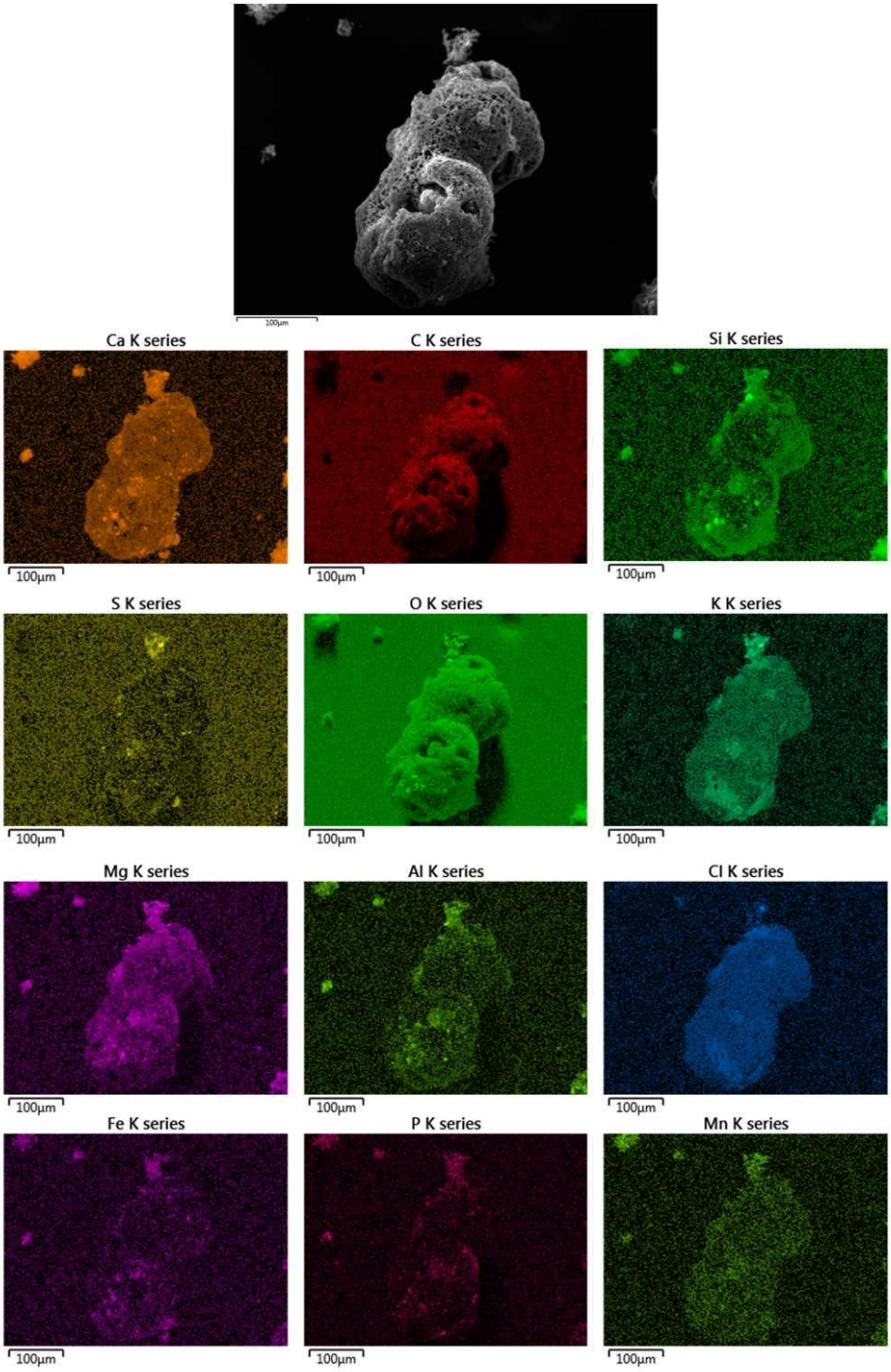

Figure 6-33: An electronmicrograph and EDS maps of a porous char particle from EUC J

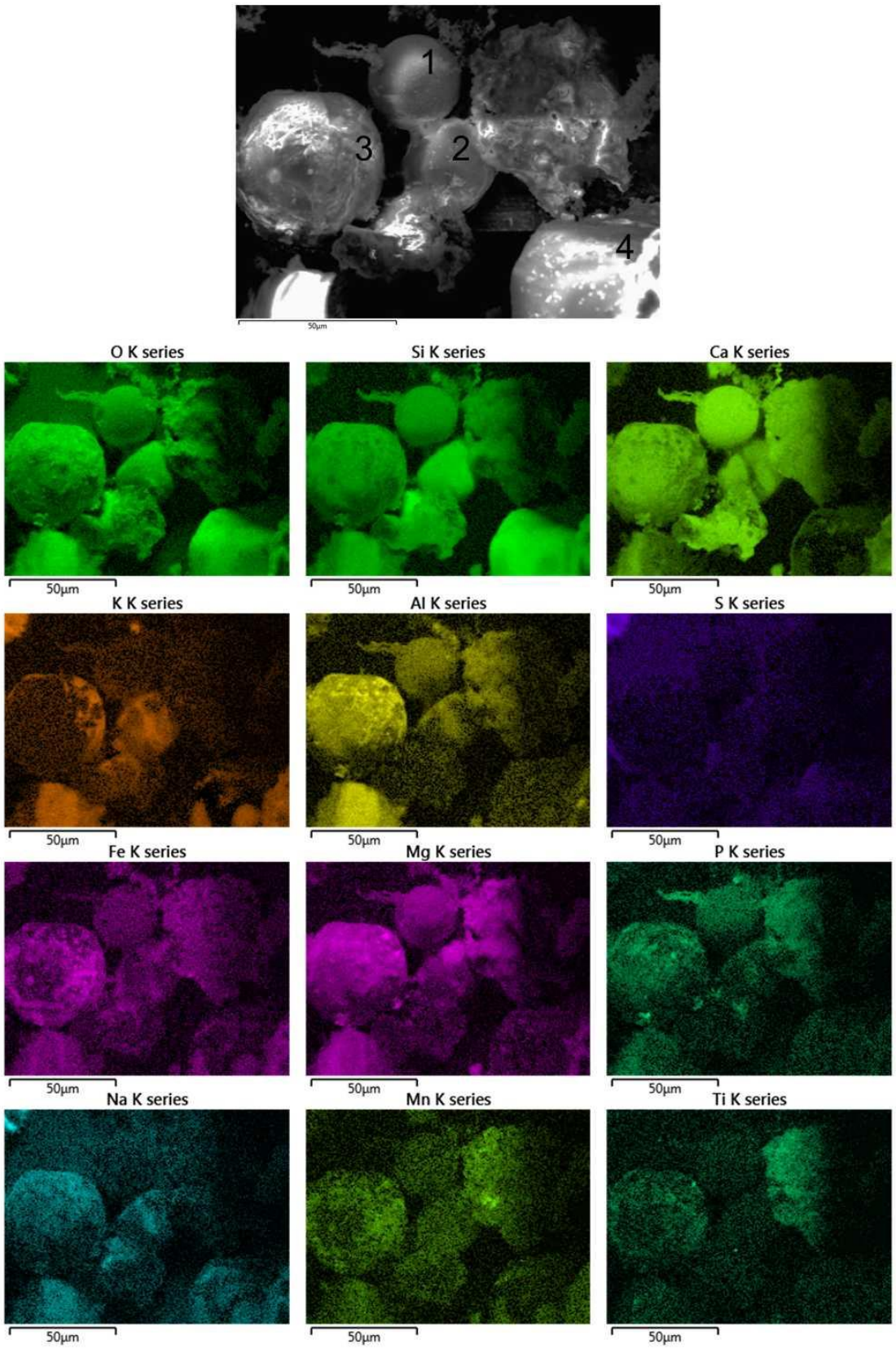

Figure 6-34: SEM electronmicrograph and EDS maps of spheres present in EUC C showing a variety of compositions between spheres and in individual spheres

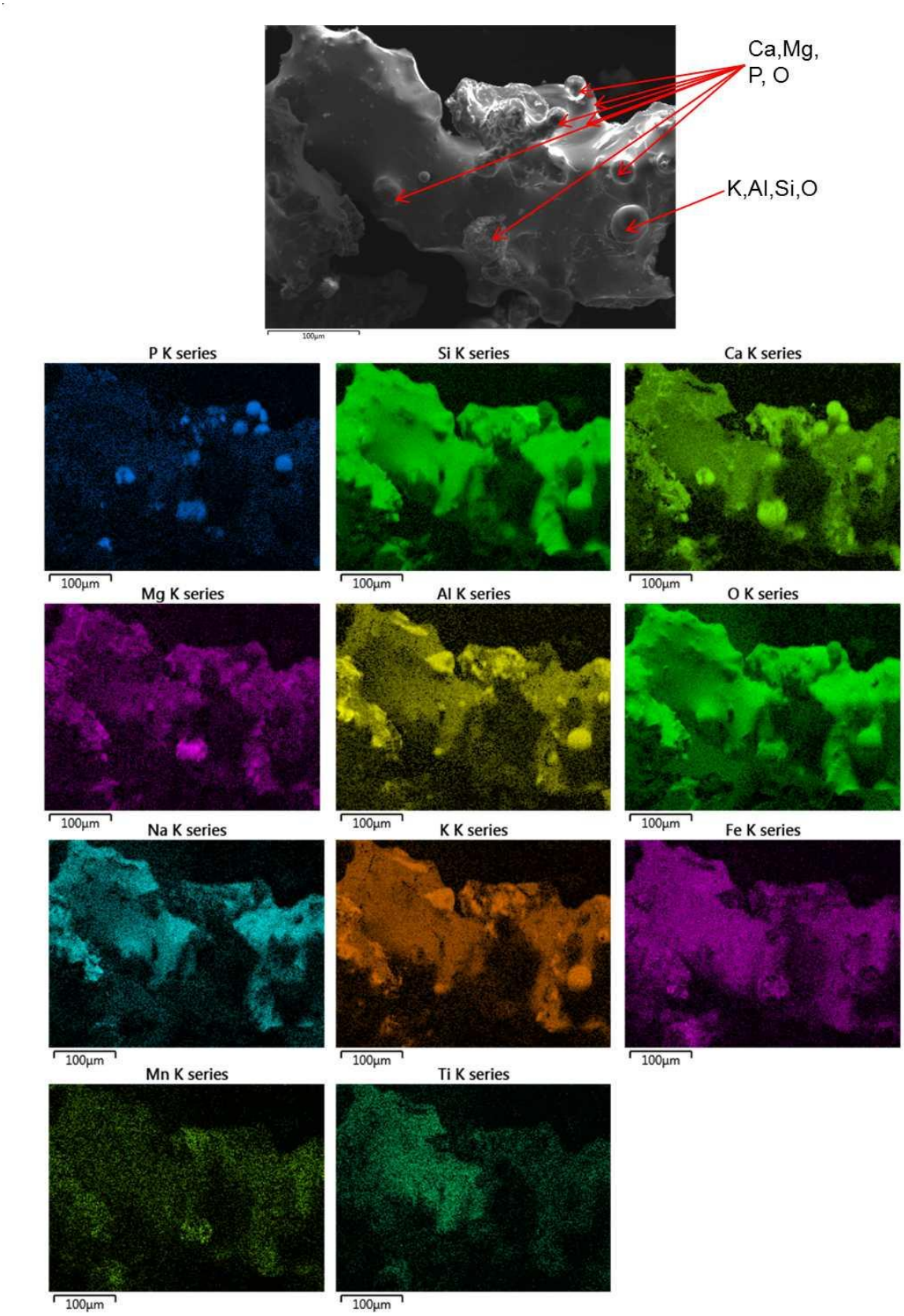

Figure 6-35: SEM Electronmicrograph and EDS maps of a melt incorporating Ca-Phosphate spheres from EUC D

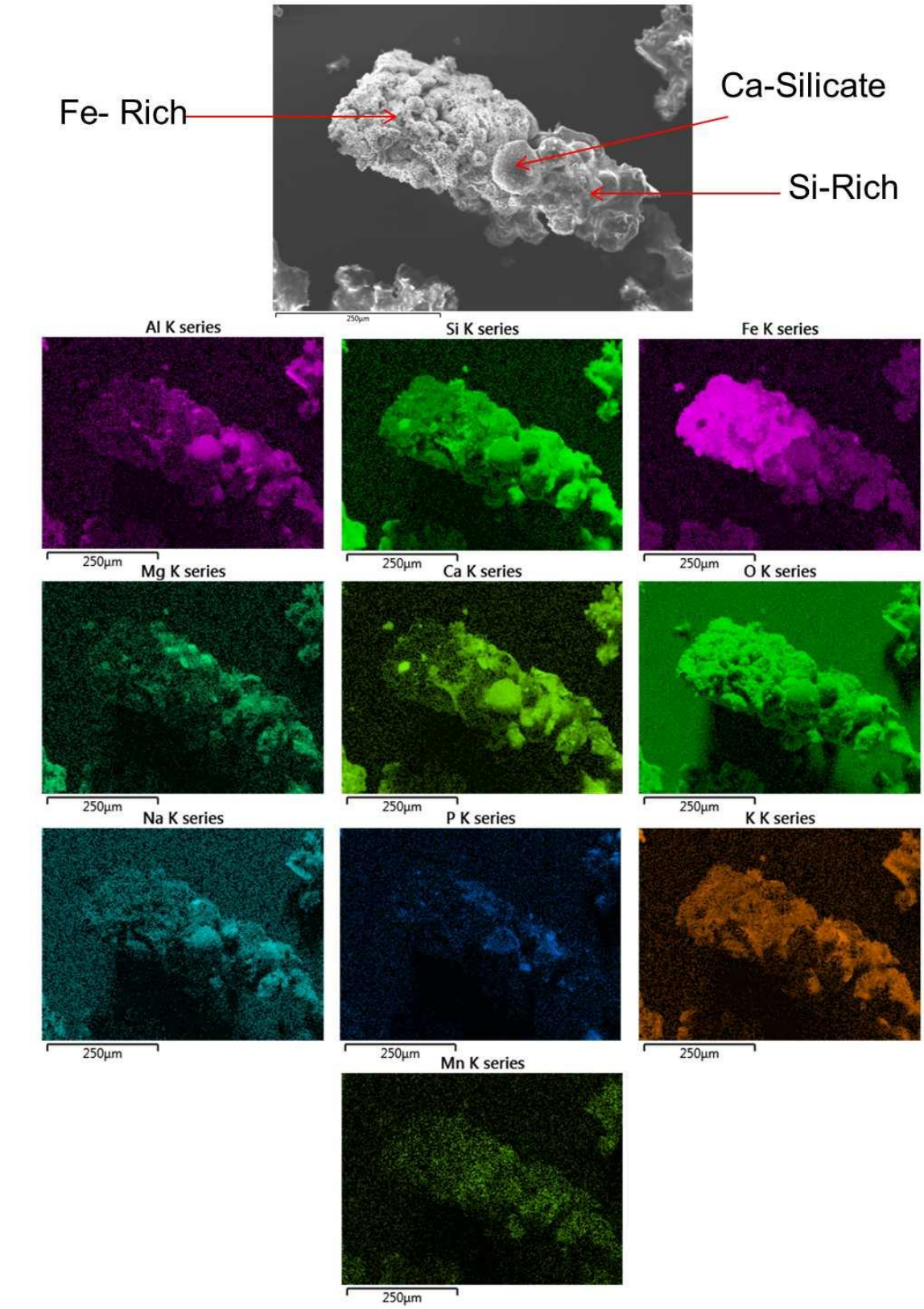

Figure 6-36: SEM micrograph and EDS maps showing an Fe scale with deposit build up from sample EUC

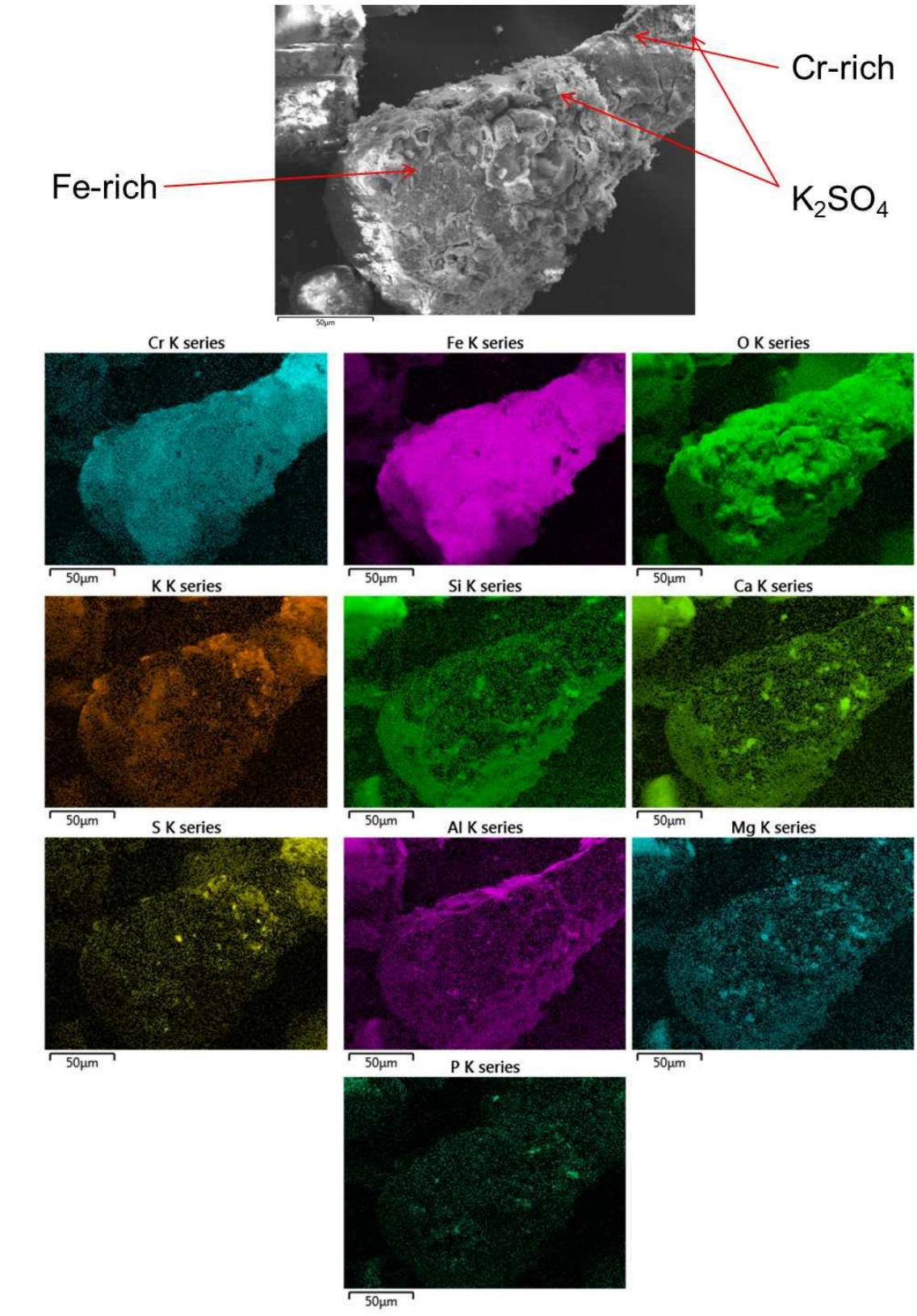

Figure 6-37: SEM Electronmicrograph and EDS maps of a corrosion scale from EUC H showing regions of Cr enrichment and K_2SO_4 deposition

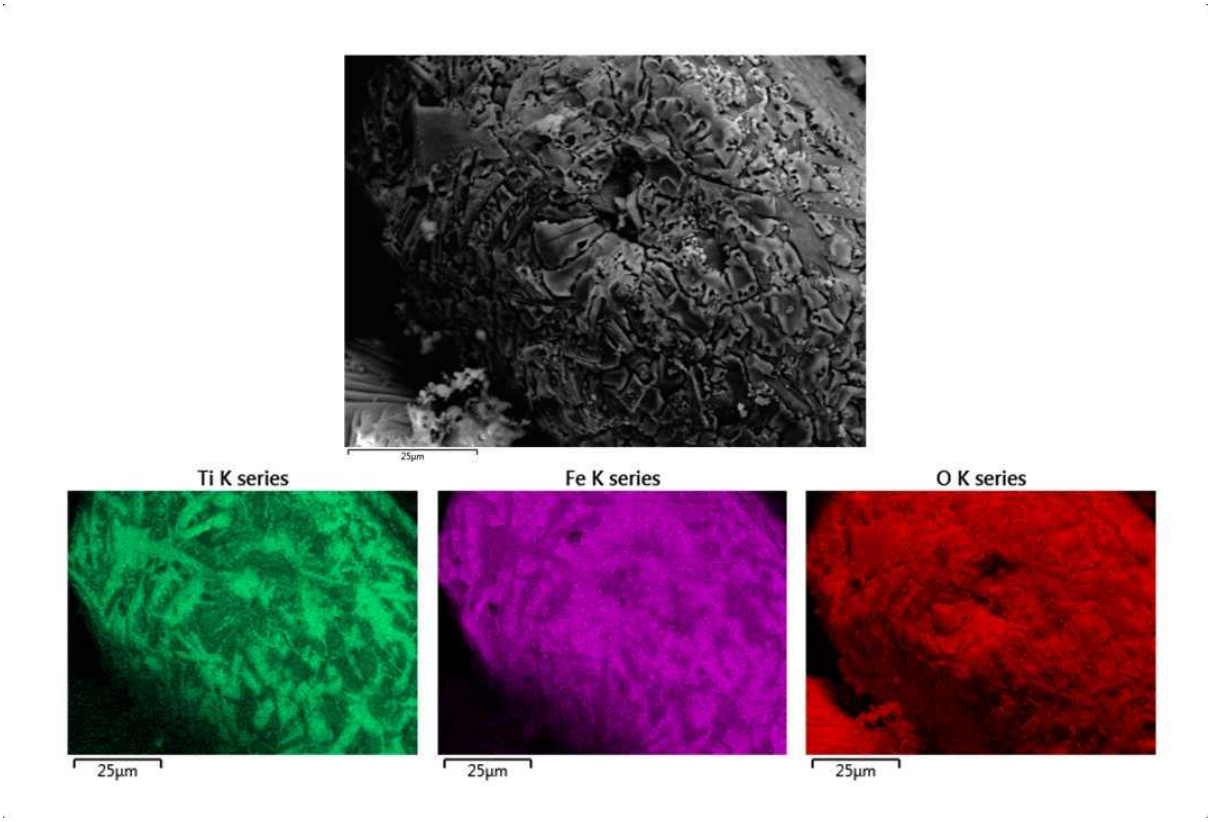

Figure 6-38: An electron micrograph and EDS maps of Fe, Ti and O deposit in sample EUC K

The deposit region highlighted with a red box in Figure 6-31k has an unusual composition. The area is a mixture of Ti, Fe, and O (Figure 6-34). The two oxides do not overlap, suggesting that there is no substitution between the two oxides. Research into the crystallisation of Fe-Ti oxides showed that immiscible oxides often formed during cooling.[228] The origin of this metal oxide deposit is unlikely to be from the alloy or coating, as Ti is not present. Instead it is more likely that this phase formed in the deposit from Ti and Fe present in the fuel.

6.4.2 Conclusions

The three Fe-oxides hematite, magnetite and wustite are identified using both PXRD and SEM-EDS analysis. These scales may have come from the alloy/coatings or they may originate from the rings used to secure the coupons to the probes. The scales, which contain Cr, are more likely to originate from the corrosion coupons / coatings as the Cr content of the fuel is minimal (1.77 mg/kg). Whilst Cr was previously observed in the deposit samples (Section 4.3.1), the close association of Cr and Fe in scales indicates that these are corrosion scale products.

The K_2SO_4 surrounding these scales also suggests that active oxidation has occurred, leading to spalling of these oxides, which leads to the scales detaching from the bulk.

There is sintering present in several of the deposit samples analysed. The formation of low melting point phases has allowed sintering to occur, as was stated in Section 4.3.1. There are also regions which have sintered and then melted; this melting can often lead to a greater degree of slagging and fouling. This can then lead to deposits flowing, which occurred in EUC G (Figure 6-32). This is undesirable as it will retard heat transfer and can create more tenacious deposits, although the formation of these melts do not appear to have increased corrosion rate.

There are also melts which did not create the flow seen on the surface of several of the samples. These melts are often multiphase, and incorporate spheres which remain intact; these spheres often comprise of Ca phosphate or K, Al silicates. This suggests that the formation of these compounds may be desirable as they will prevent the formation of hard to remove deposits, which can in turn lead to a reduction in efficiency and an increase in plant down time.

Several variations of spheres are present in the deposit samples, the spheres have a large variation in composition and surface texture. The spheres often contain multiple phases which suggests that their formation is dependent on heating rate in the flame, as opposed to the phase composition

7. Discussion and Overview

This chapter aims to present an overview of the phases formed at various stages of the combustion process. A more in depth discussion of the presence and absence of targeted phases under certain conditions then follows. Comparisons of the fuels and fuel blends will also be given, in order to give a comprehensive idea of where, and how, phases are likely to form in the combustion rig. In the comparison tables for the fuels, only 900°C and 1000°C are presented as these are the temperatures closest to those in the combustion rig.

Each of the sample sets (hemp and coal, eucalyptus and coal, and eucalyptus) are complex systems with a large number and variety of phases present. For instance, from the phases identified links to the phase diagrams CaO-SiO_2-MgO, CaO-SiO_2-Al_2O_3 can be made. Such phase formation pathways are recognised in other disciplines, for instance in refractory ceramics. Comparisons between the laboratory ashed samples and combustion rig samples show similarities, allowing patterns to be identified. The phases present ash samples indicate that predictable reactions are taking place in the combustion rig.

7.1 Hemp and Coal Discussion

The phases identified in the combustion rig samples, and the laboratory synthesised ash, are presented in Table 7-1. Various polymorphs of SiO_2 (quartz, cristobalite, and tridymite) are often present as the dominant phases in the samples, the SiO_2 content of the ash in the hemp and coal blend is 23.41wt% meaning it is around a quarter of the bulk ash matrix (Table 3-18). Tridymite and cristobalite, the high temperature polymorphs of SiO_2 are only present in samples that are settled/deposited (i.e: coupons and bottom ash for over 1 hour) meaning that the phases take time to form/ transform.

One of the phases that is of greatest concern during biomass co-firing is KCl. In the hemp and coal samples it was identified in the deposits, coupons, fly ash, and bottom ash. It was not identified in the 900°C and 1000°C samples generated in the lab; this is likely due to volatilisation earlier in the heating process and so it may have condensed in a cooler region of the furnace. The presence of KCl in deposits was unexpected as the bulk deposition mechanism of KCl is onto cooler surfaces, and the ceramic probes used for deposition were at approximately gas temperature (971-980°C). The presence of KCl in the deposits (Table 5-1) could be due to condensation of the KCl on the surface of larger particles, which then impact onto the surface of the probe/ growing deposit (Figure 2-3). KCl that did not deposit onto a surface, travelled with the flue gas in the fly ash and reached the cyclone.

As the bottom ash reached temperatures high enough to give large glassy phases, the presence of KCl was not expected. It is possible that the KCl comes from char particles which did not follow the flue gas flow and fell into the ash hopper. Decomposition in the high temperature of the bulk bottom ash, alongside its dense glassy nature, prevented the KCl from volatilising and re-entering the flue gas of the combustion rig.

The presence of KCl in the coupons (Figure 6-7) suggests that corrosion of the alloy 15Mo3 is likely to occur when hemp and coal are co-fired as fuels. KCl deposits under the diffusion/thermophoresis mechanism, meaning it condenses onto cooler surfaces. As the probes were air cooled, this environment is much cooler compared to the gas flow and is the likely point of deposition in the combustion rig. The presence of arcanite (K_2SO_4) suggests the sulphation of KCl according to Equation 6-27. The SO_2 required for this reaction will come from the coal component of the co-fired fuel blend.

The iron oxides, hematite and magnetite, are identified in the sample. In the coupons this could be either a corrosion product of 15Mo3 oxidation or a deposition phase. Other occurrences (those in the deposit and quench samples) are likely to have formed from the fuel. Magnetite is only present in the deposit and quenched samples. The reduction of hematite to magnetite in the deposit samples could be due to the unburnt C present in the combustion gas/char, which has previously been shown to lead to uncontrolled reduction[187].

As has been shown in previous chapters (4,5) the CaO-MgO-SiO_2 system comprises a large part of the ash. Seven phases have been identified in this system which are present from the hemp and coal fuel blend; these are wollastonite, larnite, diopside, akermanite, monticellite, merwinite, and forsterite, with a further two (gehlenite and augite) being from closely related systems. This system is also likely to contain Mn, which was not detected in the PXRD data.

The formation of these phases by reaction of other phases present in the ash is illustrated through Rietveld refinement of the hemp laboratory ash samples. The phase quantification of the ash shows the general trend of the SiO_2 content decreasing as the silicate content increases. This means that the SiO_2 is reacting with Ca (likely to be from the hydroxyapatite or calcite) to form the complex Ca-silicates.

The CaO comes from the decomposition of the $CaCO_3$, present in the biomass fuel, and the MgO is present as periclase, from the decomposition of dolomite. Phases from this system are more dominant in the deposit samples, which suggests that the phases form in deposit as opposed to flue gas reactions confirming that these phases take time to form.

Table 7-1: Comparison table of phases identified at multiple points during the combustion run and in synthetic ashing procedure for hemp and coal

Phase	Composition	Lab Samples		Combustion Rig Sample				
		900 °C	1000°C	Deposits Combined	Quench Combined	Coupons Combined	Cyclone Ash	Bottom Ash Combined
Quartz	SiO_2	·	·	·	·	·	·	·
Cristobalite	SiO_2					·		·
Tridymite	SiO_2							·
Sylvite	KCl			·		·	·	·
Arcanite	K_2SO_4	·		·		·		
Anhydrite	$CaSO_4$		·	·		·		
Calcite	$CaCO_3$	·		·	·	·	·	
Fairchildite	$K_2(CaCO_3)_2$					·		
Periclase	MgO	·	·	·	·	·	·	
Hematite	Fe_2O_3	·	·	·	·	·	·	
Magnetite	Fe_3O_4			·	·			
Albite	$NaAlSi_3O_8$	·	·	·		·		·
Orthoclase	$KAlSi_3O_8$		·			·		
Microcline	$KAlSi_3O_8$	·	·	·		·		
Sanidine	$KAlSi_3O_8$			·	·			
Kalsilite	$KAlSiO_4$	·	·	·	·	·	·	
Leucite	KAl_2SiO_6					·		
Wollastonite	$CaSiO_3$	·	·	·	·			
Larnite	Ca_2SiO_4		·		·			
Diopside	$CaMgSi_2O_6$	·	·	·		·		
Augite	$Ca(Mg_{0.74}Fe_{0.26})Si_2O_6$			·				
Akermanite	$Ca_2MgSi_2O_7$	·	·	·	·	·		
Gehlenite	$Ca_2Al(AlSiO_7)$	·	·	·		·		·
Monticellite	$CaMgSiO_4$				·			
Merwinite	$Ca_3MgSi_2O_8$				·			
Forsterite	Mg_2SiO_4				·	·		
Hydroxyapatite	$Ca_{10}(PO_4)_6(OH)_2$	·	·	·	·	·	·	
	$Ca_9MgK(PO_4)_7$							·
Illite	$KAl_2(Si_3Al)O_{10}(OH)_2$	·						
Andalusite	Al_2SiO_5			·				
Mullite	$Al_{2.35}Si_{0.64}O_{4.82}$		·	·	·			

As was shown in the hemp and coal laboratory ashing studies, diopside can react with excess $CaCO_3$, which decomposes to lime (CaO) at temperatures above 900°C, to form akermanite and larnite. Diopside also accepts Fe to form the phase augite, identified in the deposit samples. Augite was only identified when magnetite was also present in the deposit sample, suggesting the oxidation state of Fe is an important factor. This was previously identified by Sorenson *et al*.[188]

Akermanite ($Ca_2MgSi_2O_7$) and gehlenite ($Ca_2Al(AlSiO_7)$ are both end members of the melilite system. A solid solution exists between these two end members, *via* replacement of Mg with Al (or vice versa), and so would be present independently in the hemp and coal ash. Cultrone *et al*.[161] identified gehlenite alongside wollastonite in Ca,Mg rich clays fired at 900-1000°C to form ceramic phases. This observation is also present in the lab ashed samples and the deposit samples; however it is not true for the coupons, suggesting the wollastonite may be consumed in the formation of another phase. It is also suggested that illite and calcite may react to form gehlenite; the source of the illite in this instance is the coal.

Further Ca containing phases identified as hydroxyapatite and $Ca_9MgK(PO_4)_7$ are present in the hemp and coal samples. The hydroxyapatite is thought to originate in the hemp fuel, and may be present in the trichome structures (Figure 4-3). At temperatures above 1500°C it has been shown by Queiroz *et al.*[199] that the phase $Ca_9MgK(PO_4)_7$ forms from hydroxyapatite. The incorporation of K into the phase comes from the KCl also present in the bottom ash.

The illite identified in the laboratory synthesised ash and the coal fuel is thought to have decomposed into the sanidine and mullite phases identified; decomposition occurs between 800-1000°C. This reaction is also present in the laboratory ash as illite is present at 900°C but not 1000°C, sanidine was not detected by PXRD.

There are multiple K, Al-silicates present, and it is thought that these can interconvert. The microcline may have formed through the reaction of illite (present from the coal) with calcite, giving a Ca, Al silicate as a side product (Equation 4-18).[161] The sanidine may also have formed through high temperature transformation of microcline.[161] Also present in the coal was kaolinite; this has previously been identified as a precursor to kalsilite formation by Vassilev *et al*..[27] A reaction between kalsilite and quartz, to yield leucite, was also shown observed at temperatures between 700-950°C.[183] These temperatures were reached in multiple regions of the combustion rig.

Orthoclase ($KAlSi_3O_8$) is present in the coupon samples and the laboratory ash at 1000°C. Previous work by Frandsen *et al.*[49] shows that microcline (another K-feldspar) forms through slow cooling of orthoclase. Deposit samples and the coupon samples cooling rapidly after

removal from the combustion rig is the origin of orthoclase (the kinetic product), as microcline (the thermodynamic phase) does not have time to form.

There are very few Na containing phases identified in the samples collected from the combustion rig, with the feldspar albite being the exception. This suggests that the Na_2O identified in the ash matrix is either the albite, which may not decompose during combustion, or that the Na incorporates into other phases without causing detectable structural changes. Incorporation of Na into other crystal structures is observed through analysis of the EDS data, where there are clear regions of Na present around identified phases (Figure 5-6). This is also thought to be the case for Mn, which could also be present in an amorphous form, undetectable by PXRD.

As well as distinct trends in the phases observed in the PXRD data of the samples, there are also morphological trends. The morphology of the particle debris identified as trichomes from the hemp raw fuel is clearly visible in the samples collected from the laboratory ash (Figure 4-2), the combustion rig deposits, quench samples (Figure 5-11), coupons, and fly ash (Figure 5-15).The trichome structure is not visible in the bottom ash, as the bottom ash reaches high temperatures and forms a slag melt. This infers that the temperatures are thought to be above 1500°C, due to the formation of the phase $Ca_9MgK(PO_4)_7$. Through analysis of the EDS data, the trichomes contain Ca, Mg, P, and O, amongst other elements, suggesting that the absence of the trichomes and hydroxyapatite is therefore likely to be due to the high temperatures reached in the bottom ash, leading to a high temperature formation of $Ca_9MgK(PO_4)_7$.

In contrast to the trichome structures, which are present in both the lab and the combustion rig ash, the morphology of the bulk of the ash differs between the two. In the laboratory ash the particles have distinct shapes similar to that of the original hemp/coal structure. In contrast the combustion rig samples, particularly those formed in the flue gas prior to deposition/removal, largely contain a spherical morphology. These differences are due to the heating gradient in the combustion rig; the introduction of the fuel to a flame causes the ash formation stages outlined in Figure 2-3. The increased heating by introduction of the fuel to the flame, in comparison to the gradual temperature rise of the laboratory ashing, leads to rapid droplet expansion causing the observed spheres.

The spheres, named ceno/plerospheres by Raask,[191] are formed through rapid gas expansion catalysed by a small amount of Fe and C present in the silicate droplets. This mechanism was initially observed in coal ash. Composition can vary both between spheres,[190] and in the spheres themselves, as is shown through EDS analysis of the particles (Figure 5-9). This, similar to the morphology, can be attributed to the rapid heating the ash particles undergo.

Phases that are close to one another will react within the particle, in the high temperature environment. If these particles then deposit further, reaction of these phases will occur and additional reactions will occur. This explains the absence of complex silicates (e.g. diopside/akermanite) present in the cyclone ash, in comparison to the deposit and coupon phases.

7.2 Eucalyptus and Coal Discussion

As with the hemp and coal blend, the eucalyptus and coal blended ash samples are complex and multiphase (Table 7-2). Like the hemp and coal samples, the largest portion of the oxides in the ash matrix is SiO_2. This is reflected by the presence of the phases quartz and cristobalite, alongside the complex silicate phases also identified using PXRD analysis. Cristobalite has previously been reported to have a high affinity for alkali metals at high temperatures. This attribute, coupled with the highly porous structure of cristobalite, increases the surface area. It was previously concluded in Section 4.2.1 that this may be responsible for phases forming at lower temperatures than have previously reported. The quench sample for eucalyptus and coal contains oxides and feldspars. This supports the formation of complex silicates in deposit as opposed to in the flue gas, a conclusion also drawn from the hemp and coal data.

The $CaO\text{-}MgO\text{-}SiO_2$ system is dominant; the eucalyptus and coal fuel blend has a higher CaO content compared to hemp and coal. This difference between the basic fuel ash matrices explains the multiple phases present in separate blends. The phases present in the eucalyptus and coal blend from the $CaO\text{-}MgO\text{-}SiO_2$ system are wollastonite, diopside, akermanite, merwinite, and forsterite, with those that are closely related being gehlenite and grossular.

The conversion between wollastonite, diopside and akermanite is explained above in the present chapter and the laboratory ashing chapter (Section 4.4.1). Also present in the samples is grossular ($Ca_3Al_2(SiO_4)_3$) which was found to form alongside diopside and wollastonite[162]. In comparison to the hemp and coal ash matrix, there is a higher content of Al_2O_3 (Table 3-18). Periclase is identified in the laboratory ashed samples, deposits, coupons and bottom ash meaning it is present as a Mg source for the formation of complex silicates.

Table 7-2: Phases present in laboratory and combustion rig samples of eucalyptus and coal ash, # indicates a solid solution between two phases

Phase	Composition	Laboratory ash		Combustion rig sample			
		900°C	1000°C	Deposits Combined	Quench Combined	Coupons Combined	Bottom Ash Combined
Quartz	SiO_2	•	•	•	•	•	•
Cristobalite	SiO_2	•	•	•		•	•
Sylvite	KCl					•	
Arcanite	K_2SO_4			•		•	
Anhydrite	$CaSO_4$	•	•	•		•	
Calcite	$CaCO_3$						•
Fairchildite	$K_2Ca(CO_s)_2$	•	•			•	•
Natrite	$NaCO_3$				•		
Periclase	MgO	•	•	•		•	•
Hematite	Fe_2O_3	•	•	•	•	•	•
Magnetite	Fe_3O_4	•	•		•	•	
Aluminium oxide	Al_2O_3			•	•		
Albite	$NaAlSi_3O_8$	•	•	•		•	
Microcline	$KAlSi_3O_8$	•	•	•	•	•	
Sanidine	$KAlSi_3O_8$			•			
Kalsilite	$KAlSiO_4$	•	•	•			
Leucite	KAl_2SiO_6	•	•	•		•	•
Wollastonite	$CaSiO_3$	•	•				
Diopside	$CaMgSi_2O_6$	•	•	•		•	•
Akermanite	$Ca_2MgSi_2O_7$	•	•	#		•	#
Gehlenite	$Ca_2Al(AlSiO_7)$	•	•	#		•	#
Grossular	$Ca_3Al_2(SiO_4)_3$	•	•			•	
Anorthite	$CaAl_2Si_2O_8$					•	•
Merwinite	$Ca_3MgSi_2O_8$			•			
Forsterite	Mg_2SiO_4			•			
Hydroyapatite	$Ca_{10}(PO_4)_6(OH)_2$						•
	$Ca_9MgK(PO_4)_7$						•
Illite	$KAl_2(Si_3Al)O_{10}(OH)_2$	•	•				
Mullite	$Al_{2.35}Si_{0.64}O_{4.82}$	•	•	•	•		
	Calcium Chromium Oxide					•	
Talc	$Mg_3Si_4O_{10}(OH)_2$					•	
Nickel Oxide	NiO					•	
Chromium Oxide	Cr_2O_3					•	
Tremolite	$Ca_2(Mg,Fe)_5Si_8O_{22}(OH)_2$					•	

A large portion of Al_2O_3 in the ash is advantageous during co-firing as it increases the ash fusion temperature of the deposits which leads to a decrease in in-deposit sintering. This advantage is being investigated with the use of Al_2O_3 as an additive.[229] A decrease in sintering is desirable because sintering increases can lead to the blocking of ducts and decrease efficiency. Incorporation of the Al_2O_3 into the akermanite phase will either yield the phase gehlenite, through total replacement of the Mg, or the formation of a solid solution between akermanite and gehlenite which is observed here. These two phases are end members of the melilite family. The presence of Al_2O_3 in both the deposit and the quenched samples, alongside gehlenite, is in agreement with the formation mechanisms presented above.

The Ca,Al-silicate anorthite was also identified in the coupons and bottom ash samples. Previous research[9,10,11] has shown that a matrix content of less than 8.6% favours the formation of diopside over anorthite. As such, the presence of anorthite in the coupons and bottom ash could be due to higher temperatures than those in the other samples (i.e. the bottom ash reaches temperatures in excess of 1500°C and the gas temperature of the coupons is similar to the flame temperature), as Kurama *et al*.[209] report that at higher temperature gehlenite can react further to form anorthite.

The K,Al-silicates microcline, sanidine, kalsilite, and leucite are present in the samples. The formation of leucite in the coupon and bottom ash samples could be due to the presence of cristobalite in these samples. Which, due to the increased surface area in comparison to quartz, has an affect on reaction rate.

In contrast to the hemp and coal samples, KCl was identified in fewer samples, which is likely due to the Cl content of the eucalyptus being seven times lower than that of hemp (Table 3-1). The KCl identified in the coupons is deposited due to the diffusion/ thermophoresis mechanism. This often leads to an increase in corrosion. Figure 6-17 shows distinct KCl deposition onto an oxide scale formed during the combustion trial. Whilst KCl was only identified on one coupon it is also identified in several others via EDS. Figure 6-18 shows the presence of KCl on a scale surface alongside K_2SO_4, showing substitution has occurred. This is also shown through a linescan analysis of a sample in Figure 6-19. K_2SO_4 (Table 5-13, Figure 5-23) is also present in the deposit samples suggesting that conversion of KCl to K_2SO_4 may have occurred in the deposit, or deposited after formation in the flue gas.

Unlike the hemp and coal coupon samples, distinct iron-oxide crystals can be observed using SEM-EDS. The iron oxides hematite and magnetite are present in samples other than the coupon samples, due to the high Fe content of the eucalyptus fuel. SEM-EDS analysis allows differentiation between the scale formed in the coupons, from that of the ash matrix. There are

whiskers of hematite observed growing between the scale and the deposit (Figure 6-21).[226] Research by Pettersson *et al*.[104] concluded that these whiskers are most likely to form in areas which have undergone breakaway oxidation, therefore it is likely these whiskers are metal oxidation products.

Distince octahedral magnetite crystals are also visualised through SEM-EDS (Figure 6-20); this shows that the metal of the coupon has experienced reducing conditions during the combustion run. The presence of Mn and Ni indicates that the scales come from the 15Mo3 alloy (Table 3-4). This observation, coupled with the presence of the hematite whiskers, shows that corrosion may occur when co-firing the eucalyptus and coal fuel blend.

The oxides Cr_2O_3 and NiO are also present in the coupon samples. The NiO comes from the grease used in the lubrication of the coupon samples. The Cr_2O_3 is present from the 15Mo3 alloy. Previous research by Uusitalo *et al*.[85] and Wood *et al*.[225] indicate that Cr enrichment occurs in boiler scales in low alloy steels. Cr_2O_3 and Fe_2O_3 often form a spinel; this was not identified through PXRD analysis as the patterns of hematite and the Cr-Fe spinel have similar peak positions and intensities which are hard to distinguish from one another.

Through SEM-EDS analysis, morphology differences between the lab ashing and combustion rig samples can also be observed (i.e: no spheres (Figure 4-41) and spheres (Figure 5-23)). The increase of Al, which has often been reported to increase the sintering temperature of the ash, did not lead to significant morphological differences between the hemp and coal sintered regions and the eucalyptus and coal sintered regions. The distinct trichome structures are not visible in the eucalyptus and coal showing that these are structures distinct to the hemp fuel.

7.3 Eucalyptus Discussion

In contrast to the co-fired blends, the SiO_2 content of the ash matrix is much lower (16.92wt%, compared to 23.41 wt% hemp and coal, and 31.25 wt% eucalyptus and coal (Table 4-1)). This suggests that there will be differences in the composition of the ash formed as the lower Si content may lead to the formation of silicates with differing SiO_2 contents. The three polymorphs of SiO_2 quartz, tridymite, and cristobalite are observed in several of the samples. Tridymite is only observed in the lab samples suggesting that conditions in the combustion rig favour quartz or cristobalite. The polymorph cristobalite is only present in the samples that were present in the rig for an extended amount of time i.e: above 120 minutes. This indicates that for cristobalite to form it requires above 60 minutes (the time at high temperature in the furnace for the lab ashing studies) at elevated temperature.

As was shown in the co-fired fuel blends one of the significant ternary systems is CaO-MgO-SiO_2, with seven phases which are present in this phase diagram in this system observed, as well as those closely related phases in the CaO-Al_2O_3-SiO_2 system. The eucalyptus ash matrix contains a higher proportion of Al_2O_3 in comparison the hemp and coal blend; This increase in Al content has led to an increase in the amount of Al containing phases. These phases are mainly observed in the deposit and quench samples suggesting that they require time to form, and also that formation is dependent on what phases are in close proximity; for instance, Cordierite, a Mg, Al-silicate is present in the deposit sample.

Phases in the melilite family that were present in the eucalyptus and coal, and hemp and coal ash samples, are also present in the eucalyptus samples. Akermanite, gehlenite, solid solutions of these two phases, as well as soda melilite are present in the samples. Na is also incorporated into the melilite system. The phase containing Na that was identified in both of the fuel blends, is albite, this was not identified in the eucalyptus ash produced in the laboratory although it was present in the quenched and coupon samples. This suggests that the Na in the eucalyptus fuel is available in a more accessible form (i.e. it is released during combustion) which reacts with Al_2O_3 and SiO_2 to form the soda-melilite. The albite that is identified through PXRD could be soil contamination, when it is observed in the co-fired fuel blends it is likely to come from the coal, as the phase is present in the coal ash produced in the laboratory (Table 4-8 , Figure 4-29).

Table 7-3: Phases identified in the eucalyputs laboratory ash and combustion rig samples, # indicates a solid solution between two phases

	Composition	Sample						
		900°C	1000°C	Deposits Combined	Quench Combined	Coupons Combined	Cyclone Ash	Bottom Ash Combined
Quartz	SiO_2	•	•	•	•	•	•	•
Cristobalite	SiO_2			•		•		•
Tridymite	SiO_2	•	•					
Sylvite	KCl					•	•	
Anhydrite	$CaSO_4$	•	•	•		•	•	
Calcite	$CaCO_3$				•		•	•
Fairchildite	$K_2(CaCO_3)_2$				•	•		
Dolomite	$CaMg(CO_3)_2$				•			
Periclase	MgO	•	•	•			•	
Magnesium iron oxide	$(MgO)_{0.77}(FeO)_{0.23}$					•		
Lime	CaO			•				
Portlandite	$Ca(OH)_2$	•	•					
Hematite	Fe_2O_3	•	•	•	•	•	•	•
Magnetite	Fe_3O_4				•	•		
Wustite	FeO					•		
	$KFe_{11}O_7$		•					
Aluminium oxide	Al_2O_3			•				
Corundum	Al_2O_3			•				
Albite	$NaAlSi_3O_8$				•			•
Microcline	$KAlSi_3O_8$	•		•	•	•		•
Orthoclase	$KAlSi_3O_8$					•		
Kalsilite	$KAlSiO_4$	•	•	•	•			•
Leucite	KAl_2SiO_6			•		•		•
Wollastonite	$CaSiO_3$	•	•	•	•			•
Larnite	Ca_2SiO_4				•			
Diopside	$CaMgSi_2O_6$			•		•		•
Akermanite	$Ca_2MgSi_2O_7$	•	•	•	•	•	#	#•
Gehlenite	$Ca_2Al(AlSiO_7)$		•				#	#
Monticellite	$CaMgSiO_4$	•	•					
Merwinite	$Ca_3MgSi_2O_8$		•	•	•		•	
Forsterite	Mg_2SiO_4	•		•	•			
Soda melilite	$CaNaAlSi_2O_7$			•			•	
Grossular	$Ca_3Al_2(SiO_4)_3$			•	•			
Grossite	$CaAl_4O_7$							•
Xonotlite	$Ca_6Si_6O_{16}(OH)_2$				•			
Cordierite	$Mg_2Al_4Si_5O_8$			•				
Calcium Phosphate	$Ca_3(PO_4)_2$			•		•		
Iron Silicate	Fe_2SiO_4				•			
Mullite	$Al_{2.35}Si_{0.64}O_{4.82}$			•				•

In contrast to the fuel blends, more oxides have been identified (Table 7-3). Incorporation of K and Mg into the Fe-oxides has been observed. The high Fe content of the eucalyptus compared to the other fuel blends is likely the cause for this observation. However, as $KFe_{11}O_7$ is only present in the laboratory ashed samples, it may be that this phase was formed due to proximity, rather than being a favoured or likely phase to appear in the combustion rig. The magnesium iron oxide, observed in the coupon scales, is likely to be a reaction occurring prior to the formation of augite, a silicate closely related to the CaO-MgO-SiO system.

The phosphate hydroxyapatite that was observed in the hemp and coal ash, and in the loose bottom ash of the eucalyptus and coal ash, was not observed in the eucalyptus ash. Instead the phase $Ca_3(PO_4)_2$ is present; this is likely formed through the reaction of P_2O_5 with CaO (Equation 5-26). The source of the hydroxyapatite in the samples is not fully clear; in the hemp and coal samples it is thought to be present in the trichome structures of the raw hemp fuel which only decompose at high temperatures. The $Ca_3(PO4)_2$ is present in the deposit samples and the ash coupons, suggesting that it takes longer than an hour at high temperature to form.

The plerospheres and cenospheres that were identified and classified by Raask[191] are also identified in the eucalyptus combustion rig samples (Figure 5-37) indicating that they are not a coal specific morphology. This is due to the similar ash composition (presence of SiO_2, Al_2O_3) of the biomass fuels and coal, which suggests that alongside the other formation conditions of catalytic Fe to induce droplet swell and a small amount of C is needed in the spheres means that the spheres will be present during biomass combustion. Spheres are also identified by Valentim *et al*.[192], however rather than being silicate spheres the composition is largely P and are named phosphospheres, these have been identified in both biomass and co-fired ash in the present study (Figure 6-34).

Sintering, slagging, and fouling are severe problems related to firing biomass or co-firing biomass in power plants that were developed for other types of fuel.[53] Analysis of the data suggests sintering has occurred in all fuel types; the K or Ca-silicates and phosphates have previously been identified as causing sintering, and as such are likely responsible for the sintering in the deposits formed in the combustion rig. Figure 6-35 indicates regions of silicates and P containing regions where the spheres have joined together to form melts, these may then sinter as is the case in Figure 6-36. A slag melt formed during the combustion run on the face of probe EUC E is presented in Figure 6-32. Sintering and slag melt is also observed in the bottom ash of all of the combustion trials (Figure 5-30), showing that all of the fuels will form slag melts under extreme conditions.

7.4 Fuel comparisons and conclusions

Whilst the fuels and fuel blends had variations in the composition of the ash matrix, there are several distinct trends that can be identified in the phase formation during combustion. All three polymorphs of SiO_2 are formed during the combustion of biomass ash, with the presence of cristobalite likely aiding the formation of the complex alkali silicates observed in the ash.

The phase diagram CaO-MgO-SiO_2 can be used to accurately predict which silicates will form during the combustion of biomass/ biomass and coal, as phases from this system are present in each fuel blend/type. There is variation between the phases formed with wollastonite, akermanite, and diopside being the most commonly formed in the samples. The formation of these phases is dependent on the time that the deposited ash spends in the flue gas e.g. these phases are less likely to be observed in the quenched ash samples. The formation of phases other than those predicted by the ideal conditions (which would be ideal mixing (homogenous distribution) of the phases with no temperature gradient over the sample) are likely due to the random impaction mechanism of the particles, which makes it impossible to predict where each phase will deposit. For example, if more Mg deposits in a region compared to Ca, monticellite will form in favour of merwinite. This also accounts for the formation of forsterite (magnesium silicate) and wollastonite/larnite (calcium silicates) phases, without significant substitution by the opposite oxide.

Closely related to this above mentioned phase diagram is the CaO-Al_2O_3-SiO_2 system. The phases akermanite and gehlenite are end members in the melilite family, and so the formation of these two phases, both alone and as a solid solution is likely to occur. The eucalyptus fuel has a higher content of Al_2O_3 than the co-fired blends and therefore, coupled with the lower SiO_2 content, more Ca,Al-silicates are formed. This phase diagram also predicts the formation of the phases anorthite and mullite which have also been observed in the samples.

The K,Al-silicates that are present in the co-fired samples may form through decomposition of the kaolinite/illite present in the coal fuel. However in the eucalyptus these phases are not present. The proposed mechanism of formation for kalsilite is instead a reaction between Al_2O_3.SiO_2 and KOH/KCl present from the combustion of the biomass. This formation mechanism is also applicable for the co-fired blends, as K is present in more readily accessible (during combustion) forms in biomass compared to coal, i.e. do not require high temperature decomposition for formation. The multiple formation pathways of kalsilite, coupled with a presence in a large portion of the samples analysed, indicate that the phase is favoured in the combustion conditions observed in the combustion trials. This phase can then convert to

leucite with an excess of SiO_2, which accounts for the presence of this phase in the deposits, coupons, and bottom ash as the excess SiO_2 is either present from transport through the deposit or inertial impaction onto the kalsilite region.

Also present in the samples are K-feldspars (microcline, sanidine, and orthoclase); these feldspars are likely to originate from the soil collected during the harvesting of the biomass. However, formation can also occur during the decomposition of coal phases during combustion. Interconversion of these feldspars occured in the combustion rig and also in the lab samples. This is due to the rapid cooling of the samples, with both the coupons removed from the combustion rig and the samples removed from the furnace cooling rapidly after removal from the high temperature environment. This leads to the formation of orthoclase, the high temperature form of microcline, as the rapid cooling did not allow rearrangement to microcline.

P-containing phases in the samples vary between the co-fired ashes and the eucalyptus ash. In the co-fired blends hydroxyapatite was identified. In the case of hemp and coal it is present from the trichome structures, and may be partially present from the coal. In comparison, $Ca_3(PO_4)_2$ formed when the eucalyptus was fired alone. This suggests that the formation of hydroxyapatite was assisted by the coal. Also present in the hemp fuel are the trichome structures which comprise of silicate and phosphates; this accounts for the higher content of P_2O_5 in the ash in comparison to the two other fuels. The hydroxyapatite present converts into the phase $Ca_9MgK(PO_4)_7$ in the high temperature slag melt of the bottom ash. This phase may also have formed from the phosphospheres, first presented by Valentim *et al*.[192] these are identified in Figure 6-36.

Spheres present in the ashes, identified as plerospheres and cenospheres, were first identified by Raask[191] in coal ash. The spherical morphology is more commonly observed in samples removed from the combustion rig, this suggests that formation is dependent on the heating rate, which is higher in the combustion rig. Nucleation of KCl has also been observed on the surface of the spheres, indicating a reason for observation in the deposits onto ceramic.

The formation of phases present in the $CaO\text{-}MgO\text{-}SiO_2$ and $CaO\text{-}Al_2O_3\text{-}SiO_2$ systems, occurs on the surface of the coupons present in the boiler. The formation of deposits on these surfaces can lead to a loss in heat transfer and therefore is undesirable. The deposition of KCl onto the surface of the coupons is present in all three fuel systems analysed. The eucalyptus and coal had the widest variety of oxidation products (Table 6-5) suggesting this fuel blend was more likely to cause corrosion on a larger scale. However, these results cannot be compared with

the eucalyptus combustion run as coatings were present on the coupons. The eucalyptus co-fire had the highest SO_3 content of the fuel blends, suggesting that upon sulfation of the KCl (to yield K_2SO_4) the Cl liberated was free to attack the metal surface again initiating corrosion. The main oxidation products of the hemp and coal combustion trial were hematite and magnetite.

None of the fuels/blends were free of slagging, fouling, and sintering, suggesting that for larger trials optimum combustion conditions should be looked for more closely. The high SiO_2, K_2O, and CaO content of the fuels increases the likelihood of sintering, whereas an increase in the Al_2O_3 content of the fuel leads to the formation of phases with higher melting temperatures.

Overall, there were a wide variety of phases identified in the combustion trial samples which could be predicted relatively well using phase diagrams of the dominant oxides in the ash, coupled with in laboratory studies of the fuels used in the trials. The prediction of the formation of these phases is important information prior to full scale combustion, as phases that are likely to cause large deposit build up or high corrosion rates are desirable to avoid. The morphology range of the particles present in the deposit, quenched, and fly ash samples was not wide as the dominant morphology was the spherical particles formed due to the heating rate across the samples in the flame.

8. Overall Conclusions and Further Work

The analysis of the fuels and ashes of hemp, coal, and eucalyptus, alongside the co-fired blends of hemp and coal, and eucalyptus and coal synthesised in the laboratory enabled a profile which could be applied to a larger scale to be compiled. The formation of phases at specific temperatures and over time can directly feedback to larger scale tests and applications as problem areas (i.e. areas where these phases may grow and then form large slag melts) can then be identified. The initial ash matrix of the bulk helps to gain information about phases that may form at high temperatures i.e. the high SiO_2 and CaO content of the fuels meant Ca-silicates were likely to form. The phase systems, particularly CaO-MgO-SiO_2 and CaO-Al_2O_3-SiO_2 can be used to identify phases that are present in the samples. In samples containing a a different compostion e.g. K_2O instead of CaO the appropriate phase systems should be applied. Phase quantification of the laboratory ash samples enhanced information collected as the trend of decreasing SiO_2 whilst the complex Ca-silicated increased showed the profiling of the ash to be correct.

Multiple forms of the fly ash (deposits, quenched, and cyclone ash) and bottom ash from a large scale combustion rig have been analysed. The multiple sources of fly ash allowed a profile of ash behaviour in the large scale to be constructed. The presence of more complex silicates in the deposits compared to the quenched ash/ cyclone ash shows that these phases require time to form. Which phases deposit next to each other is also a consideration in the formation of complex silicates. The variety of temperatures and positions the samples were collected at can be applied to larger scale applications, such as full firing, as temperatures that should be avoided to reduce the formation of problem phases or gas passage angles, that will increase the chance of deposition, can be identified.

Throughout the study phase formation pathways have been identified and applied to both the laboratory synthesised ash and the combustion rig samples. The inhomogeneous nature of the samples (i.e. it is impossible to predict which particles will contain certain phases and whether they will deposit next to another particle) and the time required to form a phase are identified as key points when analysing the ash samples. Whilst some sintering, identified via SEM imaging, of the deposits has occurred they can be removed. However, if the deposits had been present in the combustion rig for longer, a greater degree of sintering may have occurred and slag melts (such as those seen on the eucalyptus coupon probes) may have formed. It is important to monitor this affect in larger scale applications where components will be left for a long time.

The morphology of the ash between the laboratory synthesised ash and the combustion rig trials differs in that spheres are the dominant morphology of the combustion rig samples. The heating rate of the combustion rig is responsible for this dominance; the spheres are designated as ceno and plerospheres (previously identified in coal) and phosphospheres (recently categorised). The presence of the spheres in the eucalyptus samples, where no coal is present, means that the mechanism of formation can also be applied to biomass ash.

One of the phases of interest in biomass combustion and co-firing is KCl, as it is cited as a precursor to corrosion and breakaway oxidation. KCl was identified in multiple samples and was shown to have a direct affect on the coupons, particularly when eucalyptus and coal were co-fired. Distinct areas of KCl attack have been observed. KCl was also present in deposits and cyclone ash meaning that not all KCl in the combustion environment deposited.

The 15Mo3 coupons showed signs of active oxidation, where scales had been removed from the coupon surface. Hematite whiskers and magnetite octahedra were also observed. This oxidation and reduction in a large scale trial shows that monitoring of components using the 15Mo3 alloy should be included in plant operation. Coatings appeared to reduce the visible signs of active oxidation.

Futher work analysing biomass fuels and ash for combustion is required. Different fuel blends should be analysed to strengthen this approach, which can also be used in conjunction with modelling. The application of these techniques to other combustion technologies, e.g. bubbling fluidised bed and circulating fluidised bed, should also be attempted, which will allow further profiling of fuels.

Further phase quantification work on the laboratory synthesised ash and the combustion rig samples is also necessary, as this will allow further trends to be identified. Analysis of the combustion rig samples will give further information about the composition of the deposits and how much the SiO_2 reacts in the deposits. The information about composition of the ashes is also likely to be useful when analysing disposal of the ashes. Little other work has been done on phase quantification of biomass ashes.

Analysis of the spheres, such as cross sectioning to find out what is inside, to gather further information about formation mechanisms should be conducted. The formation of the whiskers in the eucalyptus and coal combustion rig samples is of interest as, whilst several studies have already been attempted, a general consensus has yet to be reached.

This study has looked at the application of biomass co-firing to pulverised fuel for combustion trials, further work assessing the availability of the fuel, transport costs, and disposal should also be conducted.

9. References

1. Loo, S. Van & Koppejan, J. *The handbook of biomass combustion and co-firing*. (Earthscan, 2008).

2. Paper, E. W. Our energy future - creating a low carbon economy.

3. Nielsen, L. B., Jensen, L. S., Pedersen, C., Røkke, M. & Livbjerg, H. Field measurements of combustion aerosols from co-firing of coal and straw. *J. Aerosol Sci.* **27,** S365–S366 (1996).

4. Bauen, A., Berndes, G., Junginger, M., Londo, M. & Vuille, F. Bioenergy- a Sustainable and Reliable Energy Source. *IEA Bioenergy* 1–108 (2009). doi:ExCo: 2009:06

5. Eisentraut, A. & Brown, A. Technology Roadmap Bioenergy for Heat and Power. *Technol. Roadmaps* 1–41 (2012).

6. *Climate Change Act 2008*. (2008). at <www.legislation.gov.uk/ukpga>

7. Iain MacLeay, Harris, K., Annut, A. & Authors, and C. Digest of United Kingdom Energy Statistics (DUKES) 2014. 1–268 (2014). at <https://www.gov.uk/government/publications/digest-of-united-kingdom-energy-statistics-dukes-2013-printed-version-excluding-cover-pages>

8. Bugge, J., Kjær, S. & Blum, R. High-efficiency coal-fired power plants development and perspectives. *Energy* **31,** 1437–1445 (2006).

9. Baxter, L. & Koppejan, J. Biomass-coal Co-combustion : Opportunity for Affordable Renewable Energy. *Fuel* **84,** 1295–1302 (2005).

10. County, E. & Service, R. *Tilbury Power Station 27 February 2012 - A Fire Service Repsonse*. (2012).

11. Centre, I. C. C. Coal Online. at <http://www.coalonline.org/site/coalonline/content/home>

12. Hack, H. & Stanko, G. Update on Fireside Corrosion Resistance of Advanced Materials for Ultra-Supercritical Coal-Fired Power Plants. in *The 31st International Technical Conference on Coal …* (2006).

13. Designation, A. *Standard Classification of Coals by Rank*. *1992 Annual Book of ASTM Standards, Section 5, …* (ASTM International, 2012). doi:Standard Classification of Coals by Rank

14. Spitz, N. *et al.* Firing a sub-bituminous coal in pulverized coal boilers configured for bituminous coals. *Fuel* **87,** 1534–1542 (2008).

15. Vassilev, S. V., Baxter, D., Andersen, L. K., Vassileva, C. G. & Morgan, T. J. An overview of the organic and inorganic phase composition of biomass. *Fuel* **94,** 1–33 (2012).

16. Demirbas, A. Combustion characteristics of different biomass fuels. *Prog. Energy Combust. Sci.* **30,** 219–230 (2004).

17. Sami, M., Annamalai, K. & Wooldridge, M. Co-firing of coal and biomass fuel blends. *Prog. Energy Combust. Sci.* **27,** 171–214 (2001).

18. Demirbaş, A. Calculation of higher heating values of biomass fuels. *Fuel* **76,** 431–434 (1997).

19. Sheng, C. & Azevedo, J. L. T. Estimating the higher heating value of biomass fuels from basic analysis data. *Biomass and Bioenergy* **28,** 499–507 (2005).

20. Bryers, R. Fireside slagging, fouling, and high-temperature corrosion of heat-transfer surface due to impurities in steam-raising fuels. *Prog. energy Combust. Sci.* **22,** 29–120 (1996).

21. Burvall, J. A. N. Influence of Harvest Time and Soil Type on Fuel Quality in Reed Canary Grass (Phalaris Aruninacea L.). *Biomass and Bioenergy* **12,** 149–154 (1997).

22. Xiong, S., Zhang, Q.-G., Zhang, D.-Y. & Olsson, R. Influence of harvest time on fuel characteristics of five potential energy crops in northern China. *Bioresour. Technol.* **99,** 479–85 (2008).

23. Zub, H. W., Arnoult, S. & Brancourt-Hulmel, M. Key traits for biomass production identified in different Miscanthus species at two harvest dates. *Biomass and Bioenergy* **35,** 637–651 (2011).

24. Lewandowski, I. & Heinz, A. Delayed harvest of miscanthus—influences on biomass quantity and quality and environmental impacts of energy production. *Eur. J. Agron.* **19,** 45–63 (2003).

25. Wieck-hansen, K. *Parameters influencing straw quality important for burning in boilers*. (2005).

26. Vassilev, S. V., Baxter, D., Andersen, L. K. & Vassileva, C. G. An overview of the chemical composition of biomass. *Fuel* **89,** 913–933 (2010).

27. Vassilev, S. V., Baxter, D. & Vassileva, C. G. An overview of the behaviour of biomass during combustion: Part I. Phase-mineral transformations of organic and inorganic matter. *Fuel* **112,** 391–449 (2013).

28. Werkelin, J., Skrifvars, B.-J. & Hupa, M. Ash-forming elements in four Scandinavian wood species. Part 1: Summer harvest. *Biomass and Bioenergy* **29,** 451–466 (2005).

29. Eldrup, A. & Korshoj, B. *Bioenergy for electricity and heat - experiences from biomass-fired CHP plants in Denmark*. (2007).

30. Nikolaisen, L. *et al. Quality Characteristics of Biofuel Pellets*. (2002).

31. Vassilev, S. V., Baxter, D., Andersen, L. K. & Vassileva, C. G. An overview of the composition and application of biomass ash. Part 1. Phase–mineral and chemical composition and classification. *Fuel* **105,** 40–76 (2013).

32. Vassilev, S. V., Baxter, D., Andersen, L. K. & Vassileva, C. G. An overview of the composition and application of biomass ash. *Fuel* **105,** 19–39 (2013).

33. Vamvuka, D., Pitharoulis, M., Alevizos, G., Repouskou, E. & Pentari, D. Ash affects during combustion of lignite/biomass blends in fluidized bed. *Renew. Energy* **34,** 2662–2671 (2009).

34. Khor, A., Ryu, C., Yang, Y., Sharifi, V. N. & Swithenbank, J. Straw combustion in a fixed bed combustor. *Fuel* **86,** 152–160 (2007).

35. Hughes, E. Biomass cofiring: economics, policy and opportunities. *Biomass and Bioenergy* **19,** 457–465 (2000).

36. Epstein, E. & Bloom, A. J. *Mineral Nutrition of Plants: Principles and Perspectives*. (John Wiley & Sons, 2003).

37. Robinson, A. L., Junker, H. & Baxter, L. L. Pilot-scale investigation of the influence of coal-biomass cofiring on ash deposition. *Energy and Fuels* **16,** 343–355 (2002).

38. Shah, K. V., Cieplik, M. K., Betrand, C. I., van de Kamp, W. L. & Vuthaluru, H. B. Correlating the affects of ash elements and their association in the fuel matrix with the ash release during pulverized fuel combustion. *Fuel Process. Technol.* **91,** 531–545 (2010).

39. Stelte, W., Sanadi, A. & Shang, L. Recent developments in biomass pelletization–A review. *BioResources* **7,** 4451–4490 (2012).

40. Bergman, P. & Kiel, J. Torrefaction for biomass upgrading. *Proc. 14th Eur. Biomass Conf. Paris, Fr.* 17–21 (2005).

41. Cieplik, M. & Fryda, L. in *Solid Biofuels for Energy* 197–217 (2011). at <http://link.springer.com/chapter/10.1007/978-1-84996-393-0_9>

42. Vassilev, S. V., Baxter, D. & Vassileva, C. G. An overview of the behaviour of biomass during combustion: Part II. Ash fusion and ash formation mechanisms of biomass types. *Fuel* **117,** 152–183 (2014).

43. Christensen, K. a. & Livbjerg, H. A Field Study of Submicron Particles from the Combustion of Straw. *Aerosol Sci. Technol.* **25,** 185–199 (1996).

44. Jappe Frandsen, F. Utilizing biomass and waste for power production—a decade of contributing to the understanding, interpretation and analysis of deposits and corrosion products. *Fuel* **84,** 1277–1294 (2005).

45. Wigley, F., Williamson, J. & Gibb, W. The distribution of mineral matter in pulverised coal particles in relation to burnout behaviour. *Fuel* **76,** 1283–1288 (1997).

46. Zbogar, A., Frandsen, F., Jensen, P. A. & Glarborg, P. Shedding of ash deposits. *Prog. Energy Combust. Sci.* **35,** 31–56 (2009).

47. Karin Laursen. Ash deposition trials at three power stations in Denmark. *Fuel Energy Abstr.* **12,** 429 (1998).

48. Hansen, L. A., Nielsen, H. P. & Frandsen, F. J. Influence of deposit formation on corrosion at a straw-fired boiler. *Fuel Process. Technol.* **64,** 189–209 (2000).

49. Jensen, P. & Frandsen, F. SEM investigation of superheater deposits from biomass-fired boilers. *Energy …* **12,** 378–384 (2004).

50. Koer, S. K., Rosendahl, L. A. & Baxter, L. L. Extending the Capability of CFD Codes to Assess Ash Related Problems in Biomass Fired Boilers. *Prepr. Pap.-Am. Chem. Soc., Div. Fuel Chem* **49,** 97 (2004).

51. King, R. A review of vortex shedding research and its application. *Ocean Eng.* **4,** 141–171 (1977).

52. Baxter, L. Ash deposition during biomass and coal combustion: a mechanistic approach.

Biomass and Bioenergy **4,** 85–102 (1993).

53. Frandsen, R. B., Montgomery, M. & Larsen, O. H. Field test corrosion experiences when co-firing straw and coal: 10 year status within Elsam. *Mater. High Temp.* **24,** 343–349 (2007).

54. Coleman, K. E., Simms, N. J., Kilgallon, P. J. & Oakey, J. E. Corrosion in Biomass Combustion Systems. *Mater. Sci. Forum* **595–598,** 377–386 (2008).

55. Walsh, P., Sayre, A. & Loehden, D. Deposition of bituminous coal ash on an isolated heat exchanger tube: affects of coal properties on deposit growth. *Prog. Energy …* **16,** (1990).

56. Lokare, S. S. *et al.* Investigation of Ash Deposition Rates for a Suite of Biomass Fuels and Fuel Blends. *Energy & Fuels* 1008–1014 (2006).

57. Wells, J., Riley, G. & Williamson, J. Interactions between coal-ash and burner quarls. Part 1: Characteristics of burner refractories and deposits taken from utility boilers. *Fuel* **82,** 1859–1865 (2003).

58. Hao, Z., Kefa, C. & Ping, S. Prediction of ash deposition in ash hopper when tilting burners are used. *Fuel Process. Technol.* **79,** 181–195 (2002).

59. Biedermann, F. & Obernberger, I. Ash-related Problems during Biomass Combustion and Possibilities for a Sustainable Ash Utilisation. in *Proceeddings of the Internacional Conference 'World Renewable Energy Congress' (WREC)* 8 (2005). at <www.bios-bioenergy.at>

60. Zbogar, A., Frandsen, F. J., Jensen, P. A. & Glarborg, P. Heat transfer in ash deposits: A modelling tool-box. *Prog. Energy Combust. Sci.* **31,** 371–421 (2005).

61. Wall, T., Bhattacharya, S. & Zhang, D. The properties and thermal affects of ash deposits in coal-fired furnaces. *Prog. Energy …* **19,** 487–504 (1993).

62. Baxter, L., Gale, T., Sinquefield, S. & Sclippa, G. Influence of ash deposit chemistry and structure on physical and transport properties. *Fuel Process. Technol.* **56,** 81–88 (1998).

63. Zheng, Y., Jensen, P. A., Jensen, A. D., Sander, B. & Junker, H. Ash transformation during co-firing coal and straw. *Fuel* **86,** 1008–1020 (2007).

64. Sander, B. & Wieck-Hansen, K. Full-scale investigations on alkali chemistry and ash utilisation by co-firing of straw. *14th Eur. Biomass Conf. Paris, Fr.* (2005).

65. Baxter, L. L. *et al.* The behavior of inorganic material in biomass-fired power boilers : field and laboratory experiences. *Fuel Process. Technol.* **54,** 47–78 (1998).

66. Dayton, D. C., Belle-Oudry, D. & Nordin, A. Affect of Coal Minerals on Chlorine and Alkali Metals Released during Biomass/Coal Cofiring. *Energy & Fuels* **13,** 1203–1211 (1999).

67. Miles, T., Jr, T. M. & Baxter, L. *Alkali deposits found in biomass power plants: A preliminary investigation of their extent and nature. Volume 1*. (1995).

68. Hansen, P. F. B., Andersen, K. H. & Wieck-Hansen, K. Co-firing straw and coal in a 150-MW e utility boiler : in situ measurements. *Fuel Process. Technol.* **54,** 207–225 (1998).

69. Heinzel, T., Siegle, V., Spliethoff, H. & Hein, K. R. G. Investigation of slagging in pulverized fuel co-combustion of biomass and coal at a pilot-scale test facility. *Fuel Process. Technol.* **54,** 109–125 (1998).

70. Khodier, a. H. M., Hussain, T., Simms, N. J., Oakey, J. E. & Kilgallon, P. J. Deposit formation and emissions from co-firing miscanthus with Daw Mill coal: Pilot plant experiments. *Fuel* **101,** 53–61 (2012).

71. Defra. Waste Wood as a Biomass fuel. *Strategy* (2008). at <http://www.defra.gov.uk/environment/waste/topics/documents/wastewood-biomass.pdf>

72. Odukoya, O. O., Arowolo, T. a & Bamgbose, O. Pb, Zn, and Cu levels in tree barks as indicator of atmospheric pollution. *Environ. Int.* **26,** 11–6 (2000).

73. Dai, J. *et al.* Overview and some issues related to co-firing biomass and coal. *Can. J. Chem. Eng.* **86,** 367–386 (2008).

74. Backman, R., Hupa, M., Hitunen, M. & Peltola, K. Interaction Behaviour of Lead and Zinc with Alkalis in Fluidised Bed Combustion or Gasification of Waste Fuels. in *18th International Conference on Fluidised Bed Combustion* 651–659 (2005). doi:0.1115/FBC2005-78074

75. Wiinikka, H., Grönberg, C. & Boman, C. Emissions of Heavy Metals during Fixed-Bed Combustion of Six Biomass Fuels. *Energy & Fuels* **27,** 1073–1080 (2013).

76. Bankiewicz, D., Yrjas, P. & Hupa, M. High-Temperature Corrosion of Superheater Tube Materials Exposed to Zinc Salts †. *Energy & Fuels* **23,** 3469–3474 (2009).

77. Henriksen, N. Corrosion in Coal and Straw Co-Combustion Environments. in *Corrosion 97* (1997).

78. Backman, R., Skrifvars, B. & Yrjas, P. The influence of aerosol particles on the melting behaviour of ash deposits in biomass fired boilers. *Proc. Int. Semin. "Aerosols …* 119–131 (2005). at <http://scholar.google.com/scholar?hl=en&btnG=Search&q=intitle:The+influence+of+aerosol+particles+on+the+melting+behavior+of+ash+deposits+in+biomass+fired+boilers#3>

79. Nussbaumer, T. & Ussbaumer, T. Furnace design and combustion control to reduce emissions and avoid ash slagging. *… Energy Agency, Biomass Combust. Act. Final …* (1995).

80. Kær, S. K. The Impact of Deposits on Heat Transfer during Biomass Combustion. *ACOMP Gr.* (2005).

81. Nutalapati, D., Gupta, R., Moghtaderi, B. & Wall, T. F. Assessing slagging and fouling during biomass combustion: A thermodynamic approach allowing for alkali/ash reactions. *Fuel Process. Technol.* **88,** 1044–1052 (2007).

82. Płaza, P. P. The Development of a Slagging and Fouling Predictive Methodology for Large Scale Pulverised Boilers Fired with Coal / Biomass Blends. (Cardiff University, 2013). at <http://orca.cf.ac.uk/58453/>

83. Noguera, C. & Goniakowski, J. *Oxide Materials at the Two-Dimensional Limit*. **234,** (2016).

84. Richardson, T. *Shriers Corrosion*. (Elsevier,2009, 2009).

85. Uusitalo, M. ., Vuoristo, P. M. . & Mäntylä, T. . High temperature corrosion of coatings and boiler steels below chlorine-containing salt deposits. *Corros. Sci.* **46,** 1311–1331 (2004).

86. Nielsen, H. P., Frandsen, F. J., Dam-Johansen, K. & Baxter, L. L. The implications of chlorine-associated corrosion on the operation of biomass-fired boilers. *Prog. Energy Combust. Sci.* **26,** 283–298 (2000).

87. Zahs, A., Spiegel, M. & Grabke, H. J. Chloridation and oxidation of iron, chromium, nickel and their alloys in chloridizing and oxidizing atmospheres at 400-700°C. *Corros. Sci.* **42,** 1093–1122 (2000).

88. Cha, S. C. & Spiegel, M. Local reactions of KCl particles with iron, nickel and chromium surfaces. *Mater. Corros.* **57,** 159–164 (2006).

89. Uusitalo, M., Vuoristo, P. & Mäntylä, T. High temperature corrosion of coatings and boiler steels in oxidizing chlorine-containing atmosphere. *Mater. Sci. …* **346,** (2003).

90. Grabke, H. J., Reese, E. & Spiegel, M. The affects of chlorides, hydrogen chloride, and sulfur dioxide in the oxidation of steels below deposits. *Corros. Sci.* **37,** 1023–1043 (1995).

91. Moreea-taha, R. *Materials development for coal , biomass and waste fuel plants*. (2002).

92. Pettersson, J., Asteman, H., Svensson, J.-E. & Johansson, L.-G. KCl Induced Corrosion of a 304-type Austenitic Stainless Steel at 600°C; The Role of Potassium. *Oxid. Met.* **64,** 23–41 (2005).

93. Carter, V. E. *et al. Coatings for Protection*. (Institution of Production Engineers, 1983).

94. Antunes, R. A. & de Oliveira, M. C. L. Corrosion in biomass combustion: A materials selection analysis and its interaction with corrosion mechanisms and mitigation strategies. *Corros. Sci.* **76,** 6–26 (2013).

95. Nordgren, D. & Helgesson, A. *Memo No U08-81 Danish experiences from co-firing of straw and woods*. (2009).

96. Birks, N., Meier, G. H. & Pettit, F. S. *Introduction to the High-Temperature Oxidation of Metals*. (Cambridge University Press, 1993).

97. Heinriksen, N. & Larsen, O. H. Corrosion in Coal and Straw Co-Combustion Environments. in *Corrosion 97* 148 (1997).

98. Stalenheim, A. & Henderson, P. Materials for higher steam temperatures (up to 600°C) in biomass and waste fired plant. – A review of present knowledge. *Varmeforsk* (2011).

99. Liu, C. & Little, J. Corrosion of HR3C heat exchanger alloy in a biomass fired PF utility boiler. *Mater. …* **773,** 765–773 (2000).

100. Hussain, T., Syed, a. U. & Simms, N. J. Trends in fireside corrosion damage to superheaters in air and oxy-firing of coal/biomass. *Fuel* **113,** 787–797 (2013).

101. Dudziak, T., Hussain, T., Simms, N. J., Syed, A. U. & Oakey, J. E. Fireside corrosion degradation of ferritic alloys at 600°C in oxy-fired conditions. *Corros. Sci.* **79,** 184–191 (2014).

102. Skrifvars, B.-J., Westén-Karlsson, M., Hupa, M. & Salmenoja, K. Corrosion of superheater steel materials under alkali salt deposits. Part 2: SEM analyses of different steel materials. *Corros. Sci.* **52,** 1011–1019 (2010).

103. Eriksson, T. *Corrosion of Heat Transfer Surfaces in Co-Combustion of Fossil and Biomass Fuel*. (2000).

104. Pettersson, C., Pettersson, J., Asteman, H., Svensson, J.-E. & Johansson, L.-G. KCl-induced high temperature corrosion of the austenitic Fe–Cr–Ni alloys 304L and Sanicro 28 at 600°C. *Corros. Sci.* **48,** 1368–1378 (2006).

105. Davidsson, K. O. *et al.* Potassium, chlorine, and sulfur in ash, particles, deposits, and corrosion during wood combustion in a circulating fluidized-bed boiler. *Energy and Fuels* **21,** 71–81 (2007).

106. Skog, E. *et al.* Why Does Bio-mass and Waste Cause Severe Corrosion of Superheater Tubes. *Proc. 33rd Int. …* (2008).

107. Schütze, M., Malessa, M., Rohr, V. & Weber, T. Development of coatings for protection in specific high temperature environments. *Surf. Coatings Technol.* **201,** 3872–3879 (2006).

108. Hussain, T., Dudziak, T., Simms, N. J. & Nicholls, J. R. Fireside Corrosion Behavior of HVOF and Plasma-Sprayed Coatings in Advanced Coal/Biomass Co-Fired Power Plants. *J. Therm. Spray Technol.* **22,** 797–807 (2013).

109. Uusitalo, M., Vuoristo, P. & Mäntylä, T. High temperature corrosion of coatings and boiler steels in reducing chlorine-containing atmosphere. *Surf. Coatings Technol.* **161,** 275–285 (2002).

110. Kumar, V. & Kandasubramanian, B. Processing and design methodologies for advanced and novel thermal barrier coatings for engineering applications. *Particuology* **27,** 1–28 (2016).

111. Sidhu, T. S., Agrawal, R. D. & Prakash, S. Hot corrosion of some superalloys and role of high-velocity oxy-fuel spray coatings—a review. *Surf. Coatings Technol.* **198,** 441–446 (2005).

112. Jenkins, B. ., Baxter, L. ., Miles, T. . & Miles, T. . Combustion properties of biomass. *Fuel Process. Technol.* **54,** 17–46 (1998).

113. Vamvuka, D. & Mistakidou, E. Predicting the affect of inorganic constituents of wood residues on boiler 1. *14th Eur. Biomass Conf. , 17-21 Oct. 2005 , Paris , Fr.* 1328–1331 (2005).

114. Montgomery, M., Sander, B. & Larsen, O. H. Biomass firing: Danish experiences. *Energy Mater. Mater. Sci. Eng. Energy Syst.* **1,** 17–19 (2006).

115. Wiltsee, G. *Lessons Learned from Existing Biomass Power Plants*. *Cogeneration* (DIANE Publishing, 2000). at <http://www.osti.gov/energycitations/product.biblio.jsp?osti_id=753767>

116. Liodakis, S., Katsigiannis, G. & Kakali, G. Ash properties of some dominant Greek forest species. *Thermochim. Acta* **437,** 158–167 (2005).

117. Teixeira, E. R., Mateus, R., Camões, A. F., Bragança, L. & Branco, F. G. Comparative

environmental life-cycle analysis of concretes using biomass and coal fly ashes as partial cement replacement material. *J. Clean. Prod.* **112, Part,** 2221–2230 (2016).

118. Institute, B. S. *BS EN ISO/IEC 17025:2005 General requirements for the competence of testing and calibration laboratories*. (2005).

119. Institute, B. S. *BS EN 14778:2011 Solid Biofuels - Sampling*. (2011).

120. Institute, B. S. *BS EN 14780:2011 Solid biofuels — Sample preparation*. (2011).

121. Institute, B. S. *BS EN ISO 18134-1:2009 Solid biofuels. Determination of moisture content. Oven dry method. Total moisture. Reference method*.

122. Institute, B. S. *BS EN ISO 18123:2009 Solid biofuels. Determination of the content of volatile matter*.

123. Institute, B. S. *BS EN ISO 17225-1:201 Solid biofuels — Fuel specifications and classes Part 1 : General requirements*. (2014).

124. Institute, B. S. *BS EN 14918:2009 Solid biofuels. Determination of calorific value.*

125. Institute, B. S. *BS EN ISO 16994 Solid biofuels. Determination of total content of sulphur and chlorine*.

126. British. *BS EN ISO 16948:2015 Solid biofuels. Determination of total content of carbon, hydrogen and nitrogen. View details*.

127. Institute, B. S. *BS EN ISO 16967 Solid biofuels — Determination of major elements — Al , Ca , Fe , Mg , P , K , Si , Na and Ti (ISO*. (2015).

128. Institute, B. S. *BS EN 15297:2011 Solid biofuels — Determination of minor elements — As , Cd , Co , Cr , Cu , Hg , Mn , Mo , Ni , Pb , Sb , V and Zn*. (2011).

129. Institute, B. S. *BS EN ISO 11885:2009 Water quality — Determination of selected elements by inductively coupled plasma optical emission spectrometry (ICP-OES)*. (2009).

130. Institute, B. S. *BS EN ISO 16993:2015 Solid biofuels — Conversion of analytical results from one basis to another*. (2015).

131. Schofield, P. F.; Knight, K. S.; Covey-Crump, S. J.; Cressey, G.; Stretton, I. C. Accurate quantification of the modal mineralogy of rocks when image analysis is difficult. *Mineral. Mag.* **66,** 189–200 (2002).

132. Lambiv Dzemua, G., Gleeson, S. A. & Schofield, P. F. Mineralogical characterization of the Nkamouna Co--Mn laterite ore, southeast Cameroon. *Miner. Depos.* **48,** 155–171 (2013).

133. Pecharsky, V. & Zavalij, P. *Fundamentals of Powder Diffraction and Structural Characterization of Materials, Second Edition*. (Springer US, 2008). at <https://books.google.co.uk/books?id=2fI-AAAAQBAJ>

134. Newman, J. A. *et al.* Parts per Million Powder X-ray Diffraction. *Anal. Chem.* **87,** 10950–10955 (2016).

135. Downs, R. T. & Hall-Wallace, M. The American Mineralogist crystal structure database. *Am. Mineral.* **88,** 247–250 (2003).

136. Xing, P. *et al.* Short communication A comparative assessment of biomass ash preparation methods using X-ray fluorescence and wet chemical analysis. *Fuel* **182,** 161–165 (2016).

137. Institute, B. S. *BS EN 18122:2015 Solid biofuels — Determination of ash content*. (2015).

138. Sherman, J. The theoretical derivation of fluorescent X-ray intensities from mixtures. *Spectrochim. Acta* **7,** 283–306 (1955).

139. Thomsen, V. Basic Fundamental Parameters in X-Ray Fluorescence. *Spectroscopy* **22,** 46–50 (2007).

140. Sprang, H. A. Van. Fundamental Parameter Methods in XRF Spectroscopy. *Adv. X-ray Anal.* **42,** (2000).

141. Elam; William T. (Redmond, WA), Nicolosi; Joseph A. (Bardonia, NY), Shen; Robert B. (South Barrington, IL), Scruggs; Bruce E. (Englewood, N. Scatter spectra method for x-ray fluorescent analysis with optical components. (2005).

142. EDAX. *X-Ray Fluorescence Metrology Tools*. (2016). at <http://www.edax.com/-/media/ametekedax/files/xray_metrology/brochures/xrf_metrology_tools_tech_guide.pdf>

143. Brunner, D. *IEA Bioenergy Task 32 project Advanced characterisation methods for solid biomass fuels*. (2015).

144. Vassilev, S. V., Vassileva, C. G. & Vassilev, V. S. Advantages and disadvantages of composition and properties of biomass in comparison with coal: An overview. *Fuel* **158,** 330–350 (2015).

145. Blomberg, T. E. Free Alkali-Index for Optimising the Fuel Mixture in Biomass Co-firing. in *Proceedings of 7th International Conference on Heat Exchanger Fouling and Cleaning - Challenges and Opportunities* (2010).

146. Pronobis, M. Evaluation of the influence of biomass co-combustion on boiler furnace slagging by means of fusibility correlations. *Biomass and Bioenergy* **28,** 375–383 (2005).

147. Xiong, S., Öhman, M., Zhang, Y. & Lestander, T. Corn Stalk Ash Composition and Its Melting (Slagging) Behavior during Combustion. *Energy & Fuels* **24,** 4866–4871 (2010).

148. Weber, R., Mancini, M., Schaffel-Mancini, N. & Kupka, T. On predicting the ash behaviour using Computational Fluid Dynamics. *Fuel Process. Technol.* **105,** 113–128 (2013).

149. Niu, Y. *et al.* Further study on biomass ash characteristics at elevated ashing temperatures: the evolution of K, Cl, S and the ash fusion characteristics. *Bioresour. Technol.* **129,** 642–5 (2013).

150. Suárez-Garcıa, F. & Martınez-Alonso, A. Inorganic matter characterization in vegetable biomass feedstocks. *Fuel* **81,** (2002).

151. Prade, T., Svensson, S.-E., Andersson, A. & Mattsson, J. E. Biomass and energy yield of industrial hemp grown for biogas and solid fuel. *Biomass and Bioenergy* **35,** 3040–3049 (2011).

152. Alaru, M. *et al.* Lignin content and briquette quality of different fibre hemp plant types and energy sunflower. *F. Crop. Res.* **124,** 332–339 (2011).

153. Salentijn, E. M. J., Zhang, Q., Amaducci, S., Yang, M. & Trindade, L. M. New developments in fiber hemp (Cannabis sativa L.) breeding. *Ind. Crops Prod.* **68,** 32–41 (2015).

154. Rehman, M. S. U., Rashid, N., Saif, A., Mahmood, T. & Han, J.-I. Potential of bioenergy production from industrial hemp (Cannabis sativa): Pakistan perspective. *Renew. Sustain. Energy Rev.* **18,** 154–164 (2013).

155. Gov.uk. Hemp Growing Licence. *12 Nov* (2014). at <https://www.gov.uk/hemp-growing-licence>

156. Bates, S. *et al.* Analysis of amorphous and nanocrystalline solids from their X-ray diffraction patterns. *Pharm. Res.* **23,** 2333–49 (2006).

157. Belton, D., Deschaume, O. & Perry, C. An overview of the fundamentals of the chemistry of silica with relevance to biosilicification and technological advances. *FEBS J.* **279,** 1710–1720 (2012).

158. Schilmiller, A. L., Last, R. L. & Pichersky, E. Harnessing plant trichome biochemistry for the production of useful compounds. *Plant J.* **54,** 702–11 (2008).

159. Etienne, M. Time factor in utilization of mineral nutrients by hemp. *Plant Physiol.* 731 (1936).

160. Földvári, M. *Handbook of thermogravimetric system of minerals and its use in geological practice*. **213,** (2011).

161. Cultrone, G., Rodriguez-Navarro, C., Sebastian, E., Cazalla, O. & De La Torre, M. J. Carbonate and silicate phase reactions during ceramic firing. *Eur. J. Mineral.* **13,** 621–634 (2001).

162. Trindade, M., Dias, M., Coroado, J. & Rocha, F. Mineralogical transformations of calcareous rich clays with firing: A comparative study between calcite and dolomite rich clays from Algarve, Portugal. *Appl. Clay Sci.* **42,** 345–355 (2009).

163. Ohashi, Y. & Finger, L. W. The role of octahedral cations in pyroxenoid crystal chemistry . I . Bustamite , wollastonite , series the pectolite-schizolite-serandite. *Am. Mineral.* **63,** 274–288 (1978).

164. Jung, I.-H., Decterov, S. a. & Pelton, A. D. Critical thermodynamic evaluation and optimization of the CaO–MgO–SiO2 system. *J. Eur. Ceram. Soc.* **25,** 313–333 (2005).

165. Nakamura, S., Otsuka, R., Aoki, H. & Akao, M. Thermal expansion of hydroxyapatite-β-tricalcium phosphate ceramics. *Thermochim. Acta* **165,** 57–72 (1990).

166. Stipniece, L., Salma-Ancane, K., Jakovlevs, D., Borodajenko, N. & Berzina-Cimdina, L. The Study of Magnesium Substitution Affect on Physicochemical Properties of Hydroxyapatite. *Mater. Sci. Appl. Chem.* **28,** 51 (2013).

167. Fernández Llorente, M. J. & Carrasco García, J. E. Comparing methods for predicting the sintering of biomass ash in combustion. *Fuel* **84,** 1893–1900 (2005).

168. Neilan, J. & Thompson, D. Eucalyptus as a potential biomass species for Ireland. *Coford*

Connect. **reproducti,** (2008).

169. Gominho, J., Lourenço, A., Miranda, I. & Pereira, H. Chemical and fuel properties of stumps biomass from Eucalyptus globulus plantations. *Ind. Crops Prod.* **39,** 12–16 (2012).

170. Nussbaumer, T. Combustion and Co-combustion of Biomass: Fundamentals, Technologies, and Primary Measures for Emission Reduction †. *Energy & Fuels* **17,** 1510–1521 (2003).

171. Tao, G. *et al.* Biomass properties in association with plant species and assortments. II: A synthesis based on literature data for ash elements. *Renew. Sustain. Energy Rev.* **16,** 3481–3506 (2012).

172. K. Reisinger, C. Haslinger, M. Herger, H. H. BIOBIB - A Database for Biofuels. at <http://cdmaster2.vt.tuwien.ac.at/biobib/all.html>

173. Netherlands, E. R. C. of the. Phyllis 2, database for biomass and waste. at <https://www.ecn.nl/phyllis2>

174. Lima, M. & Lavorente, G. Affects of pretreatment on morphology, chemical composition and enzymatic digestibility of eucalyptus bark: a potentially valuable source of fermentable sugars. *Biotechnol …* 1–17 (2013).

175. Courtial, P., Téqui, C. & Richet, P. Thermodynamics of diopside, anorthite, pseudowollastonite, CaMgGeO4 olivine, and åkermanite up to near the melting point. *Phys. Chem. Miner.* **49,** 242–250 (2000).

176. Ventura, J. M. G., Tulyaganov, D. U., Agathopoulos, S. & Ferreira, J. M. F. Sintering and crystallization of akermanite-based glass–ceramics. *Mater. Lett.* **60,** 1488–1491 (2006).

177. Energy, U. . D. of. A Brief History of Coal Use. at <http://www.fossil.energy.gov/education/energylessons/coal/coal_history.html>

178. Dyjakon, A., Cieplk, M., Kallvodoka, J. & van de Kamp, W. Laboratory- and Full-Scale Investigations of Slagging and Fouling During Energy Production From Co-Combustion of Coal and Biomass. in *European Biomass Conference* 17 (2009).

179. Ahmed, M. A., Blesa, M. J. & Moliner, R. Chemical Decomposition of Iron in Spanish Coal Pyrolysis Identified by Mossbauer Spectroscopy at Different Temperatures. *Energy Sources, Part A* **29,** 1443–1456 (2007).

180. Eggleton, R. & Buseck, P. The orthoclase-microcline inversion: A high-resolution transmission electron microscope study and strain analysis. *Contrib. to Mineral. Petrol.* **133,** 123–133 (1980).

181. Lay, V. F., Kirk, C. a., Higginson, R. L., Hogg, S. C. & Davis, C. Characterisation, Analysis and comparison of multiple biomass fuels used in co-firing trials. in *23rd European Biomass Conference and Exhibition* 464–474 (2015). at <http://www.etaflorence.it/proceedings/index.asp?conference=2015>

182. Mao, H., Hillert, M., Selleby, M. & Sundman, B. Thermodynamic Assessment of the CaO-Al2O3-SiO2 System. *J. Am. Ceram. Soc.* **89,** 298–308 (2006).

183. Zhang, Y., Li, B., Rao, P., Lü, M. & Wu, J. Seeded Crystallization of Leucite. *J. Am.*

Ceram. Soc. **90,** 1615–1618 (2007).

184. Lindström, E., Boström, D. & Öhman, M. Affect of kaolin and limestone addition on slag formation during combustion of woody biomass pellets. *Proc. 14th Eur. …* 1319–1322 (2005).

185. Steenari, B. & Lindqvist, O. High-temperature reactions of straw ash and the anti-sintering additives kaolin and dolomite. *Biomass and Bioenergy* **14,** (1998).

186. Rao, Y. The kinetics of reduction of hematite by carbon. *Metall. Trans.* **2,** (1971).

187. Monsen, B. Iron ore concentrates: oxidation and reduction. (1992). at <http://brage.bibsys.no/xmlui/handle/11250/248778>

188. Sørensen, P. M. *et al.* Affect of the redox state and concentration of iron on the crystallization behavior of iron-rich aluminosilicate glasses. *J. Non. Cryst. Solids* **351,** 1246–1253 (2005).

189. Vassileva, G. Some relationships between coal rank and chemical and mineral composition. *Fuel* **75,** 1537–1542 (1996).

190. Lay, V. F., Higginson, R. L., Hogg, S. C., Kirk, C. a. & Davis, C. Analysis of deposits formed during biomass co-firing on 15Mo3 under different gas and temperature conditions. *Mater. High Temp.* **32,** 230–237 (2015).

191. Raask, E. *Mineral Impurities in Coal Combustion: Behavior, Problems, and Remedial Measures*. (Taylor & Francis, 1985).

192. Valentim, B. *et al.* Notes on the occurrence of phosphate mineral relics and spheres (phosphospheres) in coal and biomass fly ash. *Int. J. Coal Geol.* **154–155,** 43–56 (2016).

193. Mazzucato, E. & Gualtieri, a. F. Wollastonite polytypes in the CaO-SiO 2 system. *Phys. Chem. Miner.* **27,** 565–574 (2000).

194. Vu, D. H., Wang, K.-S., Chen, J.-H., Nam, B. X. & Bac, B. H. Glass–ceramic from mixtures of bottom ash and fly ash. *Waste Manag.* **32,** 2306–2314 (2012).

195. Gemmi, M., Merlini, M., Cruciani, G. & Artioli, G. Non-ideality and defectivity of the akermanite-gehlenite solid solution: An X-ray diffraction and TEM study. *Am. Mineral.* **92,** 1685–1694 (2007).

196. Pinho, S. P. & Macedo, E. A. Solubility of NaCl, NaBr, and KCl in water, methanol, ethanol, and their mixed solvents. *J. Chem. Eng. Data* **50,** 29–32 (2005).

197. Mineralogical, J. & America, S. O. F. THE CRYSTAL FORMS OF CALCIUM SULPHATE.

198. Backman, R., Skrifvars, B.-J. B. & Yrjas, P. The influence of aerosol particles on the melting behavior of ash deposits in biomass fired boilers. in *Aerosols in Biomass Combustion* 119–131 (2005). at <www.ieabcc.nl/workshops/task32_Graz_aerosols/10_Backman.pdf>

199. Queiroz, C., Fernandes, M. & Frade, J. Early steps of orthophosphate crystallisation in a Ca-Mg-K phosphosilicate glass frit. *Mater. Sci. Forum* **456,** 402–405 (2004).

200. Queiroz, C. M., Fernandes, M. H. & Frade, J. R. Particle size affects on the

crystallisation of glass with the. *Phys. Chem. Glas.* **43C,** 281–285 (2002).

201. Boström, D. & Broström, M. Ash transformation chemistry during energy conversion of biomass. *Proc. …* 1–20 (2010). at <https://pure.ltu.se/portal/files/32600542/25._Bostrom_et_al_2010_Imp._of_fuel_quality.pdf>

202. Nordgren, D., Hedman, H., Padban, N., Boström, D. & Öhman, M. Ash transformations in pulverised fuel co-combustion of straw and woody biomass. *Fuel Process. Technol.* **105,** 52–58 (2013).

203. Farny, J. A. & Kerkhoff, B. Diagnosis and Control of Alkali-Aggregate Reactions in Concrete. *Portl. Cem. Assoc.* (2007). at <http://www.cement.org/docs/default-source/fc_concrete_technology/is413-02---diagnosis-and-control-of-alkali-aggregate-reactions-in-concrete.pdf?sfvrsn=2>

204. Chisholm, J. E. Determination of cristobalite in respirable airborne dust using x-ray diffraction. *Anal. Chim. Acta* **286,** 87–95 (1994).

205. Jenkins, B., Baxter, L., Jr, T. M. & Miles, T. Combustion properties of biomass. *Fuel Process. Technol.* **54,** 17–46 (1998).

206. Linch, K. D. Respirable concrete dust--silicosis hazard in the construction industry. *Appl. Occup. Environ. Hyg.* **17,** 209–21 (2002).

207. Higgins, N., Srinivasan, N., Shah, J., Dorner, R. & Pozzobon, E. Fuel affects andmitigation strategies when cofiring pulverized biomass. in *Power-Gen Europe. Milan.* 24 (2011).

208. Kang, M. & Kang, S. Influence of Al2O3 additions on the crystallization mechanism and properties of diopside/anorthite hybrid glass-ceramics for LED packaging materials. *J. Cryst. Growth* **326,** 124–127 (2011).

209. Kurama, S. & Ozel, E. The influence of different CaO source in the production of anorthite ceramics. *Ceram. Int.* **35,** 827–830 (2009).

210. Boström, D., Skoglund, N. & Grimm, A. Ash transformation chemistry during combustion of biomass. *Energy & fuels* **26,** 85–93 (2012).

211. Su, S., Ma, H., Yang, J., Zhang, P. & Luo, Z. Synthesis of kalsilite from microcline powder by an alkali-hydrothermal process. *Int. J. Miner. …* **21,** 826–831 (2014).

212. Steenari, B.-M., Lundberg, A., Pettersson, H., Wilewska-Bien, M. & Andersson, D. Investigation of Ash Sintering during Combustion of Agricultural Residues and the Affect of Additives. *Energy & Fuels* **23,** 5655–5662 (2009).

213. Vassileva, C. G. & Vassilev, S. V. Behaviour of inorganic matter during heating of Bulgarian coals. *Fuel Process. Technol.* **87,** 1095–1116 (2006).

214. Luo, J., Qi, S., Peng, L. & Wang, J. Phytoremediation efficiency OF CD by Eucalyptus globulus transplanted from polluted and unpolluted sites. *Int. J. Phytoremediation* **18,** 308–314 (2016).

215. Wu, P., Eriksson, G. & Pelton, A. Critical evaluation and optimization of the thermodynamic properties and phase diagrams of the CaO–FeO, CaO–MgO, CaO–MnO, FeO–MgO, FeO–MnO, and MgO–. *J. Am. Ceram. …* **5,** (1993).

216. Lumpkin, G. R., Ribbe, P. H. & Lumpkin, N. E. Composition, order-disorder and lattice parameters of olivines; determinative methods for Mg-Mn and Mg-Ca silicate olivines. *Am. Mineral.* **68,** 1174–1182 (1983).

217. Chang, Y.-N. & Wei, F.-I. Review High temperature oxidation of low alloy steels. *J. Mater. Sci.* **24,** 14–22 (1989).

218. Higginson, R. L., Jepson, M. a. E. & West, G. D. Use of EBSD to characterise high temperature oxides formed on low alloy and stainless steels. *Mater. Sci. Technol.* **22,** 1325–1332 (2006).

219. Chang, Y.-N. Oxidation Behaviors of Five Low-Alloy Structural Steels at 600°C. *Corros. Sci.* **50,** 3–10 (1994).

220. Frandsen, F. *et al.* Ash and deposit formation in the biomass co-fired Masnedø combined heat and power production plant. *IFRF Combust. J.* 1–17 (2003).

221. Broström, M. *et al.* Sulfation of corrosive alkali chlorides by ammonium sulfate in a biomass fired CFB boiler. *Fuel Process. Technol.* **88,** 1171–1177 (2007).

222. Ringdalen, E. Changes in Quartz During Heating and the Possible Affects on Si Production. *Jom* **67,** 484–492 (2014).

223. Tite, M. & Maniatis, Y. Examination of ancient pottery using the scanning electron microscope. *Nature* (1975).

224. Rathossi, C. & Pontikes, Y. Affect of firing temperature and atmosphere on ceramics made of NW Peloponnese clay sediments. Part I: Reaction paths, crystalline phases, microstructure and colour. *J. Eur. Ceram. Soc.* **30,** 1841–1851 (2010).

225. Wood, G. C. I. Iron-Chromium Alloys and Stainless Steels at High Temperatures. *Corros. Sci.* **2,** 173–196 (1962).

226. Higginson, R. L. & Green, G. Whisker growth morphology of high temperature oxides grown on 304 stainless steel. *Corros. Sci.* **53,** 1690–1693 (2011).

227. Yuan, L. *et al.* The origin of hematite nanowire growth during the thermal oxidation of iron. *Mater. Sci. Eng. B* **177,** 327–336 (2012).

228. Pang, K.-N., Zhou, M.-F., Lindsley, D., Zhao, D. & Malpas, J. Origin of Fe-Ti Oxide Ores in Mafic Intrusions: Evidence from the Panzhihua Intrusion, SW China. *J. Petrol.* **49,** 295–313 (2007).

229. Niu, Y. *et al.* Experimental evaluation of additives and K2O–SiO2–Al2O3 diagrams on high-temperature silicate melt-induced slagging during biomass combustion. *Fuel* **179,** 52–59 (2016).

230. Rao, K. V. K., Naiw, S. V. N. & Murthy, K. S. Precision Lattice Parameters and Expansion of Calcite. *J. Phys. Chem. Solids* **29,** 245–248 (1968).

231. Markgraf, S. A. & Reeder, R. J. High-temperature structure refinements of calcite and magnesite. *Am. Mineral.* **70,** 590–600 (1985).

232. Fiquet, G., Richet, P., Lyon, Â. De & Lyon, Â. De. High-temperature thermal expansion of lime , periclase , corundum and spinel. 103–111 (2000).

233. Iyengar, L. Thermal expansion and Debye temperatures of KCI-KBr mixed crystals by

an X-ray method. **21,** (1986).

234. AMCSD. American Mineralogist Crystal Structure Database. at <http://rruff.geo.arizona.edu/AMS/amcsd.php>

235. Szemmelveisz, K., Szűcs, I., Palotás, Á. B., Winkler, L. & Eddings, E. G. Examination of the combustion conditions of herbaceous biomass. *Fuel Process. Technol.* **90,** 839–847 (2009).

236. Miller, S. & Miller, B. The occurrence of inorganic elements in various biofuels and its affect on ash chemistry and behavior and use in combustion products. *Fuel Process. Technol.* **88,** 1155–1164 (2007).

237. Werther, J., Saenger, M., Hartge, E.-U., Ogada, T. & Siagi, Z. Combustion of agricultural residues. *Prog. Energy Combust. Sci.* **26,** 1–27 (2000).

238. Lindberg, D., Backman, R., Chartrand, P. & Hupa, M. Towards a comprehensive thermodynamic database for ash-forming elements in biomass and waste combustion — Current situation and future developments. *Fuel Process. Technol.* **105,** 129–141 (2013).

239. Werkelin, J., Lindberg, D., Boström, D., Skrifvars, B.-J. & Hupa, M. Ash-forming elements in four Scandinavian wood species part 3: Combustion of five spruce samples. *Biomass and Bioenergy* **35,** 725–733 (2011).

240. Prade, T., Finell, M., Svensson, S.-E. & Mattsson, J. E. Affect of harvest date on combustion related fuel properties of industrial hemp (Cannabis sativa L.). *Fuel* **102,** 592–604 (2012).

241. Ma, J. F. & Yamaji, N. Functions and transport of silicon in plants. *Cell. Mol. Life Sci.* **65,** 3049–57 (2008).

242. Nakata, P. a. Advances in our understanding of calcium oxalate crystal formation and function in plants. *Plant Sci.* **164,** 901–909 (2003).

243. Cultrone, G. Carbonate and silicate phase reactions during ceramic firing. *Eur. J. Miner.* **13,** 621–634 (2001).

244. Christensen, K. A. The formation of submicron particles from the combustion of straw. (Technical University of Denmark, 1995).

245. Wall, T. F. The Properties and Thermal Affects of Ash Deposits in Coal-Fired Furnaces. *Prog. Energy Combust. Sci.* **19,** 487–504 (1993).

246. Couling, D. The Oxyfuel Research Rig at E.ON New Build & Technology. in *Coal Research Forum AGM and Combustion Division Meeting* (2012).

Appendix 1 – Calculating Patterns for High Temperature In-Situ Data

Using the program WinXPow - THEO the crystal parameters are entered and a full pattern for the specified pattern is generated. The high temperature values for KCl, $CaCO_3$, MgO, hydroxyapatite and CaO were obtained from literature[165,230–233]. Quartz data was already available in the ICDD database. Atom positions were entered from cif files (obtained from the American Mineralogist Crystal Structure Database (AMCSD)[234]). Finally, pattern parameters for geometry (reflection), monochromator (none) and profile function (pearson) were entered. This gave the generation of a pattern with predicted intensities which could then be saved as a .TIN file to put into the graphic comparison software. Where direct temperature data was not available (e.g. CaO) patterns either side were generated and checked for trend.

Appendix 1 – Publications

1. Analysis of deposits formed during biomass co-firing on 15Mo3 under different gas and temperature conditions, V. F. Lay, R. L. Higginson, S. C. Hogg, C. A. Kirk, and C. Davis, Materials At High Temperatures, Vol. 32, Iss. 1-2, 2015

http://dx.doi.org/10.1179/0960340914Z.00000000105

2. Characterisation, analysis and comparison of multiple biomass fuels used in co-firing trials V. F. Lay, R. L. Higginson, S. C. Hogg, C. A. Kirk, and C. Davis, 23rd European Biomass Conference and Exhibition 2015, 464-474

http://dx.doi.org/10.5071/23rdEUBCE2015-2AO.5.1

Analysis of deposits formed during biomass co-firing on 15Mo3 under different gas and temperature conditions

V. F. Lay*[1], R. L. Higginson[1], S. C. Hogg[1], C. A. Kirk[2] and C. Davis[3]

This paper reports on the analysis of fly ash and oxides on 15Mo3 after the co-firing of eucalyptus and a Russian coal at various temperatures and gas conditions for 50 hours. The loose deposits present have been characterised using X-ray diffraction (XRD), scanning electron microscopy (SEM) and energy dispersive X-ray spectroscopy (EDS). Results show that under reducing conditions KCl deposition is increased and a variation in oxide scale composition is observed. Complex silicates, often present as spheres are imaged through SEM.

Keywords: Low alloy steel, 15Mo3, Co-firing, Oxidation

This article is part of a special issue on Microscopy of Oxidation 9

Introduction

Low alloy steels such as 15Mo3 are often used as structural materials in power plants due to their lower cost compared to other ferritic and heat resistant steels.[1–3] 15Mo3 is typically used for boiler tubes for plants operating at temperatures up to 475°C. Oxidation can lead to serious problems including pipe failure and wall thinning at higher temperatures.[4] A review of high temperature oxidation of low alloy steels has previously been conducted by Chang and Wei,[5] and further research characterising the oxides formed from low alloy steels has been conducted by Higginson *et al.*[6] where it was concluded that low alloy steels tend to form less complex oxides such as wustite, magnetite and hematite. Later work by Chang[4] also showed that long term oxidation of metals could not be predicted as different alloys possess widely differing spalling characteristics.

The co-firing of biomass and coal is an increasingly popular method to reduce CO_2 emissions from energy generation.[7] Biomass unlike coal is considered to be carbon neutral. Power stations typically used for the combustion of coal are being adapted to also fire biomass. Ash composition from biomass can vary widely and deposits often form in different regions compared to 100% coal fired systems.[8] These deposits affect heat transfer and can often lead to premature boiler tube failure.[9] Information on oxidation products and deposit formation on 15Mo3 during the combustion of biomass is essential to minimise plant down time. The change from firing coal to co-firing presents challenges for materials due to the chemical differences between coal and biomass.

[1]Department of Materials, Loughborough University, Loughborough, Leicestershire, LE11 3TU, UK
[2]Department of Chemistry, Loughborough University, Loughborough, Leicestershire, LE11 3TU, UK
[3]E.On New Build & Technology Limited, Technology Centre, Ratcliffe-On-Soar, Nottingham, NG11 0EE, UK

*Corresponding author, email v.f.lay@lboro.ac.uk

Biomass commonly has a higher chlorine and potassium content compared to coal, which can lead to increased corrosion compared to coal firing alone.[10] Silicates and their role in combustion have been widely investigated by Vassilev *et al.*[11] in which it was suggested that they prevent the formation of harmful KCl by means of potassium capture. Frandsen[12] found that the uptake of potassium through silicates prevented the formation of corrosive KCl. K_2SO_4 is present in the samples analysed by Frandsen and so, the harmful KCl may have been sulphated through the mechanism proposed by Kassman *et al.*[13] in equation (1)

$$2KCl + SO_2 + H_2O + {}^1/_2O_2 \rightarrow K_2SO_4 + 2HCl \qquad (1)$$

Along with the capture of potassium to form alkali silicates other metals often react with the SiO_2 inherent in both the biomass and coal. Complex silicates such as feldspars form during combustion either through agglomeration of ash particles in the flue gas or via chemical reaction in the deposit itself.[8]

A Cl containing atmosphere either through the presence of deposited KCl or HCl(g) can lead to active oxidation; a schematic illustration can be seen in Fig. 1. Under reducing conditions an oxide barrier which is defective and far less protective than an oxide layer formed under conditions of high O_2 is likely to due to little O_2 present to react and form a protective layer.[14] A presence of CO at concentrations higher than 2% has previously been shown to increase the corrosive rate of HCl by 2·5 times.[15] A high $\%O_2$ indicates oxidising conditions, under which protective oxide scales are more likely to form.[14] In the high $p(O_2)$ metal chlorides diffuse to the scale surface and upon encountering a higher $p(O_2)$ gradient solid metal oxides are formed in a loosely adherent non-protective, porous layer.[15]

Deposit formation and ash phases are widely researched topics within the field of co-firing. Vassilev *et al.*[11] conducted an extensive review into the phases

© W. S. Maney & Son Ltd. 2015
Received 16 April 2014; accepted 16 May 2014
DOI 10.1179/0960340914Z.00000000105

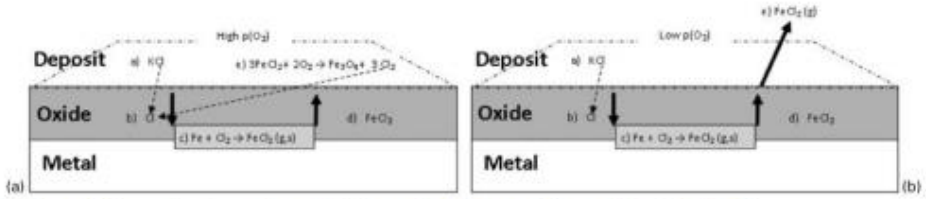

1 Active oxidation mechanisms under *a* oxidising and *b* reducing conditions adapted from Ref. 12

2 Schematic of boiler in combustion rig showing insertion points of probes *a*, *b* and *c* analysed in this study, provided by E.On

found in fly ash and deposits, their roles in corrosion and in relation to their environmental concerns. Fly ash interactions and deposition mechanisms have been discussed in great detail in 'The handbook of biomass combustion and co-firing'[8] which gives information about inorganic phase interactions. This allows insight into possible deposition mechanisms to be gathered as information on both coarse fly ash particles and aerosols are given. Zbogar *et al.*[9] discuss the six methods of particle deposition related to deposit growth:

(i) inertial Impaction
(ii) thermophoresis and diffusion
(iii) eddy deposition (flue gas flow side)
(iv) eddy deposition (non flue gas flow side)
(v) chemical reaction
(vi) condensation.

Eucalyptus is a low ash, low chlorine fuel which decreases the likelihood of large harmful deposits.[16] Knowledge of the interaction between coal and biomass when co-fired can lead to insights into the corrosive effects along with possible areas of deposition. An investigation of the corrosive effect of a eucalyptus/coal blend on 15Mo3 at varying temperatures under oxidation/reducing conditions is reported in this paper.

Materials and experimental procedure

The composition of the alloy 15Mo3 is shown in Table 1. Probes containing coupons of the alloy were exposed for 50 h in a 0·8MWth rig co-firing eucalyptus (82·8% thermal) and Russian coal (17·2% thermal). The fuel was fired in pulverised form at feed rates of 183·50 kg h^{-1} (eucalyptus) and 18·89 kg h^{-1} (coal). Corrosion coupons of 15Mo3 are a bare metal surface ground to a 0·4RA surface finish. These coupons are flush with the lining of the boiler so as to experience the same gas and temperature conditions as pipes as well as not creating any deviation of gas flow. The probes securing mechanisms were lubricated using Belzona 8211 (H.P. Anti-Seize) mineral based nickel grease. A Eurotherm temperature controller with a continuously variable output was used to drive a proportional air throttle valve, enabling the flow of cooling air to the probe to be regulated. Insertion points of the probes are shown in Fig. 2.

Samples were taken at various positions on the boiler wall and were subjected to temperatures of 425–450°C under both oxidation and reducing conditions. Sample conditions are shown in Table 2. Probes were removed after 50 h exposure and were allowed to cool and the ash debris was removed from the probes for analysis. The ash matrix composition was provided by the E.On New Build and Technology centre, elements present were

Table 1 Measured composition of alloy 15Mo3, provided by E.On

Alloy	Cr	Mn	Fe	Ni	Mo	Cu
15Mo3	0·22	0·48	98·59	0·24	0·29	0·18

determined by acid dissolution and emission spectroscopy according to ASTM D6349-09.

Ash debris was analysed using a LEO 1530VP Field Emission Gun SEM (FEGSEM) with an EDAX Genesis Energy Dispersive X-ray Spectroscopy (EDS) instrument. Samples were prepared on carbon pads, attached to aluminium stubs followed by coating with gold for 30 s. Samples were prepared for X-ray diffraction (XRD) analysis by placing between two layers of cello tape. Powder XRD data was collected using the Bruker D_8 discover diffractometer (5–65° 2θ, Co K_α radiation, 16 h). Inductively coupled plasma – optical emission spectroscopy (ICP-OES) was conducted by E.On according to the ASTM D6349-09 standard.[17]

Results and discussion

Fuel characteristics

Inherent biomass ash, those elements that are present as salts, bound in the carbon structure are often more readily available during combustion than those inorganic salts bound in coal.[8] Table 3 shows the ash matrix composition of both the biomass and coal blend, elements presented are assumed to be in the oxide form for analysis with ICP-OES, with the exception of Ca, potentially present as $CaCO_3$, due to the aggressive nature of the acid dissolution. A large percentage of the ash matrix is Si, which can also form a large percentage of coal, in the form of complex silicates such as Illite $[(K,H_2O)Al_2(Si,Al)Si_3O_{10}(OH)_2]$ and also as less complex silicates like quartz (SiO_2).[12] Si can also be present in large quantities in biomass giving skeletal system support in some plants.[8] Information on these elements present often gives important insight into phases likely to be present in any deposits formed through the co-firing of eucalyptus and Russian coal.

Sample atmospheres

Figure 3 shows gas profiles of the probes. The gas sampled was dried through a silica gel column prior to analysis the remainder of the atmosphere contains N_2/CO_2/H_2O along with low levels of various sulphur species and NO_x. Clear differences between O_2 and CO concentrations are observed between probes under oxidising and reducing atmospheres; a higher %CO indicates the conditions are reducing. The coupons are exposed at temperatures below 500°C, and therefore it is likely the corrosion will be parabolic.[15] A high $\%O_2$ indicates oxidising conditions, under which protective oxide scales are more likely to form.[14] Samples analysed in the scope of this paper do not show the full oxidation of the metal coupons as only the loose debris removed from the probes was analysed.

Table 2 Probe temperatures and atmospheres of samples analysed

Probe	Temperature/°C	Atmosphere
A	450	Reducing
B	450	Oxidising
C	425	Oxidising

Table 3 Ash matrix composition according to ASTM D6349-09

Phase	Composition ash matrix/%
SiO_2	33·20
Al_2O_3	8·66
Fe_2O_3	5·89
CaO	25·53
MgO	6·41
K_2O	11·06
Na_2O	2·80
TiO_2	0·87
BaO	0·25
Mn_3O_4	1·85
P_2O_5	2·67

XRD analysis

XRD analysis of the loose deposits from the samples shows the major component in all cases to be quartz (SiO_2). Si constitutes a large percentage of the ash residue and so it is unsurprising that SiO_2 forms a considerable amount of the deposit. During combustion refractory oxides such as SiO_2, CaO and MgO nucleate heterogeneously, the agglomeration of these compounds can lead to the formation of silicates such as sapphirine $(Mg,Al)_8(Al,Si)_6O_{20}$[8] and leucite ($KAlSi_2O_6$). The unassigned peaks in Figure 4 are thought to be due to complex interactions forming solid solutions of silicates. The low intensity of these peaks makes assignment to a specific phase/composition challenging. SEM-EDS analysis confirms the presence of silicate phases in these samples, which provides a strong basis for these tentative assignments (section on 'Spherical debris').

Hematite (Fe_2O_3) and magnetite (Fe_3O_4) are further phases identified in the XRD pattern, suggesting that the polished metal (Fe alloy) coupons have undergone oxidation. Chang *et al.*[5] in their review of low alloy metal oxidation at high temperatures state that at below 570°C only magnetite (Fe_3O_4) and hematite (Fe_2O_3) will be present as iron oxides, at higher temperatures wstite (FeO) will be formed. Previous work by Higginson *et al.*[6] characterising the phases in low alloy steels at high temperature, was consistent with these findings. Cr_2O_3 was also found to be present, even though the Cr content of the alloy is low. Reasons for this apparent enrichment will be discussed in the section on 'Iron oxidation products'.

In this study, KCl was found to be present in the sample collected under reducing conditions (Fig. 4, S). Pettersson *et al.*[18] showed that KCl deposits on the surface of a 304-type austenitic alloy lead to an increase in breakaway oxidation, particularly around grain boundaries. As greater amounts of KCl are present in the reducing atmosphere it is likely more breakaway oxidation has occurred and therefore upon cooling the scales have become loose. This could also explain the greater variation in composition of the oxides in the scales formed under the reducing atmosphere.

Table 4 XRD phases identified in samples

Symbol	Phase
M	Magnetite (Fe_3O_4)
Q	Quartz (SiO_2)
H	Hematite (Fe_2O_3)
Ca	$CaSO_4$
S	KCl
C	Cr_2O_3
N	NiO
Ni	Ni (metal)

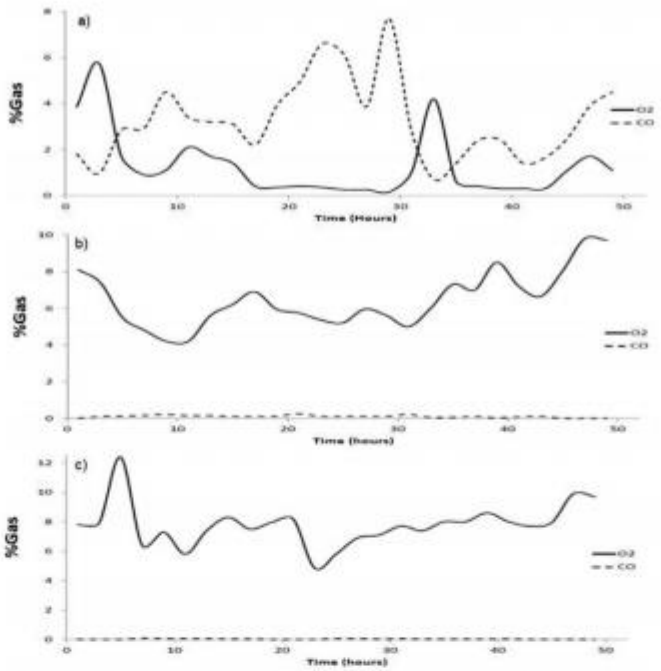

3 Gas profiles of three probes during 50 h combustion run: *a* 450°C under reducing atmosphere; *b* 450°C under oxidising atmosphere and; *c* 425°C under oxidising atmosphere

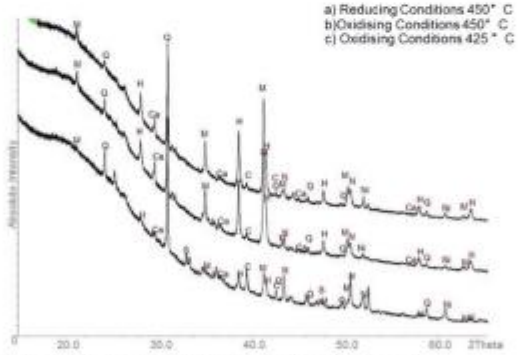

4 X-ray diffraction pattern of loose debris removed from probes (key in Table 4)

The Ni present as both NiO and elemental Ni is likely to come from the anti-seize grease used to allow coupon removal from the probe, rather than an oxidation product of the minimal amount of Ni contained in the alloy.

Deposit microscopy

The phases present in the bulk deposit have been determined by XRD (section on 'XRD analysis'). EDS analysis of the deposits, imaged using an SEM, are in agreement with the XRD analysis. However some phases are present in quantities too small to be detected using XRD. Figure 5 shows an oxide scale in profile; clear deposit and metal oxide regions can be identified. The probable mechanism of formation of these loose oxide scale fragments is breakaway oxidation followed by loss of the scales upon cooling.[19] These oxide scales have been separated from the alloy during the 50 h combustion run and are loose enough to be removed by gentle shaking. The fragments of oxide scales show significant variation in size with a range of 35–200 μm in length and 3–20 μm thickness suggesting variation in the oxidation of the metal. This thickness variation could also be due to deposit-oxide interaction.

A linescan of the scale shows K and S to be closely associated in this deposit region. This is likely to be K_2SO_4 deposited homogenously under the diffusion

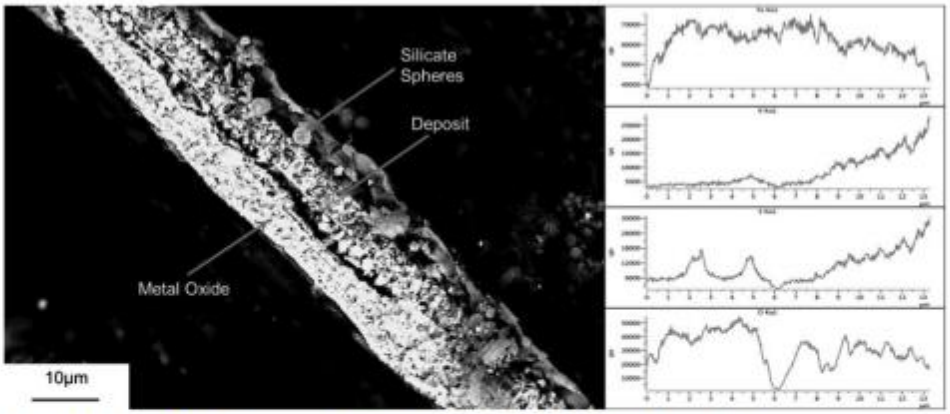

5 SEM micrograph of oxide scale formed under oxidising conditions in profile with linescan data

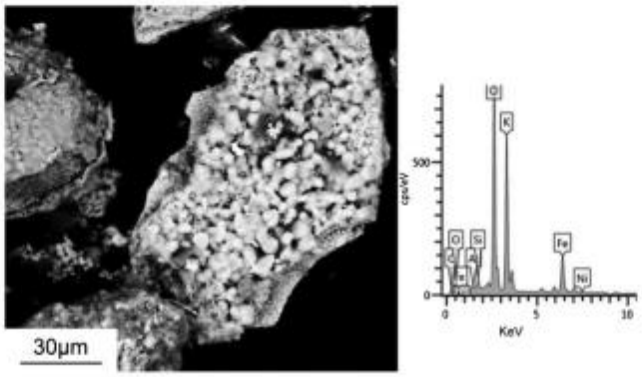

6 SEM micrograph of KCl deposition onto surface of oxide scale under reducing conditions

mechanism presented by Zbogar *et al*,[9] or KCl that has then reacted with SO_2 according to the reaction given in equation (1). In comparison, silicate spheres and refractory oxides will deposit through inertial impaction possibly undergoing further complex reactions post-deposition.[9]

Figure 6 contains an oxide flake with a large amount of KCl deposited on the surface, likely as the result of diffusion. These particles are fairly prominent suggesting a degree of homogeneous nucleation in the flue gas. Large KCl deposits were only imaged on scales found under reducing conditions.

In Fig. 7 EDS analysis of one of the scales formed in the reducing atmosphere shows the presence of different metal ions, these results fit well with the XRD analysis, showing high amounts of Cr present in the scale, unusual for such a low alloyed steel. Uusitalo *et al.*[20] report Cr enrichment in scales formed under reducing conditions on low alloy steels; this research supports these findings. Park *et al.*[21] also found surface enrichment of Cr under electrochemically reducing conditions for a low alloy steel with a 0·5%Cr content. Wood[19] stated that the initial Cr oxidation rate in metals with a low Cr content (0·2%) is more rapid in comparison to Fe and that this can lead to a Cr content maximum at the inner/outer scale interface. This oxidation rate is shown to be faster under reducing conditions than oxidising conditions.[19] An increased Cr content of the scale can apparently be explained by this preferential oxidation. Fe and Cr are present in close association with one another, possibly suggesting the presence of an Fe, Cr spinel phase. It should however be noted that the origin of the oxides may be difficult to ascertain in the present case and could be contaminants from the combustion rig, for example.

Potassium and sulphur are once again shown to closely associate with one another (Fig. 7) suggesting the presence of K_2SO_4, formed either through diffusion deposition or sulphation of KCl (equation (1)). The presence of Ni throughout the sampled region is likely due to the grease used in the lubrication of the probe.

Iron oxidation products

Magnetite

Magnetite and hematite are shown to be present from XRD analysis (section on 'XRD analysis'), on certain oxide fragments octahedral crystals characteristic of magnetite are present (Fig. 8). EDS analyses of these

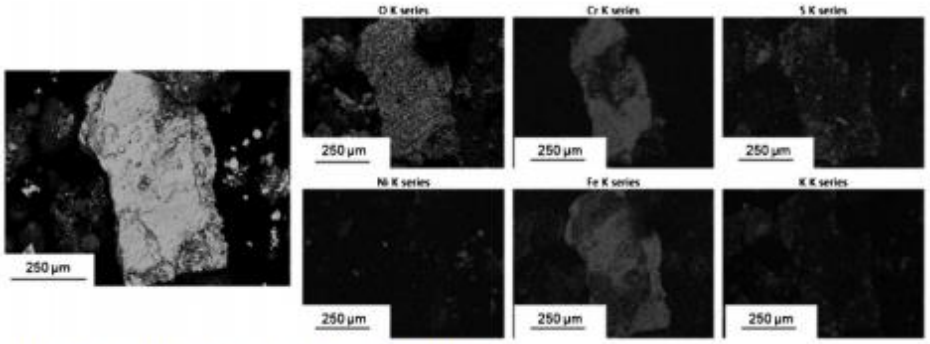

7 EDS analysis of oxide scale from reducing conditions at 450°C

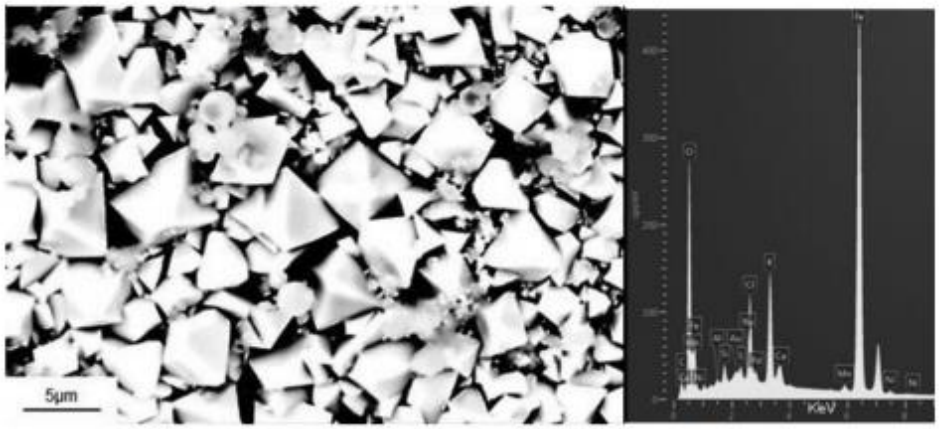

8 Magnetite octahedral crystals visible under both oxidising and reducing conditions, SEM-EDS analysis of octahedral regions

octahedral crystals show that they contain a large amount of Fe and O, alongside minor portions of K, Cl and Ni, confirming the presence of magnetite. The K and Cl, likely to be present as KCl, is thought to have induced $FeCl_2$ transport to the surface of the deposit where upon encountering the O_2 will have formed the octahedral magnetite crystals, through an active oxidation mechanism.[14]

Hematite

Cracks were often observed in the oxide scale either between the deposit and the oxide or two layers of the oxide itself. At higher magnification (Fig. 9) whiskers can be seen growing in these gaps only under oxidising conditions. Previous work by Higginson *et al.*[22] on whisker growth morphology of high temperature oxides showed these whiskers are highly likely to be hematite. Yuan *et al.*[23] found iron whisker growth often occurs on the grain boundaries of hematite/magnetite whereas Higginson *et al.*[22] and Pettersson *et al.*[18] found that whiskers were most likely to form around areas of breakaway oxidation. It is beyond the scope of the current work to speculate on the formation mechanism of the whiskers.

Spherical debris

Alongside oxide scales are other non-metallic particles formed as loosely adhering deposits. Amongst this loose fly ash there are multiple particles with different morphologies. Often during biomass combustion,

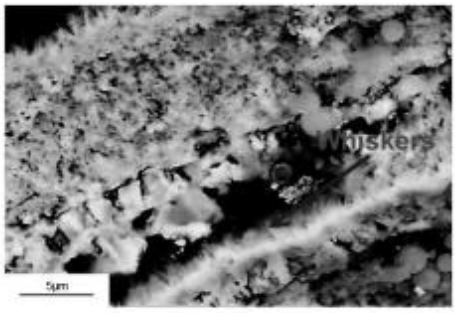

9 Whiskers, thought to be hematite present under oxidation conditions

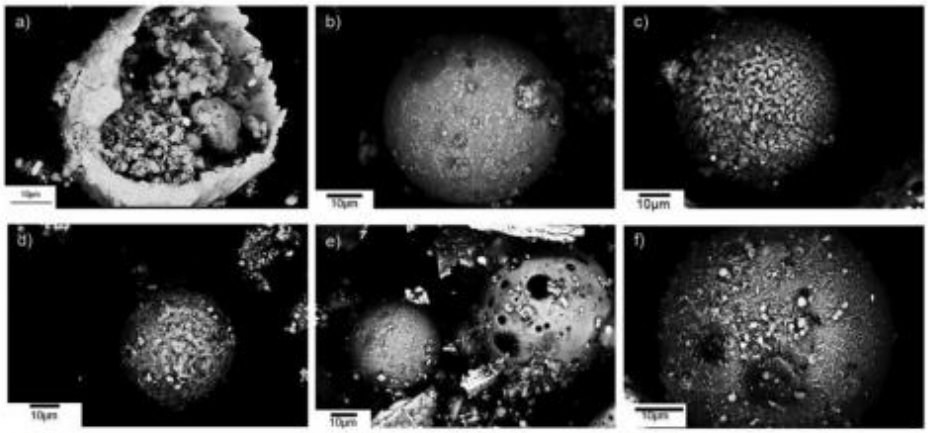

10 Spherical deposits formed under different conditions: *a–c* oxidising conditions 450°C; *d–e* oxidising conditions 425°C and; *f* reducing conditions 450°C

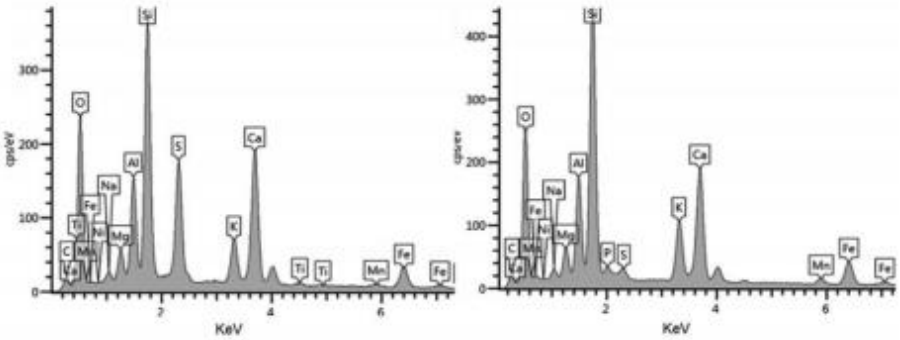

11 EDS spectrum of spheres in Fig. 10*e*

complex silicates form spherical particles either classified as a cenosphere (a microsphere of aluminosilicate glass encapsulating gas[11]) or a plerosphere (a cenosphere encapsulating smaller pre-existing particles[11]).

Figure 10 shows a plerosphere along with cenospheres present in the deposits of all three samples. Raask[24] investigated the formation both cenospheres and plerospheres. Cenosphere formation comes from the expansion of a silicate droplet, often containing a catalytic amount of iron, some carbon must be present in the slag melt in order for gas evolution to occur and so the droplet swells to a hollow sphere. Plerospheres are formed through a similar mechanism; however, mineral particles must be deposited through the droplet in order to be encapsulated in the sphere.[24] This spherical debris is thought to have deposited through the inertial impaction mechanism. However, it is thought that as the spheres have not formed large agglomerates, the reactions necessary to form these particles, took place in the flue gas prior to deposition.

Clear differences in the surfaces of the spherical particles can be seen in Fig. 10 with some containing large pores (Fig. 10*e*) and others showing signs of surface enrichment (Fig. 10*c*). The composition of the spheres formed can often be highly complex. The spectra from EDS (Fig. 11) shows the composition of the two spheres in Fig. 10*e*, illustrating two different compositions of the spherical deposits. Varying amounts of Ca and K are present in both silicate spheres along with Mg and Na suggesting the presence of the complex solid solutions as discussed in section on 'XRD analysis'. S content varies between the spheres although a high content may suggest some surface enrichment commonly undergone by aerosols such as K_2SO_4.[8] Also present in the spheres is Fe, which has been shown to be catalytically important for their formation.[24]

Conclusions

An investigation of fly ash deposition and loose oxide structure from a combustion run of co-fired eucalyptus and Russian coal under different temperatures and atmospheres has been conducted. Metal oxide scales have been observed in the loose deposits from the 15Mo3 probes and are visible under both reducing and oxidising conditions. Variation between the composition

of these scales was found, this is thought to be due to the higher occurrence of KCl under a reducing atmosphere which in turn leads to greater rates of breakaway oxidation around the grain boundaries.

Under oxidising conditions whiskers, which are thought to be hematite, have been observed, further work to establish their composition using FIB-TEM is required. Magnetite crystals with an octahedral morphology are present under all conditions, indicating that in part the 15Mo3 alloy may have undergone active oxidation in order for the oxide scales to become loose.

The variation of spherical debris present indicates complex reactions occurring both pre and post deposition. Further analysis is required to allow identification of these spheres as either plerospheres or cenospheres.

Acknowledgements

The Authors would like to express thanks to the E.On New Build and Technology Centre, the Engineering and Physical Sciences Research Council (EPRSC), Materials Knowledge Transfer Network (Materials KTN) and Loughborough University for funding this work.

References

1. H. Kassman, M. Broström, M. Berg and L.-E. Åmand: 'Measures to reduce chlorine in deposits: Application in a large-scale circulating fluidised bed boiler firing biomass', *Fuel*, 2011, **90**, 1325–1334.
2. H. Furtado and I. May: 'High temperature degradation in power plants and refineries', *Mater. Res.*, 2004, **7**, 103–110.
3. K. Persson, M. Broström, J. Carlsson, A. Nordin and R. Backman: 'High temperature corrosion in a 65 MW waste to energy plant', *Fuel Process. Technol.*, 2007, **88**, 1178–1182.
4. Y.-N. Chang: 'Oxidation behaviors of five low-alloy structural steels at 600°C', *Corros. Sci.*, 1994, **50**, 3–10.
5. Y.-N. Chang and F.-I. Wei: 'Review high temperature oxidation of low alloy steels', *J. Mater. Sci.*, 1989, **24**, 14–22.
6. R. L. Higginson, M. A. E. Jepson and G. D. West: 'Use of EBSD to characterise high temperature oxides formed on low alloy and stainless steels', *Mater. Sci. Technol.*, 2006, **22**, 1325–1332.
7. B.-J. Skrifvars, R. Backman, M. Hupa, K. Salmenoja and E. Vakkilainen: 'Corrosion of superheater steel materials under alkali salt deposits Part 1: The effect of salt deposit composition and temperature', *Corros. Sci.*, 2008, **50**, 1274–1282.
8. S. Van Loo and J. Koppejan: 'The handbook of biomass combustion and co-firing'; 2008, Sterling, VA, Earthscan.
9. A. Zbogar, F. Frandsen, P. A. Jensen and P. Glarborg: 'Shedding of ash deposits', *Prog. Energy Combust. Sci.*, 2009, **35**, 31–56.
10. B. Jenkins, L. T. M. Baxter, Jr and T. Miles: 'Combustion properties of biomass', *Fuel Process. Technol.*, 1998, **54**, 17–46.
11. S. V. Vassilev, D. Baxter, L. K. Andersen and C. G. Vassileva: 'An overview of the composition and application of biomass ash. Part 1. Phase–mineral and chemical composition and classification', *Fuel*, 2013, **105**, 40–76.
12. F. Jappe Frandsen: 'Utilizing biomass and waste for power production—a decade of contributing to the understanding, interpretation and analysis of deposits and corrosion products', *Fuel*, 2005, **84**, 1277–1294.
13. H. Kassman, L. Bäfver, L. Åmand, V. Power and C. Ab: 'Sulphation of gaseous KCl in a biomass fired CFB boiler', *Eur. Combust. Meet.*, 2009, **3**, 2–7.
14. M. Uusitalo, P. M. Vuoristo and T. Mäntylä: 'High temperature corrosion of coatings and boiler steels below chlorine-containing salt deposits', *Corros. Sci.*, 2004, **46**, 1311–1331.
15. H. P. Nielsen, F. J. Frandsen, K. Dam-Johansen and L. L. Baxter: 'The implications of chlorine-associated corrosion on the operation of biomass-fired boilers', *Prog. Energy Combust. Sci.*, 2000, **26**, 283–298.
16. J. Gominho, A. Lourenço, I. Miranda and H. Pereira: 'Chemical and fuel properties of stumps biomass from Eucalyptus globulus plantations', *Ind. Crops Prod.*, 2012, **39**, 12–16.
17. 'StandardTest method for determination of major and minor elements in coal, coke, and solid residues from combustion of coal and coke by inductively coupled plasma — atomic emission', ASTM D6349-09, i, 1–10, 2009.
18. C. Pettersson, J. Pettersson, H. Asteman, J.-E. Svensson and L.-G. Johansson: 'KCl-induced high temperature corrosion of the austenitic Fe–Cr–Ni alloys 304L and Sanicro 28 at 600°C', *Corros. Sci.*, 2006, **48**, 1368–1378.
19. G. C. I. Wood: 'Iron-chromium alloys and stainless steels at high temperatures', *Corros. Sci.*, 1962, **2**, 173–196.
20. M. A. Uusitalo, P. M. J. Vuoristo and T. A. Mäntylä: 'Elevated temperature erosion–corrosion of thermal sprayed coatings in chlorine containing environments', *Wear*, 2002, **252**, 586–594.
21. S. Park, W. Ji and J. Kim: 'Effect of chromium on the corrosion behaviour of low-alloy steels containing copper in FGD environment', *Int. J. Electrochem. Sci.*, 2013, **8**, 7498–7509.
22. R. L. Higginson and G. Green: 'Whisker growth morphology of high temperature oxides grown on 304 stainless steel', *Corros. Sci.*, 2011, **53**, 1690–1693.
23. L. Yuan, Y. Wang, R. Cai, Q. Jiang, J. Wang, B. Li, A. Sharma and G. Zhou: 'The origin of hematite nanowire growth during the thermal oxidation of iron', *Mater. Sci. Eng. B*, 2012, **177B**, 327–336.
24. E. Raask: 'Mineral impurities in coal combustion: behavior, problems, and remedial measures', 484; 1985, London, Taylor & Francis.

CHARACTERISATION, ANALYSIS AND COMPARISON OF MULTIPLE BIOMASS FUELS USED IN CO-FIRING TRIALS.

V.F. Lay[1,2], C.A. Kirk[1], R.L. Higginson[2], S.C. Hogg[2], C. Davis[3]
[1] Department of Chemistry, [2]Department of Materials, [3] E.On Technology (Ratcliffe) Ltd.
[1,2]Loughborough University, Loughborough, Leicestershire, LE11 3TU.
[3]Technology Centre, Ratcliffe-on-Soar, Nottingham, NG11 0EE.

ABSTRACT: The co-firing of biomass and coal is one method proposed for the reduction of CO_2 emissions. This paper compares synthetic laboratory ash of hemp, coal and eucalyptus and their co-ashed blends with deposits formed during the co-combustion of hemp and coal and eucalyptus and coal. Results show that whilst the results are not in complete agreement a trend towards the formation of Ca-silicates, Ca-Mg silicates and K-Al-Silicates at high temperatures is present in both laboratory ashed samples. The morphology of the particles formed through the different methods differs with larger spherical agglomerates present in the deposits.
Keywords: Ashes, Biomass, Co-Firing, Eucalyptus, Hemp,

1 INTRODUCTION

Environmental concerns arising from the frequent and widespread use of fossil fuels for energy generation have led to greater interest in the use of both dedicated biomass firing and biomass/coal co-firing [31]. The combustion of biomass is widely considered to be carbon neutral as the CO_2 absorbed in photosynthesis during plant growth is then released through combustion [54,56]. It is worth noting, that small amounts of greenhouse gases are emitted during fuel transport and processing. Therefore, to ensure that the process is as carbon neutral as possible, it is desirable that biomass is sourced locally [1]. Increases in biomass usage requires a deeper understanding of the fuels used including combustion properties, fuel characteristics (e.g: calorific value, ash composition, heavy metals present) and ash behaviour (formation of corrosion products or high melting point silicates) [235]. This important analysis should be undertaken prior to full application of the fuels [31]. A review of the behavior of a wide range of biomass during combustion has been undertaken [27,42]. Investigations into the composition of ash produced from biomass firing/co-firing have been carried out alongside the possible applications or uses of the ash including fly ash as components in concrete and for use in road surfaces [31].

Phase transformations, alongside chemical interactions during combustion and pyrolysis, have previously been identified as key questions in relation to biomass firing [27]. Multiple studies into biomass combustion and the transformation behavior of the major inorganic elements contained in the ash have been conducted on a variety of fuels [63,65,201,236,237]. Lindberg *et al.* noted that as some systems may have in excess of 20 elements present in the fuels predicting interactions and deposition will not be straight forward [238].

A study into the composition of several species of woody biomass and types of plant tissue of trees (e.g. needles, bark, stem, shoots) concluded that, due to the inhomogeneous nature of the biomass and variations in plant tissue, producing a representative composition of the whole tree is challenging [28]. Further work modelling the ashing characteristics of five types of plant tissue and comparing against laboratory ashed samples, found the theoretical results to be in good agreement with the samples [239]. The elemental composition of biomasses were found to vary between plant species and genus [171]. These studies also showed that the ash composition is likely to vary due to different mineral pathways in the plant itself, as well as sometimes being affected by differing soil characteristics.

Databases such as the BIOBIB database [172] provide useful information on fuels already analysed however, the varying nature of biomasses even between crop and harvest [22,240], may mean that the information cannot be relied upon for 100% accurate information on fuels selected for use in power plants and further analysis may be required. It was found that some entries in the database were missing >20% of values required for peer data comparison (e.g. proximal analysis (C,H,S,N,Cl), ultimate analysis (inorganic ash matrix), calorific value, ash thermal behaviour and heavy metal content) [171].

This paper is to examine the ashing characteristics of three biomasses and one coal as well as two blends (hemp-coal and eucalyptus coal) to examine interactions of phases present in the ash at various temperatures on heating. Data obtained from lab studies are compared to deposits formed during large scale co-firing trials in a $1MW_{th}$ combustion rig.

2 EXPERIMENTAL

Hemp, eucalyptus, Russian coal and two biomass-coal blends, hemp and coal (77:23 by mass) and eucalyptus and coal (88:12 by mass), were ashed in an air atmosphere, in a Carbolite CSF12/13 chamber furnace with a Eurotherm 808 controller. 1g of each sample was ashed in a clean oven dried crucible according to the temperature profile: 150°C (1 hour), 250°C (2 hours), 450°C (1h 30 mins), 575°C (3 hours) followed by cooling in a dessicator, weighing and returning to the furnace at 575°C until a constant weight (±3mg) was obtained. This was carried out in triplicate.

These ashes and ash blends were placed in a Pt crucible in an Elite BRF14/5-2416 Furnace, and heated at 100°C intervals for 1 hour between 600-1100°C. At each temperature, a small portion of each sample was removed and the ash was returned to the furnace.

Fuel analysis was provided by E.On Technology (Ratcliffe) Limited. As received data are presented in **Table I.**

Ash analysis of the bulk fuels was provided by E.On Technology (Ratcliffe) Limited. Elements present were determined by acid dissolution and emission spectroscopy according to ASTM D6349-09. (**Table II**) gives ash analysis.

Table I: Fuel composition, as received provided by E.On Technology (Ratcliffe) Limited

	Hemp	Eucalyptus	Coal
Moisture (%)	14.5	8.2	7.3
Volatile Matter (%)	56.3	76.8	35.8
Fixed Carbon (%)	13.00	14.40	48.20
Ash (%)	16.2	0.6	8.7
CV, kJ/kg	14050	18570	27440
Sulfur (%)	0.09	0.01	0.34
Chlorine (%)	0.21	0.03	0.01
Hydrogen (%)	4.43	5.63	4.48

Table II: Elements present in the ashes of fuels studies as determined by emission spectroscopy, provided by E.On Technology (Ratcliffe) Limited. (CaO as $CaCO_3$ for biomass)

Element (%)	Hemp	Eucalyptus	Coal
SiO_2	44.00	26.50	44.80
Al_2O_3	1.68	7.60	6.21
Fe_2O_3	0.84	5.13	4.50
CaO	17.70	21.80	23.10
MgO	3.89	5.88	2.55
K_2O	11.80	10.25	3.57
Na_2O	0.32	2.52	1.52
TiO_2	0.11	0.33	4.07
BaO	0.02	0.22	0.49
Mn_3O_4	0.17	2.03	0.57
P_2O_5	6.52	2.88	1.13
SO_3	1.44	2.53	3.53

Samples were collected onto ceramic probes (**Figure 1)** in the superheater region of a $1MW_{th}$ test combustion rig. They were taken *in-situ* during combustion runs of the co-firing of hemp-coal (77:23% by mass) and eucalyptus-coal (88:12% by mass). The collection times and temperatures are shown in **Table III**.

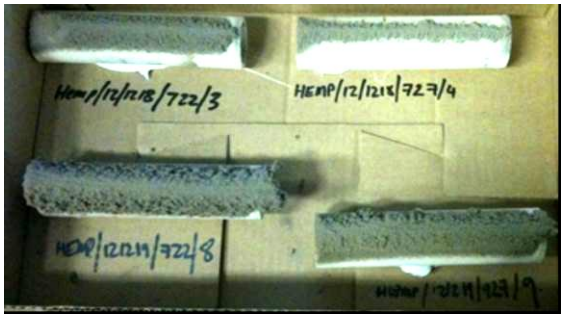

Figure 1: Hemp and coal ash deposits onto ceramic probes

Table III: Sample collection parameters for combustion rig samples (H=Hemp, E=Eucalyptus)

Sample	Duration (min)	Temperature (°C)
H1	38	971
H2	57	Not Recorded
H3	76	1013
H4	58	980
E1	163	978
E2	202	914
E3	184	1012
E4	117	932

Samples were prepared for Scanning Electron Microscopy (SEM)- Energy Dispersive X-Ray Spectroscopy (EDS) by placing the ash materials onto a carbon sticky pad attached to an aluminium stub followed by Au coating for 30s. Analysis was carried out using a Leo-Zeiss 1530VP field emission gun (FEG) with an X-Max 80mm^2 detector (20kV, 60µm aperture, backscatter detector, 8.5mm working distance) or (10kV, 30 µm aperture, SE2 detector (deposit samples)).

Samples were prepared for Powder X-Ray Diffraction (PXRD) by grinding in a pestle and mortar with acetone to a suspension and mounting on a silicon substrate. Powder XRD data were collected using the Bruker D2 PHASER diffractometer (5-60º 2θ, CuKα radiation, 15min, step size 0.0122, 4509 steps, 0.2s time step, 1-Dimentional LYNXEYE detector). Data was analysed using STOE WinXPow software suite and the ICDD 2005 database.

3 RESULTS AND DISCUSSION

Table I illustrates that the fuel compositions differ from one another, with coal and hemp containing a larger portion of ash in comparison to eucalyptus. This, in turn, is likely to have an affect on the slagging and fouling prospensity of a fuel. Larger quantities of ash lead to an increase in the likelihood of phases which can cause the well documented issues [1,53] of high deposition rate and corrosion to occur.

Table II gives the elemental composition of the ash matrices of the three fuels studied. Differences in the quantity of elements present can lead to a significant phase variation between fuels. A comparison of the phases present in laboratory ashed samples to those present in ash samples collected in the combustion rig, may show some differences. This is likely to be due to the reduction/oxidation conditions and atmosphere experienced in each environment differing, which may result in the formation of different phases.

3.1 Laboratory Ashed Samples

3.1.1 X-Ray Diffraction

PXRD data are presented in **Figures 2-4**, representing analysis of samples at 600°C, 1000°C and 1100°C . These temperatures and data sets were selected as they highlight clear differences in the phases present at different temperatures on heating. The PXRD patterns shown in **Figure 2**, show that the major component of the ash at 600°C is quartz (SiO_2). This is unsurprising due to the large percentage of Si present in each of the fuels (**Table I**). At lower temperatures SiO_2 remains largely unreacted. The role of silicates in plants is known to be largely a protection mechanism from stress [241]; it is commonly taken up as sililic acid ($Si(OH)_4$) before transport to other regions of the plant.

At lower temperatures carbonates (calcite ($CaCO_3$), fairchildite ($K_2Ca(CO_3)_2$) and dolomite ($CaMg(CO_3)_2$)) are present. The origin of calcite in the biomass fuels is thought to be via the decomposition of calcium oxalate, known to be present in the fuels [159,242]. The decomposition occurs in two steps:

$CaC_2O_4.H_2O \rightarrow CaC_2O_4 + H_2O$ 170-200°C
(Equation 1) [27]

$CaC_2O_4 \rightarrow CaCO_3 + CO_2$ 300-600°C
(Equation 2) [27]

Calcite often then undergoes a decomposition to lime (CaO) according to the reaction:

$CaCO_3 \rightarrow CaO + CO_2$ 840°C
(**Equation 3**)

Dolomite decomposition follows the path shown in **Equation 4**[162]**.**

$CaMg(CO_3)_2 \rightarrow CaCO_3 + MgO + CO_2$ 500-900°C
(Equation 4)[27]

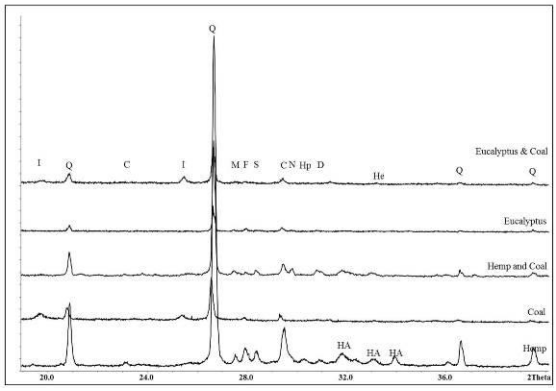

Figure 2: PXRD data of laboratory ashed samples at 600°C. A selected range (20-40°2θ) is presented for clarity. Q (Quartz, SiO_2), M (Microcline, $KAlSi_3O_8$), F (Fairchildite, K_2CaCO_3), S (Sylvite, KCl), C (Calcite, $CaCO_3$), N (Nepheline, $NaAlSiO_4$), Hp (Halite Potassian ($K_{0.4}Na_{0.6}Cl$), D (Dolomite, $CaMg(CO_3)_2$), I (Illite, $K(Al_4Si_2O_9(OH)_3)$, HA (hydroxyapatite ($Ca_{9.04}(PO_4)_6(OH)_{1.68}$), He (Hematite, Fe_2O_3). The highest intensity reflection of Periclase (MgO) is observed at 42.9°2θ, outside the range presented. **Tables V-IX** in the appendix list the full phases present in each fuel at each temperature.

The presence of lime was only observed in the sample set for hemp suggesting that upon formation it promptly reacts, most likely to form Ca-silicates.

Above 900°C silicates begin to form (**Figures 3 & 4**). Due to the differing original compositions of the fuels there are a variety of silicates formed for each fuel. All three fuels are high in Ca and therefore the presence of Ca-silicates through the pathways presented in equations 5-7 is likely.

$CaCO_3 + SiO_2 \rightarrow CaSiO_3$ (wollastonite) $+CO_2 + 2CO_2$ (**Equation 5)**[162]

$CaMg(CO_3)_2 + SiO_2 \rightarrow CaMgSi_2O_6$ (diopside) $+ 2CO_2$ (**Equation 6)**[162]

$KAl_2(Si_3Al)O_{10}(OH)_2$ (illite) $+ 2\,CaCO_3 + 4SiO_2 \rightarrow 2KAlSi_3O_8$ (leucite) $+ 2Ca_2Al_2SiO_8$ (anorthite) $+ 2CO_2 + H_2O$
(Equation 7)[243]

The formation of the Ca-silicates alongside CaMg-silicates highlights the potential for interaction between the elements and phases present in biomass and coal. For instance, eucalyptus ashed without coal was found to have more prominent peaks associated with akermanite ($Ca_2MgSi_2O_7$) in comparison to the diffraction signature of the more Mg-rich phase, diopside ($CaMgSi_2O_6$), whereas the eucalyptus-coal blend had a more prominent signature of the diopside phases. This suggests that Ca reacted preferentially over Mg to drive formation as shown by Trindade *et al.*, who found that $CaCO_3$ is consumed more rapidly than MgO in the formation of Ca-Mg silicates [162]. Therefore an increase in MgO content of the ash, derived from the dolomite present in the coal during co-ashing, may drive the reactions further towards diopside rather than akermanite.

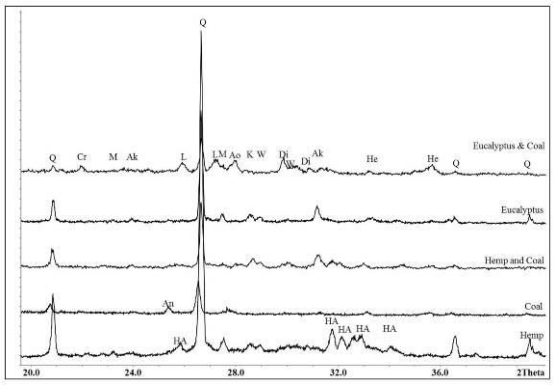

Figure 3: Laboratory ashed samples at 1000°C. A selected range (20-40°2θ) is presented for clarity. Q (Quartz, SiO_2), M (Microcline, $KAlSi_3O_8$), HA (hydroxyapatite ($Ca_{9.04}(PO_4)_6(OH)_{1.68}$), He (Hematite, Fe_2O_3), Di (Diopside, $CaMgSi_2O_6$), K (Kalsilite, $KAlSiO_4$), W (Wollastonite, $CaSiO_3$), Ak (Akermanite, $Ca_2MgSi_2O_7$), L (Leucite, $KAlSi_2O_6$), Ao (Anorthite ($CaAl_2Si_2O_8$), An (Anhydrite ($CaSO_4$)), Cr (Cristobalite, SiO_2). The highest intensity reflection of Periclase (MgO) is observed at 42.9°2θ and Mullite ($Al_{2.35}Si_{0.64}O_{4.82}$), main peak at 16.5°2θ outside the range presented.

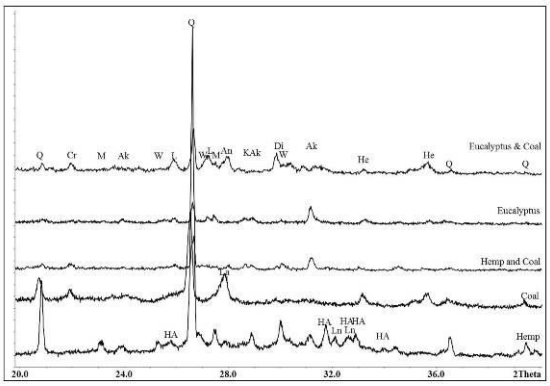

Figure 4: : Laboratory ashed samples at 1100°C. A selected range (20-40°2θ) is presented for clarity. Q (Quartz, SiO_2), M (Microcline, $KAlSi_3O_8$), HA (hydroxyapatite $Ca_{9.04}(PO_4)_6(OH)_{1.68}$), He (Hematite, Fe_2O_3), Di (Diopside, $CaMgSi_2O_6$), K (Kalsilite, $KAlSiO_4$), W (Wollastonite, $CaSiO_3$), Ak (Akermanite, $Ca_2MgSi_2O_7$), L (Leucite, $KAlSi_2O_6$), Ao (Anorthite ($CaAl_2Si_2O_8$), An (Anhydrite $CaSO_4$), Cr (Crisobalite, SiO_2),Ln (Larnite, Ca_2SiO_4). The highest intensity reflection of Periclase (MgO) is observed at 42.923 2θ and Mullite ($Al_{2.35}Si_{0.64}O_{4.82}$), main peak at 16.529 2θ outside the range presented.

Hemp ashed with coal has a greater variety of silicates present in comparison to the ashing of hemp alone (**Tables V & VII**). The lower Fe content of the hemp-coal mixture, in comparison to eucalyptus and coal, for instance may drive the formation of the feldspar anorthite ($CaAl_2Si_2O_8$). Sorenson *et al*. investigated the affects of Fe on the formation of aluminosilicate phases. They concluded that a lower iron content was more likely to yield anorthite rather than diopside, as this mineral was found to crystallise alongside augite ((Ca,Na)(Mg,Fe,Al,Ti)[(Si,Al)$_2O_6$]) in the presence of Fe [188].

Kang *et al*. classified the affects of Al_2O_3 on the diopside/anorthite system and found that below 8.6wt% Al_2O_3 favoured the formation of diopside over anorthite, Above 15.9wt% Al_2O_3 anorthite was shown to be the dominant phase [208]. The low wt% of Al_2O_3 present in the mixtures suggests a preference towards the formation of diopside. Hemp and coal has a lower Fe content than eucalyptus-coal, favouring anorthite. Increased Al from coal ash in the hemp-coal blend, potentially explains the presence of anorthite in the hemp co-ash where there is none in the hemp ash.

Kalsilite ($KAlSiO_4$) is often present in the ash samples (**Tables V-IX**). Vassilev *et al*., in their comprehensive study of biomass ash transformations state that the formation temperature of kalsilite is between 900-1100°C [27]. This corresponds well with experimental data, however it has been identified in PXRD patterns collected on samples heated below 900°C. The complex nature of the matrix may be a contributing factor in its early formation. Also present in the ash is leucite ($KAlSi_2O_6$), which may have formed from kalsilite. Previous work by Zhang *et al*. has shown kalsilite to be a precursor to leucite formation[183]. Equation 7 shows a pathway for leucite formation through a reaction with illite. Due to the presence of illite in the coal ash it is likely this is mechanism of the leucite formation at lower temperature in the eucalyptus and coal co-ash.

Hematite (Fe_2O_3) is present in the ashes of coal, eucalyptus, coal & eucalyptus and hemp & coal, which is correlated by the iron contents of the fuels (**Table II**).The Fe_2O_3 shown to be present in the hemp & coal ash is highly likely come from the coal. Vassilev *et al.* [27] state that organically bound iron in biomass fuels oxidises to hematite between 200-700°C, this may explain the presence of Fe_2O_3 in the eucalyptus ash, as the eucalyptus fuel was shown to have a high amount of Fe (**Table II**).

Sylvite (KCl) was found to be present in the hemp samples at low temperature. The eucalyptus and coal fuels have low Cl content (**Table I**) and therefore no KCl in the ashes of these fuels was detected by PXRD.

Hydroxyapatite is present in both the hemp ash and the hemp and coal ash; hemp has a relatively high level of P_2O_5 in the ash matrix (**Table II**). The hydroxyapatite could be either extraneous, from the soil or formed as a secondary phase during ashing [15,241]. Boström *et al.* [201] report that the formation of Ca-phosphate phases will occur prior to an Ca/Si interaction.

The origin of the feldspar phase microcline is thought to originate from soil contamination during harvest and processing [201].

3.1.2 Hemp Microscopy Analysis

Figure 5 shows calcium oxalate/carbonate crystals present in the hemp fuel pre-ashing. Exact information on the composition is hard to ascertain due to the high carbonaceous nature of the fuel. In plant material, it is likely the carbonate phase present is CaC_2O_4 and therefore the presence of $CaCO_3$ through the decomposition of oxalate is likely (**Equation 2**).

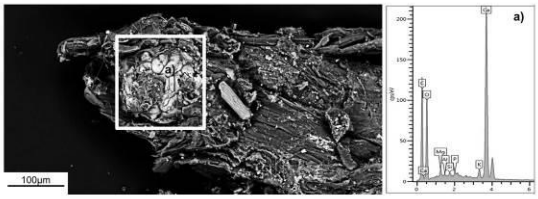

Figure 5: SEM electromicrogaph and EDS analysis of $CaC_2O_4/CaCO_3$ crystals (labelled a) present in hemp fuel.

Figure 6a shows interesting thorn-like structures on the surface of the hemp fuel. Whilst the original texture of the hemp fuel is lost during heating, largely due to its organic composition, these structures remain clearly intact through the heating process. EDS analysis of these structures (**Figure 7**) shows the major components are Ca,K,Mg,Si, P and O, suggesting they comprise of both silicates and hydroxyapatite, this would account for the stability at high temperatures.

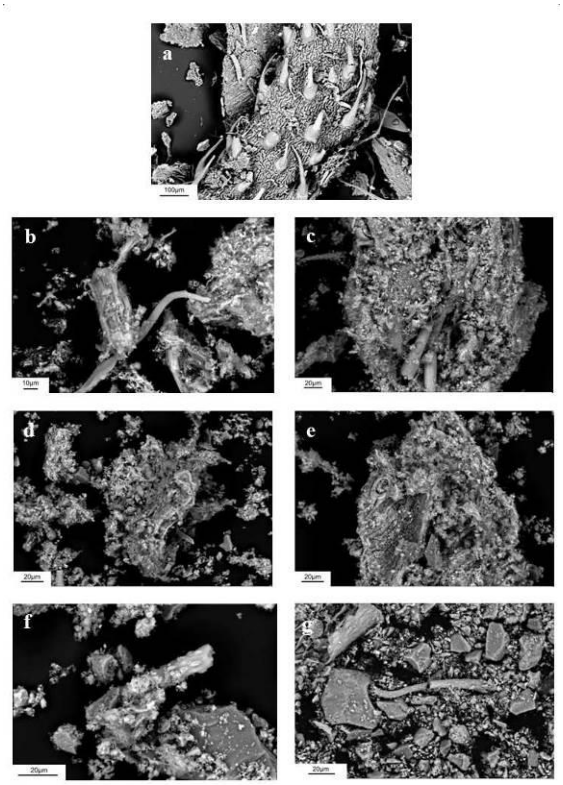

Figure 6: SEM electromicrographs of:- a) hemp fuel b) hemp ash after 1h 600°C
c) hemp ash after 1h 700°C d) hemp ash after 1h 800°C e) hemp ash after 1h 900°C f) hemp ash after 1h 1000°C g) hemp ash after 1h 1100°C

As the ashing temperature increased a higher number of glass-like particles are present. This suggests the melting, reaction and agglomeration of certain components of the fuels. EDS mapping (**Figure 8**) shows that these glassy particles largely comprise of Ca-Mg silicates alongside K-Al silicates. Ca and P also remain closely associated. This would confirm the presence of hydroxyapatite, which is thermally stable at 1100°C.

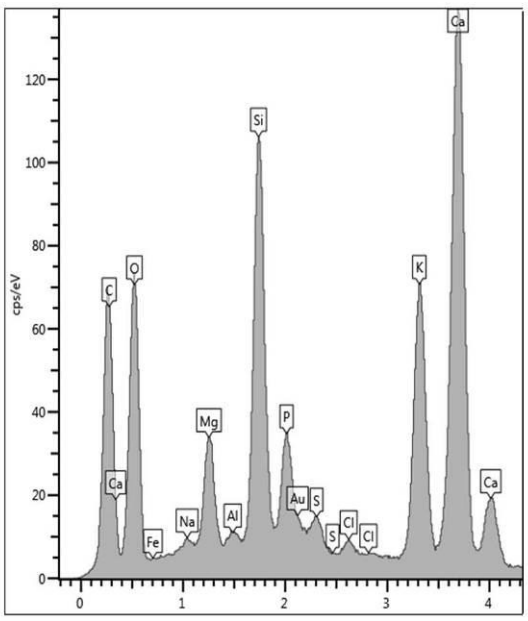

Figure 7: EDS analysis of a thorn-like structure from hemp ash sample at 800°C

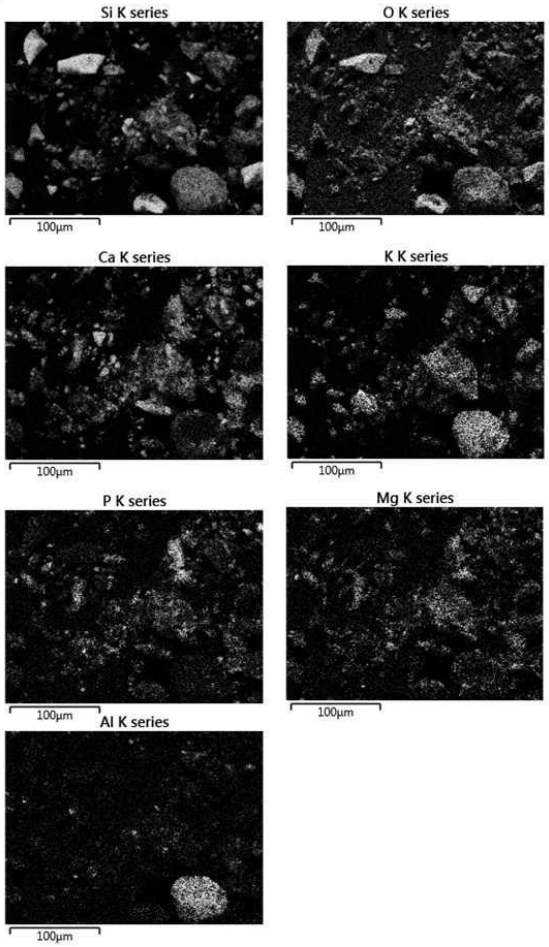

Figure 8: SEM electromicrographs EDS maps of hemp ash at 1100°C

3.1.3 Eucalyptus Microscopy Analysis

An SEM electromicrograph of the eucalyptus fuel (**Figure 9a**) shows a large degree of texture on the fuel surface. This is lost during the ashing process indicating it is cellulose, hemicellulose and lignin that form this structure. After removal of the organic material distinct crystals are observed in the fuels (**Figures 9b-9g**).

EDS analysis shows distinct K,Al,Si,O crystals (**Figure 9b**) at 600°C, thought to be microcline ($KAlSi_3O_8$) as this is the phase containing those elements present at this temperature from XRD (**Table IX**).

Present at 800°C is an anhydrite ($CaSO_4$) crystal probably originating from coal via dehydration of gypsum ($CaSO_4.2H_2O$); this indicates little reaction between certain components of eucalyptus and coal ash until higher temperatures are reached.

The Fe crystals present in **Figure 9e** are thought to originate from fuel processing.

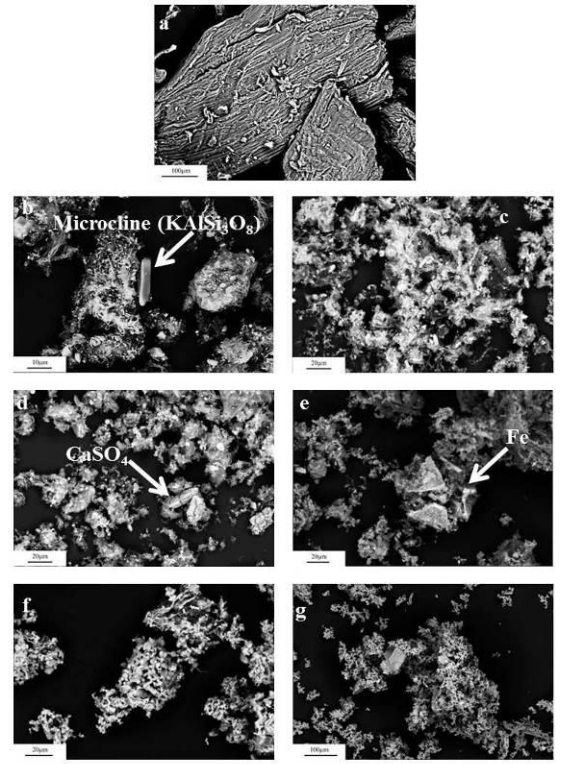

Figure 9: SEM electromicrographs of a) Eucalyptus fuel b) Eucalyptus ash after 1h 600°C c) Eucalyptus ash after 1h 700°C d) Eucalyptus ash after 1h 800°C e) Eucalyptus ash after 1h 900°C
f) Eucalyptus ash after 1h 1000°C g) Eucalyptus ash after 1h 1100°C

3.2 COMBUSTION RIG SAMPLES

To further this investigation, comparison of the data collected on samples from lab-based studies to those collected during combustion rig runs, will now be made. This part of the study focuses on comparisons between the hemp & coal and eucalyptus & coal blends.

3.2.1 P-XRD Analysis

3.2.2 Hemp and Coal Co-Fire

PXRD analysis of the hemp ash samples shows compositional differences between H1-H4 (**Table IV, Figure 10**). The phases found to be present in H2 deviate most when compared to the other samples (H1, H3, H4). Dolomite was shown to be present, with diopside being

the most significant CaMg-silicate phase. In the other samples however, the Ca-Mg silicate akermanite was found to be present. It is also worth noting that the temperature for H2 is unknown and therefore accurate interpretation of the phases present is not fully possible. The presence of dolomite alongside diopside in H2 suggests that there was not a full reaction of dolomite into Ca-Mg silicates and therefore it may have formed from reaction of CaO and MgO with atmospheric CO_2. Vassilev *et al.* show the formation of secondary carbonates between 200-900°C [31].

Variations between samples may also be attributed to temperature differences between samples (971-1013°C) and also reduction/oxidation conditions at the time of sampling [68]. The lack of KCl present in the deposits is due to the temperatures of the ceramic probes; KCl usually deposits through a diffusion/thermophoresis mechanism [46] on to a cool surface. As the temperatures of the ceramic probes used for deposition were at approximately the same temperature as the flue gas it is unlikely that KCl would be present in the samples.

A comparison of the laboratory ashed samples to the combustion rig samples shows many similarities in the phases found to be present. The presence of hydroxyapatite in both sample sets do not indicate whether it is formed during the ashing process or if it is present in the plant itself, possibly in the thorn-like structures. Microcline is only present in some of the rig samples, this suggests that it is extraneous in origin i.e: collected during harvesting from the soil. Extraneous minerals behave differently to those found in the biomass, for instance they may reach lower surface temperatures during combustion [41], or, due to their larger crystallite size (as they will not volatilize in the flame) they may also fail to be carried in the flue gas and drop into the ash hopper, explaining its absence in the rig samples.

The different silicates present in each set of samples can be attributed to the non-equilibrium state of the combustion rig and therefore, whilst the laboratory ashed samples provide some prediction of phases likely to form, in the temperatures of the rig there are some deviations in those found in the rig samples due to the different conditions.

3.2.3 Eucalyptus and Coal Co-Fire P-XRD

Comparison of the PXRD data collected for eucalyptus and coal (**Table V, Figure 11)**to that of the hemp and coal co-fire (**Table IV, Figure 10**) shows the eucalyptus and coal blend deposits to be much more uniform in composition throughout the combustion run. The lower ash content of the eucalyptus in comparison to coal (0.6 and 16.2% respectively) suggests that as there is less variation in the phases capable of forming the ash.
The similarities in phases formed in the eucalyptus co-fire (sample E1-E4) also suggest much more uniform oxidation/reduction conditions. However it should be noted that the sample collection time for eucalyptus was two-three times longer than the hemp samples (**Table III**) suggesting that residence time in the combustion environment plays a key role in reaching conditions where phases become more uniform and stable

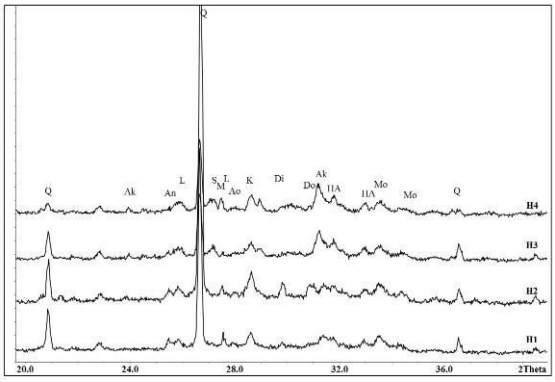

Figure 10: XRD Pattern for combustion rig samples for hemp and coal co-fire. A selected range (20-40°2θ) presented for clarity. Q (Quartz, SiO_2), M (Microcline, $KAlSi_3O_8$), Di (Diopside, $CaMgSi_2O_6$), K (Kalsilite, $KAlSiO_4$), S (Sanidine, $KAlSi_3O_8$), Ak (Akermanite, $Ca_2MgSi_2O_7$), L (Leucite, $KAlSi_2O_6$), HA (hydroxyapatite $Ca_{9.04}(PO_4)_6(OH)_{1.68}$), Mo (monticellite, $CaMgSiO_4$), Ao (Anorthite $CaAl_2Si_2O_8$), An (Anhydrite $CaSO_4$), Do (Dolomite $CaMg(CO_3)_2$) The highest intensity reflection of Periclase (MgO) is observed at 42.923 2θ and Mullite ($Al_{2.35}Si_{0.64}O_{4.82}$), main peak at 16.529 2θ outside the range presented.

Table IV: Phases identified in samples H1-H4 from hemp and coal co-fired combustion run

	H1	**H2**	**H3**	**H4**
Quartz (SiO_2)	•	•	•	•
Akermanite ($Ca_2MgSi_2O_7$)	•		•	•
Diopside ($CaMgSi_2O_6$)	•	•		•
Hematite (Fe_2O_3)			•	•
Anhydrite ($CaSO_4$)	•	•	•	
Leucite ($KAlSi_2O_6$)	•			•
Dolomite ($CaMg(CO_3)_2$)	•	•		
Hydroxylapatite ($Ca_{9.04}(PO_4)_6(OH)_{1.68}$)	•	•	•	•
Forsterite (Mg_2SiO_4)			•	
Monticellite ($CaMgSiO_4$)	•	•	•	•
Kalsilite ($KAlSiO_4$)	•	•	•	
Albite ($NaAlSi_3O_8$)	•			
Periclase (MgO)	•	•	•	•
Microcline ($KAlSi_3O_8$)		•		•
Gehlenite ($Ca_2Al_2SiO_7$)		•		
Wollastonite ($CaSiO_3$)			•	•
Sanidine ($KAlSi_3O_8$)			•	•
Mullite ($Al_{2.35}Si_{0.64}O_{4.82}$)			•	•

. Alongside Ca-Mg-silicates, Mg-silicates are also present. As has been previously stated, $CaCO_3$ preferentially reacts with SiO_2 during dolomite decomposition favouring diopside and akermanite formation, the presence of forsterite (Mg_2SiO_4) indicates that a longer residence time may lead to a greater number of chemical reactions in the ash.

Table V: Phases identified in samples E1-E4 from a eucalyptus and coal co-fired combustion run

	E1	E2	E3	E4
Quartz (SiO_2)	•	•	•	•
Akermanite ($Ca_2MgSi_2O_7$)	•	•	•	•
Diopside ($CaMgSi_2O_6$)	•	•	•	•
Hematite(Fe_2O_3)	•	•	•	•
Anhydrite ($CaSO_4$)	•	•	•	•
Leucite ($KAlSi_2O_6$)	•	•	•	•
Dolomite ($CaMg(CO_3)_2$)	•	•	•	•
Aluminium Oxide (Al_2O_3)	•	•	•	•
Forsterite (Mg_2SiO_4)	•	•	•	•
Anorthite ($CaAl_2Si_2O_8$)	•	•	•	•
Rutile (TiO_2)	•	•	•	•
Albite ($NaAlSi_3O_8$)	•	•	•	•

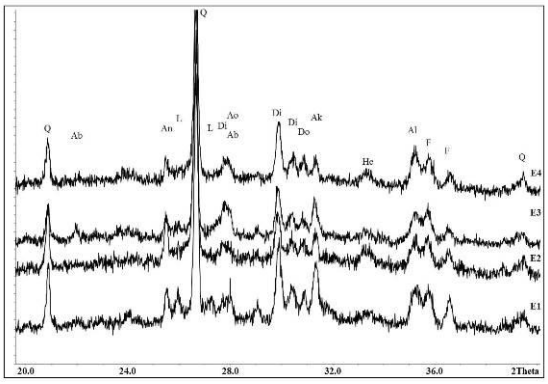

Figure 11: XRD Pattern for combustion rig samples for eucalyptus and coal co-fire. Region 20-40° is presented for clarity. Q (Quartz, SiO_2), Ab (Albite, $NaAlSi_3O_8$), Di (Diopside, $CaMgSi_2O_6$), Ak (Akermanite, $Ca_2MgSi_2O_7$), L (Leucite, $KAlSi_2O_6$), Ao (Anorthite ($CaAl_2Si_2O_8$), An (Anhydrite ($CaSO_4$)) He (Hematite, Fe_2O_3), F (Forsterite, Mg_2SiO_4) Al (aluminium oxide, Al_2O_3)

The lack of kalsilite, but presence of leucite, once again suggests that longer exposure to a high temperature environment has an affect on sample composition. **Equation 7** gives a mechanism of formation for both leucite and anorthite, with the presence of both illite and calcite in the fuel. Future work ashing the eucalyptus and coal under laboratory conditions for longer time periods would be useful for predicting the ash compounds in the combustion rig.

3.2.4 Microscopy of the Co-Fired Rig Samples

Micrographs of the co-fired samples show a distinct spherical morphology for the vast majority of particles in the deposits. The mechanism of deposition for these fly ash particles is inertial impaction, which occurs when large particles (>10µm) have too much mass/inertia to deviate from the gas flow and therefore hit the surface of the tube/deposit[46].

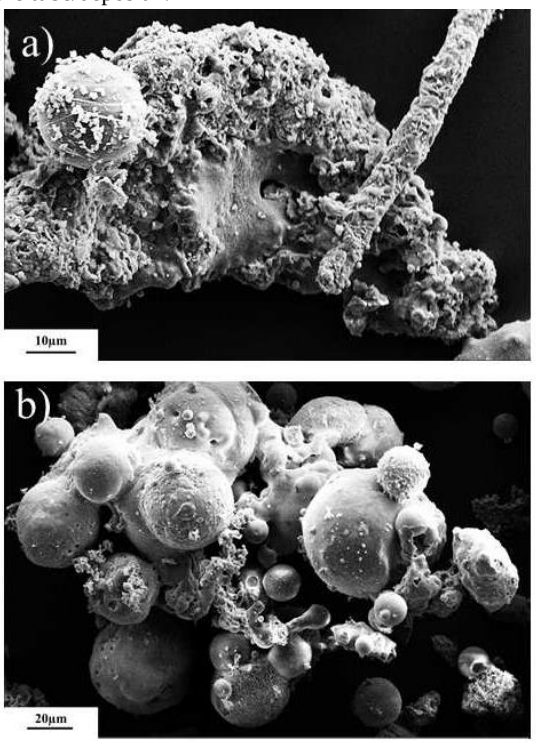

Figure 12: a) SEM electromicrograph of hemp and coal ash deposits removed from a ceramic probe showing particle agglomeration and surface deposition, sample H2. B) SEM electromicrograph of eucalyptus and coal ash deposits removed from a ceramic probe showing a large amount of spherical particles agglomerated together, sample E1.

These deposits form a characteristic elliptical shape as they form on the same side as the gas flow[48], this elliptical shape is shown in **Figure 1**. Inertial impaction in these deposits is also evidenced by the agglomerated particle morphology. Clear fusion between some of the spheres was observed (**Figure 12b**) suggesting reactions may be occurring at these interfaces.

The thorn-like structures which were present in the SEM analysis of hemp and coal (Section 3.1.2), are still observed in deposits from the hemp and coal. **Figure 13** shows EDS analysis of one of these structures which is similar to the analysis presented in **Figure 7**, suggesting the parameters for ash formation have little affect.

The particle surfaces are not always smooth (**Figure 14**) suggesting formation of phases on the surface of the particles. This often occurs through heterogenous nucleation, where refractory oxides (e.g. SiO_2, MgO, CaO etc. or KCl, K_2SO_4 or K_2CO_3) condense with the same species and often form enriched areas on particles surfaces.

In comparison to the morphology of the laboratory ashed samples the spherical particles seen in the rig deposits are much larger. Raask investigated the formation of cenospheres and plerospheres (aluminosilicate glass

microspheres encapsulating gas and smaller pre-existing particles respectively) during coal combustion[191].

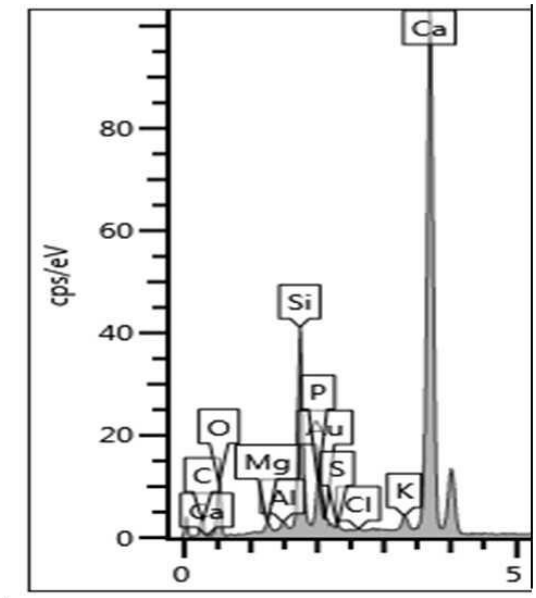

Figure 13: EDS analysis of thorn-like structure from sample H3.

The spheres, which must contain a small amount of Fe and C, form through the expansion of silicate droplets to form a hollow sphere. It is likely that this is a formation mechanism for some of the spheres present in the deposit. These spheres may also form due to the gas conditions present in the combustion rig as one of the main mechanisms in fly ash formation is agglomeration [244].

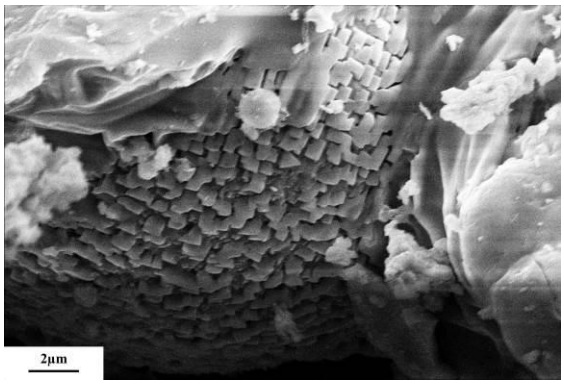

Figure 14: An SEM electromicrograph showing a spherical particle from the hemp and coal co-fire with surface enrichment of cubic crystals.

4 CONCLUSIONS

This paper highlights the benefits from carrying out controlled laboratory ashing studies of fuels to predict fly ash deposition of the same fuels in a combustion rig/power plant. There are many similarities between samples ashed in a controlled environment, at temperatures analogous to those logged during deposition of samples in the combustion rig. The differences between laboratory ashed and combustion rig fired samples indicate that the amount of time a deposit spends in the high temperature environment can have a significant affect on the phases formed.

At high temperatures the main phases, other than quartz identified as present in deposits, are Ca-silicates and Ca-Mg-silicates. These are likely to have formed through a reaction between calcite, dolomite, periclase and quartz. The formation conditions of the phases present in ash samples are similar to those conditions used during ceramic phase formation.

SEM studies have shown that the morphology of particles/phases formed during laboratory ashing of the fuels differs to the morphology from those formed under combustion rig conditions. The morphology of particles formed in the rig were more spherical with the spheres present from the combustion rig being larger and are likely formed through a cenosphere/plerosphere mechanism. The conditions required for the formation of these spheres is challenging to replicate under laboratory conditions.

We have shown that controlled laboratory studies produce useful data that can allow predictions of the phase composition of ash deposits in the combustion rig to be made. This could be used alongside modelling to provide a relatively quick, cheap and affective method of assessing a fuel prior to large scale combustion tests.

Future work on the samples includes longer ashing of the coal-biomass blends in the laboratory to determine if the phases formed are similar in composition to those exposed to the high-temperature rig environment for periods longer than 60 minutes. Phase quantification of the PXRD data is also underway to investigate how the proportions of phases alter as a function of temperature.

5 REFERENCES

[1] S.V.Vassilev, D. Baxter, L. K. Andersen, C. G. Vassileva, An overview of the composition and application of biomass ash. Part 1. Phase-mineral and chemical composition and classification, Fuel. 105 (2013) 40-76

[2] K. E. Coleman, N. J. Simms, P. J. Kilgallon, J. E. Oakley, Corrosion in biomass combustion systems, Mater. Sci. Forum. 595-598 (2008) 377-386

[3] S. S. Lokare, J. D. Dunaway, D. Moulton, D. Rogers, D. R. Tree, L. L. Baxter, Investigation of ash deposition rates for a suite of biomass fuels and fuel blends, Energy & Fuels, 20 (2006) 1008-1014

[4] S. Van Loo, J. Koppejan, The handbook of biomass combustion and co-firing, 1st Edition, Earthscan, London, 2008

[5] K. Szemmelveisz, I. Szűcs, Á.B. Palotás, L. Winkler, E.G. Eddings, Examination of the combustion conditions of herbaceous biomass, Fuel Process. Technol. 90 (2009) 839–847.

[6] S. V. Vassilev, D. Baxter, C.G. Vassileva, An overview of the behaviour of biomass during combustion: Part I. Phase-mineral transformations of organic and inorganic matter, Fuel. 112 (2013) 391–449.

[7] S. V. Vassilev, D. Baxter, C.G. Vassileva, An overview of the behaviour of biomass during combustion: Part II. Ash fusion and ash formation mechanisms of biomass types, Fuel. 117 (2014) 152–183.

[8] L.L. Baxter, T.R. Miles, B.M. Jenkins, T. Milne, D. Dayton, R.W. Bryers, et al., The behavior of inorganic material in biomass-fired power boilers : field and laboratory experiences, Fuel Process. Technol. 54 (1998) 47–78.

[9] S. Miller, B. Miller, The occurrence of inorganic elements in various biofuels and its affect on ash chemistry and behavior and use in combustion products, Fuel Process. Technol. 88 (2007) 1155–1164.
[10] J. Werther, M. Saenger, E.-U. Hartge, T. Ogada, Z. Siagi, Combustion of agricultural residues, Prog. Energy Combust. Sci. 26 (2000) 1–27.
[11] Y. Zheng, P.A. Jensen, A.D. Jensen, B. Sander, H. Junker, Ash transformation during co-firing coal and straw, Fuel. 86 (2007) 1008–1020
[12] D. Boström, M. Broström, Ash transformation chemistry during combustion of biomass, Energy & Fuels 26 (2011) 85-93.
[13] D. Lindberg, R. Backman, P. Chartrand, M. Hupa, Towards a comprehensive thermodynamic database for ash-forming elements in biomass and waste combustion — Current situation and future developments, Fuel Process. Technol. 105 (2013) 129–141.
[14] J. Werkelin, B.-J. Skrifvars, M. Hupa, Ash-forming elements in four Scandinavian wood species. Part 1: Summer harvest, Biomass and Bioenergy. 29 (2005) 451–466.
[15] J. Werkelin, D. Lindberg, D. Boström, B.-J. Skrifvars, M. Hupa, Ash-forming elements in four Scandinavian wood species part 3: Combustion of five spruce samples, Biomass and Bioenergy. 35 (2011) 725–733.
[16] G. Tao, T. a. Lestander, P. Geladi, S. Xiong, Biomass properties in association with plant species and assortments I: A synthesis based on literature data of energy properties, Renew. Sustain. Energy Rev. 16 (2012) 3481–3506
[17] G. Tao, P. Geladi, T. a. Lestander, S. Xiong, Biomass properties in association with plant species and assortments. II: A synthesis based on literature data for ash elements, Renew. Sustain. Energy Rev. 16 (2012) 3507–3522.
[18] H.H. K. Reisinger, C. Haslinger, M. Herger, BIOBIB - A DATABASE FOR BIOFUELS, (n.d.). http://cdmaster2.vt.tuwien.ac.at/biobib/all.html (accessed May 27, 2013).
[19] S. Xiong, Q.-G. Zhang, D.-Y. Zhang, R. Olsson, Influence of harvest time on fuel characteristics of five potential energy crops in northern China., Bioresour. Technol. 99 (2008) 479–85.
[20] T. Prade, M. Finell, S.-E. Svensson, J.E. Mattsson, Affect of harvest date on combustion related fuel properties of industrial hemp (Cannabis sativa L.), Fuel. 102 (2012) 592–604.
[21] R. Frandsen, M. Montgomery, O. H. Larsen, Field test corrosion experiences when co-firing straw and coal: 10 year status within Elsam, Mater. High. Temp. 24 (2007) 343–349.
[22] J.F. Ma, N. Yamaji, Functions and transport of silicon in plants., Cell. Mol. Life Sci. 65 (2008) 3049–57.
[23] M. Etienne, Time factor in utilization of mineral nutrients by hemp, Plant Physiol. (1936) 731.
[24] P. A. Nakata, Advances in our understanding of calcium oxalate crystal formation and function in plants, Plant Sci. 164 (2003) 901–909
[25] M. Trindade, M. Dias, J. Coroado, F. Rocha, Mineralogical transformations of calcareous rich clays with firing: A comparative study between calcite and dolomite rich clays from Algarve, Portugal, Appl. Clay Sci. 42 (2009) 345–355
[26] G. Cultrone, C. Rodriguez-Navarro, E.Sebastian, O. Cazalla, M. J. De La Torre, Carbonate and silicate phase reactions during ceramic firing, Eur. J. Mineral. 13 (2001) 612-634
[27] P.M. Sørensen, M. Pind, Y.Z. Yue, R.D. Rawlings, A. R. Boccaccini, E.R. Nielsen, Affect of the redox state and concentration of iron on the crystallization behavior of iron-rich aluminosilicate glasses, J. Non. Cryst. Solids. 351 (2005) 1246–1253.
[28] M. Kang, S. Kang, Influence of Al2O3 additions on the crystallization mechanism and properties of diopside/anorthite hybrid glass-ceramics for LED packaging materials, J. Cryst. Growth. 326 (2011) 124–127.
[29] Y. Zhang, B. Li, P. Rao, M. Lü, J. Wu, Seeded Crystallization of Leucite, J. Am. Ceram. Soc. 90 (2007) 1615–1618.
[30] S. V. Vassilev, D. Baxter, L.K. Andersen, C.G. Vassileva, T.J. Morgan, An overview of the organic and inorganic phase composition of biomass, Fuel. 94 (2012) 1–33.
[31] P.F.B. Hansen, K.H. Andersen, K. Wieck-Hansen, Co-firing straw and coal in a 150-MW e utility boiler : in situ measurements, Fuel Process. Technol. 54 (1998) 207–225.
[32] A. Zbogar, F. Frandsen, P.A. Jensen, P. Glarborg, Shedding of ash deposits, Prog. Energy Combust. Sci. 35 (2009) 31–56.
[33] M. Cieplik, L. Fryda, Ash Formation, Slagging and Fouling in Biomass Co-firing in Pulverised-fuel Boilers, in: Solid Biofuels for Energy, 2011: pp. 197–217.
[34] L.A. Hansen, H.P. Nielsen, F.J. Frandsen, Influence of deposit formation on corrosion at a straw-fired boiler, Fuel Process. Technol. 64 (2000) 189–209.
[35] E. Raask, Mineral Impurities in Coal Combustion: Behavior, Problems, and Remedial Measures, Taylor & Francis, 1985.
[36] K.A. Christensen, The formation of submicron particles from the combustion of straw, Technical University of Denmark, 1995.

6 ACKNOWLEDGEMENTS

The authors are grateful to the staff at LMCC for the help given during sample analysis. E.On Technology (Ratcliffe) Limited, for providing samples used in the analysis and funding alongside the EPRSC for the provision of funding.

7 APPENDIX

Due to the inhomogenous nature of the samples certain phases are only present in very small amounts and therefore may not always be observed.

Table V: Phases present in laboratory ashed samples of hemp.

Phase	Temperature (°C)					
	600	700	800	900	1000	1100
Quartz (SiO_2)	•	•	•	•	•	•
Calcite ($CaCO_3$)	•	•				
Sylvite (KCl)	•	•	•	•		
Fairchildite ($K_2Ca(CO_3)_2$)	•	•	•			
Hydroxyapatite ($Ca_{9.04}(PO_4)_6(OH)_{1.68}$)	•	•	•	•	•	•
Microcline ($KAlSi_3O_8$)	•	•	•	•	•	•
Periclase (MgO)	•	•	•	•	•	•
Halite, potassian ($K_{0.4}Na_{0.6}Cl$)	•	•	•			
Dolomite ($CaMg(CO_3)_2$	•	•	•			
Lime CaO)			•			
Wollastonite ($CaSiO_3$)			•		•	•
Diopside ($CaMgSi_2O_6$)			•	•	•	•
Akermanite ($Ca_2MgSi_2O_7$)					•	•
Larnite (Ca_2SiO_4)					•	•
Kalsilite ($KAlSiO_4$)					•	

Table VI: Phases present in laboratory ashed samples of coal.

Phase	Temperature (°C)					
	600	700	800	900	1000	1100
Quartz (SiO_2)	•	•	•	•	•	•
Calcite ($CaCO_3$)	•					
Dolomite ($CaMg(CO_3)_2$	•					
Illite ($K(Al_4Si_2O_9(OH)_3$)	•	•	•	•		
Anhydrite ($CaSO_4$)	•	•	•	•	•	
Cuprite (Cu_2O)		•		•	•	•
Hematite (Fe_2O_3)		•	•	•	•	•
Albite ($NaAlSi_3O_8$)					•	•
Labradorite ($Ca_{0.65}Na_{0.32}(Al_{1.62}Si_{2.38}O_8)$						•
Mullite ($Al_{2.35}Si_{0.64}O_{4.82}$)						•

Table VII: Phases present in laboratory ashed samples of hemp and coal

Phase	Temperature (°C)					
	600	700	800	900	1000	1100
Quartz (SiO_2)	•	•	•	•	•	•
Calcite ($CaCO_3$)	•	•	•			
Sylvite (KCl)	•	•	•			
Fairchildite ($K_2Ca(CO_3)_2$)	•	•	•			
Hydroxyapatite ($Ca_{9.04}(PO_4)_6(OH)_{1.68}$)	•	•	•	•	•	•
Microcline ($KAlSi_3O_8$)	•	•	•	•	•	•
Periclase (MgO)	•	•	•	•	•	•
Hematite (Fe_2O_3)	•	•	•	•	•	•
Dolomite ($CaMg(CO_3)_2$	•	•				
Illite ($K(Al_4Si_2O_9(OH)_3$)	•	•				
Nepheline ($NaAlSiO_4$)	•	•	•			
Wollastonite ($CaSiO_3$)				•	•	•
Diopside ($CaMgSi_2O_6$)				•	•	•
Akermanite ($Ca_2MgSi_2O_7$)				•	•	•
Kalsilite ($KAlSiO_4$)				•	•	•
Anorthite ($CaAl_2Si_2O_8$)					•	•
Larnite (Ca_2SiO_4)					•	
Mullite ($Al_{2.35}Si_{0.64}O_{4.82}$)					•	•

Table VIII: Phases present in laboratory ashed samples of eucalyptus

Phase	Temperature (°C)					
	600	700	800	900	1000	1100
Quartz (SiO_2)	•	•	•	•	•	•
Calcite ($CaCO_3$)	•	•				
Fairchildite ($K_2Ca(CO_3)_2$)	•	•				
Microcline ($KAlSi_3O_8$)	•	•		•	•	•
Sylvite (KCl)	•					
Periclase (MgO)			•	•	•	•
Hematite (Fe_2O_3)	•	•	•	•	•	•
Arcanite (K_2SO_4)	•	•	•			
Cristobalite (SiO_2)						•
Wollastonite ($CaSiO_3$)					•	•
Diopside ($CaMgSi_2O_6$)				•		
Akermanite ($Ca_2MgSi_2O_7$)				•	•	•
Leucite ($KAlSi_2O_6$)						•
Kalsilite ($KAlSiO_4$)		•	•	•	•	•
Mullite ($Al_{2.35}Si_{0.64}O_{4.82}$)						•

Table IX: Phases present in laboratory ashed samples of eucalyptus and coal

Phase	Temperature (°C)					
	600	700	800	900	1000	1100
Quartz (SiO_2)	•	•	•	•	•	•
Calcite ($CaCO_3$)	•		•			
Fairchildite ($K_2Ca(CO_3)_2$)	•	•				
Microcline ($KAlSi_3O_8$)	•	•	•	•	•	•
Illite ($K(Al_4Si_2O_9(OH)_3$)	•	•				
Periclase (MgO)		•	•	•	•	•
Hematite (Fe_2O_3)	•	•	•	•	•	•
Anhydrite ($CaSO_4$)	•	•	•	•		
Arcanite (K_2SO_4)			•			
Cristobalite (SiO_2)					•	•
Wollastonite ($CaSiO_3$)					•	
Diopside ($CaMgSi_2O_6$)					•	•
Anorthite ($CaAl_2Si_2O_8$)				•	•	•
Leucite ($KAlSi_2O_6$)				•	•	•
Kalsilite ($KAlSiO_4$)			•	•	•	•
Mullite ($Al_{2.35}Si_{0.64}O_{4.82}$)					•	•